

# Lessons from Antarctica

Twenty years on, the success of the Montreal Protocol can help inform plans to mitigate climate change.

**T**he revelation in 1985 that chemical emissions had ripped a vast hole in Earth's protective ozone layer sparked an international effort that has become one of the great environmental success stories. The Montreal Protocol, which came into force 20 years ago this year, halted the production of chlorofluorocarbons (CFCs) — the main culprits causing the hole above Antarctica — and set the schedule for phasing out most other ozone-destroying substances.

Today, stratospheric ozone levels are no longer in decline. And, although plenty of ozone-depleting chemicals remain in the atmosphere, there are signs of recovery in ozone levels at the mid-latitudes. The rapid and committed response of the world's nations has probably averted a future in which unfiltered sunlight would have scorched humans, animals and plants alike (see page 792).

Yet the Montreal Protocol is often written off as a model for curbing greenhouse-gas emissions. The international response to the ozone hole was fast — the protocol was ready for signing just two years after the hole was discovered — in part because the threat was immediate, and because chemical alternatives to CFCs had already been developed.

The situation is less clear cut for global warming — it is a slow-moving,

long-term problem for which there is no single alternative to fossil-fuel use. Nonetheless, the Montreal model has much it can offer the fight against climate change. Governments are increasingly waking up to the urgency of the threat of global warming. And there is already an arsenal of alternative-energy technologies, ranging from wind turbines to energy-conserving building design, that could be delivered quite quickly around the world — if there was a political will to make it happen.

The Montreal Protocol's Multilateral Fund offers a particularly good model for such action. Industrialized nations, which have produced the majority of the world's CFCs, have contributed more than US\$2 billion to the fund since it began operation in 1991 to help poorer nations meet their obligations under the treaty. Over time, this system has inspired a level of trust that is sorely lacking in today's global climate negotiations.

Above all, the Montreal Protocol serves as proof that the countries of the world can work together. And if nations, particularly those in the developed world, continue to take inspiration from its success, it could help divided governments find a common path towards tackling climate change. ■

## A change of tone

There is every reason to be optimistic about the Obama administration's attitude towards science.

**T**he feel-good glow that pervaded much of Washington DC after the January inauguration of President Barack Obama has faded fast this summer, as the US capital has descended into partisan gridlock over issues such as health-care reform and financial regulation.

Nevertheless, positive steps are quietly being taken. Last week, for example, White House science adviser John Holdren convened the first meeting of the 21-member President's Council of Advisors on Science and Technology (PCAST, see page 785) — a star-studded assembly of academics and industry researchers.

As with any such meeting in the early days of a new administration, the PCAST gathering was high on enthusiasm and necessarily low on evidence of effectiveness. But Holdren, who brings an extensive background in nonproliferation and energy issues to his post, noted that the council's first report, on the government's response to the H1N1 flu pandemic, is already in the pipeline for public release within a few weeks. And the meeting's lively discussions on topics such as electronic health records and research comparing the effectiveness of medical treatments suggested that members fully expect their advice to be heeded by the White House.

Also last week, Holdren and Peter Orszag, director of the White

House Office of Management and Budget, signed a memorandum to top federal officials outlining the administration's priorities as the agencies begin to prepare their budget requests for fiscal year 2011. The memo emphasized the key part played by science and technology in those priorities — including economic recovery, health care, energy and climate. And it featured the telling phrase, "sound science should inform policy decisions".

That was something not seen too often during the administration of George W. Bush, which regularly sidelined science. Last week, a report from the Bipartisan Policy Center, a think tank in Washington DC established in 2007 by four former Republican and Democratic senators, served as a reminder of how much work remains to be done to integrate science properly into political decision-making. The report makes recommendations that seem like common sense: proposed regulations should set out what science questions need to be answered, for instance, and there should be clearer conflict-of-interest rules for anyone appointed to a scientific advisory committee. Common sense on scientific matters was all too often lacking in Bush's Washington.

Many challenges await Holdren in the coming months and years, including helping to convince Congress whether major investments in science and technology are warranted, and then delivering progress reports that clearly delineate the success or failure of such investments. His White House team is far from complete; two of his office's four associate director positions — for science and for national security — remain empty and should be filled as quickly as possible with qualified nominees. But overall, science advice in the Obama era is off to a good start. ■

# RESEARCH HIGHLIGHTS

## CANCER BIOLOGY

### Suicide by nucleotide

*Cancer Cell* **16**, 103–114 (2009)

A synthetic molecule that mimics double-stranded RNA viruses can trigger melanoma cells to digest and kill themselves.

Melanoma cells often evade the immune system and deactivate cell-death pathways. But María Soengas at the Spanish National Cancer Research Centre in Madrid and her colleagues have found that the cells respond to a viral RNA mimic called polyinosine-polycytidylic acid, an adjuvant that boosts immunity.

When administered alongside the carrier molecule polyethyleneimine, the complex caused melanoma cells — but not normal cells — to digest their organelles and eventually undergo programmed cell death. The process seems to happen without the help of other immune cells: the complex efficiently killed melanoma cells in immunocompromised mice.

## ATMOSPHERIC CHEMISTRY

### Isoprene's fate

*Science* **325**, 730–733 (2009)

Isoprene emitted by trees has long been thought to form aerosols in the atmosphere, but how it does so was unclear.

Fabien Paulot of the California Institute of Technology in Pasadena and his colleagues used chemical ionization mass spectrometry to monitor the photooxidation products resulting from the reaction of isoprene with hydroxyl radicals in an experimental environmental chamber. They found that isoprene initially forms hydroxyhydroperoxides. Surprisingly, further reaction with hydroxyl radicals results in the production of dihydroxyepoxides and reformation of the hydroxyls. These epoxides are readily taken up by acidic aerosols, forming tetraols and polymers.

The researchers estimate that these epoxides account for nearly 100 teragrams of carbon in the atmosphere every year. Further understanding of this secondary aerosol formation should help to improve models of atmospheric chemistry.



G. VOCKEL/STILL PICTURES

### Stray genes

*Proc. Natl Acad. Sci. USA*  
doi:10.1073/pnas.0902129106  
(2009)

Semi-feral village dogs around the world carry complex mixtures of native and introduced genes, and could point to the origins of man's best friend.

Adam Boyko of Cornell

University in Ithaca, New York, and his colleagues analysed mitochondrial and nuclear DNA in 318 dogs from seven areas of Africa and compared them with Puerto Rican street dogs, US mutts and representatives of 126 recognized breeds. They were able to determine the mixture of indigenous and non-native breed-dog genes

in each population.

On the basis of mitochondrial DNA diversity, the authors urge closer scrutiny of recent suggestions that domesticated dogs have East Asian origins. The results also suggest that Pharaoh hounds and Rhodesian Ridgebacks, putatively African breeds, have non-African origins.

## PHYSICS

### Salt mined

*Phys. Rev. Lett.* **103**, 058501 (2009)

Mixing fresh water with salt water releases a substantial amount of energy, but scientists have struggled to find a way to harvest this inexpensively. Dorian Brogioli at the University of Milan-Bicocca, based in Monza, Italy, has proposed a new technique.

He charged two porous carbon electrodes in salty water, then flushed the device with fresh water. Salt ions diffused away from the electrodes, increasing the voltage between them from 300 to 333 millivolts. Discharging the electrodes allowed energy to be extracted. (Apparatus and technique are detailed in graphic, below.)

Brogioli estimates that the device could yield about 1.6 kilojoules per litre of fresh water, which is on a par with the power produced by costly membrane-based methods.

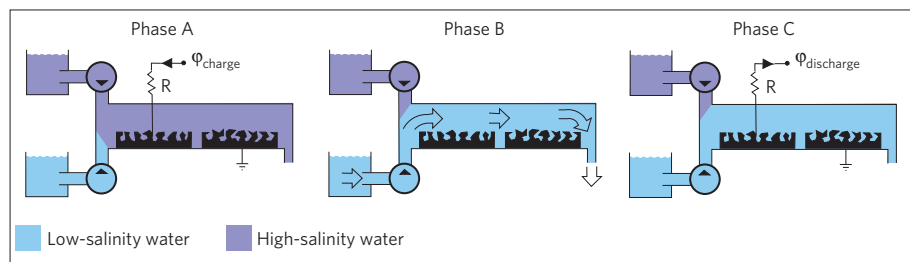
## SPECIATION

### Multiplying effects

*Proc. Natl Acad. Sci. USA* doi:10.1073/pnas.0811575106 (2009)

Duplications of the genome that result in 'polyploid' organisms seem to be responsible for more plant-speciation events than was thought.

Troy Wood of the University of Münster in Germany and his colleagues have used existing genetic data on vascular plants to establish the frequency of speciation events in which an increase in ploidy — the number of copies of the genome — occurred. They find that 15% of angiosperms and almost one-third of fern species are derived from a polyploid event that may have rendered a plant morphologically distinct from and sexually incompatible with its former brethren. This is four times higher than previous estimates and, the authors say, may



D. BROGIOLI/PHYS. REV. LETT.

still be a conservative figure.

Although polyploidy seems to play an important part in creating new species, the team found no evidence that these polyploid plant lines go on to diversify more often than non-polyploids.

## NEUROBIOLOGY

### Have guts, get nerve

*J. Neurosci.* **29**, 9683–9699 (2009)

Even in adulthood, gut neurons can renew themselves, scientists have found.

Mintsai Liu at Columbia University in New York and her colleagues compared neurons in the guts of normal mice with those from mice lacking a receptor for serotonin (5-HT<sub>4</sub>), a neurotransmitter associated with adult nerve generation in other parts of the body.

They found that knocking out this receptor, 5-HT<sub>4</sub>, prevents the proliferation of neurons usually seen in the gut of newborn mice. In normal mice, drugs that activate 5-HT<sub>4</sub> receptors promote neuron survival and stimulate stem cells to make new neurons.

The authors suggest that such drugs might be developed to repair damage to the enteric nervous system as might occur in inflammatory bowel disease.

## EVOLUTION

### Reinventing the egg

*Evolution* doi:10.1111/j.1558-5646.2009.00790.x (2009)

Many vertebrates have abandoned egg-laying for live birth. But despite some suggestive examples, convincing evidence for the evolutionary reversal of this trait has been lacking until now.

Vincent Lynch and Günter Wagner at

Yale University, New Haven, carried out a phylogenetic analysis of 41 species of boa snake using recent DNA data. The most parsimonious explanation of the phylogeny, they conclude, is that the Arabian sand boa, *Eryx jayakari* (pictured below), one of only two species of egg-laying boa, re-evolved this ability some 60 million years after the transition of the group to live birth.

*E. jayakari* also lacks the egg tooth other oviparous snakes use to tear their way out of the egg, additional evidence that egg-laying was lost and reacquired, according to the authors.



## SOIL ECOLOGY

### As different as day and night

*Biogeosciences* **6**, 1361–1370 (2009)

When it comes to warming's effects on plants, day and night are not equal.

Shiqiang Wan and his collaborators at the Chinese Academy of Sciences' Institute of Botany in Beijing set up 36 experimental plots on an Inner Mongolian steppe. They warmed some plots only during the day, others during night-time hours only, and yet

others around the clock.

Plots warmed only at night turned the steppe from a net carbon source to a net carbon sink; the extra warming overnight stimulated respiration rates, boosting the plants' daytime rate of photosynthesis and so their uptake of carbon dioxide. The effects of separate day- or night-time warming did not add up to equal the effects observed at constantly warmed plots.

Many simulations of the effects of global warming on plants look at constant temperature elevations during a 24-hour cycle, but these may not be delivering the right picture.

## MOLECULAR BIOLOGY

### A regulator's regulator

*Genes Dev.* doi:10.1101/gad.541609 (2009)

Some small, non-coding RNAs regulate gene expression by binding to messenger RNA and preventing it from being translated into protein. The regulation of one bacterial gene, however, depends not just on one but on two non-coding RNAs, one of which inhibits the other.

Lionello Bossi and his colleagues at the Centre for Molecular Genetics in Gif-sur-Yvette, France, studied the production of a bacterial protein called ChiP, which is involved in sugar uptake. In the absence of sugar, a small RNA called ChiX attaches to ChiP's messenger RNA and prevents protein synthesis. Add sugar, however, and another RNA is produced that binds ChiX and targets it for destruction, allowing production of the ChiP protein.

The discovery of this new feature of small RNAs in living cells could mean that regulatory RNAs identified computationally by sequence may in fact be targets of regulation.

## JOURNAL CLUB

**Omar Tonsi Eldakar**  
Center for Insect Science,  
University of Arizona

**An evolutionary biologist  
learns how to be remembered:  
cheat someone.**

What makes someone unforgettable? Is it their charm? Their looks? Or is it that they once stiffed you on the bill?

Like many others, I have trouble remembering people's names, even as I am being introduced to them, but certain names remain etched in

my mind forever. Few, for example, will forget Bernard Madoff, the New York financier convicted of defrauding people out of billions of dollars in a giant Ponzi scheme.

Raoul Bell and Axel Buchner at the Institute of Experimental Psychology in Düsseldorf, Germany, have explored this bias in memory (R. Bell and A. Buchner. *Evol. Psychol.* **7**, 317–330; 2009). They reveal that humans have a greater propensity to remember the names of individuals associated with cheating than names associated with trustworthiness or other unrelated behaviours.

Cooperation is immensely beneficial to humans, but with cooperation looms the ever-present risk of exploitation. Researchers have proposed that humans have a specialized brain module dedicated to detecting and remembering cheaters, to help them to steer clear of future interactions with such individuals. It has previously been suggested that the cheater memory module is tied only to facial stimuli. But using the same behaviours associated with facial stimuli in previous studies, Bell and Buchner were able to replicate these

findings using only names, which suggests a more general module for remembering cheaters.

Associating reputations with names is crucial to maintaining social norms through verbal mechanisms such as gossip. Thus memory bias for the names as well as the faces of cheaters could expand the ability of groups of individuals to avoid exploitation.

Madoff probably won't have much luck if he tries to scam people again.

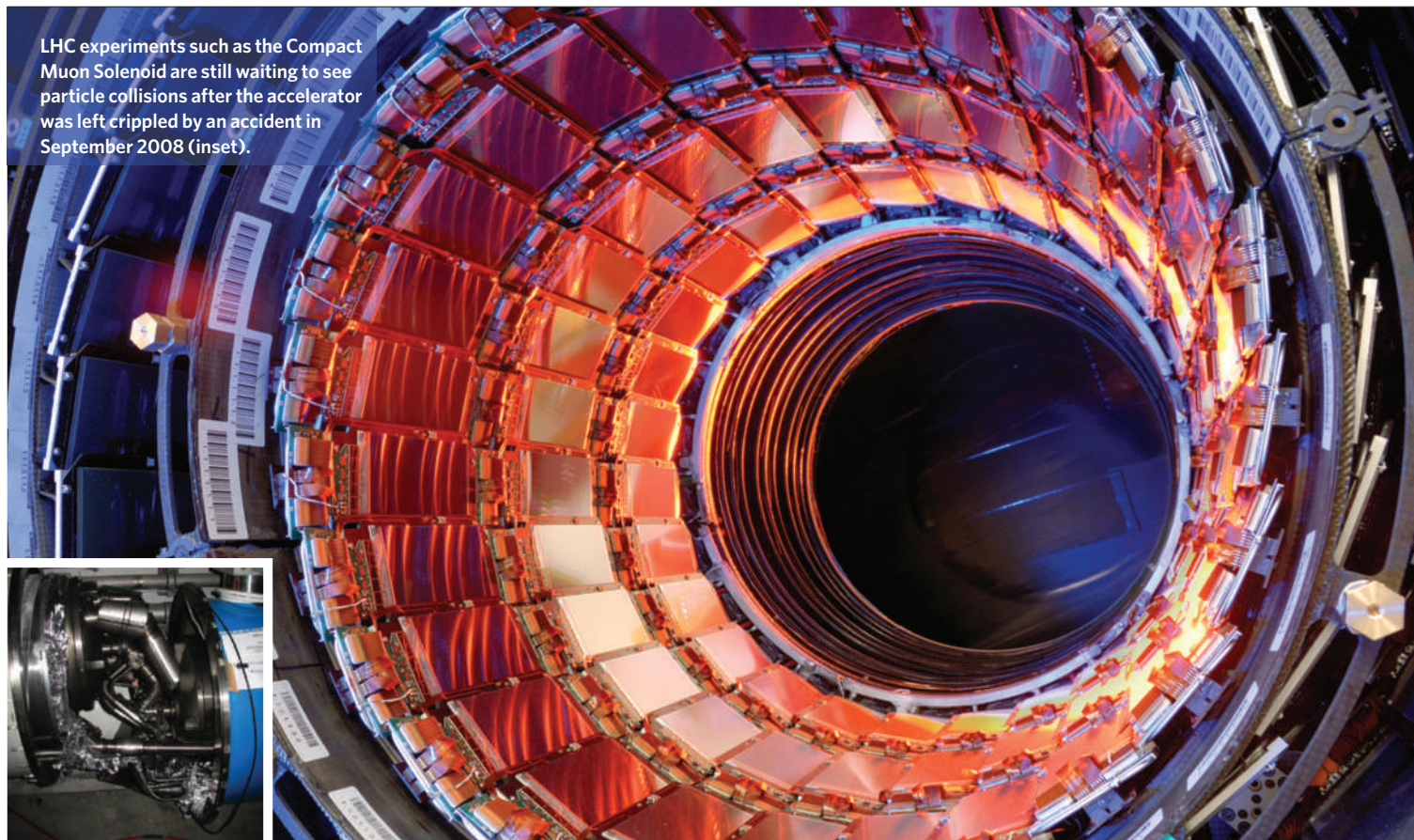
Discuss this paper at <http://blogs.nature.com/nature/journalclub>



## NEWS

M. BRICE, CERN; CERN

LHC experiments such as the Compact Muon Solenoid are still waiting to see particle collisions after the accelerator was left crippled by an accident in September 2008 (inset).



# LHC hopes for collisions by Christmas

But particle physicists will have to scale back the energies of their experiments for years.

The Large Hadron Collider (LHC) should yield its first data by Christmas, smashing protons at energies high enough to begin pushing back the boundaries of particle physics. But the world's largest particle accelerator will only be operating at half the energy that it was originally designed for, and may not reach that peak until 2011 — if at all.

The new schedule was announced by CERN, Europe's particle-physics laboratory near Geneva, Switzerland, on 6 August. The 6.5-billion Swiss franc (US\$6-billion) LHC has been offline for nearly a year, following an accident on 19 September 2008 just nine days after the facility circulated its first particle beams to worldwide fanfare. When a faulty connection burnt out between two of the superconducting magnets used to accelerate particles, 8.7 kilo-amperes of current arced outwards in a massive short-circuit. The current ripped a hole in the pipe carrying liquid helium that surrounds the superconducting wire, spewing out soot and a blast of boiling helium,

which damaged a total of 53 magnets.

During repairs this spring, a new set of problems related to faulty magnet connections was discovered. Although CERN officials believe they now have the problem in hand, they are being cautious in ramping up the beams' energies. In mid-November, protons will be injected into the 27-kilometre-long accelerator ring at low energies to show that two particle beams can circulate well in opposite directions. About four weeks later, the beams will be accelerated to about 3.5 teraelectronvolts (TeV) each, halfway to the LHC's maximum beam energy. Smashing these beams together will create showers of exotic particles, and experimenters will begin gathering the data they need to calibrate their instruments.

"We could have a Christmas present for the experimenters if we're lucky," says Steve Myers, head of CERN's accelerator department. If the initial collisions go well, Myers says, engineers

will ramp up to energies between 4 and 5 TeV per beam sometime in 2010. The beams will then shut down in October or November 2010 for six months in order to make further repairs and install more helium-release safety valves, before attempting to reach higher beam energies in 2011.

Theorists say that LHC collisions with a total energy of 7 TeV should start to reveal previously unseen particles, although it might take a little longer than hoped to accumulate evidence for their existence.

The standard model of particle physics, describing the zoo of subatomic particles and the forces that control them, begins to break down at energies above 1 TeV. Experiments at higher energies could reveal a whole new menagerie of particles predicted by a popular successor to the standard model called supersymmetry. Also within reach are particles from a hypothesized form of dark matter, believed to make

**"It's usually the simple things that cause you problems."**





**HAVE YOUR SAY**  
Comment on any of our  
News stories, online.  
[www.nature.com/news](http://www.nature.com/news)

up a quarter of the mass of the Universe. Finally, one of the most sought-after targets is the Higgs boson, the only particle predicted by the standard model that has not yet been found. The elusive boson is a marker of the Higgs mechanism, which could explain how particles have mass.

### Bad welds

The 2008 accident was caused by a faulty weld in a section of superconducting wire connecting two magnets. The subsequent months of inspections of the rest of the LHC found just four more bad welds in this type of connection — but also revealed a far more widespread problem.

The superconducting wires are surrounded by copper wires, which act as 'safety valves' to carry any sudden surge in current. The copper wire will only come into play if the superconducting wires warm up and lose their ability to conduct electricity without resistance.

Tests over the past few weeks have revealed 80 bad welds between sections of copper wire, but with roughly 10,000 copper-wire welds scattered around the LHC, not all have been inspected. This element of uncertainty means that CERN must increase the operating energy of the machine cautiously to avoid further accidents.

The cost of repairs so far is 40 million Swiss francs. Myers acknowledges there was a quality-control problem with the welds, and that the systems for detecting current surges and mitigating a catastrophic release of helium could have been improved. "It's usually the simple things that cause you problems," he says.

Peter Limon, a physicist at Fermi National Accelerator Laboratory in Batavia, Illinois, says these birth pains are "typical". Limon points out that various problems meant that Fermilab's Tevatron — currently the world's highest-energy collider — took years to reach its maximum collision energy of 1.8 TeV. With a year or two of data collection needed for the LHC to make a definitive Higgs discovery, the Tevatron still has a chance at bagging it first. Tevatron physicists plan to present the latest update on their Higgs hunt on 18 August at the Lepton-Photon conference in Hamburg, Germany.

Gordon Kane, a theorist at the University of Michigan in Ann Arbor, says that the physics community is frustrated by delays at the LHC, but adds that an extra year is not so long to hold on for the Higgs particle, given that its existence was proposed in 1964. "I'm going to be there when it's discovered," says the 72-year-old Kane, "no matter how long it takes." ■

Eric Hand

For more on the LHC, see [www.nature.com/lhc](http://www.nature.com/lhc)

## Science advisers mull priorities

An elite group of 21 US researchers met publicly for the first time last week as the new advisory panel to US President Barack Obama on scientific and technical matters. But despite an enthusiastic inaugural meeting, it will take time to know how effective the President's Council of Advisors on Science and Technology (PCAST) will be.

PCAST has already put together its first report, on the government's H1N1 pandemic strategy. Other topics likely to be high on its agenda include how science can help the economic recovery, and how best to deliver on Obama's ambitious climate and energy research portfolio.

Opening the meeting on 6 August, co-chair John Holdren called the council "a spectacular cast of leaders of our science, technology and innovation communities". Holdren, who is Obama's chief science adviser, chairs PCAST with Harold Varmus, former director of the National Institutes of Health in Bethesda, Maryland, and Eric Lander, director of the Broad Institute in Cambridge, Massachusetts. The full group boasts three Nobel laureates and 16 members of the national academies of science, engineering or medicine.

The new PCAST "has a great membership and outstanding co-chairs, but its ability to influence events depends on who listens", cautions John Marburger, who co-chaired the previous incarnation of PCAST as the science adviser to President George W. Bush. PCAST's success or failure depends mainly on its access to the president and on its interactions with various other advisory groups within the administration. These include the Office of Science & Technology Policy, which Holdren directs, and the National Science and Technology Council, composed mainly of the heads of agencies that deal with scientific matters, along with the US vice-president.

Last November, Marburger and the other outgoing PCAST co-chair, venture capitalist Floyd Kvasz, left a memo offering their successors some advice, including limiting the number of members:

under Bush, the council launched in December 2001 with 24 members and expanded to 35 in 2005. PCAST's previous incarnation focused more on technology advice, and it included fewer academic scientists and more business executives.

"The best thing about this PCAST is that it's up and running earlier in the term than the previous one," says Marburger. At the meeting last week, Holdren said that the council's speedy formation was a clear signal that Obama thinks that science and technology are crucial in addressing global challenges. On 7 August, the council met with the president for a little over an hour.

PCAST's H1N1 report had been commissioned by Obama in late June. Shortly after, the council met for two days with around a dozen experts in public health, virology and other key fields. The report, which has not yet been made public, was delivered two weeks later and addressed the value of scenario planning, communicating complex messages to the public and policy-makers, and the types of legal, social, financial and other factors that could get in the way of responding to a pandemic. "Everyone felt that it was probably the best response ever to an epidemic event," says Lander.

Last week's meeting saw council members suggesting future subjects that could attract their scrutiny. Barbara Schaal, a plant geneticist at Washington University in St Louis, suggested weighing in on the research agenda for the proposed National Institute for Food and Agriculture, an institute authorized within the US Department of Agriculture but not yet funded. Lander, also a geneticist, suggested looking at governmental approaches to cancer research, including evaluating whether the most creative approaches get support in their early days. And geochemist Daniel Schrag of Harvard University suggested tackling national strategies for research into adaptation to cope with the effects of climate change. The next PCAST meeting is slated for late October. ■

Alexandra Witze and Lizzie Buchen  
See Editorial, page 781.



John Holdren co-chairs the PCAST council.

K. WOLFF

# Ice-core researchers hope to chill out

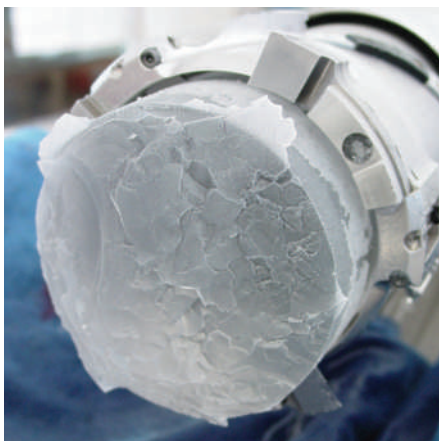
Fresh freezers needed to preserve ancient gas, scientists say.

Researchers in the United States and Europe are seeking funding so that the ice cores used to study Earth's past climate can have the same luxuriously chilly storage facilities currently enjoyed by prize tuna.

The cylindrical cores, drilled at multi-million-dollar expense from polar and glacial ice, can be kilometres long. They contain tiny bubbles of trapped air, allowing scientists to measure the concentration of carbon dioxide in the atmosphere from hundreds of thousands of years ago. The relative ratios of oxygen and nitrogen, and their isotopes, can also reveal temperature variations and help to date the trapped gas.

But oxygen is gradually lost when ice cores are stored at  $-20^{\circ}\text{C}$  to  $-30^{\circ}\text{C}$ , the standard temperature of current cold-storage facilities in the United States and Europe (M. Bender, T. Sowers and V. Lipenkov *J. Geophys. Res.* **100**, 18651–18660; 1995).

The oxygen diffuses slowly toward the core's surface and can be lost to the air, resulting in



Unless stored correctly, ice cores lose their value.

higher ratios of nitrogen to oxygen that can distort the conclusions scientists draw from them. In 2005, Japanese researchers showed that colder storage temperatures could mitigate this gas loss (T. Ikeda-Fukazawa *et al. Earth Planet.*

*Sci. Lett.* **229**, 183–192; 2005), and the ice-core storage facility at the National Institute of Polar Research, Tokyo, was subsequently upgraded with technology used to maintain cold stores for high-grade tuna at  $-50^{\circ}\text{C}$ .

US researchers are now seeking roughly \$5 million to rebuild cold-storage facilities at the US Army Cold Regions Research and Engineering Laboratory in Hanover, New Hampshire, which would also have its storage capacity increased by about 25%. Ian Baker, a materials scientist at Dartmouth College, also in Hanover, is leading the application for funding from the National Science Foundation. If the team gets its funding, Dartmouth would then manage the refurbished facility, which could be completed by 2010.

European scientists face a similar challenge. "We need a European-wide facility," says Eric Wolff at the British Antarctic Survey in Cambridge, UK. But a European Commission study in 2008 estimated that a new  $-50^{\circ}\text{C}$  facility, with associated research labs and teaching facilities,

L. AUGUSTIN/CNRS

## Flu database rocked by legal row

### EXCLUSIVE

A question mark is hanging over the future of EpiFlu, an international database created to help monitor the spread and evolution of influenza viruses. The database openly shares genetic, epidemiological and clinical data that previously had often been hoarded by countries and scientists, and is contributing to the rapid analysis of viral gene sequences from the current H1N1 pandemic.

EpiFlu has become mired in a legal dispute between the Global Initiative on Sharing Avian Influenza Data (GISAID), an international group created by leading flu researchers in August 2006 to promote data sharing (see *Nature* **442**, 981; 2006), and the Swiss Institute of Bioinformatics (SIB) in Geneva. GISAID announced a contract with the SIB in December 2006 to build the EpiFlu database. Most funding for EpiFlu came from the US Centers for Disease Control and Prevention and the Swiss government.

The row became public on 27 July, when visitors to the EpiFlu landing page on the GISAID website were met with a message from the SIB informing them that the database was currently unavailable on that site "due to contractual and

legal issues", and instead was available only to users redirected to a SIB website. The same day, the SIB e-mailed the same message to all registered users of the database.

The next day, GISAID also e-mailed users to assert that the SIB "had no right [to cut off the access to the EpiFlu Database via GISAID] or to operate the EpiFlu Database on its own".

Both SIB and GISAID officials declined to discuss the details because of the ongoing legal dispute. But the SIB alleges that GISAID has breached its contract by failing to pay its bills on time. GISAID officials say that although there had been a hiatus in its funding, they had acted in good faith and had subsequently obtained additional funds to meet some of the bills.

"GISAID continues to work with the SIB to resolve their monetary dispute," says Cheryl Bennett, an official at the GISAID Foundation's Washington DC office. "However, before the monetary dispute can fairly be resolved, GISAID must receive an accurate accounting from the SIB, which GISAID has requested but the SIB has thus far not provided."

She asserts that the SIB's continued operation of the database, including GISAID's trademark logos and data-access agreement, amounts to "misappropriation" of the database, and claims that under the terms of the contract, all EpiFlu data remain GISAID's property, giving the SIB no right to operate the database independently.

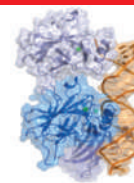
However, the SIB had written to GISAID in September 2008 declaring that it was terminating their contract. The SIB argues that GISAID has not settled its bills in full and that, under Swiss law, a default on payment renders a contract null and void, giving the SIB the rights to the database it built.

Since then, the SIB claims that it has operated the database without asking for more money from GISAID, and has taken fund-raising for the database into its own hands.

Although researchers can still access the database, public-health officials are worried by the longer-term implications of the row. Before the creation of GISAID, several countries — including Indonesia, an avian flu hotspot — had refused to share sequence data on the grounds that they got little in return. But they

**"I hope they reach the best solution for the sake of global health."**





# IMPROVING CELL REPROGRAMMING

Blocking an antitumour pathway helps produce stem cells.

[www.nature.com/news](http://www.nature.com/news)

WIKIMEDIA COMMONS

would cost €25 million (US\$35 million), and is unlikely to be funded, says Frank Wilhelms of the Alfred Wegener Institute for Polar and Marine Research in Bremerhaven, Germany, which houses one of four major ice-core facilities in Europe. The International Partnerships in Ice Core Sciences (IPICS), an organization of scientists, drillers and engineers from 18 nations, has also said that urgent action is needed to prevent ice cores degrading.

In the interim, Jeffrey Severinghaus, an IPICS steering-committee member from the Scripps Institute of Oceanography in La Jolla, California, says some institutions like his are building smaller units to keep parts of cores at  $-50^{\circ}\text{C}$ . These units can be created for about \$15,000, but the necessary freezer adaptations void warranties and there are concerns that keeping sections of ice cores in many different locations may hamper researchers' access.

His lab is currently studying oxygen/nitrogen ratios in ice cores drilled last year for the Western Antarctic Ice Sheet Divide Ice Core project, a collaboration of US research groups. Preliminary comparisons with the Byrd ice core, drilled in 1968 in Western Antarctica, show that oxygen has been lost in the older core during storage, he says.

Rex Dalton

were persuaded to share by GISAID's terms of access, similar to those of open-source software, in which all users agree to share their own data and give due credit to the originators.

"Indonesia has been supportive of GISAID from the outset," says Widjaja Lukito, a senior policy adviser at the country's ministry of health. He adds that he is watching "with great concern the problems faced by the GISAID Initiative during this pandemic phase". He says that he strongly hopes that "the parties involved will reach the best solution for the sake of global public health".

One flu scientist, who is a member of GISAID's scientific council, adds that EpiFlu is more than just the database computing infrastructure built by the SIB. Considerable effort has been invested by GISAID and its partners in "building trust" between the scientific community and countries who have sequence data to deposit, and in contributing influenza expertise.

Lawyers for both the SIB and GISAID have in the past weeks made confidential settlement offers to each other, and both say they are keen to reach a peaceful settlement. "The SIB is 100% committed to the EpiFlu database as part of the GISAID initiative. We are working very hard to find the best possible solution for all concerned," says Ron Appel, head of the SIB.

Declan Butler

## Climate data spat intensifies

A leading UK climatologist is being inundated by freedom-of-information-act requests to make raw climate data publicly available, leading to a renewed row over data access.

Since 2002, Steve McIntyre, the editor of Climate Audit, a blog that investigates the statistical methods used in climate science, has repeatedly asked Phil Jones, director of the Climatic Research Unit (CRU) at the University of East Anglia, UK, for access to monthly global surface temperature data held by the institute. But in recent weeks, Jones has been swamped by a sudden surge in demands for data.

Several organizations worldwide collect and report global average temperature data for each month. Of these, a temperature data set held jointly by CRU and the UK Met Office's Hadley Centre in Exeter, known as HadCRU, extends back the farthest, beginning in 1850. Although these data are made available in a processed format that shows the global trend, access to the raw data is restricted to academics.

Between 24 July and 29 July of this year, CRU received 58 freedom-of-information-act requests from McIntyre and people affiliated with Climate Audit, requesting access to the data or information about their use. In the past month, the UK Met Office, which receives a cleaned-up version of the raw data from CRU, has received ten requests of its own.

McIntyre, based in Toronto, Ontario, is best known for questioning the validity of the statistical analyses used to reconstruct the past 1,000 years of climate, but has more recently turned his attention to criticizing the quality of global temperature records. Jones concedes that raw climate data have imperfections — such as duplication of stations — but says that such minor errors would not alter the overall global temperature trend. McIntyre insists that he is not interested in challenging the science of climate change or in nit-picking, but is simply asking that the data be made available. "The only policy I want people to change is their data-access policy," he says.



Steve McIntyre wants access to more UK data.

Jones says he can't fulfil the requests because of confidentiality agreements signed in the 1990s with some nations, including Spain, Germany, Bahrain and Norway, that restrict the data to academic use. In some cases, says Jones, the agreements were made verbally, and in others the written records were mislaid during a move.

He says he is now working to make the data publicly available online. As *Nature* went to press, Jones was expected to post a statement on the CRU website to that effect, including any existing confidentiality agreements. Jones says any such data release "needs to be done in a systematic way".

"We're trying to make them all available," says Jones. "We're consulting with all the meteorological services — about 150 members [of

the World Meteorological Organization] — and will ask them if they are happy to release the data." A spokesperson for the Met Office confirmed this, saying "we are happy for CRU to take the lead on this, as they are their data".

But getting the all-clear from other nations won't be without its challenges, says Jones, who estimates that it could take several months. In addition, some nations may object if they make money by selling their wind, sunshine and precipitation data.

The dispute is likely to continue for some time. McIntyre is especially aggrieved that Peter Webster, a hurricane expert at the Georgia Institute of Technology in Atlanta, was recently provided with data that had been refused to him.

Webster says his team was given the station data for a very specific request that will result in a joint publication with Jones. "Reasonable requests should be fulfilled because making data available advances science," says Webster, "but it has to be an authentic request because otherwise you'd be swamped."

Indeed, Jones says he has become "markedly less responsive to the public over the past few years as a result of this".

Olive Heffernan

**"Data release needs to be done in a systematic way."**

# Return of the rat

European investment could see knock-out rats catching up with mutant mice in medical research.

The European Commission has approved the world's first major systems-biology programme to study the rat.

Known as EURATRANS — for European large-scale functional genomics in the rat for translational research — the multimillion-euro project includes collaborators in the United States and Japan. The aim of the initiative is to expand databases of genes, proteins and other biomolecules, analysing the information and translating it into a form that is useful to clinical researchers.

The effort represents a comeback for the rat, which fell from scientific prominence during the mouse-dominated genomics era, despite the unprecedented amounts of physiological data that have been gathered from it over the centuries.

"The rat is a better model than the mouse for many complex disorders that are so common in humans, like cardiovascular and psychiatric disease," says EURATRANS coordinator Norbert Hübner, a geneticist at the Max Delbrück Center for Molecular Medicine in Berlin. "The project will help rat genetics catch up with the many-years head start that mouse genetics has enjoyed."

In the late 1980s, researchers developed a technique to knock out single genes from mice using embryonic stem cells as a starting material, making it possible for geneticists to engineer the mutant strains needed to model human disease. Rat genetics proved trickier to manipulate, and the mouse's popularity as a lab animal soared.

Two things have happened in the past few years that make a major assault on the rat feasible and worthwhile, says Hübner. "First, the huge advances in sequencing and other molecular technologies, and second, the problem which was preventing the development of gene knock-out technology in rats has been overcome." Last year, Austin Smith, director of the Wellcome Trust Centre for Stem Cell Research at the University of Cambridge, UK, and his colleagues achieved this by altering the culture medium conditions used to grow embryonic cells *in vitro*<sup>1</sup>. Knock-out rats have not yet been created using these cells, but this is one of the aims of the EURATRANS



A Europe-led project could push the lab rat back into the spotlight.

project, in which Smith is also a participant.

The 16 institutions participating in EURATRANS will receive a total of €10.5 million (US\$14.9 million) from the commission, which they will match from their own resources. The money will be used to create detailed genome sequences of the eight progenitor strains of rat that gave rise to the stock rats generated at the US National Institutes of Health (NIH) laboratories in Bethesda, Maryland, the diverse genetics of which mirrors that of human populations.

The project will also apply state-of-the-art technologies in order to generate data on rat functional genomics. Thirty additional 'recombinant inbred strains' created at the Prague-based Institute of Physiology, part of the Academy of Sciences of the Czech Republic, will also get this treatment. These rats were made by crossing the two strains of rat that have already had their genomes sequenced — the Norwegian brown rat (*Rattus norvegicus*)<sup>2</sup> and the albino spontaneously hypertensive rat, which develops high blood pressure early in life. The crosses display a range of clinical phenotypes, such as variations in blood pressure and glucose tolerance, and resistance to insulin, so studying them may help researchers

to unpick the many genes involved in these pathologies.

But identifying genes is not enough to understand complex diseases, stresses Hübner. "It is a question of what happens to those genes." For example, a recent genome-wide association study in thousands of people implicated the gene for the enzyme HMGCoA reductase as a risk factor in cardiovascular disease — but found the risk to be small<sup>3</sup>. Yet the statin drugs that target this enzyme are among the most effective for cardiovascular disease. "That's why we need to integrate genomic information with other molecular information and learn more about entire molecular pathways in cells that may go wrong in disease," says Hübner.

The systems-biology approach of EURATRANS aims to integrate terabytes of information — on gene sequences, gene transcription and chemical modification, as well as proteomic and metabolomic data — in order to identify these molecular networks. The consortium will then confirm the networks' involvement in disease using appropriately engineered rats.

Smith points out that the growing use of mutant rats will come at a cost. Being larger than mice and taking longer to reach maturity, rats are more expensive to keep, although their size can also make them easier to work with. "Funding agencies will need to be persuaded that it is worth the investment," he says.

EURATRANS is one of the first projects to be approved under a reciprocal funding arrangement agreed in late 2008 between the European Union and the NIH. This means that a consortium does not have to prove, as it still does for other non-EU countries, that no laboratory with the same skills exists in Europe.

EURATRANS participant Tadao Serikawa of Kyoto University in Japan, who heads the National BioResource Project-Rat initiative, says that the global nature of the EU project is important both for exchange of skills and information, and because "it avoids redundant experiments, which saves animals, time and money and accelerates biomedical progress". ■

**Alison Abbott**

1. Buehr, M. et al. *Cell* **135**, 1287-1298 (2008).
2. Rat Genome Sequencing Project Consortium *Nature* **428**, 493-521 (2004).
3. Kathiresan, S. et al. *Nature Genet.* **40**, 189-197 (2008).

A. ZVOZNIKOV/ARDEA.COM





# CAMBRIAN HUNTER DEFANGED

*Anomalocaris* didn't have the chops to chew up trilobites.  
[www.nature.com/news](http://www.nature.com/news)

WIKIMEDIA COMMONS

## Satellite data show Indian water stocks shrinking

Unsustainable water use in India is threatening agricultural production and raising the spectre of a major water crisis.

Matthew Rodell of NASA's Goddard Space Flight Center in Greenbelt, Maryland, and colleagues used data from the Gravity Recovery and Climate Experiment (GRACE) satellites — operated by NASA and the German Aerospace Center (DLR) — to determine how groundwater levels are changing in the Indian states of Rajasthan, Punjab and Haryana, which includes the national capital of New Delhi.

Their research, published online in *Nature* this week (M. Rodell *et al.* *Nature* doi:10.1038/nature08238; 2009), found gravity anomalies suggesting a net loss of 109 cubic kilometres of water — equivalent to a mass of 109 billion tonnes — from August 2002 to October 2008.

**"If farmers could shift away from water-intensive crops and implement more efficient irrigation methods, that would help."**

The amount lost is double the capacity of India's largest surface-water reservoir, the Upper Wainganga, and almost three times the capacity of Lake Mead in Nevada, the largest reservoir in the United States.

A second study using GRACE data, by scientists at the University of Colorado and the National Center for Atmospheric Research in Boulder, has found that the most intensively irrigated areas in northern India, eastern Pakistan and parts of Bangladesh are losing groundwater at an overall rate of 54 cubic kilometres per year, consistent with Rodell's results (V. M. Tiwari *et al.* *Geophys. Res. Lett.* doi:10.1029/2009GL039401; in the press).

Groundwater depletion in northwest India is a known problem, but Rodell's data suggest that the loss rate is around 20% higher than the Indian authorities have previously estimated.

Rodell notes that rainfall during the

study period was close to the long-term climatic mean, and says that the observed groundwater depletion is unlikely to be the result of unusual dryness or variability.

The regions of Rajasthan, Punjab and Haryana have a combined population of 114 million people, and receive an average of 500 millimetres of rainfall per year — just slightly less than that of London — but with pronounced seasonal and regional differences. Although less than a third of agricultural land there is irrigated, crop irrigation accounts for up to 95% of groundwater consumption. "If farmers could shift away from water-intensive crops, such as rice, and implement more efficient irrigation methods, that would help," says Rodell.

Meanwhile, the Indian government is looking into framing regulations to reduce groundwater consumption. "Hopefully," says Rodell, "our research will give them the evidence they need to carry through."

**Quirin Schiermeier**

## Europe prepares for drugs from GM plants

The first European guidelines on crop pharming — growing transgenic plants to produce drugs — were published on 7 August, clearing an obstacle to commercial development.

The guidance was drawn up by the European Food Safety Authority in Parma, Italy, which will assess applications from scientists hoping to grow drug-producing plants on a commercial scale. The European Commission and member states will have the final say on all such plans.

Developers must detail the differences between the modified plant and the conventional crop, assess the risks of genes being passed on to other plants, consider the potential dangers to humans and animals and specify monitoring procedures. This is consistent with rules set out by the US Food and Drug Administration and the US Department of Agriculture, says Jeffrey Wolt, an expert in plant biotechnology risk assessment at Iowa State University in Ames.

Internationally, only a handful of clinical trials of plant-pharmed drugs are under way (see *Nature* 458, 951; 2009), and there are none on the market.

For a longer version of this story, see <http://tinyurl.com/m8uvzg>

## Presidential panel lays out options for NASA's future

The committee deliberating NASA's future has outlined seven possible scenarios to shape US space operations for the coming decade. The ten-person panel, chaired by Norman Augustine, retired head of aerospace giant Lockheed Martin, set out its choices in a public meeting in Washington DC on 5 August.

Five of the seven scenarios would extend the life of the International Space Station by five years to 2020; three could allow the space shuttle to continue past 2011; but only two spell out a future for Ares I, the rocket being built to replace the shuttle as the main way of getting astronauts into space.

The number of options presented to the



Norman Augustine: laying plans for NASA.

## Novartis targeted by animal-rights extremists

Militant animal-rights activists were responsible for the torching of the Alpine holiday home (pictured) of Daniel Vasella, head of the Swiss pharmaceutical company Novartis, in the early hours of 3 August, Swiss authorities assume. The chalet was destroyed but no one was hurt.

Novartis has reported at least ten other recent attacks on its employees. These include the desecration of graves of Vasella's family and the theft of his mother's ashes at the end of last month, as well as the placing of incendiary devices under the cars of Novartis's administrative chief, Ulrich Lehner, in May.

Swiss police say they expect further attacks. The Stop Huntingdon Animal Cruelty (SHAC) group has called an Action Week for 24–30 August against major customers of Huntingdon Life Sciences, a contract animal-testing company near Cambridge, UK, that has faced a sustained campaign of attacks. Novartis denies being a Huntingdon Life Sciences customer, as the SHAC website claims.



E. LEANZA/PA

president — whose administration has called for a reduced NASA budget — may change between now and 31 August, when the panel will deliver its final report.

For a longer version of this story, see <http://tinyurl.com/mrtrf5>

## Batteries feel the benefit of green car money

The US Department of Energy rolled out \$2.4 billion in stimulus grants on 5 August to develop next-generation technologies for electric cars.

The bulk of the awards, made to 48 projects in more than 20 states, will fund factories to make battery components. Smaller pots of money go to producing electric motors and other drive components, and to fund road-testing of plug-in hybrids and all-electric cars.

Established car makers and battery manufacturers took most of the money. Mark Platshon, a clean-technology analyst with VantagePoint Venture Partners in San Bruno, California, says he had hoped to see more handed to smaller, more innovative companies. "It's scaling up the existing guys with the existing technology in the existing way," he says.

For a longer version of this story, see <http://tinyurl.com/nhuy7v>

## Stalled science buildings restart in California

The University of California (UC) last week came up with US\$200 million to finance research and medical facilities despite a state-wide budget catastrophe (see *Nature* 460, 441; 2009).

Of the ten UC campuses, eight will receive funds. Santa Cruz tops the list of research allotments, receiving \$64 million for a biomedical science facility, Irvine wins \$5 million for biological, engineering and computer sciences, and Riverside gets \$4.6 million for equipment to stock newly completed materials-science and engineering buildings.

Slashing \$813 million last month from its \$3.2-billion annual budget, the UC system has forced staff to take unpaid leave and halted building work. The \$200 million was made available on 4 August after the UC system secured a commercial bank loan to buy bonds from the state of California — which used the financing to restart stalled infrastructure projects.

## German scientists found guilty of negligence

An independent investigation committee has found four scientists at the elite University of Göttingen, Germany, guilty of gross negligence because they included three unfinished manuscripts in publication lists supporting an application for research funding. But the researchers did not invent or falsify data, the committee says.

The application was for the continuation of a collaborative research centre (SFB): a highly prized award funded by the DFG, Germany's major national research agency. The collaboration was set up to study the stability of the Indonesian rainforest and had received €16.6 million (US\$22.3 million) from 2000 to June 2009 (see *Nature* 459, 23; 2009).

Investigations by the university and local public prosecutors into possible financial irregularities continue.



# FIXING THE SKY

When nations made plans to save the ozone layer, they didn't factor in global warming. **Quirin Schiermeier** reports on how two environmental problems complicate each other.

After this month, something sinister will start to take shape above Antarctica. As sunlight reappears in the polar skies after the long winter, chlorine and bromine compounds in the stratosphere will begin destroying part of the ozone layer that shelters Earth's surface from harmful ultraviolet radiation. Over the next few months, these pollutants will eliminate enough ozone to create a hole in the protective veil over the Antarctic continent.

That same phenomenon has occurred every spring since the late 1970s, although it took several years before scientists recognized and documented the emerging pattern. When, in 1985, a team of researchers from the British Antarctic Survey published a paper in *Nature* describing the ozone hole<sup>1</sup>, the world was put on high alert. At about the same time, it was becoming clear that the ozone shield over much of the planet was vulnerable to pollutants emitted into the atmosphere. That concern propelled countries in 1987 to agree to phase out the production of ozone-destroying compounds — which stands out even today as the most ambitious action ever taken to tackle a global environmental problem.

Thanks to that agreement, the Montreal Protocol, nations have made great strides towards repairing the planet's sunshield. Although the ozone hole that appears over Antarctica each year remains as bad as ever, the amount of chlorine in the atmosphere has started to decline and the

rest of the ozone layer has started to show signs of recovery from a less dramatic, but still dangerous, thinning.

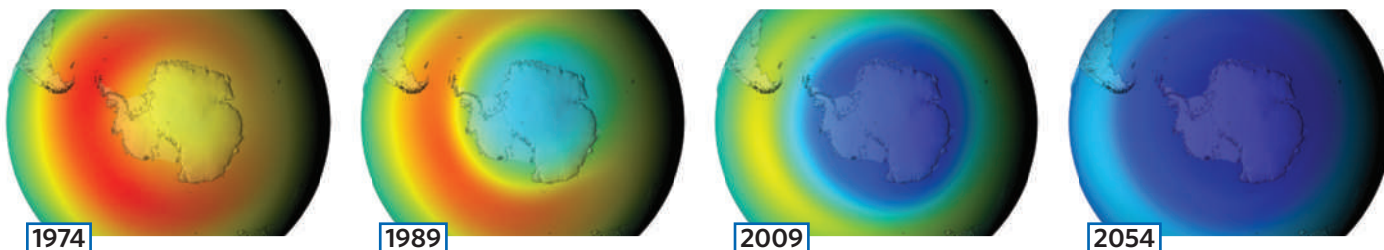
Amid the good news, however, lurk big questions about how long it will take to fix the sky. A decade ago, researchers projected that the ozone layer would fully recover by 2050, but now there is far more uncertainty in their estimates. One of the complicating factors is that greenhouse gases have altered atmospheric conditions in many ways since the Montreal Protocol was signed, some of which speed up ozone recovery and some of which delay it.

Scientists are only now gaining the necessary computing power to run long-term simulations that allow them to test which effects of climate warming might win out. These types of studies suggest that part of the global ozone layer will recover decades earlier than previously thought, whereas the Antarctic ozone hole may linger decades longer than was once hoped.

## Complex interplay

Just as the climate influences ozone, changes to the ozone layer will, in turn, alter the climate. Ozone loss over Antarctica has already affected the climate there, for example, by helping to warm the Antarctic Peninsula and thereby contributing to the destruction of several ice shelves. And it may have tilted the odds towards more frequent droughts and fires in Australia.

**In a NASA simulation, a world with no controls on chlorine and bromine pollution leads to extreme ozone loss (blue hues) over Antarctica.**



"Stratospheric ozone and surface climate are coupled in many ways," says Susan Solomon, an atmospheric chemist at the National Oceanic and Atmospheric Administration in Boulder, Colorado. "It's a fascinating interplay of which we may not yet know the whole story."

Well before the ozone hole was recognized, scientists had started to worry about the effects that humans were having on the ozone layer. In 1974, Sherwood Rowland and Mario Molina, chemists at the University of California, Irvine, warned that chlorofluorocarbons (CFCs) could break down in the stratosphere and the chlorine released could destroy atmospheric ozone<sup>2</sup>. They later shared the 1995 Nobel Prize in Chemistry with Paul Crutzen of the Max Planck Institute for Chemistry in Mainz, Germany, for their pioneering work in understanding ozone chemistry.

Concern over that global thinning and the ozone hole led to the 1987 treaty known as the Montreal Protocol on Substances that Deplete the Ozone Layer. The treaty came into effect 20 years ago and was followed up by amendments that banned the worst ozone-destroying chemicals, such as CFCs (used in refrigeration, air-conditioning and foam production) and bromine-containing halons (used in fire extinguishers). The agreements yielded quick dividends: the effective concentration of ozone-destroying compounds in the stratosphere peaked in the late-1990s and has declined since then<sup>3</sup>.

The Montreal provisions also came with a free gift for the climate because CFCs and their kin are much stronger greenhouse gases than carbon dioxide. By getting rid of those compounds, the ozone agreement has achieved five to six times greater reductions in warming effect than the Kyoto Protocol<sup>4</sup>.

"The Montreal Protocol is just the most successful piece of international environmental legislation ever," says Solomon. "It also contains the unwritten memo to climate negotiators that we need to, and can, do much better in controlling greenhouse warming than we have been doing so far."

### The 'world avoided'

A glance at a hypothetical future with no ozone protections illustrates what could have been. Paul Newman of NASA's Goddard Space Flight Center in Greenbelt, Maryland, and his colleagues, used a model that simulates chemical reactions, atmospheric circulation and solar radiation to forecast a future in which production of ozone-depleting compounds is never regulated and grows at an annual rate of 3%. By 2065, two-thirds of the ozone would be destroyed — not just over the poles but everywhere<sup>5</sup>. CFCs would virtually eliminate the global ozone layer by the end of the century. People in New York, Buenos Aires and Tokyo, like everyone else living in mid-latitudes (the temperate regions between about 30° and 60° from the Equator),

**"If you have to have an ozone hole, the best place is Antarctica. In the tropics it would be very damaging to life."**

— Susan Solomon

would be exposed to ultraviolet radiation so extreme that they would develop dangerous sunburn within 5 minutes, on average, one-third of the time it takes today. The level of DNA-mutating ultraviolet radiation would rise about six-fold, dramatically boosting skin cancer cases in humans (see 'Ozone and cancer').

But the ozone treaties will spare humans from living in a world unshielded from the might of the Sun. "The worst has been avoided," says Martin Dameris, an atmospheric and climate scientist at the German Aerospace Centre in Oberpfaffenhofen near Munich. "But it is also a reminder that we must not even think about watering down the protocol."

### Continued pollutant use

Environmental groups worry in particular about methyl bromide, which is used in agriculture to control pests. Under the provisions of the ozone-protection treaties, developed nations were supposed to stop using this compound by 2005, with developing nations following 10 years later. But lobbying by farming groups led to a stay of execution and the chemical is still in use in many developed countries. Another complicating factor is the large volume of chlorine and bromine stored in older air-conditioning and fire-fighting systems, much of which will eventually make its way into the atmosphere.

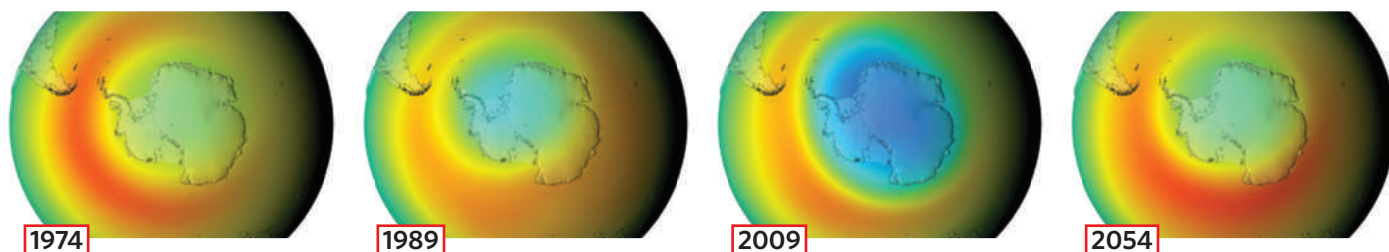
Once the chemicals get there, they linger for decades. So even though CFCs and several other ozone destroyers have been phased out, they will continue to eliminate ozone for many years. At present, stratospheric ozone concentrations around the globe are about 4% below the 1964–80 average, but the depletions differ substantially between hemispheres and latitudes. In tropical regions, there is relatively little ozone loss. Over the mid-latitudes, where the air mixes more readily with ozone-depleted air parcels from the poles, total ozone loss has reached 3% in the Northern Hemisphere, and around 6% in the Southern Hemisphere, since 1980 (ref. 3).

Although relatively minor compared with the extreme ozone loss over Antarctica each spring, the mid-latitude changes have a notable effect because so much of the population lives there. The additional ultraviolet light may cause hundreds of thousands of extra cases of skin cancer each year worldwide, with the full effects still decades away<sup>3</sup>.

But there is good news for the mid-latitudes, because ozone concentrations there have started to show signs of rebounding. "It seems as if mid-latitude ozone is going up," says Richard Stolarsky, an atmospheric chemist at Goddard. The upward trend is still not clear enough to be able to firmly establish its cause, he says, "but we're pretty confident that reduced chlorine load [in the atmosphere] is contributing to the rebound".

Although researchers once estimated that it would take

**Controls on pollution are projected to prompt a recovery of the ozone hole later this century.**





until 2050 for the mid-latitude ozone layer to recover fully, model simulations now suggest that point will come perhaps 20 years earlier, especially in the Northern Hemisphere, which is not greatly affected by the Antarctic ozone hole<sup>6</sup>. The faster recovery can be considered a benefit of global warming. As greenhouse gases trap heat in the lower atmosphere, they cool the stratosphere above, which slows down the ozone-destroying chemical reactions. Moreover, models that simulate climate and atmospheric chemistry suggest that global warming will speed up the circulation pattern that carries ozone-rich air from the tropics to the mid-latitudes, thereby boosting ozone amounts there.

### Quick reactions

Closer to the poles, however, the influence of global warming becomes less clear, especially for the Antarctic ozone hole. Cooling in the stratosphere there would, by itself, lead to more ozone destruction by stimulating the growth of polar stratospheric clouds. In the extremely dry stratosphere above Antarctica, such clouds form when temperatures drop below  $-78^{\circ}\text{C}$ , and they provide a surface for the chemical reactions that rapidly strip an oxygen atom from the three-oxygen ozone molecule.

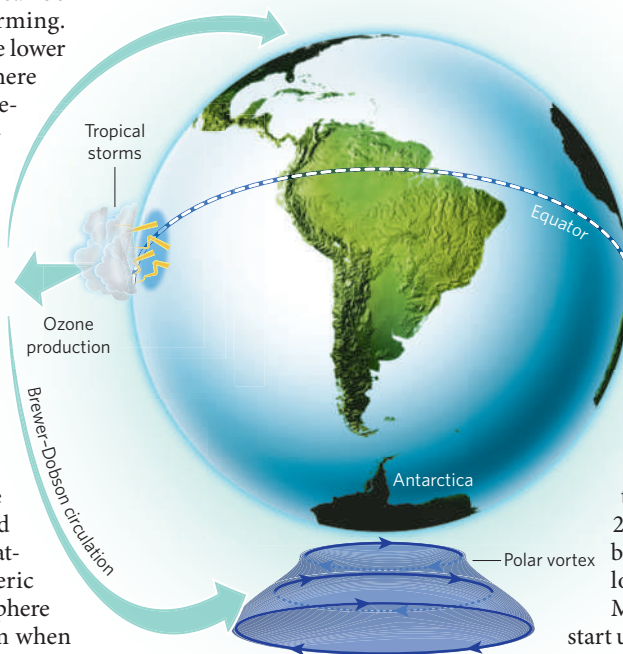
The ice particles play a powerful part. Outside the polar regions, a chlorine atom in the stratosphere can eliminate only a few hundred ozone molecules before it reacts with other gases such as nitrous oxide, breaking the cycle. But on the surface of polar ice particles, it can catalytically convert tens of thousands of ozone molecules. And it happens quickly. In the heart of the Antarctic ozone hole, between 14 and 21 kilometres above the surface, the loss rate can reach up to 3% per day<sup>3</sup>. By the beginning of October, the cloud-mediated reactions destroy nearly every ozone molecule in that altitude band.

In 1992, researchers predicted that greenhouse warming would speed up the destruction so strongly that it would cause ozone holes to open above the Arctic as well<sup>7</sup>. But that analysis left out an important effect, says John Austin, an author of the study and a modeller at the Geophysical Fluid Dynamics Laboratory in Princeton, New Jersey. Normal atmospheric flow, called the Brewer–Dobson circulation, causes air to rise into the stratosphere over the tropics, and then travel towards the higher latitudes, where it sinks back into the lower atmosphere (and heats up as it gets compressed). If climate change accelerates that cycle, it will speed up the downward flow above the polar regions, which would enhance the compression of the sinking air and raise atmospheric temperatures there. Especially in the Arctic, that heating effect in the polar stratosphere will impede ozone loss, says Austin.

With climate change acting both to warm and to cool the polar stratosphere, researchers do not yet know

### OZONE'S LONG JOURNEY

Ozone molecules are produced in the stratosphere over the tropics and are then transported towards the poles where they sink into the lower stratosphere. Over Antarctica, a vortex of winds isolates the polar stratosphere during winter and spring, which bottles up the cold air there and fosters the formation of springtime ozone holes.



**"Ozone chemistry and atmospheric dynamics influence each other. It's difficult to keep apart what's pushing from what's pulling."**

— Martin Dameris

which effect will win out. The results are not consistent from one model to the next and there is still considerable uncertainty on this topic, says Darryn Waugh, an atmospheric scientist at Johns Hopkins University in Baltimore, Maryland.

One factor holding back progress in this area is the time it takes to conduct the research. There are still relatively few groups with the computing power to run long simulations with sufficiently complex models that mimic both atmospheric chemistry and climate. In the case of the Princeton lab, it takes 3 months of continuous computing with a 100-processor system to conduct a 100-year simulation, says Austin. "I have to watch it every day," he says, to make sure that the experiment does not get stuck. "Otherwise three months turns into four or five."

For now, the ozone hole above Antarctica shows no sign of getting any better. In 2002 and 2004 the ozone loss was less severe, but in 2006 ozone levels fell to a new record low and have since remained depressed.

Most scientists don't expect the recovery to start until at least 20 years from now — a decade or so later than was projected just five years ago.

That is because models that simulate the movement of chemicals suggest that the stratosphere over Antarctica will remain saturated with ozone-destroying substances for another 10–20 years. And according to many models, it will take until 2060 or 2065 for nearly complete recovery, when polar concentrations of ozone-destroying compounds drop below their 1980s values.

The latest modelling results have raised an additional complicating factor: the influence of bromine compounds. Concentrations of bromine in the stratosphere are higher than models suggest they should be, perhaps because more bromine is making its way into the stratosphere than had been predicted. If that trend continues, a small ozone hole — about one-tenth its current size — would continue to form for decades beyond 2065, according to work done by the Princeton lab. "Even by the end of the century, you don't see complete recovery," says Austin, who cautions that this result is still preliminary.

For humans, and for most animals and plants, the extra ultraviolet light let in by the ozone hole may not present a significant problem. The peak ozone loss occurs early in the spring, when the Sun is still low over the horizon, which limits the amount of ultraviolet radiation reaching the surface.

"If you have to have an ozone hole, the best place is Antarctica," says Solomon. "If it occurred in the tropics it would be very damaging to life."

But aside from letting in slightly more radiation, the ozone hole has the indirect effect of altering the local climate, which causes atmospheric changes that can be felt throughout much of the Southern Hemisphere. Ozone

is normally an enormous source of heat for the stratosphere because it absorbs solar ultraviolet radiation. The absence of ozone throughout much of the polar stratosphere leads to a 6°C or so cooling there. Solomon has found that this cooling effect has helped to seal off the Antarctic continent by strengthening the vortex of westerly winds that flow around the polar cap<sup>8</sup>.

This discovery serves as an explanation for several puzzling features of Antarctica's climate. The strong vortex locks very cold air on the high plateaus in the continent's interior and thus shelters the coldest regions on Earth from the effects of greenhouse warming. Large parts of Antarctica have experienced a cooling trend over the past 30 years — a fact often raised by those who deny any reality to global warming. But Solomon's work shows that ozone loss helps to explain the lack of warming in the interior parts of Antarctica.

### Message in a bottle

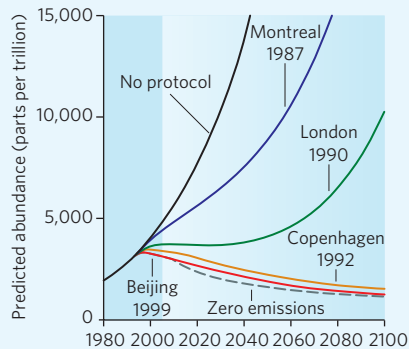
With the colder air bottled up over Antarctica, it does not flow out as frequently over the edges of the continent. That helps to explain why the Antarctic Peninsula, exposed to relatively mild oceanic air, has become one of the fastest-warming places on Earth. In the past couple of years, two large ice shelves have disintegrated along the peninsula, whereas six others show signs of retreat, sending gargantuan icebergs floating off into the Southern Ocean.

So as the ozone hole shrinks during this century, it will uncork the air bottled up over the continent. "The polar vortex won't be as tight anymore, and cold interior air could

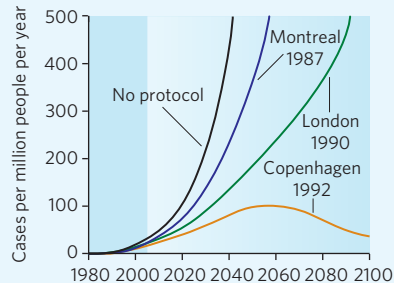
### THE TREATY THAT WORKED

Without the Montreal Protocol and its amendments, the amount of ozone-destroying compounds would continue to rise, driving up skin-cancer rates.

### OZONE-DESTROYING COMPOUNDS



### EXTRA SKIN-CANCER CASES



## Ozone and cancer

With the thinning of global ozone layer in the past 30 years, a surge in skin-cancer rates would be expected. And at first glance, that seems to have happened. The incidence of melanoma in the United States has more than doubled since 1975, with almost 69,000 cases expected to be diagnosed this year. In some parts of Australia and New Zealand, which have the highest incidence and mortality of melanoma in the world, the numbers have jumped by more than 50% since 1994.

However, attributing that trend to ozone

depletion is difficult because skin-cancer rates depend on other factors such as lifestyle, sunscreen use and how often tumours are diagnosed, all of which have changed over time. It also takes decades for skin cancer to appear after exposure. So the peak in cancer from the past thinning of the ozone layer has not yet hit.

Based on predicted increases in the amount of ultraviolet radiation, and assuming that factors other than ozone will remain unchanged, the World Meteorological Organization and United

Nations Environment Programme predict that additional skin cancer cases will top out around mid-century at 100 or so cases per million per year above 1980 levels — which would translate to at least 700,000 extra cases worldwide. Those rates should eventually return to 1980 values.

Without the Montreal Protocol and its subsequent provisions on chlorofluorocarbons, skin cancer cases would have been expected to quadruple by 2050 and to sharply increase further thereafter<sup>3</sup> (see graphic, above). **Q.S.**

make it to the peninsula more frequently," says Solomon. "That would help."

Elsewhere around Antarctica, for instance in the Ross Sea, sea-ice coverage is growing. Solomon was among the first to suggest that stronger atmospheric circulation around Antarctica may be behind that seemingly puzzling trend as well. Indeed, model experiments have recently confirmed that the ozone hole alters circulation patterns in just such a way to explain the sea-ice expansion and the overall climate changes in the Antarctic<sup>9</sup>.

Looking beyond Antarctica, James Risbey of the Center for Dynamical Meteorology and Oceanography at Monash University in Clayton, Australia, suggests that ozone loss is responsible for reduced rainfall and more frequent droughts over southern Australia. This happens, he says, because the cooling caused by ozone depletion over Antarctica has lowered atmospheric pressures there, speeding up the vortex of winds around the continent (see graphic, page 794). That pulls the rain-bearing westerly winds southwards, keeping them away from Australia. Risbey speculates that the ozone loss over Antarctica has caused a 20% reduction in rainfall in the dry season over Australia.

"Ozone chemistry and atmospheric dynamics influence each other. That's why it's difficult to keep apart what's pushing from what's pulling," says Dameris. "Much is speculation still, and there may be surprises."

His experiments with a model that simulates climate and atmospheric chemistry suggest that rising sea surface temperatures in the tropical oceans will strengthen the Brewer-Dobson circulation<sup>10</sup>. That could result in less ozone inside the tropics and more ozone outside, leading to abnormally high ozone concentrations in the mid-latitudes. That extra ozone would help protect people but it could have unwanted effects, perhaps by altering the chemistry of the stratosphere or by hindering the growth of plants, says Dameris.

Over the long term, as chlorine and bromine pollution are cleaned from the skies, climate change will take over and be the dominant human influence on ozone concentrations, he says. "Not many people have started thinking about what that might mean. It's getting about time."

**Quirin Schiermeier is Nature's Germany correspondent. Additional reporting by Richard Monastersky.**

- Farman, J. C., Gardiner, B. G. & Shanklin, J. D. *Nature* **315**, 207–210 (1985).
- Molina, M. J. & Rowland, F. S. *Nature* **249**, 810–812 (1974).
- United Nations Environment Programme *Scientific Assessment of Ozone Depletion: 2006* (UNEP, 2007); available at [www.unep.ch/ozone/Assessment\\_Panels/SAP/Scientific\\_Assessment\\_2006/index.shtml](http://www.unep.ch/ozone/Assessment_Panels/SAP/Scientific_Assessment_2006/index.shtml).
- Velders, G. J. M., Andersen, S. O., Daniel, J. S., Fahey, D. W. & McFarland, M. *Proc. Natl Acad. Sci. USA* **104**, 4814–4819 (2007).
- Newman, P. et al. *Atmos. Chem. Phys.* **9**, 2113–2128 (2009).
- Waugh, D. W. et al. *Geophys. Res. Lett.* **36**, L03805 (2009).
- Austin, J., Butchart, N. & Shine, K. P. *Nature* **360**, 221–225 (1992).
- Thompson, D. W. J. & Solomon, S. *Science* **296**, 895–899 (2002).
- Turner, J. et al. *Geophys. Res. Lett.* **36**, L08502 (2009).
- Deckert, R. & Dameris, M. *Geophys. Res. Lett.* **35**, L10813 (2008).

**See Editorial, page 781.**



# CORRESPONDENCE

## Ape and human similarities can be deceptive

**SIR** — In his Essay 'Darwin's last laugh' (*Nature* **460**, 175; 2009), Frans de Waal suggests that ape vocalizations are homologous to human laughter, which they could be — but that does not necessarily imply that apes have a sense of humour. Adaptive divergence could be at play, making humans the ones who get the jokes.

Darwin's singular contribution to the issues raised by de Waal is that, in spite of universal appreciation for the behavioural similarities between humans and other animals, these continuities can be divided into two classes. The first is a symbolic, or literary, relationship, familiar to us through Aesop: the ant is industrious, the fox is clever. The second is the result of a shared biological history, or common ancestry. Our scientific interest in the apes is presumably based on the expectation that the similarities we can identify between them and us are principally of the second type. Although critical to de Waal's argument, this type of overlap is, unfortunately, much easier to assume than to demonstrate.

The circumstances in which similarities between chimps and humans manifest often indicate the opposite — that the behaviours are not directly homologous and are being overenthusiastically interpreted. For example, infanticide by chimps is carried out by non-relatives (for reasons only they know) whereas in humans it may be carried out by the mother, or by someone acting on her behalf, mainly for cultural, social or economic reasons. In one species, the act is aggressive, violent and often cannibalistic, with no indication of the remorse that can accompany the act in the other species.

And although our feet are homologous to ape feet, the chimp's foot is principally adapted for grasping and the human

foot to weightbearing. They are similar, and are descended from a common ancestral structure, but they are by no means the same.

A genuine Darwinian approach to primate behaviour may have to acknowledge that the brains of apes (and their capabilities) may simply be different from our own, like their feet. Evolution, after all, is the production of difference. If one scholar acknowledges the adaptive divergence that has occurred between a human and a chimp over 7 million years or so of separation, and another insists that they are the same, then who is really in denial of evolution?

**Jonathan Marks** Department of Anthropology, University of North Carolina at Charlotte, Charlotte, North Carolina 28223, USA  
e-mail: jmarks@uncc.edu

## Speed of reporting isn't the issue when your work is scooped

**SIR** — In your Editorial 'How to stop blogging' (*Nature* **460**, 152; 2009), you urge the conference community to be clear from the outset about whether their meetings are 'open' or 'closed' with respect to the informal dissemination of their content. In my view (as a scientist and a blogger, <http://tinyurl.com/mf8ynx>), this risks treating early adopters of new communication technologies as scapegoats.

A few years ago, interested conference participants might have stood in front of a poster and sketched the figures for themselves; more recently, they might have snapped a digital photo while the presenter's back was turned. Key information could always be relayed by a swift phone call back to their laboratories. Now people can also tweet to the lab or the wider 'tweetersphere'.

We present information in order to disseminate it and enhance our reputations. Whether this occurs within

weeks, days or minutes is just a question of scale.

If a competitor can scoop me by tweeting or blogging my data only a few days or hours faster than he or she would have done by simply coming to my poster and taking ideas back to the laboratory, then the problem clearly lies with my own inability to conclude and publish my research — not in the progress of technology.

For the most part, the use of this technology is limited to sharing information with like-minded individuals. The nature of the conference has not changed, only the mindset of the participants.

**Ian M. Brooks** Biomedical Informatics Unit, University of Tennessee Health Science Center Clinical and Translational Science Institute, Memphis, Tennessee 38163, USA  
e-mail: ibrooks1@utmem.edu

*Readers are welcome to comment at <http://tinyurl.com/kkfe6e>*

## European bodies can help to tackle TB worldwide

**SIR** — We welcome your Editorial plea ('Orphan giant' *Nature* **459**, 1034; 2009) for stronger advocacy for tackling tuberculosis (TB), a shared global strategy and increased commitment to research and innovation. The emerging threat of drug-resistant TB in Europe, highlighted in a recent report from the European Academies Science Advisory Council (EASAC; [www.easac.eu](http://www.easac.eu)) could be an opportunity to bring European Union (EU) public-health objectives to bear on a shared global strategy.

EASAC was formed by the national science academies of EU member states to provide advice to policy-makers. Its report indicates that the EU has failed so far to respond adequately to the global TB threat, despite now being on the frontline for infection control. There is still an

opportunity for strategic leadership: the EU is in a good position to draw on its considerable strengths in science, to develop effective coordinated public-health capabilities and to contribute to solving the problem on a global scale.

The report recommends, for example, that the EU should improve its procedures for collecting, reporting and using its own TB-surveillance data. To help understand the molecular determinants of virulence and resistance, standardized characterization of pathogen strains and their drug sensitivity should be linked into user databases of genetic and clinical information. Better EU funding models for research and innovation should eventually generate new health-care products and services.

The domestic public-health objectives for the EU can be directly aligned with global policy requirements. For example, policy-makers worldwide need to extend the 'advanced market commitment' — under which governments and other sponsors pay in advance for development of vaccines — to cover TB diagnostics, drugs and vaccines. However, to avoid repetition of previous problems caused by lack of coordination among multiple initiatives, there must also be more effective interaction among EU institutions, intergovernmental and non-governmental organizations.

**Robin Fears** EASAC, The Royal Society, 6-9 Carlton House Terrace, London SW1Y 5AG, UK  
e-mail: robinfears@aol.com  
**Alimuddin Zumla** Centre for Infectious Diseases and International Health, University College London Medical School, London W1T 4JF, UK  
**Volker ter Meulen** EASAC and German Academy of Sciences Leopoldina, Postfach 110543, 6019 Halle (Saale), Germany

*Contributions to this page may be sent to [correspondence@nature.com](mailto:correspondence@nature.com). Please see the Guide to Authors at <http://tinyurl.com/373jsv>*

## BOOKS &amp; ARTS

# Africa's biotechnology battle

An influential book accuses Europe of keeping genetically modified crops out of Africa, but, by polarizing the debate, it undermines efforts to improve the continent's agriculture, warn **Ian Scoones** and **Dominic Glover**.

## Starved for Science: How Biotechnology Is Being Kept Out of Africa

by Robert Paarlberg

Harvard University Press: 2008. 256 pp.

\$24.95 (hbk), \$16.95 (pbk)

*Starved for Science* is a troubling polemic. Political scientist Robert Paarlberg argues that genetically modified (GM) crops could solve Africa's hunger and poverty, but that, through inadequate investment, external lobbying and stringent regulations, farmers are being deprived of the technology and prevented from achieving agricultural success. He lays the blame largely with European governments and non-governmental organizations for trying to foist their affluent values and precautionary sensibilities on Africa's poor.

The book has quickly become influential. Paarlberg was asked to speak about hunger alleviation in front of the US Senate Committee on Foreign Relations. The book's arguments were repeated in a major policy speech by Nina Fedoroff, science and technology adviser both to the US Secretary of State and to the administrator of the US Agency for International Development (USAID). Economist Paul Collier of the University of Oxford, UK, praised it in an article in the journal *Foreign Affairs*, and British peer Dick Taverne described it in a House of Lords debate as one of the most important books he had read in years.

But Paarlberg's account is one-sided. Just as the heated debate about GM crops had settled around a position that recognizes they can be useful in some circumstances yet are not a panacea, this book unhelpfully polarizes the matter once more.

Large parts of *Starved for Science* are uncontroversial. Paarlberg is correct in saying that there has been long-term underinvestment in African agriculture, especially in scientific research and technology development. And few would dispute that funding agricultural research offers high returns and is a key weapon in the fight against poverty and hunger. That such arguments have been ignored by policy-makers and aid programmes is also well recognized.

Where we take issue with the book is its explicit assertion that the only kind of science-based agriculture worth investing in is founded on biotechnology, and on genetic engineering in particular. In its narrow focus, *Starved for Science*



S. TORENN/PANOS

Transgenic crops are not a panacea in Africa, where low-tech farming methods can yield good results.

dismisses a slew of scientifically validated approaches to agriculture, including integrated pest and soil-fertility management, 'low-input' techniques that reduce reliance on synthetic fertilizers and pesticides, and even other forms of biotechnology. Yet such methods have performed well in African contexts (J. N. Pretty *et al. Environ. Sci. Technol.* **40**, 1114–1119; 2006).

Paarlberg's book reduces the vast and varied continent and its farmers to a series of gloomy generalizations. But a detailed look at the data reveals numerous successes. For example, in northern and western Africa, agricultural production per capita increased by more than 40% between 1981–83 and 2003–05, and total output value increased by an amount equal to that seen in Asia after the 1960s Green Revolution (see <http://tinyurl.com/lgkosx>).

Another success is that of smallholder farmers who produce hybrid maize in Zimbabwe and Kenya and cassava and cotton in West Africa (see <http://tinyurl.com/mhaebb>). Results can seem mixed overall because each technology must perform within a particular social, economic, institutional and market setting.

Paarlberg also pays too little attention to the substantial efforts that have got under way recently in Africa. International donors have, for example, lent their support to two important strategic initiatives for agriculture: the Alliance

for a Green Revolution in Africa and the African Union's Comprehensive Africa Agriculture Development Programme. Meanwhile, agricultural biotechnology has received significant backing from within Africa itself — including a thoughtful assessment from the African Union's high-level panel on biotechnology (see <http://tinyurl.com/lnc46j>). GM crop research is also under way in countries as diverse as South Africa, Burkina Faso and Malawi.

Paarlberg argues that GM crops are being "kept out" of Africa because European lobby groups have forced the imposition of "stifling regulations" based on "extreme precaution". His

roll-call of bad guys is long, from Food First, Greenpeace and the International Federation of Organic Agriculture Movements, to the United Nations and the Ford Foundation. All are blamed

for preventing a "science-based escape from rural poverty".

In fact, the pro-GM lobby has been every bit as active, bombarding decision-makers and media organizations with slick marketing materials and free trips to their corporate headquarters. The US government has sponsored schemes in Africa that provide biosafety training programmes for regulators and that promote model legal frameworks. Such projects include the US Foreign Agriculture Service's scientific exchange programmes and the

**"Players on both sides of the GM debate have fought a fierce tug-of-war over policy."**



Agricultural Biotechnology Support Project, part of the USAID Collaborative Agriculture Biotechnology Initiative.

Paarlberg's claim that external, anti-GM views have been the main influence on decision-making by national governments in Africa is not substantiated. Instead, international players on both sides of the GM debate have fought a fierce tug-of-war over policy, with African regulators and policy-makers often left as unwilling bystanders.

Meanwhile, on the ground, detailed, site-specific evidence on the performance of GM technologies indicates that a farmer's ability to reap the potential benefits depends on a range of technical, agronomic and institutional factors (see <http://tinyurl.com/ksbfxo> and <http://tinyurl.com/krmzxx>). For instance, the transgenic trait needs to be available in crop varieties that can perform in constrained environments. A good yield depends heavily on favourable soils and irrigation, which the poorest farmers typically lack. As the experiences of smallholder Bt-cotton farmers in South Africa have demonstrated, GM crop technology also needs to be supported by infrastructure and institutions if it is to benefit the poorest people.

These findings are in contrast to the triumphalism of reports that show the spread of GM crops around the world, such as that released annually by the International Service for the Acquisition of Agri-biotech Applications. Studied closely, the 2008 report shows that only 8 of the 25 countries that grew GM crops planted more than a million hectares. Almost 80% of the global GM crop of 125 million hectares was grown in just three countries: 62.5 million hectares in the United States, 21 million hectares in Argentina and almost 16 million hectares in Brazil. Moreover, the GM crops that have been commercialized to date are mostly insect-resistant Bt varieties of maize and cotton and herbicide-tolerant varieties of soya bean, designed for and mainly used by large-scale commercial farmers.

African agricultural policy-makers have some difficult decisions to make. Biotechnology will surely be part of the mix of approaches required for the future, as indicated both in the World Bank's 2008 World Development Report on agriculture and in the 2008 International Assessment of Agricultural Knowledge, Science and Technology for Development. But big uncertainties remain — including how farmers will gain access to markets where GM products are currently restricted and the potential risks of GM technologies to the environment

or health. An informed 'wait-and-see' stance thus makes sense.

What of the future? One of the pivotal arguments in *Starved for Science* is that promising pipeline technologies and longer-term research are also being held back. To make his case, Paarlberg cites the effort to develop drought-tolerant

GM maize, a major programme of the African Agricultural Technology Foundation. Supported by the Bill & Melinda Gates Foundation, it is working with a range of public and private research and development organizations. This broad initiative involves

conventional breeding, genomics applications and genetic-marker-based selection as well as genetic modification. Yet Paarlberg zeroes in on the GM solution, maintaining that this is where the necessary breakthroughs will happen.

Blue-skies research into future agricultural techniques is essential. But inflating expectations has major downsides. As occurred with medical biotechnology, hype can distort innovation. It diverts funds from other research and narrows the focus of study to

genetics rather than taking into account the wider environmental, behavioural and synergistic dynamics (P. Nightingale and P. Martin *Trends Biotechnol.* 22, 546–569; 2004). A similar process will occur in agricultural science unless we retain a balanced perspective of the options available.

A dogmatic and unscientific stance on GM crops — whether for or against — helps no one, least of all African farmers. A more evidence-based approach than Paarlberg's is needed — one that should foster diverse development pathways for agriculture underpinned by high-quality scientific research and attuned to particular circumstances.

**Ian Scoones** is a professorial fellow at the Institute of Development Studies and co-director of the ESRC STEPS Centre, University of Sussex, Brighton BN1 9RE, UK. **Dominic Glover** is a postdoctoral researcher in the Technology and Agrarian Development Group, Wageningen University, 6706 KN Wageningen, the Netherlands. e-mail: i.scoones@ids.ac.uk

For additional references, see <http://tinyurl.com/lfp2x3>.

**"Blue-skies research into future agricultural techniques is essential."**

## The world in a grain of sand

**Sand: A Journey through Science and the Imagination**  
by Michael Welland  
Oxford University Press: 2009. 352 pp.  
£18.99

On an island off the southwestern coast of Turkey, called Sedir Adasi, lies a stunning stretch of white sand known as Cleopatra's Beach. According to legend, Cleopatra's lover Mark Antony made the beach for her as a lavish gift by shipping bargeloads of sand from Egypt to the island some 2,000 years ago. There may be a grain of truth in this story, writes Michael Welland in *Sand* — the "exotic creamy white oolith" granules occur nowhere else on the island but match those on Egyptian coastal beaches west of Alexandria.

A modern mystery of sand is the origin of the silica used in making silicon for the electronics industry. After much research, Welland drew a blank. The handful of technology companies who dominate this crucial market would not disclose the source of their raw material; all the author could deduce was that silicon chips are made from "sand that has already been ultrapurified by nature: quartzite".

A popular book by a long-time professional geologist could easily have been worthy but dry. Yet *Sand* is serious and entertaining; it is the work of someone who has been in love with the stuff since he built sandcastles as a child. Nothing like it has been published before, even by the larger-than-life pioneer of sand studies, Ralph Bagnold, who serves as Welland's inspiration.

Bagnold was a British army officer who saw the Sphinx excavated in the 1920s from tonnes of preservative sand laid down over millennia. He became a desert explorer in Egypt and a formidable adversary behind enemy lines in the Second World War. He was also a scientist, and built a wind tunnel at Imperial College London to investigate the behaviour of sand grains under controlled conditions. In 1941 he published *The Physics of Blown Sand and Desert Dunes*, a classic study (see *Nature* 457, 1084–1085; 2009) that was later used by NASA to plan how its rovers should deal with Martian sand.

But Welland stretches beyond Bagnold and his deserts. *Sand* begins on the small scale, with the counter-intuitive physics of granular behaviour. Strangely, dry sand behaves like a liquid, whereas damp sand is more like a solid, provided that it is not too wet. Welland explains

PHOTO SCALA, FLORENCE/EGYPTIAN MUS., CAIRO

the stability and collapse of sand piles, and the forensic study of sand to solve murders. This leads to a discussion of the weird and wonderful microscopic life forms — such as rotifers, tardigrades, gastrotrichs, turbellarians and others — that have evolved to flourish in the spaces between shifting, abrasive sand grains. Such an environment may become the last refuge for life in the event of catastrophic climate change. Welland then addresses sand on a progressively larger scale: along the course of meandering rivers, in the formation of beaches, in deserts and mid-ocean sandbanks, in the formation of Old Red Sandstone rocks found extensively from the Arctic to the Gulf of Mexico and, finally, in sand found beyond Earth.

Welland asks how sand grains have helped humans to conceive the Universe and the infinite. He begins with Archimedes who, in the third century BC, calculated that  $10^{63}$  grains of sand would fill the Universe to the outermost sphere of the fixed stars. The author also discusses, and attractively illustrates, how sand has been used artistically in many cultures — from sand painting by Australian aboriginal communities and the North American Navajo, to Zen sand gardens in Japan and the sand sculptures created by digital methods at the Media Lab at the Massachusetts Institute



Green desert glass from Libya was carved into a scarab beetle for Tutankhamun's necklace — but how did the silica glass form?

of Technology in Cambridge. One fascinating photograph shows the 'Earthquake Rose', the pattern made by a desktop toy, a sand-tracing pendulum, during a strong earthquake in Washington state in 2001.

A personal epilogue provides the reader

with a genuine mystery. In 1922, the discovery of Tutankhamun's tomb in Egypt yielded a famous necklace with a scarab beetle carved from a glowing, yellow-green, gem-like material, which its discoverer Howard Carter did not recognize. In the 1990s, the material was shown to be a unique silica glass, 28 million years old and 98% pure, from a particular part of the Libyan desert.

Welland travels to this desolate spot and cherishes the glassy samples he finds glittering on the dunes. But, he muses, what could have produced heat that was intense enough to fuse silica? A strike from a meteorite or lightning can be ruled out because of the lack of visible impact craters or hollow fulgurite tubes, respectively. He speculates that the cause might have been an air burst from the impact of an asteroid with the atmosphere, similar to that at Tunguska in Siberia, Russia, in 1908.

With irresistible ideas such as this, Welland provides an appealing blend of science and the imagination, worthy

of the famous vision of the poet William Blake: "To see a world in a grain of sand".

Andrew Robinson is the author of *Earthshock* and *The Story of Measurement*. He is a visiting fellow of Wolfson College, Cambridge CB3 9BB, UK.

e-mail: ar471@cam.ac.uk

## D-Day forecast fictionalized

### Turbulence

by Giles Foden

Faber and Faber: 2009. 368 pp. £16.99

Fluid dynamics and weather prediction seem unpromising material for a gripping story. But Giles Foden has ingeniously dramatized what is perhaps the most important weather forecast ever made: that for the D-Day landings, the invasion of continental Europe at Normandy by the Allied forces towards the end of the Second World War. The result is a compelling tale, with meteorologists as the unlikely heroes and the turbulence of the title providing the central metaphor.

General Dwight D. Eisenhower, in command of the operation, had to be sure that the crossing of the English Channel would not be disrupted by bad weather. And he needed that assurance five days in advance — a length

of time that stretches today's forecasting techniques to their limit, and which was beyond the capability of meteorologists in 1944. Add to that the need for a low tide to evade the German sea defences, the task confronting the Allies' weather experts seemed insurmountable.

In *Turbulence*, Foden tells this story through the eyes of a fictional character, Henry Meadows, a young academic attached to the forecasting team that is led, as it was in reality, by the British meteorologist James Stagg. The decision-making process of Stagg and his fractious colleagues, including the brash American entrepreneur Irving Krick and the arrogant but astute Norwegian Sverre Petterssen, occupies the last third of the book. Stagg and Petterssen each published their own accounts in the 1970s. Although Foden's tale is steeped in that history, he allows Meadows to make the crucial, unrecognized contribution.

The story begins with Meadows being sent to rural Scotland to glean clues about forecasting from the leading authority of the day, the difficult genius Wallace Ryman. Ryman is a fictionalized version of Lewis Fry Richardson, known for his work on fractal coastlines, who Foden rightly calls "one of the unsung heroes of British science". Like Richardson, Ryman is a Quaker whose experiences in the Friends' Ambulance Unit during the First World War convinced him that war must be avoided. He shuns collaboration with the military, so Meadows must pursue his mission by stealth — an attempt that he mostly bungles.

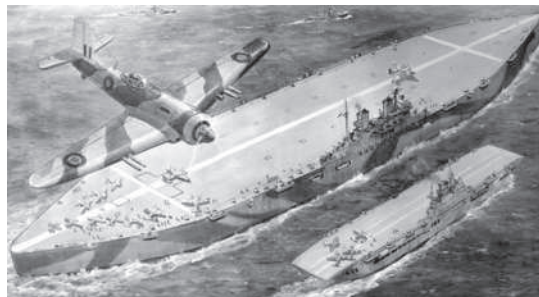
In Scotland, Meadows runs into the second wayward genius in the book, this time without a pseudonymous disguise: Geoffrey Pyke, the man behind the Habbakuk project to build aircraft carriers out of ice reinforced with wood pulp. This 'Pykrete' is extraordinarily resistant to impacts and melting. Also making a fleeting appearance is Julius Brecher, a doppelgänger for biochemist Max Perutz, who assisted Pyke during the war. This part of the plot would seem far-fetched if you didn't know that it is true.



ILLUSTRATED LONDON NEWS/MARY EVANS

Yet the Habbakuk story, however entertaining, seems tacked on. It is not central to the plot even though it supplies a framing device: Meadows recounts his wartime exploits while on board an ice ship built in 1980 for an Arab sheikh. When Meadows joins Pyke in wartime London only to see the Habbakuk project terminated, it feels like a cul-de-sac. One could carp at a few other points of creaky plotting or narrative, but that seems churlish given how splendidly the book animates a buried story of scientific endeavour and triumph.

One must also ask whether the author succeeds in creating scientists who are fully fleshed individuals. Foden complicates his task by making Meadows callow and withdrawn as a result of a childhood trauma in Africa.



Secret wartime plans included building giant ships from ice.

Meadows's fixation on his research and his social awkwardness could make him a caricature of the diffident scientist. Brecher also refracts everything through the prism of his own research topic of blood, while Ryman is the crabby boffin and Pyke the dotty one.

But Foden has a motive in shaping Meadows this way, using him to capture a sense of the dour, buttoned-up character of wartime Britain. And unlike so many fictional scientists, Meadows is believable: his discourses on turbulence and hydrodynamics are assured, even uncompromising, without the breezy 'beginner's guide' flavour that is the usual hallmark of undigested authorial research. Here Foden had the immense benefit of advice from his father-in-law, Julian Hunt, a leading expert on turbulence and meteorology and, fittingly, a recipient of the Lewis Fry Richardson medal for nonlinear geophysics. Skilfully balancing fact and fiction, *Turbulence* is dramatic, intelligent and convincing. ■

**Philip Ball** is a freelance writer. His most recent books form a trilogy called *Nature's Patterns*.

## Bling of the Bactrians

**Afghanistan: Hidden Treasures from the National Museum, Kabul**

Metropolitan Museum of Art, New York  
Until 20 September

Desire for gold has driven people out of their homes and out of their minds. So Soviet archaeologist Viktor Sarianidi cannot have been surprised when a crowd gathered to gawk at a mound he was excavating in northern Afghanistan in 1978. Tillya Tepe, the Hill of Gold, dates to the first century AD, when the land was known as Bactria, and contained the graves of six nomads — a chieftain and five women — buried with more than 20,000 golden and bejewelled belongings, some of which are now on show at the Metropolitan Museum of Art in New York.

Sarianidi sent the treasures to the National Museum in Kabul and returned to Moscow. Then came the wars. The Soviet army invaded Afghanistan in 1979, the National Museum was nearly destroyed by shelling in 1994, and in 2001 it was ransacked by the Taliban. Yet museum guards had hidden the treasures in secret vaults in the presidential palace and kept their location secret for some 25 years.

*Afghanistan* portrays the tremendous challenges of preserving a country's heritage in the face of war. "All of these artefacts were supposed to have been lost," says curator

and archaeologist Fredrik Hiebert, who was invited by the Afghans in 2003 to catalogue the crates when they were rediscovered. "Every time we opened a box, it was like a miracle." Along with the Tillya Tepe gold, the guards had concealed nearly all of the treasures from Kabul's museum.

The exhibition displays artefacts from four archaeological sites, each focusing on a major stage or civilization in Afghanistan's history. They reveal the multiple influences of the Roman, Indian, Greek and Chinese cultures that infiltrated the ancient nation. A second-millennium gold bowl unearthed at the Bronze Age settlement of Tepe Fullol in the northeast of the country is decorated with

bearded bulls, a motif from distant Mesopotamia. The third-century-BC Greek-style city of Ai Khanum, founded after Bactria's conquest by Alexander the Great, yielded two sophisticated sundials: one, carved from limestone in the form of a throne balanced on two lions' legs, was designed for Ai Khanum's latitude; the other, a unique cylindrical design, was calibrated for ancient Syene (Aswan) in Egypt. Another mechanical marvel comes from Begram, a city on the Silk Road that thrived in the first and second centuries AD. A green bronze basin is filled with sinuous metal fish, their moveable fins and tails wired to small weights that would make them 'swim' when the bowl was filled with water.

But the gold of Tillya Tepe is the most alluring. Its pastoralist owners ploughed their profits from sheep- and goat-herding into shimmering trophies ornamented with symbols of diverse cultures: Aphrodite with an Indian dot on her forehead, a dagger handle topped with a Siberian bear, Chinese-style boot buckles, Roman coins, resplendent gold jewellery and a folding gold crown composed of five 'trees' adorned with rosettes and birds. That such valuables survived "is an amazing testament to the Afghans' ability to keep a secret", Hiebert says. "The Communists came through, the mujahedin came through, the Taliban came through, and these poor underpaid museum people didn't tell them, ever. I want to tell that story to my children." ■

**Josie Glausiusz** is a writer based in New York.

e-mail: [jg@planetjosie.net](mailto:jg@planetjosie.net)



Museum staff hid this folding gold crown from Afghanistan's looters for years.

MUSÉE GUIMET/T. OLIVIER

## NEWS &amp; VIEWS

## MATHEMATICAL PHYSICS

## A tight squeeze

Henry Cohn

**How can identical particles be crammed together as densely as possible? A combination of theory and computer simulations shows how the answer to this intricate problem depends on the shape of the particles.**

We all know from experience with luggage just how difficult it is to pack objects efficiently into a limited space. These difficulties are even greater when huge numbers of objects, such as grains of wheat, are involved. From Luke the evangelist's reference to "a good measure, pressed down, shaken together and running over" all the way to modern disclaimers that contents may have settled during shipping, nobody has been able to analyse how to achieve the densest possible packings. On page 876 of this issue, Torquato and Jiao describe<sup>1</sup> remarkable computer-simulation results that show how subtle this problem can be, while offering new hope for understanding important cases.

Identical, perfect spheres are among the simplest objects to pack. It is not difficult to guess how — just look at the way cannonballs are stacked at war memorials. But theoretical analysis of the problem presents profound difficulties that were overcome only recently by Thomas Hales<sup>2</sup>, nearly four centuries after the answer was conjectured by Johannes Kepler<sup>3</sup>. Of course, most granular materials do not consist of spherical grains, and this complicates matters tremendously. For most grain shapes we cannot guess or even closely approximate the answer, let alone prove it, and it is difficult to develop even a qualitative understanding of the effects of grain shape on packing density.

Instead of perfect spheres, Torquato and Jiao study<sup>1</sup> packings of the five Platonic solids: the tetrahedron, cube, octahedron, dodecahedron and icosahedron (see Fig. 1 on page 877). These are the simplest and most symmetrical polyhedra. Needless to say, nobody expects the grains in physical materials to have these precise shapes, but they are a beautiful test case for understanding the effects of corners and edges and the role of symmetry.

The cube-packing problem is easy — cubes can fill space completely. But the densest packings of the other Platonic solids are much less obvious. They do not tile space — fill space with no gaps or overlaps — despite Aristotle's incorrect assertion<sup>4</sup> that tetrahedra do. In their simulations, Torquato and Jiao find a striking difference between two cases: the octahedron, dodecahedron and icosahedron have central symmetry (that is, each remains

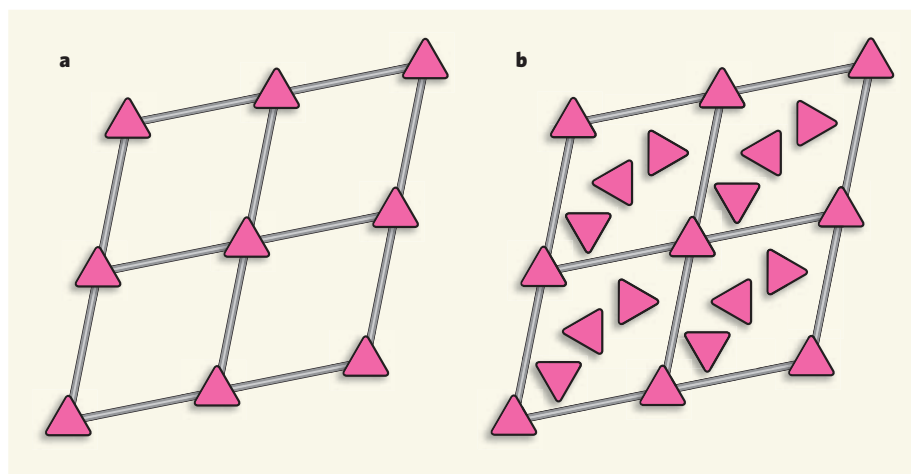


**Figure 1 | Two-dimensional view of packings.** **a**, In a two-dimensional Bravais lattice packing, there is one particle per lattice cell, and the particles are all aligned with each other. In this illustration, the particle is represented by a triangle and is located in the upper left corner of the cell. **b**, In a general, non-Bravais lattice packing, there are multiple particles per cell, and they can be arbitrarily rotated. In their computer simulations, Torquato and Jiao<sup>1</sup> show that the best packings of centrally symmetric Platonic solids turn out to be Bravais lattice packings, which is remarkable given how restricted such packings are.

unchanged by a 180° rotation about a point at its centre). But the tetrahedron does not have central symmetry, and this turns out to be the crucial distinction.

In the centrally symmetric cases, Torquato and Jiao show that the highest-density packings belong to the simplest kind, called Bravais lattice packings (Fig. 1a), although this constraint is never directly imposed on their simulations. In such arrangements, all the particles are perfectly aligned with each other, and the packing is made up of lattice cells that each contain only one particle. The densest Bravais lattice packings had been determined previously<sup>5,6</sup>, but it had seemed implausible that they were truly the densest packings, as Torquato and Jiao's simulations and theoretical analysis now suggest. By contrast, for the tetrahedron it has long been known that Bravais lattice packings are far from optimal, and in this case the authors achieve a record density: they find a non-Bravais lattice configuration (Fig. 1b) that fills up 78.20% of the space available (an improvement over the previous record<sup>7</sup> of 77.86%, or 36.73% for Bravais lattices<sup>8</sup>).

To find their packings, Torquato and Jiao

use a powerful simulation technique. Starting with an initial guess at a dense packing, they gradually modify it in an attempt to increase its density. In addition to trying to rotate or move individual particles, they also perform random collective particle motions by means of deformation and compression or expansion of the lattice's fundamental cell. With time, the simulation becomes increasingly biased towards compression rather than expansion. Allowing the possibility of expansion means that the particles are initially given considerable freedom to explore different possible arrangements, but are eventually squeezed together into a dense packing.

The new tetrahedron packing is a variant of an ingenious construction found by Chen last year<sup>7</sup>. Using physical models, she observed that tetrahedra pack well when arranged in a form Torquato and Jiao call 'wagon wheels': wheels of five tetrahedra sharing an edge, with the wheels joined in pairs at right angles (see Fig. 3a on page 878). How best to arrange these pairs of wagon wheels is not clear, but Chen used a computer algebra system (a software program that manipulates mathematical formulae)



to optimize their placement and achieved a density of 77.86%, which is a vast improvement over the previous record<sup>9</sup> of 71.75%. The authors' simulations<sup>1</sup> suggest that Chen's solution was nearly, but not quite, optimal.

Although Torquato and Jiao's improvement on Chen's packing is noteworthy, perhaps the most intriguing implication of their work is the apparent optimality of Bravais lattice packings for the centrally symmetric Platonic solids (as well as generalizations such as Archimedean polyhedra). This part of the work may seem less exciting, because the densest packings turned out to be known already. However, in a field with few clear organizing principles, this latest insight into the part played by symmetry might take on the role of a twenty-first-century Kepler conjecture. It will surely inspire many future research papers, and with any

luck we won't have to wait 400 years for a full understanding of it.

Henry Cohn is at Microsoft Research New England, One Memorial Drive, Cambridge, Massachusetts 02142, USA.  
e-mail: cohn@microsoft.com

1. Torquato, S. & Jiao, Y. *Nature* **460**, 876–879 (2009).
2. Hales, T. C. *Ann. Math.* **162**, 1065–1185 (2005).
3. Kepler, J. *Strena Seu de Nive Sexangula* [A New Year's Gift of Hexagonal Snow] (Godfrey Tampach, 1611).
4. Aristotle *On the Heavens* Book III, Pt 8 (transl. Guthrie, W. K. C.) (Harvard Univ. Press, 1939).
5. Minkowski, H. *Nachr. Akad. Wiss. Göttingen Math. Phys. Kl. II*, 311–355 (1904).
6. Betke, U. & Henk, M. *Comput. Geom.* **16**, 157–186 (2000).
7. Chen, E. R. *Discrete Comput. Geom.* **40**, 214–240 (2008).
8. Hoyleman, D. J. *Bull. Am. Math. Soc.* **76**, 135–137 (1970).
9. Conway, J. H. & Torquato, S. *Proc. Natl Acad. Sci. USA* **103**, 10612–10617 (2006).

## STEM CELLS

# Escaping fates with open states

Robert J. Sims III and Danny Reinberg

**The ability of embryonic stem cells to give rise to any cell type relies on a remodelling protein that maintains open chromatin. But the chromatin landscape of these cells may be more complex than previously thought.**

Embryonic stem (ES) cells are ideal models for studying the molecular principles that dictate cell fate. ES cells can self-renew and form every type of cell in an organism — a property called pluripotency. It is well established that DNA-binding proteins set the stage for determining cell-type specificity by orchestrating complex patterns of gene expression<sup>1</sup>. However, DNA is tightly assembled with accessory proteins into a structure called chromatin, which limits its accessibility to regulatory proteins. Chromatin can be loosely packed, or 'open', allowing DNA-binding proteins ready access to the genome. Alternatively, it can be densely compacted, or 'closed', making the DNA relatively inaccessible<sup>2</sup>. On page 863 of this issue, Gaspar-Maia *et al.*<sup>3</sup> provide evidence that chromatin structure is intimately connected with cell fate by showing that highly accessible chromatin is essential for the unique properties of stem cells.

ES cells have to achieve a delicate balance of gene regulation: they must suppress genes that result in premature differentiation, while maintaining expression of genes that allow self-renewal. Previous work<sup>4,5</sup> has shown that ES cells maintain an open chromatin structure and express a large proportion of their genes. Differentiation of ES cells into mature cell types, such as neural cells, is accompanied by closing of chromatin<sup>4</sup> and by widespread gene silencing<sup>5</sup>. As chromatin structure strongly dictates whether or not genes can be expressed, Gaspar-Maia and colleagues<sup>3</sup> examined the

role of enzymes that can modify this structure in keeping ES cells pluripotent.

The authors found that decreasing the amounts of a chromatin-remodelling protein called Chd1 impaired ES-cell proliferation and reduced expression of the DNA-binding transcription factor Oct4, which is a master regulator of ES-cell function. Chd1 has previously been shown to facilitate gene expression<sup>6</sup>, consistent with its role in Oct4 regulation. However, in this case<sup>3</sup> its depletion did not result in a global decrease in gene activity, as would be expected for a factor widely associated with active gene transcription. Instead, ES cells lacking Chd1 upregulated the expression of genes involved in nervous-system development, and they tended to differentiate into cells of the neuronal lineage<sup>3</sup>.

Whether chromatin structure is accessible or compact is determined in part by chemical modification of its core protein components, histones. For example, trimethylation of lysine 4 on histone H3 (H3K4me3) is a marker of open chromatin. Chd1 contains a motif that recognizes H3K4me3 (refs 7, 8) and indeed, when Gaspar-Maia and colleagues performed genome-wide studies of Chd1 localization on chromatin in normal ES cells, they found that Chd1 co-localizes with H3K4me3. When the authors depleted ES cells of Chd1, they observed an increase in the proportion of condensed chromatin in these cells. On the basis of their results, they surmise that Chd1 maintains an open chromatin structure in ES cells,

which is required for their pluripotency.

The interplay between Chd1, H3K4me3 and open chromatin (Fig. 1) highlighted by Gaspar-Maia and colleagues<sup>3</sup> is reinforced by findings from other studies<sup>9–13</sup>. H3K4me3 is incorporated into chromatin during active transcription<sup>9</sup>; therefore, promotion of gene expression by Chd1 might ensure that chromatin is rich in H3K4me3 and maintained in an open conformation. Chd1 has also been shown<sup>10</sup> to regulate DNA-replication-independent deposition of chromatin enriched in H3K4me3. Moreover, binding of Chd1 to chromatin may protect H3K4me3 from turnover through histone demethylation. This histone mark also prevents the binding of factors that mediate gene silencing, such as the NuRD histone-modifying complex<sup>11,12</sup> and the DNA methyltransferase subunit DNMT3L<sup>13</sup>. Loss of H3K4me3 would therefore allow increased chromatin compaction induced by NuRD and DNA methylation, highlighting the need to maintain a correct balance of H3K4me3. In addition, the histone methyltransferase Suv39H1 facilitates the formation of silent chromatin domains by methylating lysine 9 on histone H3. Suv39H1 is known to act on histones that lack methylated H3K4 (Fig. 1); thus, open chromatin would serve to counteract this repressive activity.

What Gaspar-Maia and colleagues' work<sup>3</sup> does not explain is how, despite depletion of Chd1, global ES-cell gene activation is largely unaffected while genes that drive differentiation towards the neuronal cell fate are upregulated. It is possible, though, to reconcile these findings by taking into account Chd1-mediated regulation of the distribution of H3K4me3. For instance, the p400/TIP60 complex, which turns genes on or off by changing the composition of chromatin, also seems to bind H3K4me3 (ref. 14). When the amount of H3K4me3 is reduced in ES cells, binding of p400/TIP60 to its chromatin targets is impaired<sup>14</sup>. In this way, the perturbation of H3K4me3 in the absence of Chd1 could impair gene silencing through its effects on factors such as p400/TIP60. Although unusual for somatic cells (non-gametes), in ES cells, H3K4me3 may be associated with silencing of genes at focal locations throughout chromatin<sup>15</sup>. Alternatively, widespread gene reactivation could be a consequence of indirect effects of the downregulation of ES-cell master regulatory factors such as Oct4.

Studying differentiated cells undergoing reprogramming to a pluripotent state<sup>16</sup> allows insight into the core properties of stem-cell chromatin. Cells that fail reprogramming reactivate subsets of stem-cell-related genes, but simultaneously fail to repress lineage-specific transcription factors<sup>16</sup>. Thus, the correct mix of gene expression to achieve stem-cell properties may depend more on local alterations in chromatin structure than on global chromatin reorganization. Gaspar-Maia *et al.*<sup>3</sup> show that Chd1 loss prevents the reprogramming of somatic

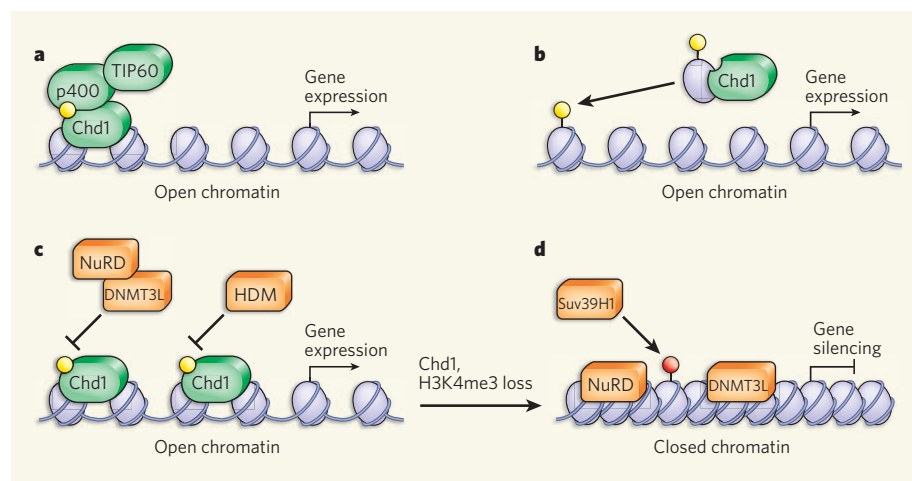


**Figure 1 | Chd1 and open chromatin.** The chromatin-remodelling protein Chd1 may maintain open chromatin in various ways in ES cells. **a**, Chd1 facilitates active transcription, which induces the placement of H3K4me3 (yellow), a histone mark conducive to open chromatin structure. The p400/TIP60 complex supports ES-cell function by binding to H3K4me3 and regulating gene expression. **b**, Chd1 may promote deposition of H3K4me3 in a DNA-replication-independent manner, maintaining open chromatin. **c**, H3K4me3 prevents binding of factors that promote closed chromatin and that mediate gene silencing, such as the NuRD histone-modifying complex and the DNA methyltransferase subunit DNMT3L. Chd1 binding may also protect H3K4me3 from turnover by histone demethylases (HDMs). **d**, Gaspar-Maia *et al.*<sup>3</sup> show that, on removal of Chd1, chromatin in ES cells is more compacted. This may be due to loss of H3K4me3, allowing binding of NuRD and DNMTs. Also, the histone methyltransferase Suv39H1 facilitates formation of silent chromatin by methylating lysine 9 on histone H3 (red). Suv39H1 preferentially methylates histones that lack H3K4me. Compaction of chromatin is associated with ES-cell differentiation, possibly due to the silencing of genes that are essential for maintaining pluripotency.

cells to a pluripotent state. A small imbalance in chromatin structure, induced by loss of Chd1, might reorganize boundaries between open and closed chromatin states; this could result in failure to maintain the appropriate

mix of specific gene expression and gene silencing, sending the ES cell down a path of differentiation.

Could the increased amount of closed chromatin observed in ES cells lacking Chd1 (ref. 3)

stem from focal changes in chromatin at genes encoding cell-lineage-specifying factors, rather than representing a genome-wide alteration in chromatin structure? Current assays do not accurately measure the physical properties of chromatin structure in cells, and novel techniques to analyse higher-order chromatin structure *in vivo* are needed to answer such complex questions. It is clear, however, that the careful maintenance of an open chromatin structure, whether global or local, by factors such as Chd1, is crucial for the preservation of pluripotency.

Robert J. Sims III is in the Department of Biology, Constellation Pharmaceuticals, Cambridge, Massachusetts 02139, USA. Danny Reinberg is at the Howard Hughes Medical Institute, Department of Biochemistry, New York University School of Medicine, New York 10016, USA.

e-mails: robert.sims@constellationpharma.com; reinbd01@nyumc.org

1. Jaenisch, R. & Young, R. *Cell* **132**, 567–582 (2008).
2. Trojer, P. & Reinberg, D. *Mol. Cell* **28**, 1–13 (2007).
3. Gaspar-Maia, A. *et al.* *Nature* **460**, 863–868 (2009).
4. Meshorer, E. *et al.* *Dev. Cell* **10**, 105–116 (2006).
5. Efroni, S. *et al.* *Cell Stem Cell* **2**, 437–447 (2008).
6. Sims, R. J. III *et al.* *Mol. Cell* **28**, 665–676 (2007).
7. Sims, R. J. III *et al.* *J. Biol. Chem.* **280**, 41789–41792 (2005).
8. Flanagan, J. F. *et al.* *Nature* **438**, 1181–1185 (2005).
9. Pavri, R. *et al.* *Cell* **125**, 703–717 (2006).
10. Konev, A. Y. *et al.* *Science* **317**, 1087–1090 (2007).
11. Zegerman, P., Canas, B., Pappin, D. & Kouzarides, T. *J. Biol. Chem.* **277**, 11621–11624 (2002).
12. Nishioka, K. *et al.* *Genes Dev.* **16**, 479–489 (2002).
13. Ooi, S. K. *et al.* *Nature* **448**, 714–717 (2007).
14. Fazio, T. G., Huff, J. T. & Panning, B. *Cell* **134**, 162–174 (2008).
15. Berstein, B. E. *et al.* *Cell* **125**, 315–326 (2006).
16. Mikkelsen, T. S. *et al.* *Nature* **454**, 49–55 (2008).

## ECOLOGY

# Elementary factors

Josep Peñuelas and Jordi Sardans

**The identification of a general connection between biogeochemistry and the structure of food webs would constitute a considerable advance in understanding ecosystems. Ecologists are on the case.**

Organisms are the products of chemical reactions, and their growth depends on the availability of various elements, especially carbon, nitrogen and phosphorus. The growth-rate hypothesis<sup>1</sup> links the relative element content of organisms to their growth rate, the idea being that fast-growing organisms need relatively more P-rich RNA, the main component of the protein-producing ribosome, to support rapid protein synthesis. Consequently, ecosystem conditions that produce organic matter with low C:P and N:P ratios would be expected to result in lower protein:RNA ratios, higher adaptive growth rates, more efficient energy transfer through a food web, and increased biomass of

large-bodied animals relative to that of small-bodied animals<sup>1</sup>. In *Global Change Biology*, Mulder and Elser<sup>2</sup> offer a first test of this association between C:N:P stoichiometry and faunal size spectrum for soil food webs.

Elser *et al.*<sup>3</sup> had previously proposed the growth-rate hypothesis (GRH) to explain differences in C:N:P ratios among zooplankton species; support for the hypothesis in that context soon appeared<sup>4</sup>. Subsequent investigations<sup>5,6</sup> revealed significant relationships between body C:N:P stoichiometry and growth rate in diverse groups of organisms. The scaling up of studies to the community level related the elemental stoichiometries of water environments and of body composition

to the body-size spectrum of food webs in aquatic ecosystems<sup>7</sup>. But investigations of such relationships in terrestrial ecosystems are only now beginning<sup>8</sup>.

Mulder and Elser<sup>2</sup> analysed the mass-abundance and body-size spectra of all soil invertebrates, fungi and bacteria in 22 grassland soils in the Netherlands. They find that the higher the availability of P in the soil (the lower the C:P ratio), the steeper is the slope of the faunal biomass size spectrum — that is, the biomass of large-bodied invertebrates becomes greater relative to that of small invertebrates. This relationship has broad implications because soil invertebrates of different sizes have different effects on soil processes. The relationship connects biogeochemistry with the structure of food webs, and — if it holds true in different settings — opens a way to developing more general laws of ecosystem structure and dynamics.

So Mulder and Elser's results<sup>2</sup> are promising. Nonetheless, the association between soil-element stoichiometry and the body-size spectrum of the food web might not simply result from faster growth of different organisms in the food web in response to low C:P



and protein:RNA ratios, as predicted by the GRH. As Mulder and Elser point out, other factors may be involved. For example, the shift in body-size spectrum might have resulted from the change from one main food resource (bacterial cells) to another (fungal remains) that Mulder and Elser found in their soils as C:P ratios decreased. The shift between these two different energy channels<sup>9</sup>, which differ in both productivity and turnover rate, could have driven the shift in invertebrate dominance from bacterium-feeding nematodes to microarthropods, which have different feeding habits and sizes. The link between C:P ratio and body-size spectrum could result from the microfauna (nematodes) coping better with P-limited conditions than the mesofauna (microarthropods).

Tests of the GRH are being extended to plants, which present a much more variable stoichiometry than animals or microbes<sup>10</sup>. In an investigation in pines just published in *Ecology Letters*, Matzek and Vitousek<sup>11</sup> find no link between foliar N:P ratio and growth rate. In comparing leaves of the same species growing at different rates as a result of different nutrient conditions, they found that the faster-growing plants had lower protein:RNA ratios but not consistently lower N:P ratios; and in comparing several species with different growth rates, they found that there was no relation between growth rate and foliar N:P or protein:RNA ratios. Their results thus deviate from the predictions of the GRH.

Matzek and Vitousek<sup>11</sup> conclude that plants adjust the balance of protein and RNA to favour either speed or efficiency of protein synthesis, depending on whether nutrient availability is high or low. According to this thinking, the balance of protein and RNA is not dictated only by the stoichiometry of elements in the leaf, nor does this balance, in isolation, dictate leaf N:P stoichiometry. In fact, the stoichiometry of plants might be decoupled from metabolic and physiological needs by storage of nutrients in vacuoles, obscuring the stoichiometric differences that would be expected given the protein:RNA ratios observed. Thus, the links between N:P stoichiometry and growth capacity in plants would seem not to be ruled by protein:RNA ratio alone.

Further assessment of the GRH evidently requires many more studies of the effects of C:N:P ratios on proteins and RNA, as well as on other different metabolic products, and on growth rates and body sizes in different taxa and ecosystems. The number of variables is bewildering, and, as is clear from these two papers<sup>2,11</sup>, the answers will not be universally straightforward.

Metabolomics analysis<sup>12</sup> is emerging as one way forward, however. Improved analytical methods and computerized interpretation of large data sets have transformed the task of quantifying more metabolic compounds — carbohydrates, amino acids and peptides, lipids, phenolics, terpenoids, alkaloids and

so on — and associating them with the corresponding elemental stoichiometries. Metabolomics should thus help to interpret the response of different groups of organisms in allocating resources to growth, storage and defence. It may also provide the elemental and metabolic budgets for different species along gradients from low to fast growth, which would allow a better test of the links between C:N:P ratio, growth rate and body-size spectrum.

This is an endeavour that goes well beyond assessment of the GRH. Such research will improve our understanding of the coupling between different levels of biological organization, from cellular metabolism to ecosystem structure and nutrient cycling. In doing so, it will help in integrating analysis of the pools and flows of chemical elements and energy studied in ecosystem ecology, with assessments of genetic fitness and the biochemical products of genomes considered in evolutionary ecology. ■

Josep Peñuelas and Jordi Sardans are in the Global Ecology Unit CSIC-CREAF-CEAB,

Center for Ecological Research and Forestry Applications, Facultat de Ciències, Universitat Autònoma de Barcelona, 08193 Bellaterra, Catalonia, Spain.

e-mails: josep.penuelas@uab.cat;  
j.sardans@creaf.uab.cat

1. Sterner, R. W. & Elser, J. J. *Ecological Stoichiometry: The Biology of Elements from Molecules to the Biosphere* (Princeton Univ. Press, 2002).
2. Mulder, C. & Elser, J. J. *Global Change Biol.* doi:10.1111/j.1365-2486.2009.01899.x (2009).
3. Elser, J. J., Dobberfuhl, D., Mackay, N. A. & Schampel, J. H. *Bioscience* **46**, 674–684 (1996).
4. Main, T., Dobberfuhl, D. R. & Elser, J. J. *Limnol. Oceanogr.* **42**, 1474–1478 (1997).
5. Gillooly, J. F., Charnov, E. L., West, G. B., Savage, V. M. & Brown, J. H. *Nature* **417**, 70–73 (2002).
6. Niklas, K. J. *Ann. Bot.* **97**, 155–163 (2006).
7. de Eyto, E. & Irvine, K. *Ecosystems* **17**, 724–736 (2007).
8. Reuman, D. C., Cohen, J. E. & Mulder, C. *Adv. Ecol. Res.* **41**, 45–85 (2009).
9. Rooney, N., McCann, K., Gellmer, G. & Moore, J. C. *Nature* **442**, 265–269 (2006).
10. Güsewell, S. *New Phytol.* **164**, 243–266 (2004).
11. Matzek, V. & Vitousek, P. M. *Ecol. Lett.* **12**, 765–771 (2009).
12. Bundy, J. G., Davey, M. P. & Viant, M. R. *Metabolomics* **5**, 3–21 (2009).

## CANCER

# More than kin and less than kind

Kevin Shannon and Mignon Loh

**A gene that is found to be mutated in a type of blood cancer exhibits properties of both a growth-suppressing tumour suppressor and a growth-promoting oncogene.**

Myeloproliferative neoplasms (MPNs) are a group of cancers characterized by excessive production of one or more types of differentiated blood cell. Mutations in genes that encode components of cellular signalling networks are a hallmark of MPNs, and cells from affected patients are often abnormally sensitive to growth factors called cytokines<sup>1</sup>. On page 904 of this issue, Sanada *et al.*<sup>2</sup> report that mutations in the *CBL* gene, which are found in a subset of patients with MPNs, contribute to the development of cancer in unexpected and complex ways, suggesting that the normal protein encoded by this gene both promotes and inhibits the growth of blood cells.

Sanada and colleagues<sup>2</sup> performed genome-wide studies of bone-marrow samples from patients with MPNs to uncover acquired genetic changes that might contribute to abnormal cellular growth. The authors were particularly interested in detecting a type of genetic alteration called acquired uniparental disomy (aUPD) that occurs in somatic cells (non-gametes). In this alteration, a region of DNA on one chromosome is lost in tumour cells, but is replaced by a copy of the corresponding segment from the partner chromosome that harbours a mutant gene. This mechanism can contribute to leukaemia through

loss of the normal copy (allele) of a tumour-suppressor gene<sup>3</sup> or by duplicating genes that promote cancer (oncogenes)<sup>4,5</sup>. Because this alteration results in replacement of the deleted DNA, the region of aUPD eludes discovery by conventional techniques. To surmount these difficulties, the authors<sup>2</sup> and other groups<sup>6–8</sup> have analysed samples using single nucleotide polymorphism (SNP) arrays — a technique that has become a valuable tool in cancer biology. One of the many advantages of SNP analysis is that it can identify aUPD by detecting a chromosomal region in which the DNA is derived from a single parental chromosome (so-called loss of heterozygosity).

Using this technique, researchers have detected aUPD spanning a region of chromosome 11 that includes the *CBL* gene in MPN specimens<sup>2,6–8</sup>, and have gone on to discover mutations in this gene. The Cbl protein is expressed in various cell types and regulates cellular signalling networks by acting as a multifunctional adaptor molecule and as an E3 ubiquitin ligase<sup>9</sup>, an enzyme that attaches a ubiquitin molecule to growth-factor receptors and other cellular proteins. Ubiquitination of growth-factor receptors triggers their internalization and degradation, thereby reducing the signalling cascades that promote cellular

## CHEMICAL BIOLOGY

## Protein picker

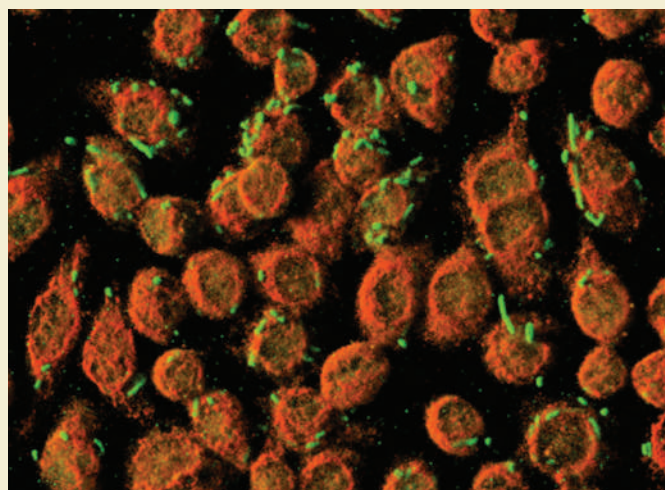
Reporting in *Nature Chemical Biology*, Ngo *et al.* describe a system for cell-selective protein labelling in mixtures of cells (J. T. Ngo *et al.* *Nature Chem. Biol.* doi:10.1038/nchembio.200; 2009). Their work is based on the principle that proteins can be tracked in experiments if they are engineered so that some of their constituent amino acids contain a tag, such as a radioactive label; tagged amino acids can be added to cells in culture, whereupon the cells incorporate them into newly formed proteins. The general problem with this approach is that all the cells in the culture become labelled, whereas it might be that only certain types of cell need to be tagged.

Ngo and colleagues' solution to that problem involves non-naturally occurring amino acids that contain azide ( $N_3$ ) groups in their side chains. Azides don't react with biological molecules, but under certain conditions they do react quickly with synthetic molecules

that contain alkyne groups (which have carbon-carbon triple bonds). Once incorporated into proteins, azide-containing amino-acid residues will thus react with alkyne-containing fluorescent dyes or affinity reagents, so tagging the proteins for imaging, detection or separation.

Non-natural amino acids are already used for protein labelling, but Ngo *et al.* take the idea further. They exploit an azide-containing amino acid that is incorporated into proteins only by cells that express a mutant of the methionyl-tRNA synthetase enzyme (which is involved in protein synthesis). When the authors added this amino acid to a co-culture of normal and mutant *Escherichia coli* cells, only the mutants were subsequently tagged with an alkyne-containing affinity reagent or fluorescent dye.

To show that their technique could be applied to mixtures of bacterial and mammalian cells, Ngo *et al.*



infected mouse macrophages with *E. coli* cells that express the mutant enzyme, in the presence of the azide-containing amino acid. They then treated the macrophages with a green alkyne-containing dye, which tagged only the bacterial cells (pictured; macrophages are stained orange, and are about 15 micrometres in diameter). The authors were also able to specifically tag newly synthesized bacterial proteins with an affinity reagent, which was then used as

a handle to isolate those proteins from the culture.

The authors' approach allows the cellular origins of proteins in complex multicellular systems to be determined. It could therefore be handy for isolating proteins from pathogens in studies of infections, for example, or for identifying the complement of proteins of a single bacterial species living in a community of many other microbial organisms.

**Andrew Mitchinson**

proliferation. The missense *CBL* mutations found in MPNs introduce amino-acid substitutions that disable ubiquitin-ligase activity.

Consistent with a previous report<sup>10</sup>, Sanada *et al.*<sup>2</sup> show that mice lacking the *Cbl* gene produce increased numbers of immature blood cells. They also find that *Cbl* inactivation promotes the development of leukaemia in mice engineered to express the pro-leukaemic *BCR-ABL* gene. Mutant Cbl proteins inhibit ubiquitination of growth-factor receptors in blood-cell lines, even in cells that retain a normal copy of the *CBL* gene<sup>2,7</sup>, and the authors demonstrate that this inhibition is associated with prolonged receptor activation and an enhanced proliferative response to cytokine growth factors. Although these studies provide evidence that *CBL* is a tumour-suppressor gene, Sanada and colleagues' data<sup>2</sup> also suggest a more complex role for *CBL* in leukaemogenesis. For example, if mutation of a single *CBL* allele is sufficient to disrupt normal ubiquitin-ligase activity, it is unclear why MPN cells also inactivate the normal copy of the gene through aUPD. The authors' findings that the effects of the mutant Cbl proteins are more pronounced in cells that lack a normal *CBL* gene suggest that other biochemical properties contribute to tumour growth. This idea is consistent with the observation that mice lacking *Cbl* do not spontaneously develop MPNs, as would be expected if the gene acted purely to suppress

tumour formation. Finally, when the authors over-expressed mutant *CBL* in fibroblasts, these cells showed cancerous properties<sup>2</sup>.

So what are we to make of *CBL*? Is it a tumour suppressor or an oncogene, or, as Shakespeare might have put it, "more than kin and less than kind"? On the one hand, there is strong selective pressure to delete the normal *CBL* allele in tumour cells, resulting in loss of ligase activity that restrains the output of activated growth-factor receptors. These are impeccable credentials for a tumour-suppressor protein. However, the blood cells of patients with MPNs invariably retain at least one gene that encodes a functional, albeit mutant, Cbl protein. Furthermore, mutated Cbl proteins seem to acquire unexpected growth-promoting functions<sup>2</sup> — this gain-of-function characteristic is not seen in blood stem cells that lack *CBL*. Such features implicate *CBL* as a bona fide oncogene.

Tumour suppressor or oncogene? Perhaps a solution to this conundrum is that this multi-domain protein fine-tunes the growth of blood stem cells and progenitor cells by simultaneously promoting and restraining growth through distinct protein-protein interactions. Recent studies offer intriguing clues about the potential growth-promoting biochemical properties of mutant Cbl proteins. First, Sanada *et al.*<sup>2</sup> find that expression of the mutant Cbl proteins is associated with aberrant

phosphorylation of STAT5, an activator of gene transcription. Aberrant phosphorylation is a biochemical feature of some types of MPN<sup>11</sup>, and although in this report<sup>2</sup> it may be due to loss of Cbl-mediated ubiquitination of cytokine receptors that activate STAT5, other mechanisms are possible. Second, *CBL* mutations and mutations in the oncogene *NRAS* were mutually exclusive in the adult MPN patients studied by the authors. *CBL* mutations were also found only in specimens from children with juvenile myelomonocytic leukaemia (a type of MPN) without mutations in *NRAS* or *KRAS*<sup>8</sup>. As this childhood leukaemia is an MPN in which a hyperactive form of the cell-signalling molecule Ras has a central role, there is likely to be a connection between mutant Cbl proteins and Ras signalling. Data suggesting that Cbl regulates Ras trafficking in cells are intriguing in this respect<sup>12</sup>. The elegant functional studies of Sanada *et al.*<sup>2</sup> thus raise fascinating questions about the nature of oncogenic Cbl-mediated interactions in MPNs and how such interactions might be targeted to treat these disorders.

Kevin Shannon and Mignon Loh are in the Department of Pediatrics and Helen Diller Family Comprehensive Cancer Center, University of California, San Francisco, San Francisco, California 94158-9001, USA. e-mails: shannonk@peds.ucsf.edu; loh@peds.ucsf.edu



1. Van Etten, R. A. & Shannon, K. M. *Cancer Cell* **6**, 547–552 (2004).
2. Sanada, M. *et al.* *Nature* **460**, 904–908 (2009).
3. Stephens, K. *et al.* *Blood* **108**, 1684–1689 (2006).
4. Fitzgibbon, J. *et al.* *Cancer Res.* **65**, 9152–9154 (2005).
5. Kralovics, R., Guan, Y. & Prchal, J. T. *Exp. Hematol.* **30**, 229–236 (2002).
6. Dunbar, A. J. *et al.* *Cancer Res.* **68**, 10349–10357 (2008).
7. Grand, F. H. *et al.* *Blood* **113**, 6182–6192 (2009).
8. Loh, M. L. *et al.* *Blood* doi:10.1182/blood-2009-01-198416 (2009).
9. Schmidt, M. H. & Dikic, I. *Nature Rev. Mol. Cell Biol.* **6**, 907–918 (2005).
10. Rathinam, C. *et al.* *Genes Dev.* **22**, 992–997 (2008).
11. Kotecha, N. *et al.* *Cancer Cell* **14**, 335–343 (2008).
12. Mor, A. & Philips, M. R. *Annu. Rev. Immunol.* **24**, 771–800 (2006).

## MICROBIAL GENETICS

# Love the one you're with

Joseph Heitman

***Candida albicans* is notorious as an opportunistic microbe that causes thrush and serious systemic disease. For geneticists, however, it offers continuing revelations into the wondrously varied sex lives of fungi.**

Sex facilitates evolution by recombining parental genomes and purging deleterious mutations. There are myriad forms, but they have three steps in common: meiosis, which halves the number of chromosomes per cell; gamete production; and cell–cell fusion. Sex in most animals involves two individuals of opposite sex, who produce distinct gametes (sperm and oocytes). In fungi, sex typically involves morphologically similar cells of opposite mating type (**a** and **α**) that reciprocally produce sex-stimulating pheromones. In other cases, fungi are self-fertile, and lone individuals can reproduce sexually. One well-known example of this is the model yeast *Saccharomyces cerevisiae*, in which a single cell divides, one of

the resulting cells switches mating type, and mating yields **a/a** diploid cells, with a double complement of chromosomes, that no longer mate but undergo meiosis. On page 890 of this issue, Alby *et al.*<sup>1</sup> report a conceptually similar but mechanistically distinct self-mating phenomenon in another yeast, the pathogenic *Candida albicans*.

*Candida albicans* resides in the human microbiota, for example in the gastrointestinal tract, and commonly causes infections. For more than a century it was thought to be strictly asexual. Then the mating-type gene locus was discovered, and most isolates were found to be **a/a** diploids that, like *S. cerevisiae*, are sterile<sup>2</sup>. Mutants with only one mating type (**a/a** or **α/α**) were

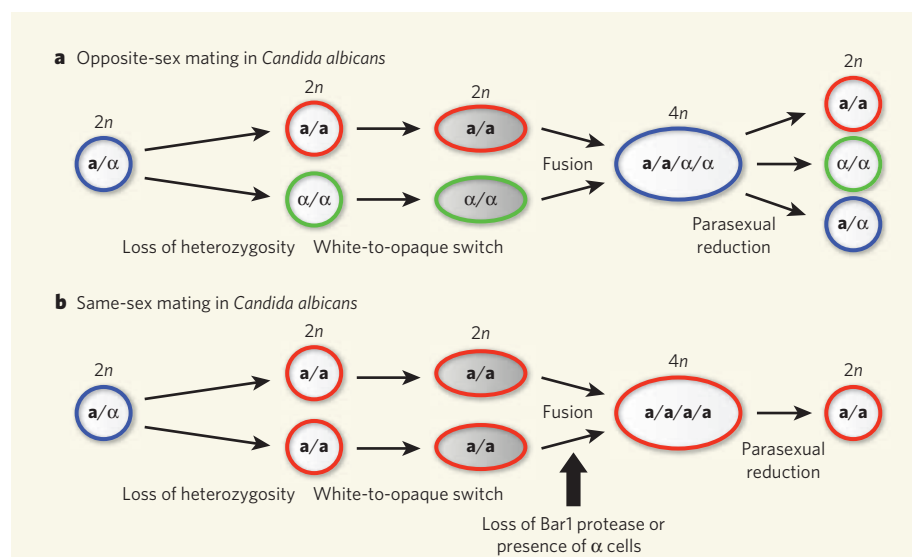


**Figure 1 | Opposite-sex and same-sex mating in *Candida albicans*.** This fungus is diploid (2n); most strains are heterozygous, having both mating-type gene forms (**a/α**), and are sterile. **a**, Opposite-sex mating involves loss of heterozygosity, yielding **a** and **α** diploid cells that then switch from the white type to the opaque type specialized for mating. Cell–cell fusion yields tetraploid (4n) cells in which parasexual chromosome reduction without recognized meiosis yields diploid progeny. **b**, Same-sex mating again involves loss of heterozygosity and the white–opaque switch. As identified by Alby *et al.*<sup>1</sup>, the same-sex path can then be advanced in two ways, both of which involve production of pheromone of the opposite mating type that promotes fusion and results in tetraploid **a** cells. If **a** cells lack Bar1 protease, they do not destroy the **α**-pheromone they produce; and in *ménage-à-trois* matings, even a few **a** cells can provide **α**-pheromone.



## 50 YEARS AGO

Most areas where there is a high prevalence of multiple sclerosis coincide in a highly suggestive fashion with areas where glaciation has played an important part in providing parent material for soils. However, the converse is certainly not true: all glacial soils cannot be correlated with areas where the prevalence of multiple sclerosis is high. Maps showing the distribution of multiple sclerotic cases in Northern Ireland, south-eastern Ontario, Sweden, and Denmark are alike in one respect—they all bear a remarkable resemblance to maps illustrating the distribution of boulders or geochemical anomalies in any map prepared for the purpose of searching in a glaciated area for buried ore bodies ... One other point appears worthy of note: higher than 'normal' quantities of lead are known to occur in those rocks ... occurring in areas where the prevalence of multiple sclerosis is high ... It should also be noted that anomalous amounts of lead may, on occasion, be accompanied by anomalous amounts of some other elements such as silver, barium, magnesium, and fluorine.

From *Nature* 15 August 1959.

## 100 YEARS AGO

It is a usual custom in pharmacological work to state the dosage of drugs as so much per kilogram of body-weight of animal or man, the subject of experiment or treatment. Prof. Benjamin Moore points out in the *Biochemical Journal* ... that this method of stating dosage is inaccurate, the dose of a drug for two individuals of different size, apart from peculiar idiosyncrasies, being proportional, not to their weights, but to their *body surfaces*, in other words, to the two-thirds powers of their weights. Thus an adult of 150 lb. weight cannot be given fifteen times the dose for an infant of 10 lb., but much more nearly a dose only six times as much. It may be that it is this principle which limits the value of some drugs.

From *Nature* 12 August 1909.

50 & 100 YEARS AGO

## CHEMICAL BIOLOGY

## Protein picker

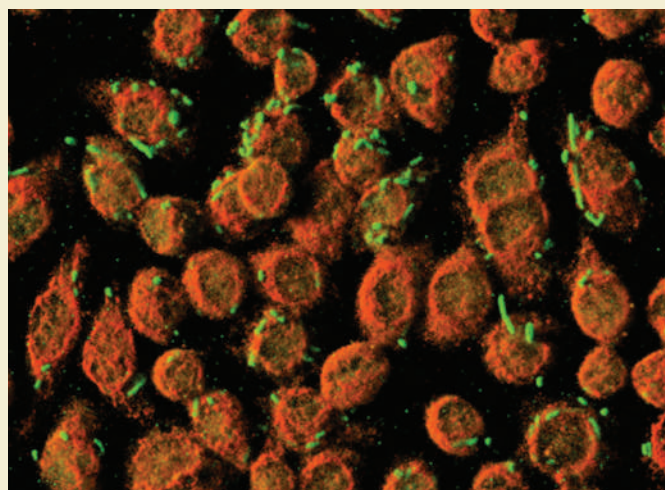
Reporting in *Nature Chemical Biology*, Ngo *et al.* describe a system for cell-selective protein labelling in mixtures of cells (J. T. Ngo *et al.* *Nature Chem. Biol.* doi:10.1038/nchembio.200; 2009). Their work is based on the principle that proteins can be tracked in experiments if they are engineered so that some of their constituent amino acids contain a tag, such as a radioactive label; tagged amino acids can be added to cells in culture, whereupon the cells incorporate them into newly formed proteins. The general problem with this approach is that all the cells in the culture become labelled, whereas it might be that only certain types of cell need to be tagged.

Ngo and colleagues' solution to that problem involves non-naturally occurring amino acids that contain azide ( $N_3$ ) groups in their side chains. Azides don't react with biological molecules, but under certain conditions they do react quickly with synthetic molecules

that contain alkyne groups (which have carbon-carbon triple bonds). Once incorporated into proteins, azide-containing amino-acid residues will thus react with alkyne-containing fluorescent dyes or affinity reagents, so tagging the proteins for imaging, detection or separation.

Non-natural amino acids are already used for protein labelling, but Ngo *et al.* take the idea further. They exploit an azide-containing amino acid that is incorporated into proteins only by cells that express a mutant of the methionyl-tRNA synthetase enzyme (which is involved in protein synthesis). When the authors added this amino acid to a co-culture of normal and mutant *Escherichia coli* cells, only the mutants were subsequently tagged with an alkyne-containing affinity reagent or fluorescent dye.

To show that their technique could be applied to mixtures of bacterial and mammalian cells, Ngo *et al.*



infected mouse macrophages with *E. coli* cells that express the mutant enzyme, in the presence of the azide-containing amino acid. They then treated the macrophages with a green alkyne-containing dye, which tagged only the bacterial cells (pictured; macrophages are stained orange, and are about 15 micrometres in diameter). The authors were also able to specifically tag newly synthesized bacterial proteins with an affinity reagent, which was then used as

a handle to isolate those proteins from the culture.

The authors' approach allows the cellular origins of proteins in complex multicellular systems to be determined. It could therefore be handy for isolating proteins from pathogens in studies of infections, for example, or for identifying the complement of proteins of a single bacterial species living in a community of many other microbial organisms.

**Andrew Mitchinson**

proliferation. The missense *CBL* mutations found in MPNs introduce amino-acid substitutions that disable ubiquitin-ligase activity.

Consistent with a previous report<sup>10</sup>, Sanada *et al.*<sup>2</sup> show that mice lacking the *Cbl* gene produce increased numbers of immature blood cells. They also find that *Cbl* inactivation promotes the development of leukaemia in mice engineered to express the pro-leukaemic *BCR-ABL* gene. Mutant Cbl proteins inhibit ubiquitination of growth-factor receptors in blood-cell lines, even in cells that retain a normal copy of the *CBL* gene<sup>2,7</sup>, and the authors demonstrate that this inhibition is associated with prolonged receptor activation and an enhanced proliferative response to cytokine growth factors. Although these studies provide evidence that *CBL* is a tumour-suppressor gene, Sanada and colleagues' data<sup>2</sup> also suggest a more complex role for *CBL* in leukaemogenesis. For example, if mutation of a single *CBL* allele is sufficient to disrupt normal ubiquitin-ligase activity, it is unclear why MPN cells also inactivate the normal copy of the gene through aUPD. The authors' findings that the effects of the mutant Cbl proteins are more pronounced in cells that lack a normal *CBL* gene suggest that other biochemical properties contribute to tumour growth. This idea is consistent with the observation that mice lacking *Cbl* do not spontaneously develop MPNs, as would be expected if the gene acted purely to suppress

tumour formation. Finally, when the authors over-expressed mutant *CBL* in fibroblasts, these cells showed cancerous properties<sup>2</sup>.

So what are we to make of *CBL*? Is it a tumour suppressor or an oncogene, or, as Shakespeare might have put it, "more than kin and less than kind"? On the one hand, there is strong selective pressure to delete the normal *CBL* allele in tumour cells, resulting in loss of ligase activity that restrains the output of activated growth-factor receptors. These are impeccable credentials for a tumour-suppressor protein. However, the blood cells of patients with MPNs invariably retain at least one gene that encodes a functional, albeit mutant, Cbl protein. Furthermore, mutated Cbl proteins seem to acquire unexpected growth-promoting functions<sup>2</sup> — this gain-of-function characteristic is not seen in blood stem cells that lack *CBL*. Such features implicate *CBL* as a bona fide oncogene.

Tumour suppressor or oncogene? Perhaps a solution to this conundrum is that this multi-domain protein fine-tunes the growth of blood stem cells and progenitor cells by simultaneously promoting and restraining growth through distinct protein-protein interactions. Recent studies offer intriguing clues about the potential growth-promoting biochemical properties of mutant Cbl proteins. First, Sanada *et al.*<sup>2</sup> find that expression of the mutant Cbl proteins is associated with aberrant

phosphorylation of STAT5, an activator of gene transcription. Aberrant phosphorylation is a biochemical feature of some types of MPN<sup>11</sup>, and although in this report<sup>2</sup> it may be due to loss of Cbl-mediated ubiquitination of cytokine receptors that activate STAT5, other mechanisms are possible. Second, *CBL* mutations and mutations in the oncogene *NRAS* were mutually exclusive in the adult MPN patients studied by the authors. *CBL* mutations were also found only in specimens from children with juvenile myelomonocytic leukaemia (a type of MPN) without mutations in *NRAS* or *KRAS*<sup>8</sup>. As this childhood leukaemia is an MPN in which a hyperactive form of the cell-signalling molecule Ras has a central role, there is likely to be a connection between mutant Cbl proteins and Ras signalling. Data suggesting that Cbl regulates Ras trafficking in cells are intriguing in this respect<sup>12</sup>. The elegant functional studies of Sanada *et al.*<sup>2</sup> thus raise fascinating questions about the nature of oncogenic Cbl-mediated interactions in MPNs and how such interactions might be targeted to treat these disorders.

Kevin Shannon and Mignon Loh are in the Department of Pediatrics and Helen Diller Family Comprehensive Cancer Center, University of California, San Francisco, San Francisco, California 94158-9001, USA. e-mails: shannonk@peds.ucsf.edu; loh@peds.ucsf.edu



1. Van Etten, R. A. & Shannon, K. M. *Cancer Cell* **6**, 547–552 (2004).
2. Sanada, M. *et al.* *Nature* **460**, 904–908 (2009).
3. Stephens, K. *et al.* *Blood* **108**, 1684–1689 (2006).
4. Fitzgibbon, J. *et al.* *Cancer Res.* **65**, 9152–9154 (2005).
5. Kralovics, R., Guan, Y. & Prchal, J. T. *Exp. Hematol.* **30**, 229–236 (2002).
6. Dunbar, A. J. *et al.* *Cancer Res.* **68**, 10349–10357 (2008).
7. Grand, F. H. *et al.* *Blood* **113**, 6182–6192 (2009).
8. Loh, M. L. *et al.* *Blood* doi:10.1182/blood-2009-01-198416 (2009).
9. Schmidt, M. H. & Dikic, I. *Nature Rev. Mol. Cell Biol.* **6**, 907–918 (2005).
10. Rathinam, C. *et al.* *Genes Dev.* **22**, 992–997 (2008).
11. Kotecha, N. *et al.* *Cancer Cell* **14**, 335–343 (2008).
12. Mor, A. & Philips, M. R. *Annu. Rev. Immunol.* **24**, 771–800 (2006).

## MICROBIAL GENETICS

# Love the one you're with

Joseph Heitman

***Candida albicans* is notorious as an opportunistic microbe that causes thrush and serious systemic disease. For geneticists, however, it offers continuing revelations into the wondrously varied sex lives of fungi.**

Sex facilitates evolution by recombining parental genomes and purging deleterious mutations. There are myriad forms, but they have three steps in common: meiosis, which halves the number of chromosomes per cell; gamete production; and cell–cell fusion. Sex in most animals involves two individuals of opposite sex, who produce distinct gametes (sperm and oocytes). In fungi, sex typically involves morphologically similar cells of opposite mating type (**a** and **α**) that reciprocally produce sex-stimulating pheromones. In other cases, fungi are self-fertile, and lone individuals can reproduce sexually. One well-known example of this is the model yeast *Saccharomyces cerevisiae*, in which a single cell divides, one of

the resulting cells switches mating type, and mating yields **a/a** diploid cells, with a double complement of chromosomes, that no longer mate but undergo meiosis. On page 890 of this issue, Alby *et al.*<sup>1</sup> report a conceptually similar but mechanistically distinct self-mating phenomenon in another yeast, the pathogenic *Candida albicans*.

*Candida albicans* resides in the human microbiota, for example in the gastrointestinal tract, and commonly causes infections. For more than a century it was thought to be strictly asexual. Then the mating-type gene locus was discovered, and most isolates were found to be **a/a** diploids that, like *S. cerevisiae*, are sterile<sup>2</sup>. Mutants with only one mating type (**a/a** or **α/α**) were

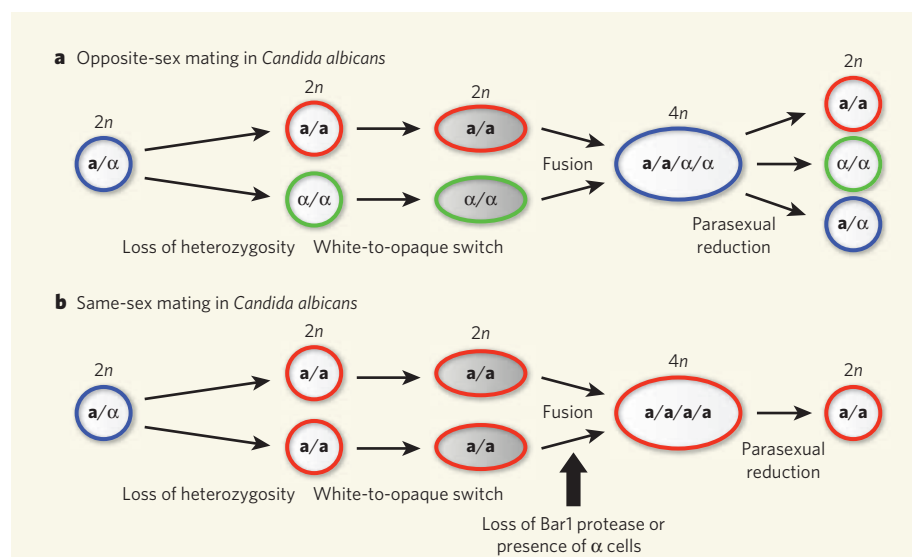


**Figure 1 | Opposite-sex and same-sex mating in *Candida albicans*.** This fungus is diploid ( $2n$ ): most strains are heterozygous, having both mating-type gene forms (**a/a**), and are sterile. **a**, Opposite-sex mating involves loss of heterozygosity, yielding **a** and **α** diploid cells that then switch from the white type to the opaque type specialized for mating. Cell–cell fusion yields tetraploid ( $4n$ ) cells in which parasexual chromosome reduction without recognized meiosis yields diploid progeny. **b**, Same-sex mating again involves loss of heterozygosity and the white–opaque switch. As identified by Alby *et al.*<sup>1</sup>, the same-sex path can then be advanced in two ways, both of which involve production of pheromone of the opposite mating type that promotes fusion and results in tetraploid **a** cells. If **a** cells lack Bar1 protease, they do not destroy the **α**-pheromone they produce; and in *ménage-à-trois* matings, even a few **a** cells can provide **α**-pheromone.



## 50 YEARS AGO

Most areas where there is a high prevalence of multiple sclerosis coincide in a highly suggestive fashion with areas where glaciation has played an important part in providing parent material for soils. However, the converse is certainly not true: all glacial soils cannot be correlated with areas where the prevalence of multiple sclerosis is high. Maps showing the distribution of multiple sclerotic cases in Northern Ireland, south-eastern Ontario, Sweden, and Denmark are alike in one respect—they all bear a remarkable resemblance to maps illustrating the distribution of boulders or geochemical anomalies in any map prepared for the purpose of searching in a glaciated area for buried ore bodies ... One other point appears worthy of note: higher than 'normal' quantities of lead are known to occur in those rocks ... occurring in areas where the prevalence of multiple sclerosis is high ... It should also be noted that anomalous amounts of lead may, on occasion, be accompanied by anomalous amounts of some other elements such as silver, barium, magnesium, and fluorine. From *Nature* 15 August 1959.

## 100 YEARS AGO

It is a usual custom in pharmacological work to state the dosage of drugs as so much per kilogram of body-weight of animal or man, the subject of experiment or treatment. Prof. Benjamin Moore points out in the *Biochemical Journal* ... that this method of stating dosage is inaccurate, the dose of a drug for two individuals of different size, apart from peculiar idiosyncrasies, being proportional, not to their weights, but to their *body surfaces*, in other words, to the two-thirds powers of their weights. Thus an adult of 150 lb. weight cannot be given fifteen times the dose for an infant of 10 lb., but much more nearly a dose only six times as much. It may be that it is this principle which limits the value of some drugs. From *Nature* 12 August 1909.

50 &amp; 100 YEARS AGO

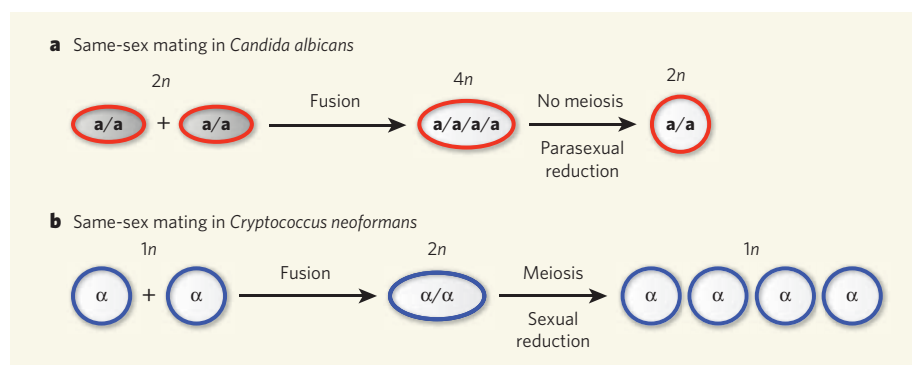


**Figure 2 | Same-sex mating in two pathogenic fungi.** Unisexual reproduction occurs in both *Candida albicans* (a) and *Cryptococcus neoformans* (b). These forms of self-fertility may result in population features (such as inbreeding and clonality) that are associated with pathogenesis. Given that two such evolutionarily divergent pathogenic fungi both undergo same-sex mating, this process is likely to be even more general among fungi. The two species are distinguished in that mating in *C. albicans* is parasexual and no spores are produced, whereas in *C. neoformans* meiosis results in the production of infectious spores.

found to mate in the laboratory or during infection<sup>2</sup>. But the low frequency of mating raised the question of whether sex occurs in nature. This was resolved by various discoveries<sup>2–4</sup>, including the observation that mating is enhanced a million-fold when cells switch from ‘white’ to an ‘opaque’ type specialized for mating.

In opposite-sex mating in *C. albicans* (Fig. 1a), cell–cell fusion produces tetraploid cells that have four copies of each chromosome ( $a/a/a/a$ ). These tetraploids undergo a ‘parasexual’ phase<sup>5</sup>, which restores the diploid state and allows limited genetic recombination but does not involve overt meiosis and does not produce spores. (The parasexual recombination that does occur requires Spo11 (ref. 6), an enzyme that acts as a recombinase during meiosis in other organisms. Thus, sex in *C. albicans* could involve cryptic meiosis or novel parasexual roles for Spo11.)

Alby *et al.*<sup>1</sup> report the discovery of a facet of *C. albicans* reproduction in which cells mate with each other via same-sex mating (Fig. 1b), rather than with the opposite mating type. This observation arose from analysing *C. albicans* mutants lacking barrier protease, an enzyme that inactivates  $\alpha$ -pheromone. Barrier was discovered in *S. cerevisiae* as a factor that interferes with mate signalling when  $a$  cells producing barrier are interposed between  $a$  and  $\alpha$  cells<sup>7</sup>. Among other things, we now know that barrier is encoded by the *BAR1* gene in a mating-type-specific manner, and that it acts on  $\alpha$ -pheromone, enabling  $a$  cells to choose mates producing the most pheromone.

Curiously, *C. albicans*  $a$  cells express genes encoding both  $a$ - and  $\alpha$ -pheromone. Alby *et al.*<sup>1</sup> observed that  $a$  cell *bar1* mutants lacking barrier produce unusual wrinkled colonies, and that these colonies were responding to pheromone. Surprisingly, they also discovered that  $a$ – $a$  cell fusion can occur both between *bar1* mutants and between wild-type and *bar1*-mutant cells. Crosses with mutant strains showed that same-sex mating occurs when  $\alpha$ -pheromone is produced by one  $a$  cell

and is sensed by  $\alpha$ -pheromone receptors on both the producing and the partner  $a$  cell.

Alby *et al.* found that same-sex mating is less efficient than opposite-sex mating, but is readily detectable, and in some cases is appreciable. They also observed same-sex mating between wild-type  $a$  cells (producing Bar1) in *ménage-à-trois* matings in which an  $\alpha$ -cell minority provided  $\alpha$ -pheromone. Under these conditions, sufficient  $\alpha$ -pheromone may overwhelm Bar1 and trigger  $a$ – $a$  cell fusion. Same-sex mating yielded tetraploid cells ( $a/a/a/a$ ) that could undergo parasexual chromosome loss to diploid progeny. Thus, *C. albicans* does not need both mating-type locus versions for the parasexual cycle, in contrast to their requirement for meiosis in *S. cerevisiae*.

Do opposite- and same-sex mating occur in nature? The original discovery of inefficient *C. albicans*  $a$ – $a$  mating fuelled speculation that it could be a lab artefact: however, a complex cellular network has been maintained that supports efficient  $a$ – $a$  mating. Population-genetics studies and identification of mating-stimulatory host conditions lend further support to the view that opposite-sex mating happens in nature<sup>2–4</sup>. That same-sex mating occurs most efficiently with mutant and not wild-type strains suggested that *bar1* mutants might occur in the population. No natural *bar1* mutants have been identified so far, however, and they might arise only transiently. Alternatively, host conditions or protease inhibitors produced by *C. albicans* ( $\alpha$ -pheromone variants) might stimulate same-sex mating in nature. Even infrequent same-sex mating in *ménage-à-trois* matings might suffice for genetic exchange in skewed mating-type populations, such as commensal biofilms on host mucosal membranes.

Although it might seem odd that yeast would mate by both opposite-sex/outcrossing and same-sex/inbreeding, *S. cerevisiae* is again instructive. The natural population consists of isolates that switch mating type and self-mate, and others that cannot switch

but are fertile with the opposite mating type. Thus, a well-defined species can evidently consist of individuals with different modes of sexual reproduction. It is striking, however, that two closely related yeasts (*C. albicans* and *S. cerevisiae*) evolved such distinct modes of self-fertility. The more evolutionarily divergent fission yeast, *Schizosaccharomyces pombe*, also switches mating type and self-mates, like *S. cerevisiae*, but independently evolved a machinery to do so. This diversity in forms of sexual reproduction illustrates the remarkable plasticity of fungi, which have evolved to exploit different environments.

A divergent pathogenic yeast, *Cryptococcus neoformans*, also reproduces unisexually<sup>8</sup>. This species has a well-defined  $a$ – $a$  sexual cycle, and the fact that the natural population is largely  $a$  unisexual was puzzling. The discovery that  $a$  cells undergo same-sex mating, yielding diploid cells that complete meiosis and produce spores (Fig. 2), suggested another route by which diversity might be maintained<sup>8</sup>. Population-genetics studies provide evidence that same-sex mating occurs in nature, and implicate the process in an outbreak of *Cryptococcus* infection<sup>9,10</sup>. That same-sex mating arose convergently in two divergent pathogenic yeasts suggests that unisexual reproduction may be linked to microbial pathogenesis, and could be even more widespread than is currently appreciated.

Transitions in sexual reproduction between inbreeding and outbreeding also occur in plants and animals. In plants, mutations in self-incompatibility loci involved in pollen recognition evoke transitions from cross-pollination to self-pollination<sup>11</sup>. One individual can thereby colonize different environmental niches, and become more cosmopolitan. Parthenogenesis — virgin birth — is restricted in mammals by genomic imprinting, but remarkable examples have been reported in Komodo dragons and sharks<sup>12,13</sup>. In these cases, otherwise sexual organisms reproduce under extreme circumstances, possibly enabling the colonization of islands or oceanic expanses by single individuals.

Joseph Heitman is in the Department of Molecular Genetics and Microbiology, Duke University Medical Center, Durham, North Carolina 27710, USA.  
e-mail: heitm001@duke.edu

- Alby, K., Schaefer, D. & Bennett, R. J. *Nature* **460**, 890–893 (2009).
- Bennett, R. J. & Johnson, A. D. *Annu. Rev. Microbiol.* **59**, 233–255 (2005).
- Daniels, K. J. *et al.* *EMBO J.* **25**, 2240–2252 (2006).
- Huang, G. *et al.* *Curr. Biol.* **19**, 330–334 (2009).
- Bennett, R. J. & Johnson, A. D. *EMBO J.* **22**, 2505–2515 (2003).
- Forche, A. *et al.* *PLoS Biol.* **6**, e110 (2008).
- Hicks, J. B. & Herskowitz, I. *Nature* **260**, 246–248 (1976).
- Lin, X., Hull, C. M. & Heitman, J. *Nature* **434**, 1017–1021 (2005).
- Fraser, J. A. *et al.* *Nature* **437**, 1360–1364 (2005).
- Lin, X. *et al.* *PLoS Genet.* **3**, e186 (2007).
- Tang, C. *et al.* *Science* **317**, 1070–1072 (2007).
- Watts, P. C. *et al.* *Nature* **444**, 1021–1022 (2006).
- Chapman, D. D. *et al.* *Biol. Lett.* **3**, 425–427 (2007).



1. Van Etten, R. A. & Shannon, K. M. *Cancer Cell* **6**, 547–552 (2004).
2. Sanada, M. *et al.* *Nature* **460**, 904–908 (2009).
3. Stephens, K. *et al.* *Blood* **108**, 1684–1689 (2006).
4. Fitzgibbon, J. *et al.* *Cancer Res.* **65**, 9152–9154 (2005).
5. Kralovics, R., Guan, Y. & Prchal, J. T. *Exp. Hematol.* **30**, 229–236 (2002).
6. Dunbar, A. J. *et al.* *Cancer Res.* **68**, 10349–10357 (2008).
7. Grand, F. H. *et al.* *Blood* **113**, 6182–6192 (2009).
8. Loh, M. L. *et al.* *Blood* doi:10.1182/blood-2009-01-198416 (2009).
9. Schmidt, M. H. & Dikic, I. *Nature Rev. Mol. Cell Biol.* **6**, 907–918 (2005).
10. Rathinam, C. *et al.* *Genes Dev.* **22**, 992–997 (2008).
11. Kotecha, N. *et al.* *Cancer Cell* **14**, 335–343 (2008).
12. Mor, A. & Philips, M. R. *Annu. Rev. Immunol.* **24**, 771–800 (2006).

## MICROBIAL GENETICS

# Love the one you're with

Joseph Heitman

*Candida albicans* is notorious as an opportunistic microbe that causes thrush and serious systemic disease. For geneticists, however, it offers continuing revelations into the wondrously varied sex lives of fungi.

Sex facilitates evolution by recombining parental genomes and purging deleterious mutations. There are myriad forms, but they have three steps in common: meiosis, which halves the number of chromosomes per cell; gamete production; and cell–cell fusion. Sex in most animals involves two individuals of opposite sex, who produce distinct gametes (sperm and oocytes). In fungi, sex typically involves morphologically similar cells of opposite mating type (*a* and  $\alpha$ ) that reciprocally produce sex-stimulating pheromones. In other cases, fungi are self-fertile, and lone individuals can reproduce sexually. One well-known example of this is the model yeast *Saccharomyces cerevisiae*, in which a single cell divides, one of

the resulting cells switches mating type, and mating yields *a/a* diploid cells, with a double complement of chromosomes, that no longer mate but undergo meiosis. On page 890 of this issue, Alby *et al.*<sup>1</sup> report a conceptually similar but mechanistically distinct self-mating phenomenon in another yeast, the pathogenic *Candida albicans*.

*Candida albicans* resides in the human microbiota, for example in the gastrointestinal tract, and commonly causes infections. For more than a century it was thought to be strictly asexual. Then the mating-type gene locus was discovered, and most isolates were found to be *a/a* diploids that, like *S. cerevisiae*, are sterile<sup>2</sup>. Mutants with only one mating type (*a/a* or  $\alpha/\alpha$ ) were

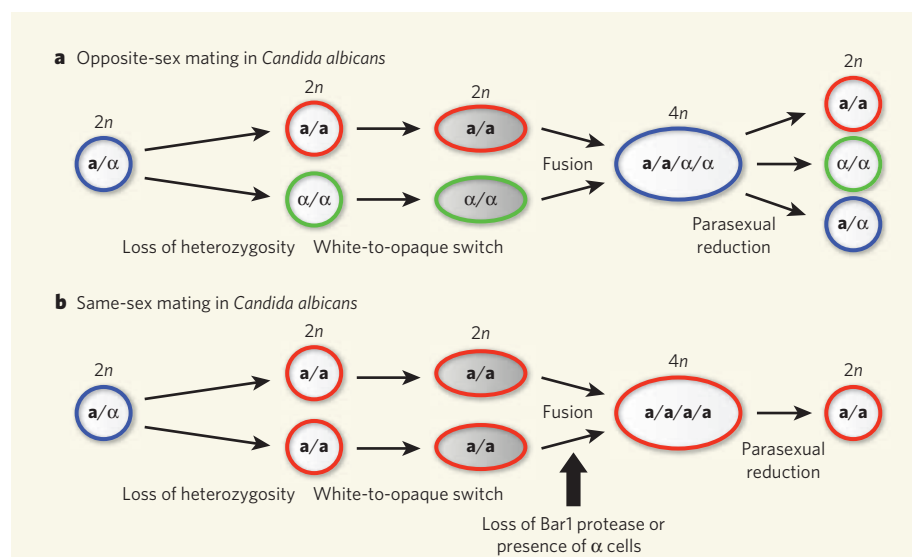


**Figure 1 | Opposite-sex and same-sex mating in *Candida albicans*.** This fungus is diploid ( $2n$ ): most strains are heterozygous, having both mating-type gene forms (*a/a*), and are sterile. **a**, Opposite-sex mating involves loss of heterozygosity, yielding *a* and  $\alpha$  diploid cells that then switch from the white type to the opaque type specialized for mating. Cell–cell fusion yields tetraploid ( $4n$ ) cells in which parasexual chromosome reduction without recognized meiosis yields diploid progeny. **b**, Same-sex mating again involves loss of heterozygosity and the white–opaque switch. As identified by Alby *et al.*<sup>1</sup>, the same-sex path can then be advanced in two ways, both of which involve production of pheromone of the opposite mating type that promotes fusion and results in tetraploid *a* cells. If *a* cells lack Bar1 protease, they do not destroy the  $\alpha$ -pheromone they produce; and in *ménage-à-trois* matings, even a few  $\alpha$  cells can provide *a*-pheromone.



## 50 YEARS AGO

Most areas where there is a high prevalence of multiple sclerosis coincide in a highly suggestive fashion with areas where glaciation has played an important part in providing parent material for soils. However, the converse is certainly not true: all glacial soils cannot be correlated with areas where the prevalence of multiple sclerosis is high. Maps showing the distribution of multiple sclerotic cases in Northern Ireland, south-eastern Ontario, Sweden, and Denmark are alike in one respect—they all bear a remarkable resemblance to maps illustrating the distribution of boulders or geochemical anomalies in any map prepared for the purpose of searching in a glaciated area for buried ore bodies ... One other point appears worthy of note: higher than 'normal' quantities of lead are known to occur in those rocks ... occurring in areas where the prevalence of multiple sclerosis is high ... It should also be noted that anomalous amounts of lead may, on occasion, be accompanied by anomalous amounts of some other elements such as silver, barium, magnesium, and fluorine. From *Nature* 15 August 1959.

## 100 YEARS AGO

It is a usual custom in pharmacological work to state the dosage of drugs as so much per kilogram of body-weight of animal or man, the subject of experiment or treatment. Prof. Benjamin Moore points out in the *Biochemical Journal* ... that this method of stating dosage is inaccurate, the dose of a drug for two individuals of different size, apart from peculiar idiosyncrasies, being proportional, not to their weights, but to their *body surfaces*, in other words, to the two-thirds powers of their weights. Thus an adult of 150 lb. weight cannot be given fifteen times the dose for an infant of 10 lb., but much more nearly a dose only six times as much. It may be that it is this principle which limits the value of some drugs. From *Nature* 12 August 1909.

50 &amp; 100 YEARS AGO

## Q&amp;A



A. RENTZ/GETTY

## TECHNOLOGY

# Hydrogen-fuelled vehicles

Louis Schlapbach

Hydrogen is hailed as a non-polluting synthetic fuel that could replace oil, especially for transport applications. The technology to make this a reality — particularly hydrogen-storage materials — has been a long time coming, but the first commercial vehicles might now be only a few years away.

## Why would hydrogen be a good transport fuel?

Hydrogen is the lightest element in the periodic table, and so molecular hydrogen has the highest energy-to-mass ratio of any chemical. Indeed, that's why it is used to propel rockets, where it is essential to minimize the mass of fuel carried. Hydrogen is carbon-free, non-toxic, and its thermal or electrochemical combustion with oxygen yields nothing but energy and water — although its combustion in air might generate nitric oxide air pollutants in controllable amounts. Another advantage is that the main source of hydrogen is water, which is essentially an unlimited resource.

## And what are the drawbacks?

The chief problem is that hydrogen is a gas at room temperature, so it takes up an impractically large amount of space. The gas must therefore be compressed in some way to make it compact enough for mobile applications. Another issue is less obvious: hydrogen is an energy carrier, not a source of energy. Unlike genuine sources of energy (such as solar radiation,

fossil hydrocarbons, hydropower and nuclear power), hydrogen is not naturally available in sufficient quantities for widespread use, and must therefore be made by splitting water into hydrogen and oxygen. Splitting requires energy, whether in the form of electricity, light, heat or chemicals. But most of that energy is recovered when hydrogen is combusted.

## Isn't hydrogen dangerously explosive?

In practice, no more so than petrol. People often think of the fire that destroyed the hydrogen-filled Zeppelin *Hindenburg* in 1937, and assume that the gas is dangerously combustible. In fact, the problem with the *Hindenburg* was its highly inflammable skin. It is true that mixtures of hydrogen and air burn over a rather broad composition range (mixtures in which 4–75% of the volume is hydrogen will burn; for comparison, mixtures of only 1–8% by volume of petrol in air will burn). Furthermore, hydrogen is more volatile than petrol, and diffuses faster through air. But comparative safety studies of fuel leaks from petrol- and hydrogen-fuelled cars, performed at the

University of Miami, clearly demonstrate that hydrogen-fuelled cars pose less of a fire risk than petrol-fuelled vehicles.

## What must be done for hydrogen to become a widely used fuel?

There are three crucial steps. First, economically viable methods must be developed to produce large quantities of hydrogen, ideally using renewable energy sources. Advanced water-splitting techniques that use electricity and some heat as energy sources are very energy-efficient, and might one day fit the bill. Second, hydrogen distribution and storage systems are required. Existing gas-distribution networks in cities and between industrial sites could be used to move large quantities of hydrogen around, but mobile hydrogen-storage vessels and filling stations are clearly necessary for transport applications. Several prototype hydrogen-filling stations already service fleets of hydrogen-fuelled buses, for example at Nagoya airport in Japan and in Berlin. But no countrywide hydrogen infrastructure has yet been set up — although Germany



has developed a tool (called H2invest) for planning such an infrastructure. The third step is to develop technologies and devices for converting the chemical energy stored in hydrogen into more useful forms of energy. Currently, hydrogen can yield thermal energy in a combustion engine or electrical energy in a fuel cell (Fig. 1).

### Could petrol-fuelled car engines be converted to use hydrogen?

Yes, by making minor modifications. But that's not a sustainable solution in the long term, as combustion engines convert chemical energy to mechanical energy (via thermal energy) with low efficiency. For example, the energy-conversion efficiency of a typical petrol-fuelled car in everyday traffic conditions is little more than 10%. Far more efficient would be a combined hydrogen-fuel-cell-electric-motor (Hy-FC-EM) system, known as a power train. But the development of an economically viable power train has proven far more difficult than was expected.

### What are the problems in developing power trains?

There are three main issues. The first is cost — fuel cells generally require catalysts that contain rare and expensive elements. The second issue is that fuel cells have short lifetimes. Nevertheless, a few companies have successfully overcome these problems to develop potentially useful hydrogen fuel cells for transport applications. The remaining big hurdle is therefore to find compact, light-weight hydrogen-storage systems capable of delivering hydrogen gas to a fuel cell at approximately room temperature, and at pressures not much greater than atmospheric pressure. To stimulate research and development in this area, in 2002 the US Department of Energy set quantitative goals for the hydrogen content of storage devices (6% by mass by 2010, then 9% by 2015). So far, the targets haven't been met, and the new US government decided to cut its funding of hydrogen-storage research, opting instead to put more money into developing batteries for fully electric vehicles. However, the US House of Representatives has subsequently voted to restore most of this funding, and the energy department has revised the targets to 5.5% by mass for 2015.

### Do the targets make sense?

No — the whole car needs to be optimized for mass, not just the fuel tank. In fact, many car manufacturers, owners and public agencies do not care if 1 tonne or more of mass is used inefficiently in heavy vehicles (which might weigh upwards of 2.5 tonnes). Concentrating efforts on the mass of the fuel tank alone is like asking an obese patient to lose weight from his left arm to control his total weight.

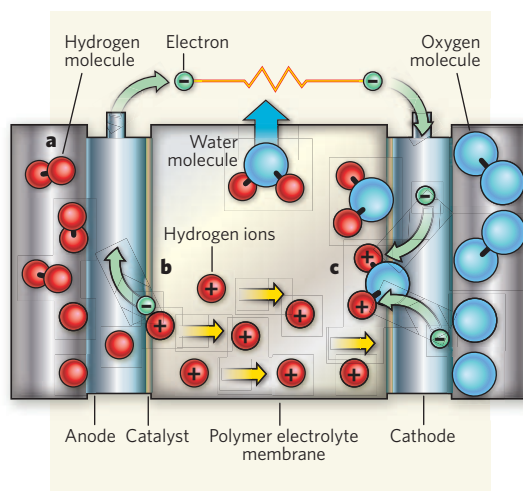


**Figure 1 | A hydrogen fuel cell.** Hydrogen is electrochemically combusted in fuel cells to produce energy. **a**, Hydrogen is channelled to the anode at one side of the cell, where the H<sub>2</sub> molecules split into hydrogen atoms. **b**, A catalyst lining the anode causes the hydrogen atoms to split into hydrogen ions (H<sup>+</sup>) and electrons. A polymer electrolyte membrane allows the hydrogen ions to pass between the anode and the cathode, but the electrons must pass through an external circuit to reach the cathode, creating a current. **c**, Oxygen is channelled to the cathode, where it reacts with electrons and hydrogen ions to form water as the only side product. The water flows out of the cell.

### How much hydrogen does a car need to store?

Using today's technologies, a safe, weight-efficient, five-seater car might weigh 1.2–1.5 tonnes. This would travel at least 500 kilometres on 30–35 litres of petrol or diesel, with the combined mass of the fuel and tank being 80 kilograms. To travel the same distance using a Hy-FC-EM power train, that car would need about 5 kilograms of hydrogen. The same car fitted with a hydrogen combustion engine would need 10 kilograms of hydrogen or more. The problem is that 5 kilograms of hydrogen at room temperature and pressure occupy about 56,000 litres — equivalent to a balloon 4.8 metres in diameter. Some method of squeezing this volume down by 1,000-fold is therefore essential.

### Can't hydrogen be stored at high pressure, or liquefied, to reduce the volume?

Yes, but this isn't practical for hydrogen storage in cars. If hydrogen behaved like an 'ideal' gas, then a pressure of 100 megapascals (100 MPa, 1,000 times that of atmospheric pressure) would be needed to compress it to 1,000th of its volume at atmospheric pressure. But hydrogen exhibits ideal-gas behaviour only up to about 10 MPa; at pressures above 50 MPa, it deviates markedly from such behaviour, requiring even more pressure to compress it further. Also, the safety issues associated with storing the gas at those high pressures become a

great concern. Compression of hydrogen above 100 MPa is therefore not a sensible option. Liquefaction certainly yields hydrogen in an extremely energy-dense form (as used for space technology), but the process requires temperatures below –250 °C. Such conditions, and the cryogenic techniques needed to obtain them, are demanding — but not infeasible — for ordinary petrol stations. The liquefaction process, however, also results in the loss of about 30% of the chemical energy of gaseous hydrogen.

### So what else can be done?

Hydrogen can be reversibly absorbed or adsorbed (accumulated at the surface) by certain solid materials, greatly reducing its volume. The gas is then released on heating or on lowering the hydrogen-gas pressure. Two main classes of hydrogen-storage material exist, corresponding to two mechanisms of sorption: physisorption, in which H<sub>2</sub> molecules are weakly adsorbed by the material, but don't react chemically with it; and chemisorption, in which H<sub>2</sub> molecules react with the material's surface, dissociating into hydrogen atoms that are absorbed into the bulk, where they form metallic, covalent or ionic bonds with the material (Fig. 2).

### What sorts of material adsorb hydrogen by physisorption?

Those that have high surface areas per unit of mass, such as some graphitic materials or high-porosity compounds. At full capacity, their hydrogen content can reach about 8% by mass. The problem is that, on planar surfaces (which occur in many materials) physisorption is weak. Temperatures below –200 °C (about the temperature of liquid nitrogen) are therefore generally needed to adsorb useful quantities of hydrogen. Physisorption is stronger in materials that have narrow, curved pores, and at surfaces decorated with hydrogen-attracting atoms. Zeolites (aluminosilicates) and metal-organic frameworks (complexes of metal ions and rigid organic molecules) might provide these features, raising the hope that hydrogen physisorption could one day be achieved at room temperature in such materials.

### And which materials use chemisorption?

Hydrogen reacts with many materials — often metals or alloys, but also other compounds — to form hydrides that can be used as hydrogen-storage media. The reactions are often fast and reversible at practically accessible temperatures (20–100 °C), so that large amounts of hydrogen can be absorbed and then recovered. Materials that have been extensively studied for hydrogen storage include: hydrides of elemental metals (magnesium, palladium, thorium); hydrides of compounds that have the formula AB<sub>3</sub> (where A and B are usually metals),

such as lanthanum–nickel hydride ( $\text{LaNi}_5\text{H}_6$ ); and ‘complex hydrides’, such as magnesium–nickel hydride ( $\text{Mg}_2\text{NiH}_4$ ) or barium–rhodium hydride ( $\text{BaRhH}_9$ ).

### How well do hydrides perform?

They easily reach hydrogen-volume densities far above that of liquid hydrogen, and can be recharged several tens of thousands of times. But because the host materials are not light, the quantity of hydrogen stored has not exceeded 4% by mass. To date, most of these compounds aren’t practically useful for mobile hydrogen storage, as their hydrogen-storage capacities per unit mass are either too small or the temperatures required to release stored hydrogen are too high. But their volumetric hydrogen-storage capacity and their safety features are impressive.

### Does that mean hydride research hasn’t been fruitful?

On the contrary, there have been many useful discoveries from this field. Metal hydrides are now used as electrodes for batteries, such as those in commercially available hybrid cars. These batteries are safe, compact and quickly rechargeable. Metal hydrides also form the basis of certain temperature sensors in aircraft, and might one day be used in intelligent coatings that control the transparency of windows. Furthermore, hydrogen-induced pulverization techniques, discovered during the course of metal-hydride research, are now used to manufacture permanent magnets.

### What’s the latest thing in hydrogen-storage materials?

Current studies focus on solid-state storage using complex hydrides of light elements (those with low atomic masses), or high-pressure tanks (35 MPa) filled with such materials. These complex hydrides include alanates (which contain  $\text{AlH}_4^-$  anions, where Al is aluminium); borohydrides (which contain  $\text{BH}_4^-$  anions, where B is boron); amide hydrides (which contain lithium, nitrogen and hydrogen); and combinations thereof. They reach attractively high hydrogen contents of 8–20% by mass. For these materials, hydride formation and decomposition proceed over several steps through intermediate compounds. Experimental and modelling efforts are aimed at fine-tuning these reactions, and finding catalysts that speed up hydrogen release. Such efforts should yield materials that charge and discharge hydrogen in a temperature range of 20–100 °C; currently, temperatures of 300 °C or more are required. But practical applications of these materials are probably still a long way off. Another approach to hydrogen storage has also recently been resurrected, having previously fallen out of favour because of poor performance. In this approach, liquid hydrocarbons are used as a source of hydrogen gas. The process generates a dehydrogenated hydrocarbon side product,

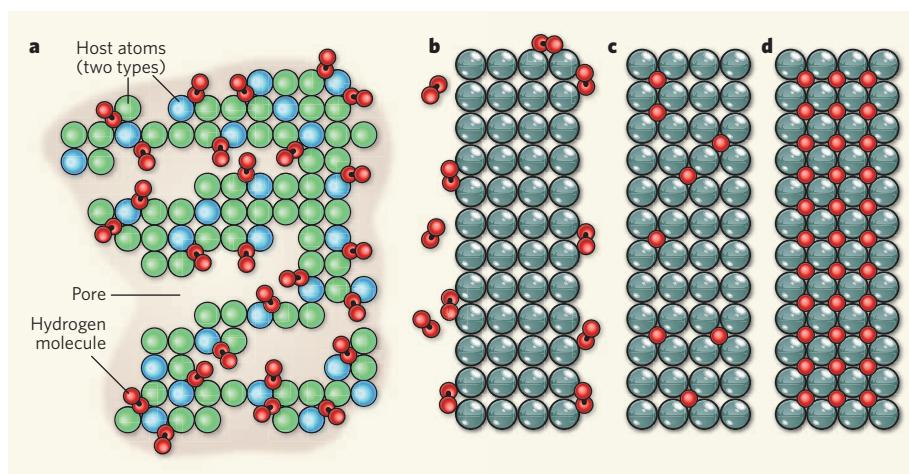


**Figure 2 | Mechanisms of hydrogen storage.** **a**, Materials that have high porosity store hydrogen using physisorption, in which the gas molecules accumulate at the surface of the material, but don’t react chemically with it. **b–d**, Certain metals, alloys and other compounds store hydrogen using chemisorption. In this process, hydrogen molecules react with the surface of the material (**b**), where they split into separate atoms. Initially, the hydrogen atoms adopt random locations in the host material (**c**). They eventually form metallic, covalent or ionic bonds with the metal atoms to yield a hydride compound, in which the hydrogen atoms adopt a regular arrangement (**d**).

which could be re-hydrogenated at a recycling centre to generate more fuel.

### When will we see hydrogen-fuelled cars on the market?

Hydrogen-powered buses in Germany and Japan have already been successful, and about 50 prototype cars — both thermal-combustion and fuel-cell types — have so far been tested, with good results. I therefore wouldn’t be surprised to see Hy-FC-EM cars for sale in about five years.

### What are the other options for powering vehicles?

Given their current dominance, oil-based fuels will undoubtedly be used in vehicles for some time to come, although uncertainties about supply mean that their days are probably numbered. New types of rechargeable battery — safer lithium and lithium–air batteries, and higher-capacity metal-hydride batteries — will also raise the market potential of fully electric city vehicles and hybrid cars. It should be noted, however, that if most car owners switched to fully electric cars, many countries would need to double their electricity production. Similarly, hydrogen production also requires energy, such as electricity.

### How will hydrogen compete with those other power sources?

This depends on trends in car design and the cost-effectiveness of hydrogen technology. Hydrogen-fuelled cars are already technically feasible, but if they are to be widely used, they must also be economically competitive with rival models that use other fuels. This will probably happen in a few years for smaller cars (those weighing about 1 tonne); a trend towards lightweight vehicles would therefore

help to kick-start the market. But although car manufacturers increasingly use lightweight, high-strength materials, the average total mass of a car has continuously increased over the past decade, as vehicles grow in size, power, comfort and safety.

### So what are the prospects for hydrogen as a fuel?

A weak trend towards customers preferring smaller vehicles does exist, and this will be strengthened as car price and fuel economy become more important to buyers. New safety devices that not only give drivers warnings, but also act directly on the car, should decrease the probability of accidents, reducing the need for heavy protection in vehicles. That would open the door to lightweight vehicles and so to hydrogen-fuelled mobility. Hydrogen therefore certainly has a place in long-term transport strategies. But to ensure success, the challenges ahead require smart goals and long-term support of the best scientists and engineers — not ‘stop-and-go’ politics from successive governments, as currently seems to be the case. ■

Louis Schlapbach is at Empa – Materials Science and Technology, CH-8600 Dübendorf, Switzerland, and the National Institute for Materials Science, Tsukuba, Japan.  
e-mail: louis.schlapbach@me.com

#### FURTHER READING

- Léon, A. (ed.) *Hydrogen Technology: Mobile and Portable Applications* (Springer, 2008).
- Züttel, A., Borgschulte, A. & Schlapbach, L. (eds) *Hydrogen as a Future Energy Carrier* (Wiley-VCH, 2008).
- Crabtree, G. W. & Dresselhaus, M. S. The hydrogen fuel alternative. *Mater. Res. Soc. Bull.* **33**, 421–428 (2008).
- Oumellal, Y., Rougier, A., Nazri, G. A., Tarascon, J.-M. & Aymard, L. Metal hydrides for lithium-ion batteries. *Nature Mater.* **7**, 916–921 (2008).
- Harris, I. R., Book, D., Anderson, P. A. & Edwards, P. P. Hydrogen storage: the grand challenge. *Fuel Cell Rev.* **1**, 17–23 (2004).
- Hydrogen and fuel cells. [www.netinform.de/h2](http://www.netinform.de/h2)



**Cover illustration**

Enzymes that contain metal atoms (yellow) at their active sites are involved in many biological processes. (Artwork by N. Spencer)

**Editor, *Nature***

Philip Campbell

**Publishing**

Nick Campbell  
Claudia Deasy

**Insights Editor**

Karl Ziemelis  
Lesley Anson

**Production Editor**

Davina Dadley-Moore

**Senior Art Editor**

Martin Harrison

**Art Editor**

Nik Spencer

**Sponsorship**

Amélie Pequignot  
Reya Silao  
Thomas Rose  
Stephen Russell

**Production**

Jocelyn Hilton

**Marketing**

Elena Woodstock  
Emily Elkins

**Editorial Assistant**

Emma Gibson

# METALLOPROTEINS

**P**roteins can catalyse a remarkably wide range of chemical reactions. Yet the main differences among polypeptides are in the side chains of naturally occurring amino acids, which account for only a small proportion of the possible chemical functionality. The diversity of function is instead made possible partly because proteins can incorporate cofactors — such as small organic molecules, single metal atoms or clusters that contain metal and non-metal atoms — into their active sites.

Almost half of all enzymes require the presence of a metal atom to function. These ‘metalloproteins’ have captivated chemists and biochemists, particularly since the 1950s, when the first X-ray crystal structure of a protein, sperm whale myoglobin, indicated the presence of an iron atom. Much is now understood about how metal clusters are assembled, how metal ions or clusters are introduced into target proteins, and which metal ions are commonly found in metalloenzymes. In addition, we are much closer to understanding the mechanisms by which metalloenzymes catalyse such a range of complex chemical reactions. But, despite more than half a century of research by chemists, biochemists and cell biologists, many discoveries remain to be made.

The articles in this Insight highlight some of the most exciting current research on metalloproteins, including how enzymes containing complex metal clusters metabolize small gaseous molecules, how proteins containing iron–sulphur clusters are assembled, and how metalloenzymes containing a single metal ion catalyse the halogenation of small organic molecules.

We are pleased to acknowledge the financial support of AstraZeneca in producing this Insight. As always, *Nature* carries sole responsibility for all editorial content and peer review.

Joshua Finkelstein, Senior Editor

## REVIEWS

### 814 Structure–function relationships of anaerobic gas-processing metalloenzymes

J. C. Fontecilla-Camps, P. Amara, C. Cavazza, Y. Nicolet & A. Volbeda

### 823 Metalloproteins and metal sensing

K. J. Waldron, J. C. Rutherford, D. Ford & N. J. Robinson

### 831 Function and biogenesis of iron–sulphur proteins

R. Lill

### 839 Molybdenum cofactors, enzymes and pathways

G. Schwarz, R. R. Mendel & M. W. Ribbe

### 848 Mechanistic considerations of halogenating enzymes

A. Butler & M. Sandy

### 855 Design of functional metalloproteins

Y. Lu, N. Yeung, N. Sieracki & N. M. Marshall

nature  
insight

# Structure–function relationships of anaerobic gas-processing metalloenzymes

Juan C. Fontecilla-Camps<sup>1</sup>, Patricia Amara<sup>1</sup>, Christine Cavazza<sup>1</sup>, Yvain Nicolet<sup>1</sup> & Anne Volbeda<sup>1</sup>

**Reactions involving H<sub>2</sub>, N<sub>2</sub>, CO, CO<sub>2</sub> and CH<sub>4</sub> are likely to have been central to the origin of life. This is indicated by the active-site structures of the enzymes involved, which are often reminiscent of minerals. Through the combined efforts of protein crystallography, various types of spectroscopy, theoretical calculations and model chemistry, it has been possible to put forward plausible mechanisms for gas-based metabolism by extant microorganisms. Although the reactions are based on metal centres, the protein matrix regulates reactivity and substrate and product trafficking through internal pathways, specific ligation and dielectricity.**

The most popular autotrophic theory of the origin of life postulates that primordial metabolisms developed on mineral iron–sulphur surfaces under reducing conditions<sup>1</sup>. During this period of the Earth's evolution, between 4.6 and 3.5 billion years (Gyr) ago, the atmosphere was probably rich in gases such as H<sub>2</sub>, CO and CO<sub>2</sub>, and its hot oceans contained relatively high concentrations of transition-metal ions such as Fe<sup>2+</sup> and Ni<sup>2+</sup> (ref. 2). Similar conditions are found around contemporary hydrothermal vents generated by plate tectonics at the ocean floor. Thermophilic methanogenic Archaea can grow around vents called black smokers, owing to the oxidation of expelled H<sub>2</sub> and the reduction of CO<sub>2</sub> to CH<sub>4</sub> (ref. 3). This biotope shows that life can thrive independently of solar energy, which was a requirement for early organisms before the emergence of photosynthesis. The oxidation of H<sub>2</sub>S by microbial symbionts of vent-associated organisms such as tube worms is not discussed here because it requires O<sub>2</sub> and is flavin based rather than metal based.

Along with H<sub>2</sub> as an energy vector, CO<sub>2</sub> was most probably used as a carbon source through an ancestral version of the Wood–Ljungdahl pathway, which generates acetyl–coenzyme A (CH<sub>3</sub>C(O)–SCoA) to be used in anabolic processes<sup>4</sup>. Conversely, nitrogenase, the enzyme capable of reducing N<sub>2</sub> to ammonia in a process crucial for life, is thought to have originally evolved as a detoxifier, neutralizing the poisonous cyanogen gas, (CN)<sub>2</sub>, present in the early atmosphere<sup>5</sup>. All these reactions took place in an anoxic environment, as it was not until about 2.2 Gyr ago that oxygen produced by photosynthetic cyanobacteria entered the atmosphere in significant amounts<sup>2</sup>. As a consequence, extant anaerobic H<sub>2</sub> and/or CO oxidizers and CO<sub>2</sub> reducers are generally confined to remaining anoxic settings, for example the bottoms of lakes and oceans and the digestive systems of animals. A notable feature of all these gas-based redox reactions is that they are catalysed by enzymes containing complex metallic active sites often reminiscent of FeS-containing mineral structures such as greigite, pyrrhotite, violarite and pyrite. This analogy constitutes the basis for the concept of primordial surface metabolism on transition-metal sulphides of the ‘iron–sulphur-world’ theory for the origin of life<sup>1</sup>. In all the gas-based reactions discussed in this Review (Table 1), catalysis seems to be metal centred, and with one exception the active site is buried. The role of the protein matrix is to determine the specificity of the reaction, provide ligands, modulate the redox potential and, in several cases, allow gas diffusion to and from the active site through hydrophobic tunnels.

Given the complexity of the active sites, it is not surprising that their assembly and insertion into the corresponding proteins typically involves

a significant number of gene products. The well-studied examples of nitrogenase and [NiFe]- and [FeFe]-hydrogenase<sup>6,7</sup> are reviewed in some detail. Perhaps the most complicated aspect of gas-based catalysis is the elucidation of its mechanism. Often, the joint efforts of spectroscopy, X-ray crystallography, computational studies and model chemistry have been required to shed light on its nature, and in certain cases there is still room for debate. In this Review, we discuss the three known classes of hydrogenase, bifunctional CO dehydrogenase (CODH)–acetyl–SCoA synthase (ACS), methyl–coenzyme M (CH<sub>3</sub>–SCoM) reductase (MCR) and nitrogenase. Four of these enzymes' active sites contain nickel, an otherwise uncommon element in biology, whereas cuboidal FeS clusters are almost ubiquitous (see page 831). The complex gas-catalysing active sites pose a formidable problem to synthetic chemists. Both biomimetic and bio-inspired models have been reported. A few examples are discussed.

## Active sites

Figure 1 shows the active sites discussed in this Review. Hydrogen catalysis is carried out by at least three well-characterized types of enzyme: [Fe]-, [FeFe]- and [NiFe]-hydrogenases. Of these, [Fe]-hydrogenases are found only in methanogens<sup>8</sup>. By contrast, [FeFe]-hydrogenases are present in bacteria and some unicellular eukaryotes, whereas their [NiFe] counterparts are found in bacteria and Archaea<sup>9</sup>. Although these proteins are phylogenetically unrelated, the three active sites contain a Fe(CO)<sub>n</sub>,

**Table 1 | A compilation of the various enzyme reactions discussed**

No.	Enzyme	Reaction
1a	Hydrogenases	H <sub>2</sub> ⇌ H <sup>+</sup> + H <sup>+</sup>
1b		H <sup>+</sup> ⇌ H <sup>+</sup> + 2e <sup>−</sup>
1c		H <sub>2</sub> ⇌ 2H <sup>+</sup> + 2e <sup>−</sup>
1d		Methenyl-H <sub>4</sub> MPT <sup>+</sup> + H <sup>+</sup> ⇌ methylene-H <sub>4</sub> MPT
2	CO dehydrogenase	CO <sub>2</sub> + 2e <sup>−</sup> + 2H <sup>+</sup> ⇌ CO + H <sub>2</sub> O
3	Acetyl–SCoA synthase	CH <sub>3</sub> –Co <sup>3+</sup> FeSP + CoAS <sup>−</sup> + CO ⇌ CH <sub>3</sub> C(O)–SCoA + Co <sup>+</sup> FeSP
4	Nitrogenase	N <sub>2</sub> + 8H <sup>+</sup> + 8e <sup>−</sup> + 16ATP ⇌ 2NH <sub>3</sub> + H <sub>2</sub> + 16ADP + 16P <sub>i</sub>
5	Methyl–SCoM reductase	CH <sub>3</sub> –SCoM + CoBSH ⇌ CH <sub>4</sub> + CoMS–SCoB

P<sub>i</sub>, inorganic phosphate.

<sup>1</sup>Laboratoire de Cristallographie et Cristallogénèse des Protéines, Institut de Biologie Structurale ‘J.P. Ebel’, CEA, CNRS, Université Joseph Fourier, 41 rue J. Horowitz, 38027 Grenoble Cedex 1, France.



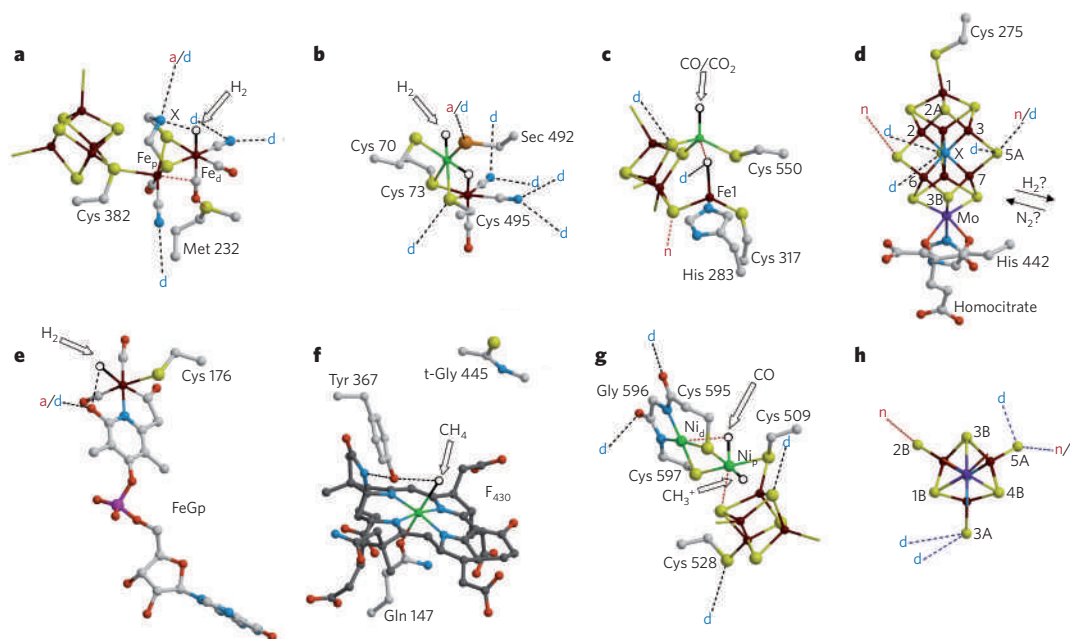


**Figure 1 | Active sites of gas-processing metalloenzymes.** **a**, [FeFe]-hydrogenase; **b**, [NiFe]-hydrogenase; **c**, nickel-dependent CO dehydrogenase; **d**, [FeMo]-nitrogenase; **e**, [Fe]-hydrogenase; **f**, methyl-SCoM reductase; **g**, acetyl-SCoA synthase; **h**, nitrogenase FeMo-co (top view). Open arrows and open spheres respectively indicate entrance/exit sites and available binding sites for gases and other substrates. We simplify the protein environments using the following symbols: d, hydrogen-bond donor; a, hydrogen-bond acceptor; and n, nucleophile<sup>86</sup>. Black and red dashed lines respectively indicate putative hydrogen-bond and other

weak interactions. Atom colour codes: molybdenum, violet; selenium, orange; nickel, green; iron, brown; sulphur, yellow; oxygen, red; nitrogen, blue; carbon, white (or grey in the F<sub>430</sub> cofactor). Subscripts p and d respectively indicate the proximal and the distal metal ions with respect to the [Fe<sub>2</sub>S<sub>4</sub>] cluster. Iron ions in FeMo-co are numbered, and inorganic sulphur ions are labelled 1A, 2A, and so on. Fe1 in **c** corresponds to a unique iron ion, and X in **d** corresponds to a central light atom that could be carbon, nitrogen or oxygen. Gp, guanylylpyridinol; Sec, selenocysteine; t-Gly, thioglycine.

unit, with  $n = 1$  in [NiFe]-hydrogenase and  $n = 2$  in [Fe]- and [FeFe]-enzymes. In addition, [NiFe]- and [FeFe]-hydrogenases have two CN<sup>−</sup> ligands that are terminally bound to one or two iron ions, respectively<sup>10</sup>, and [Fe]-hydrogenase contains a guanylylpyridinol cofactor that binds the active-site iron through an  $sp^2$ -hybridized nitrogen and a formyl carbon atom<sup>8</sup>. The protein contributes only one thiolate ligand to iron coordination. In [NiFe]-hydrogenases, protein coordination is mediated by two Fe–Ni-bridging and two nickel-binding terminal Cys thiolates<sup>11</sup>; in some enzymes, one of the latter Cys thiolates is replaced by a selenocysteinate<sup>12</sup>. In [FeFe]-hydrogenases, the active site is an [FeFe]–[Fe<sub>4</sub>S<sub>4</sub>] unit known as the H-cluster. The catalytic [FeFe] subcluster is coordinated by one Cys thiolate and a five-atom organic dithiolate ligand with a bridgehead atom that could be carbon, nitrogen or oxygen (X in Fig. 1a). Experimental studies favour nitrogen<sup>13–15</sup>, whereas a theoretical study using active-site models favoured an ether but did not rule out an amine<sup>16</sup>. The crystal structures of the three hydrogenases show vacant ligand sites at the catalytic metal, which are potentially available for H<sub>2</sub> binding. In [FeFe]- and [Fe]-hydrogenases, substrate binding would complete an octahedral coordination sphere around the iron ion. In [NiFe]-hydrogenases, the catalytic nickel ion has both a terminal coordination site and a bridging coordination site available for exogenous ligands, which, if occupied, would also result in an octahedral sphere around the metal ion.

Nickel-dependent CODH<sup>17</sup> catalyses the reversible reduction of CO<sub>2</sub> to CO (Table 1, reaction 2). Its active site, known as the C-cluster, contains an [Fe<sub>2</sub>S<sub>4</sub>] unit linked to a spectroscopically unusual iron ion (Fe1 in Fig. 1c) and a nickel ion<sup>18</sup>. The protein provides a terminal thiolate ligand to both the nickel and Fe1 and an additional His ligand to Fe1. The structure of the catalytic A-cluster of ACS consists of a [NiNi]–[Fe<sub>4</sub>S<sub>4</sub>] unit<sup>19</sup>. The nickel ion distal relative to [Fe<sub>4</sub>S<sub>4</sub>], Ni<sub>d</sub>, is bound to two consecutive main-chain nitrogen atoms and two Cys thiolates with square-planar geometry. These thiolates also bind the proximal nickel ion, Ni<sub>p</sub>, which is further coordinated by a Cys thiolate. The latter also binds one of the irons of the [Fe<sub>4</sub>S<sub>4</sub>] cluster. The proximal nickel ion is most likely involved in catalysis because it has two vacant coordination sites available for the binding of reaction

intermediates. Thus, the CODH, ACS and [NiFe]-hydrogenase active sites are similar: other than nickel, they contain iron, Cys thiolate ligands and two nickel *cis*-coordination sites available for substrate binding<sup>20</sup>.

The reduction of N<sub>2</sub> to ammonia is performed by nitrogenases<sup>21</sup> (Table 1, reaction 4). The reaction is carried out at a complex cluster, the [FeMo]-cofactor (FeMo-co)<sup>22</sup> (see page 839). The 1.16-Å-resolution crystal structure of the enzyme has redefined this cofactor as a [Mo–7Fe–9S–X] unit<sup>23</sup> (Fig. 1d, h). In the resting state of the enzyme observed in the crystals, the octahedral coordination sphere of the molybdenum ion is saturated by three bridging sulphide ions from the cluster, a bidentate homocitrate ligand and a His imidazole. The only other protein ligand is a Cys thiolate, bound to the apical iron ion at the other end of the cofactor. The other six iron ions are each bound by three sulphides and a central atom X, which, on the basis of the electron density and local charges, could be C<sup>4−</sup>, N<sup>3−</sup> or O<sup>2−</sup> (ref. 24). There is no obvious coordination site for either N<sub>2</sub> or H<sub>2</sub> (Table 1, reaction 4).

Some Archaea use specific cofactors and coenzymes for methanogenesis (Table 1, reaction 5) and anaerobic methane oxidation. The active site of the enzyme involved in methane evolution, MCR, contains a porphyrin-related F<sub>430</sub> cofactor, also known as corphin. This is the most reduced tetrapyrrole–metal complex found in nature<sup>25</sup>. Apart from binding F<sub>430</sub>, the nickel ion is axially coordinated by the oxygen of a Gln side chain. *Trans* to the latter, there is a vacant site available for substrate and product binding.

As well as binding the generally buried active sites, the protein environment finely regulates its accessibility for all substrates, including protons, coenzymes and gases that diffuse through internal tunnels (Table 1). Some of these aspects are further developed below.

## Catalysis

Possible catalytic mechanisms for the enzymes discussed here are presented in Fig. 2. The [FeFe]- and [NiFe]-enzymes are 'true' hydrogenases, in that they catalyse the reversible oxidation of molecular hydrogen to protons and electrons<sup>10,26</sup>. However, the [Fe]-hydrogenase only catalyses

the first step in the uptake reaction (Table 1, reaction 1a), transferring the resultant hydride to methenyl- $H_4MPT^+$  (Table 1, reaction 1d)<sup>27</sup>. This enzyme is also unusual in that both the active-site iron-binding guanylylpyridinol cofactor (Fig. 1e) and the substrate are found at the molecular surface<sup>8</sup>. The nickel–iron coordination geometry of [NiFe]-hydrogenases changes very little between its oxidized inactive and reduced active forms<sup>10</sup>. A hydride probably bridges the nickel and iron ions in the active form<sup>28</sup>, replacing oxygen species observed in the inactive species. The competitive inhibitor CO binds terminally to nickel in [NiFe]-hydrogenase<sup>29</sup> and to  $Fe_d$ , the distal iron ion (relative to  $[Fe_4S_4]$ ), in [FeFe]-hydrogenase<sup>30</sup> (arrows in Fig. 1). In [FeFe]-hydrogenase, one of the intrinsic CO ligands switches between terminal and bridging positions, depending on the redox state of the enzyme and, possibly, on hydride binding to the same orbital<sup>13</sup> (Fig. 2c). So far, this switch has not been reproduced by calculations using active-site models<sup>31</sup>.

The binding of active-site iron to the high-field,  $\pi$  acceptor CO and  $CN^-$  ligands (Fig. 1) promotes a low-redox state of the metal ion, making it a relatively soft Lewis acid. This, in turn, favours its binding to the soft Lewis base  $H^-$ , a probable step in catalysis (Table 1). The direction of the reaction in [FeFe]- and [NiFe]-hydrogenases is governed by the intracellular location of the enzyme, the pH and the  $H_2$  concentration. Previous work by some of us has focused on periplasmic hydrogen-uptake enzymes from sulphate-reducing bacteria<sup>10</sup>. Figure 2a shows two possible hydrogen-binding states of the active site of [NiFe]-hydrogenase: the partially oxidized electron paramagnetic resonance (EPR)-silent Ni-SI form, which may be the initial product of reductive activation (blue cycle)<sup>32</sup>; and the EPR-active Ni-C state, which has been shown to be in redox equilibrium with  $H_2$  (red cycle)<sup>33,34</sup>. The reaction of  $H_2$  with Ni-C would result in a species, reduced by two more electrons, that should be a transition state in the catalytic cycle. An equivalent

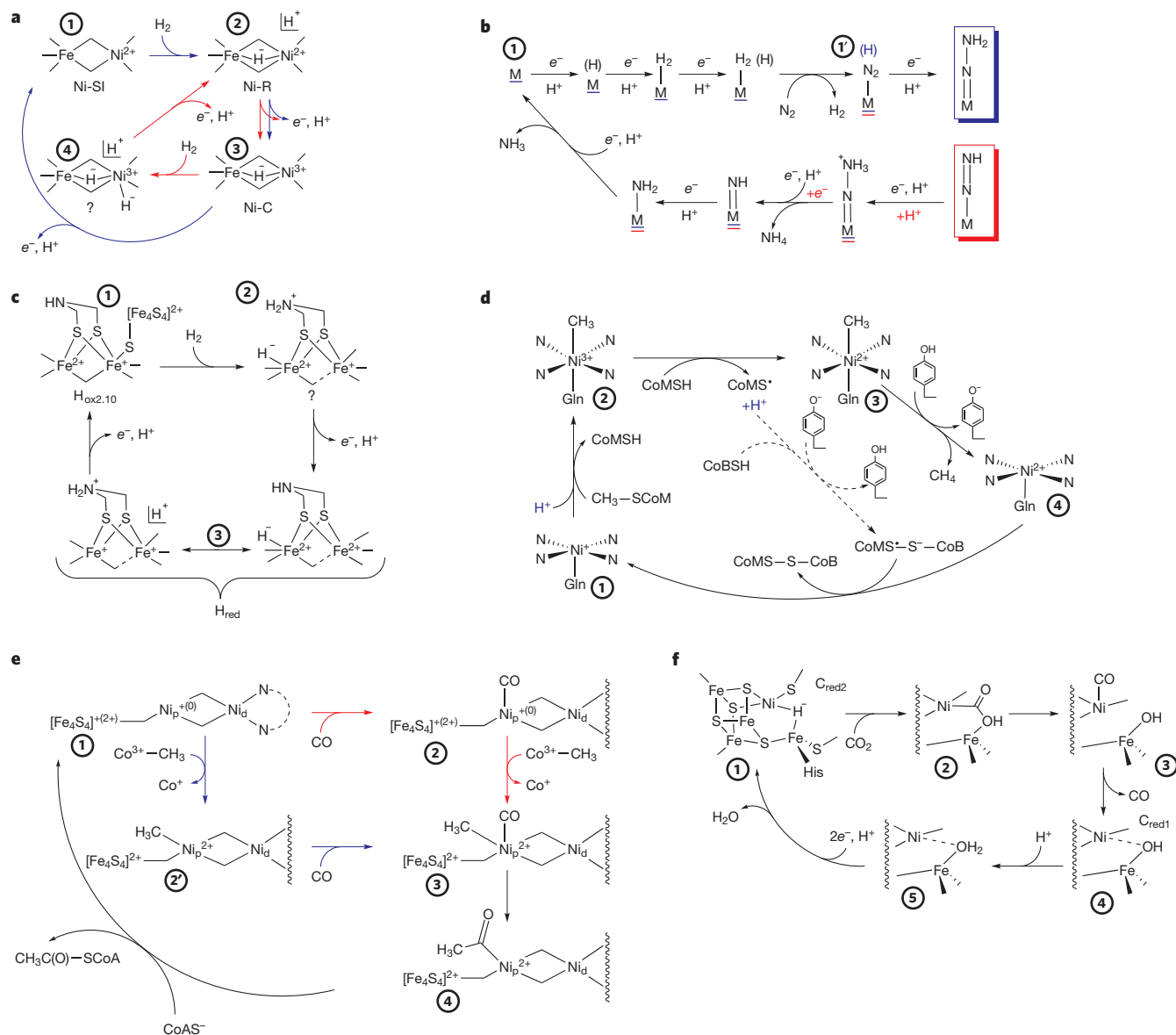


**Figure 2 | Enzymatic catalysis.** **a**, [NiFe]-hydrogenase. Blue and red cycles define Ni-SI and Ni-C as  $H_2$  acceptors, respectively<sup>32,33</sup>. **b**, Nitrogenase. The blue cycle corresponds to the complete process; it favours iron-centred catalysis<sup>30</sup>. The red cycle shows intermediate states found with a molybdenum-based model compound<sup>51</sup>; M is a metal component of FeMo-co. **c**, [FeFe]-hydrogenase. The bridgehead atom is depicted as nitrogen because it makes chemical sense and there are several lines of evidence that

favour it (see main text). **d**, Methyl-SCoM reductase. The proton donor to form  $CH_4$  is depicted as Tyr<sup>45</sup>. **e**, Acetyl-SCoA synthase. The two possible sequences of substrate binding are depicted by blue ( $CH_3$  first) and red (CO first) arrows. **f**, CO dehydrogenase. This mechanism is based on the proposition in ref. 18 and recent experimental results<sup>36,37</sup>. No catalytic mechanism for the re-interpreted active-site structure of [Fe]-hydrogenase<sup>8</sup> has been proposed. 1' and 2' correspond to alternative pathways.



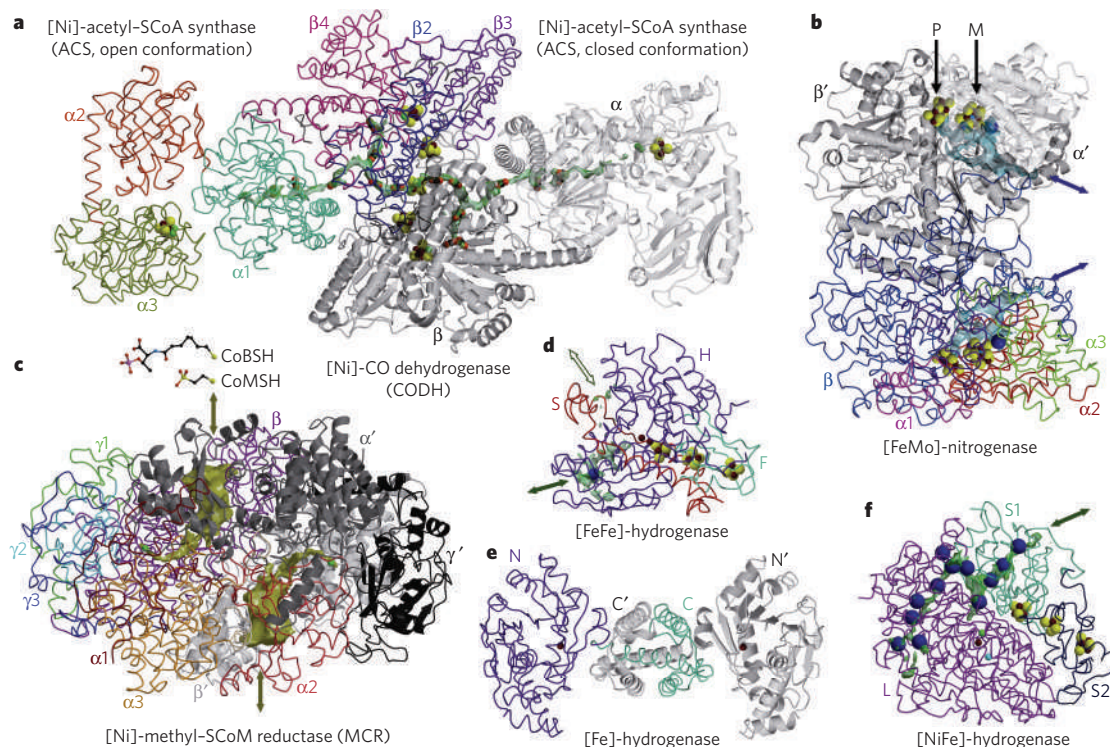


**Figure 3 | Enzyme folds and substrate tunnels.** The structures shown are of the *Moorella thermoacetica* CODH–ACS complex (a), *Azotobacter vinelandii* nitrogenase (b), *Methanothermobacter thermoautotrophicus* (formerly *Methanobacterium thermoautotrophicum*) MCR (c), *Desulfovibrio desulfuricans* [Fe]-hydrogenase (d), *Methanocaldococcus jannaschii* [Fe]-hydrogenase (e) and *Desulfovibrio fructosovorans* [NiFe]-hydrogenase (f), corresponding to Protein Danks Bank depositions with codes 1OAO<sup>19</sup>, 1M1N<sup>23</sup>, 1HBN<sup>45</sup>, 1HFE<sup>54</sup>, 3F47 (ref. 8) and 1YQW<sup>10</sup>, respectively. Selected tunnel-forming cavities are coloured green, light-blue or yellow, depending on whether they are mainly hydrophobic, hydrophilic or amphiphilic, respectively. The probe radii used to display these cavities are 0.8 Å for CODH–ACS and [NiFe]-hydrogenase, 1.4 Å for MCR, 0.6 Å for [FeFe]-hydrogenase and 1.0 Å for [FeMo]-nitrogenase. Arrows indicate proposed main gas entrance/exit sites at the enzyme surface. Crystallographically detected xenon sites are shown as large dark-blue spheres, and CO<sub>2</sub>-binding sites (in CODH–ACS) are shown as small

black and red spheres for C and O, respectively. The xenon site in [FeFe]-hydrogenase and the CO<sub>2</sub> sites in CODH–ACS correspond to our own recent results. Other atoms are coloured as in Fig. 1. For the enzymes with internal two-fold symmetry (CODH, ACS, MCR, [Fe]-hydrogenase and [FeMo]-nitrogenase), one half is depicted in grey, showing secondary structure elements as ribbons (helices) and arrows (β-sheets). All other subunits are shown as Ca traces, coloured according to domain and/or subunit. The arrows labelled P and M indicate the P-cluster and the FeMo-co in nitrogenase, respectively. All structures are shown on the same scale except CoBSH and CoMSH, which are magnified by a factor of two for clarity. Subunits are labelled using Greek symbols for CODH–ACS, MCR and nitrogenase. Domains are labelled with numbers. For the three hydrogenases, S and L respectively indicate small and large subunits, H and F respectively indicate H-cluster and ferredoxin-like domains, and N and C respectively indicate amino- and carboxy-terminal domains.

situation may apply to [FeFe]-hydrogenases because the  $H_{ox2,10}$  state, which is postulated to bind H<sub>2</sub> (ref. 14) (Fig. 2c), is the only catalytically relevant observable EPR-active species.

In the hyperthermophilic bacterium *Carboxydotherrmus hydrogenoformans*, which contains five CODHs<sup>35</sup>, CO is used both as a carbon and as a reducing power source (Table 1, reaction 2). It has been postulated that the enzyme in the CO<sub>2</sub>-binding C<sub>red2</sub> state contains a Ni<sup>2+</sup> ion and a bound Fe1–Ni-bridging hydride<sup>18</sup> (Fig. 2f). The nickel coordination seems to be square planar in most of the reaction intermediates, with the exception of the CO-bound species, in which it is tetrahedral. The proposition that the C<sub>red1</sub> state binds OH<sup>−</sup> between nickel and Fe1 (ref. 18) has been confirmed by X-ray structures<sup>36,37</sup>. CODH can form a complex with ACS that, in acetogens, functions in the anaerobic Wood–Ljungdahl pathway of CO<sub>2</sub> fixation (Table 1, reactions 2 and 3)<sup>4</sup>; in methanogens growing on acetate, it catalyses the reverse reactions as part of the acetyl–SCoA decarbonylase/synthase complex<sup>38</sup>. In the bifunctional CODH–ACS, CO produced at the C-cluster diffuses through a tunnel and binds at the A-cluster (Fig. 3).

Although the net electronic change during catalysis is zero, two electrons are required for the oxidative addition of CH<sub>3</sub><sup>+</sup> to the proximal nickel site of the A-cluster (Table 1, reaction 3; Fig. 2e). These electrons could be temporarily donated through the oxidation of Ni<sub>p</sub><sup>0</sup> to Ni<sub>p</sub><sup>2+</sup> or Ni<sub>p</sub><sup>+</sup>[Fe<sub>4</sub>S<sub>4</sub>]<sup>+</sup> to Ni<sub>p</sub><sup>2+</sup>[Fe<sub>4</sub>S<sub>4</sub>]<sup>2+</sup>, or, less likely, the formation of a disulphide bond from two thiolate ligands at the active site. Methylation of Ni<sup>0</sup> has

been shown in a model compound lacking an [Fe<sub>4</sub>S<sub>4</sub>] cluster<sup>39</sup>. However, calculations using density functional theory indicate that addition of [Fe<sub>4</sub>S<sub>4</sub>]<sup>2+</sup> to a truncated Ni<sub>d</sub><sup>2+</sup>Ni<sub>p</sub><sup>0</sup> model leads to Ni<sub>d</sub><sup>2+</sup>Ni<sub>p</sub><sup>+</sup>[Fe<sub>4</sub>S<sub>4</sub>]<sup>+</sup> (refs 40, 41), a state recently observed using Mössbauer spectroscopy<sup>42</sup>. The order of CO and CH<sub>3</sub> binding to the A-cluster is still the subject of considerable debate<sup>43,44</sup>. Figure 2e depicts the two possibilities. Another mechanism<sup>43</sup> involves the paramagnetic OC–Ni<sub>p</sub><sup>+</sup>[Fe<sub>4</sub>S<sub>4</sub>]<sup>2+</sup> state; however, the oxidative addition of CH<sub>3</sub><sup>+</sup> would require a second electron, the source of which remains undefined. After being synthesized by an insertion/migration reaction, the nascent acetyl group binds to CoAS<sup>−</sup>, regenerating the initial two-electrons-more-reduced active-site state by reductive elimination.

Regardless of their carbon source, all methanogens evolve CH<sub>4</sub> through a mechanism catalysed by MCR (Table 1, reaction 5; Figs 1 and 2d). It has been shown that in the functional active enzyme the nickel ion bound to F<sub>430</sub> is in the +1 redox state<sup>45</sup> (Fig. 1). According to the structure of the *Methanocaldococcus jannaschii* enzyme, methyl–SCoM must bind before the second substrate, CoBSH (7-thioheptanoyl–threonine phosphate), because the binding of CoBSH completely blocks access to the nickel ion. Although theoretical calculations have proposed a mechanism whereby CH<sub>4</sub> is liberated upon CH<sub>3</sub>–SCoM binding to nickel<sup>46</sup> with the transient formation of a Ni–SCoM complex, direct evidence of the formation of a stable Ni<sup>3+</sup>–CH<sub>3</sub> adduct<sup>47,48</sup> favours the mechanism depicted in Fig. 2d. The overall

reaction implies the formation of a C–H bond on the methyl group to yield CH<sub>4</sub> and CoMS–SCoB (Table 1, reaction 5; Fig. 2d). Release of CH<sub>4</sub> from the enzyme possibly occurs only after CoMS–SCoB dissociation<sup>45</sup>. The *trans*–*cis* transition of an unusual thio–oxopeptide bond (Fig. 1) has been postulated to have a negative allosteric effect on the other active site in the MCR dimer<sup>49</sup>.

Perhaps the most complex biological reaction involving gases is the reduction of N<sub>2</sub> to NH<sub>3</sub> (Table 1, reaction 4). Although the crystal structure of nitrogenase and its FeMo-co (Fig. 1) has been available for more than 15 years<sup>22</sup>, there is still considerable debate concerning the catalytic site<sup>50</sup>. In its resting state, the cofactor does not bind N<sub>2</sub> and the molybdenum ion does not have a vacant coordination site. The substrate binding site(s) at this ion may become available after reduction if some of the metal–ligand bonds are broken (for example the molybdenum–homocitrate bonds), but there is no structural evidence for this. Researchers favouring iron-based catalysis point out, for instance, site-directed mutagenesis, and crystallographic and spectroscopic studies using substrates other than N<sub>2</sub> (ref. 50), which indicate that an FeS face of FeMo-co could be involved in substrate binding. They also argue that related nitrogenases in which molybdenum has been replaced by either vanadium or iron are still active, although a substitute iron ion, in particular, should not be able to reproduce the molybdenum-based chemistry proposed in ref. 51. Intriguingly, H<sub>2</sub> formation and its subsequent evolution is a requirement for N<sub>2</sub> binding (Table 1, reaction 4; Fig. 2b). Calculations using density functional theory suggest that proton binding to the FeMo-co does not involve high activation barriers<sup>52</sup>. The discovery of an interstitial light atom in the FeMo-co has attracted much attention<sup>23</sup>. Several studies suggest that nitrogen is the most likely candidate<sup>21</sup>, either having only a structural role, stabilizing the FeMo-co<sup>21,53</sup>, or also participating in catalysis<sup>21</sup>. Figure 2b shows molybdenum- and iron-based mechanisms.

### Crystal structures and gas tunnels

Figure 3 shows the three-dimensional structures of the anaerobic gas-metabolizing enzymes discussed in this Review. They span a wide range in complexity, from relatively small monomeric and heterodimeric [FeFe]-hydrogenases<sup>54</sup>, homodimeric [Fe]-hydrogenase<sup>8</sup> and heterodimeric [NiFe]-hydrogenases<sup>11</sup> to larger homodimeric CODHs<sup>55</sup>, an (αβ)<sub>2</sub> dimer of heterodimers in nitrogenase (where α and β respectively correspond to the NifD and NifK subunits<sup>22</sup>), and dimers of heterotrimers — (αβγ)<sub>2</sub> — in the case of nickel-dependent MCR<sup>25</sup>. ACS can form an (αβ)<sub>2</sub> complex with CODH<sup>19,56</sup>. Nitrogenase, MCR and CODH have in common the presence of pseudo two-fold axes that lie perpendicular to proper two-fold axes. These pseudo-symmetry axes relate respective α and β subunits in nitrogenase and MCR, and domains β3 and β4 in CODH. Metal sites such as the nitrogenase [8Fe–7S] P-cluster<sup>53</sup> (Fig. 3) and the CODH C-cluster sit on the pseudo two-fold axes, suggesting that these complex structures evolved from simpler ones by gene duplication and divergent evolution. Indeed, most active sites are located at or close to subunit and/or domain interfaces (Fig. 3): the nickel-containing F<sub>430</sub> cofactor lies between subunits α, β, γ and α' of MCR (Fig. 1); the FeMo-co lies between three domains of the nitrogenase α-subunit; the ACS A-cluster lies close to the interface of its three domains; the H-cluster of [FeFe]-hydrogenase is bound to a region of the protein facing the ferredoxin-like domain; and the iron–guanylylpyridinol cofactor of [Fe]-hydrogenase is bound at the surface of the N-terminal domain facing the dimer-forming C terminus. An exception is the Ni–Fe site in [NiFe]-hydrogenase, which is buried in its large subunit.

Apart from [Fe]-hydrogenase, the studied enzymes have tunnels to transfer gaseous substrates and/or products to and from the active sites. In [NiFe]-hydrogenase, [FeFe]-hydrogenase, CODH and ACS, these tunnels are mainly hydrophobic. Experiments with xenon-pressurized crystals<sup>19,37,57,58</sup> have shown that this gas binds in the observed tunnels even though most of them appear too narrow to allow xenon diffusion. This, in turn, means that, even in the crystal, significant protein motions can occur.

Molecular dynamics studies of intramolecular gas diffusion have been reported for [NiFe]- and [FeFe]-hydrogenases. Initial results obtained

for [NiFe]-hydrogenases suggested that H<sub>2</sub> does not diffuse randomly in the protein matrix, but instead uses the crystallographically characterized tunnels<sup>57</sup>. In addition, large sections of the tunnels were postulated to be gas reservoirs because of the low concentration of H<sub>2</sub> in natural settings and the higher solubility of this gas in a hydrophobic medium. In the [NiFe]-hydrogenase study<sup>57</sup>, several gas molecules were allowed to diffuse from the observed xenon sites, and in some trajectories they reached the active site. These results were complemented later by a theoretical study in which an *in silico* Val-to-Ala mutation in the tunnel near the active site locally increased H<sub>2</sub> diffusion from the solvent<sup>59</sup>. However, electrochemical experiments showed that the [NiFe]-hydrogenase catalytic rate for hydrogen oxidation matches that of platinum, indicating that the protein tunnels are not a barrier to H<sub>2</sub> diffusion<sup>60</sup>. Experimentally, mutants with the Val mentioned above replaced by Met or Ile, which are bulkier, displayed significantly reduced CO and H<sub>2</sub> diffusion rates<sup>61</sup>. Molecular dynamics studies of H<sub>2</sub> and O<sub>2</sub> diffusion in [FeFe]-hydrogenase suggested two major pathways for these gases<sup>62</sup>. One coincides with a narrow hydrophobic tunnel that was previously characterized crystallographically<sup>54</sup> and found to bind one xenon atom (Fig. 3). The other tunnel depends on the dynamics of the protein matrix.

Nitrogenase contains a hydrophilic tunnel extending from the enzyme surface to the FeMo-co. A potential role for this tunnel in N<sub>2</sub> and/or H<sub>2</sub> diffusion is suggested by the presence of one xenon site next to it, close to the active site<sup>63</sup>. Because N<sub>2</sub> reduction to ammonia is slow (Table 1, reaction 4), a hydrophobic tunnel that would allow rapid gas access to the FeMo-co has not evolved. Another possible use for the hydrophilic internal pathway in nitrogenase<sup>63</sup> could be the evacuation of product as NH<sub>4</sub><sup>+</sup>. In MCR, the active site is accessible only through an amphiphilic tunnel located at the intersection of four subunits. The tunnel becomes completely obstructed after successive binding of CH<sub>3</sub>–SCoM and CoBSH. In the crystal structure with both CoMSH and CoBSH bound, a weak electron density peak, in a hydrophobic pocket between the two coenzymes, was tentatively interpreted as trapped CH<sub>4</sub> (ref. 45).

Available structures of ACS show that another way in which the protein may guide substrate access to the active site is through domain rearrangements that modify the tunnel network. In the ACS closed conformation<sup>19,56</sup>, a continuous 70-Å-long tunnel connects the C- and A-clusters such that CO produced at the C-cluster can diffuse and be used at the A-cluster without being released to the medium. The tunnel connection is interrupted in the ACS open conformation<sup>19</sup>, in which the A-cluster presumably becomes accessible to methyl transfer from the corrinoid iron–sulphur protein (Table 1, reaction 3).

In conclusion, cavity searches on three-dimensional structures and xenon-binding studies reveal at least some of the tunnels used for gas transport. Molecular dynamics simulations have shown that the size of these crystallographically observed cavities may vary owing to protein movements and that these movements may generate transient cavities that constitute additional pathways for gas diffusion.

### Active-site biosyntheses

The complex active sites discussed here (Fig. 1) are either pre-assembled in accessory scaffold proteins before being inserted or progressively built directly in the target apoenzyme. Understanding these maturation processes (Fig. 4) may be useful in explaining their evolution from a prebiotic setting and the overexpression of enzymes for potential biotechnological applications.

The extensively studied maturation of [NiFe]-hydrogenase 3 from *Escherichia coli*<sup>7</sup> involves at least the eight gene products from the *hyp* operon. These proteins are not only species specific, but in *E. coli* different hydrogenases have their own maturation machinery. The complete active site is assembled directly in the HycE apohydrogenase (Fig. 4). The [FeFe]-hydrogenase active site is also buried in the protein core (Fig. 3). The [FeFe] subcluster is covalently bound to the protein by only one Cys thiolate<sup>54</sup> (Fig. 1). So far, only three gene products, HydE, HydF and HydG, have been identified as being required for expressing an active [FeFe]-hydrogenase in *E. coli* that lack this enzyme<sup>64</sup> (Fig. 4). Nothing is known



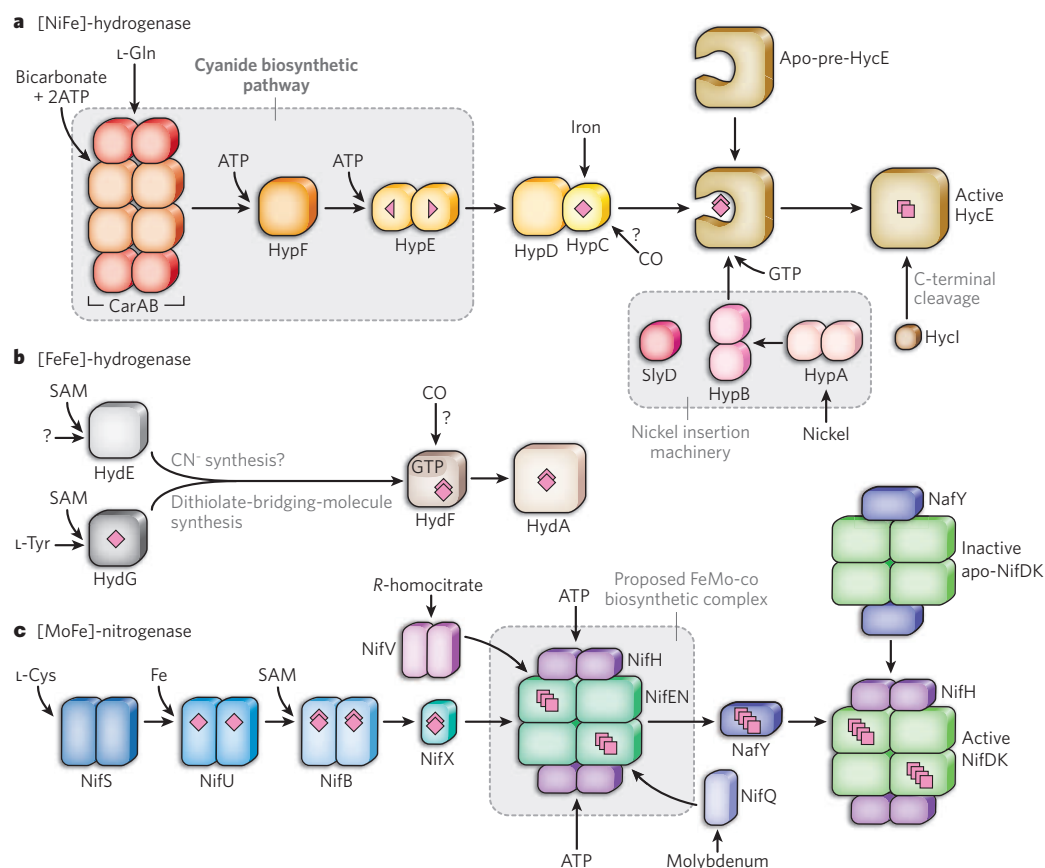


**Figure 4 | Active-site biosyntheses.** **a**, [NiFe]-hydrogenase. Biosynthesis comprises carbamoyl phosphate synthesis by CarAB from L-Gln and bicarbonate<sup>7</sup>, carbamoyl phosphate ATP-dependent conversion to AMP-OC(O)NH<sub>2</sub> by HypF, transfer of the carbamoyl moiety to the HypE C-terminal Cys, ATP-dependent dehydration of the formed thiocarbamate to thiocyanate<sup>87</sup> and CN<sup>-</sup> transfer (triangles for 1 CN<sup>-</sup>, diamond for 2 CN<sup>-</sup> ligands) to a HypCD complex containing the iron ion already bound to HypC<sup>88</sup>. An equivalent pathway for CO synthesis has not been defined, but externally supplied CO can also be incorporated, presumably<sup>89</sup> before transfer of the Fe(CN)<sub>2</sub>CO unit (double diamond) from HypC to HycE. Subsequent nickel insertion is mediated by HypA (proposed nickel carrier), HypB (GTP-dependent nickel insertase) and SlyD (affinity modulator of HypB for nickel<sup>90</sup>). Finally, HycI cleaves the C-terminal extension of HycE and the nickel-based nascent C terminus rearranges, burying the active site in the protein core (double square)<sup>91</sup>. **b**, [FeFe]-hydrogenase. HydE and HydG are radical S-adenosyl-L-methionine (SAM) proteins<sup>92</sup>. HydG resembles ThiH, which is involved in thiazole synthesis and also produces *p*-cresol and dehydroglycine from Tyr. Dehydroglycine could be used to

synthesize the small [FeFe]-bridging dithiolate molecule (diamond)<sup>93</sup>. The function of HydE is unknown, but it can bind thiocyanate and small organic molecules containing at least two carboxylate moieties at different sites<sup>94</sup>. The products of HydE and HydG (double diamond) bind to HydF, a presumed scaffold protein exhibiting GTPase activity that transfers the pre-assembled Fe<sub>2</sub>(S-C-X-C-S)(CN)<sub>2</sub>(CO)<sub>3</sub> unit next to the [Fe<sub>4</sub>S<sub>4</sub>] subcluster (double diamond), producing active [FeFe]-hydrogenase<sup>95</sup>. **c**, Nitrogenase (NifDK). The Cys desulphurase NifS directs the assembly of [FeS] clusters (diamonds) on the scaffold NifU<sup>6</sup>. These clusters serve as substrates for the radical SAM protein NifB to synthesize the NifB cofactor (double diamonds), of unknown structure, on its C-terminal domain, which is homologous to NifH<sup>6</sup>. NifX carries the cofactor to the central scaffold protein NifEN (triple square), which is homologous to NifDK<sup>6</sup>. Then R-homocitrate and molybdenum are transferred to NifEN by NifV<sup>96</sup> and NifQ, respectively<sup>97</sup>. Molybdenum delivery and insertion seem to involve ATP hydrolysis and NifH, which resembles in this respect HypB and HydF. Finally, the carrier protein NafY (also known as NifY) transfers the pre-assembled FeMo-co (quadruple square) to NifDK.

about the synthesis of CO and guanylylpyridinol or iron incorporation in [Fe]-hydrogenase (Hmd) (Fig. 1). However, in all the known methanogen genomes that contain the *hmd* gene, there is an adjacent gene, which we call *hmdB*, coding for a radical S-adenosyl-L-methionine (SAM) protein. Although *hmdB* has been annotated as biotin synthase, amino-acid sequence analysis indicates that this is not the case<sup>65</sup>. HmdB could be involved in either CO or guanylylpyridinol synthesis.

Active nitrogenase corresponds to the NifDK (α<sub>2</sub>β<sub>2</sub>) heterotetramer transiently associated with the iron protein NifH<sup>66</sup> (Fig. 4). The highly complex FeMo-co is only bound to two amino acids from the protein matrix (Fig. 1) and can be easily extracted from it<sup>67</sup>. Its biosynthetic pathway involves ten proteins (NifS, NifU, NifB, NifX, NifE, NifN, NifV, NifQ, NifH and NifY) encoded by the *nif* operon. These proteins can be functionally divided into molecular scaffolds, metalcluster carriers and enzymes. Although it is possible to assemble a functional FeMo-co *in vitro* using only iron, sulphur, molybdenum, R-homocitrate and the proteins NifB, NifH and NifEN, as well as ATP and SAM, the addition of the other Nif proteins doubles the yield of active enzyme<sup>68</sup>.

Very little is known about the synthesis of the C-cluster of CODH. It is thought that its FeS cuboidal part (Fig. 1) is assembled in the enzyme before nickel insertion<sup>69</sup>, this insertion being mediated by the proteins CooC, CooT and CooJ<sup>70,71</sup>. CooT shows low amino-acid sequence homology to HypC (Fig. 4). CooJ has a His-rich, nickel-binding motif at its C terminus, and CooC, which is responsible for nickel insertion, is similar to HypB and has low ATPase activity. No details have been reported concerning the synthesis of the ACS A-cluster. Also, the enzymes specific to the synthesis of the MCR Ni-F<sub>430</sub> cofactor and its machinery for nickel insertion are unknown. However, four amino-acid side chains are modified by specific methyltransferases<sup>72,73</sup>. Furthermore, a Gly peptide bond is converted into a thio-oxopeptide bond<sup>25,72</sup>.

Non-iron metal insertion may occur through a common mechanism in nitrogenase, [NiFe]-hydrogenase and CODH: NifH and HypB are structurally similar, and CooC has significant amino-acid sequence homology to them<sup>70,74,75</sup>. They couple metal insertion to the hydrolysis of either GTP or ATP. In the three cases, the non-iron metal (nickel or molybdenum) is bound to one or more amino acids of the target protein

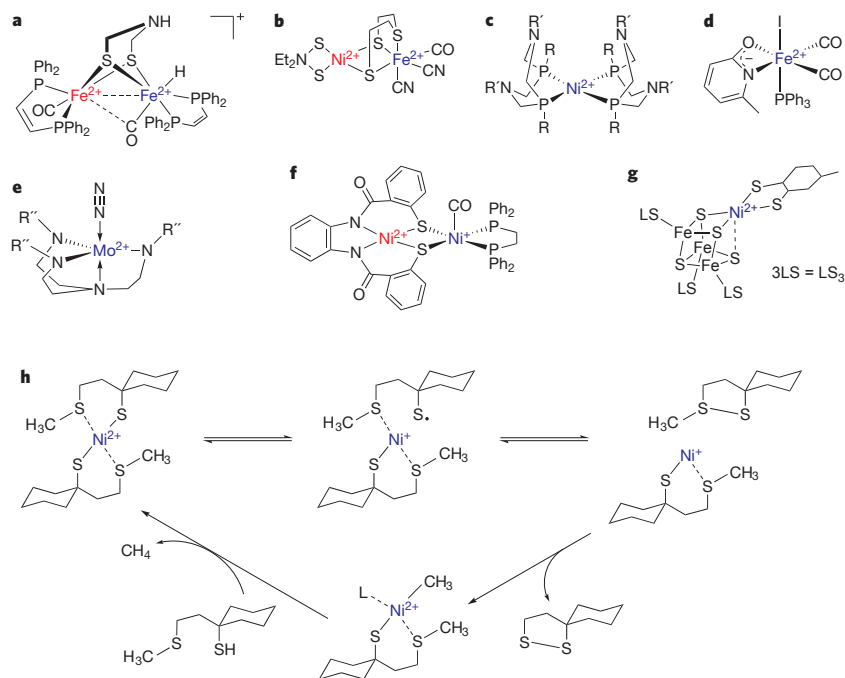


**Figure 5 | Model compounds.** **a**, [FeFe]-hydrogenase active-site model,  $[\text{Fe}_2(\text{adt})(\text{CO})_2(\text{dppv})_2(t\text{-H})]^+$  (ref. 15). **b**, [NiFe]-hydrogenase active-site biomimetic model,  $[(\text{CN})_2(\text{CO})\text{Fe}(\mu\text{-tpdt})\text{Ni}(\text{S}_2\text{CNEt}_2)]^{77}$ . **c**, Functional model of hydrogenase,  $[\text{Ni}(\text{P}^{\text{R}}_2\text{N}^{\text{R}'}_2)_2]^{2+}$ . R, phosphine or cymene; R', phosphine or benzene<sup>78</sup>. Depending on the substituent on the amine nitrogen and on the phosphorus atoms, these complexes are electrocatalysts for hydrogen production (turnover frequency,  $350\text{ s}^{-1}$ ) or for hydrogen oxidation (turnover frequency,  $10\text{ s}^{-1}$ ). **d**, [Fe]-hydrogenase active-site model,  $[\text{Fe}(\text{CO})_2(\text{PPh}_3)\text{I}(\text{hmp})]^{98}$ . This monomeric iron bis(carbonyl) pyridonate complex provided further evidence that the iron is divalent in the enzyme<sup>9</sup>. **e**, Structure of  $[\text{HIPTN}_3\text{N}]\text{Mo}(\text{N}_2)$ . This molybdenum compound is not biologically relevant, but it can reduce  $\text{N}_2$  with electrons and protons to ammonia and hydrogen<sup>51</sup>. R'', HIPT. **f**, ACS active-site model,  $[\text{Ni}(\text{dppe})\text{Ni}(\text{PhPepS})]^{99}$ , showing a labile nickel with changing coordination geometry, possible reduction to  $\text{Ni}^+$  and CO binding with an infrared frequency very close to that observed in the  $\text{OC-Ni}_p^+[\text{Fe}_4\text{S}_4]^{2+}$  state of the enzyme. **g**, CODH active-site model,  $[(\text{tdt})\text{NiFe}_3\text{S}_4(\text{LS}_3)]^{3-}$ , with a distorted square-planar diamagnetic  $\text{Ni}^{2+}$  coordination and a possible insertion of an 'exo' iron by substitution<sup>84</sup>. **h**, Mechanistic interpretation of the photoinduced formation of methane and spirodisulphide by  $\text{bis}[1\text{-}[2\text{-(methylthio)ethyl}]\text{cyclohexanethiolato}]\text{Ni}^{2+}$  via a cyclic sulphuranyl radical, without true catalytic turnover<sup>100</sup>. adt, 2-azapropene-1,3-dithiolate; dppe, diphenylphosphinoethane; dppv, *cis*-1,2-bis(diphenylphosphino)ethylene; Et, ethyl; *t*-H, terminal hydride; HIPT, hexa-isopropylterphenyl; hmp, deprotonated 2-hydroxy-6-methylpyridine;  $\text{LS}_3$ , 1,3,5-tris(4,6-dimethyl-3-mercaptophenylthio)-2,4,6-tris(*p*-tolylthio)benzene(3-); Ph, phenyl; PhPepS, *N,N'*-phenylenebis(*o*-mercaptobenzamide);  $\text{PPh}_2$ , diphenylphosphine;  $\text{PPh}_3$ , triphenylphosphine; tdt, toluene-3,4-dithiolate; tpdt, 3-thiapentanedithiolate.

and is inserted at a late stage of the assembly process. Active-site assembly in [FeFe]-hydrogenase does not involve non-iron ion insertion and proceeds by a different mechanism. Both the catalytic [FeFe] subcluster of [FeFe]-hydrogenase and the FeMo-co of nitrogenase are fully synthesized in a scaffold protein (HydF or NifEN), possibly located at the core of a multi-enzymatic complex<sup>6,7</sup>, before their insertion into the respective enzymes. The transfer of the catalytic centres as fully assembled units, along with the paucity of protein ligands and their iron/sulphur content, suggest a mineral origin. Interestingly, for both enzymes radical SAM proteins are involved at key steps in the active-site synthesis (Fig. 4). The same may apply to [Fe]-hydrogenase, underscoring the importance of radical chemistry at the early stages of life evolution.

## Model compounds

The synthesis of metalloenzyme active-site analogues is both a chemical challenge and a way to better understand the properties of their different components. Model compounds also shed light on the role of the protein environment in modulating the enzymatic properties. Depending on the desired goal, chemists use either biomimetic or bio-inspired approaches. Biomimetic approaches consist of the synthesis of both structural analogues of the enzyme active site and plausible

reaction intermediates. In the bio-inspired approach, the functional model is not structurally similar to the active site, but the reaction is the same. In general, the biomimetic compounds so far reported are not catalytically active, either because they are not identical to the biological active site or because they do not mimic the protein environment and the second coordination sphere. Synthetic catalysts are often insoluble in aqueous solvents, in which case the catalysis is performed in organic solvents. This does not have to be a drawback, because non-polar solvents may be better mimics of the protein matrix than water, although the protein interior is a mosaic of charged, polar and non-polar components, which is difficult to mimic in the laboratory. As illustrated by FeMo-co in nitrogenase<sup>67</sup>, extracted active sites may be stable but become inactive, underscoring the importance of the protein.

Figure 5 shows selected model compounds. There is a vested interest in the synthesis of mimics of hydrogenases based on nickel and/or iron instead of platinum, because the availability of platinum will not satisfy the demands of a hydrogen economy. An interesting recently reported compound related to [FeFe]-hydrogenase is a complex of two iron ions, bridged by CO and an azadithiolate (Fig. 5a), that shows the coupling of amine protonation by weak acids to hydride formation. This result favours nitrogen as bridgehead atom in the small dithiolate-containing molecule of the [FeFe] subcluster<sup>15</sup>. Although the first thiolate-bridged Ni-Fe carbonyl complex was synthesized in 1996 (ref. 76) the closest mimic of the [NiFe]-hydrogenase yet obtained was reported very recently (Fig. 5b). The infrared frequency bands from its CO(CN)<sub>2</sub> unit are very close to those from the enzyme<sup>77</sup>. However, the binuclear Ni-Fe synthetic models are not functional. One of the best catalytically active models is the mononuclear nickel complex  $[\text{Ni}(\text{P}^{\text{R}}_2\text{N}^{\text{R}'}_2)_2]^{2+}$ , in which pendant bases are incorporated in the second coordination sphere<sup>78</sup> (Fig. 5c). Concerning [Fe]-hydrogenase, an iridium-containing mimic of guanylylpyridinol has proved to be an excellent catalyst for dehydrogenation reactions. It was also very stable relative to complexes in which the guanylylpyridinol mimic lacks the 2-OH group present in its biological counterpart<sup>79</sup>. An iron-containing model is depicted in Fig. 5d.

The development of new methods to assemble iron-sulphur-thiolate and iron-molybdenum-thiolate clusters of high nuclearity led to the isolation of a cluster displaying the nitrogenase FeMo-co topology with sulphide rather than a lighter atom at its centre<sup>80</sup>. Di-iron complexes capable of cleaving the nitrogen-nitrogen bond of hydrazine with excellent catalytic activity support the possibility that di-iron centres have a role in biological  $\text{N}_2$  reduction<sup>81</sup>. Some molybdenum complexes are also efficient for the production of ammonia and are capable of reducing nitrogen, albeit with limited catalytic turnover numbers<sup>51</sup> (Fig. 5e). Carbon monoxide binding is very well characterized in ACS models. The synthesis of complexes with three coplanar  $\text{Ni}^{2+}$  centres is interesting because of the resemblance of the central nickel ion to  $\text{Ni}_p$  (ref. 82). A dinuclear nickel model sharing features with the ACS active site is shown in Fig. 5f. Although several complexes have been synthesized that involve an  $[\text{Fe}_4\text{S}_4]$  cluster leading to the formation of an  $[\text{Fe}_4\text{S}_4](\mu_2\text{-SR})\text{-Ni}_p^{2+}$  unit, none of them contains a binuclear fragment<sup>83</sup>. The two limiting steps in the synthesis of CODH models are the construction of a planar diamagnetic  $\text{Ni}^{2+}$  in an iron-sulphur cluster and the stabilization of an 'exo' iron (Fe1) bridged to the larger core fragment. A  $[(\text{tdt})\text{NiFe}_3\text{S}_4(\text{LS}_3)]^{3-}$  cluster has been synthesized for the future insertion

of an 'exo' iron by substitution<sup>84</sup> (Fig. 5g). The cleavage of the carbon–sulphur bond of methyl–SCoM in MCR poses a difficult chemical problem. The first example of biomimetic production of methane and a mixed disulphide by catalysis with a Ni<sup>2+</sup> complex was reported in 1997 (ref. 85). An interesting catalytic model was obtained through the synthesis of a substrate containing an aliphatic thiol and a methyl thioether function (Fig. 5h).

In conclusion, chemical models of enzyme active sites are useful for understanding how ligands modify the properties of metal ions, the influence of the second coordination sphere and the effect of the protein matrix. As a general rule, it seems that bio-inspired rather than biomimetic compounds may, eventually, find technological applications.

## Perspective

Now that most metal-containing enzyme active sites from anaerobic organisms have been structurally characterized in at least one state, one of the future challenges will be to obtain crystal structures of reaction intermediates. For example, a nitrogenase–N<sub>2</sub> complex or a methylated and/or carbonylated form of ACS would shed considerable light on the respective enzymatic mechanisms. Hydrogenases pose especially difficult problems for the crystallographer because substrate and product are invisible at the resolution typically obtained from protein crystals. A similar general problem is the discrimination between light atoms such as carbon, nitrogen and oxygen. In such cases, as in many others, spectroscopic, theoretical and synthetic approaches have been, and will continue to be, essential. Another aspect that will have to be further developed is our understanding of the biosynthesis of the complex active sites discussed here. Even in the best-studied cases, there remain many points to clarify. A fascinating aspect of the active-site assembly of nitrogenase and [FeFe]-hydrogenase, and most probably [Fe]-hydrogenase, is the underlying radical chemistry that leads to the synthesis of some of its components. Understanding how radical SAM enzymes carry out these reactions will be of paramount importance. As we continue to advance our knowledge concerning these ancient gas-processing enzymes, we will also be looking back into the distant past to when life first arose on this planet. ■

**Note added in proof:** A recent model of a closed form of [Fe]-hydrogenase<sup>101</sup> suggests that a 10-Å-long hydrophobic channel connecting the active-site cavity to the protein surface might be used by H<sub>2</sub>.

- Wächtershäuser, G. From volcanic origins of chemoautotrophic life to Bacteria, Archaea and Eukarya. *Phil. Trans. R. Soc. B* **361**, 1787–1806 (2006). This paper presents one of the most popular theories for the autotrophic origin of life.
- Konhauser, K. O. et al. Oceanic nickel depletion and a methanogen famine before the Great Oxidation Event. *Nature* **458**, 750–753 (2009).
- Childress, J. J. & Fischer, C. R. The biology of hydrothermal vent animals: physiology, biochemistry, and autotrophic symbioses. *Oceanogr. Mar. Biol. Annu. Rev.* **30**, 337–441 (1992).
- Ragsdale, S. W. & Pierce, E. Acetogenesis and the Wood–Ljungdahl pathway of CO<sub>2</sub> fixation. *Biochim. Biophys. Acta* **1784**, 1873–1898 (2008).
- Silver, W. S. & Postgate, J. R. Evolution of symbiotic nitrogen fixation. *J. Theor. Biol.* **40**, 1–10 (1973).
- Rubio, L. M. & Ludden, P. W. Biosynthesis of the iron–molybdenum cofactor of nitrogenase. *Annu. Rev. Microbiol.* **62**, 93–111 (2008).
- Bock, A., King, P. W., Blokesch, M. & Posewitz, M. C. Maturation of hydrogenases. *Adv. Microb. Physiol.* **51**, 1–71 (2006).
- Hironaka, T. et al. The crystal structure of C176A mutated [Fe]-hydrogenase suggests an acyl-iron ligation in the active site iron complex. *FEBS Lett.* **583**, 585–590 (2009). This paper corrects a previous interpretation of the active-site structure of [Fe]-hydrogenase.
- Vignais, P. M. & Billoud, B. Occurrence, classification, and biological function of hydrogenases: an overview. *Chem. Rev.* **107**, 4206–4272 (2007).
- Fontecilla-Camps, J. C., Volbeda, A., Cavazza, C. & Nicolet, Y. Structure/function relationships of [NiFe]- and [FeFe]-hydrogenases. *Chem. Rev.* **107**, 4273–4303 (2007). This recent review covers most aspects concerning [NiFe]- and [FeFe]-hydrogenases.
- Volbeda, A. et al. Crystal-structure of the nickel–iron hydrogenase from *Desulfovibrio gigas*. *Nature* **373**, 580–587 (1995).
- Garcin, E. et al. The crystal structure of a reduced [NiFeSe] hydrogenase provides an image of the activated catalytic center. *Structure* **7**, 557–566 (1999).
- Nicolet, Y. et al. Crystallographic and FTIR spectroscopic evidence of changes in Fe coordination upon reduction of the active site of the Fe-only hydrogenase from *Desulfovibrio desulfuricans*. *J. Am. Chem. Soc.* **123**, 1596–1601 (2001).
- Lubitz, W., Reijerse, E. & van Gestel, M. [NiFe] and [FeFe] hydrogenases studied by advanced magnetic resonance techniques. *Chem. Rev.* **107**, 4331–4365 (2007).
- Barton, B. E., Olsen, M. T. & Rauchfuss, T. B. Aza- and oxodithiolates are probable proton relays in functional models for the [FeFe]-hydrogenases. *J. Am. Chem. Soc.* **130**, 16834–16835 (2008). This paper presents model compounds, based on protonation studies, that favour azadithiolate as the small organic molecule at the active site.
- Pandey, A. S., Harris, T. V., Giles, L. J., Peters, J. W. & Szilagy, R. K. Dithiomethylether as a ligand in the hydrogenase H-cluster. *J. Am. Chem. Soc.* **130**, 4533–4540 (2008).
- Fontecilla-Camps, J. C. & Volbeda, A. in *Handbook of Metalloproteins* on-line edn (ed. Messerschmidt, A.) doi:10.1002/0470028637.met212 (Wiley, 2008).
- Volbeda, A. & Fontecilla-Camps, J. C. Structural bases for the catalytic mechanism of Ni-containing carbon monoxide dehydrogenases. *Dalton Trans.* 3443–3450 (2005).
- Darnault, C. et al. Ni–Zn–[Fe–4–S–4] and Ni–Ni–[Fe–4–S–4] clusters in closed and open subunits of acetyl–CoA synthase/carbon monoxide dehydrogenase. *Nature Struct. Biol.* **10**, 271–279 (2003).
- Volbeda, A. & Fontecilla-Camps, J. C. Structure–function relationships of nickel–iron sites in hydrogenase and a comparison with the active sites of other nickel–iron enzymes. *Coord. Chem. Rev.* **249**, 1609–1619 (2005).
- Andrade, S. L. A., Hu, Y., Ribbe, M. W. & Einsle, O. in *Handbook of Metalloproteins* on-line edn (ed. Messerschmidt, A.) doi:10.1002/0470028637.met224 (Wiley, 2008).
- Kirn, J. & Rees, D. C. Crystallographic structure and functional implications of the nitrogenase molybdenum–iron protein from *Azotobacter vinelandii*. *Nature* **360**, 553–560 (1992).
- Einsle, O. et al. Nitrogenase MoFe-protein at 1.16 Å resolution: a central ligand in the FeMo-cofactor. *Science* **297**, 1696–1700 (2002).
- Pelmenschikov, V., Case, D. A. & Noodleman, L. Ligand-bound S=1/2 FeMo-cofactor of nitrogenase: hyperfine interaction analysis and implication for the central ligand X identity. *Inorg. Chem.* **47**, 6162–6172 (2008).
- Ermiler, U., Grabarse, W., Shima, S., Goubeau, M. & Thauer, R. K. Crystal structure of methyl coenzyme M reductase: the key enzyme of biological methane formation. *Science* **278**, 1457–1462 (1997).
- Siegbahn, P. E. M., Tye, J. W. & Hall, M. B. Computational studies of [NiFe] and [FeFe] hydrogenases. *Chem. Rev.* **107**, 4414–4435 (2007).
- Shima, S., Lyon, E. J., Thauer, R. K., Mienert, B. & Bill, E. Mössbauer studies of the iron–sulfur cluster-free hydrogenase: the electronic state of the mononuclear Fe active site. *J. Am. Chem. Soc.* **127**, 10430–10435 (2005).
- Brecht, M., van Gestel, M., Buhrke, T., Friedrich, B. & Lubitz, W. Direct detection of a hydrogen ligand in the [NiFe] center of the regulatory H<sub>2</sub>-sensing hydrogenase from *Ralstonia eutropha* in its reduced state by HYSCORE and ENDOR spectroscopy. *J. Am. Chem. Soc.* **125**, 13075–13083 (2003).
- Ogata, H. et al. Structural studies of the carbon monoxide complex of [NiFe]-hydrogenase from *Desulfovibrio vulgaris* Miyazaki F: suggestion for the initial activation site for dihydrogen. *J. Am. Chem. Soc.* **124**, 11628–11635 (2002).
- Lemon, B. J. & Peters, J. W. Binding of exogenously added carbon monoxide at the active site of the iron-only hydrogenase (Cpl) from *Clostridium pasteurianum*. *Biochemistry* **38**, 12969–12973 (1999).
- Bruschi, M., Greco, C., Fantucci, P. & De Gioia, L. Structural and electronic properties of the [FeFe] hydrogenase H-cluster in different redox and protonation states. A DFT investigation. *Inorg. Chem.* **47**, 6056–6071 (2008).
- Cammack, R., Patil, D., Aguirre, R. & Hatchikian, E. C. Redox properties of the ESR-detectable nickel in hydrogenase from *Desulfovibrio gigas*. *FEBS Lett.* **142**, 289–292 (1982).
- Coremans, J. M., van Garderen, C. J. & Albracht, S. P. On the redox equilibrium between H<sub>2</sub> and hydrogenase. *Biochim. Biophys. Acta* **1119**, 148–156 (1992).
- Lill, S. O. N. & Siegbahn, P. E. M. An autocatalytic mechanism for [NiFe]-hydrogenase: reduction to Ni(I) followed by oxidative addition. *Biochemistry* **48**, 1056–1066 (2009).
- Wu, M. et al. Life in hot carbon monoxide: the complete genome sequence of *Carboxythermus hydrogeniformans* Z-2901. *PLoS Genet.* **1**, e65 (2005).
- Jeoung, J. H. & Dobbek, H. Carbon dioxide activation at the NiFe-cluster of anaerobic carbon monoxide dehydrogenase. *Science* **318**, 1461–1464 (2007).
- Gong, W. et al. Structure of the α<sub>2</sub>ε<sub>2</sub> Ni-dependent CO dehydrogenase component of the *Methanocaldococcus barkeri* acetyl–CoA decarbonylase/synthase complex. *Proc. Natl Acad. Sci. USA* **105**, 9558–9563 (2008).
- Grahame, D. A., Gencic, S. & DeMoll, E. A single operon-encoded form of the acetyl–CoA decarbonylase/synthase multienzyme complex responsible for synthesis and cleavage of acetyl–CoA in *Methanocaldococcus thermophilus*. *Arch. Microbiol.* **184**, 32–40 (2005).
- Eckert, N. A., Dougherty, W. G., Yap, G. P. A. & Riordan, C. G. Methyl transfer from methylcobaloxime to (Triphos)Ni(PPh<sub>3</sub>): Relevance to the mechanism of acetyl coenzyme A synthase. *J. Am. Chem. Soc.* **129**, 9286–9287 (2007).
- Schenker, R. P. & Brunold, T. C. Computational studies on the A cluster of acetyl-coenzyme A synthase: geometric and electronic properties of the NiFeC species and mechanistic implications. *J. Am. Chem. Soc.* **125**, 13962–13963 (2003).
- Amara, P., Volbeda, A., Fontecilla-Camps, J. C. & Field, M. J. A quantum chemical study of the reaction mechanism of acetyl-coenzyme A synthase. *J. Am. Chem. Soc.* **127**, 2776–2784 (2005).
- Tan, X., Martinho, M., Stubna, A., Lindahl, P. A. & Munck, E. Mössbauer evidence for an exchange-coupled [Fe<sub>4</sub>S<sub>4</sub>]<sup>2+</sup> Ni–P<sup>+</sup> A-cluster in isolated subunits of acetyl-coenzyme A synthase/carbon monoxide dehydrogenase. *J. Am. Chem. Soc.* **130**, 6712–6713 (2008).
- Seravalli, J. & Ragsdale, S. W. Pulse-chase studies of the synthesis of acetyl–CoA by carbon monoxide dehydrogenase/acetyl–CoA synthase — evidence for a random mechanism of methyl and carbonyl addition. *J. Biol. Chem.* **283**, 8384–8394 (2008).
- Tan, X., Surovtsev, I. V. & Lindahl, P. A. Kinetics of CO insertion and acetyl group transfer steps, and a model of the acetyl–CoA synthase catalytic mechanism. *J. Am. Chem. Soc.* **128**, 12331–12338 (2006).
- Grabarse, W. et al. On the mechanism of biological methane formation: structural evidence for conformational changes in methyl-coenzyme M reductase upon substrate binding. *J. Mol. Biol.* **309**, 315–330 (2001).



46. Harmer, J. *et al.* A nickel hydride complex in the active site of methyl-coenzyme M reductase: implications for the catalytic cycle. *J. Am. Chem. Soc.* **130**, 10907–10920 (2008).
47. Sarangi, R., Dey, M. & Ragsdale, S. W. Geometric and electronic structures of the Ni<sup>II</sup> and Methyl-Ni<sup>III</sup> intermediates of methyl-coenzyme M reductase. *Biochemistry* **48**, 3146–3156 (2009).
48. Yang, N., Reiher, M., Wang, M., Harmer, J. & Duin, E. C. Formation of a nickel–methyl species in methyl-coenzyme M reductase, an enzyme catalyzing methane formation. *J. Am. Chem. Soc.* **129**, 11028–11029 (2007).
49. Goenrich, M., Duin, E. C., Mahler, F. & Thauer, R. K. Temperature dependence of methyl-coenzyme M reductase activity and of the formation of the methyl-coenzyme M reductase red2 state induced by coenzyme B. *J. Biol. Inorg. Chem.* **10**, 333–342 (2005).
50. Seefeldt, L. C., Dance, I. G. & Dean, D. R. Substrate interactions with nitrogenase: Fe versus Mo. *Biochemistry* **43**, 1401–1409 (2004).
51. Schrock, R. R. Catalytic reduction of dinitrogen to ammonia by molybdenum: theory versus experiment. *Angew. Chem. Int. Edn* **47**, 5512–5522 (2008).  
**This paper contains a clear discussion of the issue of iron versus molybdenum concerning the catalytic site in FeMo-co.**
52. Dance, I. The chemical mechanism of nitrogenase: calculated details of the intramolecular mechanism for hydrogenation of  $\eta^2$ -N<sub>2</sub> on FeMo-co to NH<sub>3</sub>. *Dalton Trans.* 5977–5991 (2008).
53. Igarashi, R. Y. & Seefeldt, L. C. Nitrogen fixation: the mechanism of the Mo-dependent nitrogenase. *Crit. Rev. Biochem. Mol. Biol.* **38**, 351–384 (2003).
54. Nicolet, Y., Lemon, B. J., Fontecilla-Camps, J. C. & Peters, J. W. A novel FeS cluster in Fe-only hydrogenases. *Trends Biochem. Sci.* **25**, 138–143 (2000).
55. Dobbek, H., Svetlitchnyi, V., Gremer, L., Huber, R. & Meyer, O. Crystal structure of a carbon monoxide dehydrogenase reveals a [Ni-4Fe-5S] cluster. *Science* **293**, 1281–1285 (2001).
56. Doukov, T. I., Iverson, T. M., Seravalli, J., Ragsdale, S. W. & Drennan, C. L. A Ni-Fe-Cu center in a bifunctional carbon monoxide dehydrogenase/acetyl-CoA synthase. *Science* **298**, 567–572 (2002).
57. Montet, Y. *et al.* Gas access to the active site of Ni-Fe hydrogenases probed by X-ray crystallography and molecular dynamics. *Nature Struct. Biol.* **4**, 523–526 (1997).
58. Doukov, T. I., Blasiak, L. C., Seravalli, J., Ragsdale, S. W. & Drennan, C. L. Xenon in and at the end of the tunnel of bifunctional carbon monoxide dehydrogenase/acetyl-CoA synthase. *Biochemistry* **47**, 3474–3483 (2008).
59. Teixeira, V. H., Baptista, A. M. & Soares, C. M. Pathways of H<sub>2</sub> toward the active site of [NiFe]-hydrogenase. *Biophys. J.* **91**, 2035–2045 (2006).
60. Jones, A. K., Sillery, E., Albracht, S. P. J. & Armstrong, F. A. Direct comparison of the electrocatalytic oxidation of hydrogen by an enzyme and a platinum catalyst. *Chem. Commun.* 866–867 (2002).  
**This paper is an electrochemical study showing that the enzyme is as efficient as the transition metal in catalysis.**
61. Leroux, F. *et al.* Experimental approaches to kinetics of gas diffusion in hydrogenase. *Proc. Natl Acad. Sci. USA* **105**, 11188–11193 (2008).
62. Cohen, J., Kim, K., King, P., Seibert, M. & Schulten, K. Finding gas diffusion pathways in proteins: application to O<sub>2</sub> and H<sub>2</sub> transport in Cpl [FeFe]-hydrogenase and the role of packing defects. *Structure* **13**, 1321–1329 (2005).
63. Durrant, M. C. Controlled protonation of iron-molybdenum cofactor by nitrogenase: a structural and theoretical analysis. *Biochem. J.* **355**, 569–576 (2001).
64. Posewitz, M. C. *et al.* Discovery of two novel radical S-adenosylmethionine proteins required for the assembly of an active [FeFe] hydrogenase. *J. Biol. Chem.* **279**, 25711–25720 (2004).  
**This paper reports a very important discovery that has been instrumental in furthering our understanding of active-site synthesis and assembly.**
65. Nicolet, Y. & Drennan, C. L. AdoMet radical proteins — from structure to evolution — alignment of divergent protein sequences reveals strong secondary structure element conservation. *Nucleic Acids Res.* **32**, 4015–4025 (2004).
66. Bulen, W. A. & Lecomte, J. R. The nitrogenase system from *Azotobacter*: two-enzyme requirement for N<sub>2</sub> reduction, ATP-dependent H<sub>2</sub> evolution and ATP hydrolysis. *Proc. Natl Acad. Sci. USA* **56**, 979–986 (1966).
67. Shah, V. K. & Brill, W. J. Isolation of an iron-molybdenum cofactor from nitrogenase. *Proc. Natl Acad. Sci. USA* **74**, 3249–3253 (1977).
68. Curatti, L. *et al.* In vitro synthesis of the iron-molybdenum cofactor of nitrogenase from iron, sulfur, molybdenum, and homocitrate using purified proteins. *Proc. Natl Acad. Sci. USA* **104**, 17626–17631 (2007).
69. Jeon, W. B., Singer, S. W., Ludden, P. W. & Rubio, L. M. New insights into the mechanism of nickel insertion into carbon monoxide dehydrogenase: analysis of *Rhodospirillum rubrum* carbon monoxide dehydrogenase variants with substituted ligands to the [Fe<sub>3</sub>S<sub>4</sub>] portion of the active-site C-cluster. *J. Biol. Inorg. Chem.* **10**, 903–912 (2005).
70. Kerby, R. L., Ludden, P. W. & Roberts, G. P. In vivo nickel insertion into the carbon monoxide dehydrogenase of *Rhodospirillum rubrum*: molecular and physiological characterization of cooCTJ. *J. Bacteriol.* **179**, 2259–2266 (1997).
71. Jeon, W. B., Cheng, J. J. & Ludden, P. W. Purification and characterization of membrane-associated CooC protein and its functional role in the insertion of nickel into carbon monoxide dehydrogenase from *Rhodospirillum rubrum*. *J. Biol. Chem.* **276**, 38602–38609 (2001).
72. Kahnt, J. *et al.* Post-translational modifications in the active site region of methyl-coenzyme M reductase from methanogenic and methanotrophic archaea. *FEBS J.* **274**, 4913–4921 (2007).
73. Selmer, T. *et al.* The biosynthesis of methylated amino acids in the active site region of methyl-coenzyme M reductase. *J. Biol. Chem.* **275**, 3755–3760 (2000).
74. Georgiadis, M. M. *et al.* Crystallographic structure of the nitrogenase iron protein from *Azotobacter vinelandii*. *Science* **257**, 1653–1659 (1992).
75. Gasper, R., Scrima, A. & Wittinghofer, A. Structural insights into HypB, a GTP-binding protein that regulates metal binding. *J. Biol. Chem.* **281**, 27492–27502 (2006).
76. Lai, C. H., Reibenspies, J. H. & Darensbourg, M. Y. Thiolate bridged nickel-iron complexes containing both iron(0) and iron(II) carbonyls. *Angew. Chem. Int. Edn Engl.* **35**, 2390–2393 (1996).
77. Tanino, S., Li, Z., Ohki, Y. & Tatsumi, K. A dithiolate-bridged (CN)<sub>2</sub>(CO)Fe-Ni complex reproducing the IR bands of [NiFe] hydrogenase. *Inorg. Chem.* **48**, 2358–2360 (2009).  
**This paper contains the most biomimetic compounds reported so far.**
78. Dubois, M. & Dubois, D. L. The roles of the first and second coordination spheres in the design of molecular catalysts for H<sub>2</sub> production and oxidation. *Chem. Soc. Rev.* **38**, 62–72 (2009).
79. Royer, A. M., Rauchfuss, T. B. & Wilson, S. R. Coordination chemistry of a model for the GP cofactor in the Hmd hydrogenase: hydrogen-bonding and hydrogen-transfer catalysis. *Inorg. Chem.* **47**, 395–397 (2008).
80. Ohki, Y., Ikagawa, Y. & Tatsumi, K. Synthesis of new [8Fe-7S] clusters: a topological link between the core structures of P-cluster, FeMo-co, and FeFe-co of nitrogenases. *J. Am. Chem. Soc.* **129**, 10457–10465 (2007).
81. Chen, Y. *et al.* Nitrogenase model complexes [Cp\*Fe(μ-SR')<sub>2</sub>(μ-η<sup>2</sup>-R<sup>2</sup>N=NH)FeCp\*] (R' = Me, Et; R<sup>2</sup> = Me, Ph; Cp\* = η<sup>5</sup>-C<sub>5</sub>Me<sub>5</sub>): synthesis, structure, and catalytic N–N bond cleavage of hydrazines on diiron centers. *J. Am. Chem. Soc.* **130**, 15250–15251 (2008).
82. Harrop, T. C., Olmstead, M. M. & Mascharak, P. K. Binding of CO to structural models of the bimetallic subunit at the A-cluster of acetyl coenzyme A synthase/CO dehydrogenase. *Chem. Commun.* 1744–1745 (2004).
83. Rao, P. V. *et al.* On [FeS]-(μ<sub>2</sub>-SR)-M bridge formation in the synthesis of an A-cluster analogue of carbon monoxide dehydrogenase/acetyl-coenzyme A synthase. *J. Am. Chem. Soc.* **127**, 1933–1945 (2005).
84. Sun, J., Tessier, C. & Holm, R. H. Sulfur ligand substitution at the nickel(II) sites of cubane-type and cubanoid NiFe<sub>3</sub>S<sub>4</sub> clusters relevant to the C-clusters of carbon monoxide dehydrogenase. *Inorg. Chem.* **46**, 2691–2699 (2007).
85. Tada, M. & Masuzawa, Y. Biomimetic methane generation and disulfide formation by catalysis with a nickel complex. *Chem. Commun.* 2161–2162 (1997).
86. Rosenfield, R. E. Jr, Parthasarathy, R. & Dunitz, J. D. Directional preferences of nonbonded atomic contacts with divalent sulfur. 1. Electrophiles and nucleophiles. *J. Am. Chem. Soc.* **99**, 4860–4862 (1977).
87. Reissmann, S. *et al.* Taming of a poison: biosynthesis of the NiFe-hydrogenase cyanide ligands. *Science* **299**, 1067–1070 (2003).
88. Watanabe, S. *et al.* Crystal structures of [NiFe] hydrogenase maturation proteins HypC, HypD, and HypE: insights into cyanation reaction by thiol redox signaling. *Mol. Cell* **27**, 29–40 (2007).  
**This paper is a comprehensive structural analysis of active-site synthesis and assembly.**
89. Lenz, O., Zebger, I., Hamann, J., Hildebrandt, P. & Friedrich, B. Carbamoylphosphate serves as the source of CN<sup>−</sup>, but not of the intrinsic CO in the active site of the regulatory [NiFe]-hydrogenase from *Ralstonia eutropha*. *FEBS Lett.* **581**, 3322–3326 (2007).
90. Leach, M. R., Zhang, J. W. & Zamble, D. B. The role of complex formation between the *Escherichia coli* hydrogenase accessory factors HypB and SlyD. *J. Biol. Chem.* **282**, 16177–16186 (2007).
91. Rossmann, R., Maier, T., Lottspeich, F. & Bock, A. Characterization of a protease from *Escherichia coli* involved in hydrogenase maturation. *Eur. J. Biochem.* **227**, 545–550 (1995).
92. Sofia, H. J., Chen, G., Hetzler, B. G., Reyes-Spindola, J. F. & Miller, N. E. Radical SAM, a novel protein superfamily linking unresolved steps in familiar biosynthetic pathways with radical mechanisms: functional characterization using new analysis and information visualization methods. *Nucleic Acids Res.* **29**, 1097–1106 (2001).
93. Pilet, E. *et al.* The role of the maturase HydG in [FeFe]-hydrogenase active site synthesis and assembly. *FEBS Lett.* **583**, 506–511 (2009).
94. Nicolet, Y. *et al.* X-ray structure of the [FeFe]-hydrogenase maturase HydE from *Thermotoga maritima*. *J. Biol. Chem.* **283**, 18861–18872 (2008).
95. McGlynn, S. E. *et al.* HydF as a scaffold protein in [FeFe]-hydrogenase H-cluster biosynthesis. *FEBS Lett.* **582**, 2183–2187 (2008).
96. Zheng, L., White, R. H. & Dean, D. R. Purification of the *Azotobacter vinelandii* niFV-encoded homocitrate synthase. *J. Bacteriol.* **179**, 5963–5966 (1997).
97. Hernandez, J. A. *et al.* Metal trafficking for nitrogen fixation: NifQ donates molybdenum to NifEN/NifH for the biosynthesis of the nitrogenase FeMo-cofactor. *Proc. Natl Acad. Sci. USA* **105**, 11679–11684 (2008).
98. Obrist, B. V. *et al.* An iron carbonyl pyridonate complex related to the active site of the [Fe]-hydrogenase (Hmd). *Inorg. Chem.* **48**, 3514–3516 (2009).
99. Harrop, T. C., Olmstead, M. M. & Mascharak, P. K. Synthetic analogues of the active site of the A-cluster of acetyl coenzyme A synthase/CO dehydrogenase: syntheses, structures, and reactions with CO. *Inorg. Chem.* **45**, 3424–3436 (2006).
100. Signor, L. *et al.* Methane formation by reaction of a methyl thioether with a photo-excited nickel thiolate — process mimicking methanogenesis in Archaea. *Chem. Eur. J.* **6**, 3508–3516 (2000).
101. Hiramoto, T., Warkentin, E., Moll, J., Ermler, U. & Shima, S. The crystal structure of an [Fe]-hydrogenase–substrate complex reveals the framework for H<sub>2</sub> activation. *Angew. Chem. Int. Edn* doi:10.1002/anie.200902695 (2009).

**Acknowledgements** We thank D. M. Lawson and S. M. Mayer for providing data concerning the xenon sites in nitrogenase. We also thank the Commissariat à l’Energie Atomique and the Centre National de la Recherche Scientifique for institutional support, and the Agence Nationale de la Recherche and the BIOTEC programme of the European Union for funding.

**Author Information** Reprints and permissions information is available at [www.nature.com/reprints](http://www.nature.com/reprints). The authors declare no competing financial interests. Correspondence should be addressed to J.C.F.-C. (juan-carlos.fontecilla@ibs.fr).

# Metalloproteins and metal sensing

Kevin J. Waldron<sup>1</sup>, Julian C. Rutherford<sup>1</sup>, Dianne Ford<sup>1</sup> & Nigel J. Robinson<sup>1</sup>

**Almost half of all enzymes must associate with a particular metal to function. An ambition is to understand why each metal–protein partnership arose and how it is maintained. Metal availability provides part of the explanation, and has changed over geological time and varies between habitats but is held within vital limits in cells. Such homeostasis needs metal sensors, and there is an ongoing search to discover the metal-sensing mechanisms. For metalloproteins to acquire the right metals, metal sensors must correctly distinguish between the inorganic elements.**

The physical and chemical properties of a selected metal satisfy a protein's need to form structure, as for zinc-fingers, or to drive catalysis (Box 1). Proteins have also evolved to use those metals that are, or at least once were, most accessible<sup>1–3</sup>. A tenet of the cell biology of metals is that some metals tend to bind organic molecules more avidly than others. The natural order of stability for divalent metals, often called the Irving–Williams series<sup>4</sup>, sets out a resulting trend with copper and zinc forming the tightest complexes, then nickel and cobalt, followed by ferrous iron and manganese and finally, forming the weakest complexes, calcium and magnesium (Box 1). Biology must overcome this trend for some proteins to bind uncompetitive metals and for other proteins in the same cell to bind competitive metals. Cells are not ideal solutions and kinetic factors can dominate the distribution of metals, for example where metals are delivered by metallochaperones. Nonetheless, excluding the wrong metals from proteins may be more challenging than acquiring the right ones.

A truism is that there has only been selection for most metalloproteins to obtain the correct element in the context of a cellular environment, with implications for the metal status of proteins expressed in heterologous cells and *in vitro*. Two proteins, one copper protein and one manganese protein in the periplasm of a cyanobacterium, illustrate this observation<sup>5</sup>. The folding compartment for the manganese protein MncA overrides its binding preference to control its metal content. The two proteins share similar cupin folds and the same protein ligands. Both prefer copper to manganese *in vitro*, consistent with the Irving–Williams series, but the manganese protein folds before export by means of the Tat translocase. It therefore traps manganese in the cytosol rather than the periplasm. A keystone of this article will be that metal availability is controlled in the cytoplasm<sup>5–8</sup>. Metal importers, metal exporters and metal stores maintain a limited supply of competitive metals such as copper. Thus, proteins compete with other molecules for these metals rather than metals competing with other metals for proteins. To achieve this state, the amount of each metal is somehow sensed to adjust the actions of transporters (at plasma membranes or internal compartments) and storage proteins for each element<sup>9</sup>. Sensors also adjust metabolism to minimize demand for scarce metals or to exploit abundant ones. These sensors are thus pivotal to metal selectivity because their capacity to distinguish the correct metal affects metal occupancy of other metalloproteins.

Here we summarize the use and acquisition of metals by proteins, and then give an overview of how cells sense metals. Multiple bacterial metal-binding, metal-sensing transcriptional regulators are known and have recently been reviewed elsewhere<sup>9</sup>. Metal specificity of bacterial metal sensors is determined by affinity, allostery and access<sup>9</sup>. Here these

three concepts are used to question where metal discrimination lies in eukaryotic metal sensing. In yeast, some metal-responsive transcriptional regulators have been discovered, but their molecular mechanisms may harbour surprises. In mammals, one metal-binding, metal-sensing transcriptional regulator and a post-transcriptional regulator are known<sup>10,11</sup>, but innumerable metal-responsive events, including elaborate switches in protein trafficking, are controlled by largely uncharted metal sensors.

## An appraisal of metals used in proteins

The time is ripe to survey the use of metals in proteins, by exploiting bioinformatics and proteomics. Non-denaturing conditions must be used in proteomics if metal cofactors are to be retained<sup>12</sup>, and this can be technically challenging, there being a potential for metal exchange, acquisition or loss during fractionation. A commonly cited approximation is that one-third of proteins require metals. A systematic bioinformatics survey of 1,371 different enzymes for which three-dimensional structures are known estimated that 47% required metals, with 41% containing metals at their catalytic centres<sup>13</sup>. It is noteworthy that complicated metal centres<sup>14</sup> can remain poorly defined even after structure determination. Metalloenzymes occur in all six Enzyme Commission classes, accounting for 44% of oxidoreductases, 40% of transferases, 39% of hydrolases, 36% of lyases, 36% of isomerases and 59% of ligases<sup>13</sup>. Magnesium is the most prevalent metal in metalloenzymes, although it is often involved in loose partnerships with phosphate-containing substrates such as ATP and is sometimes interchangeable with manganese. The frequency of manganese in protein structures may overestimate its use *in vivo*, where magnesium is truly the cofactor (Fig. 1a).

A catalogue of the principal type of enzyme that uses each metal reveals that iron (81%), copper (93%) and molybdenum plus tungsten (81%) are most commonly used as conduits for electrons in oxidoreductases<sup>13</sup> (Fig. 1b). Cobalt and molybdenum are found almost exclusively in association with cofactors in vitamin-B<sub>12</sub>-dependent and molybdopterin-dependent enzymes (see page 839). The proportion of all proteins, not just enzymes, using metals is expected to be less than 47% and the relative contributions of the different metals may alter as the metals that perform structural roles, such as zinc in zinc-fingers, are more fully accounted for.

## Evolving metal availability and use

The metals available to organisms have altered during evolution as species have occupied new niches and in response to massive environmental changes, for example the liberation of dioxygen by photosynthesis, which significantly changed metal solubility<sup>1–3</sup>. Crucial enzymes, which

<sup>1</sup>Cell & Molecular Biosciences, Medical School, Newcastle University, Newcastle NE2 4HH, UK.

**Box 1 | The selection of metals**

At catalytic centres, metals increase acidity, electrophilicity and/or nucleophilicity of reacting species, promote heterolysis, or receive and donate electrons<sup>13</sup>. The protein's primary and secondary metal-coordination spheres tune the properties of the metal to optimize reactivity and influence metal selection. Donor ligands (S, O or N) can impart bias in favour of the correct metal. The metal-binding pocket can exclude ions with the wrong charge. Coordination geometry (octahedral, tetrahedral, square pyramidal, trigonal bipyramidal, square planar, trigonal or linear) can impart bias either in folded apoproteins if the preformed site is rigid or during folding if favourable energetics is coupled to the correct geometry. The figure shows the dominant geometries of four divalent metals in proteins<sup>98</sup>.



However, because proteins have flexibility, steric selection between metals is imperfect, especially in nascent polypeptides. Under these conditions, the relative affinities of metals for proteins are significantly governed by the ligand field stabilization energies of the metals themselves. This creates the universal orders of preference, which for divalent metals is the Irving–Williams series. There is ambiguity about the position of zinc, which is either at the top of the series or somewhere above cobalt. This ambiguity is attributed to the nephelauxetic effect<sup>99</sup>. Cuprous ions, expected to dominate in more reducing cell environments, are also competitive, and some exceptionally tight ferric complexes are known. Crucially, such affinity series underpin calculations that each metal's relative abundance in the biological locality is paramount in governing selective metal binding by proteins<sup>100</sup>, highlighting the vital contribution of cell biology to the selection of metals by metalloproteins.

cannot be readily replaced, have created dependences on metal species that were once plentiful but are now scarce. For example, under anoxic conditions iron is soluble in ferrous form, but in the presence of dioxygen ferric iron is poorly soluble; hence, plants and microbes release siderophores and plants express root-surface metal reductases to scavenge meagre amounts of iron from the environment<sup>15,16</sup>. Despite these efforts, plants remain a poor dietary source of iron and, in consequence, iron deficiency is the most common human dietary deficiency worldwide and one of the ten most prevalent causes of disease<sup>15</sup>.

In today's open oceans, the poor availability of iron, but the presence of some copper, has led organisms to replace the former and exploit the latter<sup>17,18</sup>. The oceanic diatom *Thalassiosira oceanica* has switched from using iron-containing cytochrome *c<sub>6</sub>* to using copper-containing plastocyanin<sup>17,18</sup>, which was otherwise only known in some cyanobacteria and photosynthetic organisms containing chlorophyll *b*. The sulphur isotope record also implies that ancient oceans were dominated by sulphide and, hence, metal sulphides<sup>2</sup>. Under these conditions, copper, zinc and cadmium were poorly available, but cobalt and nickel more available<sup>2</sup>. Greater volcanic–nickel input also preceded this era<sup>19,20</sup>. Enzymes that use cobalt and nickel are considered to be metal relics from these times<sup>1,2,19,20</sup>. Some carbonic anhydrases are cambialistic, capable of substituting cobalt for zinc in ocean surface waters where zinc is in short supply<sup>21</sup>. Even more noteworthy are a subset of structurally modified carbonic anhydrases from marine diatoms that have abnormal loops near the active site to facilitate metal substitution with catalytically active cadmium<sup>21–23</sup>, a rare example of enzymes that have evolved to use this normally solely toxic metal.

The exploitation of metals varies between species, and trends exist in the superkingdoms<sup>3</sup>. The slope of plots comparing the number of zinc-binding domains with the total number of protein domains encoded by each genome is greater in eukaryotes than in archaea or bacteria; the reverse trend is true for iron-, manganese- and cobalt-binding domains<sup>3</sup>. An implication is that zinc was increasingly recruited as eukaryotic genomes

became more complex, and this is especially true for multicellular eukaryotes, with a point of inflection detected at the intersection between unicellular and multicellular species<sup>3</sup>. This reflects the eukaryotic diversification of structural zinc-binding domains, notably zinc-finger and RING-finger domains, which constitute ~3% and ~1% of the human proteome, respectively<sup>24</sup>. Zinc-fingers are prevalent in the control of gene expression associated with differentiation into multiple cell types. Archaea and bacteria have, as a proportion, more iron–sulphur proteins (see page 831) but fewer haem proteins than eukaryotes, and within the bacteria aerobic species have fewer iron–sulphur cluster proteins and more haem proteins than anaerobic bacteria<sup>3</sup>.

**Metal mis-population**

It might be predicted that a consequence of proteins having tight affinities for incorrect metals is a potential for metals to mislocate, yet few such examples are documented. This rarity may reflect an exceptional efficiency of metal homeostasis or perhaps the experimental effort necessary to establish which metals are bound to proteins inside cells. Binding sites of proteins involved in metal homeostasis typically allow metal exchange, but other sites can be buried, with the metal being kinetically trapped and safe from replacement with an incorrect metal. Even so, the correct metal must somehow become trapped in the first place.

A subset of *Escherichia coli* manganese superoxide dismutase, MnSOD, is known *in vivo* to acquire iron<sup>25</sup>, which is catalytically inactive. Recombinant MnSODs from other organisms, expressed in *E. coli*, mis-populate with iron, cobalt or nickel<sup>25</sup>. Eukaryotic MnSOD, in the mitochondrial matrix, acquires catalytically inactive iron when mitochondrial manganese and/or iron homeostasis is perturbed<sup>25</sup>. Cobalt mimics hypoxia in humans possibly because cobalt replaces iron in prolyl 4-hydroxylase, which in iron-form hydroxylates the hypoxia-responsive transcription factor HIF1 (also known as HIF1A)<sup>26</sup>. The wrong metals can also mislocate to metal prosthetic groups<sup>27</sup>. A lack of specificity in ferrochelatase, the enzyme that inserts iron in the synthesis of haem, can give rise to metal mis-incorporation *in vivo* such that high concentrations of zinc protoporphyrin in the blood are used in the clinical diagnosis of iron deficiency<sup>28</sup>.

**Metallochaperones**

One way to ensure that the correct metal is acquired by a metalloenzyme is to exploit delivery proteins, that is, metallochaperones. For example, nickel is inserted into bacterial hydrogenase (see page 814) and urease by dedicated nickel metallochaperones. It is unclear where metallochaperones acquire metal. No single donor for either of two yeast copper metallochaperones emerged from a systematic analysis of mutants lacking transporters<sup>29</sup>. Metal transfer has nonetheless been observed *in vitro* between cytosolic regions of the copper importer Ctr1 and a copper chaperone<sup>30</sup>, and a recent electron crystallographic structure of Ctr1 might be exploited to visualize how this could occur<sup>31</sup>. Metal is passed from metallochaperones to cognate apoproteins by means of ligand-exchange reactions<sup>32,33</sup>. Thus, the specificity of protein contact, and of the subsequent ligand-exchange reactions, determines which proteins gain access to those metals supplied by metallochaperones. However, rather few metallochaperones are known, so most proteins are assumed to obtain metal from exchangeable cellular pools, and the contributions of metal sensors thus become vital.

**A bacterial model for metal sensing**

Bacteria have sets of metal- and DNA-binding, metal-sensing transcriptional regulators classified into families of metal de-repressors (ArsR–SmtB, CsoR–RcnR and CopY), metal co-repressors (Fur, NikR and DtxR) and metal activators (MerR)<sup>34,35</sup>. A few sensors also detect metals external to the plasma membrane. The affinities of cytosolic sensors for the metals they detect have been used to make inferences about the concentrations of metals available to proteins<sup>7,8</sup>. On the assumption that the sensors undergo metal exchange with cytosolic metal pools, their affinities become the thresholds for homeostasis. In switching from apo to holo form, metal sensors alter production of proteins to



acquire, expel or sequester metal, so the concentrations at which the sensors bind metal may not be exceeded. The affinities for metal inducers increase as the sensors detect metals farther up the Irving–Williams series<sup>9</sup>, implying that the most competitive metals are bound and buffered to exceedingly low concentrations<sup>7,8</sup>. For example, two zinc sensors of *E. coli*, Zur and ZntR, are estimated to have femtomolar zinc affinities<sup>7</sup>, which is analogous to there being fewer than one metal ion per *E. coli* cell volume (formally nanomolar).

In addition to metal affinity, the following two other factors dictate which metals a sensor detects *in vivo*.

### Access

Metal availability in the cytosol is not standardized across species<sup>25,36,37</sup>. The metals detected by a sensor can change when tested in a different bacterium, perhaps chosen because it was more tractable for experimentation<sup>36,37</sup>. Kinetic factors, perhaps mediated by protein interactions, also affect access and differ between species.

### Allostery

A manganese sensor from *Bacillus subtilis*<sup>38</sup>, a nickel sensor from *E. coli*<sup>39</sup> or *Helicobacter pylori* and a nickel/cobalt sensor from *Mycobacterium tuberculosis*<sup>36</sup> all bind metals with orders of affinity that match the Irving–Williams series. However, in these sensors only the correct metals bind in an optimal conformation to alter DNA binding allosterically.

### Metal sensors in yeast

Studies of metal-regulated gene expression have focused on a set of DNA-binding transcription factors in *Saccharomyces cerevisiae* (Fig. 2a). Functionally equivalent factors occur in other yeasts such as *Schizosaccharomyces pombe*, although the complement and mechanisms vary<sup>40,41</sup>. Metal-responsive signal transduction pathways emanating from metal sensing at the plasma membrane are either absent or yet to be discovered in yeast. Metalloregulation of these yeast DNA-binding transcription factors can involve metal-dependent change in nuclear versus cytosolic localization, metal-dependent repression of activation-domain function and metal-mediated change in DNA binding<sup>42</sup>. In *S. cerevisiae*, Zap1 responds to zinc, Mac1 plus Ace1 (also known as Cup2) to copper, and Aft1 plus Aft2 to iron (Fig. 2a).

The metal-responsive transcription factors regulate expression of a repertoire of transporters that import or compartmentalize metals<sup>42</sup> (Fig. 2b). Mac1 has also been implicated in a pathway of metal-responsive transporter degradation<sup>43</sup>. Yeast cells store excess metal in vacuoles<sup>44,45</sup>, with plasma-membrane exporters known only for cadmium and arsenic, and some yeasts have metal-sequestering metallothioneins. The factors also control metabolic switching; for example, the transcription factors Aft1 and Aft2 indirectly (through Cth1 and Cth2 (also known as Tis11)) reduce the stability of transcripts encoding iron-dependent enzymes when iron is in poor supply<sup>46,47</sup>. The iron regulon is also induced at the diauxic shift to support the enhanced iron requirements of respiration<sup>48</sup>. The extent to which the responses are triggered by metal binding to the *S. cerevisiae* transcription factors themselves has been explored.

### Metal sensing by metal binding

Mac1 and Ace1 activate transcription in response to low and, respectively, high concentrations of copper in *S. cerevisiae*<sup>49,50</sup>. Cysteine-rich motifs in both Mac1 and Ace1 can bind copper *in vitro* to form polycopper clusters that are bridged by thiolates<sup>51</sup>. Structures of the clusters have been modelled from extended X-ray absorption fine structure (EXAFS) data<sup>51</sup> (Fig. 2c). As copper concentrations increase, there is a reciprocal relationship between the loss of activation of Mac1-regulated genes and the induction of Ace1-regulated genes<sup>52</sup>. A simple model is that at some critical intracellular copper concentration, clusters form in both proteins to repress Mac1 function while activating Ace1. DNA binding by Ace1 is enhanced by copper *in vitro*<sup>49</sup>. It is not yet known whether Mac1 and Ace1 compete for the same pool of copper or whether copper is delivered by a metallochaperone. Polycopper clusters are structurally distinct and so have the potential to provide allosteric metal specificity in favour of copper through the unique protein conformations they induce.

Activation (or repression on some promoters) of gene expression in response to zinc is controlled by the Zap1 transcription factor, a process that depends on its zinc-fingers. Zap1 has two transcriptional activation domains, one of which is located within an unusual pair of zinc-fingers<sup>53</sup>. The zinc in these atypical fingers is more labile than in the standard DNA-binding zinc-fingers<sup>53</sup>. Zap1 metal regulation by means of variable zinc occupancy of these atypical fingers is strongly supported by *in vivo* observations of fluorescence resonance energy transfer (FRET) between probes on adjacent fingers<sup>54</sup> (Fig. 2d). The fluorophores only become close enough to allow energy transfer when the holo-fingers form, and this occurs only when zinc concentrations increase. Thus, for elevated zinc concentrations these atypical zinc-fingers become occupied by metal, masking the activation domain and thereby inactivating gene expression. The zinc affinities of the labile Zap1 zinc-fingers, expressed without the rest of Zap1, are in the nanomolar range<sup>53,55</sup>. This might imply that intracellular available zinc accumulates to a higher concentration in yeast than in bacteria, but perhaps the zinc affinities are tighter in intact Zap1. There is cooperative binding of zinc to the two atypical fingers of Zap1 (ref. 55), offering the potential to confer allosteric metal specificity.

### Indirect responses to metals

Iron sensing in yeast is mediated by Aft1 (ref. 56) (Fig. 2a) or its paralogue, Aft2 (ref. 57). The more extensively studied Aft1 undergoes iron-responsive nucleocytoplasmic shuttling<sup>58–60</sup>. When the iron concentration is low, Aft1 accumulates in the nucleus. Nuclear Aft1 activates transcription of a regulon that includes genes encoding iron transporters<sup>61</sup> (Fig. 2b). Details of the iron-switch are being pieced together. The switch requires cysteine residues in either Aft1 or Aft2 (refs 56, 57), two monothiol glutaredoxins (Grx3 and Grx4)<sup>60</sup> and two cytosolic proteins (Fra1 and Fra2)<sup>59</sup>. *In vitro*, Grx3 and Grx4 homodimers associate with a [2Fe–2S] cluster<sup>62</sup> and Aft1 is known to be responsive to the degree of iron–sulphur-cluster biosynthesis in the mitochondria<sup>63</sup>. Aft1 might respond to iron indirectly, with the proteins of iron–sulphur-cluster

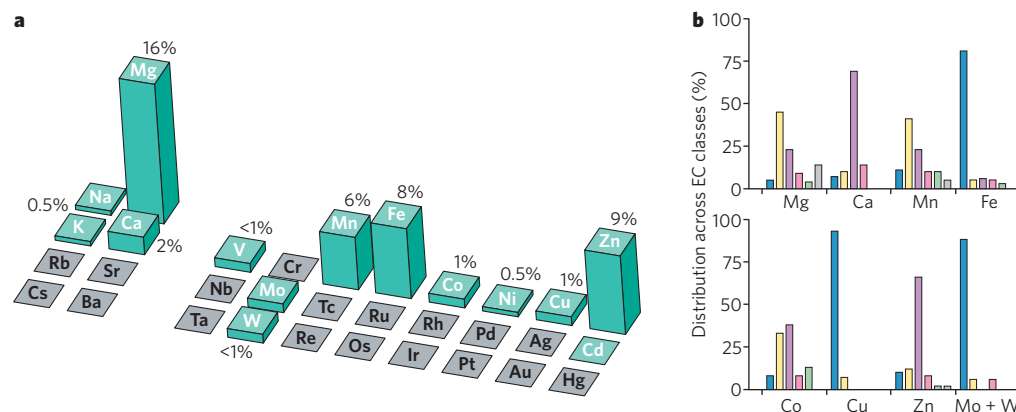


**Figure 1 | Metals used in catalysis.** **a**, The elements used as cofactors by enzymes are shown in blue. The height of each column represents the proportion of all enzymes with known structures using the respective metal. A single enzyme uses cadmium<sup>22</sup>. **b**, The proportion of proteins using the indicated metals that occur in each of the six enzyme classes: oxidoreductases (EC 1), blue; transferases (EC 2), yellow; hydrolases (EC 3), purple; lyases (EC 4), pink; isomerases (EC 5), green; ligases (EC 6), grey. EC, Enzyme Commission. Data obtained from ref. 13.

biosynthesis being the incipient discriminatory sensors.

Classical signal transduction pathways may also be involved in copper sensing, because the DNA-binding form of Mac1 is phosphorylated<sup>64</sup>. Furthermore, as hinted previously, no copper chaperone has been linked to copper delivery to the nucleus. In a search for such a donor, Mac1-responsive gene expression was systematically tested in mutants lacking each of the known copper metallochaperones<sup>65</sup>. A dependence on the copper donor for superoxide dismutase (Sod1) was discovered; however, it transpires that this is only indirect, because Mac1 needs catalytically active Sod1 in the nucleus to function<sup>65</sup>. The mere suppression of oxidative stress does not overcome the need of Mac1 for nuclear Sod1, suggesting a key role of redox changes in the nucleus for the copper response of Mac1 (ref. 65) (Fig. 2e). The activity of Sod1, itself an abundant copper enzyme, may be the indicator used to monitor copper sufficiency, raising many questions about where metal discrimination takes place.

## Metal sensing in animals

The cells of multicellular eukaryotes can respond to the metal status of the whole organism as well as to their own status, and systemic signalling molecules have been discovered such as hepcidin in animals. Many responses to metals in plants and animals occur post-transcriptionally, by adjusting messenger-RNA stability or translation, or post-translationally, by adjusting intracellular protein trafficking or degradation. With a few significant exceptions, the metal-binding, metal-sensing sites that trigger these events remain to be discovered. Plant metal homeostasis is reviewed elsewhere<sup>16,66</sup>, but the discovery of Spl7 (Crr in *Chlamydomonas*), which possibly binds (and senses) copper, should be noted.

## Metal regulation of transcription

Just one metal-binding, metal-sensing transcriptional regulator is currently known in animals, the metal-regulatory transcription

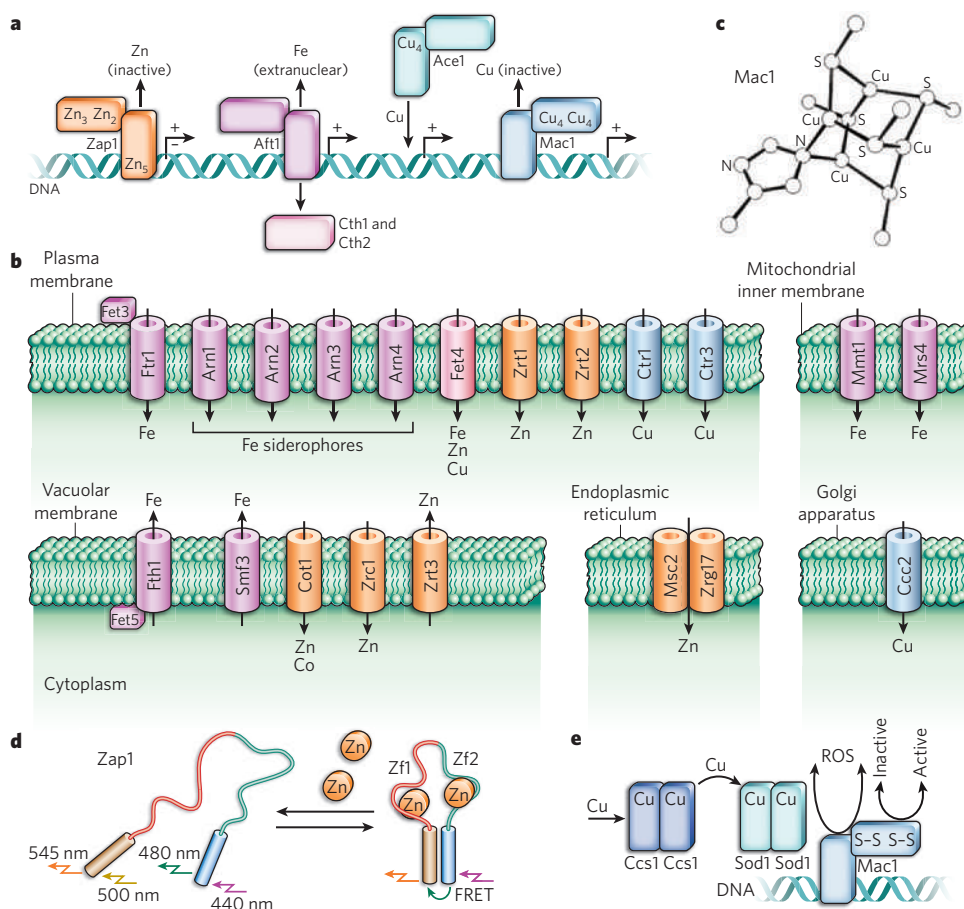


**Figure 2 | Metal sensing in *Saccharomyces cerevisiae*.** **a**, Each metal-responsive transcription factor has a DNA-binding domain and an activation domain (shown as two blocks). Zap1 (orange) has multiple sets of zinc-fingers (subscripts indicate the number of zinc atoms in each set). When zinc binds to zinc-fingers 1 and 2 (Zf1 and Zf2) in the activation domain (bound zinc indicated by Zn<sub>2</sub>), activation is repressed. Copper-cluster formation (Cu<sub>4</sub>) in Ace1 (blue-green) encourages DNA binding. By contrast, in Mac1 (blue), copper clusters inhibit activation-domain function and weaken DNA binding. Under high-iron conditions, Aft1 (pink) becomes extranuclear. These factors generally activate transcription when bound to DNA (+), but Zap1 can also act as a repressor (−). The mRNA-binding proteins Cth1 and Cth2 (pink) downregulate transcripts encoding iron-requiring proteins, and the genes encoding Cth1 and Cth2 are controlled by Aft1 and Aft2. **b**, The metal-responsive transcription factors control the expression of genes encoding a subset of metal transporters (tubes), which allow the passage of metals through various membranes in *S. cerevisiae* (pink, iron transporters; orange, zinc transporters; and blue, copper transporters). The colour of the transporter also corresponds to the specific transcription factor involved in regulation: Aft1 and/or Aft2 (pink), Zap1 (orange), and/or Mac1 (blue), with several exceptions (Fet4 is

regulated by Zap1 and Aft1; Cot1 is regulated by Aft1; Zrg17 is regulated by Zap1 but Msc2 is not; and Ccc2 is regulated by Aft1). Arrows show the direction of metal transport. Fet3 and Fet5 are ferroxidases. Fet4 is a different shade of pink because it can transport iron, zinc and copper. **c**, Copper clusters of Mac1 (or Ace1, not shown) may allow allosteric metal specificity. Model of the metal site based on X-ray absorption fine structure (EXAFS) data. Spheres represent carbon atoms unless labelled otherwise. (Panel reproduced, with permission, from ref. 51.) **d**, The binding of zinc to the zinc-fingers in Zap1 (Zf1 shown in red, and Zf2 in cyan) has been followed *in vivo* using FRET: the energy transfer between enhanced cyan fluorescent protein and enhanced yellow fluorescent protein attached to Zf2 and Zf1 was measured, providing evidence that zinc occupancy of these fingers is modulated *in vivo*. Zigzag arrows indicate the light (wavelength shown) either absorbed or emitted by the fluorescent proteins. (Panel modified, with permission, from ref. 54.) **e**, Redox chemistry is involved in regulating the activity of Mac1. Mac1 function depends on the presence of active Sod1 in the nucleus, which depends on copper being delivered to Sod1 by the metallochaperone Ccs1. The consumption or generation of a reactive oxygen species (ROS) by Sod1 might modify regulatory cysteine residues on Mac1 (ref. 65).

factor MTF1, although other DNA-binding zinc-finger proteins, such as SP1, do act downstream of unknown metal sensors<sup>67</sup>. Zinc stabilizes a complex between MTF1 and its DNA-binding site, with at least some of the sensing mechanism residing in its DNA-binding Cys<sub>2</sub>His<sub>2</sub> zinc-fingers<sup>10</sup>. MTF1 is commonly, although not exclusively, a transcriptional activator<sup>68,69</sup>, acting with other factors<sup>70</sup>. In the special case of the *Drosophila* MTF1 homologue, some of these interactions are linked to metal specificity<sup>71</sup>.

Transcription of mammalian MTF1 target genes is induced in response to metals such as copper and cadmium, not merely zinc<sup>71,72</sup>. Oddly, in a cell-free system copper or cadmium have the opposite effect, inhibiting mammalian MTF1-dependent transcription, but this is reversed simply by adding one further component, zinc metallothionein, to the reaction mixture<sup>73</sup>. Addition of apothionein, by contrast, is inhibitory<sup>73</sup>. An explanation is that cadmium and copper displace zinc from binding sites such as those of zinc metallothionein; the liberated zinc then binds to the zinc-fingers of mammalian MTF1 (Fig. 3a). Here, metal specificity is achieved through a combination of metal access and allostery.

The *Drosophila* protein MTF1 is distinct in having a copper cluster and zinc-fingers<sup>74</sup>. Flies in which the cysteine residues that coordinate the cluster are converted to alanine fail to upregulate transcription of a copper-metallothionein gene in response to a high copper concentration. Hypothetical co-regulators are proposed to interact with *Drosophila* MTF1 dependent on cluster formation. Alternative co-regulators are thought to enable *Drosophila* MTF1 to upregulate some genes in response to copper excess while upregulating others, such as that encoding the CTR1B copper importer, in response to copper limitation. Zinc can bind to the cysteine thiolate ligands of the copper cluster *in vitro* without impairing subsequent copper binding<sup>74</sup>. As for yeast copper-responsive transcription factors, structurally distinct polycopper clusters have the potential to confer allosteric metal specificity by means of the unique protein conformations they induce.

### Metal regulation of mRNA stability and translation

In a highly parsimonious way, the iron-responsive proteins IRP1 (also known as ACO1) and IRP2 (IREB2) control translation or mRNA stability reciprocally for different gene products<sup>75</sup>. A cleft in IRP1 and, by inference, IRP2 binds to iron-responsive elements (IREs) that form stem-loops in mRNAs<sup>11</sup> (Fig. 3b). IREs occur in the 5' untranslated region of mRNA encoding the ferritin iron store and in the 3' untranslated region of the mRNA encoding the transferrin receptor for iron uptake. Ferritin is needed when iron is in surplus, and transferrin receptor is needed when iron is lacking. IRP binding to the 5' region blocks translation whereas binding to the 3' region stabilizes the mRNA. An iron-sulphur cluster binds within, and hence blocks, the cleft of holo-IRP1. Thus, holo-IRP1 dissociates from mRNAs to allow translation of ferritin but degradation of transferrin-receptor mRNA when iron-sulphur clusters are sufficiently abundant to fill its cleft<sup>11</sup>. As for polycopper clusters, binding of iron-sulphur clusters to a sensor may confer allosteric metal

specificity, but because iron-sulphur clusters are themselves products of a biochemical pathway, perhaps — as noted for yeast Aft1 — metal discrimination really takes place in the cluster-assembly proteins.

### Post-translational metal regulation

Metal-responsive degradation of metal-homeostasis proteins is a general strategy that applies, for example, to IRP2 (ref. 76), to the copper chaperone CCS<sup>77</sup>, to the copper importer CTR1 (also known as SLC31A1)<sup>78</sup>, to the iron-efflux protein ferroportin<sup>79</sup> and to the zinc-uptake transporter ZIP4 (SLC39A4)<sup>80</sup> (Fig. 4). ZIP4 has three levels of post-translational regulation in response to zinc. The extracellular amino-terminal half of ZIP4 is proteolytically processed during prolonged zinc deficiency<sup>81</sup>, ZIP4 is removed from the plasma membrane to a perinuclear location when zinc becomes replete<sup>82</sup> and ZIP4 is degraded when zinc is highly elevated<sup>80</sup>. The third process involves perception of zinc by a cytoplasmic histidine-rich motif that somehow exposes a site for ubiquitination and, hence, proteasomal degradation. The same histidine-rich motif triggers ZIP4 degradation in response to cadmium, but degradation does not occur in response to iron, manganese, nickel, copper or cobalt<sup>80</sup>. The question of which elements the motif distinguishes through affinity, allostery or access awaits exploration.

As is the case for ZIP4 during the transition between low-zinc and zinc-replete conditions, other metal transporters also undergo metal-dependent trafficking (not solely for degradation). This was first observed for copper-transporting ATPase ATP7A, which redistributed from internal *trans*-Golgi membranes to the plasma membrane in cell cultures exposed to high copper concentrations<sup>83</sup> (Fig. 4). Under low-copper conditions ATP7A supplies metal to copper proteins in the *trans*-Golgi network, whereas under high-copper conditions it aids efflux. An analogous protein (ATP7B) is expressed in the liver, where it relocates to apical hepatocyte membranes under high-copper conditions to cause efflux of the surplus into bile canaliculi<sup>84</sup> (Fig. 4). Several mutations in ATP7A or ATP7B cause the transporters to remain within internal membranes, and increased trafficking to the plasma membrane rather than reduced re-internalization by endocytosis is triggered by high copper concentrations<sup>85</sup>. A nine-residue stretch of ATP7B is speculated to bind a partner in response to copper<sup>84</sup>. In this model, the copper-sensing sites are responsible for exposing the nine-residue signal but the sensor remains a mystery. One suggestion is that the acyl phosphate intermediate state of the ATPase itself exposes the nine-residue motif<sup>84</sup>. Trafficking of CTR1 in response to copper is also linked to its transport activity, and to a methionine-rich motif<sup>78</sup>. Here, the levels of catalytic activity of CTR1 and ATP7B become coupled to trafficking, and selectivity of sensing becomes a function of the selectivity of transport.

### Systemic signals of metal status

Hepcidin is a disulphide-rich peptide consisting of 25 amino acids that is synthesized and released by the liver in response to increased iron<sup>79</sup>. Hepcidin binds to ferroportin to induce internalization and lysosomal

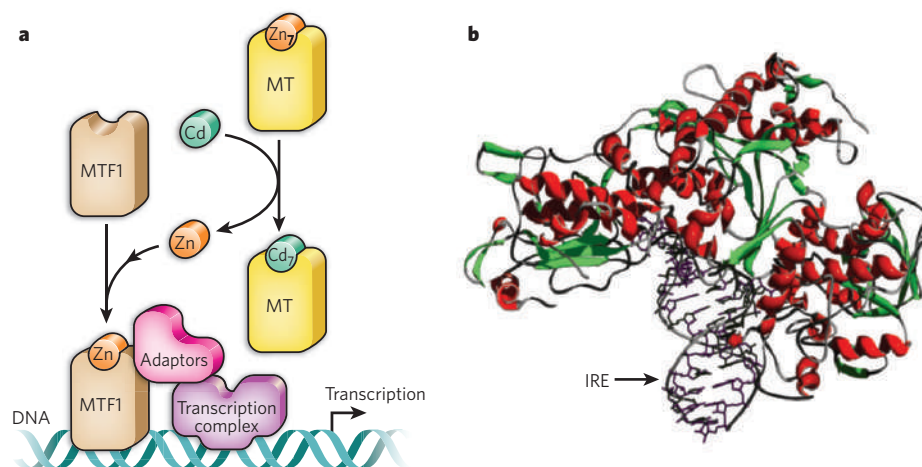


**Figure 3 | Metal sensors in animals.** **a**, MTF1 responds to cadmium *in vivo* (but not *in vitro*) indirectly, as a function of access to zinc. Cadmium binds to metallothionein (MT) more tightly than does zinc. Zinc released from metallothionein is taken up by zinc-fingers of MTF1, which in turn interacts with metal-response elements on DNA to effect the transcription of target genes through adaptor proteins<sup>73</sup>. **b**, Iron-responsive protein IRP1 ( $\alpha$ -helices, red;  $\beta$ -strands, green) in complex with an iron-regulatory element (IRE) from the 5' untranslated region of ferritin mRNA (purple, in stick format) (Protein Data Bank code 2IPY)<sup>11</sup>. Binding of IRPs to this mRNA region inhibits the translation of the iron-storage protein ferritin.



degradation<sup>79</sup>. Ferroportin is otherwise responsible for iron export into the circulation across the basolateral membrane of enterocytes<sup>86</sup> (Fig. 4). Thus, hepcidin inhibits dietary iron absorption. The mechanism by which hepcidin synthesis and release respond to iron is independent of IRPs because there are no IREs in the hepcidin mRNA. The iron signal is triggered by competition between transferrin receptors one and two for the hereditary haemochromatosis protein HFE, which is influenced by occupancy of receptor one with holo-transferrin<sup>87</sup>. Metal discrimination could be said to take place in the formation of diferric transferrin, in which the valence state of iron plays a major part in selectivity.

## Outlook

Bias in favour of the correct metal can occur during folding of a metallo-enzyme if coupled to favourable energetics<sup>88</sup> (Box 1). Perhaps some metal-coordination spheres have evolved to leave patches exposed if an incorrect metal binds, to attract folding chaperones. Such a mechanism might check that metalloproteins have enfolded the correct metals *in vivo*, a form of proofreading of metal acquisition. To understand metal occupancy, methods used decades ago to fractionate metalloproteins should be revisited, but equipped today with improved multiple-metal detection by inductively coupled plasma mass spectrometry and inordinately improved protein identification by mass fingerprinting. Mathematical methods such as principal-component analysis circumvent the need to purify holoproteins to homogeneity before identification<sup>5</sup>. Metallochaperones can influence the intracellular distribution of metals but other kinetic factors, such as interactions with metal importers (or exporters from storage compartments) or proximity to sites of metalloprotein degradation, may also create metal niches.

Metal sensors influence metal availability in cells, which in turn influences metal occupancy of metalloproteins. The contribution of allostery to metal specificity in bacterial metal sensors is predicted to be especially important for metal co-repressors and metal activators, in which metal binding to the protein must organize an active protein–DNA adduct. Another prediction is that extra ligands may have been selected adjacent to some sensory metal sites to lure the wrong metals into non-productive binding configurations. A further untested prediction is that access to

metal is partly a function of the relative affinities of a set of metal sensors<sup>9</sup>. For example, provided that a zinc sensor has the tightest affinity for zinc in the set, other sensors will never gain access to zinc even if they could otherwise bind zinc more tightly than their bona fide metal effectors.

An important question in relation to metal sensing in *S. cerevisiae* is that of what redox chemistry is associated with Aft1 and Mac1. X-ray crystal structures, plus NMR solution studies, of bacterial DNA-binding metal sensors in apo form, in holo forms with different metals, as multimers and as DNA adducts, have helped visualize metal sensing. Equivalent insight is largely missing from eukaryotic metal sensing, with one exception being IRP1 in complex with stem-loops of a ferritin transcript<sup>11</sup> (Fig. 3b). Recombinant metal-binding domains have been examined in isolation, including the zinc-fingers of Zap1 (ref. 55), those of Ace1 homologue Amt1 (also known as Mep1)<sup>89</sup> and of MTF1 (ref. 90), and the copper clusters of Ace1 (ref. 51), Mac1 (ref. 51) and *Drosophila* MTF1 (ref. 74). Technical advances in determining larger solution and crystal structures hold promise for visualizing the apo and holo forms of intact eukaryotic metal-sensing transcriptional regulators, particularly in complex with co-regulators and with DNA.

In animals, there are plenty of metal-mediated changes in the abundance of transcripts that neither contain IRP-binding sites nor are encoded by genes with promoters containing the MTF1-recognition element. For instance, ZNT5 (also known as SLC30A5) transcripts are subject to both zinc-responsive synthesis and stability through unknown factors<sup>91</sup>. Repositories of transcriptomic data catalogue a multitude of responses to altered levels of different metals in mammalian tissues or cells (see, for example, ArrayExpress (European Bioinformatics Institute; <http://www.ebi.ac.uk/microarray-as/ae/>) and the Gene Expression Omnibus (US National Center for Biotechnology Information; <http://www.ncbi.nlm.nih.gov/geo/>)). To discover unknown DNA- or RNA-binding factors, it should be possible to interrogate the sequences of metal-responsive genes to identify common nucleotide elements in those with similar responses to a metal, thereby identifying bait sequences with which to search for cognate metal regulators. Some iron-responsive genes contain the nucleotide-binding site for HIF1 (ref. 92), and one unproven

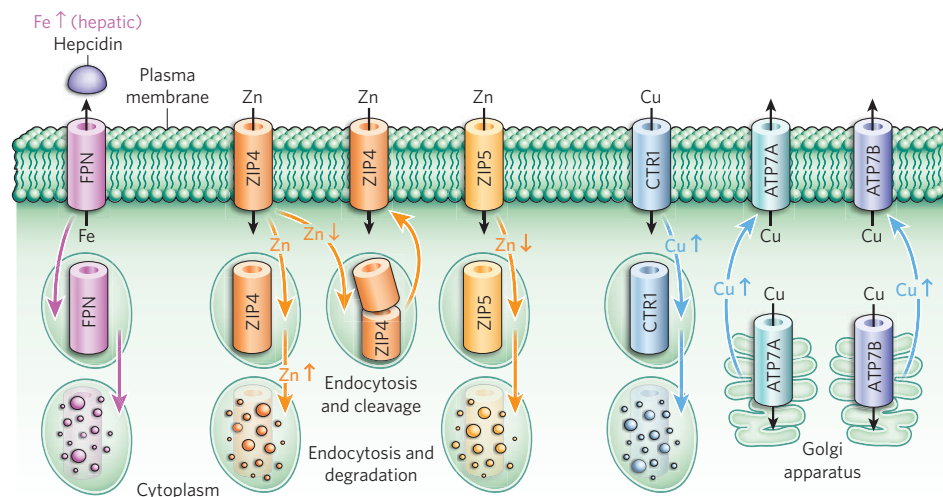


**Figure 4 | Metal-responsive trafficking and processing of metal transporters.**

Mammalian metal transporters (coloured tubes) themselves move within the cell in response to metal ions. Depending on whether the metal concentrations are high (↑), low (↓) or optimal (no arrow) for a particular transporter, the transporter can be internalized and transported within the cell (curved coloured arrows) and then degraded or cleaved. Most of the sites at which metals bind to, and are sensed by, transporters, thereby effecting these changes, remain to be discovered. Within an organism, the distribution of metal transporters can be widespread (as is the case for CTR1 and ATP7A) or restricted to particular cell types (all other transporters). In addition, in polarized cells, transporters can be expressed on the apical or basolateral side. For example, in response to high concentrations of iron,

the liver produces hepcidin (left), which binds to ferroportin (FPN) in the basolateral membranes of intestinal cells known as enterocytes, triggering the internalization and degradation of FPN. The amount of iron in the liver can thus influence how much iron is transported from the intestine into the circulation. Known distributions of metal transporters are as follows: FPN, intestine (basolateral), placental trophoblast (basolateral), and monocytes and macrophages; ZIP4, pancreatic  $\beta$ -cells, intestine (apical), embryonic visceral yolk sac (apical, in mouse) and kidney; ZIP5, pancreatic acinar cells (basolateral), embryonic visceral yolk sac (basolateral, in mouse), kidney, spleen, liver and intestine (basolateral); ATP7A, polarized cells (basolateral); ATP7B, liver (apical), mammary gland (apical), kidney (apical) and placental trophoblast (apical).

hypothesis is that HIF1 activity responds to iron through the iron dependence of its prolyl 4-hydroxylase<sup>26,93</sup>. Extracellular zinc also seems to trigger signal pathways through a G-protein-coupled mechanism<sup>94</sup>, suggesting the presence of unknown plasma-membrane metal receptors. Metazoans also somehow modify the set points for metal sensing to sustain different metal concentrations in different tissues, and all cells somehow prioritize the expression of different metalloproteins under conditions of metal deficiency.

With so many metabolic processes requiring metals, dyshomeostasis is expected to feature widely in pathologies. Aberrant copper transport is the cause of Menkes disease (mutations in ATP7A) and Wilson's disease (mutations in ATP7B)<sup>85</sup>, aberrant zinc transport is a cause of acrodermatitis enteropathica (mutations in ZIP4)<sup>81</sup>, and aberrant iron transport is a cause of haemochromatosis (mutations in ferroportin, HFE, TFR2, hepcidin or haemojuvelin)<sup>87</sup>, to name but a minuscule subset of examples. Type 2 diabetes mellitus results from interaction between environmental and genetic factors, and a linked polymorphism is found in a zinc transporter that supplies insulin granules in  $\beta$ -cells<sup>95</sup>. Perhaps progressive accumulations of competitive and/or redox-active metals in the wrong locations underlie some links between metals and multiple neurological disorders<sup>96</sup>. A more complete knowledge of metal homeostasis and, by implication, metal sensing is likely to precede an understanding of its aberrations. A knowledge of how sensors discriminate between metals has the potential to aid the development of therapies.

Changing metal availabilities over geological time fashioned the metal-protein partnerships. As dissolved CO<sub>2</sub> acidifies the modern oceans<sup>97</sup>, metal availabilities may be changing yet again. The action of carbonic anhydrase in providing substrate for oceanic photosynthetic carbon fixation by phytoplankton is central to primary productivity and to the carbon cycle through its removal of acidifying bicarbonate. It is unclear how organisms with carbonic anhydrases of differing metal requirements will respond. There is pressing interest in coupling photosynthesis to the production of biofuels such as gaseous hydrogen. Hydrogenase will have to be supplied with nickel by means of its metallochaperone, but the metallochaperone might be unable to acquire enough metal in a heterologous photosynthetic bacterium. We already know that nickel is so poorly available in a cyanobacterial cytosol that a mycobacterial nickel/cobalt sensor fails to sense nickel<sup>36</sup>. To populate metalloproteins with the correct metals in heterologous cells, special strains should be made in which bioavailable metal is adjusted, for instance by changing the affinities of metal sensors to alter the threshold concentrations within which a desired metal is buffered. A robust understanding of how metal sensors discriminate between the elements is a prerequisite to understanding and, hence, to engineering optimal 'metallation'.

1. Fraústo da Silva, J. J. R. & Williams, R. J. P. *The Biological Chemistry of the Elements* (Oxford Univ. Press, 2001).
2. Saito, M. A., Sigman, D. M. & Morel, F. M. M. The bioinorganic chemistry of the ancient ocean: the co-evolution of cyanobacterial metal requirements and biogeochemical cycles at the Archean-Proterozoic boundary? *Inorg. Chim. Acta* **356**, 308–318 (2003).
3. Dupont, C. L., Yang, S., Palenik, B. & Bourne, P. E. Modern proteomes contain putative imprints of ancient shifts in trace metal geochemistry. *Proc. Natl Acad. Sci. USA* **103**, 17822–17827 (2006).
4. Irving, H. & Williams, R. J. P. Order of stability of metal complexes. *Nature* **162**, 746–747 (1948).
5. Totter, S. *et al.* Protein-folding location can regulate manganese-binding versus copper- or zinc-binding. *Nature* **455**, 1138–1142 (2008).  
This paper shows that two proteins with similar folds and metal preferences acquire metals from opposite ends of the Irving-Williams series on the basis of where in the cell they fold, illustrating the contribution of cell biology to the selection of metals by metalloproteins.
6. Rae, T. D., Schmidt, P. J., Pufahl, R. A., Culotta, V. C. & O'Halloran, T. V. Undetectable intracellular free copper: the requirement of a copper chaperone for superoxide dismutase. *Science* **284**, 805–808 (1999).
7. Outten, C. E. & O'Halloran, T. V. Femtomolar sensitivity of metalloregulatory proteins controlling zinc homeostasis. *Science* **292**, 2488–2492 (2001).  
In this paper, the tight zinc affinities of two zinc sensors, ZntR and Zur, are estimated and used to infer a low concentration of available zinc in the bacterial cytoplasm.
8. Changela, A. *et al.* Molecular basis of metal-ion selectivity and zeptomolar sensitivity by CueR. *Science* **301**, 1383–1387 (2003).
9. Waldron, K. J. & Robinson, N. J. How do bacterial cells ensure that metalloproteins get the correct metal? *Nature Rev. Microbiol.* **7**, 25–35 (2009).  
In this paper, bacterial models for metal discrimination by metal sensors and other proteins of metal homeostasis are set out in a prelude to the current Review.

10. Laity, J. H. & Andrews, G. K. Understanding the mechanisms of zinc-sensing by metal response element binding transcription factor-1 (MTF-1). *Arch. Biochem. Biophys.* **463**, 201–210 (2007).
11. Walden, W. E. *et al.* Structure of dual function iron regulatory protein 1 complexed with ferritin IRE-RNA. *Science* **314**, 1903–1908 (2006).
12. Ferrer, M., Golyshina, O. V., Beloqui, A., Golyshin, P. N. & Timmis, K. N. The cellular machinery of *Ferroplasma acidiphilum* is iron-protein-dominated. *Nature* **445**, 91–94 (2007).
13. Andreini, C., Bertini, I., Cavallaro, G., Holliday, G. L. & Thornton, J. M. Metal ions in biological catalysis: from enzyme databases to general principles. *J. Biol. Inorg. Chem.* **13**, 1205–1218 (2008).  
In this paper, the use of different metals in enzymes is evaluated in a systematic way.
14. Lieberman, R. L. & Rosenzweig, A. C. Crystal structure of a membrane-bound metalloenzyme that catalyses the biological oxidation of methane. *Nature* **434**, 177–182 (2005).
15. Robinson, N. J., Procter, C. M., Connolly, E. L. & Guerinet, M. L. A ferric-chelate reductase for iron uptake from soils. *Nature* **397**, 694–697 (1999).
16. Palmer, C. M. & Guerinet, M. L. Facing the challenges of Cu, Fe and Zn homeostasis in plants. *Nature Chem. Biol.* **5**, 333–340 (2009).
17. Peers, G. & Price, N. M. Copper-containing plastocyanin used for electron transport by an oceanic diatom. *Nature* **441**, 341–344 (2006).
18. Strzepak, R. F. & Harrison, P. J. Photosynthetic architecture differs in coastal and oceanic diatoms. *Nature* **431**, 689–692 (2004).
19. Konhauser, K. O. *et al.* Oceanic nickel depletion and a methanogen famine before the Great Oxidation Event. *Nature* **458**, 750–754 (2009).  
This paper shows how a very early change in the availability of a metal had profound consequences for metal-protein partnerships, changing the course of evolution.
20. Saito, M. A. Less nickel for more oxygen. *Nature* **458**, 714–715 (2009).
21. Park, H., Song, B. & Morel, F. M. M. Diversity of the cadmium-containing carbonic anhydrase in marine diatoms and natural waters. *Environ. Microbiol.* **9**, 403–413 (2007).
22. Lane, T. W. *et al.* Biochemistry: a cadmium enzyme from a marine diatom. *Nature* **435**, 42 (2005).
23. Xu, Y., Feng, L., Jeffrey, P. D., Shi, Y. & Morel, F. M. M. Structure and metal exchange in the cadmium carbonic anhydrase of marine diatoms. *Nature* **452**, 56–61 (2008).
24. Lander, E. S. *et al.* Initial sequencing and analysis of the human genome. *Nature* **409**, 860–921 (2001).
25. Culotta, V. C., Yang, M. & O'Halloran, T. V. Activation of superoxide dismutases: putting the metal to the pedal. *Biochim. Biophys. Acta* **1763**, 747–758 (2006).
26. Schofield, C. J. & Ratcliffe, P. J. Oxygen sensing by HIF hydroxylases. *Nature Rev. Mol. Cell Biol.* **5**, 343–354 (2004).
27. Ranquet, C., Ollagnier-de-Choudens, S., Loiseau, L., Barras, F. & Fontecave, M. Cobalt stress in *Escherichia coli*. The effect on the iron-sulfur proteins. *J. Biol. Chem.* **282**, 30442–30451 (2007).
28. Labbé, R. F. & Dewanji, A. Iron assessment tests: transferring receptor vis-à-vis zinc protoporphyrin. *Clin. Biochem.* **37**, 165–174 (2004).
29. Portnoy, M. E., Schmidt, P. J., Rogers, R. S. & Culotta, V. C. Metal transporters that contribute to metallochaperones in *Saccharomyces cerevisiae*. *Mol. Genet. Genomics* **265**, 873–882 (2001).
30. Xiao, Z. & Wedd, A. G. A C-terminal domain of the membrane copper pump Ctr1 exchanges copper(I) with the copper chaperone Atx1. *Chem. Commun.* 588–592 (2002).
31. De Feo, C. J., Aller, S. G., Siluvai, G. S., Blackburn, N. J. & Unger, V. M. Three-dimensional structure of the human copper transporter hCTR1. *Proc. Natl Acad. Sci. USA* **106**, 4237–4242 (2009).
32. Pufahl, R. A. *et al.* Metal ion chaperone function of the soluble Cu(I) receptor Atx1. *Science* **278**, 853–856 (1997).
33. Furukawa, Y., Torres, A. S. & O'Halloran, T. V. Oxygen-induced maturation of SOD1: a key role for disulfide formation by the copper chaperone CCS. *EMBO J.* **23**, 2872–2881 (2004).
34. O'Halloran, T. V. Transition metals in control of gene expression. *Science* **261**, 715–725 (1993).
35. Giedroc, D. P. & Arunkumar, A. I. Metal sensor proteins: nature's metalloregulated allosteric switches. *Dalton Trans.* 3107–3120 (2007).  
In this paper, metal sensors of bacteria are reviewed and the important contributions of coordination chemistry and allostery are explained.
36. Cavet, J. S. *et al.* A nickel-cobalt-sensing ArsR-SmtB family repressor. Contributions of cytosol and effector binding sites to metal selectivity. *J. Biol. Chem.* **277**, 38441–38448 (2002).
37. Guedon, E. & Helmann, J. D. Origins of metal ion selectivity in the DtxR/MntR family of metalloregulators. *Mol. Microbiol.* **48**, 495–506 (2003).
38. Golyskiy, M. V., Gunderson, W. A., Hendrich, M. P. & Cohen, S. M. Metal-binding studies and EPR spectroscopy of the manganese transport regulator MntR. *Biochemistry* **45**, 15359–15372 (2006).
39. Phillips, C. M. *et al.* Structural basis of the metal specificity for nickel regulatory protein NikR. *Biochemistry* **47**, 1938–1946 (2008).
40. Labbé, S., Peña, M. M., Fernandes, A. R. & Thiele, D. J. A copper-sensing transcription factor regulates iron uptake genes in *Schizosaccharomyces pombe*. *J. Biol. Chem.* **274**, 36252–36260 (1999).
41. Pelletier, B., Beaudoin, J., Mukai, Y. & Labbé, S. Fep1, an iron sensor regulating iron transporter gene expression in *Schizosaccharomyces pombe*. *J. Biol. Chem.* **277**, 22950–22958 (2002).
42. Rutherford, J. C. & Bird, A. J. Metal-responsive transcription factors that regulate iron, zinc and copper homeostasis in eukaryotic cells. *Eukaryot. Cell* **3**, 1–13 (2004).
43. Yonkovich, J., McKendry, R., Shi, X. & Zhu, Z. Copper ion-sensing transcription factor Mac1p post-translationally controls the degradation of its target gene product Ctr1p. *J. Biol. Chem.* **277**, 23981–23984 (2002).
44. Li, L., Chen, O. S., McVey Ward, D. & Kaplan, J. CCC1 is a transporter that mediates vacuolar iron storage in yeast. *J. Biol. Chem.* **276**, 29515–29519 (2001).

45. MacDiarmid, C. W., Gaither, L. A. & Eide, D. Zinc transporters that regulate vacuolar zinc storage in *Saccharomyces cerevisiae*. *EMBO J.* **19**, 2845–2855 (2000).
46. Puig, S., Askeland, E. & Thiele, D. J. Coordinated remodelling of cellular metabolism during iron deficiency through targeted mRNA degradation. *Cell* **120**, 99–110 (2005).
47. Puig, S., Vergara, S. V. & Thiele, D. J. Cooperation of two mRNA-binding proteins drives metabolic adaptation to iron deficiency. *Cell Metab.* **7**, 555–564 (2008).
48. Haurie, V., Boucherie, H. & Sagliocco, F. The Snf1 protein kinase controls the induction of genes of the iron uptake pathway at the diauxic shift in *Saccharomyces cerevisiae*. *J. Biol. Chem.* **278**, 45391–45396 (2003).
49. Fürst, P., Hu, S., Hackett, R. & Hamer, D. Copper activates metallothionein gene transcription by altering the conformation of a specific DNA binding protein. *Cell* **55**, 705–717 (1988).
- In this paper, DNA binding by an activator of metallothionein gene transcription is shown to depend on copper binding to the activator, and a eukaryotic metal sensor is thus discovered.
50. Jungmann, J. et al. MAC1, a nuclear regulatory protein related to Cu-dependent transcription factors is involved in Cu/Fe utilization and stress resistance in yeast. *EMBO J.* **12**, 5051–5056 (1993).
51. Brown, K. R. et al. Structures of the cuprous-thiolate clusters of the Mac1 and Ace1 transcriptional activators. *Biochemistry* **41**, 6469–6476 (2002).
52. Peña, M. M., Koch, K. A. & Thiele, D. J. Dynamic regulation of copper uptake and detoxification genes in *Saccharomyces cerevisiae*. *Mol. Cell. Biol.* **18**, 2514–2523 (1998).
53. Bird, A. J. et al. Zinc fingers can act as Zn<sup>2+</sup> sensors to regulate transcriptional activation domain function. *EMBO J.* **22**, 5137–5146 (2003).
54. Qiao, W., Mooney, M., Bird, A. J., Winge, D. R. & Eide, D. J. Zinc binding to a regulatory zinc-sensing domain monitored *in vivo* by using FRET. *Proc. Natl Acad. Sci. USA* **103**, 8674–8679 (2006).
- In this paper, by exploiting constructs in which zinc occupancy of two of Zap1's zinc-fingers is coupled to energy transfer between fluorescent reporters, Zap1 is inferred to detect zinc directly through metal binding *in vivo*.
55. Wang, Z. et al. Solution structure of a Zap1 zinc-responsive domain provides insights into metalloreulatory transcriptional repression in *Saccharomyces cerevisiae*. *J. Mol. Biol.* **357**, 1167–1183 (2006).
56. Yamaguchi-Iwai, Y., Dancis, A. & Klausner, R. D. AFT1: a mediator of iron regulated transcriptional control in *Saccharomyces cerevisiae*. *EMBO J.* **14**, 1231–1239 (1995).
57. Rutherford, J. C., Jaron, S., Ray, E., Brown, P. O. & Winge, D. R. A second iron-regulatory system in yeast independent of Aft1p. *Proc. Natl Acad. Sci. USA* **98**, 14322–14327 (2001).
58. Ueta, R., Fujiwara, N., Iwai, K. & Yamaguchi-Iwai, Y. Mechanism underlying the iron-dependent nuclear export of the iron-responsive transcription factor Aft1p in *Saccharomyces cerevisiae*. *Mol. Cell. Biol.* **18**, 2980–2990 (2007).
59. Kumánovics, A. et al. Identification of FRA1 and FRA2 as genes involved in regulating the yeast iron regulon in response to decreased mitochondrial iron-sulfur cluster synthesis. *J. Biol. Chem.* **283**, 10276–10286 (2008).
60. Ojeda, L. et al. Role of glutaredoxin-3 and glutaredoxin-4 in the iron regulation of the Aft1 transcriptional activator in *Saccharomyces cerevisiae*. *J. Biol. Chem.* **281**, 17661–17669 (2006).
61. Yamaguchi-Iwai, Y., Stearman, R., Dancis, A. & Klausner, R. D. Iron-regulated DNA-binding by the AFT1 protein controls the iron regulon in yeast. *EMBO J.* **15**, 3377–3384 (1996).
62. Picciocchi, A., Saez, C., Boussac, A., Cassier-Chauvat, C. & Chauvat, F. CGFS-type monothiol glutaredoxins from the cyanobacterium *Synechocystis* PCC6803 and other evolutionary distant model organisms possess a glutathione-ligated [2Fe-2S] cluster. *Biochemistry* **46**, 15018–15026 (2007).
63. Rutherford, J. C. et al. Activation of the iron regulon by the yeast Aft1/Aft2 transcription factors depends on mitochondrial but not cytosolic iron-sulfur protein biogenesis. *J. Biol. Chem.* **280**, 10135–10140 (2005).
64. Heredia, J., Crooks, M. & Zhu, Z. Phosphorylation and Cu<sup>+</sup> coordination-dependent DNA binding of the transcription factor Mac1p in the regulation of copper transport. *J. Biol. Chem.* **276**, 8793–8797 (2001).
65. Wood, L. K. & Thiele, D. J. Transcriptional activation in yeast in response to copper deficiency involves copper-zinc superoxide dismutase. *J. Biol. Chem.* **284**, 404–413 (2009).
66. Burkhead, J. L., Gogolin Reynolds, K. A., Abdel-Ghany, S. E., Cohu, C. M. & Pilon, M. Copper homeostasis. *New Phytol.* **182**, 799–816 (2009).
67. Song, I. S. et al. Transcription factor Sp1 plays an important role in the regulation of copper homeostasis in mammalian cells. *Mol. Pharmacol.* **74**, 705–713 (2008).
68. Zheng, D., Feeney, G. P., Kille, P. & Hogstrand, C. Regulation of ZIP and ZNT zinc transporters in zebrafish gill: zinc repression of ZIP10 transcription by an intronic MRE cluster. *Physiol. Genomics* **34**, 205–214 (2008).
69. Wimmer, U., Wang, Y., Georgiev, O. & Schaffner, W. Two major branches of anti-cadmium defense in the mouse: MTF-1/metallothioneins and glutathione. *Nucleic Acids Res.* **33**, 5715–5727 (2005).
70. Li, Y., Kimura, T., Huyck, R. W., Laity, J. H. & Andrews, G. K. Zinc-induced formation of a coactivator complex containing the zinc-sensing transcription factor MTF-1, p300/CBP, and Sp1. *Mol. Cell. Biol.* **28**, 4275–4284 (2008).
71. Selvaraj, A. et al. Metal-responsive transcription factor (MTF-1) handles both extremes, copper load and copper starvation, by activating different genes. *Genes Dev.* **19**, 891–896 (2005).
72. Smirnova, I. V., Bittel, D. C., Ravindra, R., Jiang, H. & Andrews, G. K. Zinc and cadmium promote rapid nuclear translocation of metal response element-binding transcription factor-1. *J. Biol. Chem.* **275**, 9377–9384 (2000).
73. Zhang, B. et al. Activity of metal-responsive transcription factor 1 by toxic heavy metals and H<sub>2</sub>O<sub>2</sub> *in vitro* is modulated by metallothionein. *Mol. Cell. Biol.* **23**, 8471–8485 (2003).
74. Chen, X. et al. Copper sensing function of *Drosophila* metal-responsive transcription factor-1 is mediated by a tetranuclear Cu(I) cluster. *Nucleic Acids Res.* **36**, 3128–3138 (2008).
75. Rouault, T. A. The role of iron regulatory proteins in mammalian iron homeostasis and disease. *Nature Chem. Biol.* **2**, 406–414 (2006).
76. Phillips, J. D., Guo, B., Yu, Y. & Leibold, E. A. Iron regulates the intracellular degradation of iron regulatory protein 2 by the proteasome. *J. Biol. Chem.* **270**, 21645–21651 (1995).
77. Kim, B.-E., Nevitt, T. & Thiele, D. J. Mechanisms of copper acquisition, distribution and regulation. *Nature Chem. Biol.* **4**, 176–185 (2008).
78. Guo, Y., Smith, K., Lee, J., Thiele, D. J. & Petris, M. J. Identification of methionine-rich clusters that regulate copper-stimulated endocytosis of the human Ctr1 copper transporter. *J. Biol. Chem.* **279**, 17428–17433 (2004).
79. Nemeth, E. et al. Hepcidin regulates cellular iron efflux by binding to ferroportin and inducing its internalization. *Science* **306**, 2090–2093 (2004).
80. Mao, X., Kim, B.-E., Wang, F., Eide, D. J. & Petris, M. J. A histidine-rich cluster mediates the ubiquitination and degradation of the human zinc transporter, hZIP4, and protects against zinc cytotoxicity. *J. Biol. Chem.* **282**, 6992–7000 (2007).
81. Kambe, T. & Andrews, G. K. Novel proteolytic processing of the ectodomain of the zinc transporter ZIP4 (SLC39A4) during zinc deficiency is inhibited by acrodermatitis enteropathica mutations. *Mol. Cell. Biol.* **29**, 129–139 (2009).
82. Kim, B.-E. et al. Zn<sup>2+</sup>-stimulated endocytosis of the mZIP4 zinc transporter regulates its location at the plasma membrane. *J. Biol. Chem.* **279**, 4523–4530 (2004).
83. Petris, M. J. et al. Ligand-regulated transport of the Menkes copper P-type ATPase efflux pump from the Golgi apparatus to the plasma membrane: a novel mechanism of regulated trafficking. *EMBO J.* **15**, 6084–6095 (1996).
- In this paper, metal-dependent trafficking of a metal-transporter is discovered.
84. Braitermann, L. et al. Apical targeting and Golgi retention signals reside within a 9-amino acid sequence in the copper-ATPase, ATP7B. *Am. J. Physiol. Gastrointest. Liver Physiol.* **296**, G433–G444 (2009).
85. La Fontaine, S. & Mercer, J. F. Trafficking of the copper-ATPases, ATP7A and ATP7B: role in copper homeostasis. *Arch. Biochem. Biophys.* **463**, 149–167 (2007).
86. McKie, A. T. et al. A novel duodenal iron-regulated transporter, IREG1, implicated in the basolateral transfer of iron to the circulation. *Mol. Cell* **5**, 299–309 (2000).
87. Andrews, N. C. Forging a field: the golden age of iron biology. *Blood* **112**, 219–230 (2008).
88. Ma, J. K. et al. The axial ligand and extent of protein folding determine whether Zn or Cu binds to amicyanin. *J. Inorg. Biochem.* **102**, 342–346 (2008).
89. Turner, R. B. et al. Solution structure of a zinc domain conserved in yeast copper-regulated transcription factors. *Nature Struct. Biol.* **5**, 551–555 (1998).
90. Giedroc, D. P., Chen, X., Pennella, M. A. & LiWang, A. C. Conformational heterogeneity in the C-terminal zinc fingers of human MTF-1: an NMR and zinc-binding study. *J. Biol. Chem.* **276**, 42322–42332 (2001).
91. Jackson, K. A. et al. Splice variants of the human zinc transporter ZnT5 (SLC30A5) are differentially localized and regulated by zinc through transcription and mRNA stability. *J. Biol. Chem.* **282**, 10423–10431 (2007).
92. Mukhopadhyay, C. K., Mazumder, B. & Fox, P. L. Role of hypoxia-inducible factor-1 in transcriptional activation of ceruloplasmin by iron deficiency. *J. Biol. Chem.* **275**, 21048–21054 (2000).
93. Ozer, A. & Bruick, R. K. Non-heme dioxygenases: cellular sensors and regulators jelly rolled into one? *Nature Chem. Biol.* **3**, 144–152 (2007).
94. Hershinkel, M., Moran, A., Grossman, N. & Sekler, I. A zinc-sensing receptor triggers the release of intracellular Ca<sup>2+</sup> and regulates iron transport. *Proc. Natl Acad. Sci. USA* **98**, 11749–11754 (2001).
95. Sladek, R. et al. A genome-wide association study identifies novel risk loci for type 2 diabetes. *Nature* **445**, 881–885 (2007).
96. Barnham, K. J. & Bush, A. I. Metals in Alzheimer's and Parkinson's disease. *Curr. Opin. Chem. Biol.* **12**, 222–228 (2008).
97. Orr, J. C. et al. Anthropogenic ocean acidification over the twenty-first century and its impact on calcifying organisms. *Nature* **437**, 681–686 (2005).
98. Rulišek, L. & Vondrášek, J. Coordination geometries of selected transition metal ions (Co<sup>2+</sup>, Ni<sup>2+</sup>, Cu<sup>2+</sup>, Zn<sup>2+</sup>, Cd<sup>2+</sup>, and Hg<sup>2+</sup>) in metalloproteins. *J. Inorg. Biochem.* **71**, 115–127 (1998).
99. Johnson, D. A. & Nelson, P. G. Factors determining the ligand field stabilization energies of the hexaaqua 2+ complexes of the first transition series and the Irving-Williams order. *Inorg. Chem.* **34**, 5666–5671 (1995).
100. Dudev, T. & Lim, C. Metal binding affinity and selectivity in metalloproteins: insights from computational studies. *Annu. Rev. Biophys.* **37**, 97–116 (2008).

**Acknowledgements** This article describes a selection of the insights of many friends and colleagues. The authors are supported by grants BB/E001688/1 and BB/F019637/1 from the Biotechnology and Biological Sciences Research Council.

**Author Information** Reprints and permissions information is available at [www.nature.com/reprints](http://www.nature.com/reprints). The authors declare no competing financial interests. Correspondence should be addressed to N.J.R. ([n.j.robinson@ncl.ac.uk](mailto:n.j.robinson@ncl.ac.uk)).



# Function and biogenesis of iron-sulphur proteins

Roland Lill<sup>1</sup>

**Iron-sulphur (Fe-S) clusters have long been recognized as essential and versatile cofactors of proteins involved in catalysis, electron transport and sensing of ambient conditions. Despite the relative simplicity of Fe-S clusters in terms of structure and composition, their synthesis and assembly into apoproteins is a highly complex and coordinated process in living cells. Different biogenesis machineries in both bacteria and eukaryotes have been discovered that assist Fe-S-protein maturation according to uniform biosynthetic principles. The importance of Fe-S proteins for life is documented by an increasing number of diseases linked to these components and their biogenesis.**

Many proteins depend on cofactors for their function. Typically, these low-molecular-mass compounds bind to well-defined and evolutionarily conserved sequence motifs either covalently or non-covalently. Organic cofactors include various nucleotides (such as flavin mononucleotide and flavin adenine dinucleotide), vitamins (biotin, pantothenate and folate) and metal-organic compounds (haem and molybdenum cofactor). Common inorganic cofactors include various metal ions ( $\text{Mg}^{2+}$ ,  $\text{Zn}^{2+}$ ,  $\text{Mn}^{2+}$ ,  $\text{Cu}^{1+/2+}$ ,  $\text{Fe}^{2+/3+}$  and so on), which usually bind to mononuclear binding sites. The oldest and most versatile inorganic cofactors are probably Fe-S clusters, which can participate in electron transfer, catalysis and regulatory processes<sup>1</sup>. The chemically simplest Fe-S clusters are the rhombic  $[\text{2Fe-2S}]$  and the cubane  $[\text{4Fe-4S}]$  types, which contain iron ( $\text{Fe}^{2+/3+}$ ) and sulphide ( $\text{S}^{2-}$ ). Fe-S clusters are usually integrated into proteins through coordination of the iron ions by cysteine or histidine residues, yet alternative ligands (Asp, Arg, Ser, CO,  $\text{CN}^-$  and so on) are known, particularly in more complex Fe-S clusters. Several different structural folds have been recognized to coordinate these simple Fe-S clusters<sup>2</sup>. Nevertheless, it has remained difficult to predict the presence of Fe-S clusters from protein sequences. More complex Fe-S clusters, often containing other metal ions, are present in, for example, nitrogenase or hydrogenase enzymes, but are not discussed here (see pages 814 and 839).

Fe-S clusters were discovered in the early 1960s by purifying enzymes with characteristic electron paramagnetic resonance signals. Some of the first Fe-S proteins to be discovered include plant and bacterial ferredoxins and respiratory complexes I–III of bacteria and mitochondria. In the late 1960s, chemists and biochemists devised chemical reconstitution protocols to assemble Fe-S clusters into apoproteins *in vitro*, leading to the view that these cofactors can assemble spontaneously on proteins<sup>3</sup>. However, genetic, biochemical and cell-biological studies in the 1990s provided ample evidence that the maturation of Fe-S proteins in living cells is a catalysed process rather than a spontaneous one. In striking contrast to the chemical simplicity of Fe-S clusters, their biosynthesis *in vivo* appears to be a rather complex and coordinated reaction<sup>4–13</sup>. In the past decade, numerous biogenesis components were identified, and the first insights into the mechanisms of biogenesis were obtained. In this Review, I summarize our current knowledge on the biogenesis of Fe-S proteins in bacteria and eukaryotes, and emphasize the importance of Fe-S proteins for essential physiological pathways in living cells. First, I

briefly address the properties of various Fe-S clusters and the biological functions of Fe-S proteins.

## Functions of Fe-S proteins depend on cofactor properties

The most common function of Fe-S clusters, electron transfer, is based on the propensity of Fe to formally switch between oxidative states +2 and +3 (ref. 1). Within a given proteinaceous surrounding, Fe-S clusters can adopt redox potentials from –500 mV to +300 mV (ref. 2). Thus, Fe-S clusters can serve as excellent donors and acceptors of electrons in a variety of biological reactions. Examples are bacterial and mitochondrial respiratory complexes I–III, photosystem I, ferredoxins and hydrogenases. Another well-studied function of Fe-S clusters is in enzyme catalysis, a classic example being aconitase, in which a non-protein-coordinated Fe at one edge of a  $[\text{4Fe-4S}]$  cluster serves as a Lewis acid to assist  $\text{H}_2\text{O}$  abstraction from citrate (the substrate), which is converted to isocitrate. Other special cases are the radical S-adenosyl-L-methionine (SAM) enzymes biotin synthase and lipoate synthase, which bind two Fe-S clusters each. It is believed that one of these clusters is disassembled during the formation of the products biotin and lipoic acid, respectively, thus serving as a sulphur donor<sup>14</sup>. Numerous other catalytic functions are known for bacterial and eukaryotic Fe-S enzymes involved in metabolism<sup>2</sup>. However, in many cases the precise role of the Fe-S cluster is still unclear, and it is therefore possible that in some proteins the Fe-S cluster simply plays a structural role. This may be true for the recently discovered Fe-S clusters in adenosine triphosphate (ATP)-dependent DNA helicases involved in nucleotide excision repair (Rad3, XPD (also known as ERCC2), FANCI (BRIP1) and so on)<sup>15</sup>. Likewise, the precise role of the two  $[\text{4Fe-4S}]$  clusters in the ABC protein Rli1 (ABCE1 in humans) involved in ribosome biogenesis and function is unknown, despite the availability of a crystal structure of the holoprotein<sup>16,17</sup>.

A third general role of Fe-S clusters is in sensing environmental or intracellular conditions to regulate gene expression (see page 823). Examples are the bacterial transcription factors FNR, IscR and SoxR, which sense  $\text{O}_2$ , Fe-S clusters and superoxide/ $\text{NO}$ , respectively. The switch between the activating and repressed states depends on the presence or absence of an Fe-S cluster (FNR or IscR) or the redox state of the  $[\text{2Fe-2S}]$  cluster present in SoxR<sup>18</sup>. A classical example for post-transcriptional regulation of gene expression by Fe-S clusters is provided by the mammalian

<sup>1</sup>Institut für Zytobiologie, Philipps-Universität Marburg, Robert-Koch-Strasse 6, D-35033 Marburg, Germany.

cytosolic iron regulatory protein 1 (IRP1, also known as ACO1). Under iron-replete conditions, IRP1 holds a [4Fe-4S] cluster and functions as an aconitase. When the protein loses its labile cluster under iron deprivation, it can bind to stem-loop structures (termed iron-responsive elements (IREs)) in certain messenger RNAs of proteins involved in iron uptake, storage and distribution in the cell<sup>19–22</sup>. Binding of apo-IRP1 to 5'-located IREs blocks translation by inhibiting ribosome scanning to the start AUG codon, whereas association with 3'-located IREs protects mRNAs from nucleolytic degradation, leading to increased translation.

### Dedicated machineries for maturation of Fe-S proteins

The maturation of bacterial Fe-S proteins has been intensely studied in *Escherichia coli* and the azototrophic (nitrogen-fixing) *Azotobacter vinelandii*. Studies have identified three different systems for the biogenesis of bacterial Fe-S proteins: the NIF system, for specific maturation of nitrogenase in azototrophic bacteria; and the ISC assembly and SUF systems, for the generation of housekeeping Fe-S proteins under normal and oxidative-stress conditions, respectively<sup>4,9,12,13</sup>. During evolution, the latter two machineries were transferred by endosymbiosis to eukaryotes containing Fe-S proteins in mitochondria, cytosol and the nucleus. Mitochondria have retained components homologous to those of the bacterial ISC assembly system<sup>6,8</sup>, whereas plastids host proteins of the SUF machinery<sup>5,11</sup>. Assembly of Fe-S proteins in the eukaryotic cytosol and nuclei requires the assistance of both the mitochondrial ISC assembly machinery and a mitochondrial ISC export system<sup>23</sup>. Additionally, maturation of these Fe-S proteins is dependent on the essential cytosolic Fe-S-protein assembly (CIA) machinery, which is present in virtually all eukaryotes<sup>6,8</sup>. The yeast *Saccharomyces cerevisiae* has served as an excellent model organism with which to establish the first details of the complex biosynthesis pathways in eukaryotes. Recent investigations in human cell culture and other model systems have demonstrated that the entire process is highly conserved from yeast to human (see below).

Despite the obvious differences among the various biogenesis systems

found in bacteria and in eukaryotes, general biosynthetic principles seem to underlie the *in vivo* synthesis of Fe-S clusters and their assembly into apoproteins (explained in detail in Box 1). In the following, I briefly summarize our current knowledge of the components of the various assembly systems and describe their respective mechanistic functions. The special assembly pathways of nitrogenases, used by the NIF system, and hydrogenases, used by dedicated maturation systems, will not be addressed here. The reader is referred to recent reviews<sup>24–26</sup>.

### The ISC assembly systems in bacteria and mitochondria

The experimental study of Fe-S-protein biogenesis was boosted by the identification of the bacterial *isc* operon<sup>27</sup>. This discovery not only aided work on bacterial Fe-S-protein assembly, but also influenced the first attempts to identify biogenesis proteins in eukaryotes. The evolutionary relationship between bacteria and mitochondria led to the identification and functional characterization of several mitochondrial proteins homologous to the bacterial ISC system<sup>23,28</sup>. The striking similarities between the bacterial and mitochondrial ISC components and the underlying assembly mechanisms justify a comparative discussion of these related systems (Table 1).

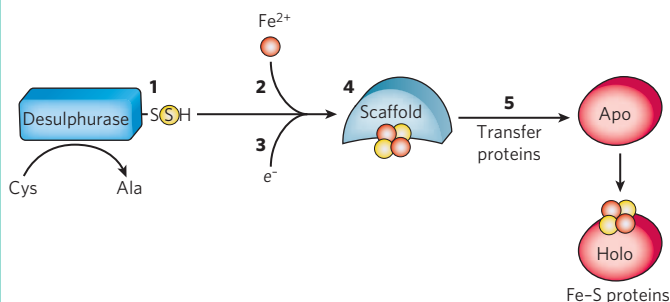
As explained in Box 1, biosynthesis of Fe-S proteins can be separated into two main steps. In the ISC systems, an Fe-S cluster is initially and transiently assembled on the scaffold proteins IscU (bacteria) and Isu1 (mitochondria), which contain three conserved Fe-S-cluster-coordinating cysteine residues<sup>29–31</sup> (Figs 1 and 2). Then the Fe-S cluster is transferred from Isu1/IscU to recipient apoproteins for incorporation into the Fe-S apoprotein by coordination with specific amino-acid residues<sup>32,33</sup>. The first reaction, Fe-S-cluster assembly on Isu1/IscU, critically depends on the function of a cysteine desulphurase as a sulphur donor (Box 1). In bacteria, this reaction is performed by IscS, which is highly similar to the founding member of this protein family, NifS, involved in nitrogenase maturation<sup>34</sup> (Fig. 1). The crystal structures of several desulphurases are known and show a dimeric two-domain protein, with one domain harbouring the pyridoxal-phosphate-binding site and a smaller domain

#### Box 1 Biosynthetic principles of Fe-S-protein biogenesis

Several systems for the biogenesis of Fe-S proteins have been identified in bacteria and in various cell compartments of eukaryotes, namely the bacterial NIF system, the bacterial and mitochondrial ISC assembly machineries, the bacterial and plastid SUF systems and the eukaryotic CIA machinery for cytosolic and nuclear Fe-S proteins. These different machineries may follow common biosynthetic rules. The overall biogenesis process can be split into two main steps: the *de novo* assembly of an Fe-S cluster on a scaffold protein, and the transfer of the Fe-S cluster from the scaffold to target apoproteins and its subsequent assembly into the polypeptide chain. Each of these steps involves the participation of several proteins and cofactors, which execute specific biosynthetic partial reactions. These reactions may define general principles that underlie all known biosynthetic systems, but for some systems the partial reactions remain to be identified.

The bold numbers in the figure correspond to the following steps.

(1) Sulphur donor. A cysteine desulphurase (termed NifS, IscS or SufS in bacteria and Nfs1-Isd11 in mitochondria) releases the sulphur required for Fe-S-cluster formation from cysteine to produce alanine. As an intermediate, a persulphide is formed on a conserved cysteine residue



of the enzyme. This persulphide may then be transferred to conserved cysteine residues of helper proteins (SufE) or directly to scaffold proteins (see below).

(2) Iron donor. Iron is unlikely to be free in solution. To guarantee its accurate delivery to scaffold proteins, specific iron donors may be needed. Such a donor function is performed by bacterial (CyaY) and mitochondrial (Yfh1) ISC components, which bind iron, the desulphurase and the scaffold protein Isu1/IscU.

(3) Electron transfer. Electrons are needed for the reduction of S<sup>0</sup> (present in cysteine) to sulphide (S<sup>2-</sup>, present in Fe-S clusters). An electron transfer function may be provided by ferredoxin reductase and ferredoxin of the ISC assembly machineries and by the central, ferredoxin-like domain of NifU in the NIF system.

(4) Scaffold proteins. These proteins serve as a platform for the *de novo* biosynthesis of an Fe-S cluster. They contain conserved cysteine residues and bind an Fe-S cluster in a labile manner, meaning that this cluster can be transferred to target proteins and stably integrated. The most highly conserved scaffolds are bacterial IscU and SufU, and eukaryotic Isu1. Other scaffolds include bacterial NifU, plastid NFU proteins and bacterial IscA and SufA.

(5) Cluster transfer proteins. Specific factors are involved in transferring the labile Fe-S clusters bound to the scaffolds to apoproteins, which are converted from the apo form to the holo form. And these transfer proteins may have three roles: to induce dissociation of the scaffold-bound Fe-S cluster; to guarantee its accurate and specific transfer to bona fide Fe-S apoproteins; and to promote correct assembly of the Fe-S cluster at the proper acceptor sites. In many cases, these cluster transfer proteins can be bypassed in experiments *in vitro* but are essential in living cells. Examples are the mitochondrial Ssq1 and Jac1 and bacterial HscA and HscB chaperones of the ISC assembly systems, and Nar1 and Cia1 of the CIA machinery.

### Table 1 | Compilation of central components involved in Fe-S-protein biogenesis

Function	Bacterial NIF	Bacterial Suf	Bacterial ISC	Mitochondrial ISC	Eukaryotic CIA
Cysteine desulphurase, sulphur donor	NifS	SufS-SufE	IscS	Nfs1-Isc11	Mitochondrial Nfs1-Isc11
U-type scaffold for Fe-S-cluster assembly	NifU (amino-terminal domain)	SufU	IscU	IscU	-
A-type scaffold for Fe-S-cluster assembly	IscA <sup>Nif</sup>	SufA	IscA, ErpA	IscA, Iba2, Iba57?	-
NFU-type scaffold for Fe-S-cluster assembly	NifU (carboxy-terminal domain)	-	NfuA	Nfu1 (also present in plastids)	-
Scaffold for Fe-S-cluster assembly	-	SufB	-	-	-
P-loop NTPase scaffold for Fe-S-cluster assembly	-	-	-	Isc1?	Cfd1-Nbp35
Electron transfer	NifU (middle domain)	-	Fdx	Isc1-Arh1	-
Iron donor	-	-	CyaY	Isc1 (frataxin)	-
Transfer of Fe-S cluster from scaffold to target proteins	-	SufC?	IscA, HscB	Isc1, Jac1, Mge1, Grx5	Nar1, Cia1
P-loop NTPase, phosphate-binding-loop nucleoside triphosphatase.					

containing the active-site cysteine that transiently carries the sulphur released from free cysteine as a persulphide<sup>35,36</sup>.

In mitochondria, the cysteine desulphurase comprises a complex consisting of the IscS-like desulphurase Nfs1 and the 11-kDa protein Isd11 (Fig. 2; refs 37, 38). Although isolated Nfs1 contains the enzymatic activity as a cysteine desulphurase and releases sulphide from cysteine *in vitro*, the Nfs1–Isd11 complex is the functional entity for sulphur transfer from Nfs1 to Isu1 *in vivo*. This reaction is aided by direct interaction between Nfs1 and Isu1 (IscS and IscU in bacteria).

On binding of iron to Isu1/Isu2, the Fe-S cluster is formed by an unknown mechanism<sup>4,12</sup>. The iron-binding protein frataxin (Yfh1 in yeast and CyaY in bacteria) is believed to function as an iron donor (Box 1) by undergoing an iron-stimulated interaction with Isu1-Nfs1 (refs 39–42). An alternative view recently suggested by *in vitro* studies is that CyaY functions as an iron-dependent regulator of the biosynthesis reaction by inhibiting IscS<sup>43</sup>. Fe-S-cluster assembly on Isu1 further depends on electron transfer from the [2Fe-2S] ferredoxin Yah1 (Fdx in bacteria), which receives its electrons from the mitochondrial ferredoxin reductase Arh1 and NADH<sup>30</sup> (Fig. 1). It is likely that the electron flow is needed for reduction of the sulphur (S<sup>0</sup>) present in cysteine to the sulphide (S<sup>2-</sup>) present in Fe-S clusters, but this remains to be verified experimentally. An additional electron requirement was suggested for the fusion of two [2Fe-2S] clusters to a [4Fe-4S] cluster by reductive coupling<sup>32,33</sup>.

The second main step of biogenesis formally comprises the release of the Fe-S cluster from Isu1/IsuU, cluster transfer to apoproteins and its assembly into the apoprotein. However, these three partial reactions have not been separated experimentally so far. The overall process is specifically assisted by a dedicated chaperone system comprising the Hsp70 ATPase Ssq1 and the DnaJ-like co-chaperone Jac1 (respectively HscA and HscB in bacteria). In mitochondria, the nucleotide exchange factor Mge1 is also required (Fig. 2), whereas in bacteria the related GrpE seems to be dispensable owing to the lability of adenosine diphosphate bound to HscA<sup>7,44</sup>. Ssq1/HscA undergoes an ATP-hydrolysis-dependent, highly specific interaction with the LPPVK motif of Isu1/IsuU<sup>45,46</sup>. This complex formation and the involvement of Jac1/HscB is thought to induce a structural change in Isu1/IsuU, thereby labilizing Fe-S-cluster binding and, thus, facilitating cluster dissociation and transfer to apoproteins<sup>47-49</sup>. An ancillary, non-essential role in Fe-S-cluster transfer from Isu1 to apoproteins is performed by the mitochondrial monothiol glutaredoxin Grx5, yet its precise function is unknown<sup>30</sup>. The plant Grx5 proteins were suggested to serve as scaffolds for the formation of [2Fe-2S] clusters<sup>50</sup>.

The aforementioned ISC proteins are required for generation of all mitochondrial Fe-S proteins, but some biogenesis components perform a more specific function. The interacting mitochondrial proteins Isa1, Isa2 and Iba57 (Table 1) are specifically involved in the maturation of a subset of Fe-S proteins, that is, members of the aconitase superfamily

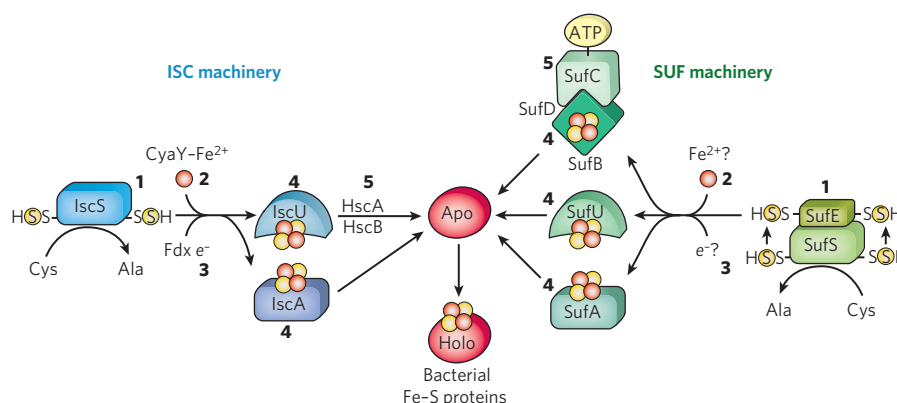


**Figure 1 | A model for Fe-S-protein biogenesis in bacteria: the ISC and SUF machineries.** For the maturation of housekeeping Fe-S proteins (to become the holo form), bacteria use one of two biogenesis systems or both systems in parallel. The ISC machinery (left) consists of the cysteine desulphurase IscS, which liberates sulphur (yellow circle) from cysteine, generating an IscS-bound persulphide (-SSH) on a conserved cysteine residue. A transient Fe-S cluster is formed on the scaffold proteins IscU and/or IscA. *De novo* Fe-S-cluster synthesis involves the transfer of iron (red circle) from the iron-binding protein CyaY (and other, unknown, factors). The [2Fe-2S] ferredoxin (Fdx) possibly serves to reduce the sulphur in cysteine to sulphide. The transiently bound Fe-S cluster is then transferred from the scaffolds to apoproteins (Apo) for coordination with specific residues (usually cysteine or histidine). Transfer from IscU is aided by the dedicated chaperone system

HscA–HscB, which binds to a conserved motif of IscU (Leu-Pro-Pro-Val-Lys). Whereas the ISC machinery is functional under normal conditions in *Escherichia coli*, the SUF machinery (right) is active under oxidative-stress and iron-limiting conditions. A SUF system is also functional in the plastids of plants. Biogenesis is initiated by the cysteine desulphurase SufS, which functions comparably to IscS except that the sulphur is first transferred to a conserved cysteine residue of SufE and bound as a persulphide. Putative iron and electron donors in this system are still unknown. Three components might be scaffolds for *de novo* Fe–S-cluster assembly: SufU and SufA, which show similarities to IscU and IscA, respectively; and SufB, which forms a stable complex with SufC–SufD. SufC is an ATPase and may facilitate Fe–S-cluster dissociation from SufB and subsequent transfer to apoproteins. The bold numbers refer to the biogenesis steps defined in Box 1.



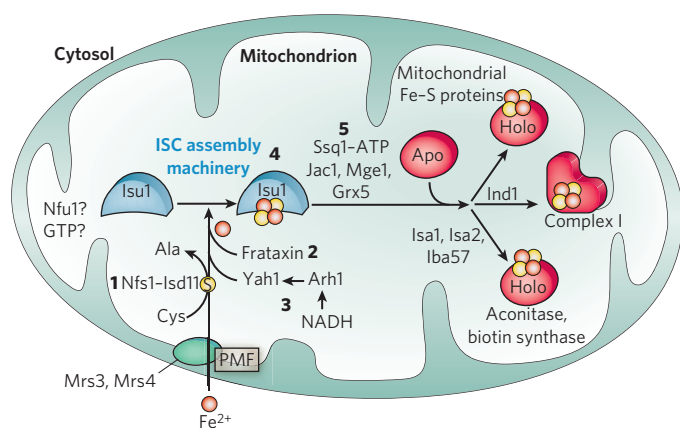


**Figure 2 | A model for Fe-S-protein assembly in mitochondria.**

Mitochondria import ferrous iron ( $\text{Fe}^{2+}$ ) from the cytosol in a membrane-potential-dependent manner (with the proton-motive force (PMF) as a source of energy). Importation is aided by the inner membrane carriers Mrs3 and Mrs4 (known as mitoferrin in mammals). The maturation of mitochondrial Fe-S proteins (to the holo form) starts with sulphur liberation from cysteine by the cysteine desulphurase complex Nfs1–Isd11. The synthesis of a transiently bound Fe-S cluster on the scaffold protein Isu1 (and Isu2 in yeast) further depends on the iron-binding protein frataxin (Yfh1 in yeast) as an iron donor and the electron-transport chain consisting of NADH, ferredoxin reductase (Arh1) and ferredoxin (Yah1), which possibly provides electrons for the reduction of sulphur to sulphide. The release of the Fe-S cluster from Isu1, and its transfer and incorporation into recipient apoproteins (Apo) are facilitated by the ATP-dependent Hsp70 chaperone Ssq1, the DnaJ-like co-chaperone Jac1, the nucleotide-exchange factor Mge1 and the monothiol glutaredoxin Grx5. Proteins of the aconitase family and radical SAM proteins such as biotin synthase specifically need Isa1, Isa2 and Iba57 in addition for maturation of their Fe-S clusters. Assembly of respiratory complex I also requires the P-loop NTPase Ind1. The roles of Nfu1 and GTP are still unclear<sup>28,100</sup>. The bold numbers refer to the biogenesis steps defined in Box 1.

and radical SAM proteins<sup>51</sup> (Fig. 2). Depletion of these proteins results in corresponding enzyme defects and auxotrophies. Similarly, a deficiency of the Isa-protein-related IscA in bacteria, in conjunction with the homologous SufA (see below; Table 1), affects the assembly of the [4Fe–4S] proteins aconitase and dihydroxy-acid dehydratase, whereas the maturation of some [2Fe–2S] proteins such as ferredoxin is unaltered<sup>52</sup>. The third bacterial member of this protein class, ErpA (Table 1), is essential for growth and involved in the maturation of an Fe-S protein of isoprenoid biosynthesis<sup>53</sup>. Several members of the Isa1/IscA protein family (Table 1) were shown *in vitro* to bind an Fe-S cluster by means of three conserved cysteine residues in two motifs characterizing these proteins<sup>4,9,12,13</sup>. SufA binds a [2Fe–2S] cluster *in vivo* that can be transferred to both [2Fe–2S] and [4Fe–4S] proteins *in vitro*<sup>54</sup>. Together, these observations may support the view that the Isa1/IscA proteins function as alternative scaffolds for a subset of Fe-S proteins (Fig. 1). However, the relative specificity of the Isu1/IscU and Isa1/IscA scaffolds and their functional cooperation will require further scrutiny *in vivo* to test the physiological relevance of this proposal, particularly because IscA was also shown to bind mononuclear iron<sup>4</sup>.

The mitochondrial P-loop NTPase Ind1 is important for the assembly of respiratory complex I (ref. 55) (Fig. 2). On the basis of its homology with the cytosolic scaffold-protein complex Cfd1–Nbp35 (see below; Table 1), it was proposed that Ind1 serves as a specific scaffold or transfer protein for the assembly of the eight Fe-S clusters into complex I. Consistent with this idea, Ind1 was shown to assemble a labile Fe-S cluster that can be passed on to apoproteins *in vitro*.

### The SUF machinery in bacteria and plastids

Deletion of the *isc* operon from *E. coli* is not associated with a major phenotype. Cell viability is affected only when the SUF biogenesis system is simultaneously inactivated<sup>56,57</sup>. The *suf* genes are organized in an

operon that is induced under iron-limiting and oxidative-stress conditions<sup>9,56</sup> (Table 1). Gene expression from the *isc* and *suf* operons is coordinately regulated by the Fe-S proteins IscR and SufR, which function as transcriptional repressors of their respective operons<sup>9</sup>. During iron deficiency or oxidative stress, the apo form of IscR additionally activates the *suf* operon. Thereby, both proteins link the efficiency of Fe-S-protein maturation to the extent of gene expression of the two operons.

Components of the SUF machinery are found in a variety of prokaryotes, including Archaea and photosynthetic bacteria. The various SUF components fulfil some of the biosynthetic conditions of Fe-S-protein biogenesis (Box 1). A complex of SufS and SufE serves as the cysteine desulphurase (Fig. 1), in which SufS acts similarly to bacterial IscS or NifS and mitochondrial Nfs1–Isd11, but functions mechanistically distinctly<sup>58–60</sup>. SufE stimulates SufS activity more than tenfold and allows the cysteine-bound persulphide intermediate on SufS to be transferred to a conserved cysteine residue on SufE, from where it is passed on to scaffold proteins<sup>61,62</sup>. Unexpectedly, SufE has a structure similar to the IscU-type scaffold proteins, but it is not known to function as one<sup>63</sup>. A specific iron donor and an electron requirement (Box 1) in the SUF system are not yet known, but corresponding steps are probably also involved in this pathway. Several SUF proteins may provide a scaffold function for *de novo* Fe-S-cluster synthesis, but their relative importance and specificity remain to be clarified (Fig. 1). SufA was discussed above as a functional IscA homologue. SufB contains several conserved cysteine residues that can assemble an Fe-S cluster<sup>9,12</sup>. SufC is an ATPase that is stimulated 100-fold by complex formation with SufB–SufD<sup>58,64</sup>. Hence, SufC is a likely candidate for a transfer protein facilitating Fe-S-cluster delivery from SufB to target proteins (Box 1). Some bacteria contain an IscU-related protein termed SufU that may or may not be encoded in the *suf* operon<sup>65,66</sup>. Notably, SufU differs from Isu1/IscU in that it lacks the HscA binding sequence LPPVK of IscU.

SUF proteins are also present in plastids, reiterating that this biosynthetic system seems to be less sensitive to high oxygen concentrations. The functionality of plastid SufS, SufE and SufA has been confirmed by *in vitro* experiments or bacterial complementation studies, but direct experimental evidence for their biogenesis function *in planta* is usually more difficult to achieve<sup>11,67</sup>. It should be mentioned in this context that in plastids the SUF proteins may not be the only proteins to support Fe-S-protein biogenesis<sup>11</sup>. An important role, possibly as scaffold proteins, is performed by NFU1, NFU2 and NFU3 (also known as Cnfu1, Cnfu2 and Cnfu3), which have homologues in photosynthetic bacteria. NFU proteins show sequence similarity in a 60-residue segment to the C-terminal domain of NfuU in bacteria and a similar segment present in Nfu1 in yeast, the function of which is unknown (Fig. 2). In particular, plastid NFU2 has been examined in more detail and shown to function as a scaffold that can assemble a [2Fe–2S] cluster *in vitro* and transfer it to apoferredoxin<sup>68</sup>. The *cnfu2* mutant plants show a dwarf phenotype with faint pale-green leaves and a deficiency in photosystem I and ferredoxins documenting the important role of NFU2 in Fe-S-protein assembly.

### Biogenesis of cytosolic and nuclear Fe-S proteins

Fe-S-protein maturation in both the cytosol and the nucleus strictly depends on the function of the mitochondrial ISC assembly machinery<sup>23,69</sup> (Fig. 3), but the molecular details of this dependence remain to be defined. In human cell culture, small amounts of some ISC proteins have been found in the cytosol<sup>10,70,71</sup>. A function for the cytosolic human homologue of Isu1 in *de novo* assembly of cytosolic Fe-S proteins could not be shown, but the protein may play a role in Fe-S-cluster repair after oxidative damage or iron deprivation. Likewise, cytosolic human Nfs1 does not support Fe-S-protein assembly in the cytosol in the absence of mitochondrial Nfs1 (ref. 72). The mitochondria-localized ISC assembly machinery is suggested to produce a (still unknown) component (X in Fig. 3) that is exported from the mitochondrial matrix to the cytosol, where it performs an essential function in the maturation process. Because, in particular, Nfs1 is required inside mitochondria to participate in cytosolic and nuclear Fe-S-protein biogenesis in both yeast and human cells, compound X is predicted to be a sulphur-containing

moiety<sup>23,72</sup>. Whether iron is also exported, possibly as part of a pre-assembled Fe–S cluster, or joins from the cytosol, is currently unknown. The export reaction is accomplished by the ABC transporter Atm1 (ABCB7 in humans) of the mitochondrial inner membrane<sup>23,73,74</sup>.

Another required component of the export reaction is the sulphhydryl oxidase Erv1, located in the intermembrane space. This enzyme has also been shown to catalyse the formation of disulphide bridges in the intermembrane space during Mia40-dependent protein import into the intermembrane space<sup>75</sup>, and thus performs a dual function. Strikingly, depletion of GSH in yeast shows a similar phenotype as the downregulation of Atm1 or Erv1, that is, defective cytosolic Fe–S-protein biogenesis and increased iron uptake in the cell and mitochondria (see below), whereas the assembly of mitochondrial Fe–S proteins is unaffected. Hence, Atm1, Erv1 and GSH have been described as the ‘ISC export machinery’ (Fig. 3).

Maturation of cytosolic and nuclear Fe–S proteins crucially involves the cytosolic Fe–S-protein assembly (CIA) machinery, which comprises five known proteins (Table 1). According to recent *in vivo* and *in vitro* studies, this process can be subdivided into two main partial reactions<sup>76</sup> (Fig. 3). First, an Fe–S cluster is transiently assembled on the P-loop NTPases Cfd1 and Nbp35 (refs 77, 78), which form a heterotetrameric complex and serve as a scaffold (Box 1). As mentioned above, this step essentially requires the mitochondrial ISC machineries. From Cfd1–Nbp35, the Fe–S cluster is transferred to apoproteins, a step that requires the CIA proteins Nar1 and Cia1. Cfd1 and Nbp35 take part in the maturation of Nar1 by assisting the assembly of two Fe–S clusters on this iron-only hydrogenase-like protein (Fig. 3). Thus, Nar1 is both a target and a component of the CIA machinery, creating a ‘chicken-and-egg’ situation for its maturation process. Nar1 holoprotein assists Fe–S-cluster transfer to target apoproteins by interacting with Cia1, a WD40 repeat protein that serves as a docking platform for binding Nar1 (ref. 79). Recently, another CIA component, termed Dre2, has been identified but its precise molecular function is currently unknown<sup>80</sup>. The protein coordinates Fe–S clusters, and is probably both a target and a component of the CIA machinery, similar to Nar1. A crucial function of the human homologues of Nar1 and Nbp35 in cytosolic Fe–S-protein biogenesis has

been experimentally verified in cultured cells using RNA-interference technology to deplete these proteins to critical levels<sup>81,82</sup>.

### The essentiality of Fe–S-protein biogenesis in eukaryotes

Most functional studies of eukaryotic Fe–S-protein biogenesis have been performed in yeast and practically all of the ISC and CIA components have been first discovered and characterized in this model system. Nevertheless, the process seems to be highly conserved in virtually all eukaryotes. This notion has now been documented in functional studies in human cell culture, mouse, zebrafish and *Drosophila* models for central components of the ISC and CIA machineries, such as Nfs1, Isu1, frataxin, Grx5, Atm1, Nbp35 and Nar1 (ref. 8). It is likely that the remaining components also have functions similar to those in yeast. Nevertheless, gene duplications of some of the ISC and CIA genes in vertebrates indicate that the process may be more complex in such eukaryotes or that the additional components perform other (non-Fe–S-related) tasks.

Most of the ISC and CIA components are essential for the viability of yeast and human cells<sup>71,72,83</sup>. In fact, Fe–S-protein biogenesis is the only known function of mitochondria that is indispensable for the viability of yeast cells. In comparison, yeast mutants in oxidative phosphorylation result in a respiratory growth defect, but they can grow on glucose-containing media. Because yeast mitochondria are not known to contain essential Fe–S proteins (apart from the ferredoxin Yah1, which is involved in Fe–S-protein biogenesis), the essential character of the mitochondrial ISC assembly machinery is explained by its role in the maturation of extra-mitochondrial Fe–S proteins. The first-known example of an essential cytosolic–nuclear Fe–S protein is the ABC protein Rli1, an Fe–S component involved in ribosome assembly and export from the nucleus<sup>16</sup>. Maturation of its Fe–S clusters strictly depends on the two mitochondrial ISC systems and the CIA machinery providing a tight link between mitochondrial function and cytosolic protein translation. Recently, two other essential (nuclear) Fe–S proteins were identified, one (Rad3) with a function in nucleotide excision repair and the other (Pri2) with a function in RNA primer synthesis for DNA replication<sup>15,84</sup>. It seems probable that their maturation requires mitochondria, possibly

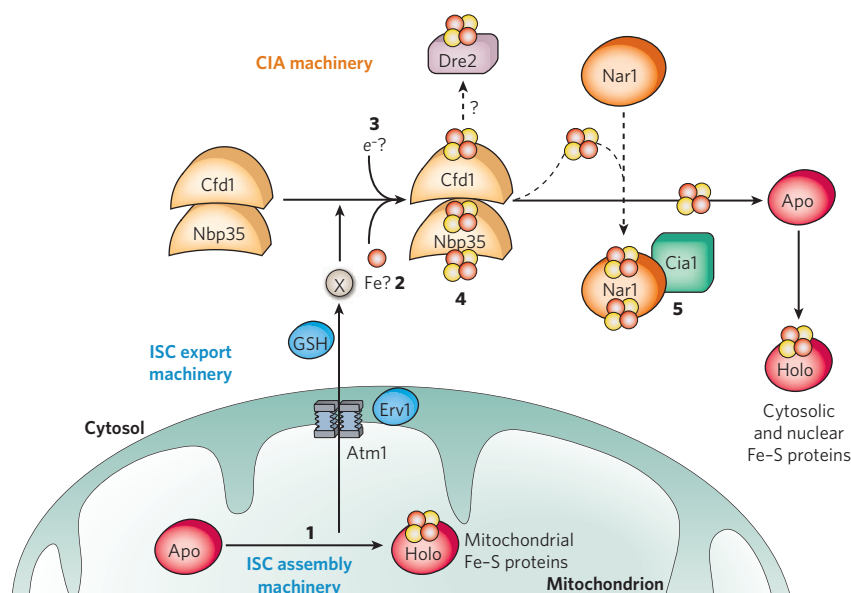


**Figure 3 | The roles of mitochondria and the CIA machinery in Fe–S-protein biogenesis in the cytosol and nucleus of eukaryotes.** Cytosolic and nuclear Fe–S-protein biogenesis requires both the mitochondrial ISC assembly and export machineries. The ABC transporter Atm1 of the mitochondrial inner membrane exports an unknown compound (X) to the cytosol for use in Fe–S-protein assembly, and is assisted by the tripeptide glutathione (GSH) and the intermembrane-space sulphhydryl oxidase Erv1, which introduces disulphide bridges into substrates. In the cytosol, the components of the CIA machinery catalyse Fe–S-protein maturation in two main steps. First,

Fe–S clusters are assembled on the P-loop NTPase complex Cfd1–Nbp35. The source of iron and the potential need for electron transfer remain to be elucidated. The Fe–S clusters bound to Cfd1–Nbp35 are labile, and, aided by the iron-only hydrogenase-like protein Nar1 and the WD40-repeat protein Cia1, can be transferred to cytosolic and nuclear apoproteins (Apo). The site of involvement of the Fe–S-cluster-containing CIA protein Dre2 is still unknown. Maturation of the two Fe–S clusters on Nar1 (and presumably on Dre2) depends on mitochondria and Cfd1–Nbp35 function. The bold numbers refer to the biogenesis steps defined in Box 1.

**Table 2 | Diseases related to Fe-S proteins and their biogenesis**

Human protein	Yeast homologue	Function	Associated disease
<b>Biogenesis components</b>			
Mitoferrin	Mrs3, Mrs4	Mitochondrial carrier; putative iron transporter	Erythropoietic protoporphyria <sup>90</sup>
ISCU	Isu1	Mitochondrial scaffold	Myopathy with exercise intolerance <sup>91,92</sup>
Frataxin	Yfh1	Iron donor for Isu1 scaffold	Friedreich's ataxia <sup>98</sup>
GLRX5	Grx5	Monothiol glutaredoxin; transfer of Fe-S clusters from Isu1 to apoproteins	Microcytic anaemia <sup>89</sup>
ADR	Arh1	Adrenodoxin reductase; electron transfer from NADH to adrenodoxin; also involved in steroid hormone biosynthesis	Tumour suppressor
ABC7	Atm1	ABC transporter, ISC export machinery component	X-linked sideroblastic anaemia and cerebellar ataxia <sup>99</sup>
<b>Fe-S proteins</b>			
Complex I	n.p.	Complex I of respiratory chain (NADH:ubiquinone oxidoreductase)	Various mitochondrial diseases such as LHON, MELAS, Leigh syndrome
Complex II	Complex II (Sdh1, Sdh2, Sdh3, Sdh4)	Complex II of respiratory chain (succinate dehydrogenase)	Tumour suppressor
XPD	Rad3	Fe-S protein involved in nucleotide excision repair	Xeroderma pigmentosum, Cockayne syndrome, trichothiodystrophy
FANCI	Rad3	Fe-S protein involved in nucleotide excision repair	Fanconi anaemia
MUTYH	Ntg2	Fe-S protein (glycosylase) involved in DNA repair	Colon cancer

n.p., not present in *S. cerevisiae*.

linking these organelles to other fundamental processes of life. This indicates that mitochondria and the process of Fe-S-protein maturation have been maintained in evolution to mature extra-mitochondrial Fe-S proteins with an essential function in gene expression. This intimate connection between the endosymbiotic host and the bacterial ancestor of mitochondria may have been decisive for the maintenance of these organelles in eukaryotes.

The crucial role of mitochondria in Fe-S-protein biogenesis has raised the pressing question of how 'amitochondriate' organisms lacking classical mitochondria (such as *Giardia*, Microsporidia and *Entamoeba*) assemble their Fe-S proteins. Genomic information on several of these organisms has provided evidence for the presence of homologues of the ISC assembly and CIA machineries, whereas genes for classical functions of mitochondria, such as respiration, haem biosynthesis or the citric-acid cycle, are missing. Cell-biological studies of several amitochondriate species have shown that the organisms harbour small double-membrane-bounded organelles, termed mitosomes, that contain homologues of the mitochondrial chaperones Hsp60 and Hsp70 as marker proteins<sup>85,86</sup>. It is now accepted that mitosomes descended from classical mitochondria by reductive evolution, that is, by successively losing functions that became dispensable owing to the usually intracellular lifestyle of these parasites. Localization and functional studies have shown that mitosomes from *Giardia* and Microsporidia in fact contain a functional set of ISC assembly proteins<sup>87,88</sup>. Fe-S-protein biogenesis therefore seems to be the remnant function of these organelles, explaining their maintenance in these species. This, however, does not readily clarify why the process of Fe-S-protein biogenesis still depends on mitosomes, that is, why the pathway still is compartmentalized and apparently cannot normally be taken over by the cytosol.

The central importance of Fe-S-protein biogenesis in mammals is impressively documented in numerous diseases associated with defects in Fe-S-protein biogenesis components or Fe-S proteins (Table 2). Depletion of frataxin, the putative iron donor for Fe-S-cluster formation on Isu1, causes the neurodegenerative disease Friedreich's ataxia, which is associated with Fe-S-protein activity defects and iron accumulation. Defects in the glutaredoxin Grx5 and in mitoferrin (Fig. 2) are associated with diseases exhibiting mainly haematological phenotypes, namely microcytic anaemia and erythropoietic protoporphyria, respectively<sup>89,90</sup>. This surprising connection between Fe-S-protein biogenesis and haematopoiesis was experimentally explained by the fact that Fe-S-protein biogenesis is crucial for the maturation of IRP1, which regulates the synthesis of several proteins involved in iron uptake, storage and utilization (see above). One such example is the erythroid

δ-aminolaevulinate synthase (ALAS2), catalysing the committed step of haem biosynthesis in mitochondria. Translation of this protein in the cytosol is largely decreased when iron is scarce or Fe-S-protein biogenesis is hampered, intimately integrating the efficiency of haem and Fe-S-protein biosynthesis, the two major iron-consuming processes in the cell. An additional connection between haem and Fe-S-protein biosynthesis may be the presence of an Fe-S cluster in mammalian ferrochelatase, the final enzyme of haem biosynthesis. A splicing defect in the *ISCU* gene in humans results in a myopathy with exercise intolerance and intracellular iron overload<sup>91,92</sup>. Some Fe-S proteins appear to be connected to human disease (Table 2). Succinate dehydrogenase (complex II of the respiratory chain) and adrenodoxin reductase (an ISC member, but not an Fe-S protein) have been described as tumour suppressors<sup>8</sup>. Mutations in the putative human Fe-S proteins XPD and FANCI cause multiple disease phenotypes including xeroderma pigmentosum and Fanconi anaemia<sup>9</sup>.

### Impact of Fe-S-protein biogenesis on other cellular processes

Defects in Fe-S-protein biogenesis in both bacteria and eukaryotes have a severe impact on several other cellular processes. On the one hand, this connection is explained by the function of particular Fe-S proteins in pathways such as amino-acid biosynthesis, the citric-acid cycle, respiration, cofactor biosyntheses (haem, biotin, lipoic acid and molybdenum cofactor) and gene expression (DNA replication, DNA repair and translation). On the other hand, some ISC components perform a second (moonlighting) function in other cellular processes. For instance, thio modification of transfer RNAs requires IscS in bacteria and mitochondrial Nfs1-Isd11 as a sulphur donor<sup>8,93,94</sup>. Thio and other modifications of tRNAs depend on the function of Fe-S proteins both in bacteria (for example, MiaB) and eukaryotes (for example, Elp3). Furthermore, the mitochondrial [2Fe-2S] ferredoxin Yah1, together with its reductase Arh1 and Cox15, is required for the hydroxylation of protohaem for the synthesis of haem A of cytochrome oxidase. The mammalian homologue of Yah1, adrenodoxin, plays a long-known role in steroid biosynthesis.

An intimate connection exists between Fe-S-protein biogenesis in mitochondria and iron regulation in the cell. The mechanisms of this regulatory pathway are fundamentally different in yeast and mammalian cells, yet the input (iron requirement for Fe-S-protein biogenesis) and the outcome (iron-uptake regulation) of the regulatory chain are similar. In yeast, iron uptake and intracellular distribution are mainly regulated by a transcriptional mechanism involving the transcription factors Aft1 and Aft2 (ref. 95). In the absence of iron, Aft1 and Aft2 translocate to the nucleus, where they activate genes of the iron regulon including iron



transporters, siderophore transporters and proteins for intracellular iron distribution. Low iron concentrations inside mitochondria or defects in mitochondrial Fe–S-protein biogenesis (that is, ISC protein deficiencies) activate Aft1–Aft2 and lead to a concomitant iron accumulation in mitochondria. Thus, mitochondria have a crucial role in regulating cellular iron homeostasis. The regulatory mechanism includes both the ISC assembly and ISC export systems, suggesting that the same or a similar molecule as that exported by Atm1 to the CIA machinery may communicate the iron status of the mitochondrial matrix to Aft1 and Aft2 (ref. 96). Strikingly, the yeast CIA proteins have no major role in iron sensing and regulation, refuting the idea that a canonical cytosolic or nuclear Fe–S protein may be responsible for the regulatory function in iron homeostasis.

In mammals, cellular iron regulation occurs predominantly at the post-transcriptional level and involves both the Fe–S protein IRP1 (see above) and iron-regulatory protein 2, which has no Fe–S cluster yet is degraded under iron-replete conditions<sup>19–21</sup>. Insertion of the Fe–S cluster into IRP1 has been shown to require mitochondrial Nfs1, Isu1, frataxin, Grx5, ABCB7, Nbp35 and Nar1 (refs 71–74, 81, 82, 89, 97). Hence, in mammals, both the ISC and the CIA machineries are critical for the regulation of cellular iron uptake, creating the notable difference from yeast, in which the CIA machinery is not needed.

## Outlook

Despite the impressive progress in research on Fe–S-protein biogenesis during the past decade, exciting years of further exploration are ahead of us, ranging from basic structural, biochemical and cell-biological research to physiology and molecular medicine. Only some of the most pressing problems to be solved in future research can be mentioned here. The solving of three-dimensional structures of the various ISC and CIA proteins, in particular of the holo forms of different Fe–S scaffolds, will facilitate the elucidation of the molecular mechanisms of *de novo* Fe–S-cluster assembly in living cells. It will be crucial to combine *in vitro* and *in vivo* approaches to verify the physiological relevance of findings with isolated proteins. The specificity of, and differing needs for, the various scaffold proteins has to be clarified to understand their individual roles. The mechanisms of Fe–S-cluster transfer from the scaffold proteins must be dissected into partial steps, and the precise roles of the transfer-assisting proteins will have to be understood. It will be important to elucidate the conversion of [2Fe–2S] clusters to [4Fe–4S] clusters and define the function of participating biogenesis components.

Novel biogenesis components, in particular the iron and electron donors of the SUF and CIA machineries, will be identified and their function characterized. A particularly pressing question is the isolation and chemical characterization of the substrate exported from mitochondria to assist extra-mitochondrial Fe–S-protein biogenesis. This achievement will crucially depend on the development of an *in vitro* reconstitution protocol for the export process. It is possible that new moonlighting functions of Fe–S-protein biogenesis components will be identified. In that respect, it will be interesting to clarify the function of the nuclear form of Nfs1. Advances in isolating mitochondria will make it possible to test their suggested function in cellular Fe–S-protein biogenesis experimentally. Finally, new diseases associated with this fundamental process of life will allow us to understand the physiological consequences of Fe–S-protein defects. It is clear that thorough molecular insights into the mechanisms of Fe–S-protein biogenesis are prerequisite for the future development of therapeutic strategies in the treatment of Fe–S diseases. ■

- Beinert, H., Holm, R. H. & Münck, E. Iron-sulfur clusters: nature's modular, multipurpose structures. *Science* **277**, 653–659 (1997).
- Meyer, J. Iron-sulfur protein folds, iron-sulfur chemistry, and evolution. *J. Biol. Inorg. Chem.* **13**, 157–170 (2008).
- Malik, R. & Rabinowitz, J. C. The reconstitution of clostridial ferredoxin. *Biochem. Biophys. Res. Commun.* **23**, 822–827 (1966).
- Johnson, D. C., Dean, D. R., Smith, A. D. & Johnson, M. K. Structure, function and formation of biological iron-sulfur clusters. *Annu. Rev. Biochem.* **74**, 247–281 (2005).
- Balk, J. & Lobreaux, S. Biogenesis of iron-sulfur proteins in plants. *Trends Plant Sci.* **10**, 324–331 (2005).
- Lill, R. & Mühlenhoff, U. Iron-sulfur protein biogenesis in eukaryotes: components and mechanisms. *Annu. Rev. Cell Dev. Biol.* **22**, 457–486 (2006).
- Vickery, L. E. & Cupp-Vickery, J. R. Molecular chaperones HscA/Ssq1 and HscB/Jac1 and their roles in iron-sulfur protein maturation. *Crit. Rev. Biochem. Mol. Biol.* **42**, 95–111 (2007).
- Lill, R. & Mühlenhoff, U. Maturation of iron-sulfur proteins in eukaryotes: mechanisms, connected processes, and diseases. *Annu. Rev. Biochem.* **77**, 669–700 (2008).
- Ayala-Castro, C., Saini, A. & Outten, F. W. Fe–S cluster assembly pathways in bacteria. *Microbiol. Mol. Biol. Rev.* **72**, 110–125 (2008).
- Rouault, T. A. & Tong, W. H. Iron-sulfur cluster biogenesis and human disease. *Trends Genet.* **24**, 398–407 (2008).
- Xu, X. M. & Möller, S. G. Iron-sulfur cluster biogenesis systems and their crosstalk. *ChemBioChem* **9**, 2355–2362 (2008).
- Fontecave, M. & Ollagnier-de-Choudens, S. Iron-sulfur cluster biosynthesis in bacteria: mechanisms of cluster assembly and transfer. *Arch. Biochem. Biophys.* **474**, 226–237 (2008).
- Bandyopadhyay, S., Chandramouli, K. & Johnson, M. K. Iron-sulfur cluster biosynthesis. *Biochem. Soc. Trans.* **36**, 1112–1119 (2008).
- Booker, S. J., Cicchillo, R. M. & Grove, T. L. Self-sacrifice in radical S-adenosylmethionine proteins. *Curr. Opin. Chem. Biol.* **11**, 543–552 (2007).
- Rudolf, J., Makranton, V., Ingledew, W. J., Stark, M. J. & White, M. F. The DNA repair helicases XPD and FancJ have essential iron-sulfur domains. *Mol. Cell* **23**, 801–808 (2006).
- Kispaal, G. *et al.* Biogenesis of cytosolic ribosomes requires the essential iron-sulphur protein Rli1p and mitochondria. *EMBO J.* **24**, 589–598 (2005).
- Karcher, A., Schele, A. & Hopfner, K. P. X-ray structure of the complete ABC enzyme ABCE1 from *Pyrococcus abyssi*. *J. Biol. Chem.* **283**, 7962–7971 (2008).
- Imlay, J. A. Cellular defenses against superoxide and hydrogen peroxide. *Annu. Rev. Biochem.* **77**, 755–776 (2008).
- Walden, W. E. *et al.* Structure of dual function iron regulatory protein 1 complexed with ferritin IRE-RNA. *Science* **314**, 1903–1908 (2006).
- Rouault, T. A. The role of iron regulatory proteins in mammalian iron homeostasis and disease. *Nature Chem. Biol.* **2**, 406–414 (2006).
- Wallander, M. L., Leibold, E. A. & Eisenstein, R. S. Molecular control of vertebrate iron homeostasis by iron regulatory proteins. *Biochim. Biophys. Acta* **1763**, 668–689 (2006).
- Volz, K. The functional duality of iron regulatory protein 1. *Curr. Opin. Struct. Biol.* **18**, 106–111 (2008).
- Kispaal, G., Csere, P., Prohl, C. & Lill, R. The mitochondrial proteins Atm1p and Nfs1p are required for biogenesis of cytosolic Fe/S proteins. *EMBO J.* **18**, 3981–3989 (1999). This paper and reference 28 functionally characterize the first components of the mitochondrial ISC assembly machinery and show the role of mitochondria for both cytosolic Fe–S-protein biogenesis and iron homeostasis.
- Rubio, L. M. & Ludden, P. W. Biosynthesis of the iron-molybdenum cofactor of nitrogenase. *Annu. Rev. Microbiol.* **62**, 93–111 (2008).
- Hu, Y., Fay, A. W., Lee, C. C., Yoshizawa, J. & Ribbe, M. W. Assembly of nitrogenase MoFe protein. *Biochemistry* **47**, 3973–3981 (2008).
- Leach, M. R. & Zamble, D. B. Metallocluster assembly of the hydrogenase enzymes. *Curr. Opin. Chem. Biol.* **11**, 159–165 (2007).
- Zheng, L., Cash, V. L., Flint, D. H. & Dean, D. R. Assembly of iron-sulfur clusters. Identification of an *iscSUA-hscBA-fdx* gene cluster from *Azotobacter vinelandii*. *J. Biol. Chem.* **273**, 13264–13272 (1998). This paper describes the *isc* operon encoding components of the bacterial ISC assembly machinery.
- Schilke, B., Voisine, C., Beinert, H. & Craig, E. Evidence for a conserved system for iron metabolism in the mitochondria of *Saccharomyces cerevisiae*. *Proc. Natl Acad. Sci. USA* **96**, 10206–10211 (1999).
- Yuvaniyama, P., Agar, J. N., Cash, V. L., Johnson, M. K. & Dean, D. R. NifS-directed assembly of a transient [2Fe–2S] cluster within the NifU protein. *Proc. Natl Acad. Sci. USA* **97**, 599–604 (2000). This paper introduces the concept of *de novo* Fe–S-cluster assembly on a scaffold protein.
- Mühlenhoff, U., Gerber, J., Richhardt, N. & Lill, R. Components involved in assembly and dislocation of iron-sulfur clusters on the scaffold protein Isu1p. *EMBO J.* **22**, 4815–4825 (2003). This paper defines various stages of mitochondrial Fe–S-protein assembly and verifies the scaffold concept *in vivo*.
- Raulfs, E. C., O'Carroll, I. P., Dos Santos, P. C., Unciuleac, M. C. & Dean, D. R. *In vivo* iron-sulfur cluster formation. *Proc. Natl Acad. Sci. USA* **105**, 8591–8596 (2008).
- Unciuleac, M. C. *et al.* *In vitro* activation of apo-aconitase using a [4Fe–4S] cluster-loaded form of the IscU [Fe–S] cluster scaffolding protein. *Biochemistry* **46**, 6812–6821 (2007).
- Chandramouli, K. *et al.* Formation and properties of [4Fe–4S] clusters on the IscU scaffold protein. *Biochemistry* **46**, 6804–6811 (2007).
- Zheng, L., White, R. H., Cash, V. L., Jack, R. F. & Dean, D. R. Cysteine desulfurase activity indicates a role for NifS in metallocluster biosynthesis. *Proc. Natl Acad. Sci. USA* **90**, 2754–2758 (1993). This paper identifies and characterizes the founding member of cysteine desulfurases.
- Kaiser, J. T. *et al.* Crystal structure of a NifS-like protein from *Thermotoga maritima*: implications for iron-sulfur cluster assembly. *J. Mol. Biol.* **297**, 451–464 (2000).
- Cupp-Vickery, J. R., Urbina, H. & Vickery, L. E. Crystal structure of IscS, a cysteine desulfurase from *Escherichia coli*. *J. Mol. Biol.* **330**, 1049–1059 (2003).
- Wiedemann, N. *et al.* Essential role of Isd11 in iron-sulfur cluster synthesis on Isu scaffold proteins. *EMBO J.* **25**, 184–195 (2006).
- Adam, A. C., Bornhövd, C., Prokisch, H., Neupert, W. & Hell, K. The Nfs1 interacting protein Isd11 has an essential role in Fe/S cluster biogenesis in mitochondria. *EMBO J.* **25**, 174–183 (2006).
- Gerber, J., Mühlenhoff, U. & Lill, R. An interaction between frataxin and Isu1/Nfs1 that is crucial for Fe/S cluster synthesis on Isu1. *EMBO Rep.* **4**, 906–911 (2003).
- Layer, G., Ollagnier-de Choudens, S., Sanakis, Y. & Fontecave, M. Iron-sulfur cluster biosynthesis: characterization of *Escherichia coli* CyaY as an iron donor for the assembly of [2Fe–2S] clusters in the scaffold IscU. *J. Biol. Chem.* **281**, 16256–16263 (2006).
- Bencze, K. Z. *et al.* The structure and function of frataxin. *Crit. Rev. Biochem. Mol. Biol.* **41**, 269–291 (2006).

42. Wang, T. & Craig, E. A. Binding of yeast frataxin to the scaffold for Fe-S cluster biogenesis. *Isu. J. Biol. Chem.* **283**, 12674–12679 (2008).
43. Adinolfi, S. *et al.* Bacterial frataxin CyaY is the gatekeeper of iron-sulfur cluster formation catalyzed by IscS. *Nature Struct. Mol. Biol.* **16**, 390–396 (2009).
44. Schilke, B. *et al.* Evolution of mitochondrial chaperones utilized in Fe-S cluster biogenesis. *Curr. Biol.* **16**, 1660–1665 (2006).
45. Cupp-Vickery, J. R., Silberg, J. J., Ta, D. T. & Vickery, L. E. Crystal structure of IscA, an iron-sulfur cluster assembly protein from *Escherichia coli*. *J. Mol. Biol.* **338**, 127–137 (2004).
46. Dutkiewicz, R. *et al.* Sequence-specific interaction between mitochondrial Fe-S scaffold protein Isu and Hsp70 Ssa1 is essential for their *in vivo* function. *J. Biol. Chem.* **279**, 29167–29174 (2004).
47. Chandramouli, K. & Johnson, M. K. HscA and HscB stimulate [2Fe-2S] cluster transfer from IscU to apoferredoxin in an ATP-dependent reaction. *Biochemistry* **45**, 11087–11095 (2006).  
**This paper and reference 49 define the role of heat-shock proteins in Fe-S-cluster transfer from scaffold to target proteins in vitro.**
48. Andrew, A. J., Dutkiewicz, R., Kniezner, H., Craig, E. A. & Marszalek, J. Characterization of the interaction between the J-protein Jac1 and the scaffold for Fe-S cluster biogenesis, Isu1. *J. Biol. Chem.* **281**, 14580–14587 (2006).
49. Bonomi, F., Iametti, S., Morleo, A., Ta, D. & Vickery, L. E. Studies on the mechanism of catalysis of iron-sulfur cluster transfer from IscU [2Fe2S] by HscA/HscB chaperones. *Biochemistry* **47**, 12795–12801 (2008).
50. Bandyopadhyay, S. *et al.* Chloroplast monothiol glutaredoxins as scaffold proteins for the assembly and delivery of [2Fe-2S] clusters. *EMBO J.* **27**, 1122–1133 (2008).
51. Gelling, C., Dawes, I. W., Richhardt, N., Lill, R. & Mühlenhoff, U. Mitochondrial Iba57p is required for Fe/S cluster formation on aconitase and activation of radical SAM enzymes. *Mol. Cell. Biol.* **28**, 1851–1861 (2008).
52. Tan, G., Lu, J., Bitoun, J. P., Huang, H. & Ding, H. IscA/SufA paralogs are required for the [4Fe-4S] cluster assembly in enzymes of multiple physiological pathways in *Escherichia coli* under aerobic growth conditions. *Biochem J.* **420**, 463–472 (2009).
53. Loiseau, L. *et al.* ErpA, an iron sulfur (Fe S) protein of the A-type essential for respiratory metabolism in *Escherichia coli*. *Proc. Natl Acad. Sci. USA* **104**, 13626–13631 (2007).
54. Gupta, V. *et al.* Native *Escherichia coli* SufA, coexpressed with SufBCDSE, purifies as a [2Fe-2S] protein and acts as an Fe-S transporter to Fe-S target enzymes. *J. Am. Chem. Soc.* **131**, 6149–6153 (2009).
55. Bych, K. *et al.* The iron-sulphur protein Ind1 is required for effective complex I assembly. *EMBO J.* **27**, 1736–1746 (2008).
56. Takahashi, Y. & Tokumoto, U. A third bacterial system for the assembly of iron-sulfur clusters with homologs in archaea and plastids. *J. Biol. Chem.* **277**, 28380–28383 (2002).
57. Tokumoto, U., Kitamura, S., Fukuyama, K. & Takahashi, Y. Interchangeability and distinct properties of bacterial Fe-S cluster assembly systems: functional replacement of the isc and suf operons in *Escherichia coli* with the nifS-like operon from *Helicobacter pylori*. *J. Biochem.* **136**, 199–209 (2004).
58. Outten, F. W., Wood, M. J., Munoz, F. M. & Storz, G. The SufE protein and the SufBCD complex enhance SufS cysteine desulfurase activity as part of a sulfur transfer pathway for Fe-S cluster assembly in *E. coli*. *J. Biol. Chem.* **278**, 45713–45719 (2003).  
**This paper and reference 59 describe the first functional analyses and interactions of the Suf proteins.**
59. Loiseau, L., Ollagnier-de-Choudens, S., Nachin, L., Fontecave, M. & Barras, F. Biogenesis of Fe-S cluster by the bacterial Suf system: SufS and SufE form a new type of cysteine desulfurase. *J. Biol. Chem.* **278**, 38352–38359 (2003).
60. Kessler, D. Enzymatic activation of sulfur for incorporation into biomolecules in prokaryotes. *FEMS Microbiol. Rev.* **30**, 825–840 (2006).
61. Layer, G. *et al.* SufE transfers sulfur from SufS to SufB for iron-sulfur cluster assembly. *J. Biol. Chem.* **282**, 13342–13350 (2007).
62. Sendra, M., Ollagnier de Choudens, S., Lascoux, D., Sanakis, Y. & Fontecave, M. The Suf iron-sulfur cluster biosynthetic machinery: sulfur transfer from the SUFS-SUFE complex to SUFA. *FEBS Lett.* **581**, 1362–1368 (2007).
63. Liu, G. *et al.* High-quality homology models derived from NMR and X-ray structures of *E. coli* proteins YgdK and Suf E suggest that all members of the YgdK/Suf E protein family are enhancers of cysteine desulfurases. *Protein Sci.* **14**, 1597–1608 (2005).
64. Nachin, L., Loiseau, L., Expert, D. & Barras, F. SufC: an unorthodox cytoplasmic ABC/ATPase required for [Fe-S] biogenesis under oxidative stress. *EMBO J.* **22**, 427–437 (2003).
65. Liu, J. *et al.* Structural characterization of an iron-sulfur cluster assembly protein IscU in a zinc-bound form. *Proteins* **59**, 875–881 (2005).
66. Riboldi, G. P., Verli, H. & Frazzoni, J. Structural studies of the *Enterococcus faecalis* SufU [Fe-S] cluster protein. *BMC Biochem.* **10**, 3 (2009).
67. Ye, H., Pilon, M. & Pilon-Smits, E. A. CpnifS-dependent iron-sulfur cluster biogenesis in chloroplasts. *New Phytol.* **171**, 285–292 (2006).
68. Yabe, T. *et al.* The *Arabidopsis* chloroplastic NifU-like protein CnfU, which can act as an iron-sulfur cluster scaffold protein, is required for biogenesis of ferredoxin and photosystem I. *Plant Cell* **16**, 993–1007 (2004).
69. Gerber, J., Neumann, K., Prohl, C., Mühlenhoff, U. & Lill, R. The yeast scaffold proteins Isu1p and Isu2p are required inside mitochondria for maturation of cytosolic Fe/S proteins. *Mol. Cell. Biol.* **24**, 4848–4857 (2004).
70. Rouault, T. A. & Tong, W. H. Iron-sulphur cluster biogenesis and mitochondrial iron homeostasis. *Nature Rev. Mol. Cell Biol.* **6**, 345–351 (2005).
71. Tong, W. H. & Rouault, T. A. Functions of mitochondrial ISC and cytosolic ISCU in mammalian iron-sulfur cluster biogenesis and iron homeostasis. *Cell Metab.* **3**, 199–210 (2006).  
**This paper and references 72, 73, 89 and 97 demonstrate the general conservation of Fe-S-protein biogenesis in vertebrates.**
72. Biederbick, A. *et al.* Role of human mitochondrial Nfs1 in cytosolic iron-sulfur protein biogenesis and iron regulation. *Mol. Cell. Biol.* **26**, 5675–5687 (2006).
73. Pondarre, C. *et al.* The mitochondrial ATP-binding cassette transporter Abcb7 is essential in mice and participates in cytosolic iron-sulphur cluster biogenesis. *Hum. Mol. Genet.* **15**, 953–964 (2006).
74. Cavadini, P. *et al.* RNA silencing of the mitochondrial ABCB7 transporter in HeLa cells causes an iron-deficient phenotype with mitochondrial iron overload. *Blood* **109**, 3552–3559 (2007).
75. Mesecke, N. *et al.* A disulfide relay system in the intermembrane space of mitochondria that mediates protein import. *Cell* **121**, 1059–1070 (2005).
76. Netz, D. J., Pierik, A. J., Stümpfig, M., Mühlenhoff, U. & Lill, R. The Cfd1-Nbp35 complex acts as a scaffold for iron-sulfur protein assembly in the yeast cytosol. *Nature Chem. Biol.* **3**, 278–286 (2007).  
**This paper defines various stages of cytosolic Fe-S-protein assembly and identifies Cfd1-Nbp35 as a cytosolic scaffold.**
77. Roy, A., Solodovnikova, N., Nicholson, T., Antholine, W. & Walden, W. E. A novel eukaryotic factor for cytosolic Fe-S cluster assembly. *EMBO J.* **22**, 4826–4835 (2003).  
**This paper identifies Cfd1 as the first extra-mitochondrial Fe-S-protein biogenesis component.**
78. Hausmann, A. *et al.* The eukaryotic P-loop NTPase Nbp35: an essential component of the cytosolic and nuclear iron-sulfur protein assembly machinery. *Proc. Natl Acad. Sci. USA* **102**, 3266–3271 (2005).
79. Srinivasan, V. *et al.* Structure of the yeast WD40 domain protein Cia1, a component acting late in iron-sulfur protein biogenesis. *Structure* **15**, 1246–1257 (2007).
80. Zhang, Y. *et al.* Dre2, a conserved eukaryotic Fe/S cluster protein, functions in cytosolic Fe/S protein biogenesis. *Mol. Cell. Biol.* **28**, 5569–5582 (2008).
81. Song, D. & Lee, F. S. A role for IOP1 in mammalian cytosolic iron-sulfur protein biogenesis. *J. Biol. Chem.* **283**, 9231–9238 (2008).
82. Stehling, O. *et al.* Human Nbp35 is essential for both cytosolic iron-sulfur protein assembly and iron homeostasis. *Mol. Cell. Biol.* **28**, 5517–5528 (2008).
83. Lill, R. & Mühlenhoff, U. Iron-sulfur protein biogenesis in eukaryotes. *Trends Biochem. Sci.* **30**, 133–141 (2005).
84. Klinge, S., Hirst, J., Maman, J. D., Krude, T. & Pellegrini, L. An iron-sulfur domain of the eukaryotic primase is essential for RNA primer synthesis. *Nature Struct. Mol. Biol.* **14**, 875–877 (2007).
85. van der Giezen, M. & Tovar, J. Degenerate mitochondria. *EMBO Rep.* **6**, 525–530 (2005).
86. Embley, T. M. & Martin, W. Eukaryotic evolution, changes and challenges. *Nature* **440**, 623–630 (2006).
87. Tovar, J. *et al.* Mitochondrial remnant organelles of *Giardia* function in iron-sulphur protein maturation. *Nature* **426**, 172–176 (2003).
88. Goldberg, A. V. *et al.* Localization and functionality of microsporidian iron-sulphur cluster assembly proteins. *Nature* **452**, 624–628 (2008).
89. Wingert, R. A. *et al.* Deficiency of *glutaredoxin 5* reveals Fe-S clusters are required for vertebrate haem synthesis. *Nature* **436**, 1035–1039 (2005).
90. Shaw, G. C. *et al.* Mitoferrin is essential for erythroid iron assimilation. *Nature* **440**, 96–100 (2006).
91. Mochel, F. *et al.* Splice mutation in the iron-sulfur cluster scaffold protein ISCU causes myopathy with exercise intolerance. *Am. J. Hum. Genet.* **82**, 652–660 (2008).
92. Olsson, A., Lind, L., Thornell, L. E. & Holmberg, M. Myopathy with lactic acidosis is linked to chromosome 12q23.3–24.1 and caused by an intron mutation in the ISCU gene resulting in a splicing defect. *Hum. Mol. Genet.* **17**, 1666–1667 (2008).
93. Mueller, E. G. Trafficking in persulfides: delivering sulfur in biosynthetic pathways. *Nature Chem. Biol.* **2**, 185–194 (2006).
94. Nakai, Y., Nakai, M., Lill, R., Suzuki, T. & Hayashi, H. Thio modification of yeast cytosolic tRNA is an iron-sulfur protein-dependent pathway. *Mol. Cell. Biol.* **27**, 2841–2847 (2007).
95. Kaplan, J., McVey Ward, D., Crisp, R. J. & Philpott, C. C. Iron-dependent metabolic remodeling in *S. cerevisiae*. *Biochim. Biophys. Acta* **1763**, 646–651 (2006).
96. Rutherford, J. C. *et al.* Activation of the iron-regulon by the yeast Aft1/Aft2 transcription factors depends on mitochondrial, but not cytosolic iron-sulfur protein biogenesis. *J. Biol. Chem.* **280**, 10135–10140 (2005).
97. Stehling, O., Elsässer, H. P., Brückel, B., Mühlenhoff, U. & Lill, R. Iron-sulfur protein maturation in human cells: evidence for a function of frataxin. *Hum. Mol. Genet.* **13**, 3007–3015 (2004).
98. Campuzano, V. *et al.* Friedreich's ataxia: autosomal recessive disease caused by an intronic GAA triplet repeat expansion. *Science* **271**, 1423–1427 (1996).
99. Bekri, S. *et al.* Human ABC7 transporter: gene structure and mutation causing X-linked sideroblastic anemia with ataxia (XLSEA/A) with disruption of cytosolic iron-sulfur protein maturation. *Blood* **96**, 3256–3264 (2000).
100. Amutha, B. *et al.* GTP is required for iron-sulfur cluster biogenesis in mitochondria. *J. Biol. Chem.* **283**, 1362–1371 (2008).

**Acknowledgements** I wish to thank all present and past members of my group for their excellent and dedicated work. Generous financial support from the Deutsche Forschungsgemeinschaft (SFB 593 and TR1, Gottfried-Wilhelm Leibniz programme and GRK 1216), the Max-Planck Gesellschaft, the von Behring-Röntgen-Stiftung, the German-Israeli Foundation for Scientific Research and Development, the Alexander von Humboldt-Stiftung, Rhön Klinikum AG and Fonds der Chemischen Industrie is gratefully acknowledged. I apologize to all colleagues whose original work could not be discussed or cited owing to length limitations.

**Author Information** Reprints and permissions information is available at [www.nature.com/reprints](http://www.nature.com/reprints). The author declares no competing financial interests. Correspondence should be addressed to the author ([lill@staff.uni-marburg.de](mailto:lill@staff.uni-marburg.de)).

# Molybdenum cofactors, enzymes and pathways

Günter Schwarz<sup>1</sup>, Ralf R. Mendel<sup>2</sup> & Markus W. Ribbe<sup>3</sup>

**The trace element molybdenum is essential for nearly all organisms and forms the catalytic centre of a large variety of enzymes such as nitrogenase, nitrate reductases, sulphite oxidase and xanthine oxidoreductases. Nature has developed two scaffolds holding molybdenum in place, the iron–molybdenum cofactor and pterin-based molybdenum cofactors. Despite the different structures and functions of molybdenum-dependent enzymes, there are important similarities, which we highlight here. The biosynthetic pathways leading to both types of cofactor have common mechanistic aspects relating to scaffold formation, metal activation and cofactor insertion into apoenzymes, and have served as an evolutionary ‘toolbox’ to mediate additional cellular functions in eukaryotic metabolism.**

Molybdenum is bioavailable as molybdate ( $\text{MoO}_4^{2-}$ ). Once molybdate enters the cell, it is subsequently incorporated by complex biosynthetic machineries into metal cofactors<sup>1,2</sup>. All enzymes that depend on molybdenum catalyse redox reactions by taking advantage of the versatile redox chemistry of the metal, which is controlled by the cofactor itself and the enzyme environment<sup>3</sup>. Within the enzyme, molybdenum shuttles between three oxidation states (+4, +5 and +6), thereby catalysing two-electron reduction–oxidation (redox) reactions. In most cases, regeneration of the active site involves single-electron steps, resulting in a paramagnetic molybdenum intermediate. Molybdenum enzymes are found in nearly all organisms, with *Saccharomyces* as a prominent eukaryotic exception<sup>4</sup>. Many anaerobic archaea and some bacteria are molybdenum independent but require tungsten for their growth. Tungstate, which is 100-fold less abundant than molybdate, is enriched in deep-sea hydrothermal vents, reflecting conditions on the primitive Earth. Many of the known tungsten-dependent hyperthermophilic bacteria and archaea are found in such vents<sup>5</sup>.

In nature, two very different systems have developed to control the redox state and catalytic power of molybdenum, which functions as an efficient catalyst in oxygen-transfer reactions. In either case, at least three sulphur and two oxygen atoms form ligands to molybdenum (Fig. 1). One type of molybdenum cofactor is the iron–sulphur-cluster-based iron–molybdenum cofactor (FeMo-co) that is unique to the molybdenum nitrogenase<sup>6</sup>, with one [4Fe–3S] and one [Mo–3Fe–3S] partial cubane bridged by three sulphides and one  $\mu_6$  central atom, X (which may be carbon, oxygen or nitrogen)<sup>7</sup>. The molybdenum of FeMo-co is further coordinated by homocitrate (Fig. 1a). The core structure of the other type of molybdenum cofactor (Moco) is a pterin-based cofactor (molybdopterin or metal-binding pterin (MPT)), with a C6-substituted pyrano ring, a terminal phosphate and a unique dithiolate group binding molybdenum<sup>8</sup>. The metal can be attached to one or two pterin moieties with additional terminal oxygen and sulphur ligands (Fig. 1c, d). Both cofactors are oxygen sensitive and very unstable outside their respective apoenzymes.

In this Review, we give a short overview of the different families of molybdenum-containing enzymes, focusing on the biosynthetic

machineries that lead to the ‘biological’ activation of the metal in different molybdenum cofactors.

## Molybdenum-dependent enzymes

On the basis of cofactor composition and catalytic function, molybdenum-dependent enzymes can be grouped into two categories: bacterial nitrogenases containing an FeMo-co in the active site, and pterin-based molybdenum enzymes. The second category is divided into three families, exemplified by sulphite oxidase, xanthine oxidase and dimethyl sulphoxide reductase (DMSOR), which each have a distinct active-site structure<sup>3</sup> (Fig. 1). Tungsten-dependent formate dehydrogenase is classified as part of the DMSOR family, whereas aldehyde:ferredoxin oxidoreductases form a separate family of tungsten-cofactor (W-co) containing enzymes found only in archaea. The biochemistry of W-co enzymes has been summarized very recently<sup>5</sup>.

## Molybdenum nitrogenase

Nitrogenases provide the biochemical machinery for nucleotide-dependent reduction of dinitrogen ( $\text{N}_2$ ) to ammonia ( $\text{NH}_3$ )<sup>6</sup>. The overall reaction catalysed by nitrogenases is usually depicted as  $\text{N}_2 + 8\text{H}^+ + 16\text{MgATP} + 8\text{e}^- \rightarrow 2\text{NH}_3 + \text{H}_2 + 16\text{MgADP} + 16\text{P}_i$ , where  $\text{P}_i$  denotes an inorganic phosphate. This reaction not only represents a major entry point of reduced nitrogen into the global nitrogen cycle, but also embodies the complex chemistry of breaking the triple bond of  $\text{N}_2$  under ambient conditions (see page 814). Three homologous nitrogenase systems have been identified so far<sup>9</sup>. The best-characterized molybdenum nitrogenase is a binary enzyme system comprising two redox-active metalloproteins (Fig. 2a). One, designated Fe-protein, is an  $\alpha_2$  homodimer with one [4Fe–4S] cluster bridged between the subunits and one MgATP-binding site located in each subunit; the other, termed MoFe-protein, is an  $\alpha_2\beta_2$  heterotetramer containing two unique metal centres: the P-cluster, an [8Fe–7S] cluster that is ligated between each  $\alpha\beta$ -subunit dimer; and the FeMo-co, a [Mo–7Fe–9S–X–homocitrate] cluster (where X may be carbon, oxygen or nitrogen) that is buried within each  $\alpha$ -subunit<sup>7,10</sup> (Fig. 1a). Catalysis by molybdenum nitrogenase probably involves the repeated association and dissociation of Fe-protein and MoFe-protein

<sup>1</sup>Institute of Biochemistry, Department of Chemistry & Centre for Molecular Medicine, University of Cologne, 47 Zulpicher Street, 50674 Cologne, Germany. <sup>2</sup>Institute of Plant Biology, Braunschweig University of Technology, 1 Humboldt Street, 38106 Braunschweig, Germany. <sup>3</sup>Department of Molecular Biology and Biochemistry, School of Biological Sciences, University of California, Irvine, California 92697, USA.



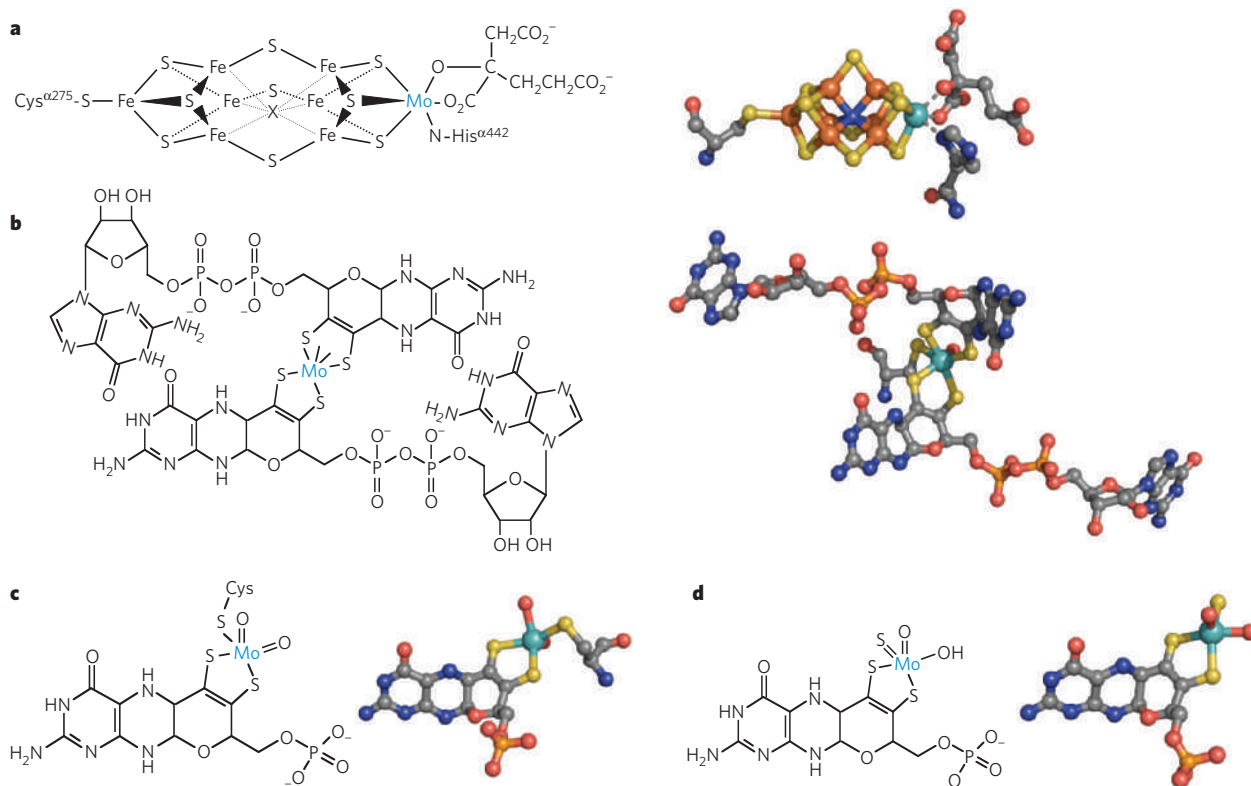


**Figure 1 | Molybdenum-containing cofactors.** Chemical and three-dimensional structures of FeMo-co (a), Mo-bis-MGD (b) and the Moco from enzymes of the sulphite oxidase (c) and xanthine oxidase (d) families. The three-dimensional structures were taken from the crystal structures

of nitrogenase<sup>7</sup>, NarG–NarH–NarI<sup>15</sup>, *Pichia pastoris* nitrate reductase<sup>17</sup> and bovine xanthine oxidase<sup>24</sup>. Structures are shown in ball-and-stick presentation (Mo, cyan; C, grey; O, red; S, yellow; Fe, brown; N, blue) and rendered with PYMOL (<http://www.pymol.org/>).

and ATP-dependent transfer of electrons from the [4Fe–4S] cluster of Fe-protein, through the P-cluster, to the FeMo-co of MoFe-protein, where substrate reduction eventually takes place<sup>6</sup>.

### Molybdenum enzymes with a pterin cofactor

More than 50 different pterin-containing molybdenum enzymes are known and classified on the basis of the coordination chemistry of molybdenum in their active site<sup>11–13</sup>. All eukaryotic molybdenum enzymes belong exclusively to either the sulphite oxidase or the xanthine oxidase family with a simple MPT-type cofactor (Fig. 1c, d). They differ in the nature of the third Mo–S ligand, which is either provided by an enzyme-derived cysteine (sulphite oxidase) or as a terminal sulphido ligand (xanthine oxidase). By contrast, members of the DMSOR family coordinate molybdenum by two pterin moieties, each carrying in addition guanosine monophosphate, which together form a Mo–bis-MPT guanine dinucleotide cofactor (Mo–bis-MGD; Fig. 1b). Detailed mechanistic aspects of all these enzyme families have been discussed elsewhere<sup>3,12–14</sup>.

Members of the DMSOR family are very diverse in reaction, function and structure<sup>11</sup>. Whereas DMSOR of *Rhodobacter sphaeroides* is monomeric and lacks other redox centres, DMSOR from *Escherichia coli* is a membrane-bound enzyme composed of three subunits (DmsA, DmsB and DmsC) with high similarity to *E. coli* dissimilatory nitrate reductase<sup>11</sup> (Fig. 2b). Both represent complex members of this family and additionally harbour a [3Fe–4S] cluster in the catalytic Mo–bis-MGD-containing subunit (NarG), four [4Fe–4S] clusters in the electron-transfer subunit (NarH) and a pair of type-*b* cytochromes in the membrane-spanning subunit (NarI), together forming a dimer of trimers<sup>15</sup>. By contrast with the tricyclic pyranopterin structure of Moco in all known molybdenum and tungsten enzymes, NarG–NarH–NarI shows the presence of an open bicyclic structure in one of the pterins<sup>15</sup>, suggesting a reversible cyclization during catalysis. Most members of the DMSOR family function under anaerobic conditions whereby their

respective cofactors serve as terminal electron acceptors in respiratory metabolism.

Animal sulphite oxidase and eukaryotic nitrate reductase are dimeric enzymes forming another family of molybdenum enzymes with a high degree of structural conservation<sup>16,17</sup>. In addition to the molybdenum domain, they both harbour a cytochrome-*b*<sub>5</sub>-type haem domain that either receives electrons from the molybdenum centre (sulphite oxidase; Fig. 2c) or donates electrons to the molybdenum site (nitrate reductase). However, animal sulphite oxidase shuttles electrons derived from sulphite oxidation towards cytochrome *c*, whereas nitrate reductase receives electrons needed for nitrate reduction from NADPH. The catalytic cycle of sulphite oxidase involves sulphite oxidation coupled to molybdenum reduction, followed by two individual electron-transfer steps through the cytochrome *b*<sub>5</sub> domain to cytochrome *c*, a process associated with large spatial movements of the sulphite oxidase haem domain<sup>13</sup>. Sulphite oxidases and homologous enzymes are also found in plants and bacteria, where they either form a homodimer of two molybdenum subunits lacking the haem domain (plants)<sup>18,19</sup> or assemble into a heterodimer of a single molybdenum- and cytochrome *c*-containing subunit (bacteria)<sup>20</sup>. Sulphite dehydrogenase from *Starkeya novella* is localized in the periplasm, whereas plant sulphite oxidase functions in peroxisomes, generating H<sub>2</sub>O<sub>2</sub> on transfer of electrons to dioxygen<sup>21</sup>. Plant, fungal and algal nitrate reductases are localized in the cytosol and provide the second major entry point for nitrogen into the living world. By comparison with sulphite oxidase, nitrate reductase contains an additional carboxy-terminal FAD domain where either NADH (plant and algae) or NADPH (fungi) provides reducing equivalents for nitrate reduction<sup>22</sup>.

All members of the xanthine oxidase family (also termed molybdenum hydroxylases) catalyse hydroxylations of carbon centres (in aldehydes and aromatic heterocycles) using oxygen derived from water<sup>12</sup>. They are molybdo-flavoenzymes forming homodimers in eukaryotes with three distinct domains in each subunit (Fig. 2d). Xanthine oxidase is the key enzyme in purine degradation, catalysing oxidation of hypoxanthine via

xanthine to uric acid. Electrons derived from substrate hydroxylation are transferred through [2Fe–2S] clusters and FAD to either molecular oxygen, yielding superoxide anions (xanthine oxidase)<sup>12</sup> or NAD<sup>+</sup> (xanthine dehydrogenase)<sup>23</sup>. In bacteria, such as *Rhodobacter capsulatus*, xanthine dehydrogenase assembles from two different subunits, harbouring the Moco on one subunit and the iron-containing and FAD-containing domains on the other subunit and showing a remarkable structural and functional similarity to the bovine enzyme<sup>24,25</sup>. Eukaryotic aldehyde oxidases, which are derived from ancient gene duplications of xanthine oxidase, convert a wide range of aromatic and non-aromatic aldehydes and function in detoxification (animals)<sup>26</sup> and hormone synthesis (abscisic acid, plants)<sup>27</sup>. Bacterial members of the xanthine oxidase family contain a mono-MPT cytosine dinucleotide cofactor and include aldehyde oxidoreductases<sup>28</sup> and carbon monoxide dehydrogenase<sup>29</sup>, the latter being characterized by a special dinuclear Cu–S–Mo centre. Apart from substrate-dependent production of reactive oxygen species, xanthine oxidase and aldehyde oxidases show NADH oxidase activity with simultaneous production of superoxide<sup>30</sup>, which has a number of proposed physiological functions in the metabolism of reactive oxygen species during stress response<sup>23</sup>.

Recently a new mitochondria-associated molybdenum enzyme was found in mammals<sup>31</sup> that promotes reduction of *N*-hydroxylated amidines in concert with cytochrome *b<sub>5</sub>* and cytochrome *b<sub>5</sub>* reductase, a reaction that may be associated with cellular detoxification. It remains unclear what molybdenum-enzyme family this enzyme belongs to, but its occurrence is widespread, homologues having been found among plants and bacteria.

### Biosynthesis of FeMo-co

Assembly of nitrogenase FeMo-co is a considerable chemical feat because of its complexity and intricacy. Recent progress in the chemical synthesis of FeMo-co analogues has provided significant insights into this process<sup>32</sup>. Elucidation of the biosynthesis of FeMo-co, on the other hand, is further complicated by the large ensemble of participating gene products<sup>1,33</sup>. The exact functions of these gene products and the precise sequence of events in FeMo-co assembly have remained unclear until recently, when the characterization of a number of assembly-related intermediates afforded a better understanding of this biosynthetic ‘black box’ (Fig. 3).

### Formation of the Fe–S core of FeMo-co

Assembly of FeMo-co is probably initiated by NifU and NifS, which mobilize iron and sulphur for the assembly of small Fe–S fragments (see page 831). NifS is a pyridoxal phosphate-dependent cysteine desulphurase and is responsible for the formation of a protein-bound cysteine persulphide that is subsequently donated to NifU for the sequential formation of [2Fe–2S] and [4Fe–4S] clusters<sup>34,35</sup> (Fig. 3). These small Fe–S clusters are then transferred to NifB and further processed into a large Fe–S core that possibly contains all the iron and sulphur necessary for the generation of a mature cofactor<sup>36</sup>. The exact function of NifB in this process is unclear. Nevertheless, NifB is an indispensable constituent of FeMo-co biosynthesis, as deletion of *nifB* results in the generation of a cofactor-deficient MoFe-protein<sup>37</sup>. Sequence analysis indicates that NifB contains a CXXXCXXC (where X is any amino acid) signature motif at the amino terminus, which is typical for a family of radical *S*-adenosyl-L-methionine (SAM)-dependent enzymes<sup>1,38</sup>. In addition, there is an abundance of potential ligands in the NifB sequence that are available to coordinate the entire complement of iron atoms of FeMo-co<sup>1</sup>. Thus, formation of the Fe–S core on NifB may represent a new synthetic route to bridged metal clusters that relies on radical chemistry at the SAM domain of NifB. For example, NifB could link two [4Fe–4S] subcubanes by inserting a sulphur atom along with the central atom, X, thereby building a fully complemented Fe–S core that could be rearranged later into the core structure of FeMo-co (Fig. 3).

### Insertion of molybdenum into the Fe–S core on NifEN

The function of NifEN (NifE–NifN) as a scaffold protein for FeMo-co maturation was initially proposed on the basis of a significant degree of sequence homology between NifEN and the MoFe-protein, which has

led to the hypothesis that NifEN contains a ‘P-cluster site’ that houses a P-cluster homologue and an ‘FeMo-co site’ that hosts the conversion of FeMo-co precursor to a mature cofactor<sup>1,33</sup>. Whereas the P-cluster homologue in NifEN was identified earlier as a [4Fe–4S] cluster<sup>33</sup>, a molybdenum-free precursor of FeMo-co was captured on NifEN only recently<sup>39</sup>. Iron K-edge X-ray absorption spectroscopy reveals that this precursor closely resembles the Fe–S core of the mature FeMo-co despite slightly elongated interatomic distances<sup>40</sup> (Fig. 3). This finding implies that, instead of being assembled by the previously postulated mechanism that involves the coupling of [4Fe–3S] and [Mo–3Fe–3S] subclusters, the FeMo-co is assembled by having the complete Fe–S core structure in place before the insertion of molybdenum.

The precursor on NifEN can be converted, *in vitro*, to a fully complemented FeMo-co on incubation with Fe-protein, MgATP, molybdate and homocitrate<sup>41</sup>. Iron and molybdenum K-edge X-ray absorption spectroscopy reveals that the FeMo-co on NifEN is nearly identical in structure to the native cofactor in MoFe-protein, except for an asymmetric coordination of molybdenum that is probably due to the presence of a different ligand environment at the molybdenum end of the cofactor in NifEN<sup>41</sup>. Homocitrate is supplied by NifV (that is, homocitrate

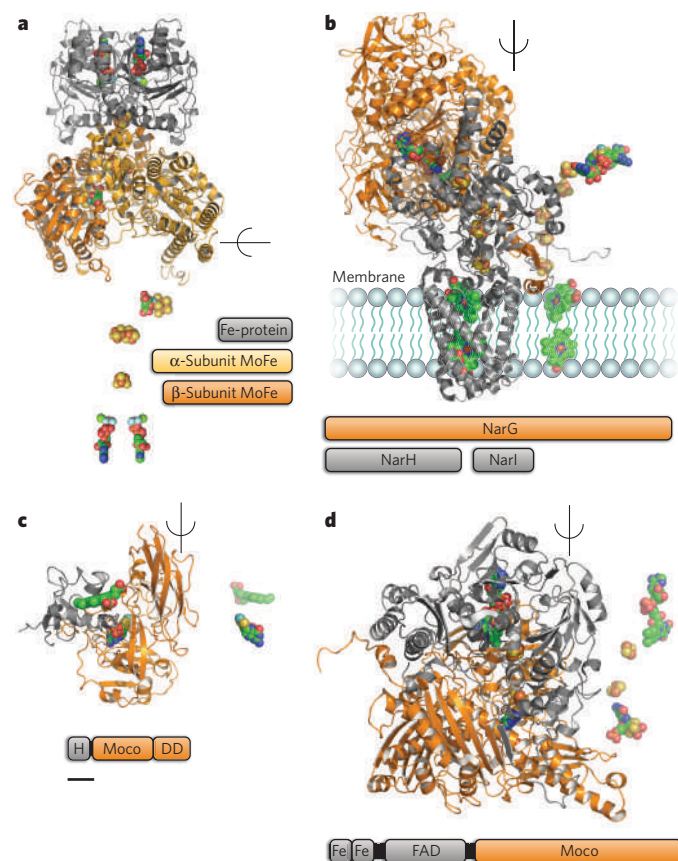


**Figure 2 | Three-dimensional structures of representative members of molybdenum-containing enzymes.** **a**, Molybdenum nitrogenase from *Azotobacter vinelandii*<sup>17</sup>; **b**, *E. coli* membrane-bound dissimilatory nitrate reductase A (NarG–NarH–NarJ)<sup>15</sup>; **c**, chicken sulphite oxidase<sup>16</sup>; **d**, bovine xanthine oxidase<sup>24</sup>. All enzymes shown operate as dimers of which one half is shown as a ribbon diagram with bound cofactors as spheres. For clarity, in the other half of the dimer, only the cofactors are shown, highlighting their spatial arrangement to maintain intramolecular electron transfer. The domain or subunit that binds the molybdenum-containing cofactor is rendered in orange. The FeMo-co-containing nitrogenase MoFe-protein assembles from two different subunits into a heterotetramer ( $\alpha_2\beta_2$ ). Subunit compositions and domain structures are depicted below (DD, dimerization domain; FAD, FAD domain; Fe, [2Fe–2S] cluster; H, haem domain; Moco, Moco-binding domain). A scale bar 100 residues long is provided beneath **c** to indicate protein size. Structures were rendered with PYMOL and coloured as follows: Mo, cyan; C, green; O, red; N, blue; S, yellow; Fe, brown.



synthase) *in vivo*<sup>42</sup>, but molybdenum mobilization within the cell that occurs before the intervention of Fe-protein remains a topic of debate<sup>43,44</sup>. Nevertheless, the fact that the cluster is completely converted before its exit from NifEN points to Fe-protein having a significant role in FeMo-co maturation.

Fe-protein re-isolated after incubation with molybdate, homocitrate and MgATP is 'loaded' with molybdenum and homocitrate that can be subsequently inserted into the precursor on NifEN<sup>45</sup>. The molybdenum K-edge X-ray absorption spectrum of the loaded Fe-protein is consistent with a decreased number of Mo=O bonds (two or three instead of the four found in molybdate) as well as a decrease in the effective oxidation state of molybdenum due to either a change in the formal oxidation state of molybdenum or a change in molybdenum ligation. Interestingly, the electron paramagnetic resonance spectrum of loaded Fe-protein assumes a line shape intermediate between those of the MgADP- and MgATP-bound states of the Fe-protein<sup>45</sup>. This observation is consistent with that from the initial crystallographic analysis of an ADP-bound form of Fe-protein, in which molybdenum is attached at a position that corresponds to the  $\gamma$ -phosphate of ATP<sup>46</sup>. Such an ADP/molybdenum-binding mode (Fig. 4a) may reflect the initial attachment of molybdenum to Fe-protein, particularly when the structural analogy between phosphate and molybdate is considered. Remarkably, similar nucleotide-assisted processes are proposed for the molybdenum insertion in pterin-based cofactors (see below; Fig. 4b).

### Insertion of FeMo-co into apo-MoFe-protein

The completion of FeMo-co assembly on NifEN signals the delivery of FeMo-co to its destined location in MoFe-protein. The absolute requirement of intermediary FeMo-co carrier(s) between NifEN and MoFe-protein was precluded by the observations of unaffected nitrogen-fixing activity of the host after deletions of proposed carrier-encoding gene(s)<sup>47</sup> and direct FeMo-co transfer between NifEN and MoFe-protein on protein-protein interactions<sup>41</sup>. Sequence comparison between NifEN and MoFe-protein reveals that certain residues that either provide a covalent ligand or tightly pack FeMo-co within the polypeptide matrix of MoFe-protein are not duplicated in the corresponding NifEN sequence. It is possible, therefore, that the respective

cluster sites in NifEN and MoFe-protein are brought into close proximity, allowing the subsequent diffusion of FeMo-co from its biosynthetic site in NifEN (low-affinity site) to its binding site in MoFe-protein (high-affinity site). On its delivery to MoFe-protein, FeMo-co interacts with a number of MoFe-protein residues en route to its target location within the protein. Identification of these residues<sup>48–50</sup> was assisted by the crystallographic analysis of a P-cluster-intact yet FeMo-co-deficient form of MoFe-protein, which contains a positively charged funnel in the  $\alpha$ -subunit that is of sufficient size to accommodate the insertion of the negatively charged FeMo-co<sup>37</sup>.

### Biosynthesis of pterin-based molybdenum cofactors

Although widespread in all kingdoms, Moco is synthesized by a conserved biosynthetic pathway divided into four steps according to the biosynthetic intermediates: cyclic pyranopterin monophosphate (cPMP), MPT and MPT-AMP. The biosynthetic pathway has been summarized in detail<sup>2</sup> with particular focus on plants<sup>51</sup>, bacteria<sup>52</sup> and humans<sup>53</sup>, and is believed to be very similar to W-co synthesis<sup>52</sup>. In prokaryotes a final modification by a nucleotide can occur, whereas in MPT-type enzymes Moco maturation either involves a terminal sulphuration (xanthine oxidase family) or cysteine ligation to the apoenzyme (sulphite oxidase family).

### Synthesis of the metal-binding pterin

Biosynthesis starts with the conversion of GTP into cPMP (previously identified as precursor Z; ref. 54) catalysed by two proteins: a radical SAM enzyme (for example MoaA in bacteria) harbouring two oxygen-sensitive [4Fe-4S] clusters, and an accessory hexameric protein involved in pyrophosphate release (for example MoaC in bacteria)<sup>55</sup>. MoaA harbours an N-terminal Fe-S cluster involved in radical SAM generation and a MoaA-specific C-terminal Fe-S cluster crucial for substrate binding<sup>55</sup>. Although the reaction mechanism of cPMP synthesis is not yet fully understood, it is well established that each carbon of the ribose and purine is incorporated into cPMP<sup>55,56</sup>. Furthermore, the structure of cPMP as a fully reduced pyranopterin with a terminal cyclic phosphate and geminal diol (Fig. 5) supports its physicochemical properties<sup>57</sup>. With respect to the observed geminal diol, it remains to be

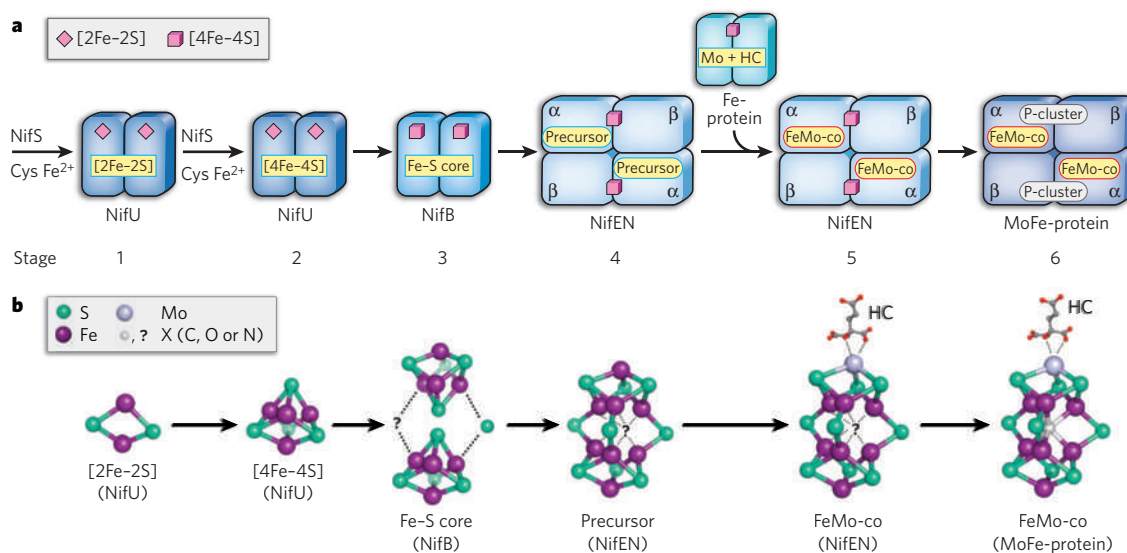


**Figure 3 | Biosynthesis of FeMo-co.** **a**, Sequence of events during FeMo-co assembly. The biosynthetic flow of FeMo-co is NifU–NifS → NifB → NifEN → MoFe-protein. The combined action of NifU–NifS generates small Fe–S fragments on NifU (stages 1 and 2), which are used as building blocks for the formation of a large Fe–S core on NifB (stage 3). This Fe–S core is further processed into a molybdenum-free precursor (stage 4), which can be converted to a mature FeMo-co on NifEN on Fe-protein-mediated insertion of molybdenum and homocitrate (stage 5). After the completion of FeMo-co assembly on NifEN, FeMo-co is delivered to its destined location in MoFe-protein (stage 6). The permanent metal

centres of the scaffold proteins are coloured pink; the transient cluster intermediates are coloured yellow. HC, homocitrate. **b**, Structures of intermediates during FeMo-co assembly. Shown are the cluster types that have been identified (on NifU, NifEN and MoFe-protein) or proposed (for NifB). Hypothetically, NifB could bridge two [4Fe-4S] clusters by inserting a sulphur atom along with the central atom, X, thereby generating an Fe–S scaffold that could be rearranged into a precursor closely resembling the core structure of the mature FeMo-co. In the case of the NifEN-associated precursor, only the 8Fe model is shown. The potential presence of X in the intermediates of FeMo-co biosynthesis is indicated by a question mark.



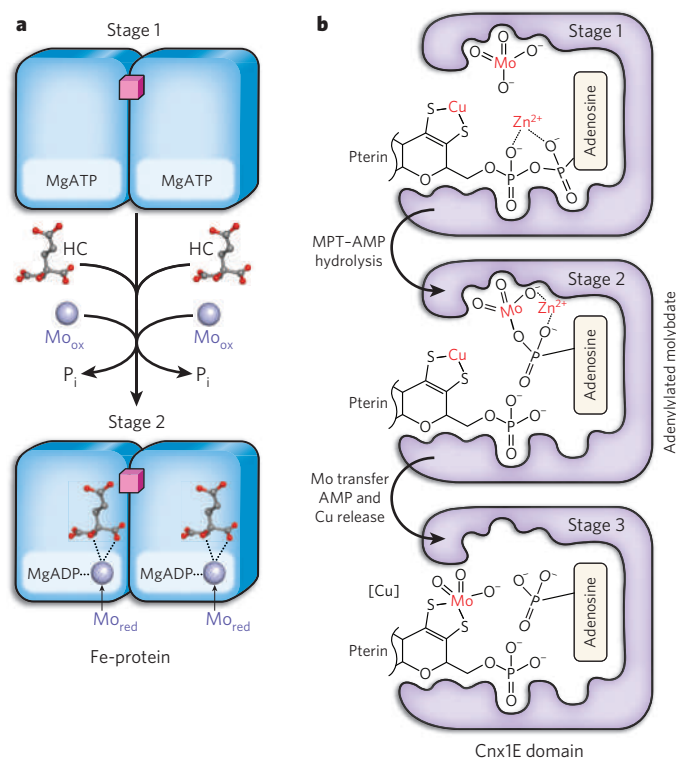


**Figure 4 | Proposed mechanisms for molybdate activation in FeMo-co and Moco biosynthesis.** **a**, For FeMo-co synthesis, in a MgATP-dependent process Fe-protein (stage 1) reduces molybdenum from a more oxidized state, such as molybdate ( $\text{Mo}_{\text{ox}}$ ), to a more reduced state ( $\text{Mo}_{\text{red}}$ ).  $\text{Mo}_{\text{red}}$  probably occupies the position of the  $\gamma$ -phosphate of MgATP (stage 2), which is released on ATP hydrolysis. Subsequently,  $\text{Mo}_{\text{red}}$ , in complex with homocitrate, can be inserted into the FeMo-co precursor, resulting in the formation of a mature FeMo-co on NifEN. **b**, In Moco biosynthesis, adenylylated MPT (MPT-AMP) and molybdate bind first in a cooperative manner to the Cnx1E domain (stage 1); subsequently,  $\text{Zn}^{2+}$  or  $\text{Mg}^{2+}$  promotes hydrolysis of the pyrophosphate bond in MPT-AMP. Stage 2 depicts the formation of a hypothetical reaction intermediate (adenylylated molybdate), which is thought to represent an unstable transition state that will immediately react with MPT, thus replacing bound copper at the MPT dithiolate (stage 3). The function of copper is still unknown, and it remains unclear whether molybdenum insertion is dependent on copper. According to the coordination of adenylylated molybdate, as well as the required modification of Moco in molybdenum enzymes of the sulphite oxidase and xanthine oxidase families (cysteine binding or sulphuration), released Moco is proposed to carry three oxo ligands.

determined at which point interconversion into a keto function takes place<sup>58</sup>. The functions of MoaA and MoaC are conserved throughout evolution, as eukaryotic orthologues are able to restore Moco biosynthesis in bacteria<sup>59</sup>.

To form the MPT dithiolate, two sulphur atoms are incorporated into cPMP by MPT synthase, a heterotetrameric complex of two small (MoaD in *E. coli*) and two large (MoaE in *E. coli*) subunits. MoaD carries a sulphur atom as thiocarboxylate at the conserved C-terminal double-glycine motif<sup>60</sup>, which is deeply buried in the large subunit to form the active site<sup>61</sup>. As one sulphur atom is bound per small subunit, a two-step mechanism for MPT dithiolate synthesis with the formation of a singly sulphurated intermediate has been demonstrated<sup>62</sup>. MPT synthase homologues in higher eukaryotes have been identified and characterized<sup>2</sup>. The expression of human MPT synthase is unusual, as both subunits are encoded by a bicistronic messenger RNA<sup>63</sup>.

In a separate reaction, sulphur is transferred to the small subunit of MPT synthase (Fig. 5). For this, in *E. coli* MoeB catalyses the adenylation of the C-terminal glycine residue of MoaD<sup>64</sup> in a process that is notably similar to the action of the ubiquitin-activating enzyme Uba1<sup>65</sup>. Together with MoaD, which has a ubiquitin-like fold, MPT synthase

provides an evolutionary origin for ubiquitin-like protein conjugation. AMP-activated MoaD becomes sulphurated by sulphide transfer, which is catalysed by a cysteine desulfurase<sup>66</sup> and a rhodanese<sup>67</sup>; the latter is fused in eukaryotes, as the C-terminal domain, to an MoeB-homologous domain<sup>68</sup>.

### Metal insertion and nucleotide attachment

On completion of MPT synthesis, the metal is transferred by a multistep reaction. Whereas *E. coli* encodes two separate proteins involved in this step, eukaryotes catalyse metal transfer by homologous two-domain proteins, such as Cnx1 (plants) and gephyrin (human) (Fig. 5), pointing to a functional cooperation between their domains. The physiological functions of their domains were discovered by determining the crystal structure of the N-terminal G domain of Cnx1 in complex with substrate and product<sup>69</sup>. The latter was found to be MPT-AMP, a common intermediate in bacterial and eukaryotic Moco synthesis<sup>70</sup> synthesized by G domains and homologous proteins (MogA in bacteria)<sup>71</sup>. Subsequently, a transfer of MPT-AMP to the E domain in Cnx1 was demonstrated<sup>72</sup>. In the presence of divalent cations and molybdate, bound MPT-AMP is hydrolysed and molybdenum is transferred to the MPT dithiolate, resulting in Moco release. This Moco most probably carries two oxo ligands and one OH group depicted (Figs 4a and 5) in a deprotonated form<sup>72</sup>, as supported by preliminary spectroscopic data derived from a storage-protein-bound Moco (see below; G.S., unpublished observation). There is no experimental evidence for a reduction of molybdenum at this state.

W-co biosynthesis is believed to be conserved up to MPT formation<sup>5</sup>, with differences in metal transfer. The tungsten-dependent archaeon *Pyrococcus furiosus* and related thermophiles lack *mogA*; instead, they all express genes encoding an MoaB-like protein, which also catalyses MPT adenylation, confirming MPT-AMP as an essential and general prerequisite before metal insertion<sup>73</sup>. Furthermore, *P. furiosus* expresses two different MoeA-like proteins, suggesting metal-selective activities<sup>5</sup>.

Finally, enzymes of the DMSOR family need to be further modified by the attachment of a nucleotide molecule (Fig. 5), a reaction dependent on the preceding metal insertion<sup>72</sup>. In *E. coli*, MoaB catalyses the conversion of MPT and GTP to Mo-bis-MGD<sup>74</sup>. Interaction studies with proteins catalysing metal insertion and Mo-bis-MGD formation identified a transient Moco-synthesizing machinery comprising MogA, MoeA, MoaB and molybdenum-enzyme-specific chaperones<sup>75</sup>.

### Cofactor maturation, storage and transfer

Molybdenum hydroxylases such as aldehyde oxidase and xanthine oxidase require a final step of maturation to gain enzymatic activity, namely the addition of a terminal sulphido ligand to the molybdenum centre, which is catalysed by a Moco sulphurase (that is, Aba3 in plants or HMCS (also known as MOCOS) in humans), a two-domain protein<sup>76</sup> acting as a homodimer (Fig. 6). In a pyridoxal phosphate-dependent manner, the N-terminal NifS-like domain abstracts sulphur from L-cysteine and forms a persulphide intermediate on a conserved cysteine residue<sup>77</sup>. Subsequently this sulphur is transferred via a second cysteine persulphide intermediate to bound Moco. Both of these steps are catalysed by the C-terminal Moco-binding domain of Aba3 (ref. 78), which selectively stabilizes sulphurated Moco. The same mechanism operates in HMCS (R.R.M., unpublished observations). Among prokaryotes, no homologues to eukaryotic Moco sulphurases have been found. However, for xanthine dehydrogenase from *R. capsulatus*, its enzyme-specific chaperone XdhC was found to fulfil Moco sulphuration<sup>79</sup>. By contrast with enzymes of the xanthine oxidase family, sulphite oxidase and nitrate reductase incorporate Moco without further modification. The proposed tri-oxo coordination of molybdenum in mature Moco<sup>72</sup> (Figs 4b and 5) suggests a simple mechanism of cysteine ligation to the molybdenum accompanied by loss of one of the oxygens as water.

As Moco is highly unstable once liberated from proteins, it was assumed that Moco does not occur in a 'free state'; rather, Moco might be bound to a carrier protein that protects and stores it until further use. Whereas some

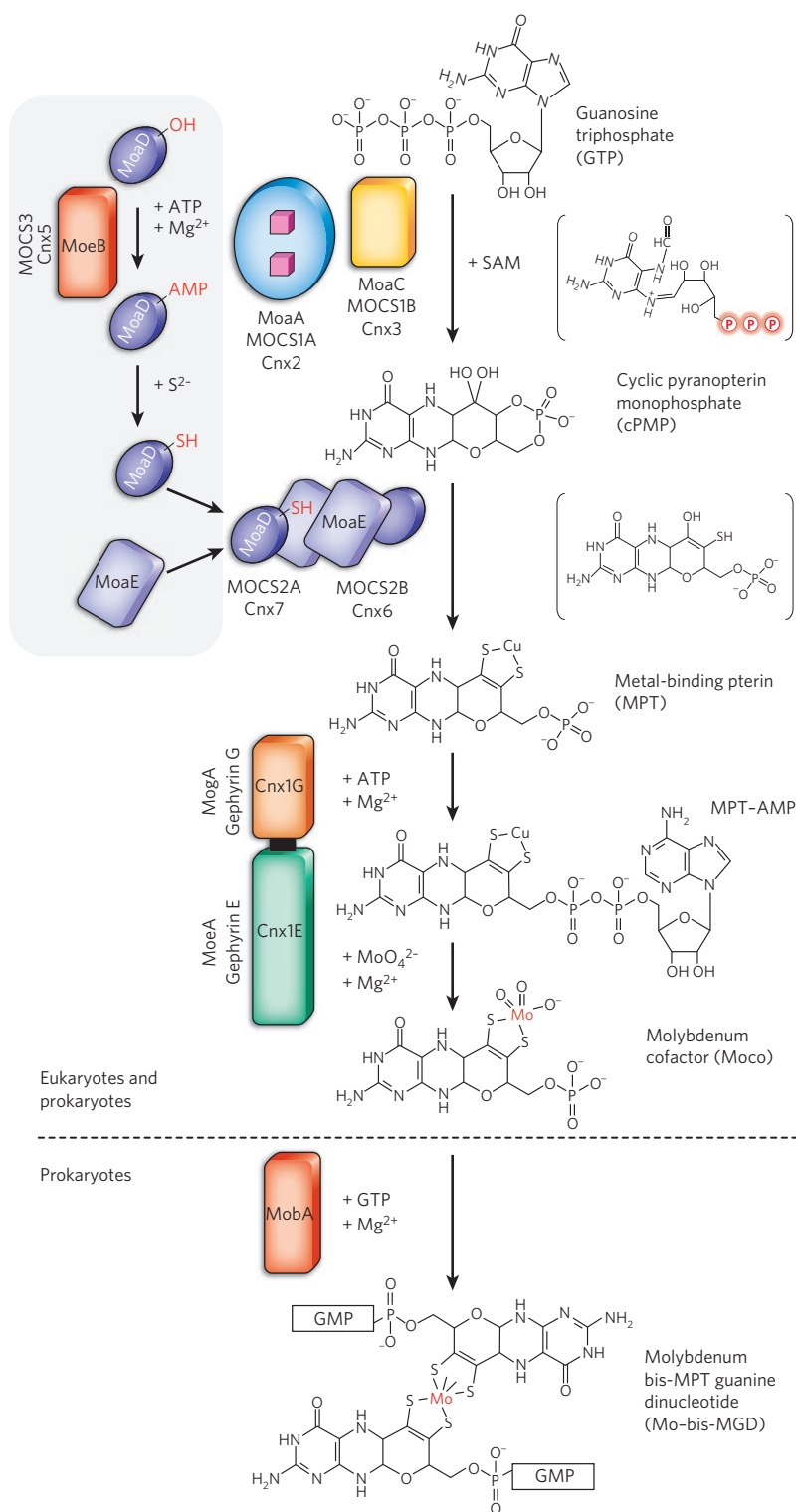


**Figure 5 | Biosynthesis of the pyranopterin-based molybdenum cofactors.** Shown is a generalized scheme of the pathway based on data derived from studies in *E. coli*, plants and humans. All known/characterized intermediates of the pathway are presented sequentially in the four steps in which Moco is synthesized. A fifth step present only in prokaryotes results in the formation of Mo-bis-MGD. Proposed (first step)<sup>55</sup> or partially characterized (second step) intermediates<sup>62</sup> are indicated in parentheses (circled P, phosphate group). The intermediate of the second step has been suggested on the basis of mechanistic studies of MPT synthase yielding an intermediate with a linear phosphate<sup>62</sup>. Proteins catalysing the individual steps are depicted in different colours, and a similar shade is applied to domains/proteins involved in nucleotide transfer. Homologous proteins from *E. coli* ('Mo' nomenclature), humans ('MOCS' nomenclature except gephyrin) and plants ('Cnx' nomenclature) are shown for comparison. The separate pathway regenerating MPT synthase is grouped within the grey box. For simplicity, only the MoeB protein is shown. We note that eukaryotes express fusion proteins that contain a MoeB domain and a C-terminal rhodanese-like domain involved in sulphur transfer to the small subunit of MPT synthase.

bacteria have molybdate-binding proteins such as Mop<sup>80</sup>, the alga *Chlamydomonas reinhardtii* produces a homotetrameric protein<sup>81</sup> that holds four Moco molecules in a surface-exposed binding pocket<sup>82</sup>. In higher plants, gene families with 8–12 homologous Moco-binding proteins have been discovered recently (R.R.M., unpublished observations). It is still unclear whether these proteins represent a buffer in which to store Moco or whether they are part of the default pathway for Moco allocation and insertion into molybdenum enzymes, a mechanism poorly understood in eukaryotes. Because Moco is deeply buried within the holoenzymes, it needs to be incorporated before the completion of folding and oligomerization of enzyme subunits/domains; for this, many bacterial molybdenum enzymes require the presence of chaperones, such as NarJ for *E. coli* nitrate reductase, TorD for trimethylamine *N*-oxide reductase and DmsD for DMSOR, which bind and protect the apoenzymes, assist in cofactor insertion and control transmembrane targeting<sup>83</sup>.

## Molybdenum homeostasis and disorders

### Cellular uptake

Bacterial molybdenum uptake requires specific systems to scavenge molybdate in the presence of competing anions. This involves a high-affinity ATP-binding cassette (ABC) transporter: molybdate is captured by one component, a periplasmic molybdate-binding protein (ModA), and transferred to another, the transmembrane channel (ModB). The crystal structure of an ABC transporter from *Archaeoglobus fulgidus*<sup>84</sup> suggests a conserved two-state mechanism by which ATP hydrolysis and the release of ADP plus P<sub>i</sub> at the cytoplasmic protein (ModC) controls conformation of the transmembrane protein, ModB. For tungstate, two ABC-type transporters, TupA–TupB–TupC and WtpA–WtpB–WtpC, have been identified<sup>73</sup>, the latter being highly selective for tungstate over molybdate owing to a unique octahedral substrate coordination<sup>85</sup>.

Algae and multicellular plants are the only eukaryotes for which the molybdate-uptake mechanisms have been recently determined. Two proteins belonging to the large sulphate-carrier family have been shown to transport molybdate with high affinity<sup>86–88</sup>. Unexpectedly, none of them was found to reside in the plasma membrane. Contradictory reports localized them to the endomembrane system<sup>86</sup> or the mitochondrial envelope<sup>88</sup>. It is likely that additional transporters, not only in autotrophs but also in animals, will be discovered soon.

### Molybdenum-iron and -copper crosstalk

Molybdenum metabolism is strictly dependent on iron metabolism at different levels. FeMo-co biosynthesis and nitrogenase maturation are based on the synthesis of complex Fe–S clusters, and enzymes participating in the first step of Moco biosynthesis contain two [4Fe–4S] clusters<sup>55</sup>. Furthermore, all molybdenum hydroxylases and several members

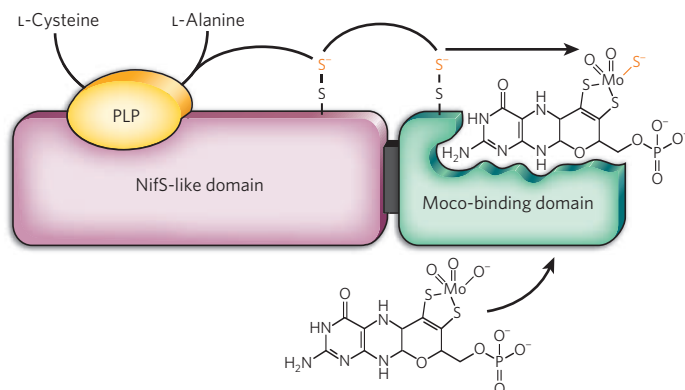


**Figure 6 | Domain structure and function of Moco sulphurase Aba3 from *Arabidopsis thaliana*.** The Aba3 protein and other homologues act as dimers catalysing the sulphuration of Moco, a reaction needed for the activation of molybdenum hydroxylases. Each Aba3 monomer can be divided into two domains, an N-terminal domain showing sequence homology to cysteine desulphurases (NifS-like enzymes) and a C-terminal domain that binds Moco. Recently, it was shown that a persulphide sulphur generated by the NifS-like domain is transferred to the C-terminal domain for the conversion of bound desulpho-Moco into sulphurated Moco, which is subsequently required to activate the target enzymes of Aba3 (that is, xanthine dehydrogenase and aldehyde oxidase). PLP, pyridoxal phosphate.

of the DMSOR family use Fe-S clusters for intramolecular electron transfer. Finally, enzymes of the sulphite oxidase family contain haem cofactors.

Recently, another link between the metabolic pathways of molybdenum and iron was discovered. In plants (and most probably also in animals), enzymes catalysing cPMP synthesis, such as Cnx2 and Cnx3, were localized within the mitochondrial matrix (R.R.M., unpublished observations), which necessitates the export of cPMP from mitochondria into the cytosol. Here, the mitochondrial ABC-type transporter Atm3 (also known as Sta1) from *A. thaliana* seems to fulfil a dual function: it not only exports Fe-S-cluster precursors to the cytosol<sup>89</sup>, but it is somehow also involved in cPMP translocation. Atm3-deficient plants showed defects in Fe-S-dependent cytosolic enzymes and accumulated large amounts of cPMP in mitochondria; consequently, activities of all molybdenum enzymes were strongly reduced (R.R.M., unpublished observations).

Only a few cases and conditions of limited molybdate availability have been reported so far<sup>5,90</sup>. Among these, the shortage of molybdenum in Australian farmland triggered excessive fertilization, resulting in molybdenum overload of the soil that caused pathological symptoms of molybdenosis in animals; this, in particular in ruminants, triggered secondary copper deficiency<sup>91</sup>. Later, these molybdenum-induced conditions of copper deficiency revealed the pathology of two copper-homeostasis disorders: Menkes disease (copper deficiency) and Wilson's disease (copper overload)<sup>92</sup> (see page 823). Consequently, potent copper chelators such as tetrathiomolybdates were used to treat Wilson's disease and a number of other disorders that are linked to copper homeostasis, such as neurodegeneration, cancer and inflammation<sup>93</sup>.

Another antagonism between molybdenum and copper has been found recently. The crystal structure of Cnx1G, which catalyses MPT adenylation, revealed the presence of a covalently bound copper ion (most probably Cu<sup>1+</sup>) at the MPT dithiolate in both the substrate- and product-bound states<sup>69</sup>. The function of copper during Moco biosynthesis is still unknown. It may participate in the sulphur-transfer reaction enabled by MPT synthase, act as a protecting group for MPT and/or function within molybdenum insertion<sup>72</sup>. *In vitro* studies suggested a competition between copper and molybdenum during Moco formation<sup>69</sup>, ultimately raising the question of whether Moco biosynthesis might be affected under conditions of copper overload or deficiency<sup>92</sup>.

### Molybdenum cofactor deficiency

Human Moco deficiency (MoCD) results in the complete loss of sulphite oxidase, xanthine oxidase and aldehyde oxidase activity. Patients

diagnosed with MoCD are classified into three groups according to the affected steps within the biosynthetic pathway (Fig. 7a). They are characterized by progressive neurological damage, leading to early childhood death in most cases<sup>94</sup>. Symptoms are mainly caused by the deficiency of sulphite oxidase protecting the organs (in particular the brain) from elevated concentrations of toxic sulphite.

The function of sulphite oxidase is important, as it represents the last step in the oxidative degradation of sulphur-containing amino acids and lipids. Mainly in liver, sequential events in cysteine catabolism through cysteine sulphinate (cytosol) and  $\beta$ -sulphinyl pyruvate (mitochondria) lead to the formation of sulphite (Fig. 7b). Sulphite oxidase, localized in the intermembrane space, oxidizes sulphite to sulphate. Under conditions of Moco or sulphite oxidase deficiency, sulphite accumulates in plasma and serum, crosses the blood-brain barrier and rapidly triggers neuronal death<sup>94</sup>. Impaired ATP synthesis has been suggested as one possible mechanism of sulphite toxicity<sup>95</sup>. Sulphite accumulation also triggers the reduction of cystine (Fig. 7b), the main carrier for cysteine in serum and plasma, which consequently causes the formation of S-sulphocysteine<sup>94</sup> (Fig. 7b), a potential agonist of glutamate receptors<sup>96</sup>. The latter may explain the observed seizures, convulsions, contractions and twitching associated with MoCD, causing damage of cortical neurons as documented by abnormal magnetic resonance imaging of the brain and loss of white matter<sup>94</sup>.

To study MoCD, an animal model with *Mocs1* knockout has been constructed<sup>97</sup>. Homozygous mice displayed a severe phenotype that reflects all biochemical characteristics of human Moco-deficient patients. They failed to thrive, and died within the first 12 days of life. The lethal

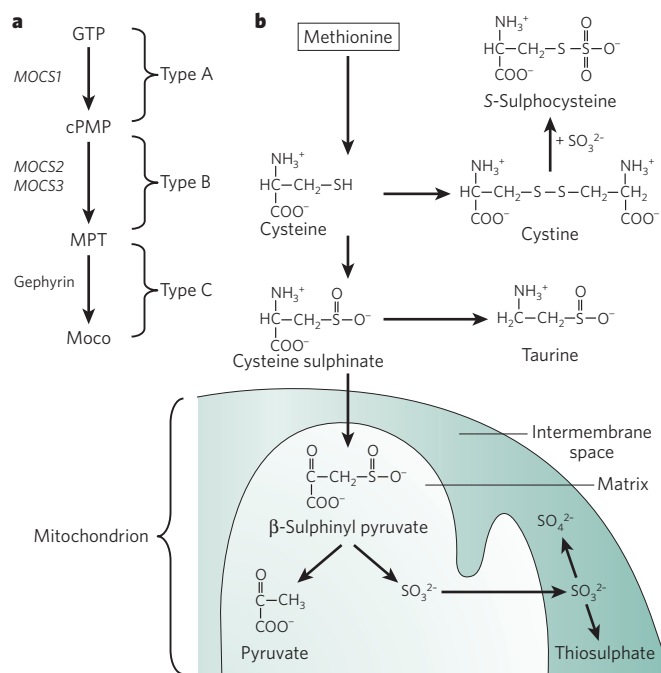


**Figure 7 | Human Moco deficiency.** a, Classification of Moco-deficient patients<sup>53</sup> according to the three distinguishable steps in human Moco biosynthesis. Genes encoding proteins catalysing the individual steps are shown. Type-A patients cannot form cPMP, whereas type-B patients accumulate cPMP, which is excreted in the urine. So far, only one type-C patient has been described, with a deletion of gephyrin due to an early stop codon in the gephyrin gene<sup>99,100</sup>, a protein also needed for the formation of inhibitory synapses. b, Degradation pathway of methionine and cysteine. Catabolic intermediates are depicted and metabolites that accumulate in Moco-deficient patients owing to increased sulphite concentrations are S-sulphocysteine, thiosulphate and taurine. Simultaneously, cystine concentrations are very low. S-Sulphocysteine is thought to make a major contribution to neurodegeneration because of its structural similarity to glutamate. We note that sulphite is formed from spontaneous decomposition of  $\beta$ -sulphinyl pyruvate. Sulphite crosses the mitochondrial inner membrane and is oxidized in the intermembrane space by molybdenum-dependent sulphite oxidase.



phenotype could be effectively neutralized by repeated injection of cPMP, which was purified from *E. coli*<sup>98</sup>. Mice treated with cPMP developed normally, gained weight and reached adulthood and fertility like their wild-type littermates. Notably, withdrawal of cPMP from *Mocs1*-knockout mice caused death within 10–14 days. These promising results were verified by a recent clinical trial (G.S., unpublished observations).

## Conclusion

The versatile redox chemistry of molybdenum is mirrored by the plethora and complexity of enzymes using molybdenum and, to some extent, tungsten. Nature has developed two very different systems to control the redox state and catalytic power of molybdenum. Although the contribution of each cofactor scaffold to the overall chemistry of a given enzyme requires further investigation, it is likely that the various scaffolds represent pathways generating sulphur-containing chelators that can trap, activate and control the transition elements as catalysts.

Future research in the field of molybdenum enzymes is likely to focus on the mechanistic details of cofactor biosynthesis, cofactor allocation and the functions of cofactors in particular enzymes. Further understanding of the differences between molybdenum and tungsten biochemistry will help to explain the unique presence of molybdenum in eukaryotes and to answer fundamental questions regarding functional specificity, metal selectivity, regulation, allocation, compartmentalization and assembly of this fascinating family of enzymes and cofactors.

As seen for both FeMo-co and Moco biosynthesis, different assembly machineries can use similar mechanisms, such as the radical SAM-based chemistry and the nucleotide-assisted molybdenum activation, which are employed for the synthesis of both cofactors. The role of molybdenum in other homeostatic circuits, such as copper and iron metabolism, awaits further investigation, which could address questions regarding the pathophysiology of related metabolic disorders. Finally, the biosynthetic machineries of these cofactors or the enzymes themselves (for example nitrogenase) are ancient natural inventions. Some of the proteins are precursors of those with specialized functions in eukaryotes, such as ubiquitin-like protein conjugation (MPT synthesis)<sup>64</sup> and G-protein-based signalling<sup>3</sup>; others, such as gephyrin, which is crucial for synaptogenesis<sup>99</sup>, have gathered additional functions. ■

- Dos Santos, P. C., Dean, D. R., Hu, Y. & Ribbe, M. W. Formation and insertion of the nitrogenase iron-molybdenum cofactor. *Chem. Rev.* **104**, 1159–1173 (2004).
- Schwarz, G. Molybdenum cofactor biosynthesis and deficiency. *Cell. Mol. Life Sci.* **62**, 2792–2810 (2005).
- Hille, R. Molybdenum and tungsten in biology. *Trends Biochem. Sci.* **27**, 360–367 (2002).
- Zhang, Y. & Gladyshev, V. N. Molybdoproteomes and evolution of molybdenum utilization. *J. Mol. Biol.* **379**, 881–899 (2008).
- Beyers, L. E., Hagedoorn, P.-L. & Hagen, W. R. The bioinorganic chemistry of tungsten. *Coord. Chem. Rev.* **253**, 269–290 (2009).
- Burgess, B. K. & Lowe, D. J. Mechanism of molybdenum nitrogenase. *Chem. Rev.* **96**, 2983–3012 (1996).
- Einsle, O. et al. Nitrogenase MoFe-protein at 1.16 Å resolution: a central ligand in the FeMo-cofactor. *Science* **297**, 1696–1700 (2002).
- Rajagopalan, K. V. & Johnson, J. L. The pterin molybdenum cofactors. *J. Biol. Chem.* **267**, 10199–10202 (1992).
- Eady, R. R. Structure–function relationships of alternative nitrogenases. *Chem. Rev.* **96**, 3013–3030 (1996).
- Schindelin, H. et al. Structure of ADP-AIF<sub>4</sub><sup>−</sup>-stabilized nitrogenase complex and its implications for signal transduction. *Nature* **387**, 370–376 (1997).
- Rothery, R. A., Workun, G. J. & Weiner, J. H. The prokaryotic complex iron-sulfur molybdoenzyme family. *Biochim. Biophys. Acta* **1778**, 1897–1929 (2008). This paper is a systematic and comprehensive overview of prokaryotic molybdenum-containing enzymes of the DMSOR family.
- Hille, R. Molybdenum-containing hydroxylases. *Arch. Biochem. Biophys.* **433**, 107–116 (2005). This paper is a comprehensive overview of structure and reaction mechanisms of molybdenum-containing hydroxylases of the xanthine oxidase family.
- Feng, C., Tollin, G. & Enemark, J. H. Sulfite oxidizing enzymes. *Biochim. Biophys. Acta* **1774**, 527–539 (2007).
- Moura, J. J., Brondino, C. D., Trincão, J. & Romão, M. J. Mo and W bis-MGD enzymes: nitrate reductases and formate dehydrogenases. *J. Biol. Inorg. Chem.* **9**, 791–799 (2004).
- Bertero, M. G. et al. Insights into the respiratory electron transfer pathway from the structure of nitrate reductase A. *Nature Struct. Biol.* **10**, 681–687 (2003).
- Kisker, C. et al. Molecular basis of sulfite oxidase deficiency from the structure of sulfite oxidase. *Cell* **91**, 973–983 (1997).
- Fischer, K. et al. Crystal structure of the yeast nitrate reductase molybdenum domain provides insight into eukaryotic nitrate assimilation. *Plant Cell* **17**, 1167–1179 (2005).
- Eilers, T. et al. Identification and biochemical characterization of *Arabidopsis thaliana* sulfite oxidase. A new player in plant sulfur metabolism. *J. Biol. Chem.* **276**, 46989–46994 (2001).
- Schrader, N. et al. The crystal structure of plant sulfite oxidase provides insights into sulfite oxidation in plants and animals. *Structure* **11**, 1251–1263 (2003).
- Kappler, U. & Bailey, S. Molecular basis of intramolecular electron transfer in sulfite-oxidizing enzymes is revealed by high resolution structure of a heterodimeric complex of the catalytic molybdopterin subunit and a c-type cytochrome subunit. *J. Biol. Chem.* **280**, 24999–25007 (2005).
- Hansch, R. et al. Plant sulfite oxidase as novel producer of H<sub>2</sub>O<sub>2</sub>: combination of enzyme catalysis with a subsequent non-enzymatic reaction step. *J. Biol. Chem.* **281**, 6884–6888 (2006).
- Campbell, W. H. Nitrate reductase structure, function and regulation: bridging the gap between biochemistry and physiology. *Annu. Rev. Plant Physiol. Plant Mol. Biol.* **50**, 277–303 (1999).
- Mendel, R. R. & Bittner, F. Cell biology of molybdenum. *Biochim. Biophys. Acta* **1763**, 621–635 (2006).
- Enroth, C. et al. Crystal structures of bovine milk xanthine dehydrogenase and xanthine oxidase: structure-based mechanism of conversion. *Proc. Natl Acad. Sci. USA* **97**, 10723–10728 (2000).
- Truglio, J. J. et al. Crystal structures of the active and alloxanthine-inhibited forms of xanthine dehydrogenase from *Rhodospirillum rubrum*. *Structure* **10**, 115–125 (2002).
- Garattini, E. et al. Mammalian molybdo-flavoenzymes, an expanding family of proteins: structure, genetics, regulation, function and pathophysiology. *Biochem. J.* **372**, 15–32 (2003).
- Seo, M. et al. The *Arabidopsis* aldehyde oxidase 3 (AO3) gene product catalyzes the final step in abscisic acid biosynthesis in leaves. *Proc. Natl Acad. Sci. USA* **97**, 12908–12913 (2000).
- Neumann, M. et al. A periplasmic aldehyde oxidoreductase represents the first molybdopterin cytosine dinucleotide cofactor containing molybdo-flavoenzyme from *Escherichia coli*. *FEBS J.* **276**, 2762–2774 (2009).
- Dobbeek, H. et al. Catalysis at a dinuclear [CuS<sub>2</sub>Mo(=O)OH] cluster in a CO dehydrogenase resolved at 1.1-Å resolution. *Proc. Natl Acad. Sci. USA* **99**, 15971–15976 (2002).
- Harrison, R. Structure and function of xanthine oxidoreductase: where are we now? *Free Radic. Biol. Med.* **33**, 774–797 (2002).
- Havemeyer, A. et al. Identification of the missing component in the mitochondrial benzamidoxime prodrug-converting system as a novel molybdenum enzyme. *J. Biol. Chem.* **281**, 34796–34802 (2006).
- Groisman, S. & Holm, R. Biomimetic chemistry of iron, nickel, molybdenum, and tungsten in sulfur-ligated protein sites. *Biochemistry* **48**, 2310–2320 (2009). This paper is a comprehensive review of the chemical synthesis of analogues of pterin cofactors of molybdenum enzymes and the FeMo-co and P-cluster of nitrogenase MoFe-protein.
- Hu, Y. et al. Assembly of nitrogenase MoFe protein. *Biochemistry* **47**, 3973–3981 (2008). This paper reports a recent development in the biosynthesis of the FeMo-co and P-cluster of nitrogenase MoFe-protein.
- Smith, A. D. et al. NifS-mediated assembly of [4Fe-4S] clusters in the N- and C-terminal domains of the NifU scaffold protein. *Biochemistry* **44**, 12955–12969 (2005).
- Johnson, D. C., Dean, D. R., Smith, A. D. & Johnson, M. K. Structure, function, and formation of biological iron-sulfur clusters. *Annu. Rev. Biochem.* **74**, 247–281 (2005).
- Allen, R. M., Chatterjee, R., Ludden, P. W. & Shah, V. K. Incorporation of iron and sulfur from NifB cofactor into the iron-molybdenum cofactor of dinitrogenase. *J. Biol. Chem.* **270**, 26890–26896 (1995).
- Schmid, B. et al. Structure of a cofactor-deficient nitrogenase MoFe protein. *Science* **296**, 352–356 (2002).
- Curatti, L., Ludden, P. W. & Rubio, L. M. NifB-dependent *in vitro* synthesis of the iron-molybdenum cofactor of nitrogenase. *Proc. Natl Acad. Sci. USA* **103**, 5297–5301 (2006).
- Hu, Y., Fay, A. W. & Ribbe, M. W. Identification of a nitrogenase FeMo cofactor precursor on NifEN complex. *Proc. Natl Acad. Sci. USA* **102**, 3236–3241 (2005).
- Corbett, M. C. et al. Structural insights into a protein-bound iron-molybdenum cofactor precursor. *Proc. Natl Acad. Sci. USA* **103**, 1238–1243 (2006). This paper is the first X-ray absorption spectroscopy/extended X-ray absorption fine structure (XAS/EXAFS)-based structural analysis of the FeMo-co precursor on NifEN.
- Hu, Y. et al. FeMo cofactor maturation on NifEN. *Proc. Natl Acad. Sci. USA* **103**, 17119–17124 (2006).
- Zheng, L., White, R. H. & Dean, D. R. Purification of the *Azotobacter vinelandii* nifV-encoded homocitrate synthase. *J. Bacteriol.* **179**, 5963–5966 (1997).
- Imperial, J., Ugalde, R. A., Shah, V. K. & Brill, W. J. Role of the nifQ gene product in the incorporation of molybdenum into nitrogenase in *Klebsiella pneumoniae*. *J. Bacteriol.* **158**, 187–194 (1984).
- Hernandez, J. A. et al. Metal trafficking for nitrogen fixation: NifQ donates molybdenum to NifEN/NifH for the biosynthesis of the nitrogenase FeMo-cofactor. *Proc. Natl Acad. Sci. USA* **105**, 11679–11684 (2008).
- Hu, Y. et al. Nitrogenase Fe protein: a molybdate/homocitrate insertase. *Proc. Natl Acad. Sci. USA* **103**, 17125–17130 (2006).
- Georgiadis, M. M. et al. Crystallographic structure of the nitrogenase iron protein from *Azotobacter vinelandii*. *Science* **257**, 1653–1659 (1992).
- Rubio, L. M. et al. Cloning and mutational analysis of the γ gene from *Azotobacter vinelandii* defines a new family of proteins capable of metallocluster binding and protein stabilization. *J. Biol. Chem.* **277**, 14299–14305 (2002).
- Hu, Y. et al. Molecular insights into nitrogenase FeMoco insertion: TRP-444 of MoFe protein α-subunit locks FeMoco in its binding site. *J. Biol. Chem.* **281**, 30534–30541 (2006).

49. Hu, Y., Fay, A. W. & Ribbe, M. W. Molecular insights into nitrogenase FeMo cofactor insertion: the role of His 362 of the MoFe protein a subunit in FeMo cofactor incorporation. *J. Biol. Inorg. Chem.* **12**, 449–460 (2007).
50. Fay, A. W., Hu, Y., Schmid, B. & Ribbe, M. W. Molecular insights into nitrogenase FeMo cofactor insertion — the role of His 274 and His 451 of MoFe protein a subunit. *J. Inorg. Biochem.* **101**, 1630–1641 (2007).
51. Schwarz, G. & Mendel, R. R. Molybdenum cofactor biosynthesis and molybdenum enzymes. *Annu. Rev. Plant Biol.* **57**, 623–647 (2006).
52. Schwarz, G., Hagedoorn, P. L. & Fischer, K. In *Molecular Microbiology of Heavy Metals* (eds Nies, D. H. & Silver, S.) 421–451 (Springer, 2007).
53. Reiss, J. & Johnson, J. L. Mutations in the molybdenum cofactor biosynthetic genes *MOCS1*, *MOCS2*, and *GEPH*. *Hum. Mutat.* **21**, 569–576 (2003).
54. Wuebbens, M. M. & Rajagopalan, K. V. Structural characterization of a molybdopterin precursor. *J. Biol. Chem.* **268**, 13493–13498 (1993).
55. Hanzelmann, P. & Schindelin, H. Binding of 5'-GTP to the C-terminal FeS cluster of the radical S-adenosylmethionine enzyme MoaA provides insights into its mechanism. *Proc. Natl Acad. Sci. USA* **103**, 6829–6834 (2006).  
**This paper describes the structural basis of radical SAM-based conversion of GTP into cPMP.**
56. Wuebbens, M. M. & Rajagopalan, K. V. Investigation of the early steps of molybdopterin biosynthesis in *Escherichia coli* through the use of *in vivo* labeling studies. *J. Biol. Chem.* **270**, 1082–1087 (1995).
57. Santamaria-Araujo, J. A. *et al.* The tetrahydropyranopterine structure of the sulfur-free and metal-free molybdenum cofactor precursor. *J. Biol. Chem.* **279**, 15994–15999 (2004).
58. Daniels, J. N., Wuebbens, M. M., Rajagopalan, K. V. & Schindelin, H. Crystal structure of a molybdopterin synthase-precursor Z complex: insight into its sulfur transfer mechanism and its role in molybdenum cofactor deficiency. *Biochemistry* **47**, 615–626 (2008).
59. Hanzelmann, P., Schwarz, G. & Mendel, R. R. Functionality of alternative splice forms of the first enzymes involved in human molybdenum cofactor biosynthesis. *J. Biol. Chem.* **277**, 18303–18312 (2002).
60. Gutzke, G., Fischer, B., Mendel, R. R. & Schwarz, G. Thiocarboxylation of molybdopterin synthase provides evidence for the mechanism of dithiolene formation in metal-binding pterins. *J. Biol. Chem.* **276**, 36268–36274 (2001).
61. Rudolph, M. J., Wuebbens, M. M., Rajagopalan, K. V. & Schindelin, H. Crystal structure of molybdopterin synthase and its evolutionary relationship to ubiquitin activation. *Nature Struct. Biol.* **8**, 42–46 (2001).
62. Wuebbens, M. M. & Rajagopalan, K. V. Mechanistic and mutational studies of *Escherichia coli* molybdopterin synthase clarify the final step of molybdopterin biosynthesis. *J. Biol. Chem.* **278**, 14523–14532 (2003).
63. Stallmeyer, B. *et al.* Human molybdopterin synthase gene: identification of a bicistronic transcript with overlapping reading frames. *Am. J. Hum. Genet.* **64**, 698–705 (1999).
64. Lake, M. W., Wuebbens, M. M., Rajagopalan, K. V. & Schindelin, H. Mechanism of ubiquitin activation revealed by the structure of a bacterial MoeB–MoaD complex. *Nature* **414**, 325–329 (2001).
65. Lee, I. & Schindelin, H. Structural insights into E1-catalyzed ubiquitin activation and transfer to conjugating enzymes. *Cell* **134**, 268–278 (2008).
66. Leimkuhler, S. & Rajagopalan, K. V. A sulfurtransferase is required in the transfer of cysteine sulfur in the *in vitro* synthesis of molybdopterin from precursor Z in *Escherichia coli*. *J. Biol. Chem.* **276**, 22024–22031 (2001).
67. Forlani, F. *et al.* The cysteine-desulfurase IscS promotes the production of the rhodanese RhdA in the persulfurated form. *FEBS Lett.* **579**, 6786–6790 (2005).
68. Matthies, A., Rajagopalan, K. V., Mendel, R. R. & Leimkuhler, S. Evidence for the physiological role of a rhodanese-like protein for the biosynthesis of the molybdenum cofactor in humans. *Proc. Natl Acad. Sci. USA* **101**, 5946–5951 (2004).
69. Kuper, J. *et al.* Structure of the molybdopterin-bound Cnx1G domain links molybdenum and copper metabolism. *Nature* **430**, 803–806 (2004).  
**This paper reports the first protein-complex structures of Moco intermediates and the identification of a novel reaction intermediate essential for metal transfer.**
70. Bevers, L. E. *et al.* Function of MoaB proteins in the biosynthesis of the molybdenum and tungsten cofactors. *Biochemistry* **47**, 949–956 (2008).
71. Llamas, A., Mendel, R. R. & Schwarz, G. Synthesis of adenylated molybdopterin: an essential step for molybdenum insertion. *J. Biol. Chem.* **279**, 55241–55246 (2004).
72. Llamas, A. *et al.* The mechanism of nucleotide-assisted molybdenum insertion into molybdopterin. A novel route toward metal cofactor assembly. *J. Biol. Chem.* **281**, 18343–18350 (2006).
73. Bevers, L. E., Hagedoorn, P. L., Krijger, G. C. & Hagen, W. R. Tungsten transport protein A (WtpA) in *Pyrococcus furiosus*: the first member of a new class of tungstate and molybdate transporters. *J. Bacteriol.* **188**, 6498–6505 (2006).
74. Stevenson, C. E. M. *et al.* Crystal structure of the molybdenum cofactor biosynthesis protein MoaA from *Escherichia coli* at near-atomic resolution. *Structure* **8**, 1115–1125 (2000).
75. Vergnes, A. *et al.* Involvement of the molybdenum cofactor biosynthetic machinery in the maturation of the *Escherichia coli* nitrate reductase A. *J. Biol. Chem.* **279**, 41398–41403 (2004).
76. Bittner, F., Oreb, M. & Mendel, R. R. ABA3 is a molybdenum cofactor sulfurase required for activation of aldehyde oxidase and xanthine dehydrogenase in *Arabidopsis thaliana*. *J. Biol. Chem.* **276**, 40381–40384 (2001).
77. Heidenreich, T., Wollers, S., Mendel, R. R. & Bittner, F. Characterization of the NifS-like domain of ABA3 from *Arabidopsis thaliana* provides insight into the mechanism of molybdenum cofactor sulfuration. *J. Biol. Chem.* **280**, 4213–4218 (2005).
78. Wollers, S. *et al.* Binding of sulfated molybdenum cofactor to the C-terminal domain of ABA3 from *Arabidopsis thaliana* provides insight into the mechanism of molybdenum cofactor sulfuration. *J. Biol. Chem.* **283**, 9642–9650 (2008).  
**This paper describes the mechanism and platform principle of Moco sulphuration in eukaryotes.**
79. Neumann, M. *et al.* *Rhodobacter capsulatus* XdhC is involved in molybdenum cofactor binding and insertion into xanthine dehydrogenase. *J. Biol. Chem.* **281**, 15701–15708 (2006).
80. Pau, R. N. & Lawson, D. M. Transport, homeostasis, regulation, and binding of molybdate and tungstate to proteins. *Met. Ions Biol. Syst.* **39**, 31–74 (2002).
81. Ataya, F. S. *et al.* *Mcp1* encodes the molybdenum cofactor carrier protein in *Chlamydomonas reinhardtii* and participates in protection, binding, and storage functions of the cofactor. *J. Biol. Chem.* **278**, 10885–10890 (2003).
82. Fischer, K. *et al.* Function and structure of the molybdenum cofactor carrier protein from *Chlamydomonas reinhardtii*. *J. Biol. Chem.* **281**, 30186–30194 (2006).
83. Sargent, F. Constructing the wonders of the bacterial world: biosynthesis of complex enzymes. *Microbiology* **153**, 633–651 (2007).
84. Hollenstein, K., Frei, D. C. & Locher, K. P. Structure of an ABC transporter in complex with its binding protein. *Nature* **446**, 213–216 (2007).  
**This paper provides the first structural insight into the family of molybdate and tungstate ABC transporters**
85. Hollenstein, K. *et al.* Distorted octahedral coordination of tungstate in a subfamily of specific binding proteins. *J. Biol. Inorg. Chem.* **14**, 663–672 (2009).
86. Tomatsu, H. *et al.* An *Arabidopsis thaliana* high-affinity molybdate transporter required for efficient uptake of molybdate from soil. *Proc. Natl Acad. Sci. USA* **104**, 18807–18812 (2007).
87. Tejada-Jimenez, M. *et al.* A high-affinity molybdate transporter in eukaryotes. *Proc. Natl Acad. Sci. USA* **104**, 20126–20130 (2007).
88. Baxter, I. *et al.* Variation in molybdenum content across broadly distributed populations of *Arabidopsis thaliana* is controlled by a mitochondrial molybdenum transporter (MOT1). *PLoS Genet.* **4**, e1000004 (2008).
89. Chen, S. *et al.* Functional characterization of AtATM1, AtATM2, and AtATM3, a subfamily of *Arabidopsis* half-molecule ATP-binding cassette transporters implicated in iron homeostasis. *J. Biol. Chem.* **282**, 21561–21571 (2007).
90. Suttle, N. F. The interactions between copper, molybdenum, and sulphur in ruminant nutrition. *Annu. Rev. Nutr.* **11**, 121–140 (1991).
91. Mason, J. Thiomolybdates: mediators of molybdenum toxicity and enzyme inhibitors. *Toxicology* **42**, 99–109 (1986).
92. Mercer, J. F. The molecular basis of copper-transport diseases. *Trends Mol. Med.* **7**, 64–69 (2001).
93. Brewer, G. J. Anticopper therapy against cancer and diseases of inflammation and fibrosis. *Drug Discov. Today* **10**, 1103–1109 (2005).
94. Johnson, J. L. & Duran, M. In *The Metabolic and Molecular Bases of Inherited Disease* (eds Scriver, C. R., Beaudet, A. L., Sly, W. S. & Valle, D.) 3163–3177 (McGraw-Hill, 2001).
95. Zhang, X., Vincent, A. S., Halliwell, B. & Wong, K. P. A mechanism of sulfite neurotoxicity: direct inhibition of glutamate dehydrogenase. *J. Biol. Chem.* **279**, 43035–43045 (2004).
96. Tan, W. H. *et al.* Isolated sulfite oxidase deficiency: a case report with a novel mutation and review of the literature. *Pediatrics* **116**, 757–766 (2005).
97. Lee, H.-J. *et al.* Molybdenum cofactor-deficient mice resemble the phenotype of human patients. *Hum. Mol. Genet.* **11**, 3309–3317 (2002).
98. Schwarz, G. *et al.* Rescue of lethal molybdenum cofactor deficiency by a biosynthetic precursor from *Escherichia coli*. *Hum. Mol. Genet.* **13**, 1249–1255 (2004).  
**This paper describes the successful therapeutic use of a Moco intermediate (cPMP) to cure Moco deficiency.**
99. Stallmeyer, B. *et al.* The neurotransmitter receptor-anchoring protein gephyrin reconstitutes molybdenum cofactor biosynthesis in bacteria, plants, and mammalian cells. *Proc. Natl Acad. Sci. USA* **96**, 1333–1338 (1999).
100. Reiss, J. *et al.* A mutation in the gene for the neurotransmitter receptor-clustering protein gephyrin causes a novel form of molybdenum cofactor deficiency. *Am. J. Hum. Genet.* **68**, 208–213 (2001).

**Acknowledgements** Support from the Deutsche Forschungsgemeinschaft (G.S., R.R.M.), the Bundesministerium für Bildung und Forschung (G.S.), the Fonds der Chemischen Industrie (G.S.), the European Union (R.R.M.) and the US National Institutes of Health (grant GM-67626; M.W.R.) is gratefully acknowledged, as is the contribution of all co-workers, especially graduate students and post-docs, during the past ten years.

**Author Information** Reprints and permissions information is available at [www.nature.com/reprints](http://www.nature.com/reprints). The authors declare no competing financial interests. Correspondence should be addressed to G.S. ([gschwarz@uni-koeln.de](mailto:gschwarz@uni-koeln.de)).

# Mechanistic considerations of halogenating enzymes

Alison Butler<sup>1</sup> & Moriah Sandy<sup>1</sup>

**In nature, halogenation is a strategy used to increase the biological activity of secondary metabolites, compounds that are often effective as drugs. However, halides are not particularly reactive unless they are activated, typically by oxidation. The pace of discovery of new enzymes for halogenation is increasing, revealing new metalloenzymes, flavoenzymes, S-adenosyl-L-methionine (SAM)-dependent enzymes and others that catalyse halide oxidation using dioxygen, hydrogen peroxide and hydroperoxides, or that promote nucleophilic halide addition reactions.**

Halogenated natural products have been isolated in abundance from marine eukaryotic organisms, but also increasingly from microorganisms that inhabit marine and terrestrial environments (Fig. 1). These halogenated compounds range from peptides, polyketides, indoles, terpenes, acetogenins and phenols to volatile halogenated hydrocarbons (for example bromoform, chloroform and dibromomethane) that are produced on a very large scale<sup>1–3</sup>. Many halogenated marine metabolites possess biological activities of pharmacological interest, including anticancer, antifungal, antibacterial, antiviral and anti-inflammatory activities. The biogenesis of these compounds has intrigued scientists for decades.

The first halogenating enzyme to be discovered, in the 1960s, was the haem (iron-containing porphyrin) chloroperoxidase (CPO) from the terrestrial fungus *Caldariomyces fumago*, which produces the chlorinated natural product caldariomycin<sup>4</sup>. Some time later, haloperoxidase enzymes were proposed in the biogenesis of certain halogenated marine natural products<sup>5,6</sup>, although this was long before haloperoxidases or other halogenating enzymes had been discovered in marine organisms. Since the discovery of haem CPO, other haem haloperoxidases<sup>7–9</sup>, vanadium haloperoxidases<sup>10–12</sup> and non-haem iron halogenases<sup>13</sup>, as well as non-metallo-, flavin-dependent halogenases<sup>14</sup>, SAM-dependent chlorinases and fluorinases<sup>15</sup>, and methyl halide transferases<sup>16</sup>, have been discovered. For recent reviews, see refs 14, 15, 17–23.

Haloperoxidases catalyse electrophilic halogenation reactions, whereas the non-haem iron halogenases catalyse radical halogenation reactions and SAM-dependent halogenases catalyse nucleophilic halogenation reactions. Haloperoxidases have traditionally been classified on the basis of the most electrophilic halide that is readily oxidized. Thus, chloroperoxidases oxidize chloride, bromide and iodide by hydrogen peroxide (H<sub>2</sub>O<sub>2</sub>), whereas iodoperoxidases oxidize only iodide in this way. Hydrogen peroxide lacks the thermodynamic potential to oxidize fluoride; thus, enzymes catalysing fluorination are not peroxidases. The overall stoichiometry of the haloperoxidase reaction is consumption of one equivalent of H<sub>2</sub>O<sub>2</sub> per halogenated product produced (Fig. 2, reaction 1).

One class of halogenase, the non-haem iron enzymes, uses dioxygen (O<sub>2</sub>) to activate halide (Fig. 2, reaction 2); these enzymes catalyse radical halogenation reactions at aliphatic carbon sites. The overall stoichiometry is consumption of one equivalent of  $\alpha$ -ketoglutaric acid and O<sub>2</sub> per halogenated equivalent produced (Fig. 2, reaction 2). Flavin-dependent halogenases activate O<sub>2</sub> by means of formation of flavin-bound hydroperoxide, which then oxidizes the halide (Fig. 2, reaction 3). This class of halo-

genating enzyme is a two-component system in which a flavin reductase is required to keep the halogenase reduced for catalytic turnover. These enzymes catalyse reactions that more closely resemble the electrophilic haloperoxidases that are mediated by 'HOX-like' species. Finally, SAM-dependent enzymes catalyse nucleophilic substitution, generating 5'-halo-5'-deoxyadenosine and L-methionine (Fig. 2, reaction 4). In this review we focus on the mechanisms of metalloenzyme-catalysed halogenation reactions, emphasizing the activation of halides by O<sub>2</sub> and H<sub>2</sub>O<sub>2</sub>, and the nature of the halogenation step.

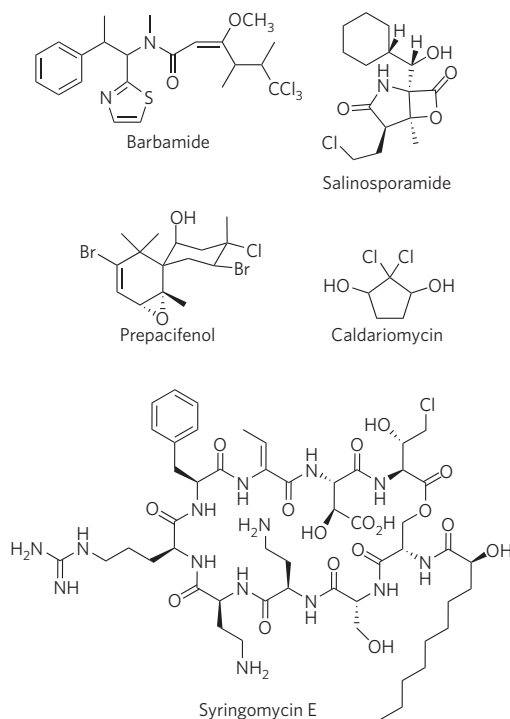
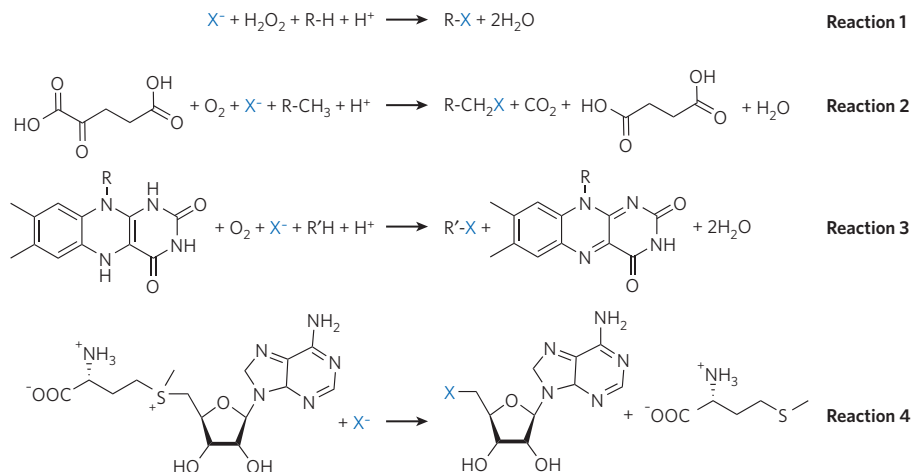


**Figure 1 | Halogenated natural products.** A few examples of halogenated natural products that have been discovered in the past few decades. These natural products have been isolated from marine eukaryotic organisms, as well as microorganisms that inhabit marine and terrestrial environments.

<sup>1</sup>Department of Chemistry and Biochemistry, University of California, Santa Barbara, California 93106, USA.



**Figure 2 | Biologically relevant halogenation reactions.** Four distinct classes of enzyme have been discovered that carry out halogenation reactions. Reaction 1, which encompasses electrophilic halogenation, is catalysed by haloperoxidases such as the haem-containing or vanadate-containing enzymes. Reaction 2 is carried out by  $\alpha$ -ketoglutarate-dependent non-haem iron halogenases and is characteristic of radical halogenation at unactivated C–H centres. Reaction 3 is catalysed by flavin-dependent halogenases. Reaction 4 shows the SAM-dependent halogenase reaction. X, halogen atom; R, R', alkyl group.



### Haem haloperoxidases

The fungus *C. fumago*, from which the first haloperoxidase, Fe(III)-haem CPO, was derived<sup>4</sup>, produces the chlorinated natural product caldariomycin, which is thought to be synthesized by CPO. The optimal pH for chlorination turnover by haem CPO is pH 2.7 (ref. 4). Interestingly, CPO is used to catalyse a number of oxidation reactions in the absence of chloride. These oxidation reactions are generally carried out at neutral pH, whereas chlorination occurs only at low pH. The active site of Fe(III)-haem CPO contains Fe(III)-protoporphyrin IX coordinated by the thiolate side chain of a cysteine in the proximal position<sup>24</sup>. Recently the X-ray structure of Fe(III)-haem CPO was determined with the substrate, 1,3-cyclopentanedione (CPD), bound in one of the two channels leading to the haem iron centre (Fig. 3)<sup>25</sup>. In addition, halide-binding sites were identified at the protein surface near the opening of the second, narrower, channel leading to the haem iron moiety, as well as within this channel and at the other end of the channel, near the haem iron site<sup>25</sup>.

A haem bromoperoxidase isolated from the marine green alga *Penicillium capitatus* contains a distal His ligand in place of the cysteine ligand in Fe(III)-haem CPO<sup>7,8</sup>. This enzyme uses bromide preferentially, although under certain conditions it can catalyse chlorination reactions<sup>8</sup>. Although the thiolate ligand was initially thought to be important for CPO activity, and His for bromoperoxidase activity in the haem haloperoxidases, a haem CPO with a distal His ligand has been isolated from

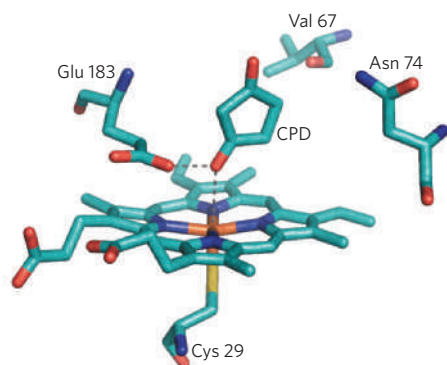


**Figure 3 | Structure of the active site of haem CPO from *C. fumago*, with a bound substrate, 1,3-cyclopentanedione<sup>25</sup>.** The active site of CPO contains Fe(III)-protoporphyrin IX coordinated by the thiolate side chain of a Cys in the proximal position. Two channels have been identified that lead to the haem active site. The substrate, 1,3-cyclopentanedione (CPD), has been located in the broader of the two channels in a recent X-ray structure, and halides were located within the narrower channel<sup>25</sup>. Glu 183 is located close to the haem iron centre and is proposed to assist in formation of both compound 0 and compound I (Fig. 4). The carbon backbone is shown in teal green, oxygen in red, nitrogen in blue, sulphur in yellow and the Fe(III) centre in orange; the dashed lines indicate hydrogen bonding.

the marine worm *Notomastus lobatus*<sup>9</sup>. This enzyme is unusual in that it requires a partner flavoprotein for activity.

The haem iron centre functions as a redox catalyst (Fig. 4). Hydrogen peroxide oxidizes the haem Fe(III) centre to compound I, the Fe(IV)-oxo  $\pi$ -cation radical species ( $\text{O}=\text{Fe}(\text{IV})\text{-haem}^{+\bullet}$ ), via the short-lived compound-0 state, characterized as a peroxo-anion complex,  $\text{HOO-Fe}(\text{III})\text{-haem}^{26}$ . Glu 183 is proposed to assist in formation of both compound 0 and compound I. Compound I oxidizes chloride by two electrons, reforming the haem Fe(III) centre. Characterization of the state that is generated immediately following chloride oxidation has generated much discussion<sup>27</sup>. At issue is whether  $\text{OCl}^-$  is a ligand to the Fe(III)-haem at the distal site, whether it is released from the enzyme active site or whether it is otherwise trapped within the enzyme substrate pocket but not coordinated to Fe(III)-haem. The oxidized chlorine intermediate can then chlorinate the organic substrate or react with a second equivalent of  $\text{H}_2\text{O}_2$ , producing  $\text{O}_2$  (in the singlet excited state). Although caldariomycin (Fig. 1) is not a chiral compound, interest in stereospecific and regiospecific halogenation reactions has been widespread.

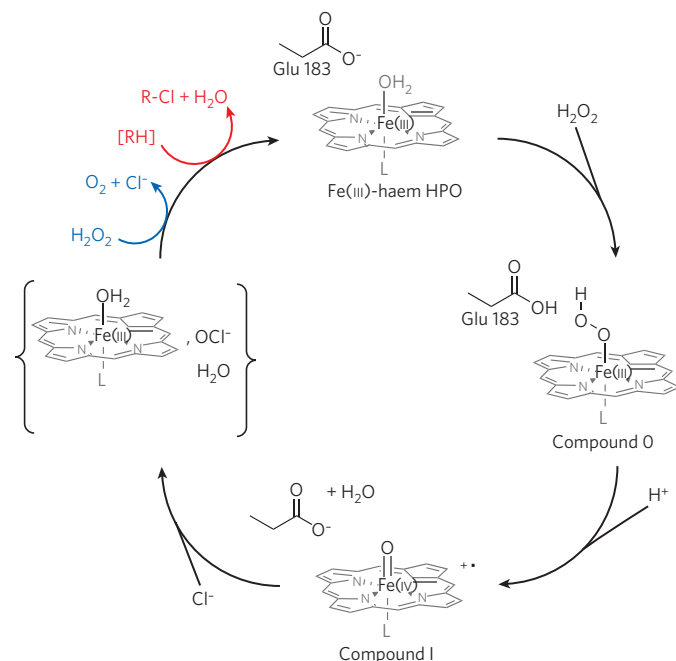


**Figure 4 | Proposed catalytic cycle for haem CPOs<sup>24-27</sup>.** The Fe(III)-haem resting state is oxidized by  $\text{H}_2\text{O}_2$ , forming compound I. Compound I oxidizes chloride by two electrons, reforming the haem Fe(III) centre and generating an oxidized chlorine intermediate that is formally at the oxidation level of  $\text{OCl}^-$ . This oxidized chlorine intermediate could chlorinate the organic substrate (shown in red) or oxidize a second equivalent of  $\text{H}_2\text{O}_2$  (shown in blue), depending on the reaction conditions. L, cysteine.

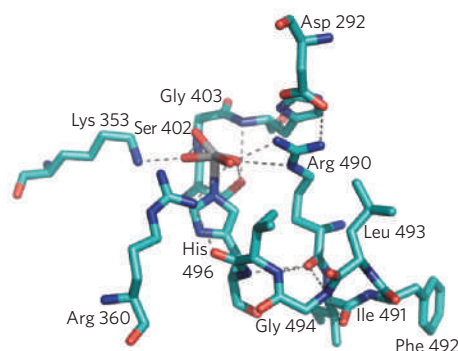


**Figure 5 | Structure of the active site of V-CPO from *C. inaequalis*<sup>35</sup>.** The V(v)-containing active site shown here for V-CPO is very similar in all the V-HPOs. A conserved His residue is a ligand to vanadate. The carbon backbone is shown in teal green, oxygen in red, nitrogen in blue and the V(v) centre in grey; the dashed lines indicate hydrogen bonding.

Numerous kinetic and spectroscopic investigations along with product analyses have tried to probe the nature of the halogenating intermediate. Several experimental results suggest that the oxidized chlorine intermediate may not escape from the active site during turnover<sup>27</sup>. A key result arising from  $\text{Cl}^-$  oxidation by compound I, which is the rate-limiting step during turnover, is the  $^{35}\text{Cl}/^{37}\text{Cl}$  isotope effect. During chlorination of 1,3,5-trimethoxybenzene or 3,5-dimethylphenol in the presence of excess chloride (with a known chlorine isotopic composition,  $-0.76 \pm 0.07\%$ ),  $^{35}\text{Cl}$  is preferentially incorporated into the chlorinated organic products. The kinetic isotope effect,  $k_{35}/k_{37}$  (the ratio of isotope reaction rate constants), of 1.012 for 1,3,5-trimethoxybenzene or 1.011 for 3,5-dimethylphenol is significantly more than that observed in the uncatalysed, molecular chlorination reaction with hypochlorite under otherwise identical conditions<sup>28</sup>. The observed chloride isotope fractionation establishes that the oxidized chlorine intermediate is not in exchange equilibration with bulk  $\text{Cl}^-$ ,  $\text{Cl}_2$ ,  $\text{OCl}^-$ ,  $\text{HOCl}$  or other possible chlorine species outside the enzyme active site. Thus, this experiment suggests that the oxidized chlorine intermediate is trapped in the enzyme active-site pocket and that chlorination occurs within the enzyme active-site channel.

### Vanadium haloperoxidases

The first vanadium haloperoxidase (V-HPO) was discovered in marine kelp in the early 1980s<sup>10,11</sup>. Since that time, vanadium bromoperoxidases

(V-BPOs) have been isolated from the three major classes of marine seaweed, and vanadium CPOs (V-CPOs) have been isolated from fungi<sup>29</sup> and are predicted to be present in marine bacteria<sup>30</sup>. V-HPOs are undoubtedly important in the biosynthesis of many halogenated marine natural products (see below), and have recently been shown to be involved in iodide accumulation in marine macroalgae (kelp)<sup>31</sup>. Although chlorinated natural products have not been isolated from the fungi containing V-CPO, these enzymes may be important in fungus-mediated chlorination and degradation of lignin<sup>32</sup>.

The vanadate site in V-HPOs is positioned at the bottom of a channel 15–20 Å deep, at the core of the four-helix bundle scaffold (Fig. 5)<sup>33–35</sup>. Vanadium is coordinated to the protein by a single axial His ligand in a trigonal bipyramidal coordination geometry. The three equatorial oxygens of vanadate are hydrogen-bonded to two conserved Arg residues, a Lys, a Ser and the backbone of a Gly amide, thereby decreasing the overall negative charge around the vanadate ion. The proposed apical water/hydroxide ligand is hydrogen-bonded to a His. The X-ray structures of V-BPO (*Corallina officinalis*<sup>34</sup>, *Ascophyllum nodosum*<sup>33</sup>) and V-CPO (*Curvularia inaequalis*<sup>35</sup>) are remarkably similar, and are nearly superimposable when the structures are overlaid at the V(v) centre<sup>33</sup>. The striking similarity of the active sites raises questions about the molecular basis of the halide selectivity and the reactivity towards halide oxidation. One noticeable difference in the overlay is the presence of Phe 397 in V-CPO but His in V-BPO. This extra His residue does not interact directly with vanadate, although it has been proposed that the His side chain participates as a proton donor and acceptor during catalysis<sup>23,36,37</sup> and, thus, could affect the overall oxidation potential of the oxo-peroxo-V(v) moiety.

In contrast to the haem haloperoxidases that function as redox catalysts, V-HPOs function as Lewis acid catalysts of halide oxidation by  $\text{H}_2\text{O}_2$ . The catalytic reaction is initiated by coordination of one equivalent of  $\text{H}_2\text{O}_2$  to the resting V(v) state of the enzyme (Fig. 6a). The X-ray structure of the peroxo adduct of V-CPO reveals that a Lys side chain is hydrogen-bonded to the coordinated peroxide. This is probably an essential feature of the catalytic reaction because it would increase the potential of the oxo-peroxo-V(v) centre for halide oxidation. The oxo-peroxo-V(v) species can then oxidize the halide by two electrons, forming an oxidized halogen that is formally at the  $\text{X}^+$  oxidation state or, more probably, at that of the hypohalite anion,  $\text{OX}^-$ . Electrophilic halogenation results from reaction of ' $\text{OX}^-$ ' either with the organic substrate or, in the absence of a good organic substrate, with a second equivalent of  $\text{H}_2\text{O}_2$ , forming  $\text{O}_2$  (which has been shown to be in the singlet excited state during turnover with  $\text{Br}^-$ )<sup>38</sup> and the halide,  $\text{X}^-$ . Radical halogenation reactions have not been observed with the V-HPO enzymes.

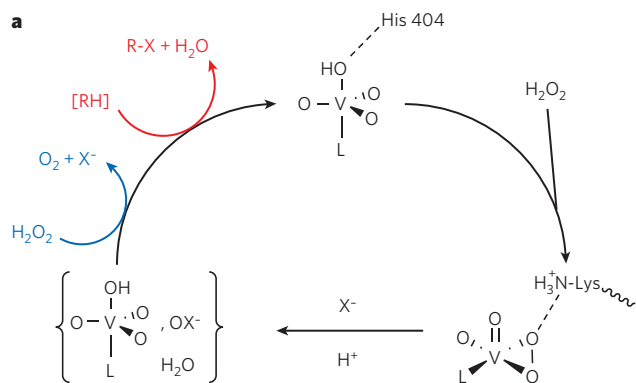
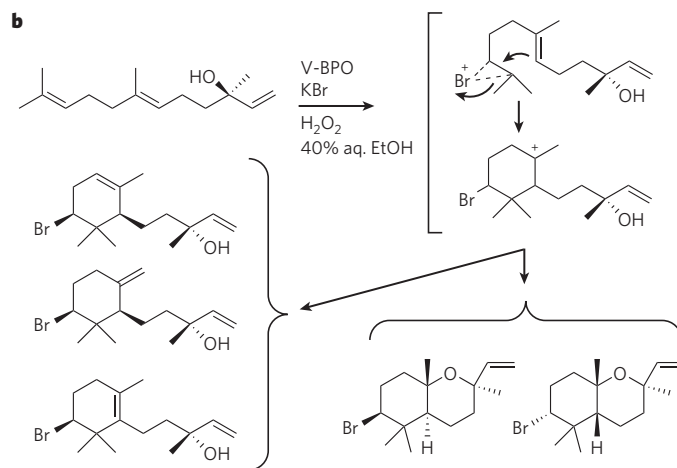


**Figure 6 | Mechanistic considerations of V-HPOs.** **a**, Proposed catalytic cycle for V-HPOs<sup>12,21,23,37</sup>. The catalytic reaction is initiated by coordination of one equivalent of  $\text{H}_2\text{O}_2$  to the resting V(v) state of the enzyme. Hydrogen bonding from a Lys side chain to V(v)-coordinated peroxide most probably assists halide oxidation by increasing the oxidation potential of the oxo-peroxo-V(v) moiety. After halide oxidation, the oxidized halogen intermediate, ' $\text{OX}^-$ ', could brominate the organic



substrate (shown in red) or oxidize a second equivalent of  $\text{H}_2\text{O}_2$ , forming singlet oxygen (shown in blue). **b**, V-BPO-catalysed formation of  $\alpha$ -,  $\beta$ - and  $\gamma$ -snyderol and (+)-3 $\beta$ -bromo-8-epicaparrapi oxide natural products from (E)-(+)-nerolidol<sup>41</sup>. The formation of single diastereomers of  $\alpha$ -,  $\beta$ - and  $\gamma$ -snyderol suggests that the reaction proceeds through a common intermediate, initially formed by electrophilic bromination of a single face of the terminal alkene site in (E)-(+)-nerolidol. L, ligand.

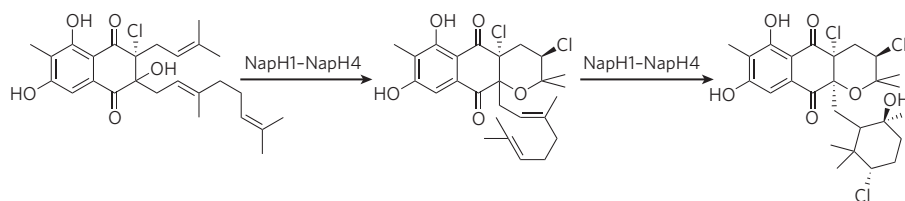


**Figure 7 | Proposed biosynthesis of the napyradiomycins A80915A–A80915D<sup>30</sup>.** The sequence of reactions depicts chlorination and cyclization of the isoprene and the geranyl units in a manner analogous to V-BPO-catalysed bromination and cyclization of terpenes shown in Fig. 6b.

Initial reports suggested that V-BPO lacked organic-substrate specificity because a wide range of brominated organic compounds could be produced. However, few compounds are brominated as efficiently as would be indicated by the stoichiometric consumption of one equivalent of  $\text{H}_2\text{O}_2$  per brominated organic equivalent produced (Fig. 2, reaction 1). Instead, during halogenation reactions of many compounds, far more  $\text{H}_2\text{O}_2$  is consumed in the halide-assisted  $\text{H}_2\text{O}_2$ -disproportionation reaction than brominated product is formed, consistent with escape of HOBr from the active site as occurs with poor organic substrates.

Terpenes, which are the biogenic precursors to many halogenated terpene natural products, are substrates for V-BPO that do react stoichiometrically during turnover, such that one equivalent of  $\text{H}_2\text{O}_2$  is consumed per equivalent of terpene reacted, at least with the red algal V-BPOs<sup>39–41</sup>. For example, V-BPO catalyses the bromination of the sesquiterpene (*E*)-(+)-nerolidol, which is accompanied by terpene cyclization, and consumption of one equivalent of  $\text{H}_2\text{O}_2$  in the formation of  $\alpha$ -,  $\beta$ - and  $\gamma$ -snyderol and (+)-3 $\beta$ -bromo-8-epicaparrapi oxide (Fig. 6b)<sup>41</sup>. Single diastereomers of  $\beta$ - and  $\gamma$ -snyderol and mixed diastereomers of (+)-3 $\beta$ -bromo-8-epicaparrapi oxide (diastereomeric excess, 20–25%) are produced in the V-BPO-catalysed reaction with (*E*)-(+)-nerolidol, whereas two diastereomers of these compounds are formed in the synthesis with 2,4,4,6-tetrabromocyclohexa-2,5-dienone<sup>41</sup>.

The formation of single diastereomers of the snyderols in the V-BPO reaction indicates that only one face of the terminal alkene of (*E*)-(+)-nerolidol is brominated. Moreover, the halogenating species is trapped within the active site, although speciation within the active site, such as HOBr/OBr<sup>−</sup>/Br<sub>2</sub>, V(v)-OBr or a possible bromamine or acyl hypobromite species, among other possibilities, cannot be addressed explicitly. Thus, the active-site channel would seem to play a role by holding the terpene substrate in place such that only one face of the terminal alkene is presented to the vanadium centre. Differences between the active-site channels, in terms of terpene-substrate selectivity, is a topic of current interest.

Recent cluster analysis of the napyradiomycin biosynthetic gene cluster (*nap*) from the marine sediment *Streptomyces* sp. strain CNQ-525 and the actinomycete *Streptomyces aculeolatus* NRRL 18442 revealed multiple open-reading-frame sequences that could encode multiple V-CPOs and a flavin-dependent halogenase. Functional expression of the biosynthetic cluster leads to formation of chlorinated compounds (Fig. 7); however, a functional V-CPO has not yet been isolated<sup>30</sup>.

Phylogenetic analysis of V-HPOs shows that the *nap* V-CPOs form a clade distinct from the marine algal V-BPO clade (*A. nodosum*, *Corallina pilulifera* and *C. officinalis*) and the fungal V-CPO clade (*C. inaequalis* and *Embellisia didymospora*)<sup>30</sup>. All of the V-HPOs have a set of conserved residues that comprise the His ligand to vanadate (His 496 in the number sequence of *C. inaequalis* V-CPO) and five of the other amino acids at the active site, most of which are involved in hydrogen-bonding to vanadate oxygen atoms. However, His 404, a residue that is found within hydrogen-bonding distance of the vanadate apical oxygen, is absent in the putative

*nap* V-CPOs<sup>30</sup>. It will be interesting to learn the effects that the His 404 substitutions (Ser, Phe) have on halide oxidation reactivity.

In an interesting display of chemical defence, some marine algae have evolved a means to disrupt bacterial quorum sensing and, thus, mitigate the effects of bacterial colonization of an alga's surface. Quorum sensing is the mechanism by which bacteria sense cell density and regulate such phenotypic responses as biofilm formation, virulence, swarming motility and bioluminescence. Many bacteria use acyl homoserine lactones as their signalling molecules to activate a receptor-mediated cascade of events dependent on sufficient cell density<sup>42</sup>.

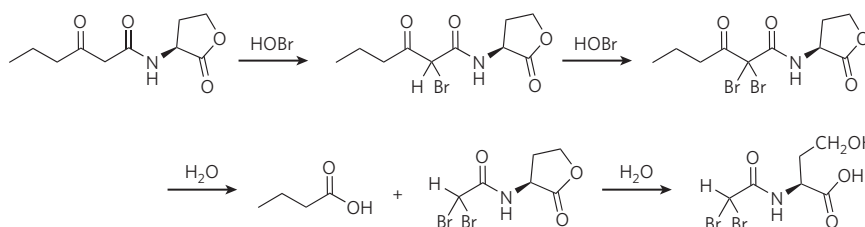
The lack of microbial fouling of the marine red alga *Delisea pulchra* has intrigued marine ecologists for some time<sup>43</sup>. *Delisea pulchra* produces halogenated furanones that have been shown to inhibit quorum sensing by interfering with the receptor-mediated phenotypic responses of certain bacteria<sup>43</sup>. Intriguingly, the 3-oxo-acyl homoserine lactones are readily susceptible to electrophilic halogenation at C2, as demonstrated by reaction with aqueous HOX/OX<sup>−</sup>/X<sub>2</sub> as well as by the V-HPO of *Laminaria digitata* (Fig. 8)<sup>44</sup>. The brominated products disrupt quorum sensing efficiently, as demonstrated with engineered reporter strains of *Agrobacterium tumefaciens* and *Chromobacterium violaceum*<sup>44</sup>. Some marine algae have haloperoxidases on their surfaces, suggesting that they use a double-pronged approach of attacking 3-oxo-acyl homoserine lactones secreted by bacteria attempting to colonize their surface, in addition to producing halogenated compounds to disrupt quorum sensing.

### Non-haem iron halogenases

A number of halogenated natural products, such as syringomycin E, barbamide and jamaicamide, contain halogen substituents at an unactivated carbon centre<sup>13,18,20,22</sup>. The biosynthesis of these compounds is catalysed by a new class of  $\alpha$ -ketoglutarate ( $\alpha$ KG)-dependent, non-haem iron ( $\text{Fe}_{\text{NH}}$ ) halogenase enzymes that comprise a divergent subset of the larger class of  $\text{Fe}_{\text{NH}}-\alpha$ KG oxygenases. In the oxygenase family of enzymes, the bidentate complex of  $\alpha$ KG coordinated to  $\text{Fe}(\text{II})$  is bound in the enzyme active site by coordination to a conserved set of two His ligands and either an Asp or a Glu ligand that form a facial triad at the octahedral iron site. The pentadentate ligation leaves a vacant coordination site for  $\text{O}_2$  coordination. Dioxygen activation is coupled to the oxidative decarboxylation of  $\alpha$ KG, a co-substrate in the overall enzyme reaction and a source of two of the four electrons required to reduce  $\text{O}_2$  to  $\text{H}_2\text{O}$  (Fig. 2, reaction 2).

A distinguishing characteristic of the  $\text{Fe}_{\text{NH}}-\alpha$ KG halogenases is the absence of the carboxylate protein ligand (that is, Glu or Asp). As shown in the X-ray structure of SyrB2, which was the first  $\text{Fe}_{\text{NH}}$  halogenase to be discovered (Fig. 9)<sup>45</sup>,  $\text{Fe}(\text{II})$  is coordinated by the two conserved His ligands and a halide ligand. The conserved Glu/Asp residue has been replaced with Ala; this means that the  $(\text{His})_2(\text{Asp}/\text{Glu})$  triad of the oxygenases has been changed to  $(\text{His})_2(\text{Ala})$ , thus creating a vacancy for the halide.

**Figure 8 | Bromination of 3-oxo-hexanoyl homoserine lactone and subsequent hydrolysis of the dibromo product<sup>60</sup>.** Many bacteria secrete acyl homoserine lactone compounds, which they use as signalling molecules to sense cell density. The 3-oxo class of acyl homoserine lactone is readily susceptible to electrophilic halogenation at C2 with aqueous bromine solutions containing HOBr and Br<sub>2</sub>, as shown in this sequence of reactions.





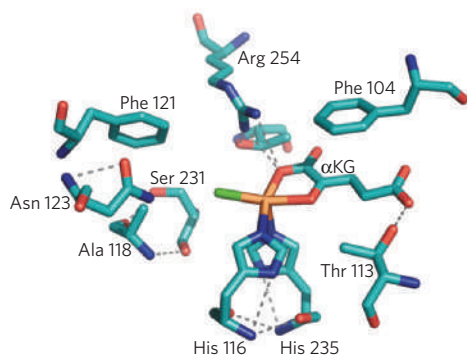


**Figure 9 | Structure of the active site of  $\text{Fe}_{\text{NH}}\text{-}\alpha\text{KG}$  in SyrB2 from *P. syringae*<sup>45</sup>.** The active site comprises  $\text{Fe(II)}$  coordinated to two conserved His ligands and a halide ligand. A conserved Glu/Asp residue found in  $\text{Fe}_{\text{NH}}\text{-}\alpha\text{KG}$  oxygenases has been replaced by Ala, creating a vacancy for the halide coordination. The carbon backbone is shown in teal green, oxygen in red, nitrogen in blue and the chloride ligand to the non-haem  $\text{Fe(II)}$  centre (orange) in bright green; the dashed lines indicate hydrogen bonding.

The catalytic cycle of the halogenases (Fig. 10) resembles the reaction sequence of the  $\text{Fe}_{\text{NH}}\text{-}\alpha\text{KG}$  oxygenases up to the point of formation of the oxo-ferryl species<sup>46,47</sup>. The halogenation reaction begins with association of the organic substrate in the enzyme active site, which triggers a change in the resting state enabling the subsequent coordination of  $\text{O}_2$  by  $\text{Fe(II)}$  in  $(\text{His})_2(\text{X})\text{Fe(II)}_{\text{NH}}\text{-}\alpha\text{KG}$  (Fig. 10)<sup>47</sup>. On the basis of the ‘HAG’ mechanism of the  $\text{Fe}_{\text{NH}}\text{-}\alpha\text{KG}$  oxygenases<sup>46</sup>, Matthews *et al.*<sup>47</sup> have proposed a series of states (I, II and III; Fig. 10) that lead to hydrogen-atom abstraction by the haloferryl ( $\text{X-Fe(IV)=O}$ ) species. The oxygenase and halogenase mechanisms diverge at this point. The halogenase mechanism proceeds by a rebound attack by the halogen atom at the iron centre ( $\text{Fe(III)-X}$ ) on the organic radical leading to the halogenated organic compound and  $\text{Fe(II)}$ , as opposed to rebound by the hydroxyl radical ( $\text{Fe(III)-OH}$ ) in the oxygenase mechanism. The hydrogen-atom abstraction step shows a large deuterium kinetic isotope effect, which has also been observed with other  $\alpha\text{KG}$ -dependent hydroxylases<sup>47</sup>.

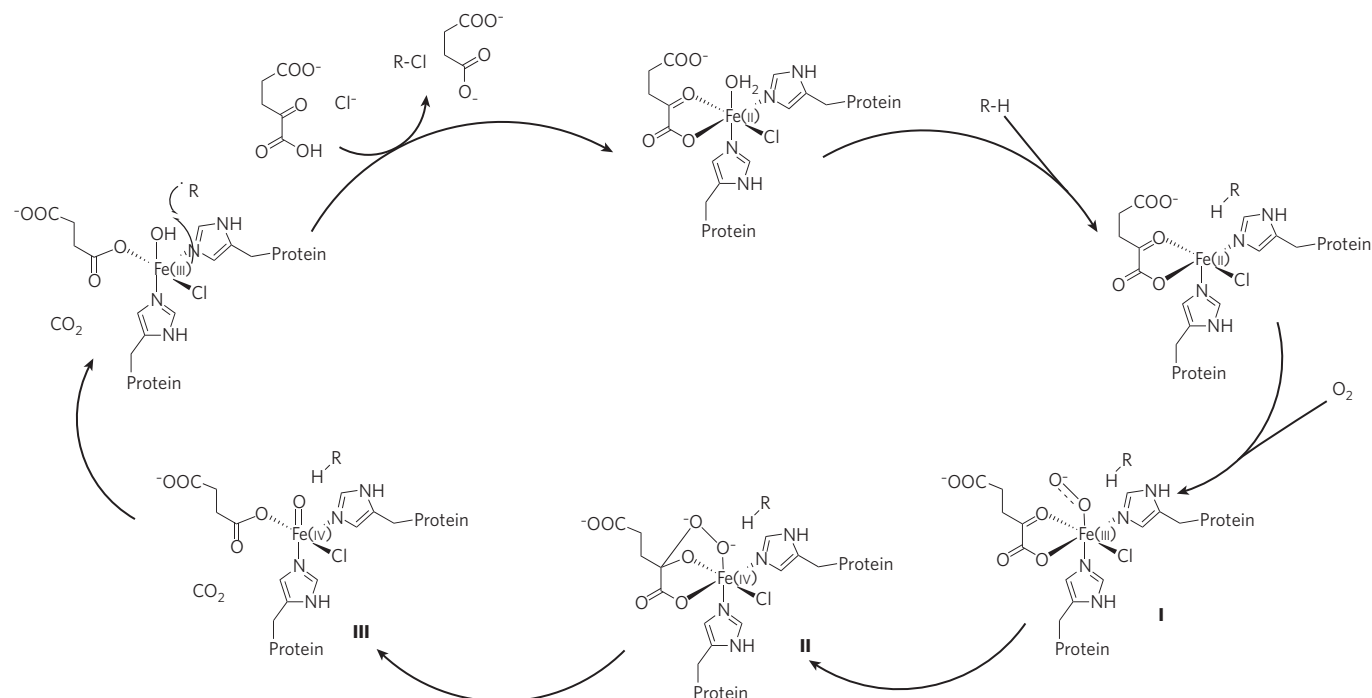


**Figure 10 | Proposed catalytic cycle of  $\text{Fe}_{\text{NH}}\text{-}\alpha\text{KG}$  halogenases.** The reaction is triggered on binding of the organic substrate, inducing a conformational change such that the resting  $\text{Fe(II)}_{\text{NH}}\text{-}\alpha\text{KG}$  state can then react with  $\text{O}_2$ . The

The ‘substrate triggering’ mechanism in the  $\text{Fe}_{\text{NH}}\text{-}\alpha\text{KG}$  halogenases (Fig. 10) proposed by Matthews *et al.*<sup>47</sup> is consistent with the biosynthesis of syringomycin E (Fig. 1), in which L-threonine is chlorinated by the  $\text{Fe}_{\text{NH}}\text{-}\alpha\text{KG}$  halogenase component, SyrB2, of the non-ribosomal peptide synthetase biosynthetic gene cluster in *Pseudomonas syringae* B301D (Fig. 11)<sup>48</sup>. A number of other  $\text{Fe}_{\text{NH}}$  halogenases have also been identified or predicted<sup>22</sup>, including BarB1 and BarB2 from *Lyngbya majuscula*, which are involved in the trichlorination of L-leucine of barbamide<sup>49</sup>; CytC3 enzymes involved in the sequential chlorination of L-aminobutyrate<sup>50</sup>; and even CmaB, which chlorinates the  $\gamma$  position of L-*allo*-isoleucine (Fig. 11), among others<sup>22,51</sup>. In this last reaction,  $\gamma\text{-Cl-L-}allo\text{-isoleucine}$  undergoes a  $\gamma$ -elimination reaction catalysed by the enzyme CmaC, leading to cyclopropyl ring formation and the release of chloride, a process that has been termed cryptic chlorination<sup>51</sup>.

PCR cloning of halogenase homologues has been useful in the discovery of new  $\text{Fe}_{\text{NH}}\text{-}\alpha\text{KG}$  halogenases<sup>52</sup>. Of particular interest are the  $\text{Fe}_{\text{NH}}\text{-}\alpha\text{KG}$  halogenase components, CurA and JamE, of *L. majuscula*, which were predicted to be involved in the biosyntheses of curacin A through cryptic halogenation<sup>52</sup> and jamaicamide A through vinyl chloride formation<sup>53</sup>. Very recently, Gu *et al.*<sup>54</sup> demonstrated the remarkable sequence identity of CurA and JamE, at 92%, yet curacin A and jamaicamide A are structurally very different. In the Cur pathway a  $\beta$ -branched cyclopropane is formed, whereas in the Jam pathway a vinyl chloride is formed. The evolution of these metabolic pathways within the same organism is striking. Chlorination occurs at a carboxylated  $\gamma$ -carbon in both pathways, a reaction not previously observed in other halogenases. As depicted in Fig. 12, the biosynthetic pathways diverge after chlorination at the decarboxylation step. After formation of  $\alpha,\beta$ -enoyl thioester (I  $\rightarrow$  II in Fig. 12) in the Cur pathway, the NADPH-dependent Cur enoyl reductase domain was found to catalyse formation of the cyclopropyl unit, presumably by intramolecular nucleophilic displacement of  $\text{Cl}^-$ . This reaction is new and distinct from the cryptic chlorination reaction catalysed by CmaB (Fig. 11d). However, in the Jam pathway a  $\beta,\gamma$ -enoyl thioester of the 3-methyl-4-chloroglutaconyl decarboxylation product is formed (I  $\rightarrow$  III in Fig. 12) that is not a substrate for the Jam enoyl reductase. The Jam enoyl reductase domain is a reductase for the  $\alpha,\beta$ -enoyl thioester solely, and thus is not functional in the biosynthesis of jamaicamide.

scheme shows a series of states — I, II, and III — that lead to hydrogen-atom abstraction by the haloferryl ( $\text{X-Fe(IV)=O}$ ) species. The halogenation reaction can then proceed as described in the main text. Adapted from ref. 47.

## Non-metallo-haloperoxidases

Not all biological halogenation is catalysed by metalloenzymes. A large class consists of the flavin-dependent halogenases (Fig. 2, reaction 2; for a current review, see ref. 18). These enzymes carry out halogenation reactions, such as in the biosynthesis of rebeccamycin. Halogenation by perhydrolase enzymes has also been demonstrated, although the biological relevance of this enzyme activity is not known<sup>15</sup>.

A significant class of non-metallo-halogenating enzymes use SAM as a co-substrate. The first of the SAM-dependent halogenases to be discovered was the methyl chloride transferase enzyme in seaweeds and other plants, which is responsible for the production of profuse levels of methyl chloride<sup>17,55</sup>, raising questions about its biological function. Other SAM-dependent halogenases, including chlorinase<sup>56</sup> and fluorinase<sup>15,56–59</sup> enzymes, are now known. These enzymes catalyse nucleophilic halogenation reactions, rather than electrophilic or radical halogenation reactions. The SAM-dependent chlorinase SalL, from the marine bacterium *Salinospora tropica*, chlorinates SAM by nucleophilic chloride addition generating 5'-chloro-5'-deoxyadenosine as a precursor to chloroethylmalonyl-CoA, which is ultimately incorporated into salinosporamide A<sup>57</sup>. SalL will also accept Br<sup>−</sup> and I<sup>−</sup> but not F<sup>−</sup> directly. The fluorinase is the first step in the biosynthesis of fluoroacetate and 4-fluorothreonine from the soil bacterium *Streptomyces cattleya* at the C5' site of SAM in a S<sub>N</sub>2 reaction that occurs with inversion of configuration<sup>59</sup>.

## Outlook

In the past five years, more halogenating enzymes have been identified than in the four decades after the discovery of the first halogenating enzyme, haem CPO (*C. fumago*). The pace of discovery of new haloperoxidases and halogenases is bound to continue to increase with the use of genomic and bioinformatic approaches. We will undoubtedly continue to isolate new halogenated natural products and uncover new biosynthetic pathways that co-opt halogenating enzymes for new purposes.

However, in the four-and-a-half decades since the discovery of haem CPO, fundamental questions remain about the mechanism of the halogenating enzymes. At first glance, the intricate balance between halogenation and hydroxylation in the Fe<sub>NH</sub>-αKG enzymes would seem to be mediated by the replacement of a carboxylic-acid-containing amino acid, Glu or Asp (with Ala in the halogenases), creating a vacant coordination site for halide coordination to iron. But relatively few structures are known for the Fe<sub>NH</sub>-αKG halogenases. It is not yet known how the Fe<sub>NH</sub>-αKG active sites vary in this class of enzyme or what the elements of discrimination and selectivity are that exist within these enzyme active sites. The 45-year-old question regarding the nature of the halogenating moiety in the haloperoxidases remains unanswered.

New spectroscopic techniques able to provide faster snapshots during turnover may be revealing. With significant advances in the sensitivity of isotope mass spectrometers, investigations of halogen isotope effects may have a more prominent role in mechanistic investigations, particularly now for <sup>79</sup>Br/<sup>81</sup>Br fractionation. Within the V-HPOs, elucidating the factors that control halide selection and positioning, as well as the organic substrate selectivity, will be particularly interesting. The struc-

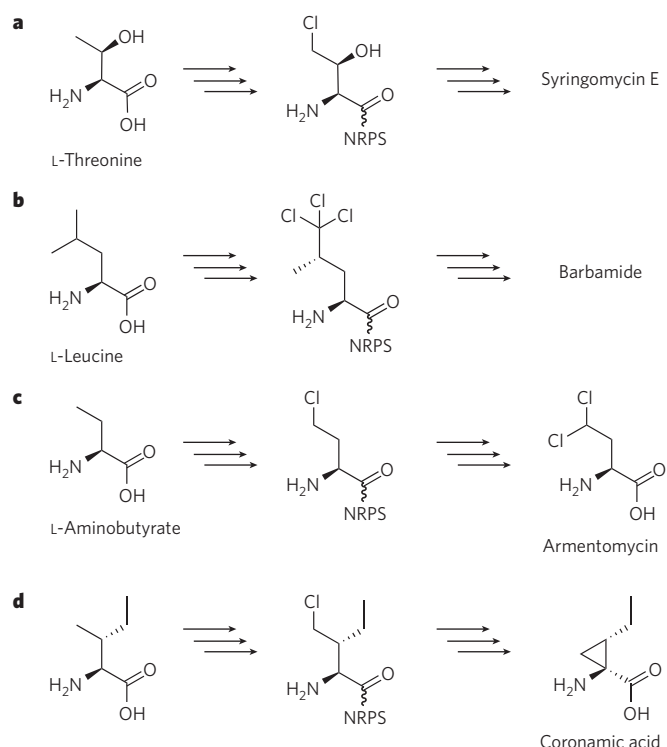


**Figure 11 | Examples of Fe<sub>NH</sub>-αKG halogenase reactions.** Fe<sub>NH</sub>-αKG halogenases have been identified in the biosynthesis of a number of natural products, such as syringomycin E (**a**; Fig. 1), barbamide (**b**; Fig. 1), armentomycin (**c**) and coronamic acid (**d**). The triple arrows mean that multiple reaction steps and different enzymes are required for the indicated conversions. NRPS, non-ribosomal peptide synthetase.

tures of the V-HPOs are fully superimposable at the V(v) centre, yet we know relatively little about the role that the active-site channel has in organic-substrate selectivity, and why some halogenated products predominate in one alga but not another related alga with a very similar haloperoxidase. In consideration of cryptic halogenation, it is not known what other natural products are formed via halogenated intermediates, including possibly in polymerization reactions.

The parallel between haem, non-haem iron and flavin-dependent halogenase enzymes and haem, non-haem iron and flavin-dependent oxygenase enzymes is striking. In addition to these three types of oxygenase enzyme, other oxygenases are also well known, including copper and manganese enzymes. Other metalloenzymes may be involved in halogenation reactions. In retrospect, it is not surprising that marine organisms evolved V-HPOs, given the halide content of the oceans and the fact that vanadium is the second most abundant transition-metal ion in seawater. Organisms living in other salty environments with unique transition-metal-ion compositions also may have evolved new metalloenzymes that carry out halogenation reactions.

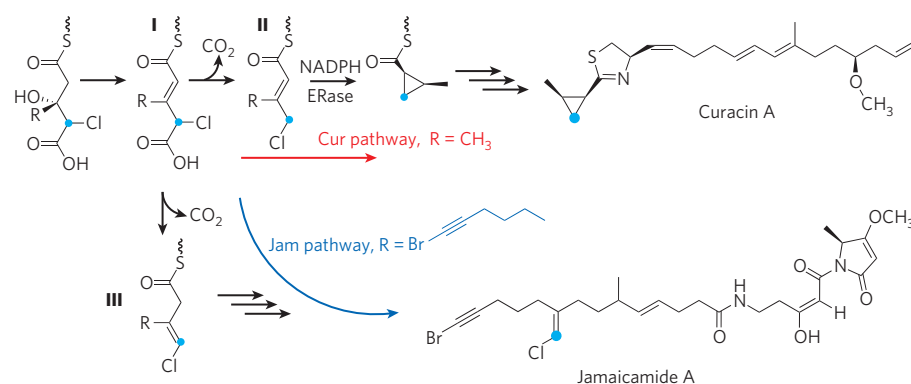


**Figure 12 | Parallel assemblies in the biosynthesis of curacin A and jamaicamide A.** The pathways diverge after chlorination. ERase, enoyl reductase. The blue dot shows the β-branching carbon atom. Adapted from ref. 54. In the Cur pathway, compound I is converted to an α-β-enoyl thioester (II), which is a substrate for the Cur ERase. In the Jam pathway, compound I is converted to a β-γ-enoyl thioester (III), which is not a substrate for the Jam ERase.

1. Faulkner, D. J. Marine natural products. *Nat. Prod. Rep.* **19**, 1–48 (2002).
2. Gribble, G. W. Naturally occurring organohalogen compounds. *Acc. Chem. Res.* **31**, 141–152 (1998).
3. Carpenter, L. J. & Liss, P. S. On temperate sources of bromoform and other reactive bromine gases. *J. Geophys. Res.* **105**, 20539–20547 (2002).
4. Hager, L. P., Morris, D. R., Brown, F. S. & Eberwein, H. Chloroperoxidase. II. Utilization of halogen anions. *J. Biol. Chem.* **241**, 1769–1777 (1966).
5. Fenical, W. Halogenation in the Rhodophyta: a review. *J. Phycol.* **11**, 245–259 (1975).
6. Wolinsky, L. E. & Faulkner, D. J. A biomimetic approach to the synthesis of *Laurencia* metabolites. Synthesis of 10-bromo- $\alpha$ -chamigrene. *J. Org. Chem.* **41**, 597–600 (1976).
7. Manthey, J. A. & Hager, L. P. Characterization of the catalytic properties of bromoperoxidase. *Biochemistry* **28**, 3052–3057 (1989).
8. Manthey, J. A. & Hager, L. P. Characterization of the oxidized states of bromoperoxidase. *J. Biol. Chem.* **260**, 9654–9659 (1985).
9. Roach, M. P. *et al.* *Notomastus lobatus* chloroperoxidase and *Amphitrite ornata* dehaloperoxidase both contain histidine as their proximal heme iron ligand. *Biochemistry* **36**, 2197–2202 (1997).
10. Vilter, H. Peroxidases from Phaeophyceae. III. Catalysis of halogenation by peroxidases from *Ascophyllum nodosum* (L.) Le Jol. *Bot. Mar.* **26**, 429–435 (1983).
11. Vilter, H. Peroxidases from Phaeophyceae. A vanadium(v)-dependent peroxidase from *Ascophyllum nodosum*. *Phytochemistry* **23**, 1387–1390 (1984).
12. Wever, R., Plat, H. & De Boer, E. Isolation procedure and some properties of the bromoperoxidase from the seaweed *Ascophyllum nodosum*. *Biochim. Biophys. Acta* **830**, 181–186 (1985).
13. Vaillancourt, F. H., Yin, J. & Walsh, C. T. SyrB2 in syringomycin E biosynthesis is a nonheme Fe<sup>II</sup>  $\alpha$ -ketoglutarate- and O<sub>2</sub>-dependent halogenase. *Proc. Natl Acad. Sci. USA* **102**, 10111–10116 (2005).
14. Chen, X. & van Pée, K.-H. Catalytic mechanisms, basic roles, and biotechnological and environmental significance of halogenating enzymes. *Acta Biochim. Biophys. Sin. (Shanghai)* **40**, 183–193 (2008).
15. Deng, H. & O'Hagan, D. The fluorinase, the chlorinase and the duf-2 enzymes. *Curr. Opin. Chem. Biol.* **12**, 582–592 (2008).
16. Wuosmaa, A. M. & Hager, L. P. Methyl chloride transferase: a carbocation route for biosynthesis of halometabolites. *Science* **249**, 160–162 (1990).
17. Blasiak, L. C. & Drennan, C. L. Structural perspective on enzymatic halogenation. *Acc. Chem. Res.* **42**, 147–155 (2009).
18. Wagner, C., Omari, E. M. & König, G. M. Biohalogenation: nature's way to synthesize halogenated metabolites. *J. Nat. Prod.* **72**, 540–553 (2009).
19. Neumann, C. S., Fujimori, D. G. & Walsh, C. T. Halogenation strategies in natural product biosynthesis. *Chem. Biol.* **15**, 99–109 (2008).
20. Fujimori, D. G. & Walsh, C. T. What's new in enzymatic halogenations. *Curr. Opin. Chem. Biol.* **11**, 553–560 (2007).
21. Littlechild, J., Rodriguez, E. G. & Isupov, M. Vanadium containing bromoperoxidase — insights into the enzymatic mechanism using X-ray crystallography. *J. Inorg. Biochem.* **103**, 617–621 (2009).
22. Vaillancourt, F. H., Yeh, E., Vosburg, D. A., Garneau-Tsodikova, S. & Walsh, C. T. Nature's inventory of halogenation catalysts: oxidative strategies predominate. *Chem. Rev.* **106**, 3364–3378 (2006).
- This review summarizes the halogenating enzymes with particular insight into the Fe<sub>NH</sub>- $\alpha$ KG halogenases.
23. Butler, A. & Carter-Franklin, J. N. A role for vanadium bromoperoxidase in the biosynthesis of halogenated marine natural products. *Nat. Prod. Rep.* **21**, 180–188 (2004).
24. Sundaramoorthy, M., Turner, J. & Poulos, T. L. The crystal structure of chloroperoxidase: a heme peroxidase-cytochrome P450 functional hybrid. *Structure* **3**, 1367–1378 (1995).
25. Kuhnle, K., Blankenfeldt, W., Turner, J. & Schlinching, I. Crystal structures of chloroperoxidase with its bound substrates and complexed with formate, acetate and nitrate. *J. Biol. Chem.* **281**, 23990–23998 (2006).
26. Wagenknecht, H.-A. & Wolf-Dietrich, W. Identification of intermediates in the catalytic cycle of chloroperoxidase. *Chem. Biol.* **4**, 367–372 (1997).
27. Libby, R. D., Beachy, T. M. & Phipps, A. K. Quantitating direct chlorine transfer from enzyme to substrate in chloroperoxidase-catalyzed reactions. *J. Biol. Chem.* **271**, 21820–21827 (1996).
28. Reddy, C. M. *et al.* A chlorine isotope effect for enzyme-catalyzed chlorination. *J. Am. Chem. Soc.* **124**, 14526–14527 (2002).
- This paper established <sup>35</sup>Cl/<sup>37</sup>Cl isotope fractionation for the first time in a haloperoxidase during turnover.
29. Van Schijndel, J. W. P. M., Vollenbroek, E. G. M. & Wever, R. The chloroperoxidase from the fungus *Curvularia inaequalis*: a novel vanadium enzyme. *Biochim. Biophys. Acta* **1161**, 249–256 (1993).
30. Winter, J. M. *et al.* Molecular basis for chloronium-mediated meroterpenoid cyclization. Cloning, sequencing, and heterologous expression of the napyradiomycin biosynthetic gene cluster. *J. Biol. Chem.* **282**, 16362–16368 (2007).
31. Küpper, F. C. *et al.* Iodide accumulation provides help with an inorganic antioxidant impacting atmospheric chemistry. *Proc. Natl Acad. Sci. USA* **105**, 6954–6958 (2008).
32. Ortiz-Bermudez, P. *et al.* Chlorination of lignin by ubiquitous fungi has a likely role in global organochlorine production. *Proc. Natl Acad. Sci. USA* **104**, 3895–3900 (2007).
33. Weyand, M. *et al.* X-ray structure determination of a vanadium-dependent haloperoxidase from *Ascophyllum nodosum* at 2.0 Å resolution. *J. Mol. Biol.* **293**, 595–611 (1999).
34. Isupov, M. N. *et al.* Crystal structure of dodecameric vanadium-dependent bromoperoxidase from the red algae *Coralina officinalis*. *J. Mol. Biol.* **299**, 1035–1049 (2000).
35. Messerschmidt, A. & Wever, R. X-ray structure of a vanadium containing enzyme: chloroperoxidase from the fungus *Curvularia inaequalis*. *Proc. Natl Acad. Sci. USA* **93**, 392–396 (1996).
36. Colpas, G. J., Hamstra, B. J., Kampf, J. W. & Pecoraro, V. L. Functional models for vanadium haloperoxidases: reactivity and mechanism of halide oxidation. *J. Am. Chem. Soc.* **118**, 3469–3478 (1996).
37. Hemrika, W., Rokus, R., Macedo-Ribeiro, S., Messerschmidt, A. & Wever, R. Heterologous expression of the vanadium-containing chloroperoxidases from *Curvularia inaequalis* in *Saccharomyces cerevisiae* and site-directed mutagenesis of the active site residues His<sup>496</sup>, Lys<sup>353</sup>, Arg<sup>360</sup>, and Arg<sup>490</sup>. *J. Biol. Chem.* **274**, 23820–23827 (1999).
38. Everett, R. R., Kanofsky, J. R. & Butler, A. Mechanism of dioxygen formation catalyzed by vanadium bromoperoxidase. Steady state kinetic analysis and comparison to the mechanism of bromination. *J. Biol. Chem.* **265**, 15671–15679 (1990).
39. Tschirret-Guth, R. A. & Butler, A. Evidence for organic substrate binding to vanadium bromoperoxidase. *J. Am. Chem. Soc.* **116**, 411–412 (1994).
40. Carter-Franklin, J. N., Parrish, J. D., Tschirret-Guth, R. A., Little, R. D. & Butler, A. Vanadium haloperoxidase-catalyzed bromination and cyclization of terpenes. *J. Am. Chem. Soc.* **125**, 3688–3689 (2003).
41. Carter-Franklin, J. N. & Butler, A. Vanadium bromoperoxidase-catalyzed biosynthesis of halogenated marine natural products. *J. Am. Chem. Soc.* **126**, 15060–15066 (2004).
- This paper shows diastereoselectivity of a V-BPO-catalysed reaction for the first time in the bromination and cyclization of the terpene (E)-(+)-nerolidol.
42. Wang, Y. J., Huang, J. J. & Leadbetter, J. R. Acyl-HSL signal decay: intrinsic to bacterial cell-cell communications. *Adv. Appl. Microbiol.* **61**, 27–58 (2007).
43. Steinberg, P. D., de Nys, R. & Kjelleberg, S. in *Marine Chemical Ecology* (eds McClintock, J. B. & Baker, B. J.) 355–387 (CRC, 2001).
44. Borchardt, S. A. *et al.* Reaction of acylated homoserine lactone bacterial signaling molecules with oxidized halogen antimicrobials. *Appl. Environ. Microbiol.* **67**, 3174–3179 (2001).
45. Blasiak, L. C., Vaillancourt, F. H., Walsh, C. T. & Drennan, C. L. Crystal structure of the non-haem iron halogenase SyrB2 in syringomycin biosynthesis. *Nature* **440**, 368–371 (2006).
46. Hanauske-Abel, H. M. & Popowicz, A. M. The HAG mechanism: a molecular rationale for the therapeutic application of iron chelators in human diseases involving the 2-oxoacid utilizing dioxygenases. *Curr. Med. Chem.* **10**, 1005–1019 (2003).
47. Matthews, M. L. *et al.* Substrate-triggered formation and remarkable stability of the C–H bond-cleaving chloroferryl intermediate in the aliphatic halogenase, SyrB2. *Biochemistry* **48**, 4331–4343 (2009).
- This paper provides significant mechanistic insight into the reactions catalysed by the Fe<sub>NH</sub>- $\alpha$ KG halogenases in comparison with those catalysed by the Fe<sub>NH</sub>- $\alpha$ KG oxygenases.
48. Galonic, D. P., Vaillancourt, F. H. & Walsh, C. T. Halogenation of unactivated carbon centers in natural product biosynthesis: trichlorination of leucine during barbamide biosynthesis. *J. Am. Chem. Soc.* **128**, 3900 (2006).
49. Chang, Z. *et al.* The barbamide biosynthetic gene cluster: a novel marine cyanobacterial system of mixed polyketide synthase (PKS)-non ribosomal peptide synthetase (NRPS) origin involving an unusual trichloroleucyl starter unit. *Gene* **296**, 235–247 (2002).
50. Ueki, M. *et al.* Enzymatic generation of the antimetabolite  $\gamma$ ,  $\gamma$ -dichloroaminobutyrate by NRPS and mononuclear iron halogenase action in a streptomycete. *Chem. Biol.* **13**, 1183–1191 (2006).
51. Vaillancourt, F. H., Yeh, E., Vosburg, D. A., O'Connor, S. E. & Walsh, C. T. Cryptic chlorination by a non-haem iron enzyme during cyclopropyl amino acid biosynthesis. *Nature* **436**, 1191–1194 (2005).
- This paper is the first report of cyclopropyl formation via a chlorinated precursor.
52. Chang, Z. *et al.* Biosynthetic pathway and gene cluster analysis of curacin A, an antitubulin natural product from the tropical marine cyanobacterium *Lyngbya majuscula*. *J. Nat. Prod.* **67**, 1356–1367 (2004).
53. Edwards, D. J. *et al.* Structure and biosynthesis of the jamaicamides, new mixed polyketide-peptide neurotoxins from the marine cyanobacterium *Lyngbya majuscula*. *Chem. Biol.* **11**, 817–833 (2004).
54. Gu, L. *et al.* Metamorphic enzyme assembly in polyketide diversification. *Nature* **459**, 731–735 (2009).
- This paper demonstrates coevolution of enzymes for metabolic diversification in the biosynthetic pathways leading to  $\beta$ -branched cyclopropane in curacin A and a vinyl chloride in jamaicamide A.
55. Ni, X. & Hager, L. P. cDNA cloning of *Batis maritima* methyl chloride transferase and purification of the enzyme. *Proc. Natl Acad. Sci. USA* **95**, 12866–12871 (1998).
56. Eustaquio, A. S., Pojer, F., Noe, J. P. & Moore, B. S. Discovery and characterization of a marine bacterial SAM-dependent chlorinase. *Nature Chem. Biol.* **4**, 69–74 (2008).
57. Dong, C. *et al.* Crystal structure and mechanism of a bacterial fluorinating enzyme. *Nature* **427**, 561–565 (2004).
58. Deng, H. *et al.* The fluorinase from *Streptomyces cattleya* is also a chlorinase. *Angew. Chem. Int. Ed.* **45**, 759–762 (2006).
59. Cadicamo, C. D., Courtieu, J., Deng, H., Meddour, A. & O'Hagan, D. Enzymatic fluorination in *Streptomyces cattleya* takes place with an inversion of configuration consistent with an SN2 reaction mechanism. *ChemBioChem* **5**, 685–690 (2004).
60. Michels, J. J., Allain, E. J., Borchardt, S. A., Hu, P. & McCoy, W. F. Degradation pathway of homoserine lactone bacterial signal molecules by halogen antimicrobials identified by liquid chromatography with photodiode array and mass spectrometric detection. *J. Chromatogr. A* **898**, 153–165 (2000).

**Acknowledgements** A.B. greatly acknowledges US National Science Foundation Division of Chemistry award number 0719553 for support of her research.

**Author Information** Reprints and permissions information is available at [www.nature.com/reprints](http://www.nature.com/reprints). The authors declare no competing financial interests. Correspondence should be addressed to A.B. ([butler@chem.ucsb.edu](mailto:butler@chem.ucsb.edu)).



# Design of functional metalloproteins

Yi Lu<sup>1</sup>, Natasha Yeung<sup>1</sup>, Nathan Sieracki<sup>1</sup> & Nicholas M. Marshall<sup>1</sup>

**Metalloproteins catalyse some of the most complex and important processes in nature, such as photosynthesis and water oxidation. An ultimate test of our knowledge of how metalloproteins work is to design new metalloproteins. Doing so not only can reveal hidden structural features that may be missing from studies of native metalloproteins and their variants, but also can result in new metalloenzymes for biotechnological and pharmaceutical applications. Although it is much more challenging to design metalloproteins than non-metalloproteins, much progress has been made in this area, particularly in functional design, owing to recent advances in areas such as computational and structural biology.**

Metalloproteins account for nearly half of all proteins in nature. Protein metal-binding sites are responsible for catalysing important biological processes, such as photosynthesis, respiration, water oxidation, molecular oxygen reduction and nitrogen fixation. Much effort has been devoted to understanding the structure and function of metalloproteins, as summarized by other reviews in this Insight. The ultimate test is to use this knowledge to design new metalloproteins that reproduce the structures and functions of native metalloproteins<sup>1–3</sup>. Metalloprotein design is not just an intellectual exercise that duplicates biochemical and biophysical studies of native metalloproteins. This ‘bottom-up’ approach can also elucidate structural features that may remain hidden in those studies. Whereas biochemical and biophysical studies mostly reveal individual features that result in a loss of function, design requires the incorporation of all the structural features needed to attain a function. Equipped with insights from design processes, it may be possible to design new metalloproteins with improved properties such as higher stability and greater efficiency, or to impart them with functions not found in nature, for use in an even wider range of biotechnological and pharmaceutical applications.

Metalloprotein design, however, has proven to be more challenging than the design of non-metalloproteins. Both fields require the issue of polypeptide design to be addressed, but metalloprotein design involves metal ions, which are much larger in number than amino acids, and geometries that are much more variable. Conversely, most metal-binding sites are highly chromatic and display distinctive magnetic properties, making it easier to characterize the designed metalloprotein using metal-based spectroscopic techniques rather than X-ray crystallography or nuclear magnetic resonance (NMR), thus shortening design cycles. Therefore, the field of metalloprotein design has enjoyed much success recently, owing to advances in biophysical, computational and structural biology. The field is also progressing from purely structural to more functional designs, and from the design of the primary coordination sphere to that of the secondary coordination sphere and beyond. We summarize these advances here, with a focus on creating new and functional metal-binding sites in either *de novo*-designed or native protein scaffolds. In addition, the emerging area of designing novel metalloproteins with functions enhanced beyond those available in nature, through the introduction of unnatural amino acids or non-native metal cofactors, is covered. We also summarize the methodologies used in achieving these goals.

## Metalloprotein design in *de novo*-designed scaffolds

The purest and most challenging form of metalloprotein design is *de novo* design, or design ‘from scratch’. *De novo* design of a metalloprotein

involves constructing a polypeptide sequence that is not directly related to any natural protein and that folds precisely into a defined three-dimensional structure that binds a metal ion<sup>4</sup>. Most work in this area has focused on introducing metal-binding sites into designed  $\alpha$ -helical bundles (Fig. 1), which are among the first *de novo*-designed proteins<sup>4</sup>. These  $\alpha$ -helical bundles are a common scaffold for a number of haem proteins in nature. Therefore, not surprisingly, haem centres were among the first, and are some of the most common, metal centres incorporated into *de novo*  $\alpha$ -helical bundles<sup>5</sup>, from mono-haem binding<sup>6</sup> (Fig. 1a) to multi-haem maquettes<sup>7</sup> (Fig. 1b), mimicking long-range electron-transfer proteins. These proteins were rationally designed by direct comparison with native proteins, such as cytochrome *bc*<sub>1</sub>, for clues to the placement of essential haem-binding and structure-stabilizing residues. In addition to electron-transfer<sup>8</sup> and proton-coupled exchange<sup>9</sup> functions, a functional aniline hydroxylase<sup>10</sup>, peroxidase<sup>11</sup> and oxygenase<sup>12</sup> have also been engineered into *de novo*-designed proteins. An exciting development in this field is the design of a di-haem-containing four-helix bundle with oxygen transport properties, whose O<sub>2</sub> affinities and exchange timescales match those of natural globins<sup>13</sup>. Remarkably, this designed protein binds O<sub>2</sub> even tighter than carbon monoxide, a desirable property that most native O<sub>2</sub>-binding haem proteins do not have. A key to its success is a reduction of helical-interface mobility to exclude water from the haem-binding site, thereby reducing haem oxidation and increasing O<sub>2</sub>-binding stability.

In addition to haem, other metal ions/cofactors have been engineered into helical bundles by introducing metal-binding ligands at specific locations to mimic those in native proteins. Examples are the Cys<sub>2</sub>His<sub>2</sub> ligand set found in zinc-finger proteins<sup>14</sup> and the His<sub>3</sub> set in carbonic anhydrase<sup>15</sup>. The X-ray crystal structure of an arsenic-bound three-stranded coiled-coil protein (Fig. 1c), which resembles the putative tris-Cys metal-binding environment of the natural arsenic-binding protein, ArsR, has been reported, affording the first biologically relevant thiolate mimic of an AsS<sub>3</sub> coordination<sup>16</sup>. Metal-binding ligands Glu and His have also been introduced by retrostructural analysis, whereby the active site of a protein can be separated into idealized secondary structural components (for example an  $\alpha$ -helix and a  $\beta$ -hairpin) and mathematically described as a root-mean-squared deviation from the idealized structure. This strategy led to the construction of dinuclear metalloproteins in  $\alpha$ -helical bundles that can bind two Zn(II), Co(II) or Fe(II), with the Zn(II) crystal structure (Fig. 1d) shown to be structurally analogous to the di-iron site of ribonucleotide reductase and ferritin<sup>17</sup>. One of these di-iron proteins was reported to catalyse

<sup>1</sup>Department of Chemistry, University of Illinois at Urbana-Champaign, Urbana, Illinois 61801, USA.

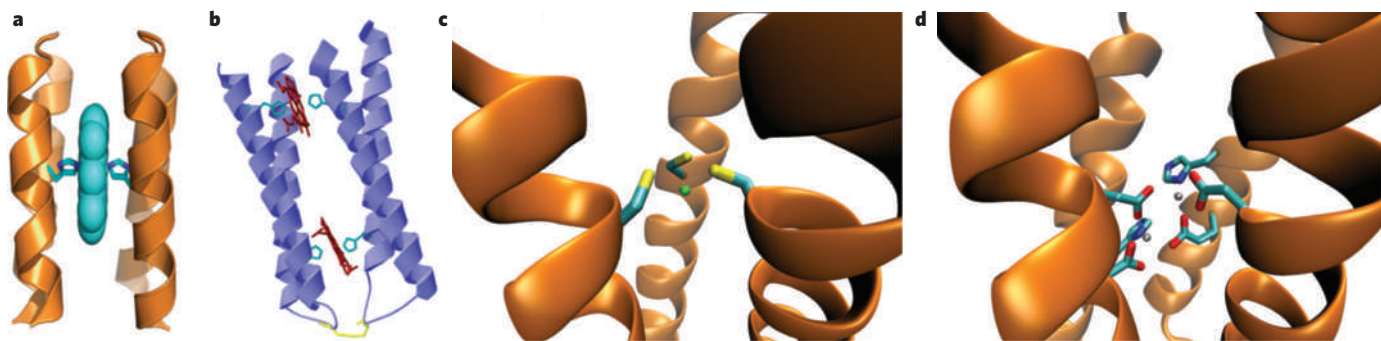


**Figure 1 | Designed metalloproteins using *de novo*-designed scaffolds.**

**a**, Computer model of a bis-histidine-ligated mono-haem  $\alpha$ -helical bundle. The haem cofactor (central molecule) is in cyan, and the relevant haem-binding His ligands are shown in stick format, with nitrogen in blue and carbon in cyan. (Panel modified from ref. 6 courtesy of W. DeGrado.)

**b**, Computer model of a bis-histidine-ligated multi-haem four- $\alpha$ -helical bundle. Haem cofactors are shown in red. Relevant haem-binding His ligands are shown in cyan, and the disulphide bond is shown in yellow.

(Panel modified from ref. 7 courtesy of P. L. Dutton.) **c**, X-ray crystal structure of As(III)-bound three-stranded coiled-coil protein (Protein Data Bank (PDB) code 2JGO)<sup>16</sup>. As(III) is represented as a green ball; relevant metal-ion-binding Cys ligands are indicated in stick format, with sulphur in yellow and carbon in cyan. **d**, X-ray crystal structure of di-Zn(II) due ferro 1 (PDB code 1EC5)<sup>17</sup>. Zn(II) ions are represented by grey balls; relevant metal-ion-binding His and Glu ligands are also indicated in stick format, with nitrogen in blue, oxygen in red, and carbon in cyan.

the two-electron oxidation of 4-aminophenol, similar to the reaction catalysed by di-iron phenol oxidases<sup>18,19</sup>.

Motivated by the natural occurrence of Cys-rich coordination sites in proteins, the introduction of Cys ligands led to the development of  $\alpha$ -helical coiled-coil metalloproteins capable of binding Co(II), Fe(II), Zn(II), Cd(II), Hg(II) and As(III)<sup>20–22</sup>. One interesting property of these *de novo*-designed proteins is that they can stabilize unusual metal-coordination states, for example three-coordinate Hg(II) stabilized by a tri-helical bundle, in preference to more normal coordination states, such as the bis-coordination often preferred by Hg(II)<sup>23,24</sup>. In other cases, metal binding can actually direct the folding and assembly of an  $\alpha$ -helical bundle from either a random coil or a less-folded or misfolded state, as has been shown for Cd(II)<sup>25</sup> and Hg(II)<sup>26</sup> binding to Cys-containing peptides predisposed to form helices. Interestingly, geometry-selective binding of two different Cd(II) atoms in one designed protein has been achieved and confirmed by the correlation of <sup>113</sup>Cd NMR and <sup>111m</sup>Cd perturbed-angular-correlation spectroscopy<sup>27,28</sup>.

In stark contrast to the design of  $\alpha$ -helical proteins, *de novo* design of  $\beta$ -structure proteins is still in its infancy, because there are few model systems with which to study  $\beta$ -sheets in isolation from other protein structures. The *de novo* design of a redox-active rubredoxin mimic, RM1, is a rare example of a structural and functional metallo- $\beta$ -sheet protein<sup>29</sup>. RM1 was shown to bind iron and reversibly cycle between the Fe(II) and Fe(III) oxidation states, mimicking native rubredoxin. The RM1  $\beta$ -hairpin structure was designed computationally by constraining the positions of the peptide that were strategic in mimicking and/or stabilizing the  $\beta$ -structure and by subsequently using another computer program, SCADS<sup>30</sup>, to select the most probable amino acids for the remaining positions.

### Metalloprotein design in native protein scaffolds

Designing metalloproteins using *de novo*-designed scaffolds offers the prospect of complete control over a protein's structure and metal-binding properties, but our current knowledge of protein folding limits the number of *de novo*-designed scaffolds to only a few types, such as the  $\alpha$ -helical bundles discussed above. It has been observed that proteins containing  $\beta$ -sheets tend to support more rigid and more pre-organized metal-binding sites than  $\alpha$ -helical proteins, which are inherently more flexible<sup>31</sup>. The Protein Data Bank contains many more natural protein scaffold types (~1,000) than it does *de novo*-designed scaffolds (<http://scop.mrc-lmb.cam.ac.uk/scop/count.html#scop-1.73>), and most of the natural protein scaffolds maintain the same fold and are of a similar stability even after numerous mutations. Therefore, metalloprotein design using native protein scaffolds instead of those designed *de novo* provides many more scaffold choices that are more tolerant to mutations, allowing less concern over decreased protein stability when

incorporating metal-binding sites into proteins. When chosen carefully, native proteins are also easier to crystallize than *de novo*-designed scaffolds, making three-dimensional characterization possible, which is critical to success. Perhaps the strongest argument for designing metalloproteins by using native scaffolds is that nature uses a similar approach — the same scaffold is often seen in numerous proteins with diverse metal-binding motifs and functions, suggesting that these native scaffolds are robust and modifiable. For example, the  $\beta$ -barrel fold has been shown to be used by ~600 types of protein, with diverse functions such as oxidase, reductase, amylase and dismutase activities. Discovering how nature is able to use the same scaffold to design a variety of metal-binding sites is an important goal of metalloprotein design<sup>1</sup>.

Biochemical techniques, such as site-directed mutagenesis, have been used extensively to study the function of metalloproteins. The loss of function accompanied by certain mutations (usually to highly conserved residues) allows the identification of residues essential for function. Although serving a different purpose, the same mutagenesis techniques can be used in metalloprotein design to impart new function into a protein scaffold by introducing residues that bind metal ions. This can be accomplished through the redesign of existing metal-binding sites to introduce novel functionality, the introduction of mononuclear metal-binding sites into proteins that do not bind metal ions natively, or the introduction of homonuclear or heteronuclear metal-binding sites into proteins. Design is often aided by empirical approaches based on prior knowledge and experience, the use of computer programs (rational design) or combinatorial selections.

The redesign of an existing metal-binding site to introduce new function or metal specificity is the simplest form of metalloprotein design, as this approach relies on the structural differences between template and target proteins and is amenable to empirical approaches as mentioned above. Despite its simplicity, this approach is still powerful in elucidating structural features important for the change in, or gain of, function by redesign. Haem proteins have been extensively redesigned in this way. They are one of the most diverse classes of protein, having functions ranging from electron transfer to small-molecule (for example oxygen and nitric oxide) transport, sensing and activation<sup>5,32,33</sup>. By systematically changing the characteristics of haem proteins, researchers have been able to convert one type of haem protein into another and to introduce new function or substrate specificity into a haem protein<sup>32–34</sup>.

The selectivity of designed metalloproteins for specific metals has also been used for the purpose of metal-sensing applications. Ratiometric Zn(II) sensors have been created by designing Zn(II)-binding sites into green fluorescent proteins and by taking advantage of the resultant fluorescent signal variations due to Zn(II)-dependent conformational changes<sup>35–37</sup>. The metal-binding site of NikR, a DNA-binding protein,



has been redesigned to bind  $\text{UO}_2^{2+}$  rather than its native  $\text{Ni}^{2+}$  cofactor<sup>38</sup> (Fig. 2a), resulting in an artificial protein that binds DNA only in the presence of  $\text{UO}_2^{2+}$ . In addition to sensors, designed metal-binding sites have allowed modulation of protein–protein interactions<sup>39,40</sup>, which are at the heart of many diverse biological functions. Because of complicated non-covalent interactions, it has been difficult to control the protein–protein interactions well. These designed metal-binding sites allow specific control over them.

More complex redesign of metal-binding sites may require rational design using computational biology, such as the simultaneous incorporation and adjustment of functional elements to convert the Gly II enzyme from a glyoxalase, which hydrolyses thioester bonds, to a  $\beta$ -lactamase<sup>41</sup>. In this case, to impart the new functionality, the metal-binding site had to be significantly redesigned to change the metal-binding geometry, as well as the substrate-binding pocket.

Although redesign of metal-binding sites can offer insight into the different structural features possessed by the template and target proteins, it cannot tell us about the structural features common to the metal-binding sites of both proteins. Introducing metal-binding sites into a protein location where no native metal-binding site is found can overcome this limitation, although this approach is more complex. A common strategy is to base the design on structural homology between the template protein (which contains no metal ions) and the target metalloprotein, in order to introduce metal-binding sites into the template protein at the positions corresponding to those in which they are found in the metalloprotein. Using this strategy, new  $\text{Zn}(\text{II})$ -binding sites have been introduced into charybdotoxin<sup>42</sup> and retinol-binding protein<sup>43</sup> to mimic carbonic anhydrase.

When there is no structural homology, computer-aided design using programs such as METAL-SEARCH<sup>44</sup> and DEZYMER<sup>45</sup> has become indispensable. A  $\text{Ca}(\text{II})$ <sup>46</sup>, a  $\text{Pb}(\text{II})$ <sup>47</sup> and an  $[\text{Fe}(\text{Cys})_4]$ <sup>45</sup> rubredoxin centre have all been designed into scaffold proteins using computer-aided design. In the case of an artificial rubredoxin site designed into the non-metalloprotein thioredoxin, it was found to undergo several rounds of air oxidation and reduction by  $\beta$ -mercaptoethanol, similar to native rubredoxins<sup>45</sup>.

Even more difficult in metalloenzyme design is the introduction into proteins of dinuclear metal-binding sites or metal clusters. An example is the binuclear  $\text{Cu}_A$  centre, consisting of two copper ions bridged by two Cys thiolates, with each copper ion also coordinated to a His nitrogen (Fig. 2b). New  $\text{Cu}_A$  centres were designed into the cupredoxins azurin<sup>48,49</sup> and amicyanin<sup>50,51</sup>, using a technique called loop-directed mutagenesis, in which the copper-binding loop of a cupredoxin is replaced by the corresponding loop in cytochrome *c* oxidase (COX; also known as CcO), which has similar structural homology. Loop-directed mutagenesis has also been used to introduce lanthanide-binding sites into a helix–turn–helix motif by drafting a calcium-binding EF-hand loop, and such a designed protein has been shown to promote DNA and phosphate hydrolysis<sup>52</sup>.

Heteronuclear bimetallic centres are also found in many natural proteins, and perform important biological functions such as oxygen reduction, lignin degradation and nitric oxide reduction. Designing metalloproteins to mimic the enzymes that carry out these complex reactions is even more challenging than designing homonuclear metal-binding sites because of the need to selectively place and bind two or more different metal centres. An example is the haem– $\text{Cu}_B$  centre in COX, where three His molecules bind a  $\text{Cu}(\text{II})$  ion that is  $\sim 4.5 \text{ \AA}$  away from the haem centre. Computer-aided design was used to introduce the His molecules above the haem of myoglobin at positions corresponding to those in COX<sup>53</sup> (Fig. 2c). Copper binding was confirmed by multiple spectroscopic techniques. Further studies showed the importance of the  $\text{Cu}_B$  site in  $\text{O}_2$  binding and reduction, as well as the significance of a proton network<sup>54</sup>. This designed protein also displays interesting functional properties, such as nitric oxide reduction<sup>55</sup>, similar to certain members of the COX family. A  $\text{Mn}(\text{II})$ -binding site has also been designed into cytochrome *c* peroxidase, resulting in a haem– $\text{Mn}(\text{II})$  protein that structurally and functionally mimics manganese

peroxidase<sup>56</sup>. Manganese peroxidase is a protein involved in lignin biodegradation, which is a critical step in biomass conversions from plant materials to biofuels.

In addition to discrete metal-binding sites, metal nanoparticles have been introduced into proteins<sup>57</sup>, including platinum nanoparticles into ferritin<sup>58</sup> and a small heat-shock protein<sup>59</sup>. The former catalyses size-selective alkene hydrogenation and the latter catalyses hydrogen production.

Although approaches based on empirical knowledge and rational design using computer programs have been relatively successful in designing metalloproteins, it is still difficult to design certain metalloproteins, especially functional ones, owing to the large number of potential interactions within the active site of a metalloenzyme. In this case, combinatorial design and directed evolution of new metalloenzymes is another powerful method. For example, directed evolution has been extensively applied to antibodies to develop new metalloenzymes. Using phage display, the 7G12 antibody protein was evolved to bind specifically to haem, with which the oxidation of tyramine could be catalysed<sup>60</sup>. A similar technique has recently been used to find antibodies specific for inorganic ligands, such as 2,2'-bis(diphenylphosphino)-1,1'-binaphthyl (BINAP) and 1,1'-bi-2-naphthol (BINOL), with the goal of developing completely new metalloenzymes<sup>61</sup>. Another striking example of this approach is the

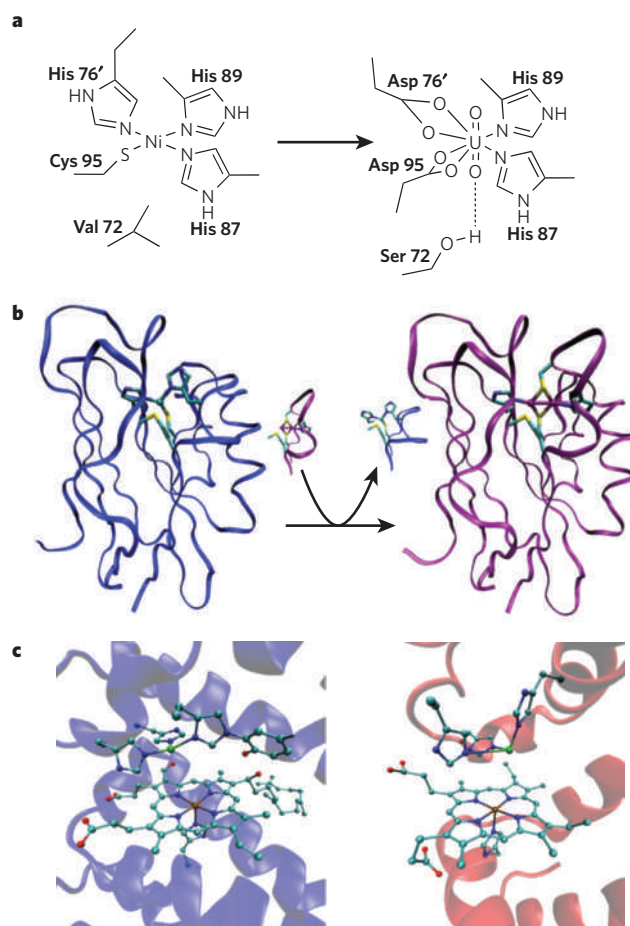


**Figure 2 | Designed metalloproteins using native scaffolds.** **a**, Native nickel-binding site of NikR (left) and the redesigned  $\text{UO}_2^{2+}$ -binding site of the NikR variant (right). **b**, Scheme showing the replacement of the copper-binding loop of blue copper azurin (blue; PDB code 4AZU) with the copper-binding loop from the  $\text{Cu}_A$ -containing subunit of COX (purple) to yield the dinuclear, purple  $\text{Cu}_A$  azurin construct (PDB code 1CC3). **c**, Catalytic haem– $\text{Cu}_B$  centre in COX (left; PDB code 1AR1) and the designed haem–copper model in sperm whale myoglobin (right). For panels **b** and **c**, active-site nitrogen is shown in blue, oxygen in red, carbon in cyan, sulphur in yellow and iron in brown; copper is shown in purple or blue (to match the protein) in **b** and green in **c**.



use of directed evolution to obtain a new form of cytochrome P450 with the ability to hydroxylate propane selectively, a function that has not yet been achieved using small-molecule catalysts<sup>62</sup>.

### Designing unnatural metalloproteins

Metalloprotein design using *de novo*-designed or native protein scaffolds has succeeded in providing valuable insights into the fundamental rules that govern protein structure and function. Replicating native protein structure and function, although challenging, is not the only goal of protein designers; they want to build proteins with properties that exceed those found in nature<sup>63</sup>. In recent years, the repertoire of functional groups such as amino acids or cofactors available to protein designers has been expanded beyond that available in biological systems.

A myriad of techniques have been developed for the incorporation of unnatural amino acids into a protein scaffold, each with its own advantages and limitations<sup>63</sup>. Total synthesis of proteins using solid-phase peptide synthesis allows the incorporation of any synthetic amino acid for which successful protection and deprotection techniques can be applied<sup>64</sup>, but cost and size constraints limit the use of total synthesis to smaller proteins (~60–100 amino acids). Native chemical ligation, involving covalent attachment of two synthetic peptides, has expanded this size<sup>65</sup>, but cost is still an issue, at least for very large proteins. Expressed-protein ligation, which involves the coupling of a bacterially expressed peptide fragment with a synthetic peptide fragment containing unnatural amino acids, has reduced the cost and extended the protein size even further, but it often requires a Cys residue at the point of ligation to maximize ligation efficiency<sup>66</sup> (methods have been developed to use other residues at the point of ligation, but with less efficiency). Methods not restricted by protein size include auxotroph generation<sup>67</sup>, chemical residue modification<sup>68</sup>

and cavity complementation<sup>69</sup>, but these methods have limited versatility in terms of the variety of unnatural amino acids that can be incorporated. A promising and versatile technique is the use of custom evolved transfer-RNA synthetase molecules for *in vitro* and *in vivo* translation of new residues through recognition of the amber stop codon<sup>70</sup>. A major contribution resulting from this approach was the design of a DNA-cleaving protein through site-specific genetic incorporation of the DNA-cleaving agent (2,2'-bipyridin-5-yl)alanine into a DNA-binding protein<sup>71</sup>. On addition of Cu(II) or Fe(II) and reducing agent to the protein, a double-stranded DNA substrate was cleaved at its consensus sequence. The variety of unnatural amino acids that this technique can incorporate is greater than that which can be used in auxotroph generation, chemical residue modification or cavity complementation, but less than that which can be used in total synthesis, native chemical ligation or expressed-protein ligation.

The expansion of the amino-acid regime has made significant contributions to the systematic determination of the role of each amino acid in tuning the activity of the metal centre to a given reactivity, and in increasing the breadth of chemical transformations performed by proteins. For instance, replacement of haem-binding His residues in *de novo*-designed four- $\alpha$ -helical bundles with 4- $\beta$ -(pyridyl)-L-alanine and 1-methyl-L-histidine has resulted in an increase in the reduction potential of the metal site for the pyridyl system and a preference for five-coordinate low-spin haem in the 1-methyl-L-histidine system<sup>72</sup>. In another system, introduction of bulky penicillamine ligands in place of Cys molecules led to the creation of an open metal-binding site in a ferredoxin model peptide<sup>73</sup>. This methodology resulted in the isolation of the first water-stable CdS<sub>3</sub> complex through subtle manipulation of steric crowding around the metal centre<sup>74</sup>. Furthermore, substitution of L-amino acids for their D-enantiomers resulted in fine control between three- and four-coordinate Cd(II) complexes in a *de novo*-designed metallopeptide<sup>75</sup>. Finally, the role of a conserved Tyr residue near the active site of rubredoxin was probed using a set of unnatural Tyr analogues in which the *para*-OH group was replaced with -H (as in native Phe), -F, -CN and -NO<sub>2</sub> groups, spanning a range of electron withdrawing strengths<sup>76</sup> (Fig. 3a). Interestingly, a linear correlation was found between the reduction potential of the rubredoxin and the Hammett  $\sigma_p$  value, but no such trend was observed with dipole moment or *para*-substituent size.

A powerful advantage of introducing unnatural amino acids is the ability to probe the role of the amide backbone, because site-directed mutagenesis using natural amino acids cannot modify the protein backbone. Both the carbonyl and nitrogen functionalities of the protein backbone have been implicated in critical and specific hydrogen-bonding interactions, either directly to the metal or to the metal ligands. For example, the Fe<sub>4</sub>S<sub>4</sub> cluster of high-potential iron proteins has such an amide interaction, which was found to be responsible for stabilizing the reduced form through attenuation of a metal-bound sulphur<sup>77</sup>. Replacement of this amide linkage with an ester linkage indeed resulted in a lowering of the reduction potential by ~100 mV.

Through the use of expressed-protein ligation, the metal-bound Cys and Met residues in the electron-transfer protein azurin were replaced with isostructurally similar unnatural amino acids<sup>78,79</sup> (Fig. 3b). Replacing Cys with selenocysteine resulted in significantly different spectral features, but did little to affect the reduction potential. By contrast, replacing methionine with selenomethionine and other isostructural variants resulted in spectral features similar to those of the wild-type protein, but with significantly different reduction potentials. The use of unnatural amino acids helped to identify the hydrophobicity of the residues at this position as the major factor in tuning the reduction potential of the protein, resulting in new metalloproteins with reduction potentials beyond those found in native azurin and its variants.

The repertoire of non-native functionalities has also been expanded through the incorporation into the protein scaffold of metal-containing cofactors not found in nature. Biological systems incorporate metal cofactors such as haem by both non-covalent and covalent means. Of the covalent approaches in nature, both single-point and dual-point

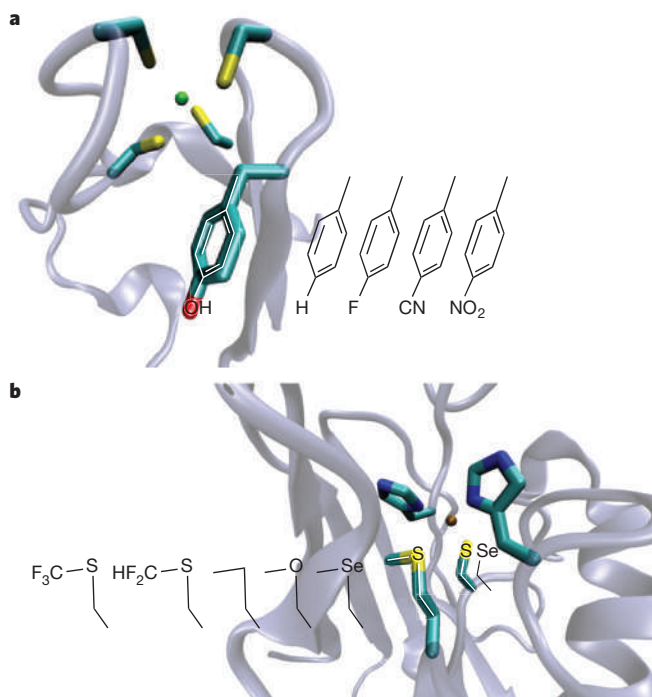


**Figure 3 | Site-specific incorporation of unnatural amino acids into a protein scaffold for the tuning of metalloprotein functional properties.** **a**, Crystal structure of rubredoxin (PDB code 1CAA), showing iron (green) and four Cys residues (in stick format). The -OH group in the highlighted phenylalanine has been replaced with an -H, -F-, -CN- or -NO<sub>2</sub> group<sup>76</sup>. **b**, Crystal structure of azurin (PDB code 4AZU), showing copper (brown) and one Cys, one Met and two His residues (in stick format). The highlighted Cys has been replaced with selenocysteine<sup>78</sup>, and the highlighted Met has been replaced with selenomethionine, oxomethionine, norleucine and di- and trifluoromethionine<sup>79</sup>. For both panels, active-site nitrogen is shown in blue, oxygen in red, carbon in cyan and sulphur in yellow.

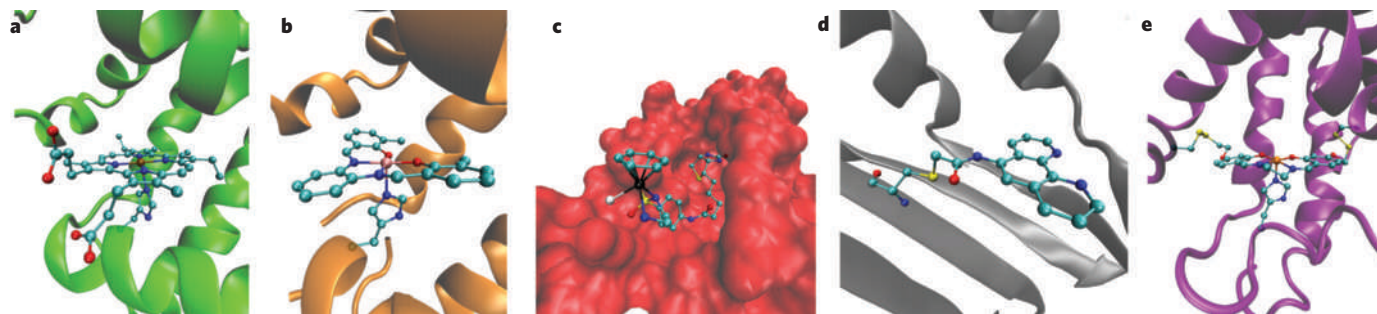


**Figure 4 | Examples of strategies for the incorporation of non-native metal cofactors into protein scaffolds.** **a**, Myoglobin (protein backbone shown in green) in which native haem *b* has been replaced non-covalently with iron porphycene (stick and ball illustration); generated from the structure with PDB code 2D6C (ref. 82). Iron is shown as a brown sphere. **b**, Myoglobin (protein backbone in orange) in which native haem *b* has been replaced non-covalently with Cr(3,3'-Me<sub>2</sub>-salophen) (stick and ball illustration); generated from the structure with PDB code 1J3F (ref. 86). Chromium is shown as a pale pink sphere. **c**, Streptavidin (protein backbone in red) into which biotinylated  $\eta^6$ -(benzene)RuCl (stick and ball illustration) has been incorporated non-covalently; generated from the structure with PDB code

2QCB (ref. 91). Ruthenium is shown as a black sphere. **d**, Adipocyte lipid-binding protein (protein backbone in grey) to which 1,10-phenanthroline (stick and ball illustration) has been attached covalently through a single point, Cys 117; generated from the structure with PDB code 1A18 (ref. 94). **e**, Myoglobin (with Leu72Cys and Tyr103Cys) (protein backbone in magenta) in which a Mn-salen complex (stick and ball illustration) is anchored covalently at two points; generated from native myoglobin structure and structural modelling<sup>95</sup>. Manganese is shown as an orange sphere. For all active-site stick and ball illustrations, nitrogen is shown in blue, oxygen in red, carbon in cyan and sulphur in yellow.

anchoring strategies are used to position the prosthetic group within the protein scaffold. These strategies have been used for the incorporation of non-native metal cofactors, with the non-covalent approach being the most extensively used strategy. For example, replacement of the native haem cofactor in myoglobin with less symmetrical structural isomers such as porphycene (Fig. 4a) has resulted in new or enhanced O<sub>2</sub>-binding affinity or O<sub>2</sub>-activation activities<sup>80–82</sup>. In addition to native protein scaffolds, *de novo*-designed  $\alpha$ -helical bundles have also been engineered to bind non-biological haem cofactors in preference to biological haems<sup>83,84</sup>.

In addition to haem analogues, other planar moieties similar to haem have been substituted into haem proteins. For example, strong binding of manganese, iron and chromium Schiff-base complexes into a myoglobin scaffold was observed after careful design of the protein to relieve steric repulsion in the active site<sup>57,85,86</sup> (Fig. 4b). Such rational design has resulted in new asymmetrical catalysts capable of oxidation-rate enhancement and chiral induction.

It is much more challenging to incorporate non-planar metal-containing cofactors into proteins in which there is no native binding site. One way to do so is through derivatization of the catalyst with a moiety exhibiting natural bio-affinity for a protein target, through, for example, the use of the high-affinity biotin–streptavidin couple (association constant,  $K_a \sim 10^{15} \text{ M}^{-1}$ ). In this way, metal cofactors such as a ruthenium catalyst have been incorporated into the streptavidin scaffold through covalent attachment to a biotin moiety<sup>87–89</sup> (Fig. 4c), resulting in artificial biocatalysts with new activities, including hydrogenation of alkenes, transfer hydrogenation of ketones, and carbon–carbon bond formation through allylic alkylation (with up to 99% enantiomeric excess)<sup>88–91</sup>.

Although the use of biotin and avidin/streptavidin to incorporate non-native metal cofactors is powerful, not all cofactors are amenable to such a strategy, as binding affinity and location may not be readily controlled. Covalent attachment is an effective and versatile method for linking a cofactor to the protein at a defined location through selective conjugation techniques involving engineered or native Cys or Lys residues. This strategy has been used to attach DNA-cleaving agents such as 1,10-phenanthroline-copper and iron–EDTA to DNA-binding proteins for the generation of artificial nucleases<sup>92</sup>, and in the case of 1,10-phenanthroline-copper (Fig. 4d) for enantioselective hydrolysis<sup>93,94</sup>.

The single-point covalent approach mentioned above makes it possible to attach a non-native cofactor at a defined location, but it does not necessarily fix the conformation of the cofactor inside the protein. For example, single covalent attachment of a 4-(2-methanesulphonylthio-ethoxy)salicylidene-1,2-ethanediamino-manganese(III) (Mn-salen) cofactor to apo myoglobin through a single Cys-selective linker

resulted in only 12% enantiomeric excess towards sulfoxidation of thioanisole<sup>95</sup>, suggesting that the Mn-salen conformation may be too flexible inside myoglobin to facilitate high enantioselectivity. Addition of a second linker (Fig. 4e) to the cofactor together with selective cavity positioning led to a significant increase in catalytic efficiency (more than a sevenfold increase) and enantioselectivity (increased from 12% to 88%)<sup>95,96</sup>. Furthermore, it has been shown that such incorporation of Mn-salen into a myoglobin scaffold significantly enhances the chemoselectivity in oxidation of thioanisole with H<sub>2</sub>O<sub>2</sub>, almost eliminating over-oxidation to the sulphone product through electrostatic exclusion of the sulfoxide product from the site<sup>96</sup>.

### Lessons learned and future challenges

Tremendous progress has been made in this exciting field of synthetic biology. Success is measured not only by how closely the designed protein resembles the native protein, but also by the insights gained from the process. For example, the crystal structure of a designed Cu<sub>A</sub>

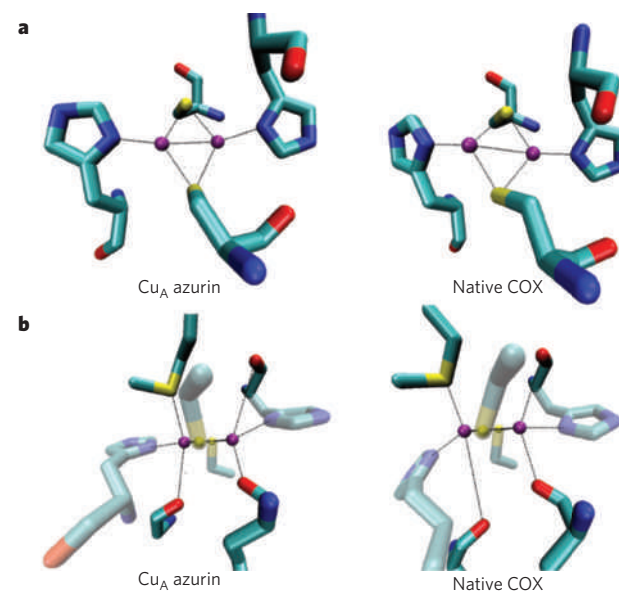


**Figure 5 | Close match between a designed metalloprotein and its native target protein.** Crystal structures of a designed Cu<sub>A</sub> site in azurin (left; PDB code 1CC3)<sup>49</sup> and a Cu<sub>A</sub> site in native COX (right; PDB code 1AR1) as viewed from above the Cu<sub>2</sub>(S<sub>2</sub>Cys)<sub>2</sub> plane (**a**) and along the Cu<sub>2</sub>(S<sub>2</sub>Cys)<sub>2</sub> plane (**b**). Active-site nitrogen is shown in blue, oxygen in red, carbon in cyan, sulphur in yellow and copper in purple.



site is almost identical to that of native Cu<sub>A</sub>, including both primary and secondary coordination spheres<sup>49</sup> (Fig. 5), indicating that metalloprotein design can lead to structures closely resembling those in nature. More importantly, two metal-binding sites, native blue copper and the designed Cu<sub>A</sub> centre, were placed in the same azurin scaffold, allowing the electron-transfer properties of two different metal centres to be compared in the same protein<sup>97</sup> — a task that is difficult, if not impossible, to do by studying native proteins. Such a comparison provided deeper insight that the Cu<sub>A</sub> centre is a more efficient electron-transfer centre than the blue copper centre<sup>97</sup>.

Given the initial successes, now is a good time to summarize the lessons learned and to recognize future challenges. Essential to success is the recognition that structural biology must have a major role in the design process. Some early metalloprotein designs generated much excitement in the field, only to be shown by X-ray crystallography to contain a different metal-binding site than originally designed. Although spectroscopy is invaluable in providing support for design, more concrete evidence from three-dimensional structural characterization is essential. In addition to confirming the initial design, it provides detailed information on what has or has not been designed correctly, thus providing insights for the next level of design.

Furthermore, design of the primary coordination sphere is often not enough to confer structure and/or function. Consideration of the environment surrounding the primary coordination sphere is critical to successful design. One main example is water molecules found at specific locations inside the protein, where the associated hydrogen-bonding interactions have essential roles in many metalloproteins, including cytochrome P450, haem oxygenase (HO) and COX<sup>33</sup>. For example, even though a Cu<sub>B</sub> centre that structurally mimics the haem–copper centre in COX was designed into myoglobin<sup>53</sup>, its function mimics HO rather than COX when O<sub>2</sub> is used as an oxidant<sup>54</sup>. When H<sub>2</sub>O<sub>2</sub> was used as an oxidant, a ferryl species, a putative intermediate in COX activity, was observed. These results suggest that the extra protons introduced through H<sub>2</sub>O<sub>2</sub> are important for function<sup>54</sup>. The introduction of an additional hydrogen-bonding donor through the replacement of the type-*b* haem in myoglobin with a type-*o* haem, resembling the haem found in COX, allowed suppression of HO activity and promotion of COX activity<sup>98</sup>.

Metalloprotein design has focused mainly on the positive design of structural features responsible for correct metal-site geometry and function. However, negative design to prevent competing metal-site geometries and unwanted functions is also critical. For example, in designing dinuclear metalloproteins in a helical bundle, there was a possibility that undesirable heterotetrameric motifs and homooligomers would form because the protein comprised different peptides. To circumvent this problem, a computational algorithm was included to destabilize these interactions<sup>99</sup>.

The final lesson is that metalloprotein design often results in lower stability because of changes made to the protein scaffold. Sometimes, the stability is so low that even if the design is valid, not enough stable protein can be obtained to prove the design. The stability of the protein must be improved, even if function may not be improved directly. A good example of this was demonstrated in cytochrome P450: only after the protein was stabilized by further mutations could the initial design confer new activity<sup>100</sup>.

The majority of the successes in the field of metalloprotein design are derived from the construction of a geometrically correct, sterically compatible primary coordination sphere sufficient to reproduce the structure and function of a desired metal centre, such as a bis-histidine haem or His<sub>2</sub>Cys<sub>2</sub> tetrahedral Zn(II) site. However, many metal-binding sites in proteins, such as the type-1 copper and Cu<sub>A</sub> centres, are not necessarily in their preferred metal-ion geometric states. Therefore, one future challenge is to design metal sites and metal clusters with unique geometric requirements. Other challenges include the design of metal sites at the interface of two or more proteins, which occur often in proteins but have not been designed until recently<sup>39,40</sup>, and the design of metal-binding sites from membrane proteins, which has

also been rarely achieved. A greater challenge is the design of protein metal-binding sites requiring helpers called metallochaperones. Consideration of the interactions between metal ions and protein hosts is not enough to confer function, making their interactions with metallochaperones necessary in the design process. In addition to metal-binding-site design, functional metalloproteins also require the design of a substrate-binding site for catalysis. A higher level of complexity involves coupling the redox reaction of a designed metal-binding site to proton transfer, conformational change or charge separation.

To meet these challenges, advances in a number of fields are required. The most important requirement is the development of better computer programs for designing metal-binding sites in proteins, including consideration of structural features beyond the primary coordination sphere. In contrast to well-defined force fields for peptide bonds and amino-acid side chains, most force fields for metal-binding sites are ill-defined because there are many more variables involved in defining a metal-binding site. These variables include variation in the identity of the metal ion, different oxidation states of the same metal ions and different ligand and geometric preferences of different metal ions. Density functional theory has been an excellent tool in defining small metal complexes. Extending its success to metal-binding sites in proteins, together with other leading algorithms, such as QM/MM (quantum mechanics/molecular mechanics), is required for the successful rational design of metalloproteins. Despite these challenges, metalloprotein design will remain a vibrant field in which researchers will continue to design metalloproteins with novel functions and gain new insights.

1. Lu, Y., Berry, S. M. & Pfister, T. D. Engineering novel metalloproteins: design of metal-binding sites into native protein scaffolds. *Chem. Rev.* **101**, 3047–3080 (2001).
2. Barker, P. D. Designing redox metalloproteins from bottom-up and top-down perspectives. *Curr. Opin. Struct. Biol.* **13**, 490–499 (2003).
3. Lu, Y. Metalloprotein and metallo-DNA/RNAzyme design: current approaches, success measures and future challenges. *Inorg. Chem.* **45**, 9930–9940 (2006).
4. DeGrado, W. F., Summa, C. M., Pavone, V., Nastri, F. & Lombardi, A. *De novo* design and structural characterization of proteins and metalloproteins. *Annu. Rev. Biochem.* **68**, 779–819 (1999).
5. Reedy, C. J. & Gibney, B. R. Heme protein assemblies. *Chem. Rev.* **104**, 617–649 (2004).
6. Choma, C. T. et al. Design of a heme-binding four-helix bundle. *J. Am. Chem. Soc.* **116**, 856–865 (1994).
7. Robertson, D. E. et al. Design and synthesis of multi-heme proteins. *Nature* **368**, 425–432 (1994).
8. Case, M. A. & McLendon, G. L. Metal-assembled modular proteins: toward functional protein design. *Acc. Chem. Res.* **37**, 754–762 (2004).
9. Huang, S. S., Koder, R. L., Lewis, M., Wand, A. J. & Dutton, P. L. The HP-1 maquette: from an apoprotein structure to a structured hemoprotein designed to promote redox-coupled proton exchange. *Proc. Natl Acad. Sci. USA* **101**, 5536–5541 (2004).
10. Sasaki, T. & Kaiser, E. T. Helichrome: synthesis and enzymic activity of a designed hemeprotein. *J. Am. Chem. Soc.* **111**, 380–381 (1989).
11. Das, A. & Hecht, M. H. Peroxidase activity of *de novo* heme proteins immobilized on electrodes. *J. Inorg. Biochem.* **101**, 1820–1826 (2007).
12. Monien, B. H., Drepper, F., Sommerhalter, M., Lubitz, W. & Haehnel, W. Detection of heme oxygenase activity in a library of four-helix bundle proteins: towards the *de novo* synthesis of functional heme proteins. *J. Mol. Biol.* **371**, 739–753 (2007).
13. Koder, R. L. et al. Design and engineering of an O<sub>2</sub> transport protein. *Nature* **458**, 305–309 (2009).  
This paper reports the design of an O<sub>2</sub> transport protein that has O<sub>2</sub> affinities and exchange timescales that match those of natural globins.
14. Klemba, M. & Regan, L. Characterization of metal binding by a designed protein: single ligand substitutions at a tetrahedral Cys<sub>2</sub>His<sub>2</sub> site. *Biochemistry* **34**, 10094–10100 (1995).
15. Handel, T. & DeGrado, W. F. *De novo* design of a Zn<sup>2+</sup>-binding protein. *J. Am. Chem. Soc.* **112**, 6710–6711 (1990).
16. Touw, D. S., Nordman, C. E., Stuckey, J. A. & Pecoraro, V. L. Identifying important structural characteristics of arsenic resistance proteins by using designed three-stranded coiled coils. *Proc. Natl Acad. Sci. USA* **104**, 11969–11974 (2007).
17. Lombardi, A. et al. Retrostructural analysis of metalloproteins: application to the design of a minimal model for diiron proteins. *Proc. Natl Acad. Sci. USA* **97**, 6298–6305 (2000).  
This paper reports the use of a novel method to design functional metalloproteins that do not contain haem.
18. Kaplan, J. & DeGrado, W. F. *De novo* design of catalytic proteins. *Proc. Natl Acad. Sci. USA* **101**, 11566–11570 (2004).
19. Calhoun, J. R. et al. Oxygen reactivity of the biferrous site in the *de novo* designed four helix bundle peptide DFsc: nature of the 'intermediate' and reaction mechanism. *J. Am. Chem. Soc.* **130**, 9188–9189 (2008).
20. Matzapetakis, M. et al. Comparison of the binding of cadmium(II), mercury(II), and arsenic(III) to the *de novo* designed peptides TRI L12C and TRI L16C. *J. Am. Chem. Soc.* **124**, 8042–8054 (2002).
21. Ghosh, D., Lee, K. H., Demeler, B. & Pecoraro, V. L. Linear free-energy analysis of mercury(II) and cadmium(II) binding to three-stranded coiled coils. *Biochemistry* **44**, 10732–10740 (2005).



22. Petros, A. K., Reddi, A. R., Kennedy, M. L., Hyslop, A. G. & Gibney, B. R. Femtomolar Zn(II) affinity in a peptide-based ligand designed to model thiolate-rich metalloprotein active sites. *Inorg. Chem.* **45**, 9941–9958 (2006).
23. Dieckmann, G. R. *et al.* De novo design of mercury-binding two- and three-helical bundles. *J. Am. Chem. Soc.* **119**, 6195–6196 (1997).
24. Ghosh, D. & Pecoraro, V. L. Probing metal–protein interactions using a *de novo* design approach. *Curr. Opin. Chem. Biol.* **9**, 97–103 (2005).
25. Kharenko, O. A. & Ogawa, M. Y. Metal-induced folding of a designed metalloprotein. *J. Inorg. Biochem.* **98**, 1971–1974 (2004).
26. Farrer, B. T. & Pecoraro, V. L. Hg(II) binding to a weakly associated coiled coil nucleates an encoded metalloprotein fold: a kinetic analysis. *Proc. Natl Acad. Sci. USA* **100**, 3760–3765 (2003).
27. Iranzo, O., Jakusch, T., Lee, K.-H., Hemmingsen, L. & Pecoraro, V. L. The correlation of  $^{113}\text{Cd}$  NMR and  $^{111m}\text{Cd}$  PAC spectroscopies provides a powerful approach for the characterization of the structure of Cd(II)-substituted Zn(II) proteins. *Chem. Eur. J.* **15**, 3761–3772 (2009).
28. Peacock, A. F. A., Iranzo, O. & Pecoraro, V. L. Harnessing nature's ability to control metal ion coordination geometry using *de novo* designed peptides. *Dalton Trans.* 2271–2280 (2009).  
This paper describes an excellent demonstration of the use of a *de novo*-designed peptide to control metal-binding-site geometry.
29. Nanda, V. *et al.* De novo design of a redox-active minimal rubredoxin mimic. *J. Am. Chem. Soc.* **127**, 5804–5805 (2005).  
This paper reports a rare example of a designed metalloprotein in a *de novo*-designed  $\beta$ -structure-containing protein.
30. Kono, H. & Saven, J. G. Statistical theory for protein combinatorial libraries. Packing interactions, backbone flexibility, and the sequence variability of a main-chain structure. *J. Mol. Biol.* **306**, 607–628 (2001).
31. Williams, R. J. P. Energised (entatic) states of groups and of secondary structures in proteins and metalloproteins. *Eur. J. Biochem.* **234**, 363–381 (1995).
32. Ueno, T., Ohki, T. & Watanabe, Y. Molecular engineering of cytochrome P 450 and myoglobin for selective oxygenations. *J. Porphyrins Phthalocyanines* **8**, 279–289 (2004).
33. Yeung, N. & Lu, Y. One heme, diverse functions: using biosynthetic myoglobin models to gain insights into heme copper oxidases and nitric oxide reductases. *Chem. Biodivers.* **5**, 1437–1454 (2008).
34. Ozaki, S.-I., Matsui, T. & Watanabe, Y. Conversion of myoglobin into a highly stereospecific peroxxygenase by the L29H/H64L mutation. *J. Am. Chem. Soc.* **118**, 9784–9785 (1996).
35. Jensen, K. K., Martini, L. & Schwartz, T. W. Enhanced fluorescence resonance energy transfer between spectral variants of green fluorescent protein through zinc-site engineering. *Biochemistry* **40**, 938–945 (2001).
36. Evers, T. H., Appelhof, M. A., de Graaf-Heuvelmans, P. T., Meijer, E. W. & Merckx, M. Ratiometric detection of Zn(II) using chelating fluorescent protein chimeras. *J. Mol. Biol.* **374**, 411–425 (2007).
37. Mizuno, T., Murao, K., Tanabe, Y., Oda, M. & Tanaka, T. Metal-ion dependent GFP emission *in vivo* by combining a circularly permuted green fluorescent protein with an engineered metal ion-binding coiled-coil. *J. Am. Chem. Soc.* **129**, 11378–11383 (2007).
38. Wegner, S. V., Boyaci, H., Chen, H., Jensen, M. P. & He, C. Engineering a uranyl-specific binding protein from NikR. *Angew. Chem. Int. Edn Engl.* **48**, 2339–2341 (2009).
39. Salgado, E. N., Faraone-Mennella, J. & Tezcan, F. A. Controlling protein–protein interactions through metal coordination: assembly of a 16-helix bundle protein. *J. Am. Chem. Soc.* **129**, 13374–13375 (2007).
40. Matthews, J. M., Loughlin, F. E. & Mackay, J. P. Designed metal-binding sites in biomolecular and bioinorganic interactions. *Curr. Opin. Struct. Biol.* **18**, 484–490 (2008).
41. Park, H. S. *et al.* Design and evolution of new catalytic activity with an existing protein scaffold. *Science* **311**, 535–538 (2006).
42. Vita, C., Roumestand, C., Tom, F. & Menez, A. Scorpion toxins as natural scaffolds for protein engineering. *Proc. Natl Acad. Sci. USA* **92**, 6404–6408 (1995).
43. Müller, H. N. & Skerra, A. Grafting of a high-affinity Zn(II)-binding site on the  $\beta$ -barrel of retinol-binding protein results in enhanced folding stability and enables simplified purification. *Biochemistry* **33**, 14126–14135 (1994).
44. Desjarlais, J. R. & Clarke, N. D. Computer search algorithms in protein modification and design. *Curr. Opin. Struct. Biol.* **8**, 471–475 (1998).
45. Benson, D. E., Wisz, M. S., Liu, W. & Hellinga, H. W. Construction of a novel redox protein by rational design: conversion of a disulfide bridge into a mononuclear iron-sulfur center. *Biochemistry* **37**, 7070–7076 (1998).
46. Yang, W. *et al.* Rational design of a calcium-binding protein. *J. Am. Chem. Soc.* **125**, 6165–6171 (2003).
47. Shete, V. S. & Benson, D. E. Protein design provides lead(II) ion biosensors for imaging molecular fluxes around red blood cells. *Biochemistry* **48**, 462–470 (2009).
48. Hay, M., Richards, J. H. & Lu, Y. Construction and characterization of an azurin analog for the purple copper site in cytochrome c oxidase. *Proc. Natl Acad. Sci. USA* **93**, 461–464 (1996).
49. Robinson, H. *et al.* Structural basis of electron transfer modulation in the purple Cu<sub>A</sub> center. *Biochemistry* **38**, 5677–5683 (1999).
50. Dennison, C., Vijgenboom, E., de Vries, S., van der Oost, J. & Canters, G. W. Introduction of a Cu<sub>A</sub> site into the blue copper protein amicyanin from *Thiobacillus versutus*. *FEBS Lett.* **365**, 92–94 (1995).
51. Jones, L. H., Liu, A. & Davidson, V. L. An engineered Cu<sub>A</sub> amicyanin capable of intermolecular electron transfer reactions. *J. Biol. Chem.* **278**, 47269–47274 (2003).
52. Franklin, S. J. & Welch, J. T. The helix–turn–helix as a scaffold for chimeric nuclease design. *Comments Inorg. Chem.* **26**, 127–164 (2005).
53. Sigman, J. A., Kwok, B. C. & Lu, Y. From myoglobin to heme–copper oxidase: design and engineering of a Cu<sub>B</sub> center into sperm whale myoglobin. *J. Am. Chem. Soc.* **122**, 8192–8196 (2000).
54. Sigman, J. A., Kim, H. K., Zhao, X., Carey, J. R. & Lu, Y. The role of copper and protons in heme–copper oxidases: kinetic study of an engineered heme–copper center in myoglobin. *Proc. Natl Acad. Sci. USA* **100**, 3629–3634 (2003).
55. Zhao, X., Yeung, N., Russell, B. S., Garner, D. K. & Lu, Y. Catalytic reduction of NO to N<sub>2</sub>O by a designed heme copper center in myoglobin: implications for the role of metal ions. *J. Am. Chem. Soc.* **128**, 6766–6767 (2006).
56. Yeung, B. K. S., Wang, X., Sigman, J. A., Petillo, P. A. & Lu, Y. Construction and characterization of a manganese-binding site in cytochrome c peroxidase: towards a novel manganese peroxidase. *Chem. Biol.* **4**, 215–221 (1997).
57. Abe, S., Ueno, T. & Watanabe, Y. Artificial metalloproteins exploiting vacant space: preparation, structures, and functions. *Top. Organomet. Chem.* **25**, 25–43 (2009).
58. Ueno, T. *et al.* Size-selective olefin hydrogenation by a Pd nanocluster provided in an apo-ferritin cage. *Angew. Chem. Int. Edn Engl.* **43**, 2527–2530 (2004).
59. Varpness, Z., Peters, J. W., Young, M. & Douglas, T. Biomimetic synthesis of a H<sub>2</sub> catalyst using a protein cage architecture. *Nano Lett.* **5**, 2306–2309 (2005).
60. Yin, J., Mills, J. H. & Schultz, P. G. A catalysis-based selection for peroxidase antibodies with increased activity. *J. Am. Chem. Soc.* **126**, 3006–3007 (2004).
61. Rasmussen, B. S. *et al.* Enantioselective proteins: selection, binding studies and molecular modeling of antibodies with affinity towards hydrophobic BINOL derivatives. *ChemBiochem* **8**, 1974–1980 (2007).
62. Fasan, R., Chen, M. M., Crook, N. C. & Arnold, F. H. Engineered alkane-hydroxylating cytochrome P450BM3 exhibiting natively catalytic properties. *Angew. Chem. Int. Edn Engl.* **46**, 8414–8418 (2007).  
This paper describes a good example of evolving metalloproteins with new and more demanding activities.
63. Lu, Y. Design and engineering of metalloproteins containing unnatural amino acids or non-native metal-containing cofactors. *Curr. Opin. Chem. Biol.* **9**, 118–126 (2005).  
This paper is a good review of the emerging field of metalloprotein design using unnatural amino acids and non-native metal-containing cofactors.
64. Merrifield, B. Concept and early development of solid-phase peptide synthesis. *Methods Enzymol.* **289**, 3–13 (1997).
65. Dawson, P. E., Muir, T. W., Clark-Lewis, I. & Kent, S. B. H. Synthesis of proteins by native chemical ligation. *Science* **266**, 776–779 (1994).
66. Muir, T. W. Semisynthesis of proteins by expressed protein ligation. *Annu. Rev. Biochem.* **72**, 249–289 (2003).
67. Ikeda, Y. *et al.* Synthesis of a novel histidine analog and its efficient incorporation into a protein *in vivo*. *Protein Eng.* **16**, 699–706 (2003).
68. Qi, D., Tann, C.-M., Haring, D. & Distefano, M. D. Generation of new enzymes via covalent modification of existing proteins. *Chem. Rev.* **101**, 3081–3111 (2001).
69. Barrick, D. Depletion and replacement of protein metal ligands. *Curr. Opin. Biotechnol.* **6**, 411–418 (1995).
70. Noren, C. J., Anthony-Cahill, S. J., Griffith, M. C. & Schultz, P. G. A general method for site-specific incorporation of unnatural amino acids into proteins. *Science* **244**, 182–188 (1989).
71. Lee, H. S. & Schultz, P. G. Biosynthesis of a site-specific DNA cleaving protein. *J. Am. Chem. Soc.* **130**, 13194–13195 (2008).  
This paper reports the first example of introducing unnatural amino acids that bind metal ions with functional properties.
72. Privett, H. K., Reedy, C. J., Kennedy, M. L. & Gibney, B. R. Nonnatural amino acid ligands in heme protein design. *J. Am. Chem. Soc.* **124**, 6828–6829 (2002).
73. Petros, A. K., Shaner, S. E., Costello, A. L., Tierney, D. L. & Gibney, B. R. Comparison of cysteine and penicillamine ligands in a Co(II) maquette. *Inorg. Chem.* **43**, 4793–4795 (2004).
74. Lee, K.-H., Cabello, C., Hemmingsen, L., Marsh, E. N. G. & Pecoraro, V. L. Using nonnatural amino acids to control metal–coordination number in three-stranded coiled coils. *Angew. Chem. Int. Edn Engl.* **45**, 2864–2868 (2006).
75. Peacock, A. F. A., Hemmingsen, L. & Pecoraro, V. L. Using diastereopeptides to control metal ion coordination in proteins. *Proc. Natl Acad. Sci. USA* **105**, 16566–16571 (2008).
76. Low, D. W. & Hill, M. G. Rational fine-tuning of the redox potentials in chemically synthesized rubredoxins. *J. Am. Chem. Soc.* **120**, 11536–11537 (1998).
77. Low, D. W. & Hill, M. G. Backbone-engineered high-potential iron proteins: effects of active-site hydrogen binding on reduction potential. *J. Am. Chem. Soc.* **122**, 11039–11040 (2000).  
This paper demonstrates the power of using unnatural amino acids in tuning metalloprotein redox potentials using backbone positions.
78. Berry, S. M., Gieselman, M. D., Nilges, M. J., Van der Donk, W. A. & Lu, Y. An engineered azurin variant containing a selenocysteine copper ligand. *J. Am. Chem. Soc.* **124**, 2084–2085 (2002).
79. Berry, S. M., Ralle, M., Low, D. W., Blackburn, N. J. & Lu, Y. Probing the role of axial methionine in the blue copper center of azurin with unnatural amino acids. *J. Am. Chem. Soc.* **125**, 8760–8768 (2003).  
This paper presents a clear demonstration of using isostructural unnatural amino acids in fine-tuning the redox properties of metalloproteins.
80. Hayashi, T. & Hisaeda, Y. New functionalization of myoglobin by chemical modification of heme–propionates. *Acc. Chem. Res.* **35**, 35–43 (2002).
81. Matsuo, T., Hayashi, T. & Hisaeda, Y. Reductive activation of dioxygen by a myoglobin reconstituted with a flavohemin. *J. Am. Chem. Soc.* **124**, 11234–11235 (2002).
82. Hayashi, T. *et al.* Crystal structure and peroxidase activity of myoglobin reconstituted with iron porphyrine. *Inorg. Chem.* **45**, 10530–10536 (2006).
83. Cochran, F. V. *et al.* Computational *de novo* design and characterization of a four-helix bundle protein that selectively binds a nonbiological cofactor. *J. Am. Chem. Soc.* **127**, 1346–1347 (2005).
84. Bender, G. M. *et al.* De novo design of a single-chain diphenylporphyrin metalloprotein. *J. Am. Chem. Soc.* **129**, 10732–10740 (2007).
85. Ohashi, M. *et al.* Preparation of artificial metalloenzymes by insertion of chromium Schiff base complexes into apomyoglobin mutants. *Angew. Chem. Int. Edn Engl.* **42**, 1005–1008 (2003).
86. Ueno, T. *et al.* Crystal structures of artificial metalloproteins: tight binding of

- FeIII(Schiff-base) by mutation of Ala71 to Gly in apo-myoglobin. *Inorg. Chem.* **43**, 2852–2858 (2004).
87. Wilson, M. E. & Whitesides, G. M. Conversion of a protein to a homogeneous asymmetric hydrogenation catalyst by site-specific modification with a diphosphinerhodium(I) moiety. *J. Am. Chem. Soc.* **100**, 306–307 (1978).
88. Collot, J. *et al.* Artificial metalloenzymes for enantioselective catalysis based on biotin-avidin. *J. Am. Chem. Soc.* **125**, 9030–9031 (2003).
89. Steinreiber, J. & Ward, T. R. Artificial metalloenzymes as selective catalysts in aqueous media. *Coord. Chem. Rev.* **252**, 751–766 (2008).
90. Letondor, C. *et al.* Artificial transfer hydrogenases based on the biotin-(strept)avidin technology: fine tuning the selectivity by saturation mutagenesis of the host protein. *J. Am. Chem. Soc.* **128**, 8320–8328 (2006).
91. Creus, M. *et al.* X-ray structure and designed evolution of an artificial transfer hydrogenase. *Angew. Chem. Int. Edn Engl.* **47**, 1400–1404 (2008).
92. Chen, C.-H. B., Milne, L., Landgraf, R., Perrin, D. M. & Sigman, D. S. Artificial nucleases. *ChemBiochem* **2**, 735–740 (2001).
93. Davies, R. R. & Distefano, M. D. A semisynthetic metalloenzyme based on a protein cavity that catalyzes the enantioselective hydrolysis of ester and amide substrates. *J. Am. Chem. Soc.* **119**, 11643–11652 (1997).
94. Ory, J. J. *et al.* Structural characterization of two synthetic catalysts based on adipocyte lipid-binding protein. *Protein Eng.* **11**, 253–261 (1998).
95. Carey, J. R. *et al.* A site-selective dual anchoring strategy for artificial metalloprotein design. *J. Am. Chem. Soc.* **126**, 10812–10813 (2004).
96. Zhang, J., Garner, D. K., Liang, L., Chen, Q. & Lu, Y. Protein scaffold of a designed metalloenzyme enhances the chemoselectivity in sulfoxidation of thioanisole. *Chem. Commun.* 1665–1667 (2008).
97. Farver, O., Lu, Y., Ang, M. C. & Pecht, I. Enhanced rate of intramolecular electron transfer in an engineered purple Cu<sub>A</sub> azurin. *Proc. Natl Acad. Sci. USA* **96**, 899–902 (1999).
- This paper presents an excellent demonstration of the power of metalloprotein design to place two metal-binding sites into the same protein scaffold for direct comparison of functional properties.**
98. Wang, N., Zhao, X. & Lu, Y. Role of heme types in heme-copper oxidases: effects of replacing a heme *b* with a heme *o* mimic in an engineered heme-copper center in myoglobin. *J. Am. Chem. Soc.* **127**, 16541–16547 (2005).
99. Summa, C. M., Rosenblatt, M. M., Hong, J.-K., Lear, J. D. & DeGrado, W. F. Computational *de novo* design, and characterization of an A<sub>2</sub>B<sub>2</sub> diiron protein. *J. Mol. Biol.* **321**, 923–938 (2002).
100. Bloom, J. D., Labthavikul, S. T., Otey, C. R. & Arnold, F. H. Protein stability promotes evolvability. *Proc. Natl Acad. Sci. USA* **103**, 5869–5874 (2006).

**Acknowledgements** We thank W. F. DeGrado, B. R. Gibney and P. L. Dutton for providing images used in Figure 1, N. Nagraj for help with editing the manuscript, and the US National Science Foundation (CHE 05-52008) and National Institutes of Health (GM062211) for financial support.

**Author Information** Reprints and permissions information is available at [www.nature.com/reprints](http://www.nature.com/reprints). The authors declare no competing financial interests. Correspondence should be addressed to Y.L. (yi-lu@illinois.edu).

# Chd1 regulates open chromatin and pluripotency of embryonic stem cells

Alexandre Gaspar-Maia<sup>1,2,3</sup>, Adi Alajem<sup>4</sup>, Fanny Polesso<sup>1,2</sup>, Rupa Sridharan<sup>5</sup>, Mike J. Mason<sup>5</sup>, Amy Heidersbach<sup>2</sup>, João Ramalho-Santos<sup>6</sup>, Michael T. McManus<sup>2</sup>, Kathrin Plath<sup>5</sup>, Eran Meshorer<sup>4</sup> & Miguel Ramalho-Santos<sup>1,2</sup>

**An open chromatin largely devoid of heterochromatin is a hallmark of stem cells. It remains unknown whether an open chromatin is necessary for the differentiation potential of stem cells, and which molecules are needed to maintain open chromatin. Here we show that the chromatin remodelling factor Chd1 is required to maintain the open chromatin of pluripotent mouse embryonic stem cells. Chd1 is a euchromatin protein that associates with the promoters of active genes, and downregulation of Chd1 leads to accumulation of heterochromatin. Chd1-deficient embryonic stem cells are no longer pluripotent, because they are incapable of giving rise to primitive endoderm and have a high propensity for neural differentiation. Furthermore, Chd1 is required for efficient reprogramming of fibroblasts to the pluripotent stem cell state. Our results indicate that Chd1 is essential for open chromatin and pluripotency of embryonic stem cells, and for somatic cell reprogramming to the pluripotent state.**

The genome of eukaryotic cells is organized into accessible euchromatin that is permissive for gene activation, and packaged heterochromatin that is largely silenced. Different cellular states may be defined at least in part by differential allocation of genomic regions to specific chromatin domains<sup>1</sup>. Several types of stem cells in organisms ranging from planarians<sup>2</sup> to mammals<sup>3,4</sup> have been reported to have an open chromatin largely devoid of heterochromatin. This phenomenon has been analysed in greater detail in pluripotent mouse embryonic stem (ES) cells. These cells have an open, 'loose' chromatin with high rates of histone protein exchange, and accumulate regions of more rigid heterochromatin after differentiation<sup>5,6</sup>. An open chromatin correlates with a globally permissive transcriptional state, and has been proposed to contribute to the developmental plasticity, or pluripotency, of ES cells<sup>6</sup>. Although there is a strong correlation between open chromatin and the undifferentiated state of stem cells, it remains unknown whether open chromatin is necessary for stem cell potential. Furthermore, little is known about the molecules that may regulate open chromatin in stem cells. Here we report the identification of the chromatin remodeller Chd1 as an essential regulator of open chromatin and pluripotency of ES cells, and of somatic cell reprogramming to pluripotency.

## Chd1 regulates ES cell self-renewal

We have recently characterized the transcriptional profiles of pluripotent stem cells, including ES cells, and the cells in the mouse embryo from which they are derived (ref. 7 and G. Wei, R.-F. Yeh, M. Hebrok and M.R.-S., unpublished observations). These studies led to the identification of chromatin remodellers and transcription factors up-regulated in pluripotent cells. To test the role of 41 candidate factors in the regulation of pluripotency, we carried out an RNA interference (RNAi) screen in ES cells (Supplementary Fig. 1). ES cells expressing green fluorescent protein (GFP) under the control of the *Oct4* promoter (*Oct4*-GiP) were infected with a short hairpin RNA

(shRNA)-expressing lentiviral vector, pSicoR-mCherry<sup>8</sup>. Using 1–2 shRNAs per candidate target gene, we identified 18 genes that when downregulated led to defects in expansion of ES cells, and 7 that led to lower activity of the *Oct4* promoter. *Chd1* was the only gene with phenotypes in both assays that had not been previously implicated in ES cells (Supplementary Fig. 1).

Chd1 is a chromatin-remodelling enzyme that belongs to the chromodomain family of proteins and contains an ATPase SNF2-like helicase domain<sup>9</sup>. The two chromodomains in Chd1 are essential for recognition of histone H3 di- or tri-methylated at lysine 4 (H3K4me2/3; ref. 10), and Chd1 has been implicated in transcriptional activation in yeast<sup>11</sup>, *Drosophila*<sup>12</sup> and mammalian cells<sup>13</sup>. Recent transcription factor location studies indicate that the *Chd1* gene is bound in mouse ES cells by Oct4 (also known as Pou5f1), Sox2, Nanog, Smad1, Zfx and E2f1, suggesting that it is a target of several regulators of pluripotency and self-renewal<sup>14</sup>.

RNAi against *Chd1* in *Oct4*-GiP ES cells, using two independent shRNAs targeting different regions of the messenger RNA, led to a decrease in the expansion of ES cells and to lower *Oct4*-GFP levels (Fig. 1a, b and Supplementary Fig. 2a). Control cells were infected with empty pSicoR-mCherry or with pSicoR-mCherry expressing an shRNA targeting GFP (empty and GFP RNAi, respectively), and behaved like uninfected cells (Supplementary Figs 1d and 2a). Downregulation of *Chd1* mRNA after RNAi was confirmed by reverse transcription followed by quantitative PCR (qRT-PCR) (Supplementary Fig. 2b). Endogenous *Oct4* downregulation was confirmed in Chd1-deficient (*Chd1* RNAi) ES cells (Supplementary Fig. 3a). *Oct4* downregulation induced differentiation into the trophoblast lineage<sup>15</sup> (marked by *Cdx2* and *Eomes*), unlike knockdown of *Chd1*, indicating that the *Chd1* RNAi phenotype is not simply one of trophoblast differentiation due to the loss of *Oct4* (Supplementary Fig. 3).

*Chd1* downregulation decreased clonogenic potential in two independent ES cell lines (*Oct4*-GiP and E14), but *Chd1* RNAi cells were

<sup>1</sup>Departments of Ob/Gyn and Pathology, Center for Reproductive Sciences and Eli and Edythe Broad Center of Regenerative Medicine and Stem Cell Research, University of California, San Francisco, 513 Parnassus Avenue, San Francisco, California 94143-0525, USA. <sup>2</sup>Diabetes Center, University of California, San Francisco, California 94143-0534, USA. <sup>3</sup>PhD Programme in Biomedicine and Experimental Biology (BEB), Center for Neuroscience and Cell Biology, University of Coimbra, 3004-517 Coimbra, Portugal. <sup>4</sup>Department of Genetics, Institute of Life Sciences, The Hebrew University of Jerusalem, Jerusalem 91904, Israel. <sup>5</sup>Department of Biological Chemistry and Eli and Edythe Broad Center of Regenerative Medicine and Stem Cell Research, University of California, Los Angeles, PO Box 951737, Los Angeles, California 90095, USA. <sup>6</sup>Center for Neuroscience and Cell Biology, University of Coimbra, 3004-517 Coimbra, Portugal.



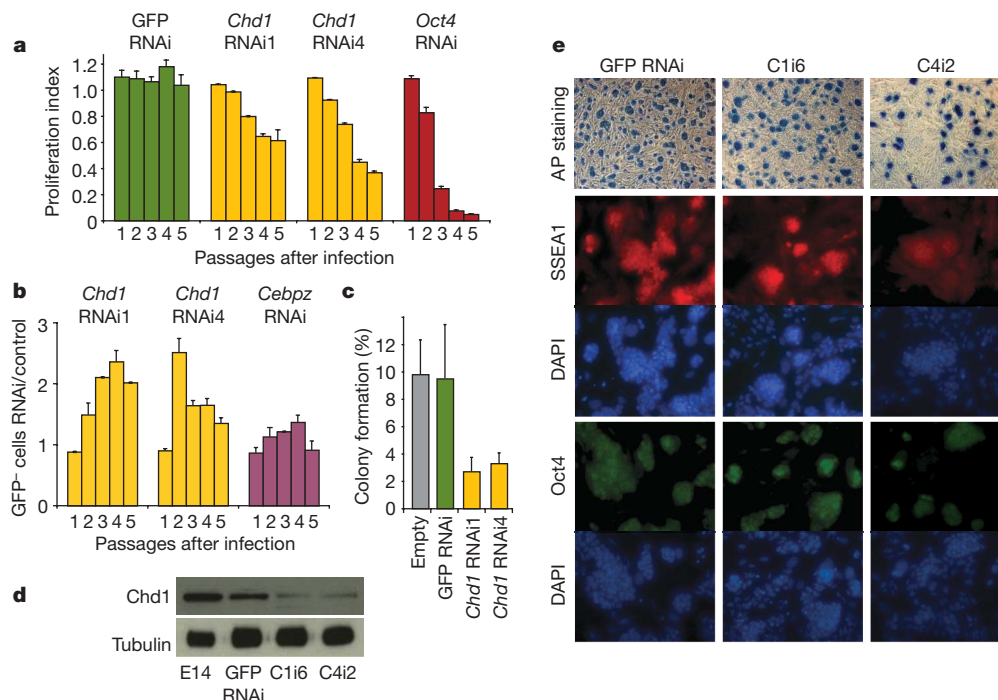


**Figure 1 | *Chd1* RNAi ES cells have decreased self-renewal but maintain expression of markers of the undifferentiated state.** **a**, A competition assay shows that downregulation of *Chd1* in Oct4-GiP ES cells using two independent shRNAs (*Chd1* RNAi1 and *Chd1* RNAi4) leads to a decreased proliferative capacity. The proliferation index represents the population of mCherry<sup>+</sup> cells relative to cells infected with empty vector, at each time point. Experiments were done in triplicate and are represented as mean and s.d. ( $n = 3$ ). **b**, Downregulation of *Chd1* leads to reduced activity of the Oct4–GFP reporter, as measured by the ratio between the percentage of GFP-negative cells in RNAi and in empty vector. *Chd1* RNAi cells have a twofold increase of GFP-negative cells relative to controls for at least one passage. Downregulation of a different gene that affects only proliferation

still able to form ES-like colonies (Fig. 1c), unlike *Oct4* RNAi ES cells. ES cell clones constitutively expressing either of the two shRNAs against *Chd1* were established, and sustained *Chd1* downregulation was verified by qRT–PCR (see below Supplementary Fig. 5) and western blot (Fig. 1d). Control lines were established using empty and GFP RNAi viruses. As described later, the two shRNAs targeting *Chd1* led to identical phenotypes in marker gene expression, transcriptional profile, differentiation potential and chromatin state, relative to controls. Results were validated in the two independent ES cell lines Oct4–GiP and E14. The data are from analyses in standard E14 ES cells not expressing GFP. *Chd1* RNAi ES cells, even though they have a self-renewal defect, form compact colonies and express markers of ES cells, such as SSEA1, alkaline phosphatase and Oct4 (Fig. 1e), indicating that they maintain at least some aspects of the undifferentiated state.

### ***Chd1* is required for ES cell pluripotency**

To gain insight into the state of *Chd1* RNAi ES cells, we determined their global gene expression profiles using Affymetrix mouse Gene 1.0 ST microarrays (Supplementary Fig. 4). We anticipated that we would find a pattern of downregulated genes in *Chd1* RNAi cells, because *Chd1* is known to be associated with active transcription<sup>13</sup>. As expected, both *Chd1* and *Oct4* were found to be downregulated in *Chd1* RNAi ES cells. Surprisingly, however, very few other genes were significantly downregulated (only 25 genes were downregulated more than twofold and none more than threefold at 90% confidence, Supplementary Fig. 4b and Supplementary Data 1). These data indicate that, at least with the low levels of *Chd1* still present in *Chd1* RNAi ES cells, there is a global maintenance of the ES cell transcriptome. On the

(*Cebpz*) has little effect on Oct4–GFP expression. Data are mean and s.d. ( $n = 3$ ). **c**, The efficiency of colony formation in *Chd1* RNAi ES cells was decreased relative to controls (empty and GFP RNAi). Data are mean and s.d. ( $n = 3$ ), and are representative of two independent experiments.

**d**, Immunoblot with whole cell extracts from parental E14 cells, GFP RNAi and two *Chd1* RNAi ES cell clones (C1i6 and C4i2) using antibodies against *Chd1* or  $\alpha$ -tubulin. **e**, *Chd1* RNAi cells still express markers of undifferentiated ES cells, such as alkaline phosphatase (AP; shown in bright field; original magnification,  $\times 100$ ), and SSEA1 and Oct4 (shown with immunofluorescence; original magnification,  $\times 400$ ). Nuclei were stained with 4,6-diamidino-2-phenylindole (DAPI).

other hand, a larger group of genes was upregulated in *Chd1* RNAi ES cells (Supplementary Fig. 4b and Supplementary Data 1). A Gene Ontology (GO) analysis of the list of upregulated transcripts showed a significant enrichment for genes involved in neurogenesis (Supplementary Fig. 4c), such as *nestin* and *Blbp* (also known as *Fabp7*), which was confirmed by qRT–PCR (Supplementary Fig. 5d).

The maintenance of the ES cell transcriptome and the unexpected expression of neural markers were further analysed by immunofluorescence for *nestin*, *Blbp* and Oct4. Oct4 was detected in *Chd1* RNAi colonies, but cells between the colonies stained strongly for *Blbp* (Fig. 2a) and *nestin* (Supplementary Fig. 4e). No staining for *nestin* or *Blbp* was detected in control ES cells. These results were confirmed with fluorescence-activated cell sorting (FACS) using the ES cell marker SSEA1 (Supplementary Fig. 5). In summary, *Chd1* RNAi ES cells can be propagated with many of the hallmarks of the undifferentiated state, but have a high propensity for neuronal differentiation.

We next tested the differentiation potential of *Chd1* RNAi ES cells *in vitro* by the formation of embryoid bodies. *Chd1* RNAi embryoid bodies did not form the typical outer layer of primitive endoderm, as marked by immunofluorescence of embryoid body sections with *Afp* and *Gata4* (Fig. 2b). Similarly, yolk sac endoderm cysts were reduced or not observed in *Chd1* RNAi embryoid bodies (Supplementary Fig. 6a), which showed downregulation of primitive endoderm markers (*Gata4*, *Afp*, *Hnf4a* and *Lamb*) by qRT–PCR (Supplementary Fig. 6b). The loss of primitive endoderm in *Chd1* RNAi embryoid bodies was comparable to that in embryoid bodies lacking an essential regulator of primitive endoderm, *Gata6* (ref. 16) (Fig. 2b). Beating foci, indicative of cardiac mesoderm differentiation, were not detected in *Chd1* RNAi embryoid bodies, whereas they could be readily

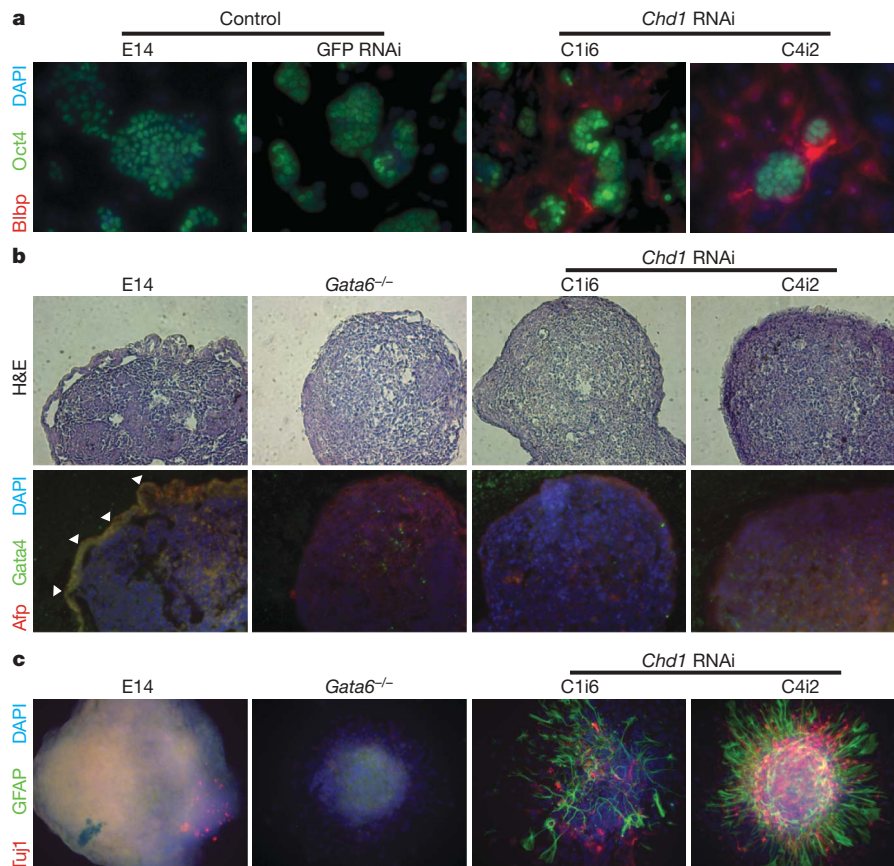


**Figure 2 | *Chd1* is required for ES cell pluripotency.** **a**, Immunofluorescence analysis of *Chd1* RNAi cells shows expression of Blbp (red), but in a population not expressing the ES cell marker Oct4 (green). Original magnification,  $\times 400$ . **b**, Paraffin sections of 6 day embryoid bodies were stained for Afp (red) and Gata4 (green), or haematoxylin and eosin (H&E). The loss of the primitive endoderm layer (highlighted in control GFP RNAi by white arrowheads) in *Chd1* RNAi embryoid bodies is similar to that

observed in embryoid bodies mutant for *Gata6*. Original magnification,  $\times 100$ . **c**, A significant increase in neural differentiation is observed, as detected by staining embryoid bodies (plated on matrigel) for astrocytes (GFAP in green) and neurons (Tuj1 in red), in 12 day *Chd1* RNAi embryoid bodies, relative to controls. Nuclei were stained with DAPI. Original magnification,  $\times 200$ .

quantified in control embryoid bodies (Supplementary Fig. 6c). However, beating foci were also not observed in *Gata6*<sup>-/-</sup> embryoid bodies, indicating that the loss of cardiac mesoderm differentiation in *Chd1* RNAi embryoid bodies may be secondary to the loss of primitive endoderm. Immunostaining of *Chd1* RNAi embryoid bodies plated on matrigel showed a marked increase of neurons (stained with Tuj1) and astrocytes (stained with Gfap) relative to controls (Fig. 2c). This increase in neural differentiation is not secondary to the loss of primitive endoderm, because *Gata6*<sup>-/-</sup> embryoid bodies did not show such phenotype (Fig. 2c). Furthermore, *Chd1* RNAi ES cells gave rise to teratomas with abundant neuronal differentiation when compared to wild-type ES cells (Supplementary Fig. 7). These results indicate that downregulation of *Chd1* leads to loss of primitive endoderm, with consequential loss of cardiac mesoderm differentiation, and abnormally high levels of neural differentiation that derives from a propensity already detected in the undifferentiated state.

### ***Chd1* is a euchromatin protein in ES cells**

We then sought to understand the potential changes in the chromatin state of *Chd1* RNAi ES cells that may underlie their differentiation defects. Previous studies<sup>11–13</sup> indicated that *Chd1* associates with euchromatin by binding to H3K4me3, although genome-wide location studies had not been performed. We carried out chromatin immunoprecipitation (ChIP)-chip for *Chd1* in wild-type ES cells, and compared the genome-wide location of *Chd1* to that of H3K4me3, RNA polymerase II (Pol II) and H3K27me3. These data

showed that *Chd1* binding strongly correlates with that of Pol II and H3K4me3 (Fig. 3 and Supplementary Fig. 8). Bivalent domains, simultaneously enriched for both the activating H3K4me3 mark and repressive H3K27me3 mark<sup>17</sup>, are largely devoid of *Chd1* (Fig. 3a and Supplementary Fig. 8). Interestingly, GO analysis indicated that the strongest *Chd1* and Pol II targets are enriched for roles in DNA binding, translation and chromatin assembly genes, and that this enrichment is not strictly correlated with expression levels (Fig. 3b and Supplementary Data 2). *Chd1* binding also correlates with H3K4me3 enrichment after differentiation: during embryoid body formation, the levels of both H3K4me3 and *Chd1* are decreased at the *Oct4* promoter and increased at the endodermal regulator *Gata4* promoter (Supplementary Fig. 9). These data indicate that *Chd1* associates globally with euchromatin in ES cells, and may preferentially target genes with roles in chromatin organization and transcription.

### ***Chd1* is required for maintenance of open chromatin**

To investigate the effects of *Chd1* downregulation on ES cell chromatin, we performed immunofluorescence for histone marks of euchromatin and heterochromatin. Surprisingly, foci of heterochromatin marks such as H3K9me3 and HP1 $\gamma$  (also known as Cbx3), which normally appear as dispersed foci in ES cells<sup>5</sup>, were markedly increased in *Chd1* RNAi ES cells (Fig. 4a and Supplementary Fig. 10). No obvious differences were observed in staining for H3K4me3 or H3K27me3 between *Chd1* RNAi ES cells and controls (data not shown). As described earlier, *Chd1* RNAi ES cells are prone to spontaneous neural

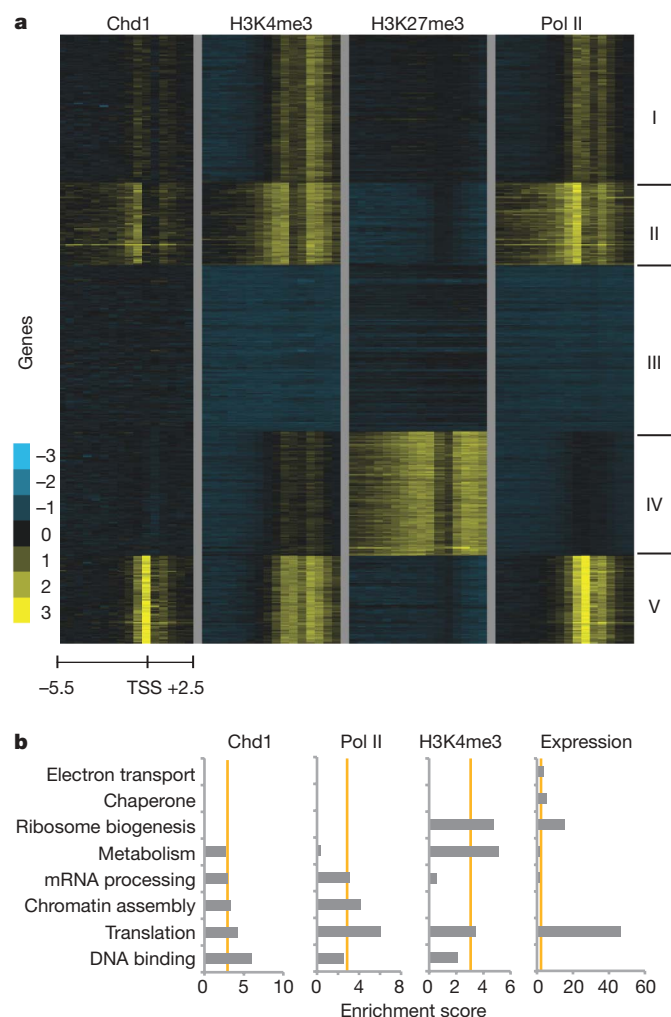


**Figure 3 | Chd1 associates with euchromatic promoter regions in ES cells.**  
**a**, K-means clustering of Chd1, H3K4me3, H3K27me3 and RNA Pol II binding in ES cells. Chd1 binding correlates with binding of H3K4me3 and RNA Pol II but is excluded from bivalent domains (cluster IV) in ES cells. Each row represents the binding pattern along the  $-5.5$  kilobase (kb) to  $+2.5$  kb promoter region relative to the transcription start site (TSS).  
**b**, Functional categorization of Chd1 targets. Gene Ontology (GO) terms associated with the 200 genes most strongly bound by Chd1 or RNA Pol II, or enriched for H3K4me3, as well as the top 200 genes in expression level in ES cells. Categories above an enrichment score of three (x axis) are considered significantly enriched. Sixty-nine genes overlap between the Chd1 and the RNA Pol II top 200 gene lists, versus 27 for Chd1 and expression, and 13 for Chd1 and H3K4me3.

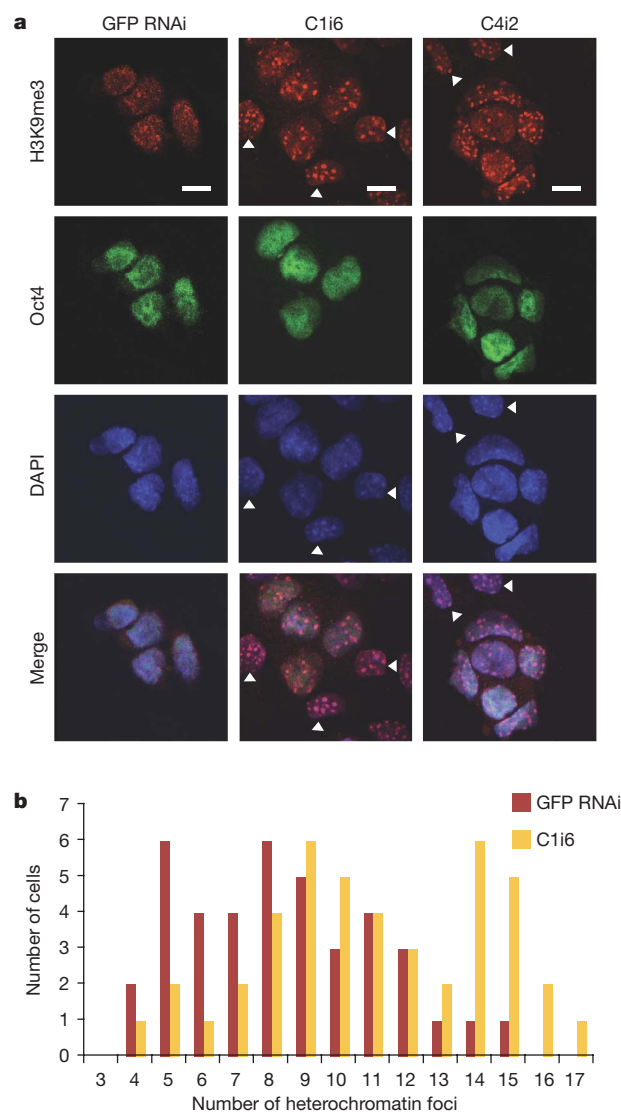


**Figure 4 | Chd1 is required to maintain open chromatin in ES cells.**  
**a**, Analysis of H3K9me3 staining by immunofluorescence. Co-staining for H3K9me3 and Oct4 distinguishes between ES-like cells (Oct4-positive) and differentiating cells (Oct4-negative, white arrowheads). Oct4-positive *Chd1* RNAi ES-like cells have increased heterochromatin foci. Scale bar, 10  $\mu$ m.  
**b**, Quantification of the increase of heterochromatin foci per nucleus in *Chd1* RNAi ES-like cells, as seen by H3K9me3 staining in Oct4-positive cells;  $P < 0.0005$ .

differentiation, and it has been shown that ES cell-derived neural precursors accumulate heterochromatin<sup>5</sup>. It was therefore important to evaluate whether the accumulation of heterochromatin is a consequence of commitment to the neural lineage, or whether it is present in ES-like cells before differentiation. Co-staining with H3K9me3 and Oct4 revealed that Oct4-positive ES-like cells, located in the centre of compact colonies that stain for other markers of the undifferentiated state (Fig. 1e), have accumulated high levels of heterochromatin in *Chd1* RNAi cells (Fig. 4a, quantified in 4b). Moreover, we analysed the global chromatin dynamics of *Chd1* RNAi cells by fluorescence recovery after photobleaching (FRAP) using a GFP-tagged histone H1. H1 is a linker protein involved in condensing nucleosomes that has been shown to rapidly exchange in the hyperdynamic chromatin of undifferentiated ES cells<sup>5</sup>. H1 showed a significant decrease in recovery in heterochromatin of *Chd1* RNAi ES cells, indicating that the rapid exchange of H1 is compromised (Supplementary Fig. 11). These results indicate that, despite a global maintenance of the transcriptome,

morphology, and marker gene expression of ES cells, *Chd1* RNAi ES-like cells are not fully undifferentiated: their chromatin is condensed.

Heterochromatin formation is induced by methylation of H3K9 by the enzymes ESET (also known as Setdb1), Suv39H1/2, G9a (Ehmt2) or Glp (Ehmt1)<sup>18</sup>, and reversed by the action of H3K9 demethylases such as Jmjd1a (Kdm3a) and Jmjd2c (Kdm4c). Jmjd1a and Jmjd2c have been shown to regulate genes expressed in ES cells and to repress differentiation<sup>19</sup>. All of these H3K9 methyltransferases and demethylases are expressed in *Chd1* RNAi ES cells at similar levels to control ES cells (Supplementary Data 1). Therefore, the accumulation of heterochromatin in *Chd1* RNAi ES cells is not likely to be due to the differential expression of known H3K9 methyltransferases or demethylases. These results indicate that the capacity to induce heterochromatin formation exists in undifferentiated ES cells, despite the presence of H3K9 demethylases, and that heterochromatinization is countered, directly or indirectly, by Chd1. Our data suggest that ES cells exist in a dynamic state of opposing epigenetic influences of euchromatin and heterochromatin, and that the



euchromatin protein Chd1 is required to maintain the heterochromatin-poor pluripotent stem cell state.

### Chd1 is required for efficient induction of pluripotency

Given the role of Chd1 in maintaining pluripotency of ES cells, we hypothesized that it may also be involved in the re-acquisition of pluripotency during somatic cell reprogramming. We analysed the effect of *Chd1* downregulation (Fig. 5a, b) in the reprogramming of Oct4–GFP mouse embryonic fibroblasts (MEFs) to induced pluripotent stem (iPS) cells<sup>20–24</sup>. Downregulation of *Chd1*, using two independent shRNAs in three separate experiments, led to a significant reduction in the number of iPS cell colonies, scored both by morphology and GFP expression. This was not due to a delay in colony formation, as colony counts at later time points showed the same relative reduction in reprogramming efficiency after *Chd1* RNAi treatment (data not shown). The iPS cell colonies that did form in *Chd1* RNAi wells either had not been infected by the RNAi virus or had silenced it, as assessed both by *Chd1* qRT–PCR and mCherry fluorescence (Supplementary Figs 12 and 13). Downregulation of *Chd1* could potentially affect proliferation of MEFs, which would confound the calculation of reprogramming efficiency. However, no significant changes in MEF growth rates were found between control and *Chd1* RNAi (Fig. 5c). Moreover, *Chd1* RNAi does not alter the expression level of the exogenous reprogramming factors (data not shown). In summary, our data show that downregulation of Chd1 does not affect the expansion of fibroblasts but inhibits their reprogramming by induction of pluripotency.

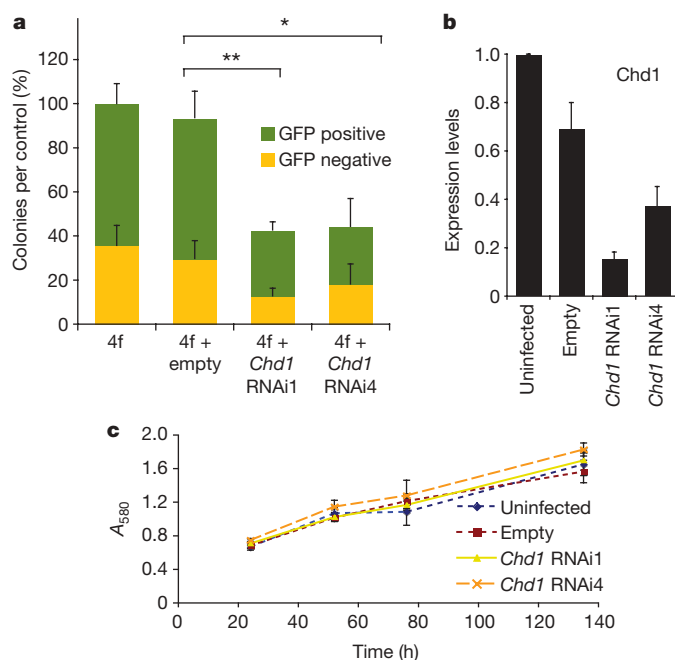


**Figure 5 | Chd1 is required for efficient induction of pluripotency.** **a**, The percentage of reprogrammed colonies was scored both by morphology and GFP expression, and normalized to the total number of colonies obtained in the control (four factors only, '4f'). The values are represented as mean and s.d. of the averages of three independent experiments, each one done in duplicate or triplicate. The total number of colonies in control wells (4f or 4f + empty) in the three separate experiments varied between 200 and 500 per 6-well. The efficiency of induction of pluripotency is significantly reduced after *Chd1* RNAi treatment. Unpaired *t*-test was performed using the total number of colonies obtained, comparing the control (empty) with RNAi against *Chd1* (*Chd1* RNAi1 and *Chd1* RNAi4). \**P* < 0.0001, \*\**P* < 0.00001. **b**, *Chd1* downregulation after RNAi was confirmed by qRT–PCR. The values are represented as mean of absolute expression and s.d. (*n* = 3). **c**, Mean growth rate of MEFs measured by the MTT assay and s.d. (*n* = 6). No differences in MEF growth rate were observed after *Chd1* RNAi treatment.

### Discussion

We show here that Chd1 is required for open chromatin and pluripotency of ES cells. ES cells have been reported to be 'poised' for differentiation by the presence of bivalent domains (marked by H3K4me3 and H3K27me3) in developmental regulatory genes<sup>17</sup>. We speculate that the opposing influences of euchromatin and heterochromatin (marked by H3K9me3) may be a further mechanism for maintaining ES cells in a state poised for differentiation. Chd1 is also highly expressed in human ES cells relative to differentiated cells (Supplementary Fig. 14)<sup>25</sup>, suggesting that its role in pluripotent stem cells may be conserved. Interestingly, it is possible that other stem cells maintain their differentiation potential using a similar mechanism, because *Chd1* has also been identified as a gene upregulated in adult haematopoietic and neural stem/progenitor cells<sup>26</sup>. Furthermore, our data show that Chd1 is required for efficient generation of iPS cells. Fibroblasts have much higher levels of heterochromatin than pluripotent stem cells<sup>5</sup> (and data not shown), and therefore a global opening of the chromatin is expected to be a component of reprogramming. Our data suggest that Chd1 may contribute to opening the chromatin and enabling transcription-factor-mediated reprogramming to occur, although the precise mechanisms remain to be determined.

It is unclear how Chd1, a protein associated with euchromatin, acts to counter heterochromatinization. Recent genetic studies in yeast indicate that euchromatin-associated factors prevent spreading of heterochromatin to euchromatic regions<sup>27,28</sup>. Further studies will be required to determine whether Chd1 has a similar role in ES cells. An intriguing possibility is that Chd1 may mediate incorporation of the histone variant H3.3, which is generally associated with active genes and is less prone to H3K9 methylation<sup>29</sup>. In support of this model, Chd1 has recently been shown to be required in the *Drosophila* oocyte for incorporation of H3.3 into sperm chromatin, a step necessary for development<sup>30</sup>. In addition, a genome-wide analysis of the chromatin state of *Chd1* RNAi ES cells may provide insight into the differential sensitivity of endoderm and neural lineages to chromatin condensation.

### METHODS SUMMARY

The RNAi screen was performed in Oct4–GFP ES cells using the lentiviral vector pSicoR–mCherry. A proliferation index was derived from a competition assay between infected and non-infected cells analysed by flow cytometry over five passages. Oct4–GFP and E14 *Chd1* RNAi and control ES cell clones were expanded from mCherry<sup>+</sup> cells isolated by FACS, and validated by qRT–PCR for *Chd1* downregulation. ES clones and embryoid bodies were grown in standard culture conditions. For expression microarray experiments, RNA from E14 *Chd1* RNAi and control clones was amplified and hybridized to Affymetrix Mouse Gene 1.0 ST arrays. Normalized data was analysed in dChip. Gene Ontology analyses were done with MAPPFinder or DAVID. For ChIP–chip, immunoprecipitated DNA was amplified and hybridized to Agilent G4490 promoter arrays. Data were extracted as previously described<sup>31</sup> and visualized using Cluster 3.0 and Treeview. ChIP, qRT–PCR and western blotting were performed using standard protocols. Immunofluorescence was performed on matrigel-coated chamber slides, with ES cells or embryoid bodies plated 2 days before fixation, or on paraffin-sectioned embryoid bodies. Teratomas were generated by subcutaneous injection of ES cells into SCID mice. FRAP analysis<sup>5</sup> and induction of pluripotency<sup>24</sup> were performed as described previously. Cell proliferation was measured using the MTT assay.

**Full Methods** and any associated references are available in the online version of the paper at [www.nature.com/nature](http://www.nature.com/nature).

Received 7 April; accepted 18 June 2009.

Published online 8 July 2009.

- Mikkelsen, T. et al. Dissecting direct reprogramming through integrative genomic analysis. *Nature* **454**, 49–55 (2008).
- Reddien, P. W. & Sanchez-Alvarado, A. Fundamentals of planarian regeneration. *Annu. Rev. Cell Dev. Biol.* **20**, 725–757 (2004).
- Terstappen, L. W. et al. Sequential generations of hematopoietic colonies derived from single nonlineage-committed CD34<sup>+</sup>CD38<sup>−</sup> progenitor cells. *Blood* **77**, 1218–1227 (1991).
- Spangrude, G. J., Heimfeld, S. & Weissman, I. L. Purification and characterization of mouse hematopoietic stem cells. *Science* **241**, 58–62 (1988).

5. Meshorer, E. *et al.* Hyperdynamic plasticity of chromatin proteins in pluripotent embryonic stem cells. *Dev. Cell* **10**, 105–116 (2006).
6. Efroni, S. *et al.* Global transcription in pluripotent embryonic stem cells. *Cell Stem Cell* **2**, 437–447 (2008).
7. Grskovic, M. *et al.* Systematic identification of *cis*-regulatory sequences active in mouse and human embryonic stem cells. *PLoS Genet.* **3**, e145 (2007).
8. Ventura, A. *et al.* Cre-lox-regulated conditional RNA interference from transgenes. *Proc. Natl Acad. Sci. USA* **101**, 10380–10385 (2004).
9. Woodage, T. *et al.* Characterization of the CHD family of proteins. *Proc. Natl Acad. Sci. USA* **94**, 11472–11477 (1997).
10. Sims, R. J. *et al.* Human but not yeast CHD1 binds directly and selectively to histone H3 methylated at lysine 4 via its tandem chromodomains. *J. Biol. Chem.* **280**, 41789–41792 (2005).
11. Simic, R. *et al.* Chromatin remodeling protein Chd1 interacts with transcription elongation factors and localizes to transcribed genes. *EMBO J.* **22**, 1846–1856 (2003).
12. Stokes, D. G., Tartof, K. D. & Perry, R. P. CHD1 is concentrated in interbands and puffed regions of *Drosophila* polytene chromosomes. *Proc. Natl Acad. Sci. USA* **93**, 7137–7142 (1996).
13. Sims, R. J. *et al.* Recognition of trimethylated histone H3 lysine 4 facilitates the recruitment of transcription postinitiation factors and pre-mRNA splicing. *Mol. Cell* **28**, 665–676 (2007).
14. Chen, X. *et al.* Integration of external signaling pathways with the core transcriptional network in embryonic stem cells. *Cell* **133**, 1106–1117 (2008).
15. Niwa, H., Miyazaki, J. & Smith, A. G. Quantitative expression of Oct-3/4 defines differentiation, dedifferentiation or self-renewal of ES cells. *Nature Genet.* **24**, 372–376 (2000).
16. Morrissey, E. E. *et al.* GATA6 regulates HNF4 and is required for differentiation of visceral endoderm in the mouse embryo. *Genes Dev.* **12**, 3579–3590 (1998).
17. Bernstein, B. E. *et al.* A bivalent chromatin structure marks key developmental genes in embryonic stem cells. *Cell* **125**, 315–326 (2006).
18. Lachner, M. & Jenuwein, T. The many faces of histone lysine methylation. *Curr. Opin. Cell Biol.* **14**, 286–298 (2002).
19. Loh, Y.-H. *et al.* Jmjd1a and Jmjd2c histone H3 Lys 9 demethylases regulate self-renewal in embryonic stem cells. *Genes Dev.* **21**, 2545–2557 (2007).
20. Takahashi, K. & Yamanaka, S. Induction of pluripotent stem cells from mouse embryonic and adult fibroblast cultures by defined factors. *Cell* **126**, 663–676 (2006).
21. Okita, K., Ichisaka, T. & Yamanaka, S. Generation of germline-competent induced pluripotent stem cells. *Nature* **448**, 313–317 (2007).
22. Maherali, N. *et al.* Directly reprogrammed fibroblasts show global epigenetic remodeling and widespread tissue contribution. *Cell Stem Cell* **1**, 55–70 (2007).
23. Wernig, M. *et al.* *In vitro* reprogramming of fibroblasts into a pluripotent ES-cell-like state. *Nature* **448**, 318–324 (2007).
24. Blueloch, R., Venere, M., Yen, J. & Ramalho-Santos, M. Generation of induced pluripotent stem cells in the absence of drug selection. *Cell Stem Cell* **1**, 245–247 (2007).
25. Skottman, H. *et al.* Gene expression signatures of seven individual human embryonic stem cell lines. *Stem Cells* **23**, 1343–1456 (2005).
26. Ramalho-Santos, M. *et al.* “Stemness”: transcriptional profiling of embryonic and adult stem cells. *Science* **298**, 597–600 (2002).
27. Kimura, A., Umehara, T. & Horikoshi, M. Chromosomal gradient of histone acetylation established by Sas2p and Sir2p functions as a shield against gene silencing. *Nature Genet.* **32**, 370–377 (2002).
28. Venkatasubrahmanyam, S. *et al.* Genome-wide, as opposed to local, antisilencing is mediated redundantly by the euchromatic factors Set1 and H2A.Z. *Proc. Natl Acad. Sci. USA* **104**, 16609–16614 (2007).
29. McKittrick, E., Gaffken, P. R., Ahmad, K. & Henikoff, S. Histone H3.3 is enriched in covalent modifications associated with active chromatin. *Proc. Natl Acad. Sci. USA* **6**, 1525–1530 (2004).
30. Konev, A. Y. *et al.* CHD1 motor protein is required for deposition of histone variant H3.3 into chromatin *in vivo*. *Science* **317**, 1087–1090 (2007).
31. Sridharan, R. *et al.* Role of the murine reprogramming factors in the induction of pluripotency. *Cell* **136**, 364–377 (2009).

**Supplementary Information** is linked to the online version of the paper at [www.nature.com/nature](http://www.nature.com/nature).

**Acknowledgements** The authors wish to thank A. Smith for Oct4-GiP ES cells, M. S. Parmacek for *Gata6*<sup>−/−</sup> ES cells, R. P. Perry and D. G. Stokes for the Chd1 antibody, M. Bigos and V. Stepps at the Flow Cytometry Core Facility and L. Ta and C. Barker at the Genomics Core Facility of the Gladstone Institutes for expert assistance, C. Chiu for technical assistance, members of the Santos laboratory, in particular M. Grskovic for advice, and A. Kriegstein, D. Melton, A. Alvarez-Buylla, D. Stainier, R. Blueloch, B. Panning, J. Reiter and M. Grskovic for discussions and critical reading of the manuscript. A.G.-M. was the recipient of a predoctoral fellowship from the Foundation for Science and Technology (POCI2010/FSE), Portugal. R.S. was the recipient of a CIRM postdoctoral training grant. This work was supported by grants from the Sandler Family to M.T.M., CIRM Young Investigator Award and NIH Director’s New Innovator Award to K.P., Israel Science Foundation (ISF 215/07), European Union (IRG-206872) and Alon Fellowship to E.M., and NIH Director’s New Innovator Award, California Institute for Regenerative Medicine and Juvenile Diabetes Research Foundation to M.R.-S.

**Author Contributions** A.G.-M., J.R.-S., M.T.M., K.P., E.M. and M.R.-S. planned the project; A.G.-M., A.A., F.P., R.S., M.J.M. and A.H. performed the experiments; A.G.-M., A.A., F.P., R.S., M.J.M., K.P., E.M. and M.R.-S. analysed the data; and A.G.-M., K.P., E.M. and M.R.-S. wrote the manuscript.

**Author Information** Expression and ChIP-chip microarray data are deposited in the Gene Expression Omnibus (GEO) under accession number GSE16462. Reprints and permissions information is available at [www.nature.com/reprints](http://www.nature.com/reprints). Correspondence and requests for materials should be addressed to M.R.-S. ([mrsantos@diabetes.ucsf.edu](mailto:mrsantos@diabetes.ucsf.edu)).

## METHODS

**ES cell culture and differentiation.** Mouse E14 and Oct4-GiP ES cells<sup>32</sup> were plated on 0.1% gelatin-coated plates or on a feeder layer of irradiated MEFs, and maintained in DMEM (Invitrogen) supplemented with 15% knockout serum replacement (Invitrogen), 1 mM L-glutamine, 0.1 mM nonessential amino acids, 100 µg ml<sup>-1</sup> penicillin, 100 µg ml<sup>-1</sup> streptomycin, 1 mM sodium pyruvate, 0.1 mM 2-mercaptoethanol and recombinant LIF. Mouse *Gata6*<sup>-/-</sup> ES cells<sup>16</sup> were grown in identical conditions except that fetal bovine serum was used instead of knockout serum replacement. Embryoid bodies were formed by plating ES cells in non-attachment conditions (suspension culture) with ES cell medium with fetal bovine serum and in the absence of LIF, for 16 days. Contractile foci were counted under an inverted microscope using triplicates of 10-cm dishes per ES cell clone.

**RNAi and competition assay.** The genes tested in the RNAi screen were the following: *Ap2gamma* (also known as *Tcfap2c*), *Brca1*, *Cebpz*, *Chd1*, *Ddx18*, *Dmrt1*, *Dppa2*, *Dppa3* (*Stella*), *Dppa4*, *Eed*, *Foxd3*, *Hells*, *Mybl2*, *c-Myc*, *Mychp*, *Nmyc1* (*Mycn*), *Nanog*, *Nfya*, *Nfyb*, *Nr0b1*, *Nr5a2*, *Oct4*, *Pramel4*, *Pramel5*, *Rex1* (*Zfp42*), *Rex2*, *Rbm35a* (*Esrp1*), *Sall4*, *Six4*, *Sox2*, *Suz12*, *Tcfcp2l1*, *Terf1*, *Tex292* (*Cirh1a*), *Utf1*, *Zic3*, A030007L17Rik (*Ggc2*), and Affymetrix MG-U74Av2 probe sets 160906\_i\_at, 135189\_f\_at, 97154\_f\_at and 98524\_f\_at. shRNA sequences were selected according to published criteria<sup>33</sup>: GFP RNAi, ACAGCCACAACGTCTATAT; *Oct4* RNAi, GAACCTGGCTAAGCTTCCA; *Chd1* RNAi1, ACATTATGATGGAGCTAAA; *Chd1* RNAi4, GTGCTACT ACAACCATTTA. All other sequences are in Supplementary Table 1. Oligonucleotides coding for the shRNAs were designed and cloned into the lentiviral vector pSicoR-mCherry as described<sup>7</sup>. Lentiviruses were produced as described<sup>8</sup>. For transduction, 10<sup>6</sup> ES cells were incubated with virus in 1 ml of ES cell medium (multiplicity of infection 5–10). After 1 h rotating at 37 °C, 2.5–3 × 10<sup>5</sup> cells were plated per gelatinized well of a 12-well plate. A competition assay<sup>34</sup> was performed by analysing cells that were passaged every two or three days. Flow cytometry was performed on a LSRII and analysed using the Flojo software. Proliferation index was measured, for every passage, by dividing the percentage of mCherry<sup>+</sup> (shRNA) with the percentage of mCherry<sup>+</sup> (empty virus). Loss of Oct4-GFP activity was measured by dividing the percentage of GFP<sup>+</sup> cells (shRNA) with the percentage of GFP<sup>+</sup> (empty virus). The calculation of the loss of Oct4/GFP expression was done with total GFP<sup>+</sup> cells rather than just GFP<sup>+</sup>/mCherry<sup>+</sup> to account for potential silencing of the mCherry construct after differentiation or non-cell autonomous effects. Proliferation index data are averages of triplicates (*n* = 3) and standard error bars. mCherry<sup>+</sup> ES cells were isolated using a FACSDiVa (BD Biosciences) cell sorter.

**Colony formation assay and clonal derivation.** E14 and Oct4-GiP ES cells were infected with lentiviruses containing shRNAs or empty virus alone, as described above. mCherry<sup>+</sup> cells were sorted on day 5 after infection using a FACSDiVa (BD Biosciences) cell sorter. Five thousand cells were plated per 10-cm dish in triplicates. After 10 days in culture, individual clones were picked per each condition (empty virus, GFP RNAi, *Chd1* RNAi1 or RNAi4) and propagated in standard ES cell growth conditions. Plates were stained for alkaline phosphatase using a Vector kit and colonies were counted. Results are averages of triplicates and standard error bars.

**Expression microarrays.** Uninfected parental E14 ES cells, one clone infected with empty pSicoR-mCherry, one GFP RNAi clone and four *Chd1* RNAi clones, three from *Chd1* RNAi1 (C115, C116 and C119) and one from *Chd1* RNAi4 (C412) were grown on gelatin in ES cell culture medium. Total RNA was isolated using the RNeasy kit (Qiagen) with in-column DNase digestion. Three-hundred nanograms of total RNA per sample were amplified and hybridized to Affymetrix Mouse Gene 1.0 ST arrays according to the manufacturer's instructions at the Genomics Core Facility of the Gladstone Institutes. These arrays assay for the expression of about 35,500 transcripts. Data were normalized using robust multi-array normalization. Hierarchical clustering and calculations of differential gene expression were done using dChip (<http://www.dchip.org>)<sup>35</sup>. The full normalized data are in Supplementary Data 1. The lower bound of the 90% confidence interval of the fold change (LCB) was used as a conservative estimate of the fold change. Five-hundred-and-thirty-one transcripts with LCB > 2 in *Chd1* RNAi relative to controls were analysed in MAPPFinder<sup>36</sup> for enrichment of gene ontology terms. Terms with *P* values adjusted for multiple testing ≤ 0.01 were considered enriched.

**Immunohistochemistry.** ES cells or embryoid bodies were plated on chamber glass slides pre-coated with matrigel. ES cells were plated on a layer of irradiated MEFs. After 2 days, cells were fixed with 4% paraformaldehyde, permeabilized with PBT (PBS plus 0.1% Triton X-100) and blocked with 2% BSA plus 1% goat or donkey serum in PBT. Slides were immunostained with primary antibody in blocking solution. Alternatively, embryoid bodies in suspension (at day 6) were fixed, paraffin-embedded, sectioned (50 µm), and stained for haematoxylin and eosin or immunostained.

Primary antibodies used: SSEA1 (MC-480, Developmental Studies Hybridoma Bank (DSHB), 1:200), Oct4 (sc5279, Santa Cruz, 1:100; sc9081; Santa Cruz; 1:50), nestin (MAB353, Chemicon, 1:200), BLBP (ab32423, Abcam, 1:200), Afp (sc8977, Santa Cruz, 1:200), Gata4 (sc1237, Santa Cruz, 1:50), Tuj1 (MMS-435P, Covance, 1:250), GFAP (Z0334, Dako, 1:500), H3K4me3 (ab8580, Abcam, 1:200), H3K9me3 (07-449, Upstate, 1:100; ab8898, Abcam, 1:100), H3K27me3 (07-449, Upstate, 1:100), HP1gamma (MAB3450, Chemicon, 1:500). Secondary antibodies: Alexa Fluor 488/594 conjugated secondary antibodies (anti-mouse, anti-rabbit, or anti-goat, 1:500, Molecular Probes). Nuclei were counterstained with DAPI. The MC-480 antibody developed by D. Solter was obtained from the DSHB developed under the auspices of the NICHD and maintained by University of Iowa.

**qRT-PCR.** RNA was isolated according to the RNeasy kit (Qiagen), and reverse-transcribed using the iScript first strand cDNAsynthesis kit (BioRad). The cDNA reaction was diluted 1:5 in TE buffer and used in Sybr Green real-time PCR reactions (BioRad). Housekeeping genes used were ubiquitin-b and ribosomal protein L7. PCR primer sequences are available on request. Reactions were run in replicates on a MyiQ qPCR machine (BioRad) according to the manufacturer's instructions. Cycle threshold values were imported into the REST software<sup>37</sup> for fold-change calculations, using the housekeeping genes as controls. Values are presented in log<sub>2</sub> scale or in absolute expression levels compared with parental E14 RNA unless otherwise indicated.

**SSEA1 cell sorting.** ES cells (GFP RNAi control and *Chd1* RNAi clones) were collected by trypsinization, washed in ice-cold PBS, first resuspended in staining medium (HBSS, Ca/Mg-free, no phenol red, 2% FBS) with primary mouse antibody anti-SSEA1 (MC-480, DSHB, 1:50) for 30 min on ice, and then in secondary anti-mouse IgM-PE (406507, BioLegends, 1:100) for 30 min on ice. Propidium iodide (P3566; Invitrogen) was added and live SSEA1<sup>+</sup> and SSEA1<sup>-</sup> cells were isolated using a FACSDiVa (BD Biosciences) cell sorter.

**Western blotting.** Whole cell extracts were prepared and measured using the Bradford assay (BioRad) for protein content. From whole ES cell extracts 30 µg of protein were resolved on SDS-PAGE gel (10%) using a rabbit antibody against Chd1 (1:2,000, from R. Perry<sup>12</sup>) and a goat anti-rabbit HRP (1:10,000). The loading control used was  $\alpha$ -tubulin, detected with a mouse antibody (1:1,000, Sigma T9026). From embryoid body extracts (at day 12), 10 µg of protein were resolved on a 10% SDS-PAGE gel using an antibody against Tuj1 (1:1,000) and anti-goat HRP (1:10,000). Detection was performed using the ECL kit according to manufacturer's instructions (Amersham).

**FRAP analysis.** Transfection of H1-GFP into ES cells and FRAP analysis were performed as described<sup>3</sup>.

**Generation of teratomas.** Teratomas were produced by injecting 3 × 10<sup>6</sup> cells subcutaneously in the flanks of SCID mice. Tumour tissue samples developed in 12 weeks and were fixed overnight in 4% paraformaldehyde before paraffin embedding. Sections were stained with haematoxylin and eosin with a standard protocol.

**ChIP.** ChIP was performed essentially as described by Upstate Biotechnology, with some minor changes described below: chromatin was cross-linked by incubating cells on plates with PBS containing 20 mM dimethylpiperimidate (DMP; Sigma) and 0.25% dimethylsulphoxide (DMSO) for 1 h at room temperature. Cells were re-fixed with 2% paraformaldehyde for another hour at room temperature, scraped and centrifuged at 1,350g for 5 min. Pellets were resuspended in SDS lysis buffer and sonicated to obtain fragments of ~200–1,000 base pairs (bp) as verified on a gel. Reactions were centrifuged at 13,000g for 10 min and the supernatants were used. Antibodies used (3 µg each): Chd1 (PAB-10569, Orbigen), H3K4me3 (ab8580, Abcam) IgG (ab46540, Abcam). DNA was purified by phenol-chloroform extraction, followed by ethanol precipitation. DNA concentration was determined using a Nanodrop spectrophotometer (NanoDrop Technologies) and 5–10 ng were used in Sybr Green real-time PCR reactions (see earlier) ran in duplicates or triplicates. Primer sequences are available on request. Fold enrichment over input was calculated using the 2<sup>-ΔC<sub>t</sub></sup> method corrected with IgG C<sub>t</sub> values. The HoxA3 primer set was used as a control gene because it corresponds to a region known to lack H3K4me3 (ref. 17).

**ChIP-chip.** ChIP and hybridization onto Agilent promoter microarrays was performed as described<sup>22</sup>. In brief 500 µg of crosslinked ES chromatin was immunoprecipitated with 10 µg of Chd1 antibody (Allele Biotech PAB-10568) or hypophosphorylated RNA polymerase II (8WG16). The eluate was reverse crosslinked, RNase- and proteinase-K-treated and purified. Equal amounts of input and immunoprecipitated samples were amplified using the WGA2 kit (Sigma), labelled with the Bioprime kit (Invitrogen) and hybridized onto Agilent mouse promoter arrays (G4490) according to manufacturer's instructions. Data were extracted as previously described<sup>31</sup>. Data were visualized using the Cluster 3.0 and Treeview programs. Bound genes were determined using the Young laboratory algorithm<sup>38</sup>. H3K4me3 and H3K27me3 data, as well as the algorithm to generate the 500-bp window presentation were previously published<sup>22</sup>. In K-means clustering, each row



represents the binding pattern along the  $-5.5$  to  $+2.5$  kb promoter region relative to the TSS, reiterated four times to present the data for each immunoprecipitation. The 8 kb promoter region is divided into sixteen 500 bp fragments that display the average log ratio of probe signal intensity with blue, yellow and grey representing lower-than-average, higher-than-average and missing values for enrichment due to lack of probes in those regions, respectively. The odds ratio for binary correlation of Chd1 binding strength was calculated as the ratio of the probability of a gene being bound by Chd1 divided by the probability of it being bound by H3K4me3 (or RNA Pol II or H3K27me3) to the probability of a gene being bound by Chd1 divided by the probability of the gene being unbound by H3K4me3 (or RNA Pol II or H3K27me3).

**Reprogramming.** Reprogramming was performed as previously described<sup>24</sup>, with minor changes: Oct4-GFP MEFs were reprogrammed using lentiviral infection (day 0) of four transcription factors (*Oct4*, *Sox2*, *nMyc* and *Klf4*). RNAi lentiviral vectors (empty, *Chd1* RNAi1, *Chd1* RNAi4) were used to infect MEFs 4 days before the addition of the four factors. At day 1, MEFs were also plated for a MTT assay to quantify growth rates and for RNA collection for qRT-PCR for *Chd1*. An optimization of the protocol was also used and described in Supplementary Fig. 12 (as reported previously<sup>39</sup>). iPS colonies were scored (13 to 16 days after addition of the four factors) by GFP fluorescence, using a scale according to the number of cells in a colony that were GFP positive, as described in Supplementary Fig. 12b (GFP-positive refers to all the colonies with any GFP-positive cells), or by their morphology under bright field (GFP-negative).

**MTT assay.** The growth rate of MEFs was measured using an indirect method. Yellow MTT is reduced by mitochondrial enzymes into a purple formazan and the absorbance measured as a result of the number of viable cells. For the MTT

assay, MEFs were plated at 5,000 cells per well in a 96-well plate and analysed 24, 52, 76 and 135 h after plating. At the indicated time points, ES cell medium (without LIF) was replaced with 100  $\mu$ l  $1 \text{ mg ml}^{-1}$  3-(4,5-dimethylthiazol-2-yl)-2,5-diphenyltetrazolium bromide (MTT) (Molecular Probes) in DMEM. After incubation at  $37^\circ\text{C}$  for 3 h, the MTT solution was removed. One-hundred microlitres of DMSO was added to dissolve precipitate for 10 min at  $37^\circ\text{C}$  and 5 min at room temperature. Absorbance was recorded at 540 nm using a Spectramax M2 microplate reader (Molecular Devices).

32. Ying, Q. L., Nichols, J., Evans, E. P. & Smith, A. G. Changing potency by spontaneous fusion. *Nature* **416**, 545–548 (2002).
33. Reynolds, A. *et al.* Rational siRNA design for RNA interference. *Nature Biotechnol.* **22**, 326–330 (2004).
34. Ivanova, N. *et al.* Dissecting self-renewal in stem cells with RNA interference. *Nature* **442**, 533–538 (2006).
35. Li, C. & Wong, W. H. Model-based analysis of oligonucleotide arrays: expression index computation and outlier detection. *Proc. Natl Acad. Sci. USA* **98**, 31–36 (2001).
36. Doniger, S. W. *et al.* MAPPFinder: using Gene Ontology and GenMAPP to create a global gene-expression profile from microarray data. *Genome Biol.* **4**, R7 (2003).
37. Pfaffl, M. W., Horgan, G. W. & Dempfle, L. Relative expression software tool (REST) for group-wise comparison and statistical analysis of relative expression results in real-time PCR. *Nucleic Acids Res.* **30**, e36 (2002).
38. Boyer, L. A. *et al.* Polycomb complexes repress developmental regulators in murine embryonic stem cells. *Nature* **441**, 349–353 (2006).
39. Wernig, M. *et al.* A drug-inducible transgenic system for direct reprogramming of multiple somatic cell types. *Nature Biotechnol.* **26**, 916–924 (2008).

# The diversity of type Ia supernovae from broken symmetries

D. Kasen<sup>1</sup>, F. K. Röpke<sup>2</sup> & S. E. Woosley<sup>1</sup>

Type Ia supernovae result when carbon-oxygen white dwarfs in binary systems accrete mass from companion stars, reach a critical mass and explode. The near uniformity of their light curves makes these supernovae good ‘standard candles’ for measuring cosmic expansion<sup>1–4</sup>, but a correction must be applied to account for the fact that the brighter ones have broader light curves<sup>5</sup>. One-dimensional modelling, with a certain choice of parameters, can reproduce this general trend in the width–luminosity relation<sup>6–8</sup>; but the processes of ignition and detonation have recently been shown to be intrinsically asymmetric<sup>9–13</sup>, so parameterization must have its limits. Here we report multi-dimensional modelling of the explosion physics and radiative transfer, which reveals that the breaking of spherical symmetry is a critical factor in determining both the width–luminosity relation and the observed scatter about it. The deviation from spherical symmetry can also explain the finite polarization detected in the light from some supernovae<sup>14</sup>. The slope and normalization of the width–luminosity relation has a weak dependence on certain properties of the white dwarf progenitor, in particular the trace abundances of elements other than carbon and oxygen. Failing to correct for this effect could lead to systematic overestimates of up to 2 per cent in the distance to remote supernovae.

In the most established model for type Ia supernovae, a carbon fusion flame is ignited near the centre of the white dwarf and initially burns in a sub-sonic and turbulent deflagration, then transitions near the white dwarf surface to a supersonic detonation<sup>15,16</sup>. The detonation is needed in order to match the observed energetics and nucleosynthesis<sup>17</sup>. The energetic stage of the explosion lasts only a second or so, but synthesizes radioactive <sup>56</sup>Ni that powers the subsequent light curve and determines its luminosity. In previous one-dimensional models, the <sup>56</sup>Ni yield depended on the choices of parameters representing the speed of the subsonic burning front and the density at which the front makes a transition to a detonation wave<sup>18</sup>. However, these parameters are actually a consequence of multi-dimensional instabilities not captured in one dimension, and so were not highly constrained by physics. Ignition in the one-dimensional models also occurred at the very centre of the star, and the transition to detonation happened simultaneously on a symmetric spherical shell. Both of these assumptions are now doubted.

The starting point of our simulations is a standard 1.4-solar-mass white dwarf composed of 50% carbon and 50% oxygen with a central density of  $2.9 \times 10^9 \text{ g cm}^{-3}$ . The propagation of the burning is followed in two spatial dimensions using a level set to track the flame’s location and a turbulent subgrid model adopted from the chemical combustion community to describe its motion<sup>12</sup>. The resulting debris are then post-processed using a multi-dimensional radiative transport code<sup>19</sup> to determine the emergent radiation. Model variations consist of how the white dwarf is ignited and the criteria for making the transition to detonation, both of which are

based on insights from recent three-dimensional studies, as described below. Variations in the trace abundance of elements other than carbon/oxygen (the metallicity) of the progenitor star over a range from one-third to three times solar are also explored, to mimic the evolution in supernova environment that may have occurred over aeons of cosmic time.

Simulations show<sup>9,20</sup> that just before ignition the white dwarf undergoes a ‘simmer phase’ characterized by dipolar convection, with material flowing out of the centre in a directed plume then circulating back in through the opposite side. The hottest points in the flow, and therefore where ignition occurs, are found on one side of the star displaced slightly from the centre. As the simulations have been computed at much lower Reynolds number ( $\sim 1,000$ ) than the true star ( $\sim 10^{14}$ ), the real flow may be even less ordered, retaining a dipole flavour but contaminated by higher multipoles, making ignition a much more chaotic process. The geometry of ignition may also be influenced by the rotation rate of the star. In our models, we therefore varied the number of ignition points, their distance from the centre of the star, and the solid angle in which they were distributed.

The physics of a putative transition to detonation, though still uncertain, has also been elucidated in recent studies<sup>21–23</sup>. As the deflagration flame propagates into lower-density material, it thickens and slows to the point that turbulent eddies can mix hot ‘fuel’ and cold ‘ash’, causing the burning rate to become highly irregular and potentially explosive. Like ignition, detonation should be a stochastic process which occurs only for the most extreme and intermittent turbulent energies, and may occur many times in different places. We therefore varied the criterion (the critical Karlovitz number) for instituting a detonation (Supplementary Information).

Figure 1 shows the final chemical structure (100 s after ignition) of the stellar debris for a sample of models. The inner regions of material, which were burned primarily in the turbulent, Rayleigh–Taylor unstable deflagration phase, consist of a patchy mixture of <sup>56</sup>Ni, intermediate-mass elements, and stable iron-group isotopes produced by electron capture (mostly <sup>54</sup>Fe and <sup>58</sup>Ni). The subsequent detonation produced a smoother distribution of intermediate-mass elements in the outer layers of the star. The synthetic model light curves, colours, and spectral time series agree very well with those of real events observed over the two months after explosion<sup>24</sup> (Fig. 2), offering a strong validation of the model’s predicted velocity structure and chemical stratification. On the other hand, it has been suggested that the mixing of electron-capture elements throughout the inner layers—a feature generic to all multi-dimensional deflagration calculations—may be inconsistent with spectral observations of some type Ia supernovae taken at late phases<sup>25</sup>.

The models predict a range of <sup>56</sup>Ni yields, from 0.3 to 1.1 solar masses, depending on the initial conditions. Perhaps counter-intuitively, models with more robust ignition generally synthesize

<sup>1</sup>Department of Astronomy and Astrophysics, UCSC, Santa Cruz, California 95064, USA. <sup>2</sup>Max-Planck-Institut für Astrophysik, Karl-Schwarzschild-Strasse 1, D-85741 Garching, Germany.

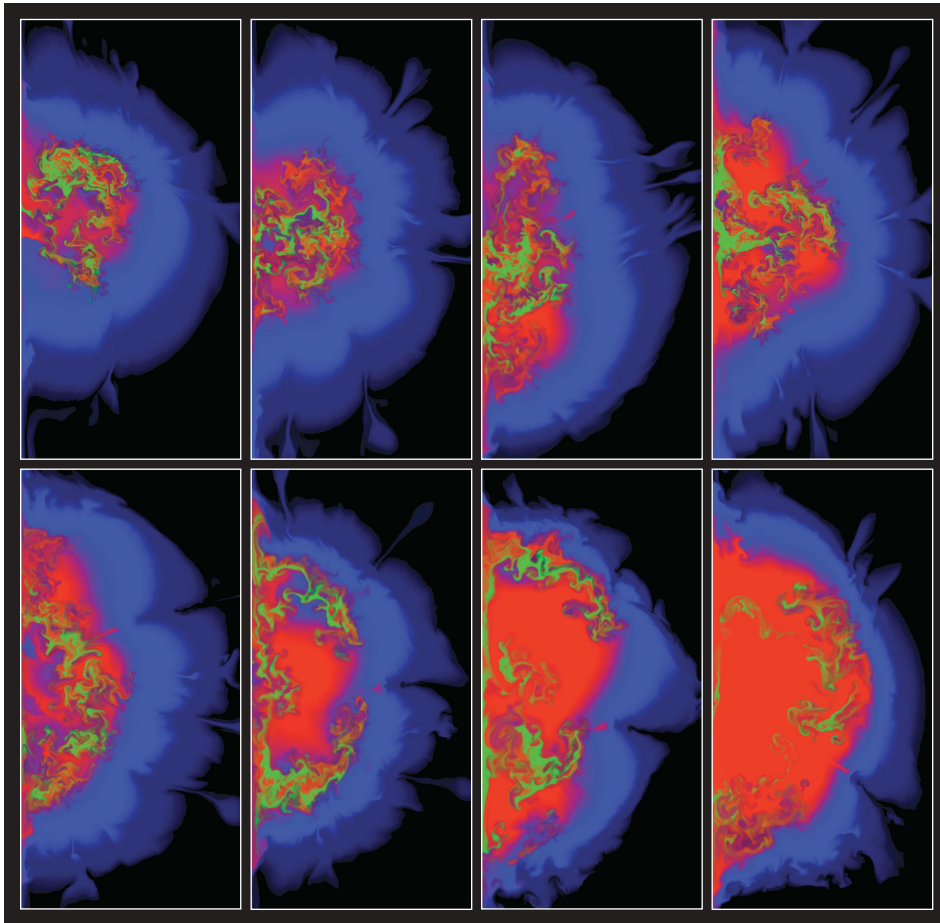


**Figure 1 | Chemical structure of the ejected debris 100 s after ignition for a subset of the explosion models with different ignition and detonation conditions.** Blue, intermediate-mass elements (that is, silicon, sulphur, calcium); green, stable iron-group elements produced by electron capture; and red,  $^{56}\text{Ni}$ . The  $^{56}\text{Ni}$  production increases (left to right) for models which undergo relatively more burning in the detonation as compared to the deflagration phase of the explosion. The turbulent inner regions reflect Rayleigh–Taylor and other instabilities that develop during the initial deflagration phase of burning. The subsequent detonation wave enhances the  $^{56}\text{Ni}$  production in the centre by burning remaining pockets of fuel. The lower-density outer layers of debris, processed only by the detonation, consist of smoothly distributed intermediate-mass elements.

less  $^{56}\text{Ni}$ . A strong ignition (that is, numerous, symmetrically distributed ‘sparks’) increases the amount of burning in the deflagration phase during which the star expands and the density declines. This reduces the  $^{56}\text{Ni}$  produced in the subsequent detonation wave. A weak or asymmetrical ignition, on the other hand, gives little deflagration burning and minimal pre-expansion, so that the detonation synthesizes abundant  $^{56}\text{Ni}$ . For similar reasons, the  $^{56}\text{Ni}$  mass also depended on the detonation criteria, as noted in previous one-dimensional calculations<sup>18</sup>.

Given the range in  $^{56}\text{Ni}$  masses, the model peak luminosities vary by a factor of three,  $(0.7\text{--}2.1) \times 10^{43} \text{ erg s}^{-1}$ ; this spans the range of

normal type Ia supernovae, though does not reproduce the more extreme and peculiar sub- and super-luminous events<sup>26</sup>. A substantial amount of the dispersion in luminosities of type Ia supernovae may therefore be the result of the stochastic and asymmetrical nature of the explosion itself, apart from any variations in the properties of the progenitor star. The r.m.s. dispersion in brightness depends on the wavelength band considered, being 45% in the blue, 27% in the red, and only 21% in the near-infrared ( $\sim 1.25 \mu\text{m}$  wavelength). This reflects a self-regulating property of the radiative transfer—dimmer models are relatively cooler, and so radiate a greater percentage of their flux at longer wavelengths. The models thus confirm observational

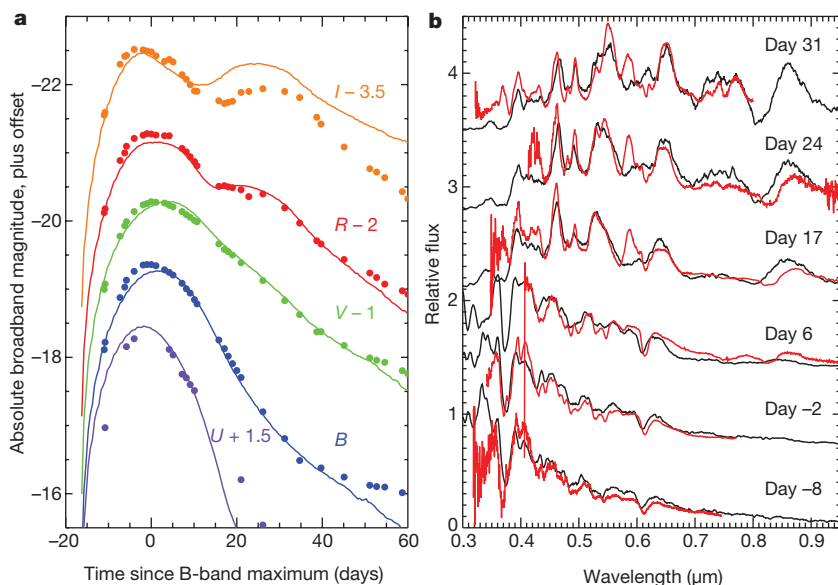


**Figure 2 | Synthetic multi-colour light curves and spectra of a representative explosion model compared to observations of a normal type Ia supernova.** **a**, The angle-averaged light curves of model DFD\_iso\_06\_dc2 (solid lines) show good agreement with filtered observations of SN 2003du<sup>24</sup> (filled circles) in wavelength bands corresponding to the ultraviolet (U), optical (B, V, R) and near-infrared (I). **b**, The synthetic spectra of the model (black lines) compare well to observations of SN 2003du (red lines) taken at times marked in days relative to B-band light-curve maximum. Over time, as the remnant expands and thins, the spectral absorption features reflect the chemical composition of progressively deeper layers of debris, providing a strong test of the predicted compositional stratification of the model.



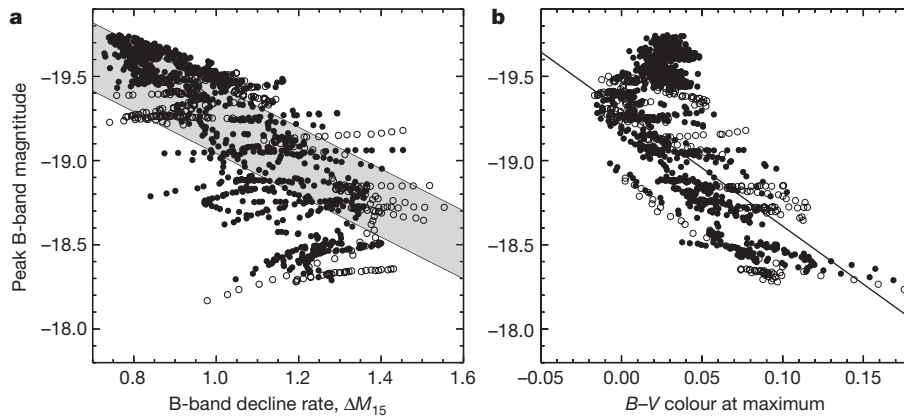


**Figure 3 | Correlation of the peak brightness of the models with their light-curve duration and colour.** The sample includes 44 models each plotted for 30 different viewing angles with equal probability of being observed. Solid circles denote models computed with the most likely range of detonation criteria, while open circles denote more extreme values. **a**, Relation between the peak brightness  $M_B$  (measured in the logarithmic magnitude scale) and the light-curve decline rate parameter  $\Delta M_{15}$ , defined as the decrease in B-band brightness from peak to 15 days after peak. The shaded band shows the approximate slope and spread of the observed width–luminosity relation (WLR). **b**, Relation between  $M_B$  and the colour parameter  $B - V$  measured at peak. The solid line shows the slope of the observed relation of ref. 6 but with the normalization shifted, as the models are systematically redder than

indications that type Ia supernovae are nearly standard (as opposed to merely standardizable) candles in the near-infrared<sup>27</sup>.

Without introducing any artificial tuning, the luminosity of the models correlates with the light-curve decline rate, giving a width–luminosity relation (WLR) similar to that observed (Fig. 3). A correlation is also found between brightness and the colour measured at peak. The r.m.s. scatter in the model WLR alone is 24%, while using both decline rate and colour reduces the dispersion to 21%—similar to, but slightly greater than, the  $\sim 16\%$  that is observed<sup>28</sup>. The larger diversity seen in the models suggests that additional important physics may constrain the ignition and detonation conditions to a range narrower than that considered here. As in observations, the calibration of the models can be improved by using additional

observed type Ia supernovae by  $\sim 7\%$ , probably due to the approximate treatment of non-local thermodynamic equilibrium effects. In observational studies, these two relations are usually fitted jointly as:

$M_B = M_{B,0} + \alpha(s - 1) - \beta[(B - V)_{\text{Bmax}} + (B - V)_0]$ , where  $s$  is a stretch parameter,  $(B - V)_{\text{Bmax}}$  is the colour measured at the light curve peak, and  $M_{B,0}$  is the fitted B-band magnitude of a  $s = 1$  supernova. We take the colour of a fiducial supernova,  $(B - V)_0 = 0$ , and determine stretch using the first-order relation  $s = 1 - (\Delta M_{15} - 1.1)/1.7$ . We find for the models fitted values of  $\alpha = 2.25$ ,  $\beta = 4.45$  and  $M_{B,0} = -19.27$ , which are in reasonable agreement with those derived from the recent observational sample of ref. 3:  $\alpha = 1.52$ ,  $\beta = 1.57$  and  $M_{B,0} = -19.31 + 5\log_{10}(H_0/70)$ , where  $H_0$  is the Hubble parameter.

information from the light curve. For example, including the shape of the light curve in several optical and near-infrared wavelength bands reduces the scatter to only 15%.

For a given mass of  $^{56}\text{Ni}$ , the residual scatter in the model WLR reflects individual features of the supernova debris structure. The turbulent deflagration phase imprints density and chemical inhomogeneities, which lead to variations in the timescale for photons to diffuse out of the debris. In addition, the global asymmetry—due to asymmetric ignition conditions or off-centre detonation points—gives rise to anisotropic emission, so that the brightness and duration of most models vary by 20–30%, depending of the angle from which they are viewed. Although the adoption of a two-dimensional geometry may exaggerate global asymmetries, spectropolarization observations reveal that type Ia supernovae typically possess asphericity near or just below the level predicted here<sup>14</sup>. Dimmer supernovae tend to be more polarized, an observation consistent with our finding that dimmer models are more asymmetric owing to relatively more burning in the turbulent deflagration phase.

There are both theoretical suggestions<sup>29</sup> and observational indications<sup>30</sup> that the metallicity of the white dwarf will affect the  $^{56}\text{Ni}$  yield at the  $\sim 10\%$  level. This is because the extra neutrons in trace elements such as  $^{22}\text{Ne}$  lead to an increased synthesis of neutronized iron group elements ( $^{54}\text{Fe}$  and  $^{58}\text{Ni}$ ) at the expense of  $^{56}\text{Ni}$ . To test the first-order effect of metallicity on the light curves, we varied the  $^{56}\text{Ni}$  and metal abundances in the ejecta models according to predicted nucleosynthetic results. The resulting light curves (Fig. 4) show that both the peak luminosity and light-curve duration decline with metallicity, in a manner roughly consistent with the WLR. Application of the WLR should therefore partially correct for metallicity variations, but with a residual error due to the different slope and normalization of the WLR at different metallicity. For extreme metallicity variations (from 0.3 to 3.0 times the solar value), this effect can lead to errors in the inferred distance to the supernova as large as 4%. The actual metallicity evolution over the range probed by cosmology experiments is much smaller than this, and we estimate that systematic errors in distance will probably be less than 2%.

The models suggest that a substantial amount of the scatter in the observed WLR arises from the random substructures and viewing-angle effects that are predicted by simulations of multi-dimensional explosions. In cosmological standard candle applications, these

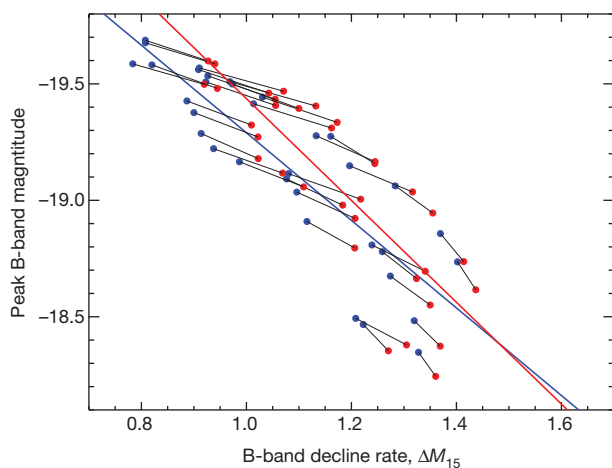


**Figure 4 | Effect of the metal content of the progenitor star population on the WLR.** The models explore two extreme values of the metallicity: 3 times (red points) and 0.3 times the solar value (blue points). For clarity, each model has been averaged over all viewing angles, and black lines connect similar explosion models of differing metallicity. The coloured lines are linear fits to the WLR of the two metallicity samples separately. The diversity introduced by metallicity variations follows the general width–luminosity trend, but the slightly different normalization and slope of the relation for different metallicity samples indicates a potential source of systematic error in distance determinations.

translate to easily reducible statistical errors. On the other hand, additional diversity arises from variations in metallicity and other properties of the progenitor star (for example, carbon/oxygen ratio, central density, rotation), which may introduce a source of systematic error. Simulation offers one means to test how such variations influence the supernova light curve; for future dark-energy experiments, this will help to anticipate and limit errors arising from a shift in progenitor demographics over cosmic time.

Received 29 September 2008; accepted 26 June 2009.

1. Riess, A. G. *et al.* Observational evidence from supernovae for an accelerating universe and a cosmological constant. *Astron. J.* **116**, 1009–1038 (1998).
2. Perlmutter, S. *et al.* Measurements of  $\Omega$  and  $\Lambda$  from 42 high-redshift supernovae. *Astrophys. J.* **517**, 565–586 (1999).
3. Astier, P. *et al.* The Supernova Legacy Survey: measurement of  $\Omega_m$ ,  $\Omega_\Lambda$  and  $w$  from the first year data set. *Astron. Astrophys.* **447**, 31–48 (2006).
4. Wood-Vasey, W. M. *et al.* Observational constraints on the nature of dark energy: first cosmological results from the ESSENCE supernova survey. *Astrophys. J.* **666**, 694–715 (2007).
5. Phillips, M. M. *et al.* The reddening-free decline rate versus luminosity relationship for Type Ia supernovae. *Astron. J.* **118**, 1766–1776 (1999).
6. Höflich, P. *et al.* Maximum brightness and postmaximum decline of light curves of Type Ia supernovae: a comparison of theory and observations. *Astrophys. J.* **472**, 81L–L84 (1996).
7. Pinto, P. A. & Eastman, R. G. The type Ia supernova width-luminosity relation. *N. Astron.* **6**, 307–319 (2001).
8. Kasen, D. & Woosley, S. E. On the Type Ia supernova width luminosity relation. *Astrophys. J.* **656**, 661–665 (2007).
9. Kuhlén, M., Woosley, S. E. & Glatzmaier, G. A. Carbon ignition in Type Ia supernovae. II. A three-dimensional numerical model. *Astrophys. J.* **640**, 407–416 (2006).
10. Livne, E., Asida, S. M. & Höflich, P. On the sensitivity of deflagrations in a Chandrasekhar mass white dwarf to initial conditions. *Astrophys. J.* **632**, 443–449 (2005).
11. Gamezo, V. N., Khokhlov, A. M. & Oran, E. S. Three-dimensional delayed-detonation model of Type Ia supernovae. *Astrophys. J.* **623**, 337–346 (2005).
12. Reinecke, M., Hillebrandt, W. & Niemeyer, J. C. Three-dimensional simulations of Type Ia supernovae. *Astron. Astrophys.* **391**, 1167–1172 (2002).
13. Livne, E. Delayed detonation at a single point in exploding white dwarfs. *Astrophys. J.* **527**, L97–L100 (1999).
14. Wang, L. & Wheeler, J. C. Spectropolarimetry of supernovae. *Annu. Rev. Astron. Astrophys.* **46**, 433–474 (2008).
15. Khokhlov, A. Delayed detonation model for type Ia supernovae. *Astron. Astrophys.* **245**, 114–128 (1991).
16. Hillebrandt, W. & Niemeyer, J. C. Type Ia supernova explosion models. *Annu. Rev. Astron. Astrophys.* **38**, 191–230 (2000).
17. Höflich, P. & Khokhlov, A. Explosion models for Type Ia supernovae: a comparison with observed light curves, distances,  $H_0$ , and  $Q_0$ . *Astrophys. J.* **457**, 500–528 (1996).
18. Höflich, P., Khokhlov, A. M. & Wheeler, J. C. Delayed detonation models for normal and subluminous type Ia supernovae: absolute brightness, light curves, and molecule formation. *Astrophys. J.* **444**, 831–847 (1995).
19. Kasen, D., Thomas, R. C. & Nugent, P. Time-dependent Monte Carlo techniques for the light curves, spectra, and polarization of supernovae. *Astrophys. J.* **651**, 366–380 (2006).
20. Woosley, S. E. *et al.* Type Ia supernovae. *Jour. Phys. Conf. Ser.* **78**, 012081 (2007).
21. Woosley, S. E. Type Ia supernovae: burning and detonation in the distributed regime. *Astrophys. J.* **668**, 1109–1117 (2007).
22. Aspdén, A. *et al.* Turbulence-flame interactions in Type Ia supernovae. *Astrophys. J.* **689**, 1173–1185 (2008).
23. Woosley, S. E., Kerstein, A., Sankaran, V. & Röpke, F. Type Ia supernova: calculations of turbulent flames using the linear eddy model. *Astrophys. J.* (submitted); preprint at (<http://www.arxiv.org/abs/0811.3610>) (2008).
24. Stanishchev, V. *et al.* SN 2003du, 480 days in the life of a normal Type Ia supernova. *Astron. Astrophys.* **469**, 645–661 (2007).
25. Höflich, P. *et al.* Signature of electron capture in iron-rich ejecta of SN 2003du. *Astrophys. J.* **617**, 1258–1266 (2004).
26. Branch, D., Fisher, A. & Nugent, P. On the relative frequencies of spectroscopically normal and peculiar Type Ia supernovae. *Astron. J.* **106**, 2383–2391 (1993).
27. Krisciunas, K., Phillips, M. M. & Suntzeff, N. B. Hubble diagrams of Type Ia supernovae in the near-infrared. *Astrophys. J.* **602**, L81–L84 (2004).
28. Hamuy, M. *et al.* The Hubble diagram of the Calan/Tololo Type Ia supernovae and the value of  $H_0$ . *Astron. J.* **112**, 2398–2407 (1996).
29. Timmes, F. X., Brown, E. F. & Truran, J. W. On variations in the peak luminosity of supernovae. *Astrophys. J.* **590**, L83–L86 (2003).
30. Howell, D. A. *et al.* The effect of progenitor age and metallicity on luminosity and  $^{56}\text{Ni}$  yield in Type Ia supernovae. *Astrophys. J.* **691**, 661–671 (2009).

**Supplementary Information** is linked to the online version of the paper at [www.nature.com/nature](http://www.nature.com/nature).

**Acknowledgements** D.K. and S.E.W. thank the Max Planck Institute for Astrophysics for hospitality during a visit when much of this research was carried out. Support for this work was provided by the DOE SciDAC Program. Support for D.K. was provided by NASA through a Hubble fellowship grant awarded by the Space Telescope Science Institute, which is operated by the Association of Universities for Research in Astronomy, Inc., for NASA. The research of F.K.R. is supported through the Emmy Noether Program of the German Research Foundation. We are grateful for computer time provided by NERSC and ORNL through an INCITE award.

**Author Contributions** D.K. developed and ran the radiative transfer calculations used to generate synthetic light curves and spectra of the models, and performed analysis and comparison to observations. F.K.R. set up the initial model conditions and ran the series of hydrodynamical explosion models. S.E.W. provided insight into the parameterization of ignition, detonation and electron capture, and assisted with the analysis.

**Author Information** Reprints and permissions information is available at [www.nature.com/reprints](http://www.nature.com/reprints). Correspondence and requests for materials should be addressed to D.K. ([kasen@ucolick.org](mailto:kasen@ucolick.org)).

# Storms in the tropics of Titan

E. L. Schaller<sup>1</sup>, H. G. Roe<sup>2</sup>, T. Schneider<sup>3,4</sup> & M. E. Brown<sup>3</sup>

Methane clouds, lakes and most fluvial features on Saturn's moon Titan have been observed in the moist high latitudes<sup>1–6</sup>, while the tropics have been nearly devoid of convective clouds and have shown an abundance of wind-carved surface features like dunes<sup>7,8</sup>. The presence of small-scale channels and dry riverbeds near the equator observed by the Huygens probe<sup>9</sup> at latitudes thought incapable of supporting convection<sup>10–12</sup> (and thus strong rain) has been suggested to be due to geological seepage or other mechanisms not related to precipitation<sup>13</sup>. Here we report the presence of bright, transient, tropospheric clouds in tropical latitudes. We find that the initial pulse of cloud activity generated planetary waves that instigated cloud activity at other latitudes across Titan that had been cloud-free for at least several years. These observations show that convective pulses at one latitude can trigger short-term convection at other latitudes, even those not generally considered capable of supporting convection, and may also explain the presence of methane-carved rivers and channels near the Huygens landing site.

Insolation on Titan varies seasonally during Saturn's 29.5-year orbit because of its 27° obliquity. The frequent presence of tropospheric clouds near the south pole at the southern summer solstice<sup>1,2</sup> led to the hypothesis that seasonally varying insolation controlled Titan's cloud locations<sup>1</sup>. Recent observations have shown that Titan's clouds display more complicated behaviour, including clouds at southern mid-latitudes<sup>14,15</sup> and clouds associated with lakes near the north pole<sup>6</sup>. Titan general circulation models have predicted that the majority of convective cloud activity should occur near the summer poles, with some cloud activity occurring at mid-latitudes, and very little in the tropics<sup>10–12,16</sup>. Although there are differences in the precise locations and frequencies of clouds in these models, they all predict that the equatorial regions should generally be the driest locations on the moon throughout most of Titan's year. In contrast with these predictions, images taken during the descent of the Huygens probe through Titan's atmosphere in January 2005 revealed small-scale channels and streams that appeared to have been carved by fluids (presumably methane) at equatorial (10° S) latitudes<sup>17</sup>. The morphologies of these channels also suggested that a high precipitation rate was needed to form them<sup>18</sup>.

Unlike the Earth, which is approximately 65% cloud covered throughout the year<sup>19</sup>, observations of Titan since 1990 have generally revealed a small amount of tropospheric cloud activity, covering only a small fraction (less than 1%) of Titan's disk<sup>7,20,21</sup>. However, on two occasions (September 1995 and October 2004; refs 22 and 23) clouds were observed to brighten dramatically, covering 5–7% of the surface, and, in the case of the October 2004 event, were found to last for at least a month. To determine the frequencies and causes of these short-lived cloud brightenings, which are thought to be associated with significant amounts of methane precipitation<sup>24</sup>, we developed a long-term observing programme with the National Aeronautics and Space Administration (NASA) Infrared Telescope Facility (IRTF) to determine the percentage of tropospheric cloud coverage of Titan's disk on a frequent (nearly nightly) basis<sup>25</sup>.

Although 138 nights of observations spread over 2.2 years revealed extremely low levels of cloud activity (0.3% coverage)<sup>25</sup>, on 13 April 2008 we observed an increase in flux at surface- or troposphere-probing wavelengths of brightness comparable to that of the events from 1995 and 2004 (Fig. 1). The following night we triggered adaptive optics observations with the Near Infrared Imager (NIRI) on the Gemini North telescope. These infrared images revealed a large cloud system in Titan's troposphere centred at 29° S, 247° W and with a latitudinal extent of  $\pm 15^\circ$ . In observations over the next three nights, the brightness centroid of this cloud system moved with an apparent eastward velocity of  $3 \pm 1 \text{ m s}^{-1}$ . The system also spread out in a southeastward direction, and finally rotated completely off the limb on 17 April. On 16–17 and 20–23 April, clouds also appeared near the south pole (81–60° S), with brightnesses not seen in the previous three years<sup>7</sup> (Figs 2 and 3).

The south pole was not predicted to be capable of supporting convective clouds during the season these clouds were observed (one year before vernal equinox)<sup>10,12,26</sup>, and clouds of this brightness had not been observed since November 2004 despite frequent imaging<sup>7</sup> and IRTF spectral monitoring<sup>25</sup>. Thus the appearance of relatively bright south polar clouds 3–7 days after the largest increase in Titan cloud activity observed in over three years points to a causal relationship. The south polar clouds were probably instigated by an atmospheric teleconnection mediated by planetary Rossby waves, formed from the initial pulse of cloud activity that occurred between 9 and 13 April. Rossby waves are large-scale atmospheric waves familiar from the

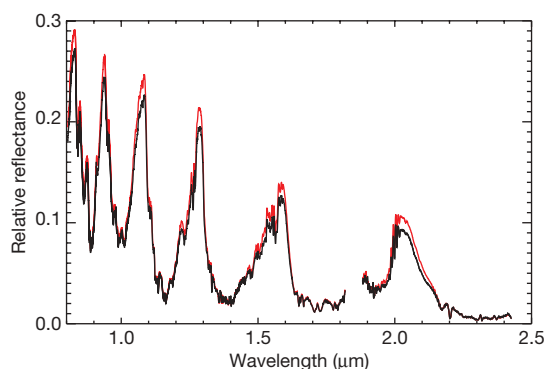


**Figure 1 | Titan IRTF spectra.** Near-infrared spectra of Titan from 28 March and 13 April 2008. Both spectra have approximately the same central longitude (227° W), but the spectrum from 13 April (red) shows increased flux in the transparent regions of Titan's atmosphere (0.8, 0.95, 1.2, 1.6 and 2.0  $\mu\text{m}$ ) while staying the same brightness in the high-opacity regions. Gemini images from the following night show the presence of a large extended cloud centred at 29° S, 247° W. Large cloud outbursts such as these (where Titan's clouds are seen to increase by over a factor of ten over typical levels) have been observed on only two other occasions<sup>22,23</sup>. The methane rainout from these large storms is thought to be responsible for carving Titan's streams and valley networks<sup>18,24</sup>.

<sup>1</sup>Institute for Astronomy, University of Hawaii, Honolulu, Hawaii 96822, USA. <sup>2</sup>Lowell Observatory, Flagstaff, Arizona 86001, USA. <sup>3</sup>Geological and Planetary Sciences, <sup>4</sup>Environmental Science and Engineering, California Institute of Technology, Pasadena, California 91125, USA.



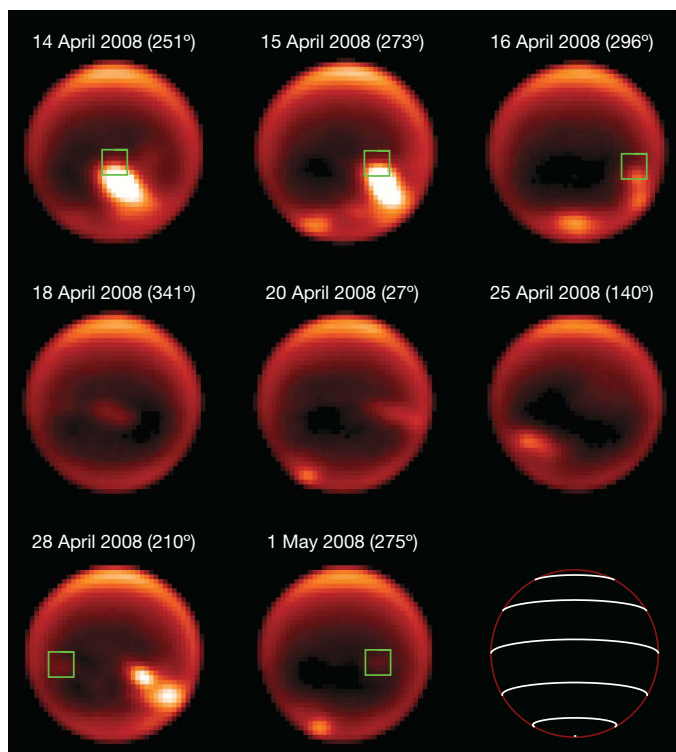


**Figure 2 | Gemini adaptive optics images of Titan.** Titan sub-Earth longitude and Universal Time date are noted for each observation. Images were taken through the H2(1-0) (2.1  $\mu\text{m}$ ) filter that probes to Titan's troposphere. Clouds were first detected on 13 April 2008 by our whole-disk spectroscopic monitoring programme with IRTF (Fig. 1). Clouds were subsequently detected in tropical, polar, and temperate latitudes using the Gemini adaptive optics system. Images from 28 April 2008 and 1 June 2008 show a faint cloud persisting over the same location as the northwesternmost extent of the initial large cloud from 14 April 2008 (15° S, 250° W; green box), perhaps indicating that the initial cloud outburst may have been localized here (see also Fig. 3).

Earth's atmosphere, which can propagate in the zonal and meridional directions. They can instigate cloud activity by modifying the temperature structure of the atmosphere and by inducing convergent flow near the surface. For a wave generated in the tropics to reach 72° S latitude in 3–7 days, it needs to travel with a meridional velocity of 3–8  $\text{m s}^{-1}$ . Deep (barotropic) Rossby waves with wavenumbers of  $\sim 2$

have zonal and meridional group velocities consistent with the observed propagation velocities (see Supplementary Information). Such long waves are probably the only ones able to propagate out of low-latitude generation regions (see Supplementary Information).

In addition to cloud activity near the south pole, on 18–20 April we also observed cloud activity from 20–12° S latitude, which are the closest latitudes to the equator we have ever observed cloud activity from the ground. Given the near lack of cloud activity at these low latitudes in all other observations (even from Cassini<sup>27,28</sup>), it is likely that these clouds were also triggered by the initial outburst. The near-equatorial clouds persisted for several days and had extended streak-like morphologies, similar to the mid-latitude clouds observed from 2003 to 2006 (refs 14, 15).

On 24 and 25 April 2008, the initial cloud rotated back onto the observable limb, decreased in brightness from that of the initial outburst but still moving with the same velocity of  $\sim 3 \text{ m s}^{-1}$  as in the initial three days of observations (Figs 2 and 3). South polar cloud activity was nearly non-existent. However, the image from 28 April shows that the same cloud system had grown significantly brighter, perhaps caused by the initial wave re-instigating cloud activity downstream. This new pulse of cloud activity, comparable in brightness to the original pulse from 14 April, displayed a similar morphology to the clouds seen on 15 and 16 April. Similarly, days later, clouds were also observed near the south pole and at near-equatorial latitudes. These observations demonstrate that a convective pulse at one latitude can trigger cloud activity at other latitudes thought to be incapable of supporting convective cloud activity. The cloud activity observed near the south pole indicates that for this short time period, convection was remarkably vigorous. Clouds appeared and re-appeared over different longitudes only days apart, indicating the likely formation and reformation of these cloud systems (similar to what was observed in October 2004). The precise locations where clouds formed were probably related to local surface conditions and methane abundances. An extremely dry location on Titan might not form clouds even if wave activity favoured it—whereas a methane lake might need only a small trigger to generate cloud activity above it (note that all of the south polar clouds that formed during this event were centred near 72° S, the latitude of Ontario Lacus).

Subsequent frequent observations from both Gemini and IRTF (30 distinct nights) revealed little to no cloud activity from 15 May to the end of the observable Titan season from the ground (7 July), indicating that the total duration of the increased cloud activity was less than one month. The duration of this period of increased cloud activity matched that of the last such outburst, which occurred in

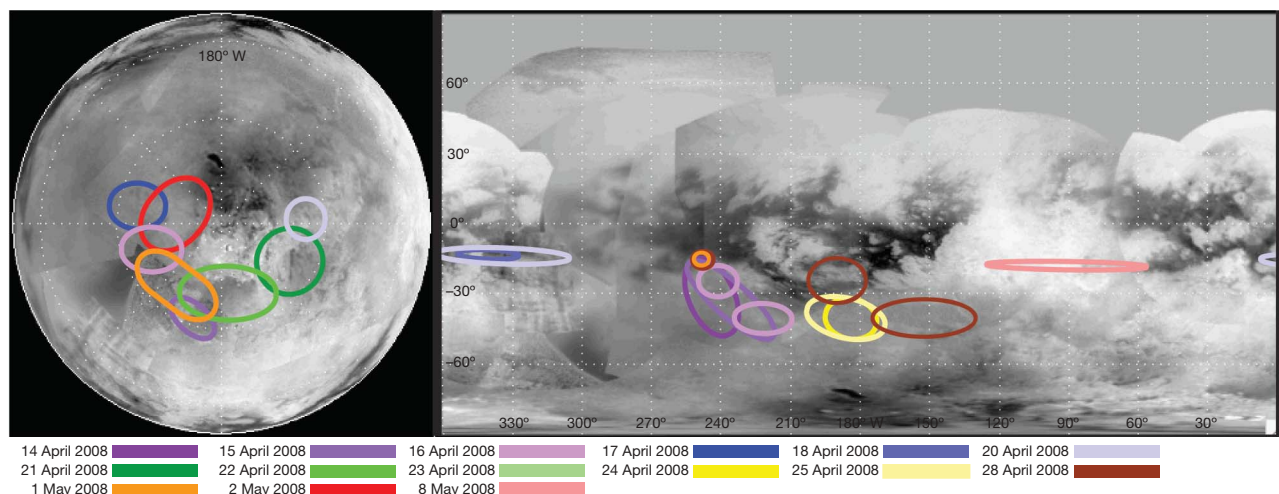


**Figure 3 | Titan cloud locations.** Cassini ISS surface maps (from <http://ciclops.org>) with locations of clouds from 14 April to 8 May 2008. No clouds were observed on 23 April 2008. Clouds that are located poleward of 55° S latitude are shown on the pole-projected surface map. Both maps show

latitude lines in 30° increments. The northwesternmost latitudes encompassed by the initial pulse of cloud activity on 14 April show the continued presence of a small cloud for at least 19 days after the initial event, indicating a potential tie to the surface.

October 2004 and lasted for approximately 30 days. Large cloud outbursts such as these are thought to be associated with significant amounts of precipitation<sup>24</sup> and probably play a major part in shaping the geological features on the surface of Titan.

One of the most intriguing questions is the cause and precise location of the initial pulse of cloud activity. Observations from 28 April and 1 May show that the northwesternmost regions encompassed by the initial pulse of cloud activity (15° S, 250° W) still remain bright in the 2.1- $\mu$ m images, indicating the continued presence of a small cloud (Figs 2 and 3). This region could have been the location of the initial pulse of cloud activity given the subsequent southeastward velocity of the bright cloud features. The Cassini ISS surface map in this region is unremarkable. Although several locations on Titan have been suggested to show evidence for cryovolcanic activity<sup>14,29</sup> (specifically regions that are bright at 5  $\mu$ m), this region is not one of them. The difficulty of forming large convective clouds at tropical latitudes, combined with the continued brightness of this region for at least 19 days, may point to a potential connection to the surface. If the surface were locally heated from below only slightly, parcels of air could be more easily lifted up to the level of free convection, leading to deep convective clouds. Additionally or alternatively, an injection of methane from the subsurface at this location could have a similar effect by lowering the level of free convection. The brightness and rapid formation of the initial cloud system indicates that the region centred on 15° S, 250° W is a good candidate location for observing surface changes due to methane rainout and, if the initial pulse were indeed tied to the surface, perhaps also recent cryovolcanism.

Received 5 March; accepted 2 June 2009.

1. Brown, M. E., Bouchez, A. H. & Griffith, C. A. Direct detection of variable tropospheric clouds near Titan's south pole. *Nature* **420**, 795–797 (2002).
2. Roe, H. G., de Pater, I., Macintosh, B. A. & McKay, C. P. Titan's clouds from Gemini and Keck adaptive optics imaging. *Astrophys. J.* **581**, 1399–1406 (2002).
3. Stofan, E. R. *et al.* The lakes of Titan. *Nature* **445**, 61–64 (2007).
4. Lorenz, R. D. *et al.* Fluvial channels on Titan: Initial Cassini RADAR observations. *Planet. Space Sci.* **56**, 1132–1144 (2008).
5. Brown, R. H. *et al.* The identification of liquid ethane in Titan's Ontario Lacus. *Nature* **454**, 607–610 (2008).
6. Brown, M. E. *et al.* Discovery of lake-effect clouds on Titan. *Geophys. Res. Lett.* **36**, L01103 (2009).
7. Schaller, E. L., Brown, M. E., Roe, H. G., Bouchez, A. H. & Trujillo, C. A. Dissipation of Titan's south polar clouds. *Icarus* **184**, 517–523 (2006).
8. Barnes, J. W. *et al.* Spectroscopy, morphometry, and photoclinometry of Titan's dunefields from Cassini/VIMS. *Icarus* **195**, 400–414 (2008).
9. Soderblom, L. A. *et al.* Topography and geomorphology of the Huygens landing site on Titan. *Planet. Space Sci.* **55**, 2015–2024 (2007).
10. Mitchell, J. T., Pierrehumbert, R. T., Frierson, D. M. & Caballero, R. The dynamics behind Titan's methane clouds. *Icarus* **103**, 18421–18426 (2006).
11. Mitchell, J. L. The drying of Titan's dunes: Titan's methane hydrology and its impact on atmospheric circulation. *J. Geophys. Res. Planets* **113**, E08015 (2008).

12. Rannou, P., Montmessin, F., Hourdin, F. & Lebonnois, S. The latitudinal distribution of clouds on Titan. *Science* **311**, 201–205 (2006).
13. Griffith, C. A., McKay, C. P. & Ferri, F. Titan's tropical storms in an evolving atmosphere. *Astrophys. J.* **687**, L41–L44 (2008).
14. Roe, H. G., Brown, M. E., Schaller, E. L., Bouchez, A. H. & Trujillo, C. A. Geographic control of Titan's mid-latitude clouds. *Science* **310**, 477–479 (2005).
15. Griffith, C. A. *et al.* The evolution of Titan's mid-latitude clouds. *Science* **310**, 474–477 (2005).
16. Tokano, T. *et al.* Methane drizzle on Titan. *Nature* **442**, 432–435 (2006).
17. Lebreton, J.-P. *et al.* An overview of the descent and landing of the Huygens probe on Titan. *Nature* **438**, 758–764 (2005).
18. Perron, J. T. *et al.* Valley formation and methane precipitation rates on Titan. *J. Geophys. Res. Planets* **111**, E11001 (2006).
19. Rossow, W. B. & Schiffer, R. A. Advances in understanding clouds from ISCCP. *Bull. Am. Meteorol. Soc.* **80**, 2261–2287 (1999).
20. Griffith, C. A., Hall, J. L. & Geballe, T. R. Detection of daily clouds on Titan. *Science* **290**, 509–513 (2000).
21. Bouchez, A. H. & Brown, M. E. Statistics of Titan's south polar tropospheric clouds. *Astrophys. J.* **618**, L53–L56 (2005).
22. Griffith, C. A., Owen, T., Miller, G. A. & Geballe, T. Transient clouds in Titan's lower atmosphere. *Nature* **395**, 575–578 (1998).
23. Schaller, E. L., Brown, M. E., Roe, H. G. & Bouchez, A. H. A large cloud outburst at Titan's south pole. *Icarus* **182**, 224–229 (2006).
24. Hueso, R. & Sánchez-Lavega, A. Methane storms on Saturn's moon Titan. *Nature* **442**, 428–431 (2006).
25. Schaller, E. L., Brown, M. E. & Roe, H. G. Seasonal change in Titan's cloud activity observed with IRTF/SpeX. *Astron. J.* (submitted).
26. Tokano, T. Meteorological assessment of the surface temperatures on Titan: constraints on the surface type. *Icarus* **173**, 222–242 (2005).
27. Turtle, E. P. *et al.* Cassini imaging of Titan's high-latitude lakes, clouds, and south-polar surface changes. *Geophys. Res. Lett.* **36**, L02204 (2009).
28. Brown, M. E., Roberts, J. & Schaller, E. L. Clouds on Titan during the Cassini prime mission: a complete analysis of the VIMS data. *Icarus* (submitted).
29. Barnes, J. W. *et al.* A 5-micron-bright spot on Titan: evidence for surface diversity. *Science* **310**, 92–95 (2005).

Supplementary Information is linked to the online version of the paper at [www.nature.com/nature](http://www.nature.com/nature).

**Acknowledgements** E.L.S. is supported by a Hubble Postdoctoral Fellowship. H.G.R. is supported by the NASA Planetary Astronomy Program. M.E.B. is supported by an NSF Planetary Astronomy grant. We thank IRTF telescope operators, D. Griep, W. Golisch, P. Sears and E. Volquardsen. The IRTF is operated by the University of Hawaii under a cooperative agreement with the Planetary Astronomy Program of the NASA Science Mission Directorate. Gemini Observatory is operated by the Association of Universities for Research in Astronomy, Inc., under a cooperative agreement with the NSF on behalf of the International Gemini partnership.

**Author Contributions** E.L.S. analysed and interpreted the IRTF and Gemini observations and wrote the paper. H.G.R. was responsible for the Gemini observations, data reduction, and analysis. T.S. helped interpret the observations. T.S. and E.L.S. wrote the Supplementary Information. M.E.B. supervised the project. All authors discussed the results and implications and commented on the manuscript.

**Author Information** Reprints and permissions information is available at [www.nature.com/reprints](http://www.nature.com/reprints). Correspondence and requests for materials should be addressed to E.L.S. ([schaller@ifa.hawaii.edu](mailto:schaller@ifa.hawaii.edu)).

## LETTERS

# Dense packings of the Platonic and Archimedean solids

S. Torquato<sup>1,2,3,4,5</sup> & Y. Jiao<sup>4</sup>

Dense particle packings have served as useful models of the structures of liquid, glassy and crystalline states of matter<sup>1–4</sup>, granular media<sup>3,5</sup>, heterogeneous materials<sup>3</sup> and biological systems<sup>6–8</sup>. Probing the symmetries and other mathematical properties of the densest packings is a problem of interest in discrete geometry and number theory<sup>9–11</sup>. Previous work has focused mainly on spherical particles—very little is known about dense polyhedral packings. Here we formulate the generation of dense packings of polyhedra as an optimization problem, using an adaptive fundamental cell subject to periodic boundary conditions (we term this the ‘adaptive shrinking cell’ scheme). Using a variety of multi-particle initial configurations, we find the densest known packings of the four non-tiling Platonic solids (the tetrahedron, octahedron, dodecahedron and icosahedron) in three-dimensional Euclidean space. The densities are 0.782..., 0.947..., 0.904... and 0.836..., respectively. Unlike the densest tetrahedral packing, which must not be a Bravais lattice packing, the densest packings of the other non-tiling Platonic solids that we obtain are their previously known optimal (Bravais) lattice packings. Combining our simulation results with derived rigorous upper bounds and theoretical arguments leads us to the conjecture that the densest packings of the Platonic and Archimedean solids with central symmetry are given by their corresponding densest lattice packings. This is the analogue of Kepler’s sphere conjecture for these solids.

A large collection of non-overlapping solid objects (particles) in  $d$ -dimensional Euclidean space  $\mathbb{R}^d$  is called a packing. The packing density  $\phi$  is defined as the fraction of space  $\mathbb{R}^d$  covered by the particles. A problem that has been a source of fascination to mathematicians and scientists for centuries is the determination of the densest arrangement(s) of particles that do not tile space and the associated maximal density  $\phi_{\max}$  (ref. 9). Most previous work has focused on spherical particles, but even for this simple shape the problem is notoriously difficult. Indeed, Kepler’s conjecture concerning the densest sphere packing arrangement was only proved by Hales in 2005 (ref. 10).

Attention has very recently turned to finding the maximum-density packings of nonspherical particles in  $\mathbb{R}^3$ , including ellipsoids<sup>12</sup>, tetrahedra<sup>13,14</sup>, and superballs<sup>15</sup>. Very little is known about the densest packings of polyhedral particles that do not tile space, including the majority of the Platonic and Archimedean solids studied by the ancient Greeks. The difficulty in obtaining dense packings of polyhedra is related to their complex rotational degrees of freedom and to the non-smooth nature of their shapes.

The Platonic solids (mentioned in Plato’s *Timaeus*) are convex polyhedra with faces composed of congruent convex regular polygons. There are exactly five such solids: the tetrahedron, icosahedron, dodecahedron, octahedron and cube (see Fig. 1). An Archimedean solid is a highly symmetric, semi-regular convex polyhedron composed of two or more types of regular polygons meeting in identical

vertices. There are thirteen Archimedean solids (see Fig. 1). We note that the tetrahedron (P1) and truncated tetrahedron (A1) are the only Platonic and Archimedean solids, respectively, that are not centrally symmetric. A particle is centrally symmetric if it has a centre  $C$  that bisects every chord through  $C$  connecting any two boundary points of the particle. We will see that this type of symmetry is fundamental in determining the nature of the dense packing arrangements.

Some definitions are in order here. A lattice  $\Lambda$  in  $\mathbb{R}^3$  is an infinite set of points generated by a set of discrete translation operations (defined by integer linear combinations of a basis of  $\mathbb{R}^3$ ) (ref. 4). A (Bravais) lattice packing is one in which the centroids of the non-overlapping particles are located at the points of  $\Lambda$ , each oriented in the same direction. The space  $\mathbb{R}^3$  can then be geometrically divided into identical regions  $F$  called fundamental cells, each of which contains just the centroid of one particle. Thus, the density of a lattice packing is given by

$$\phi = \frac{v_{\text{particle}}}{V_F} \quad (1)$$

where  $v_{\text{particle}}$  is the volume of a particle and  $V_F$  is the volume of a fundamental cell. A periodic packing of particles is obtained by placing a fixed non-overlapping configuration of  $N$  particles (where  $N \geq 1$ ) with arbitrary orientations in each fundamental cell of a lattice  $\Lambda$ . Thus, the packing is still periodic under translations by  $\Lambda$ , but the  $N$  particles can occur anywhere in the chosen cell subject to the non-overlap condition. The density of a periodic packing is given by

$$\phi = \frac{Nv_{\text{particle}}}{V_F} \quad (2)$$

We formulate the problem of generating dense packings of non-overlapping polyhedra within an adaptive fundamental cell subject to periodic boundary conditions as an optimization problem (see Methods Summary). We call this optimization scheme the ‘adaptive shrinking cell’ (ASC). Figure 2 illustrates a simple sequence of configuration changes for a four-particle packing.

Finding the densest packings of regular tetrahedra is part of the eighteenth problem in Hilbert’s famous set of problems. The densest (Bravais) lattice packing of tetrahedra (which requires all of the tetrahedra to have the same orientations) has the relatively low density  $\phi_{\max}^{\text{lattice}} = 18/49 = 0.367 \dots$  and each tetrahedron touches 14 others<sup>16</sup>. Recently, Conway and Torquato showed that the densest packings of tetrahedra must not be Bravais lattice packings, and found packings with density as large as  $\phi \approx 0.72$  (ref. 13). P. Chaikin, S. Wang and A. Jaoshvili experimentally generated jammed disordered packings of nearly tetrahedral dice with  $\phi \approx 0.75$  (unpublished work). Chen<sup>14</sup> has recently discovered a periodic packing of tetrahedra with  $\phi = 0.7786 \dots$ , which we call the ‘wagon-wheels’ packing because the basic subunits consist of

<sup>1</sup>Department of Chemistry, <sup>2</sup>Princeton Center for Theoretical Science, <sup>3</sup>Princeton Institute for the Science and Technology of Materials, <sup>4</sup>Department of Mechanical and Aerospace Engineering, Princeton University, Princeton, New Jersey 08544, USA. <sup>5</sup>School of Natural Sciences, Institute for Advanced Study, Princeton, New Jersey 08540, USA.



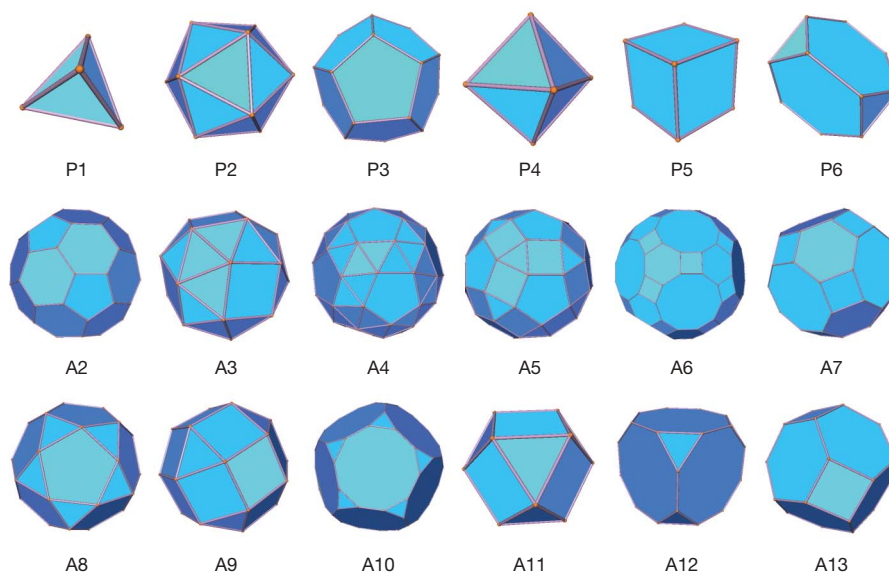


**Figure 1 | The five Platonic solids and the 13 Archimedean solids.** The five Platonic solids are the tetrahedron (P1), icosahedron (P2), dodecahedron (P3), octahedron (P4) and cube (P5). The 13 Archimedean solids are the truncated tetrahedron (A1), truncated icosahedron (A2), snub cube (A3), snub dodecahedron (A4), rhombicuboctahedron (A5), truncated

icosidodecahedron (A6), truncated cuboctahedron (A7), icosidodecahedron (A8), rhombicuboctahedron (A9), truncated dodecahedron (A10), cuboctahedron (A11), truncated cube (A12), and truncated octahedron (A13). The cube (P5) and truncated octahedron (A13) are the only Platonic and Archimedean solids, respectively, that tile space.

two orthogonally intersecting ‘wagon wheels’. A wagon wheel consists of five contacting tetrahedra packed around a common edge (see figure 1a of ref. 13).

We begin by solving the ASC scheme to obtain dense packings of tetrahedra using initial configurations based upon low-density versions of the aforementioned packings. Initial conditions based on periodic copies of the wagon-wheels packing with 72 particles per cell lead to the densest packing of tetrahedra reported to date with  $\phi = 0.782021\dots$  (see Fig. 3). Its lattice vectors and other characteristics are given in the Supplementary Information. The preference for face-to-face (not vertex-to-face) contacts and the lack of central symmetry ensure that dense tetrahedral packings must be non-lattice structures.

To obtain dense packings of icosahedra, dodecahedra and octahedra, we use a wide range of initial configurations. These include multi-particle configurations (with  $N$  ranging from 20 to 343) of random ‘dilute’ packings and a variety of lattice packings with a wide range of densities. For icosahedra, dodecahedra and octahedra, we obtain final packings with densities at least as large as  $0.836315\dots$ ,  $0.904002\dots$  and  $0.947003\dots$ , respectively, which are extremely close in structure and density to their corresponding optimal lattice packings with

$\phi_{\max}^{\text{lattice}} = 0.836357\dots$  (ref. 17),  $\phi_{\max}^{\text{lattice}} = (5 + \sqrt{5})/8 = 0.904508\dots$  (ref. 17) and  $\phi_{\max}^{\text{lattice}} = 18/19 = 0.947368\dots$  (ref. 18), respectively. Figure 3 shows the optimal lattice packings of icosahedra, dodecahedra and octahedra, in which each particle contacts 12, 12 and 14 others, respectively. Our simulation results strongly suggest that the optimal lattice packings of the centrally symmetric Platonic solids are indeed the densest packings of these particles, especially since these arise from a variety of initial dilute multi-particle configurations within an adaptive fundamental cell.

We can show that the maximal density  $\phi_{\max}$  of a packing of congruent nonspherical particles of volume  $v_{\text{particle}}$  is bounded from above according to:

$$\phi_{\max} \leq \phi_{\max}^{\text{upper bound}} = \min \left[ \frac{v_{\text{particle}}}{v_{\text{sphere}}} \frac{\pi}{\sqrt{18}}, 1 \right] \quad (3)$$

where  $v_{\text{sphere}}$  is the volume of the largest sphere that can be inscribed in the nonspherical particle and  $\pi/\sqrt{18}$  is the maximal sphere-packing density. The proof is given in the Supplementary Information. The upper bound (3) will be relatively tight for packings of nonspherical particles provided that the asphericity  $\gamma$  (equal to the ratio of the circumradius to the inradius, see online-only Methods) of the particle

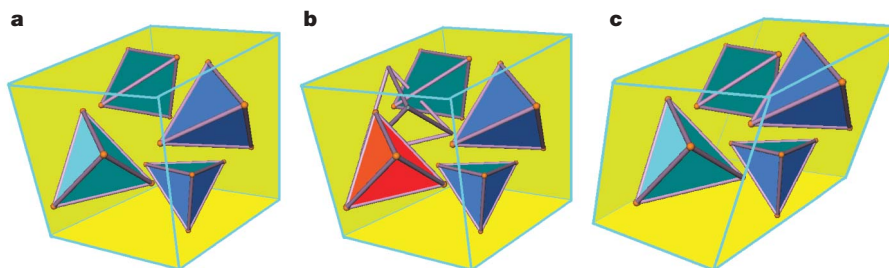


**Figure 2 | Sequential changes of a four-particle packing configuration according to the design variables in the ASC algorithm.** By efficiently exploring the design-variable space, which consists of the particle configurational space and the space of lattices (owing to our use of an adaptive fundamental cell), the ASC scheme enables us to find a point in the design-variable space in the neighbourhood of the starting point that has a higher packing density than the initial density. The process is continued until the deepest minimum of the objective function (a maximum of packing

density) is obtained, which could be either a local or global optimum. Here we show such a sequence. **a**, An initial configuration of four particles. **b**, A trial move of a randomly selected particle (red) that is rejected because it overlaps another particle. This is determined precisely using the separation axis theorem<sup>26</sup>. **c**, A trial move that is accepted, which results in a deformation and compression (small in magnitude) changing the fundamental cell shape and size as well as the relative distances between the particles.

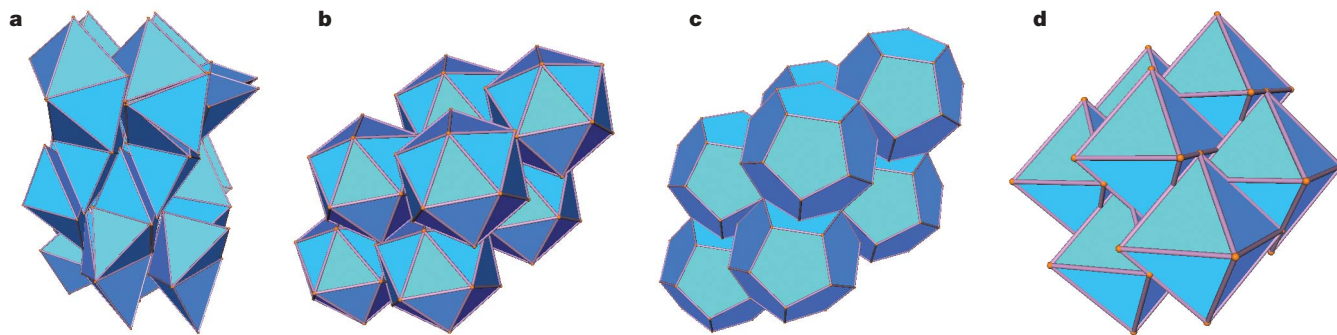


**Figure 3 | Portions of the densest packing of tetrahedra obtained from our simulations, and the optimal lattice packings of the icosahedra, dodecahedra and octahedra to which our simulations converge.** All of these packings are at least locally jammed, that is, each particle cannot be translated or rotated while fixing the positions and orientations of all the other particles<sup>27,28</sup>. We emphasize that even though the latter three cases begin with complex multi-particle initial configurations in the large fundamental (repeating) cell, they all converge to packings in which a

smaller repeat unit contains only one centroid, that is, they all converge to Bravais lattice packings and, in fact, the corresponding densest lattice packings. **a**, Tetrahedral packing. We depict the 72 particles in the fundamental cell of this non-lattice packing. Within the cell, the particles are characterized by short-range translational order and a preference for face-to-face contacts (see Supplementary Information). **b**, Optimal lattice packing of icosahedra. **c**, Optimal lattice packing of dodecahedra. **d**, Optimal lattice packing of octahedra.

is not large. Bound (3) cannot generally be sharp (that is, exact) for a nontiling, nonspherical particle, so any packing whose density is close to the upper bound (3) is nearly optimal, if not optimal.

Figure 4 compares the density of the densest lattice packings of the Platonic and Archimedean solids to the corresponding upper bounds on the maximal density for such packings. The central symmetry of the majority of the Platonic and Archimedean solids and their associated relatively small asphericities explain the corresponding small differences between  $\phi_{\max}^{\text{lattice}}$  and  $\phi_{\max}^{\text{upper bound}}$  and is consistent with our simulation findings that strongly indicate that their optimal arrangements are their respective densest lattice packings.

Why should the densest packings of the centrally symmetric solids be their corresponding optimal lattice packings? First, face-to-face contacts allow such polyhedral packings to achieve higher densities because they enable the contacting centroids around each particle to come closer together. Second, face-to-face contacts are maximized

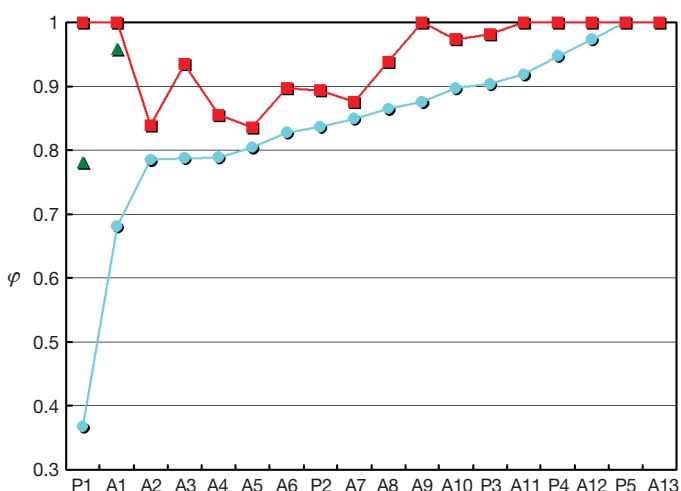


**Figure 4 | Comparison of the densest known lattice packings (blue circles) of the Platonic and Archimedean solids<sup>16–18</sup> to the corresponding upper bounds (red squares) obtained from bound (3).** The large asphericity and lack of central symmetry of the tetrahedron (P1) and truncated tetrahedron (A1) are consistent with the large gaps between their upper-bound densities and densest-lattice-packing densities, and the fact that there are non-lattice packings with densities appreciably greater than  $\phi_{\max}^{\text{lattice}}$  (green triangles). The truncated tetrahedron is the only non-centrally symmetric Archimedean solid, the densest known packing of which is a non-lattice packing with two particles per fundamental cell and a density at least as high as  $23/24 = 0.958333\dots$  (ref. 13).

when each particle has the same orientation because of the central symmetry and the equivalence of the three principal axes (associated with the small asphericity) of the solid. This is consistent with a lattice packing, the densest of which is the optimal one. These arguments in conjunction with our simulation results for the Platonic solids and rigorous bounds lead us to the following conjecture: The densest packings of the centrally symmetric Platonic and Archimedean solids are given by their corresponding optimal lattice packings. This is the analogue of Kepler's sphere conjecture for these solids.

There is no reason to believe that denser packings of tetrahedra cannot be achieved by using even better initial conditions than those based on the wagon-wheels packing and a larger number of particles. We observe that the densest packings of all of the Platonic and Archimedean solids reported here as well as the densest known packings of superballs<sup>15</sup> and ellipsoids<sup>12</sup> have densities that exceed the optimal sphere packing density  $\phi_{\max}^{\text{sphere}} = \pi/\sqrt{18} = 0.7408\dots$  These results are consistent with Ulam's conjecture<sup>19</sup>, which may be violated if the convex particle has little or no symmetry, but a counterexample has yet to be given.

How does our conjecture extend to other polyhedral packings? It is natural to group the infinite families of prisms and antiprisms<sup>20</sup> with the Archimedean solids. A prism is a polyhedron having bases that are parallel, congruent polygons and sides that are parallelograms. An antiprism is a polyhedron having bases that are parallel, congruent polygons and sides that are alternating bands of triangles. Prisms with an even number of sides and antiprisms are centrally symmetric and so it may be that Bravais lattices of such solids are optimal. However, prisms with an odd number of sides are not centrally symmetric and thus their optimal packings may not be Bravais lattices. In future work, we will determine whether our conjecture extends to prisms and antiprisms.

## METHODS SUMMARY

The objective function in our ASC optimization scheme is taken to be the negative of the packing density  $\phi$ . Starting from an initial packing configuration in the fundamental cell, the positions and orientations of the polyhedra are design variables for the optimization. Importantly, we also allow the boundary of the fundamental cell to deform as well as shrink or expand such that there is a net shrinkage (increase of the density) in the final state. Thus, the deformation and compression/expansion of the cell boundary are also design variables. We are not aware of any packing algorithm that employs both a sequential search of the configurational space of the particles and the space of lattices via an adaptive fundamental cell that shrinks on average to obtain dense packings. The ASC has a number of novel features that distinguish it from previous packing algorithms that have been devised for spheres<sup>21–23</sup>, ellipsoids<sup>24,25</sup> and superballs<sup>15</sup> (see online-only Methods for details).

**Full Methods** and any associated references are available in the online version of the paper at [www.nature.com/nature](http://www.nature.com/nature).

**Received 29 April; accepted 24 June 2009.**

1. Bernal, J. D. in *Liquids: Structure, Properties, Solid Interactions* (eds Hughel, T. J.) 25–50 (Elsevier, 1965).
2. Zallen, R. *The Physics of Amorphous Solids* (Wiley, 1983).
3. Torquato, S. *Random Heterogeneous Materials: Microstructure and Macroscopic Properties* (Springer, 2002).
4. Chaikin, P. M. & Lubensky, T. C. *Principles of Condensed Matter Physics* (Cambridge Univ. Press, 2000).
5. Edwards, S. F. in *Granular Matter* (eds Mehta, A.) 121–140 (Springer, 1994).
6. Liang, J. & Dill, K. A. Are proteins well-packed? *Biophys. J.* **81**, 751–766 (2001).
7. Purohit, P. K., Kondev, J. & Phillips, R. Mechanics of DNA packaging in viruses. *Proc. Natl Acad. Sci. USA* **100**, 3173–3178 (2003).
8. Gevertz, J. L. & Torquato, S. A novel three-phase model of brain tissue microstructure. *PLOS Comput. Biol.* **4**, e1000152 (2008).
9. Conway, J. H. & Sloane, N. J. A. *Sphere Packings, Lattices and Groups* (Springer, 1998).
10. Hales, T. C. A proof of the Kepler conjecture. *Ann. Math.* **162**, 1065–1185 (2005).
11. Cohn, H. & Elkies, N. New upper bounds on sphere packings. I. *Ann. Math.* **157**, 689–714 (2003).
12. Donev, A., Stillinger, F. H., Chaikin, P. M. & Torquato, S. Unusually dense crystal ellipsoid packings. *Phys. Rev. Lett.* **92**, 255506 (2004).
13. Conway, J. H. & Torquato, S. Packing, tiling and covering with tetrahedra. *Proc. Natl Acad. Sci. USA* **103**, 10612–10617 (2006).
14. Chen, E. R. A dense packing of regular tetrahedra. *Discrete Comput. Geom.* **40**, 214–240 (2008).
15. Jiao, Y., Stillinger, F. H. & Torquato, S. Optimal packings of superballs. *Phys. Rev. E* **79**, 041309 (2009).
16. Hoylman, D. J. The densest lattice packing of tetrahedra. *Bull. Am. Math. Soc.* **76**, 135–137 (1970).
17. Betke, U. & Henk, M. Densest lattice packings of 3-polytopes. *Comput. Geom.* **16**, 157–186 (2000).
18. Minkowski, H. Dichteste gitterförmige Lagerung kongruenter Körper. *Nachr. Akad. Wiss. Göttingen Math. Phys. Kl. II* 311–355 (1904).
19. Gardner, M. *The Colossal Book of Mathematics: Classic Puzzles, Paradoxes, and Problems* Ch. 10, 135 (Norton, 2001).
20. Cromwell, P. R. *Polyhedra* (Cambridge Univ. Press, 1997).
21. Jodrey, W. S. & Tory, E. M. Computer simulation of close random packing of equal spheres. *Phys. Lett. A* **32**, 2347–2351 (1985).
22. Rintoul, M. D. & Torquato, S. S. Hard-sphere statistics along the metastable amorphous branch. *Phys. Rev. E* **58**, 532–537 (1998).
23. Uche, O. U., Stillinger, F. H. & Torquato, S. Concerning maximal packing arrangements of binary disk mixtures. *Physica A* **342**, 428–446 (2004).
24. Donev, A., Torquato, S. & Stillinger, F. H. Neighbor list collision-driven molecular dynamics for nonspherical hard particles. I. Algorithmic details. *J. Comput. Phys.* **202**, 737–764 (2005).
25. Donev, A., Torquato, S. & Stillinger, F. H. Neighbor list collision-driven molecular dynamics for nonspherical hard particles. II. Applications to ellipses and ellipsoids. *J. Comput. Phys.* **202**, 765–793 (2005).
26. Golshtein, E. G. & Tretyakov, N. V. *Modified Lagrangians and Monotone Maps in Optimization* (Wiley, 1996).
27. Torquato, S. & Stillinger, F. H. Multiplicity of generation, selection, and classification procedures for jammed hard-particle packings. *J. Phys. Chem. B* **105**, 11849–11853 (2001).
28. Donev, A., Connelly, R., Stillinger, F. H. & Torquato, S. Underconstrained jammed packings of nonspherical hard particles: ellipses and ellipsoids. *Phys. Rev. E* **75**, 051304 (2007).

**Supplementary Information** is linked to the online version of the paper at [www.nature.com/nature](http://www.nature.com/nature).

**Acknowledgements** We are grateful to H. Cohn and J. Conway for comments on our manuscript. S.T. thanks the Institute for Advanced Study for its hospitality during his stay there. This work was supported by the National Science Foundation under award numbers DMS-0804431 and DMR-0820341. The figures showing the polyhedra were generated using the AntiPrism package developed by A. Rossiter.

**Author Contributions** S.T. devised the algorithm and upper bounds, performed theoretical analysis, and wrote the paper. Y.J. implemented the algorithm, performed theoretical analysis, commented on the manuscript and created all of the figures.

**Author Information** Reprints and permissions information is available at [www.nature.com/reprints](http://www.nature.com/reprints). Correspondence and requests for materials should be addressed to S.T. ([torquato@princeton.edu](mailto:torquato@princeton.edu)).



## METHODS

The ASC optimization problem could be solved using various techniques, depending on the shapes of the particles. For example, for spheres, we have shown that linear programming techniques can efficiently produce optimal solutions (unpublished work). However, for polyhedra, the complex non-overlap conditions make the ASC scheme inefficient to solve using linear programming methods. For polyhedral particles, we solve the ASC optimization problem using a standard Monte Carlo procedure with a Metropolis acceptance rule for trial moves to search the design-variable space efficiently, which contains both the configuration space of the particles and the space of lattices.

In our implementation, a polyhedral particle is represented by the position of its centroids as well as the coordinates of all its vertices relative to the centroid. Although this representation contains redundant information, it is a convenient way to deal with the rotational motions of the polyhedra. To search the configuration space of the particles, small random trial moves of arbitrarily selected particles are attempted sequentially for each particle. Each trial move is equally likely to be a translation of the centroid of the particle or a rotation of the particle about a randomly oriented axis through its centroid.

The space of lattices is searched by deforming/compressing/expanding the fundamental cell, which is completely characterized by a strain tensor in the linear regime (that is, small strain limit). The trace of the strain tensor determines the volume change of the fundamental cell and is involved in the objective function. The off-diagonal components of the tensor determine the shape change of the cell. The positions of the particles centroids are relative coordinates with respect to the lattice vectors. When the strain tensor is applied to the lattice vectors, although the relative coordinates of the centroids remain the same, the Euclidean distances between the particles will change. Thus, the deformation/compression/expansion of the fundamental cell at least in part allows for collective particle motions, which is more efficient for finding a direction in the design-variable space leading to a higher packing density. Moreover, it is the overall compression of the fundamental cell that causes the packing density to increase, not the growth of the particles, as in most molecular dynamics and Monte Carlo hard-particle packing algorithms<sup>15,21–25</sup>. It should be noted that for polyhedral particles, an algorithm that employs particle growth with an adaptive non-shrinking fundamental cell is computationally less efficient than the ASC scheme, which fixes the particle size while allowing the cell to shrink on average. Whereas a ‘growth’ algorithm requires manipulating the coordinates of the vertices of all of the particles, our ‘shrinkage’ method (in which the particle sizes are kept fixed) requires only the computation of the six strain components.

In the simulation, starting from an initial configuration of polyhedral particles, a trial configuration can be generated by moving (translating and rotating) a randomly chosen particle or by a random deformation and compression/expansion of the fundamental cell. If this causes interparticle overlaps, the trial configuration is rejected; otherwise, if the fundamental cell shrinks in size (which makes the density  $\phi$  higher), the trial configuration is accepted. On the other hand, if the cell expands in size, the trial configuration is accepted with a specified probability  $p_{\text{acc}}$ , which is made to decrease as  $\phi$  increases and approaches zero at the jamming limit<sup>27</sup> (that is, locally maximally dense packing) is reached. In particular, we find  $p_{\text{acc}}$  with an initial value  $p_{\text{acc}} \approx 0.35$  that decreases as a power law with an exponent equal to  $-1$ , works well for most systems that we studied. The ratio of the number of particle motions to the number of cell trial moves should be greater than unity (especially towards the end of the simulation), because compressing a dense packing could cause many overlaps between the particles. Depending on the initial configuration, the magnitudes of the particle motions and the strain components need to be chosen carefully to avoid the system getting stuck in some shallow local minimum.

A crucial aspect of any packing algorithm is the need to check for interparticle overlaps under attempted particle motions. Hard polyhedron particles, unlike spheres, ellipsoids and superballs, do not possess simple ‘overlapping’ functions. (The overlap function of a pair of strictly convex and smooth particles is a function of the positions, orientations and shapes of the two particles, whose value indicates whether the two particles overlap or not, or whether they are tangent to one another.) The separation axis theorem<sup>26</sup> enables us to check for interparticle overlaps for polyhedra up to the numerical precision of the machine. In particular, the theorem states that two convex polyhedra are separated in space if and only if there exists an axis, on which the projections of the vertices of the two polyhedra do not overlap. The separation axis is either perpendicular to one of the faces of the polyhedra or perpendicular to a pair of edges, one from each polyhedron. Thus, this reduces the number of axes that need to be checked from infinity to  $[E(E-1)/2 + 2F]$ , where  $E$  and  $F$  are the number of edges and number of faces of the polyhedra, respectively. A pre-check using the circumradius and inradius of the polyhedra dramatically speeds up the simulations, that is, two particles are guaranteed to overlap if the centroidal separation is smaller than twice the inradius and guaranteed not to overlap if the centroidal separation is larger than twice the circumradius. The circum-sphere is the smallest sphere containing the particle. The insphere is the largest sphere that can be inscribed in the particle.

The cell method and near-neighbour list<sup>24,25</sup> are also used to improve the efficiency of the simulation, but are appropriately modified to incorporate the adaptive fundamental cell.

## LETTERS

# Atlantic hurricanes and climate over the past 1,500 years

Michael E. Mann<sup>1</sup>, Jonathan D. Woodruff<sup>2</sup>, Jeffrey P. Donnelly<sup>3</sup> & Zhihua Zhang<sup>1</sup>

Atlantic tropical cyclone activity, as measured by annual storm counts, reached anomalous levels over the past decade<sup>1</sup>. The short nature of the historical record and potential issues with its reliability in earlier decades, however, has prompted an ongoing debate regarding the reality and significance of the recent rise<sup>2–5</sup>. Here we place recent activity in a longer-term context by comparing two independent estimates of tropical cyclone activity over the past 1,500 years. The first estimate is based on a composite of regional sedimentary evidence of landfalling hurricanes, while the second estimate uses a previously published statistical model of Atlantic tropical cyclone activity driven by proxy reconstructions of past climate changes. Both approaches yield consistent evidence of a peak in Atlantic tropical cyclone activity during medieval times (around AD 1000) followed by a subsequent lull in activity. The statistical model indicates that the medieval peak, which rivals or even exceeds (within uncertainties) recent levels of activity, results from the reinforcing effects of La-Niña-like climate conditions and relative tropical Atlantic warmth.

A number of past studies have attempted to place modern Atlantic tropical cyclone activity in a longer-term context using regional proxy evidence of past landfalling Atlantic hurricanes (tropical cyclones with maximum sustained surface winds exceeding 74 miles per hour)<sup>6–8</sup>. Some studies<sup>4</sup> have sought to infer past changes in activity from plausible local conditioning factors such as wind strength and sea surface temperature (SST), though the interpretations of these studies have been contested<sup>5</sup>. Qualitative comparisons between palaeo-hurricane reconstructions appear to show some temporal coherence<sup>8,9</sup>. However, no past studies have attempted to synthesize multiple records from distinct regions into a basin-integrated reconstruction of Atlantic hurricane activity. Moreover, no past studies have sought to quantitatively relate estimated variations in hurricane or tropical

cyclone activity to reconstructions of the key large-scale climate factors known to have a significant influence on modern Atlantic tropical cyclone activity. Here we produce an empirical record of past landfalling Atlantic hurricane activity by combining information from multiple sedimentary records of hurricane-induced overwash. Further, we compare these resulting estimates to independent statistical model predictions of past tropical cyclone activity driven by proxy-based large-scale climate reconstructions.

Sediment-based overwash reconstructions of hurricane landfall are limited in number, but span a wide geographic area across the North Atlantic basin affected by hurricanes. Our compilation includes (see Fig. 1) a site from the Caribbean (Vieques, Puerto Rico<sup>6,9,10</sup>), one from the US Gulf Coast<sup>7</sup>, one from the southeastern US coast<sup>11</sup>, three from the mid-Atlantic coast (one from New York<sup>8</sup> and two from New Jersey<sup>12,13</sup>) and two from southeastern New England (one from Rhode Island<sup>14</sup> and another from Massachusetts<sup>15</sup>), yielding five distinct regional series. We obtained a probabilistic estimate of past basin-wide landfalling hurricane activity using an appropriately weighted combination of the information from these five regional series, and incorporating radiocarbon age model uncertainties.

An independent estimate of past tropical cyclone activity was obtained using a statistical model for Atlantic tropical cyclone counts. This previously developed and validated<sup>3,16</sup> statistical model conditions annual Atlantic tropical cyclone counts on three key large-scale climate state variables tied to historical variations in Atlantic tropical cyclone counts: (1) the SST over the main development region (MDR) for tropical Atlantic tropical cyclones, which reflects the favourability of the local thermodynamic environment; (2) the El Niño/Southern Oscillation (ENSO), which influences the amount of (unfavourable) vertical wind shear; and (3) the North Atlantic Oscillation (NAO), which affects the tracking of storms,

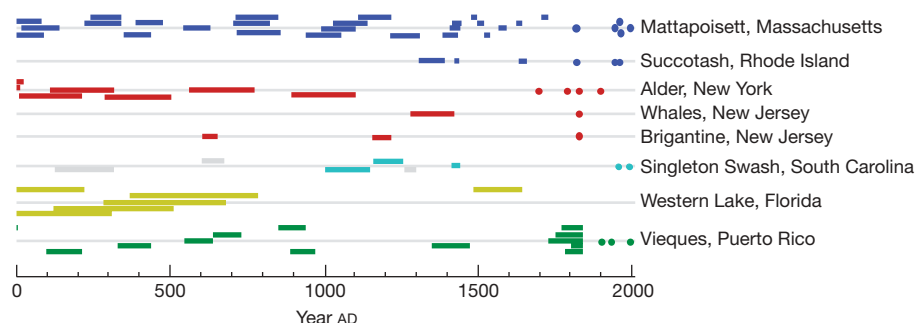


**Figure 1 | Overwash sediment records of landfalling hurricanes.** Event histories are shown for New England (blue), Mid-Atlantic (red), the southeastern US coast (turquoise; grey denotes oyster-bed events not used for reasons discussed by ref. 28 and in the Supplementary Information), the

Gulf Coast (yellow) and the Caribbean (green). The horizontal width of shaded rectangles indicates the  $\pm 1\sigma$  age model uncertainties. Circles indicate historical hurricane events.

<sup>1</sup>Department of Meteorology and Earth and Environmental Systems Institute, Pennsylvania State University, University Park, Pennsylvania 16802, USA. <sup>2</sup>Department of Geosciences, University of Massachusetts, Amherst, Massachusetts 01003, USA. <sup>3</sup>Department of Geology and Geophysics, Woods Hole Oceanographic Institution, Woods Hole, Massachusetts 02543, USA.

determining how favourable an environment they encounter. The statistical model was driven by proxy-based reconstructions<sup>17,18</sup> of these three state variables (Fig. 2), yielding a predicted history of Atlantic tropical cyclone counts for past centuries.

We compared the sediment-based record against the above statistical estimate of basin-wide tropical cyclone activity (Fig. 3), guided by a working assumption that an appropriately weighted composite of regional landfalling hurricane activity varies, at multidecadal and longer timescales, in rough proportion to basin-wide tropical cyclone activity. Although the validity of this assumption can (as discussed further below) be questioned, it is worth noting that the sediment-based record tracks the observed long-term changes in tropical cyclone count over the historical period remarkably well (inset, Fig. 3). On the basis of previously published results, the required storm strength required for overwash and deposition varies among sites<sup>19</sup>, although qualitatively similar results were obtained assuming uniform sensitivity (category 3 or greater storms) among sites (Supplementary Information). We down-weighted the Vieques data after AD 1700 to account for an estimated<sup>9,10</sup> artificial inflation of overwash deposit occurrences at the site due to increased sedimentation rates in recent centuries.

Our two entirely independent estimates of past tropical cyclone activity were found to be statistically consistent (that is, they overlap

within their estimated 95% confident intervals), with certain exceptions, which are discussed below. Jointly, the two independent records suggest periods of high activity (that is, comparable to current levels) during a medieval era of roughly AD 900–1100. Both estimates also suggest a general decrease in the level of activity after about AD 1200<sup>6,9</sup>.

Of particular interest is the medieval peak in activity, which matches or even exceeds current levels of activity within uncertainties for the statistical model. The peak arises in the statistical model from a combination of (see Fig. 2) La-Niña-like conditions during the medieval era which have been discussed elsewhere<sup>20–22</sup> and relatively warm SSTs in the tropical North Atlantic at that time<sup>23,24</sup>, with both of these factors having a substantial role in the statistical model predictions (Supplementary Information). In contrast, this interval is followed by a combination of relatively cold Atlantic SSTs and more El-Niño-like conditions in the tropical Pacific, leading to a relative lull in modelled tropical cyclone activity in subsequent centuries before the modern increase. This finding is in contrast to some other recent work<sup>4</sup>, because we do not find hurricane activity during the 1970s to be anomalously low in comparison with that over the past few centuries.

There are also some noteworthy discrepancies between the two independent estimates of past Atlantic tropical cyclone activity provided in this study. There is some independent historical

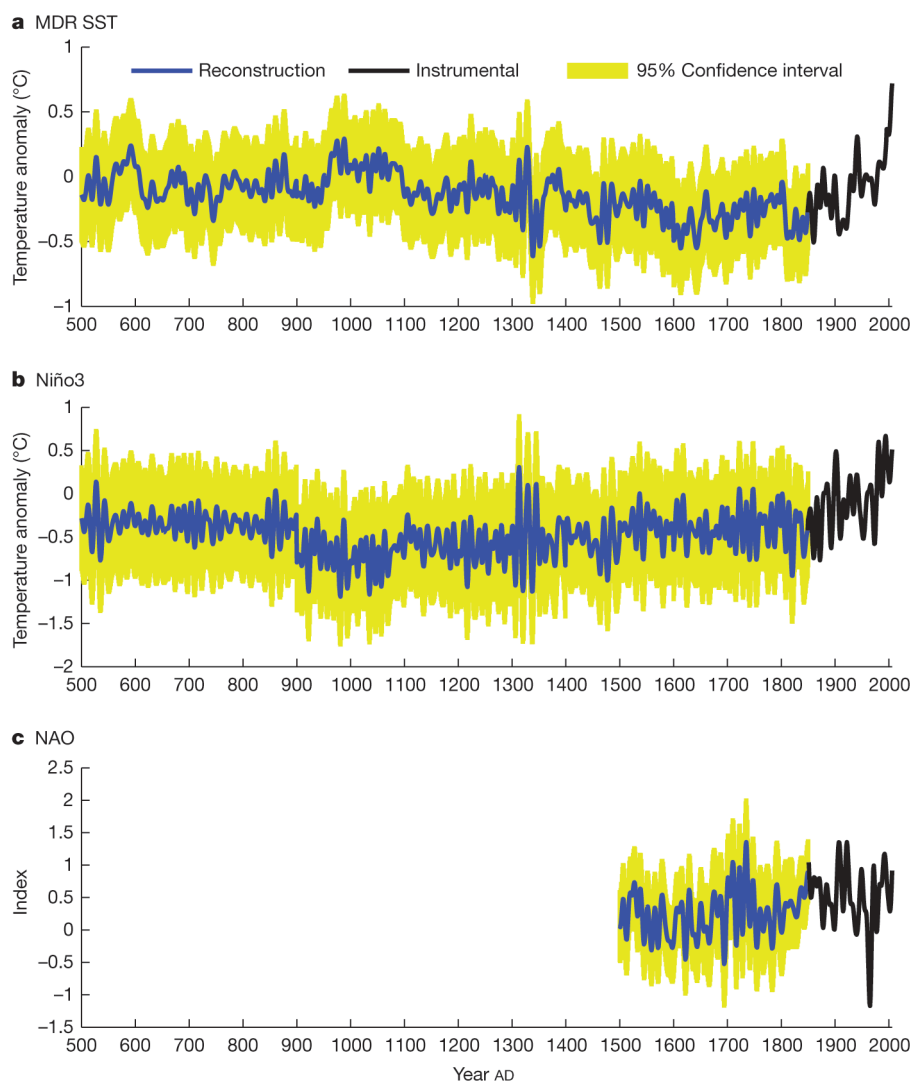


**Figure 2 | Proxy reconstructions used in statistical model estimates of Atlantic tropical cyclone counts.** **a**, The MDR SST<sup>17</sup>; **b**, the Niño3 SST<sup>17</sup>; and **c**, the boreal winter NAO<sup>18</sup>. Positive indices are associated with enhanced (a) and diminished (b, c) tropical cyclone activity, respectively<sup>16</sup>. The

corresponding instrumental series<sup>17,18</sup> are shown for comparison. All series are decadal smoothed<sup>30</sup>, and 95% uncertainty intervals are indicated by yellow shading.



documentary evidence for increased tropical cyclone activity in the Caribbean during the 1760s–1780s<sup>25</sup>, and a modest peak at this time is evident in the statistical model estimate. The sediment-based estimate, however, displays a peak that is later (early nineteenth century), and of considerably greater magnitude. The medieval peak in the sediment-based record falls slightly later than in the statistical model estimate, and is of greater duration. The peak in activity indicated by the sediment record in the mid-fifteenth century is not seen in the statistical model results.

There are a number of plausible explanations for the differences between the two records. Landfalling hurricanes do not vary in fixed proportion to the total number of storms generated on decadal time-scales<sup>1</sup>. A form of the well known ‘ergodic hypothesis’ holds that on increasingly longer averaging timescales (for example, the centennial timescale variations of interest in this study), variations in totals among the considerably sparser group of landfalling hurricanes will more closely mirror those in the larger group of basin-wide tropical cyclones. However, certain predictors, such as the NAO, influence not only the basin-wide activity but also the prevailing regions of landfall, and given an incomplete coastal observing network, a change in the latter could potentially masquerade as a change in the former. The sites used to produce a basin-wide sediment composite record may simply not be representative enough of the true, full basin-wide activity. This caveat applies in particular to the Caribbean, Gulf Coast and southeast US coast, because we are relying on just one record in each case to estimate past tropical

cyclone activity in these regions. A jackknife estimate of uncertainty based on the removal of any one of the five contributing regions (Fig. 3) nonetheless suggests that the main features of our basin-wide composite are reasonably robust (the individual jackknife surrogates are shown in Supplementary Information).

The sediment record could be contaminated by influences unrelated to hurricane strikes such as alterations to barrier morphology<sup>26,27</sup>. Also, potential biases in the proxy-based palaeoclimate reconstructions<sup>17,18</sup> used to drive the statistical model would of course lead to biases in the statistical model predictions themselves. Finally, there is the possibility that other potential tropical cyclone influences (for example, the West African monsoon<sup>6</sup>) not accounted for in the statistical model (that is, that are not correlated with the three predictors used), may have had a more important role in the past than is evident during the modern interval.

Such uncertainties and caveats notwithstanding, the striking consistency of certain key features such as the medieval peak in Atlantic tropical cyclone activity and subsequent lull using two entirely independent approaches to estimating past activity suggest that these features are real, and provides some degree of additional validation of our current understanding of the primary factors governing long-term changes in Atlantic tropical cyclone activity. Paths forward that may further improve our understanding include, among other things, development of a more extensive and diverse set of multi-proxy estimates of past landfalling hurricane activity, and improved reconstructions of the past histories of key large-scale

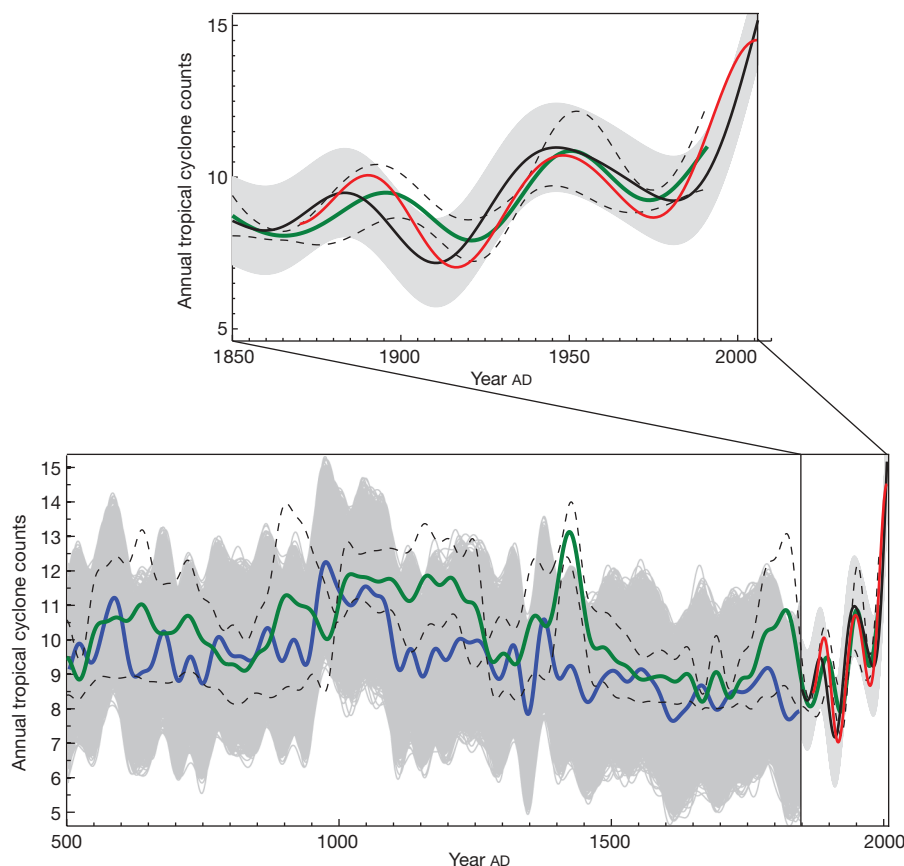


**Figure 3 | Long-term Atlantic tropical cyclone counts.** Modern Atlantic tropical cyclone counts (red) compared both with statistical model estimates of tropical cyclone activity based on modern instrumental (AD 1851–2006; black) and proxy-reconstructed (AD 500–1850; blue) climate indices and an estimate of basin-wide landfalling Atlantic hurricane activity (AD 500–1991) derived from regional composites of overwash sediments (green). All series were smoothed<sup>30</sup> at multidecadal (>40-year) timescales. The sediment composite record was standardized to have the same mean and multidecadal variance as the statistical model estimates. Uncertainties for the statistical

model estimates (grey shading, indicating 95% confidence intervals) take into account the uncertainty in the statistical model itself (grey shading), and—in the case of the proxy-reconstructed indices (grey shading), the additional uncertainty due to the uncertainties in the proxy-reconstructed climate indices. Uncertainties for the sediment composite record (thin dashed black curves indicating upper and lower limits of the 95% confidence interval) are derived from jackknifing of the full composite with respect to each of the five contributing regional estimates, as discussed in the text.

climate phenomena influencing Atlantic tropical cyclones such as ENSO.

## METHODS SUMMARY

**Sediment hurricane landfall records.** Regional sediment series were weighted with respect to inverse modern return periods for landfalling tropical cyclones<sup>19</sup> and summed to yield basin-wide composites of tropical cyclone activity. We used a Monte Carlo approach to generate an ensemble of such composites consistent with the event chronologies and age model uncertainties. A basin-wide landfalling hurricane activity series was defined by the maximum rate of activity for each year over this ensemble, that is, the maximum rate of activity for each year that is consistent with the event chronologies within uncertainties. We examined sensitivity both to the contributions of individual regions (issues of reliability have been raised with some events in the Gulf Coast<sup>27</sup> and southeastern US coast<sup>28</sup> records), and to the assumed threshold of the sites to overwhelm from varying strengths of hurricanes (Supplementary Information).

**Statistical model.** We used a statistical model of tropical cyclone counts as conditioned on<sup>3,16</sup>: the MDR SST, the ENSO (measured by the boreal winter Niño3 SST index), and the boreal winter NAO index. The tropical cyclone count series was first corrected for a modest estimated undercount<sup>3</sup> before the mid-twentieth-century undercount, although similar results were obtained (Supplementary Information) using the largest<sup>2,29</sup> published estimates of undercount bias. The statistical model, which is trained on the modern historical record, has been shown in independent statistical validation experiments<sup>3,16</sup> to resolve roughly 50% of the interannual and longer-term variations in Atlantic tropical cyclone counts. The model, in this study, was driven by decadal smoothed proxy reconstructions of the three required climate indices to yield predictions of tropical cyclone activity over past centuries. The MDR SST and Niño3 reconstructions were derived from proxy-based surface temperature patterns spanning the past 1,500 years<sup>17</sup>. Though an NAO reconstruction was available only for the past 500 years<sup>18</sup>, the NAO influence was found to be very minor (Supplementary Information).

**Full Methods** and any associated references are available in the online version of the paper at [www.nature.com/nature](http://www.nature.com/nature).

Received 6 March; accepted 14 June 2009.

- Holland, G. J. & Webster, P. J. Heightened tropical cyclone activity in the North Atlantic: natural variability or climate trend? *Phil. Trans. R. Soc. A*. doi:10.1098/rsta.2007.2083 (2007).
- Landsea, C. W. Counting Atlantic tropical cyclones back to 1900. *Eos* **88**, 197–208 (2007).
- Mann, M. E., Sabbatelli, T. A. & Neu, U. Evidence for a modest undercount bias in early historical Atlantic tropical cyclone counts. *Geophys. Res. Lett.* **34**, doi:10.1029/2007GL031781 (2007).
- Nyberg, J. *et al.* Low Atlantic hurricane activity in the 1970s and 1980s compared to the past 270 years. *Nature* **447**, 698–702 (2007).
- Neu, U. Is recent major hurricane activity normal? *Nature* **451**, E5 (2008).
- Donnelly, J. P. & Woodruff, J. D. Intense hurricane activity over the past 5,000 years controlled by El Niño and the West African monsoon. *Nature* **447**, 465–468 (2007).
- Liu, K. B. & Fearn, M. L. Reconstruction of prehistoric landfall frequencies of catastrophic hurricanes in northwestern Florida from lake sediment records. *Quat. Res.* **54**, 238–245 (2000).
- Scileppi, E. & Donnelly, J. P. Sedimentary evidence of hurricane strikes in western Long Island, New York. *Geochem. Geophys. Geosyst.* **8**, 1–25 (2007).
- Woodruff, J. D., Donnelly, J. P., Emanuel, K. A. & Lane, P. Assessing sedimentary records of paleohurricane activity using modeled hurricane climatology. *Geochem. Geophys. Geosyst.* **9**, doi:10.1029/2008GC002043 (2008).
- Woodruff, J. D. *et al.* Reconstructing relative flooding intensities responsible for hurricane induced deposits from Laguna Playa Grande, Vieques, Puerto Rico. *Geology* **36**, 391–394 (2008).
- Scott, D. B., Collins, E. S., Gayes, P. T. & Wright, E. Records of prehistoric hurricanes on the South Carolina coast based on micropaleontological and

sedimentological evidence, with comparison to other Atlantic Coast records. *GSA Bull.* **115**, 1027–1039 (2003).

- Donnelly, J. P. *et al.* Sedimentary evidence of intense hurricane strikes from New Jersey. *Geology* **29**, 615–618 (2001).
- Donnelly, J. P., Butler, J., Roll, S., Wengren, M. & Webb, T. A backbarrier overwash record of intense storms from Brigantine, New Jersey. *Mar. Geol.* **210**, 107–121 (2004).
- Donnelly, J. P. *et al.* 700 yr sedimentary record of intense hurricane landfalls in southern New England. *Geol. Soc. Am. Bull.* **113**, 714–727 (2001).
- Boldt, K., Lane, P., Woodruff, J. D. & Donnelly, J. P. Sediment evidence of hurricane-induced coastal flooding in southeastern New England over the last two millennia. *Mar. Geol.* (submitted).
- Sabbatelli, T. A. & Mann, M. E. The influence of climate state variables on Atlantic Tropical Cyclone Occurrence Rates. *J. Geophys. Res.* **112**, doi:10.1029/2007JD008385 (2007).
- Mann, M. E. *et al.* Global signatures of the Little Ice Age and the medieval climate anomaly and plausible dynamical origins. *Science* (submitted).
- Luterbacher, J. *et al.* Extending North Atlantic Oscillation reconstructions back to 1500. *Atmos. Sci. Lett.* **2**, 114–124 (2002).
- Elsner, J. B., Jagger, T. H. & Liu, K. B. Comparison of hurricane return levels using historical and geological records. *J. Appl. Met. Climatol.* **47**, 368–374 (2008).
- Cobb, K. M. *et al.* El Niño–Southern Oscillation and tropical Pacific climate during the last millennium. *Nature* **424**, 271–276 (2003).
- Mann, M. E., Cane, M. A., Zebiak, S. E. & Clement, A. Volcanic and solar forcing of the tropical Pacific over the past 1000 years. *J. Clim.* **18**, 447–456 (2005).
- Graham, N. E. *et al.* Tropical Pacific–mid-latitude teleconnections in medieval times. *Clim. Change* **83**, 241–285 (2007).
- Keigwin, L. D. The Little Ice Age and Medieval Warm Period in the Sargasso Sea. *Science* **274**, 1504–1508 (1996).
- Richey, J. N. *et al.* 1400 yr multiproxy record of climate variability from the northern Gulf of Mexico. *Geology* **35**, 423–426 (2007).
- García-Herrera, R., Gimeno, J., Ribera, P. & Hernández, E. New records of Atlantic hurricanes from Spanish documentary sources. *J. Geophys. Res.* **110**, D03109, doi:10.1029/2004JD005272 (2005).
- Lambert, W. J., Aharon, P. & Rodríguez, A. B. An assessment of the Late Holocene record of severe storm impacts from Lake Shelby, Alabama. *Trans. Gulf Coast Assoc. Geol. Soc.* **53**, 443–452 (2003).
- Otvos, E. G. Discussion of “Prehistoric landfall frequencies of catastrophic hurricanes.” (Liu and Fearn, 2000). *Quat. Res.* **57**, 425–428 (2002).
- Hippensteel, S. P., Martin, R. E. & Harris, M. S. Records of prehistoric hurricanes on the South Carolina coast based on micropaleontological and sedimentological evidence, with comparison to other Atlantic Coast records. *Geol. Soc. Am. Bull.* **117**, 250–256 (2005).
- Mann, M. E., Emanuel, K. A., Holland, G. J. & Webster, P. J. Atlantic tropical cyclones revisited. *Eos* **88**, 349–350 (2007).
- Mann, M. E. Smoothing of climate time series revisited. *Geophys. Res. Lett.* **35**, doi:10.1029/2008GL034716 (2008).

**Supplementary Information** is linked to the online version of the paper at [www.nature.com/nature](http://www.nature.com/nature).

**Acknowledgments** We thank C. Landsea for comments on the manuscript. M.E.M. and Z.Z. acknowledge support from the ATM programme of the National Science Foundation (grant ATM-0542356). J.P.D. acknowledges support from the EAR and OCE programmes of the National Science Foundation (grants EAR-0519118 and OCE-0402746), the Risk Prediction Initiative at the Bermuda Institute for Ocean Sciences, and the Inter-American Institute for Global Change Research. This is a contribution of IGCP 495—‘Holocene land–ocean interactions: driving mechanisms and coastal responses’.

**Author Contributions** M.E.M. performed the statistical reconstructions of tropical cyclone and hurricane activity. J.D.W. and J.P.D. provided the sediment overwash records of hurricane landfall and their uncertainties. J.D.W. provided the landfall return period estimates. Z.Z. provided the climate reconstructions used and their uncertainties. M.E.M. primarily wrote the paper. All authors discussed the results and provided input on the manuscript.

**Author Information** Reprints and permissions information is available at [www.nature.com/reprints](http://www.nature.com/reprints). Correspondence and requests for materials should be addressed to M.E.M. (mann@psu.edu).

## METHODS

**Formation of regional sediment series and composites.** Regional landfalling hurricane chronologies were formed by combining sediment overwash records that fall within the same distinct five regions back to AD 500. The regions and associated records are:

- (1) New England (two records): Mattapoisett Marsh, Massachusetts, 250 BC to present, latitude 41° 39' 8" N, longitude 70° 47' 13" W (ref. 15); and Succotash Marsh, Rhode Island, AD 1300 to present, 41° 22' 45" N, 71° 31' 17" W (ref. 14)
- (2) the Mid-Atlantic (three records): Alder Island, New York, 238 BC to present, 40° 35' 54" N, 73° 34' 45" W (ref. 8); Brigantine, New Jersey, AD 600 to present, 39° 25' 14" N, 74° 21' 11" W (ref. 13); and Whale Beach, New Jersey, AD 1300 to present, 39° 11' N, 74° 40' 17" W (ref. 12)
- (3) the southeast US Atlantic Coast: Singleton Swash, South Carolina, AD 223 to present, 33° 46' N; 78° 47' W (ref. 11)
- (4) the Gulf Coast: Western Lake, Florida, 1726 BC to present, 30° 19' 38" N; 86° 08' 55" W (ref. 11)
- (5) the Caribbean: Laguna Playa Grande Lake, Vieques, Puerto Rico, 3461 BC to present, 18° 5' 31" N; 65° 31' 3" W (refs 6, 9 and 10)

As discussed in the main article, potential biases have been noted for some of the records used, including the Western Lake record<sup>27</sup> and the Singleton Swash record<sup>28</sup>. For the Singleton Swash record, we made an explicit attempt to deal with certain known problems as discussed in the 'Processing of individual sediment records' section below.

**Processing of individual sediment records.** The three oyster-bed termination events (AD 223, AD 652, and AD 1283) from the Singleton Swash, South Carolina, record were not included in our analysis because of the uncertainty regarding the attribution for oyster reef terminations to hurricanes<sup>11,28</sup>, as well as potentially significant and undefined age uncertainties related to reservoir effects for the dated oyster shell material. In the absence of such a correction, the chronologies of these events do not meet the age control required for our analyses.

We adjusted the Vieques, Puerto Rico, record, on the basis of the likelihood of an artificial trend in sensitivity of hurricane landfall at the site owing to a substantial increase in sedimentation rates since AD 1700 (refs 9, 10). Following ref. 9, we assumed that changes in sedimentation rates result in an undercounting of approximately 11% after 1700 AD compared to 32% before AD 1700, and so we down-weighted the post-AD 1700 Vieques record by a factor of 11%/32% (that is, approximately one-third). Alternatively, we performed an analysis in which the Vieques record was not used subsequent to AD 1700 (see Supplementary Information).

**Formation of regional sediment composite series.** In the process of forming regional composites, we attempted to eliminate redundant representation of unique events among multiple contributing records. Multiple events among contributing sites within a region that fell within the 1 $\sigma$  age model uncertainties of each other were consolidated to represent a single assumed landfall event. This decision was motivated by the fact that known landfall events falling within the modern historical observational period are often recorded at more than one site within an identified region. The date and 1 $\sigma$  ranges for the consolidated events were defined as the average of the dates and ranges of the contributing events. When multiple events from one site fell within the age model uncertainties of an event from another site, the consolidation was done for the event for the first site that was closest in nominal age to that of the second site.

**Formation of a basin-wide sediment composite series.** To estimate basin-wide hurricane activity from the available regional composites, we normalized each regional event composite by the number of events in that composite, and then weighted the normalized sequence of events by the estimated modern return period for that region (see 'Estimation of return periods' section below). This process ensures that each site contributes to the estimated basin average in proportion to the modern frequency of landfalling hurricanes for that region, simulating the process by which any underlying basin-wide activity is expressed in terms of regional landfall activity. The results of the analysis were not especially sensitive, however, to whether or not the data were normalized, as shown in Supplementary Fig. 1. The basin-wide composite was considered as terminating in the year of the last recorded event. The latest such year in any of the chronologies was 1991.

**Monte Carlo ensembles.** A nominal chronology of basin-wide landfalling hurricane occurrences is defined by the weighted composite as described in the 'Formation of a basin-wide sediment composite series' section above. However, this nominal chronology does not take into account age model uncertainties in the chronologies. To take into account the impact of age model uncertainties, we performed Monte Carlo experiments using ensembles of 2000 realizations in which the individual events in the regional chronologies were randomly perturbed within their estimated  $\pm 1\sigma$  radiocarbon age model uncertainties. We then defined a probabilistic time series of basin-wide landfalling

hurricane rates as the maximum values over this ensemble, that is, the time sequence of the maximum occurrence rates for each year that are consistent with the event chronologies and their uncertainties.

**Estimation of return periods.** We estimated landfall return periods for weighting our sites on the basis of estimated return frequencies for storms striking within a 270-km radius of the site, obtained by the HURISK statistical modelling described in ref. 19. The radius of 270 km was chosen in order to have a large enough area for obtaining appropriate statistics using the HURISK model, yet small enough that the return periods reflect the relative activity at a site compared to the others within the composite. The radius of hurricane impact for each site is probably less than 270 km, and therefore the return periods for overwash at each site would probably be longer than those predicted using this radius. However, these derived return periods are used only to obtain relative weights when assimilating the different records, with actual return frequencies determined by the reconstructions themselves.

It is likely that the various sites differ in the category of storm they are sensitive to. For example, the Alder Island and Mattapoisett sites are probably recording storms of category 2 or greater<sup>8,15</sup>. Although there are no modern deposits at Western Lake, Florida, making it difficult to assess the exact sensitivity of the site, ref. 7 estimates a likely sensitivity to a storm of category 4 or greater. The remaining sites are probably sensitive to storms of category 3 or greater.

The return periods for storms at each respective site based on the HURISK model given the above-assumed sensitivities are as follows (parentheses indicate the 5% and 95% uncertainties in years). (1) Mattapoisett, Massachusetts ( $\geq$ category 2): 8.52 years (6.31, 13.09); (2) Alder Island, New York ( $\geq$ category 2): 10.15 years (7.35, 16.43); (3) Singleton Swash, South Carolina ( $\geq$ category 3): 7.84 years (5.90, 11.69); (4) Western Lake, Florida ( $\geq$ category 4): 45.66 years (27.69, 129.98); (5) Vieques, Puerto Rico ( $\geq$ category 3): 5.37 years (4.22, 7.39).

All distinct events were included in regional composites, so the chronologies of the regional composites are dominated by the individual sites with the largest number of contributing events and shortest return periods. Return periods for the regional composites were therefore defined by the most active site contributing to the composite. The mid-Atlantic composite was accordingly assigned the Alder Island return period, while the New England composite was assigned the Mattapoisett return period.

For comparison, we also examined the case where the HURISK return periods used for weighting were instead assigned based on an assumption of uniform sensitivity to a major hurricane (that is, a storm of category 3 or greater) passing within 270 km of each site. (1) Mattapoisett, Massachusetts: 23.81 years (15.5, 51.3); (2) Alder Island, New York: 25.71 years (16.25, 61.45); (3) Singleton Swash, South Carolina: 7.84 years (5.90, 11.69); (4) Western Lake, Florida: 8.78 years (6.58, 13.16); (5) Vieques, Puerto Rico: 5.37 years (4.22, 7.39).

Alternative results from those shown in the main article based on using these latter landfall return period estimates are provided in Supplementary Information. For completeness, we also considered the extreme (and rather implausible) case where all sites are assumed to have equal return periods (Supplementary Information). In all cases, the basic features of the basin-averaged record are preserved (for example, the elevated activity during the interval AD 900–1100), but the detailed evolution differs.

Finally, an assessment was made of the robustness of the basin-wide composite with respect to the contributions of each of the five distinct regions using a traditional jackknife analysis wherein each of the five regions were eliminated one-by-one, and composites were performed using only the four remaining regions. The resulting five jackknife surrogates are shown in the Supplementary Information. The spread among the five jackknife surrogates defines the standard errors shown in Fig. 3 for the sediment composite record.

**Modern calibration and validation of statistical model.** The statistical model was trained over the full (1870–2006) 137-year interval of overlap between the available instrumental climate state variables and historical tropical cyclone count record as in ref. 3, and the same split calibration/validation procedure, wherein the model was alternatively calibrated and validated over the half-intervals 1870–1938 and 1939–2006, was used. The same instrumental data products were used as in ref. 3, including blended HadCRU/ERSST/Kaplan<sup>31–33</sup> instrumental SST products for the Aug–Oct MDR SST and Dec–Feb Niño indices, and the CRU (ref. 34) Dec–Mar NAO series. We note that the Niño3 index of ENSO (rather than the Niño3.4 index favoured in ref. 3) was used, because a palaeoclimate reconstruction is available only for the Niño3 index and not for the Niño3.4 index. As noted in ref. 3, however, which Niño index is used has very little influence on the resulting statistical model (statistical model resolved variance is 45%/41% for full calibration/validation, as compared with 50%/43% in ref. 3). For sake of comparison, the instrument record-based statistical model was extended back in time from 1870 to AD 1851 using the longer-term instrumental data provided by refs 17 and 18, as shown in Fig. 2.



As discussed in the main text, the historical tropical cyclone record was corrected for an estimated average undercount of 1.2 storms before aircraft reconnaissance began (pre-1944) as in ref. 3, but the conclusions of our study are insensitive to whether this estimate, or the more sizeable undercount bias argued by Landsea *et al.* (see refs 2, 29) is used (Supplementary Information). Additional tests performed elsewhere<sup>35</sup> have used an alternative series we term the 'MDR residual' (MDR SST minus the global tropical mean SST during Aug–Oct), which has been argued in certain studies<sup>36,37</sup> to be a better predictor of tropical Atlantic tropical cyclone counts than the MDR SST itself. These tests reveal the MDR residual to be an inferior predictor to MDR SST across all reconstruction skill metrics; in particular, the statistical model cannot reproduce the positive trend of the past two decades when the MDR residual is used as a predictor instead of MDR SST.

The statistical model was examined for adequacy with respect to regression assumptions (that is, that the assumption of Poisson-distributed regression residuals is met), based on  $\chi^2$  and likelihood-ratio tests. The statistical model trained over the full 137-year period has a residual deviance of  $D = 107.98$  with  $N = 133$  degrees of freedom. A  $\chi^2$  test indicates  $\alpha = 0.945$  (that is, a 95% chance that we would be incorrect in rejecting the null hypothesis of Poisson-distributed residuals). The null deviance (that is, the residual deviance for an assumed fixed-rate Poisson process) is  $D = 196.91$  with  $N = 136$  degrees of freedom. A likelihood test based on the difference  $\Delta D = 88.93$  with  $N = 3$  degrees of freedom indicates a statistical significance of  $P = 0.0$  for the statistical model itself (that is, a 0% chance that we would be incorrect in rejecting the hypothesis that the model coefficients for the three predictors are all zero).

**Statistical prediction of tropical cyclone counts using proxy reconstructions.** Here the model was applied to decadal resolved reconstructions of MDR SST and Niño3 described by ref. 17 and the decadal smoothed winter NAO index of ref. 18. For the instrumental interval (1851 to present), standard errors due to uncertainties in the model coefficients were calculated from the residual decadal

variance diagnosed from the validation residuals (standard errors were averaged for the early and late intervals of the split calibration/validation procedure). For the pre-1851 statistical model estimates, which are driven by reconstructed climate indices, there is an additional component of uncertainty due to the uncertainties in the climate indices themselves. This contribution was estimated by Monte Carlo simulations in which the statistical model was driven with an ensemble of 2000 randomly perturbed versions of the statistical predictors consistent with their estimated uncertainties<sup>17</sup>, and an additional random term due to the uncertainties in the model coefficients.

Finally, to determine the separate roles of the individual predictors, we performed statistical model runs in which each of the predictors (NAO, MDR SST and Niño3) was kept constant at its modern climatological mean value, while the other two predictors were allowed to vary (Supplementary Information).

31. Rayner, N. A. *et al.* Global analyses of sea surface temperature, sea ice, and night marine air temperature since the late nineteenth century. *J. Geophys. Res.* **108**, doi:10.1029/2002JD002670 (2003).
32. Smith, T. M. & Reynolds, R. W. Extended reconstruction of global sea surface temperatures based on COADS data (1854–1997). *J. Clim.* **16**, 1495–1510 (2003).
33. Kaplan, A. *et al.* Analyses of global sea surface temperatures 1856–1991. *J. Geophys. Res.* **103**, 18567–18589 (1998).
34. Jones, P. D., Jónsson, T. & Wheeler, D. Extension to the North Atlantic Oscillation using early instrumental pressure observations from Gibraltar and South-West Iceland. *Int. J. Climatol.* **17**, 1433–1450 (1997).
35. Sabbatelli, T. A., Mann, M. E. & Miller, S. K. Semi-empirical projections of future Atlantic tropical cyclone activity. *J. Geophys. Res.* (submitted).
36. Knutson, T. R., Sirutis, J. J., Garner, S. T., Vecchi, G. A. & Held, I. M. Simulated reduction in Atlantic hurricane frequency under twenty-first-century warming conditions. *Nature Geosci.* **1**, 359–364 (2008).
37. Vecchi, G. A. & Soden, B. J. Increased tropical Atlantic wind shear in model projections of global warming. *Geophys. Res. Lett.* **34**, doi:10.1029/2006GL028905 (2007).

## LETTERS

# Glacial effects limiting mountain height

D. L. Egholm<sup>1</sup>, S. B. Nielsen<sup>1</sup>, V. K. Pedersen<sup>1</sup> & J.-E. Lesemann<sup>1</sup>

The height of mountain ranges reflects the balance between tectonic rock uplift, crustal strength and surface denudation. Tectonic deformation and surface denudation are interdependent, however, and feedback mechanisms—in particular, the potential link to climate—are subjects of intense debate<sup>1,2</sup>. Spatial variations in fluvial denudation rate caused by precipitation gradients are known to provide first-order controls on mountain range width, crustal deformation rates and rock uplift<sup>3,4</sup>. Moreover, limits to crustal strength<sup>5</sup> are thought to constrain the maximum elevation of large continental plateaus, such as those in Tibet and the central Andes. There are indications that the general height of mountain ranges is also directly influenced by the extent of glaciation through an efficient denudation mechanism known as the glacial buzzsaw<sup>6–9</sup>. Here we use a global analysis of topography and show that variations in maximum mountain height correlate closely with climate-controlled gradients in snowline altitude for many high mountain ranges across orogenic ages and tectonic styles. With the aid of a numerical model, we further demonstrate how a combination of erosional destruction of topography above the snowline by glacier-sliding and commensurate isostatic landscape uplift caused by erosional unloading can explain observations of maximum mountain height by driving elevations towards an altitude window just below the snowline. The model thereby self-consistently produces the hypsometric signature of the glacial buzzsaw, and suggests that differences in the height of mountain ranges mainly reflect variations in local climate rather than tectonic forces.

Distinctive alpine landforms, such as broad ‘U’-shaped, flat-floored valleys, hanging valleys, cirques, horns and knife-edged ridges (arêtes), are considered the fingerprints of glacial erosion. These glacial landforms exist in most of Earth’s mountain chains, produced by present and past glaciers. A majority of these landforms are associated with pronounced topographic relief consisting of over-steepened valley sides, headwalls and near-orthogonal tributary junctions often occupied by spectacular waterfalls. Perhaps not surprisingly, glaciations have accordingly been assumed to increase average relief mainly by incising valley systems, leaving high elevation peaks and hillslopes almost unaffected, and producing significant isostatically driven peak uplift<sup>10</sup>.

However, it has recently been discovered that glaciated orogens in the Himalayas<sup>6</sup>, the Andes<sup>7</sup>, the Sierra Nevada (USA)<sup>11</sup> and the Cascade Range<sup>8</sup> hold a striking coincidence of snowline altitudes, glacier equilibrium line altitudes (ELA) and elevations with a high proportion of surface area, suggesting that operation of a glacial buzzsaw denudation mechanism may be effective in reducing surface topography above the snowline and concentrating it at the snowline.

Apatite <sup>4</sup>He/<sup>3</sup>He ratio and (U–Th)/He thermochronometry studies from British Columbia<sup>12</sup> and the St Elias orogen in Alaska<sup>13</sup> support the notion of rapid glacial erosion at altitudes near and above the snowline, and indicate that climatically controlled snowline lowering dramatically increased average erosion rates during the late Cenozoic.

The geomorphic signature of the glacial buzzsaw is a concentration of surface area at elevations corresponding to the glacial ELA or the snowline<sup>6–9,11</sup>, which roughly coincide for temperate glaciers<sup>14</sup>. In hypsometric distributions (Fig. 1a), this reveals itself as a local maximum (representing a high proportion of surface area) at an altitude corresponding to the snowline<sup>6,15</sup>. To explore the prevalence of the glacial buzzsaw, we thus analysed the global distribution of hypsometric maxima (Fig. 1b) and surface area (Fig. 1c) using the Shuttle Radar Topography Mission<sup>16</sup> (SRTM) digital elevation models (DEMs) and compared this with observations of modern and Last Glacial Maximum (LGM) snowline altitudes<sup>17,18</sup>. We focus on the latitude dependence because the variation in snowline altitude is larger with latitude than with longitude (or with time); see Supplementary Figs 1–4 for more details of the analysis.

The analysis first reveals how only little surface area and practically no hypsometric maxima occur at elevations above the local modern snowline altitude (Fig. 1b and c). Second, below the snowline, surface area is concentrated in readily recognizable tectonically uplifted plateaus and near sea level, where alluvial plains increasingly dominate as they grade to sea level (Fig. 1c). The modern snowline seems to closely follow the 10<sup>–6</sup> contour of normalized surface area (the blue end of the colour scale in Fig. 1c), emphasizing its influence on high-altitude hypsometry.

When a DEM tile has topography above the snowline, its highest hypsometric maximum generally exists between the modern and LGM snowlines (Fig. 2). This pattern is recognized globally in every mountain range with sufficient height to intersect the LGM snowline (Supplementary Fig. 4). Hence, the abundance of hypsometric maxima just below the modern snowline and the absence of hypsometric maxima above the snowline are largely independent of tectonic uplift rate, lithology and general tectonic setting. For example, the Himalayas are in an intra-continental setting caused by continent–continent collision between India and Asia, whereas the high topography in western North and South America and in New Zealand is adjacent to oceans and caused by subduction and related volcanism. Yet, all show similar correlation between the distribution of hypsometric maxima and the local snowline altitude.

It further appears that glacial erosion controls the maximum height of mountains, as most summit elevations are confined to altitudes <1,500 m above the local snowline (Fig. 2). Although some of the highest peaks are evidently not included in the analysis owing to data gaps, this general trend suggests that glacial erosion restricts the height of mountains by limiting the relief that can be maintained between mountain peaks and the snowline<sup>1</sup>. The recorded outliers (Fig. 2) represent solitary peaks of primarily volcanic origin and most exist in the Andes, implying that formation and ongoing build-up of high volcanoes can outpace glacial buzzsaw denudation. Notable exceptions to the trend also exist in the Transantarctic Mountains outside the data set where a reduction or even non-existence of the glacial buzzsaw mechanism is likely, as non-eroding polar glaciers (frozen at the bed) dominate where the ice cover is relatively thin<sup>19</sup>.

<sup>1</sup>Department of Earth Sciences, Aarhus University, DK-8000 Aarhus, Denmark.

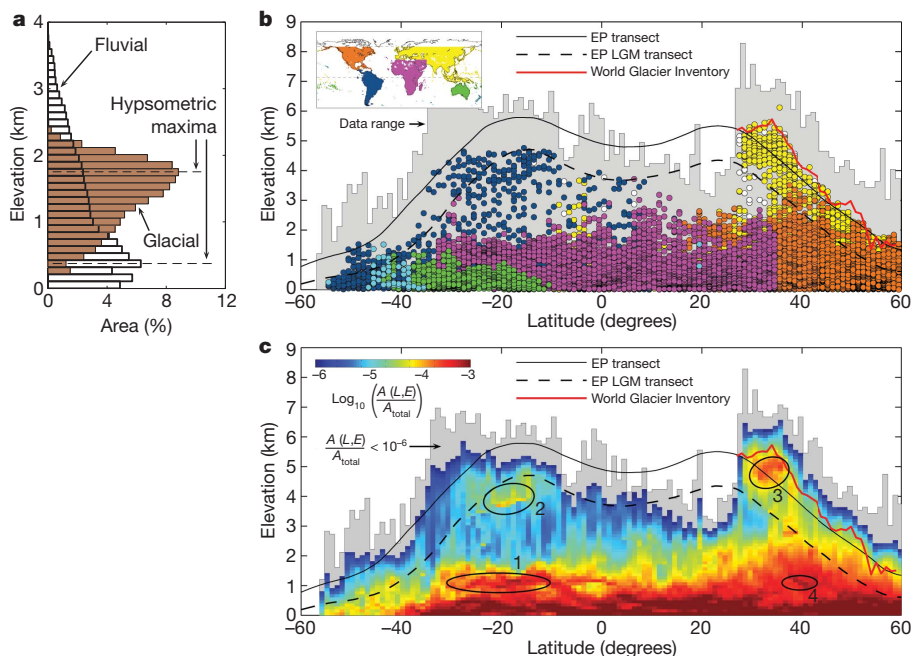


**Figure 1 | Global prevalence of the glacial buzzsaw.** **a**, Hypsometric distributions from a fluvial (northern Andes) and a glacial (Cascade Range, USA) landscape. Both hypsometries contain local maxima, but at different elevations. The hypsometric distributions each represent a  $1^\circ \times 1^\circ$  DEM with coordinates (lower left corner) ( $09^\circ$  N,  $71^\circ$  W) for the fluvial landscape and ( $48^\circ$  N,  $121^\circ$  W) for the glacial. **b**, Global distribution of hypsometric maxima as function of latitude and elevation. Each hypsometric maximum found in the data set is represented by a circle coloured by its DEM database entry (upper left inset). Hypsometric maxima derived from DEMs with more than 5% data gaps are white. The grey shaded area represents the total data coverage set by the maximum elevation at each latitude. Also shown are the

modern (black line) and LGM (dashed line) snowline transects along the east Pacific (EP) coasts of North and South America<sup>17</sup> and more than 13,000 modern snowline observations from the World Glacier Inventory<sup>18</sup> averaged in bins of  $1^\circ$  latitude where available (red line). **c**, Distribution of surface area (A) based on latitude (L) and elevation (E) within the data set. Colours show area at a given latitude and elevation normalized by the total area ( $A_{total}$ ) of the data set. Note the logarithmic colour scale. The grey zone has very little area and falls outside the colour scale, but serves to outline the total data range. Ellipses mark tectonically uplifted plateaus: 1, South Africa; 2, the Altiplano (Andes), 3, the Tibetan plateau; and 4, the Tarim basin. (See also Supplementary Figs 1–4.)

Generally, the presence of a hypsometric maximum indicates that dynamic processes (tectonic, erosional or depositional) concentrate surface elevation within a narrow altitude interval. Thus, the high

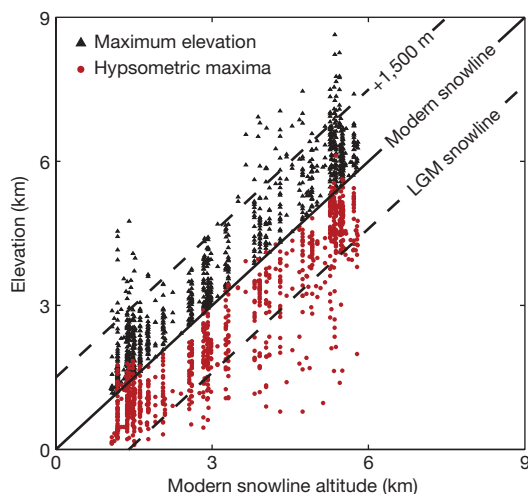


**Figure 2 | Maximum elevations and hypsometric maxima elevations correlate with local snowline altitudes.** Shown are all maximum DEM elevations (peaks) above the modern snowline and their associated highest hypsometric maxima. Most peaks are less than 1,500 m above the snowline, and apart from few exceptions all hypsometric maxima are found below the modern snowline and less consistently above the LGM snowline (the two snowlines largely demarcate the amplitude of the late Cenozoic climate variations). At latitudes  $>27^\circ$  N, local snowline observations<sup>18</sup> (latitude- and longitude-dependent) are used, whereas the east Pacific snowline transects<sup>17</sup> are used independent of longitude for DEMs with latitude  $<27^\circ$  N.

density of hypsometric maxima at low elevation (Fig. 1b and Supplementary Fig. 2) reflects, among other processes, fluvial erosion and deposition controlled by a base level ultimately set by the sea. Following this reasoning, and the findings of others<sup>6–9,11,15</sup>, the abundance of hypsometric maxima associated with snowline altitudes and the general absence of hypsometric maxima above the snowline (Fig. 1) likewise suggest that glaciers concentrate surface area just below the snowline, which thereby acts like a local base level for glacial erosion, leaving only a limited amount of topography (horns and arêtes) rising above this level<sup>6</sup> (Fig. 1c). In large trunk valleys and fjords, glacial erosion is, however, known to reach far below the snowline<sup>20</sup>.

This erosional pattern is confirmed by computational model experiments coupling the flow equations of ice with glacial erosion driven by sliding of warm-based glaciers. As an example illustrating the imprint of glacial erosion, we simulate the evolution of an initially fluvial landscape during a dramatic lowering of the snowline altitude. The Sierra Nevada mountain range in southern Spain ( $37^\circ$  N,  $3^\circ$  W) is used as the initial landscape as it was little affected by Quaternary glaciations, and only few cirque valleys near the highest summit areas above 2,500 m bear testimony to the past appearance of alpine glaciers. The landscape is thus largely fluvial (Fig. 3a), with relatively narrow river valleys emanating from the 60-km-long central ridge running broadly east–west. Accordingly, the hypsometric distribution derived from SRTM data<sup>16</sup> shows gradual decrease of surface area with increasing height above the 1,300 m contour line and with no indication of a local maximum (Fig. 3b).

To fully isolate the effects of glacial erosion and isostasy, the model does not include tectonic uplift, fluvial erosion or periglacial processes. In order to prevent slopes from steepening unrealistically, the model does, however, include nonlinear hillslope diffusion simulating mass wasting on the steepest slopes<sup>21</sup>. In the model, the snowline



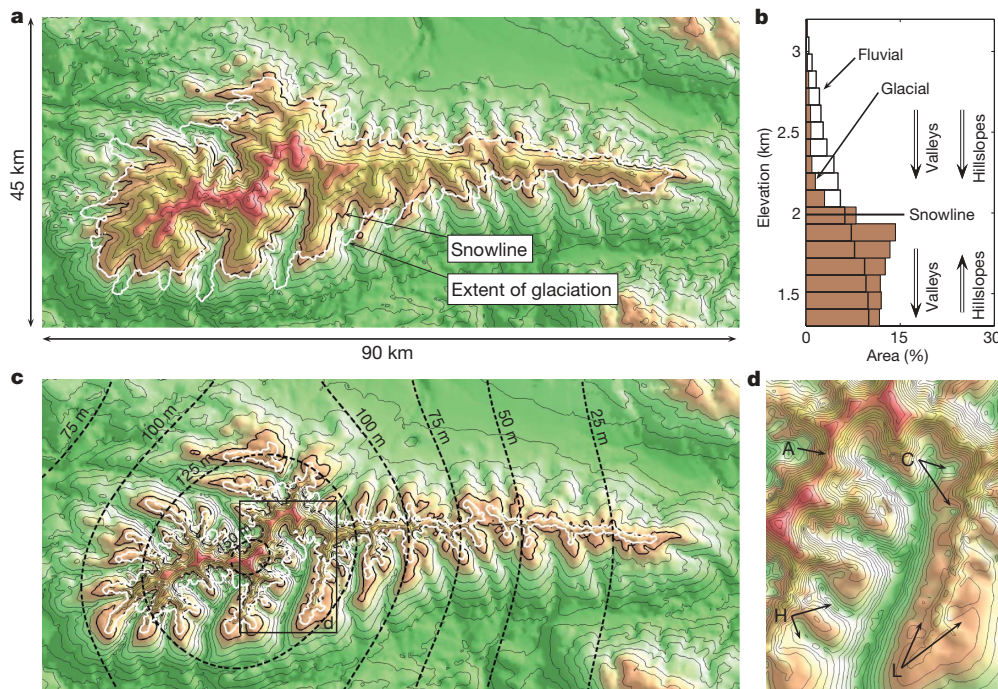


**Figure 3 | Numerical model of glacial erosion in the Sierra Nevada (Spain).** **a**, Initial fluvial topography derived from 90 m SRTM data<sup>16</sup>. The thick black contour line represents the model snowline altitude after 100 kyr, while the white contour line shows the extent of glaciers at time 100 kyr. **b**, Hypsometry before and after glacial erosion. A hypsometric maximum develops owing to denudation of hillslopes and small valleys above the snowline combined with isostatic uplift of unglaciated surfaces below the snowline. To some degree, the deep erosion of trunk valleys opposes the development of a hypsometric maximum by lowering their surface area to

elevations far below the snowline. **c**, Model topography after glacial erosion to a stage where only narrow and steep ridges (arêtes) remain above the snowline. Valleys are widened and deepened below the snowline. The amplitudes of isostatic rock uplift are shown by dashed contour lines. **d**, Enlarged view of a catchment exhibiting classical glacial erosion features including arêtes (A), cirques (C), hanging valleys (H), and low-relief areas (L) produced by the glacial buzzsaw. For more information on model results, see Supplementary Figs 5–10.

altitude is reduced from 3,000 m to 2,000 m (comparable to a 20° northward shift and conditions as found at present in, for example, British Columbia, Canada) over a period of 100 kyr, and in this stage the total ice volume grows until a quasi-steady state balance between total glacier accumulation and ablation is established. This leads into a longer phase (400 kyr) of glacial erosion and isostatic compensation. Although isostasy causes peak uplift<sup>22</sup>, the ice volume decreases owing to overall erosional destruction of catchment area above the snowline. Hence, after 500 kyr the total ice volume is reduced to 20% of its maximum value (Supplementary Fig. 5).

In agreement with the glacial buzzsaw hypothesis, this model experiment reveals (Fig. 3b) how snowline lowering self-consistently leads to emergence of a hypsometric maximum just below the snowline owing to erosion of surface topography at, and above, the snowline and compensatory isostatic uplift affecting the entire landscape, including unglaciated hillslopes at lower altitudes.

The model results also highlight the variable influence of topography on ice flow. Trunk valley glaciers initially reach far below the snowline and cause deep valley incision. Their large catchments allow for sufficient ice flux below the snowline and erosion along most portions of the glacier in this region. The largest tributary catchments undergo more limited erosion than trunk valleys and develop hanging valleys, which often exhibit cirques near their headwalls (Fig. 3c and d). In smaller tributaries and on hillslopes, the key control on erosion appears to be the limited catchment area, which does not allow for ice influx to exceed ablation below the snowline and, in effect, the snowline acts like a climatic base level limiting the down-valley extent of glacial erosion. Glaciers with small catchment areas are thus fundamentally restricted by the snowline and unable to incise the landscape much below this level. Instead, they slowly erode headward into the landscape, leaving behind low-relief surfaces (Fig. 3d) at an altitude just below the snowline: the signature of the

glacial buzzsaw. These low-relief surfaces are, however, separated by pronounced overdeepening in trunk valleys.

Isostatic uplift varies from ~200 m in the centre of the mountain range to 20 m in the upper right corner of the model (Fig. 3c). Thus, surface elevation increases in areas of the model where erosion rates are low. This applies to the highest arêtes and peaks as well as the lower parts of the hillslopes, which before glacial erosion were at altitudes below the snowline and therefore unglaciated. When the latter undergo isostatic uplift, some eventually pass the snowline and experience modification by glacial erosion as described above and further add to the hypsometric maxima.

In addition to classical features of alpine glaciation ('U'-shaped valleys, hanging valleys, overdeepenings, ridges and cirques; Fig. 3d), our model thus predicts that alpine glacial landscapes will naturally undergo strong erosion at and above the snowline. This erosion and its coupling with flexural isostasy produce the high proportion of surface area below the snowline, in agreement with global hypsometric observations. The concentration of surface area occurs in the temperature window (~0 °C) where periglacial processes (not included in the present model) are most effective. Thus, low-relief landscapes in the vicinity of the snowline will probably be further developed by frost cracking and frost creep<sup>23</sup>. This will effectively plane off and further flatten remnant short-wavelength topography into smooth low-curvature surfaces similar to those documented in the Laramide ranges of the western United States<sup>23–25</sup>.

Active tectonic uplift counteracts the erosional destruction of topography above the snowline or balances it<sup>26</sup>, but the evidence presented here and the results of other studies<sup>6–9,11–13</sup> indicate that glacial buzzsaw erosion is capable of keeping pace with any modern tectonic uplift rate. Therefore, the relationship between tectonism and climate is such that climate and latitude ultimately control the height to which tectonic processes can drive topography<sup>6,7</sup>.

## METHODS SUMMARY

The SRTM data set covers all land area within 120° of latitude (60° S to 60° N). Each of the 14,546 DEMs samples an area of 1° × 1° with 3-arcsec resolution. For every DEM, we calculated the hypsometric distribution using 40 bins uniformly spaced between the DEM's minimum and maximum values, and systematically sampled the elevation(s) to any existing local maximum (see Supplementary Figs 1–4 for more details on the topographic analysis).

In the numerical model, the general treatment of ice motion and glacial erosion closely resembles other two- and three-dimensional models<sup>27–29</sup> of glacial landscape evolution. The numerical model is however based on the second-order shallow ice approximation<sup>30</sup> (SOSIA), which allows for simulating long-term glacier evolution at a higher resolution by accounting for important higher-order effects related to a rugged basal topography, rapid ice flow accelerations, and large gradients in longitudinal stress and ice thickness.

**Full Methods** and any associated references are available in the online version of the paper at [www.nature.com/nature](http://www.nature.com/nature).

**Received 27 February; accepted 29 June 2009.**

- Whipple, K. X., Kirby, E. & Brocklehurst, S. H. Geomorphic limits to climate-induced increases in topographic relief. *Nature* **401**, 39–43 (1999).
- Whipple, K. X. The influence of climate on the tectonic evolution of mountain belts. *Nature Geosci.* **2**, 97–104 (2009).
- Beaumont, C., Fullsack, P. & Hamilton, J. in *Thrust Tectonics* (ed. McClay, K. R.) 1–18 (Chapman & Hall, 1992).
- Willett, S. D. Orogeny and orography: the effects of erosion on the structure of mountain belts. *J. Geophys. Res.* **104**, 28957–28981 (1999).
- Beaumont, C., Jamieson, R. A., Nguyen, M. H. & Medvedev, S. Crustal channel flows: 1. Numerical models with application to the tectonics of the Himalayan-Tibetan orogen. *J. Geophys. Res.* **109**, B06406 (2004).
- Brozovic, N., Burbank, D. & Meigs, A. Climatic limits on landscape development in the northwestern Himalaya. *Science* **276**, 571–574 (1997).
- Montgomery, D. R., Balco, G. & Willett, S. D. Climate, tectonics, and the morphology of the Andes. *Geology* **29**, 579–582 (2001).
- Mitchell, S. G. & Montgomery, D. R. Influence of a glacial buzzsaw on the height and morphology of the Cascade Range in central Washington State, USA. *Quat. Res.* **65**, 96–107 (2006).
- Foster, D., Brocklehurst, S. H. & Gawthorpe, R. L. Small valley glaciers and the effectiveness of the glacial buzzsaw in the northern Basin and Range, USA. *Geomorphology* **102**, 624–639 (2008).
- Molnar, P. & England, P. Late Cenozoic uplift of mountain ranges and global climate change: chicken or egg? *Nature* **346**, 29–34 (1990).
- Brocklehurst, S. H. & Whipple, K. X. Glacial erosion and relief production in the Eastern Sierra Nevada, California. *Geomorphology* **42**, 1–24 (2002).
- Shuster, D. L., Ehlers, T. A., Rusmoren, M. E. & Farley, K. A. Rapid glacial erosion at 1.8 Ma revealed by <sup>4</sup>He/<sup>3</sup>He thermochronometry. *Science* **310**, 1668–1670 (2005).
- Berger, A. L. & Spotila, J. A. Denudation and deformation in a glaciated orogenic wedge: the St. Elias orogen, Alaska. *Geology* **36**, 523–526 (2008).
- Paterson, W. S. B. *The Physics of Glaciers* 3rd edn (Butterworth-Heinemann, 1994).
- Brocklehurst, S. H. & Whipple, K. X. Hypsometry of glaciated landscapes. *Earth Surf. Process. Landforms* **29**, 907–926 (2004).
- Farr, T. G. et al. The Shuttle Radar Topography Mission. *Rev. Geophys.* **45**, RG2004, doi:10.1029/2005RG000183 (2007).
- Broecker, W. S. & Denton, G. H. The role of ocean-atmosphere reorganizations in glacial cycles. *Geochim. Cosmochim. Acta* **53**, 2465–2501 (1989).
- National Snow and Ice Data Center. World glacier inventory (2009). ([http://nsidc.org/data/docs/noaa/g01130\\_glacier\\_inventory](http://nsidc.org/data/docs/noaa/g01130_glacier_inventory)).
- Stern, T. A., Baxter, A. K. & Barrett, P. J. Isostatic rebound due to glacial erosion within the Transantarctic Mountains. *Geology* **33**, 221–224 (2005).
- Brocklehurst, S. H. & Whipple, K. X. Assessing the relative efficiency of fluvial and glacial erosion through simulation of fluvial landscapes. *Geomorphology* **75**, 283–299 (2006).
- Roering, J. J., Kirchner, J. W. & Dietrich, W. E. Evidence for nonlinear, diffusive sediment transport and implications for landscape morphology. *Wat. Resour. Res.* **35**, 853–870 (1999).
- Montgomery, D. R. Valley incision and the uplift of mountain peaks. *J. Geophys. Res.* **99**, 13913–13921 (1994).
- Anderson, R. S. Modeling of tor-dotted crests, bedrock edges and parabolic profiles of the high alpine surfaces of the Wind River Range, Wyoming. *Geomorphology* **46**, 35–58 (2002).
- Small, E. E. & Anderson, R. S. Pleistocene relief production in Laramide Mountain Ranges, western U.S. *Geology* **26**, 123–126 (1998).
- Munroe, J. S. Investigating the spatial distribution of summit flats in the Uinta Mountains of northeastern Utah, USA. *Geomorphology* **75**, 437–449 (2006).
- Brocklehurst, S. H. & Whipple, K. X. Response of glacial landscapes to spatial variations in rock uplift rate. *J. Geophys. Res.* **112**, F02035, doi:10.1029/2006JF000667 (2007).
- Harbor, J. M., Hallet, B. & Raymond, C. F. A numerical model of landform development by glacial erosion. *Nature* **333**, 347–349 (1988).
- MacGregor, K. R., Anderson, R. S., Anderson, S. P. & Waddington, E. D. Numerical simulations of glacial-valley longitudinal profile evolution. *Geology* **28**, 1031–1034 (2000).
- Tomkin, J. H. & Braun, J. The influence of alpine glaciation on the relief of tectonically active mountain belts. *Am. J. Sci.* **302**, 169–190 (2002).
- Baral, D. R., Hutter, K. & Greve, R. Asymptotic theories of large-scale motion, temperature, and moisture distribution in land-based polythermal ice sheets: A critical review and new developments. *Appl. Mech. Rev.* **54**, 215–256 (2001).

**Supplementary Information** is linked to the online version of the paper at [www.nature.com/nature](http://www.nature.com/nature).

**Acknowledgements** We thank K. Hutter and N. Kirchner for assistance with the implementation of the SOSIA. We also thank C. Clark, J. A. Piotrowski, B. H. Jacobsen, M. Sandiford, R. Brown and O. Humlum for comments. J. Braun and S. Brocklehurst are thanked for reviews that improved the manuscript considerably.

**Author Contributions** D.L.E. and S.B.N. designed the study. V.K.P. and D.L.E. performed the global topographic analysis. D.L.E. implemented the SOSIA and performed the numerical modelling. All four authors contributed to writing the paper in the order listed.

**Author Information** Reprints and permissions information is available at [www.nature.com/reprints](http://www.nature.com/reprints). Correspondence and requests for materials should be addressed to D.L.E. (david@geo.au.dk).

## METHODS

**Overview.** The present numerical landscape evolution model serves to demonstrate how the glacial buzzsaw denudation mechanism inherently follows from already established assumptions on glacier dynamics and glacial erosion. Compared to existing modelling studies<sup>31–35</sup>, there are no new assumptions. The governing equations are, however, solved using a novel approach (Supplementary Information). This allows prediction of three-dimensional patterns of glacial erosion on a much finer scale than previously because it considers the effects of steep bed topography and gradients in horizontal stress within the ice. Importantly, this permits modelled erosion patterns to be analysed at the scale of the well-known glacial landforms (hanging valleys, cirque valleys, and so on).

The mechanism of glacial buzzsaw erosion is very robust when varying model parameters controlling, for example, ice flow velocities, erosion rates and subglacial water pressure. This is because the buzzsaw signal arises primarily because of ablation patterns caused by the atmospheric temperature gradient. In other words, the downward restriction of small glaciers does not depend on the exact nature of the ice flow, but on the fact that small glaciers quickly melt when passing the snowline altitude.

**Modelling ice flow and glacial erosion.** Ice motion is the sum of internal deformation and basal sliding. The internal deformation is governed by Glen's flow law,  $\epsilon_{ij} = A\tau_e^2\tau_{ij}$ , relating components of the strain rate tensor,  $\epsilon_{ij}$ , to components of the deviatoric stress tensor,  $\tau_{ij}$ .  $\tau_e$  is the effective stress<sup>36</sup> and  $A = 2.25 \times 10^{-17} \text{ Pa}^{-3} \text{ yr}^{-1}$  is the Arrhenius constant for ice at temperatures around  $-10^\circ\text{C}$  (ref. 37).

The sliding velocity is assumed aligned with the basal shear stress,  $\tau_s$ , and of magnitude given by the generalized Weertman law<sup>38</sup>:  $u_s = C_s|\tau_s|^m/(p_i - p_w)^n$ . Here  $C_s = 2 \times 10^{-9} \text{ m Pa}^{-2} \text{ yr}^{-1}$  is a sliding coefficient,  $p_i$  is the ice overburden pressure normal to the bed and  $p_w$  is the meltwater pressure at the bed. We follow others<sup>31–35</sup> and assume a constant ratio between melt water and overburden pressures,  $p_w = 0.2p_i$ , and that  $m = 3$  and  $n = 1$ . Although there is some experimental support<sup>39,40</sup> for the latter choice,  $m$  and  $n$  are poorly constrained parameters. We have, therefore, explored the sensitivity of the modelling results to variations in  $m$  and  $n$ , and in agreement with ref. 41 we find that changing the parameters mainly affects the shape of valleys and not our conclusions regarding erosional patterns of the buzzsaw denudation mechanism.

Mass balance is calculated as the sum of accumulation,  $M_a$ , surface ablation,  $M_s$ , and basal melting,  $M_b$ , all in units of  $\text{m yr}^{-1}$ ;  $M_a = -0.1\min(0, T_s)$ ,  $M_s = -0.15\max(0, T_s)$  and  $M_b = -0.05\max(T_m, T_b)$ . Here  $T_s$  (in units of  $^\circ\text{C}$ ), given by  $T_0 - 5h$ , is the ice surface temperature at altitude  $h$  (in units of km);  $T_b$  is basal temperature as predicted from one-dimensional temperature profiles including conduction and vertical advection of heat<sup>32</sup>;  $T_m = -0.00087H$  is the melting point of ice ( $H$  is ice thickness in units of m).  $T_0$  is reduced from  $15^\circ\text{C}$  to  $10^\circ\text{C}$  during the initial 100 kyr. The downward migration of the snowline allows wet-based glacial erosion to affect, at varying degrees and different times, all altitudes in the landscape above the final snowline altitude. This ensures that the highest peaks and arêtes (which after 100 kyr are in a temperature window with non-eroding cold-based ice) have experienced glacial erosion and gives them a realistic glacial appearance. The slow downwards migration of the snowline can be understood as (1) a slow and long-term average temperature decline (averaging shorter term second order variations) or (2) tectonic uplift that transports topography slowly upwards through the snowline altitude.

We assume that the local glacial erosion rate normal to the bed is primarily governed by abrasion and quarrying, and hence<sup>42,43</sup>, proportional to local sliding rates:  $e = k_e|u_s|$ .  $k_e$  is calibrated to  $1 \times 10^{-4}$  by requiring average erosion rates to be less than  $1 \text{ mm yr}^{-1}$ , which is a conservative estimate<sup>42</sup>. Depending on the altitude and the thickness of the ice, the model glaciers above the snowline can be

frozen to the bed. The basal sliding rate is then zero and ice transport is solely due to internal deformation.

The Stokes mechanical equilibrium equations are solved using the second-order shallow ice approximation<sup>36</sup> (SOSIA) and a finite volume formulation (see Supplementary Information for details) with an irregular grid and explicit time integration. The higher-order method allows for solving the ice flow equations accurately, also when basal topography is steep and when significant gradients in longitudinal and transverse stress are present. The irregular grid consists of 31,480 Voronoi cells with average spacing of 400 m.

**Modelling hillslope processes.** In order to prevent surface slopes from increasing unrealistically, we include mass wasting on steep slopes using a nonlinear diffusion model<sup>44,45</sup>. The model expresses the flux of material,  $q = -\kappa s/[1 - (s/s_c)^2]$ , as a function of surface slope,  $s$ .  $\kappa = 1 \text{ m}^2 \text{ yr}^{-1}$  is the diffusivity of low gradient hillslopes, while  $s_c = 1.0$  defines a critical slope near which the effective diffusivity increases towards infinity.

**Modelling flexural isostasy.** Flexural isostasy is incorporated by coupling the erosion model to a two-dimensional uniform thin elastic plate<sup>45</sup> with an elastic thickness of 10 km. The densities of the eroding crust and the asthenosphere are  $2,800 \text{ kg m}^{-3}$  and  $3,300 \text{ kg m}^{-3}$ , respectively. Erosional unloading and the weight of the ice cause deflections of the plate, which are fed back into the model as vertical surface movements. The relatively small size of the Sierra Nevada mountain range combined with the elastic thickness of 10 km effectively limits the amplitudes of isostatic uplift following erosion. The model presented is thus conservative with respect to how isostasy contributes to the mechanism of the glacial buzzsaw.

- Harbor, J. M., Hallet, B. & Raymond, C. F. A numerical model of landform development by glacial erosion. *Nature* **333**, 347–349 (1988).
- Braun, J., Zwart, D. & Tomkin, J. A new surface-processes model combining glacial and fluvial erosion. *Ann. Glaciol.* **28**, 282–290 (1999).
- MacGregor, K. R., Anderson, R. S., Anderson, S. P. & Waddington, E. D. Numerical simulations of glacial-valley longitudinal profile evolution. *Geology* **28**, 1031–1034 (2000).
- Jamieson, S. S. R., Hulton, N. R. J. & Hagdorn, M. Modelling landscape evolution under ice sheets. *Geomorphology* **97**, 91–108 (2008).
- Tomkin, J. H. Numerically simulating alpine landscapes: the geomorphologic consequences of incorporating glacial erosion in surface process models. *Geomorphology* **103**, 180–188 (2009).
- Baral, D. R., Hutter, K. & Greve, R. Asymptotic theories of large-scale motion, temperature, and moisture distribution in land-based polythermal ice sheets: a critical review and new developments. *Appl. Mech. Rev.* **54**, 215–256 (2001).
- Hooke, R. L. Flow law for polycrystalline ice in glaciers: comparison of theoretical predictions, laboratory data, and field measurements. *Rev. Geophys. Space Phys.* **19**, 664–672 (1981).
- Paterson, W. S. B. *The Physics of Glaciers* 3rd edn (Butterworth-Heinemann, 1994).
- Budd, W. F., Keage, P. L. & Blundy, N. A. Empirical studies of ice sliding. *J. Glaciol.* **23**, 157–170 (1979).
- Bindschadler, R. The importance of pressurized subglacial water in separation and sliding at the glacier bed. *J. Glaciol.* **29**, 3–19 (1983).
- Harbor, J. M. Application of a general sliding law to simulating flow in a glacier cross-section. *J. Glaciol.* **38**, 182–190 (1992).
- Hallet, B. Glacial quarrying: a simple theoretical model. *Ann. Glaciol.* **22**, 1–8 (1996).
- Humphrey, N. F. & Raymond, C. F. Hydrology, erosion and sediment production in a surging glacier: Variegated Glacier, Alaska, 1982–83. *J. Glaciol.* **40**, 539–552 (1994).
- Roering, J. J., Kirchner, J. W. & Dietrich, W. E. Evidence for nonlinear, diffusive sediment transport and implications for landscape morphology. *Wat. Resour. Res.* **35**, 853–870 (1999).
- Pelletier, J. *Quantitative Modeling of Earth Surface Processes* (Cambridge Univ. Press, 2008).



## LETTERS

# Pelvic claspers confirm chondrichthyan-like internal fertilization in arthrodires

Per Ahlberg<sup>1</sup>, Kate Trinajstić<sup>2,3,4</sup>, Zerina Johanson<sup>5</sup> & John Long<sup>6,7,8</sup>

Recent finds<sup>1,2</sup> demonstrate that internal fertilization and viviparity (live birth) were more widespread in the Placodermi, an extinct group of armoured fishes, than was previously realized. Placoderms represent the sister group of the crown group jawed vertebrates (Gnathostomata)<sup>3,4</sup>, making their mode(s) of reproduction potentially informative about primitive gnathostome conditions. An ossified pelvic fin basipterygium discovered in the arthrodire *Incisoscutum ritchiei* was hypothesized to be identical in males and females, with males presumed to have an additional cartilaginous element or series forming a clasper. Here we report the discovery of a completely ossified pelvic clasper in *Incisoscutum ritchiei* (WAM 03.3.28) which shows that this interpretation was incorrect: the basipterygium described previously<sup>1</sup> is in fact unique to females. The male clasper is a slender rod attached to a square basal plate that articulates directly with the pelvis. It carries a small cap of dermal bone covered in denticles and small hooks that may be homologous with the much larger dermal component of the ptyctodont clasper.

The presence of embryos within an adult female of the placoderm *Incisoscutum ritchiei*, a member of the Arthrodira, was recently described<sup>1</sup>. This demonstrated that live birth and internal fertilization among placoderms are not restricted to the Ptyctodontida, where embryos have been described in *Materpiscis attenboroughi* and *Austroptyctodus gardineri*<sup>2</sup>. Ptyctodont males possess modified pelvic elements, or claspers<sup>5,6</sup>, used in living male chondrichthyans for internal fertilization. The existence of a pelvic clasper in *Incisoscutum ritchiei*, hypothesized previously<sup>1</sup>, can now be confirmed in WAM 03.3.28 and demonstrates sexual dimorphism in an arthrodire for the first time (Fig. 1a, b). The clasper, previously misidentified as the left pelvis of this individual, is composed of perichondral bone and articulates directly with the pelvic girdle (Fig. 1b), unlike sharks where the clasper articulates with a more proximal basipterygial element. The distal end of the clasper is thin and rod-like. Its tip is covered by a small, distinct cap of dermal bone, ornamented with small pits and denticles. The proximal part of the clasper is expanded into a plate pierced by four foramina, two larger above two smaller (Fig. 1b). The anatomy of the pelvic clasper most probably corresponds to the core of an erectile element, as in extant sharks. The basal element previously described<sup>1</sup> in *Incisoscutum ritchiei* (WAM 04.10.02) is reinterpreted as the female basipterygium, rather than a proximal element common to both sexes. This female element is also seen in BMNH P50934, one of the specimens containing embryos. In both ptyctodonts and *Incisoscutum* the distal ends of the claspers are capped by a covering of dermal bone. However, in ptyctodonts the dermal bone covering is extensive and so far no internal element has been discovered<sup>7</sup>,

suggesting that the endoskeleton was unossified, whereas in *Incisoscutum* the internal skeleton is perichondrally ossified and only the distal tip is covered by dermal bone. Notwithstanding these differences of emphasis between the dermal and endoskeletal components, the claspers appear to share a common architecture that suggests homology between the two groups. We tentatively infer that claspers characterize the whole of the Ptyctodontida and Arthrodira; further

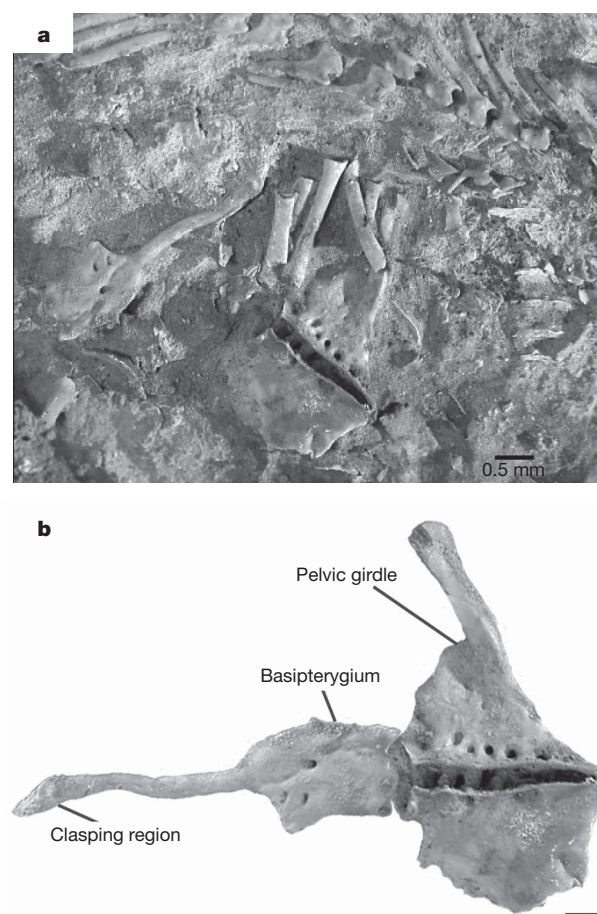


**Figure 1 | The male pelvic girdle of *Incisoscutum ritchiei* WAM 03.3.28. a, Pelvic girdle in dorsal view; b, pelvic girdle restored.**

<sup>1</sup>Subdepartment of Evolutionary Organismal Biology, Department of Physiology and Developmental Biology, Uppsala University, Norbyvägen 18A, 752 36 Uppsala, Sweden. <sup>2</sup>Western Australian Organic and Isotope Geochemistry Centre, Department of Applied Chemistry, Curtin University, Perth, Western Australia 6102, Australia. <sup>3</sup>Earth and Planetary Sciences, Western Australian Museum, Perth, Western Australia 6000, Australia. <sup>4</sup>School of Earth and Environment, The University of Western Australia, Perth, Western Australia 6009, Australia. <sup>5</sup>Department of Palaeontology, Natural History Museum, Cromwell Road, London SW7 5BD, UK. <sup>6</sup>Museum Victoria, PO Box 666, Melbourne, Victoria 3001, Australia. <sup>7</sup>Research School of Earth Sciences, The Australian National University, Canberra, Australian Capital Territory 2600. <sup>8</sup>School of Geosciences, Monash University, Clayton, Victoria 3800, Australia.

study of well-preserved arthrodires should be undertaken to test this hypothesis.

Received 3 April; accepted 28 May 2009.

Published online 13 July 2009.

- Long, J. A., Trinajstić, K. & Johanson, Z. Devonian arthrodire embryos and the origin of internal fertilization in vertebrates. *Nature* **457**, 1124–1126 (2009).
- Long, J. A., Trinajstić, K., Young, G. C. & Senden, T. Live birth in the Devonian period. *Nature* **453**, 650–652 (2008).
- Goujet, D. & Young, G. C. in *Recent Advances in the Origin and Early Radiation of Vertebrates* (eds Arratia, G., Wilson, M. V. H. & Cloutier, R.) 109–126 (Dr Friedrich Pfeil, 2004).
- Brazeau, M. D. The braincase and jaws of a Devonian 'acanthodian' and modern gnathostome origins. *Nature* **457**, 305–308 (2009).
- Miles, R. S. Observations on the ptyctodont fish, *Rhamphodopsis* Watson. *J. Linn. Soc. London Zool.* **47**, 99–120 (1967).
- Miles, R. S. & Young, G. C. in *Problems in Vertebrate Evolution* (eds Andrews, S. M., Miles, R. S. & Walker, A. D.) 123–198 (Linnean Soc. Symp. Series 4, 1977).
- Young, G. C. The relationships of placoderm fishes. *Zool. J. Linn. Soc.* **88**, 1–57 (1986).

**Acknowledgements** We thank M. Siverson for access to specimens at the Western Australian Museum. J.L. and K.T. are supported by Australian Research Council Discovery grants, and field work at Gogo in 2001 was supported by an Australian Geographic grant. P.A. is supported by the Swedish Research Council. K. Bifield prepared the specimen.

**Author Contributions** J.L. found WAM 03.3.28 and supervised the preparation, P.A. correctly identified the clasper, and all authors contributed to the description of the material.

**Author Information** Reprints and permissions information is available at [www.nature.com/reprints](http://www.nature.com/reprints). Correspondence and requests for materials should be addressed to K.T. ([kttrinajs@bigpond.net.au](mailto:kttrinajs@bigpond.net.au)).

## LETTERS

# Homothallic and heterothallic mating in the opportunistic pathogen *Candida albicans*

Kevin Alby<sup>1</sup>, Dana Schaefer<sup>1</sup> & Richard J. Bennett<sup>1</sup>

*Candida albicans* is the most common fungal pathogen in humans, causing both debilitating mucosal infections and potentially life-threatening systemic infections<sup>1,2</sup>. Until recently, *C. albicans* was thought to be strictly asexual, existing only as an obligate diploid. A cryptic mating cycle has since been uncovered in which diploid *a* and  $\alpha$  cells undergo efficient cell and nuclear fusion, resulting in tetraploid *a/a* mating products<sup>3–6</sup>. Whereas mating between *a* and  $\alpha$  cells has been established (heterothallism), we report here two pathways for same-sex mating (homothallism) in *C. albicans*. First, unisexual populations of *a* cells were found to undergo autocrine pheromone signalling and same-sex mating in the absence of the Bar1 protease. In both *C. albicans* and *Saccharomyces cerevisiae*, Bar1 is produced by *a* cells and inactivates mating pheromone  $\alpha$ , typically secreted by  $\alpha$  cells<sup>7–10</sup>. *C. albicans*  $\Delta$ bar1 *a* cells were shown to secrete both *a* and  $\alpha$  mating pheromones;  $\alpha$ -pheromone activated self-mating in these cells in a process dependent on Ste2, the receptor for  $\alpha$ -pheromone. In addition, pheromone production by *a* cells was found to promote same-sex mating between wild-type *a* cells. These results establish that homothallic mating can occur in *C. albicans*, revealing the potential for genetic exchange even within unisexual populations of the organism. Furthermore, Bar1 protease has an unexpected but pivotal role in determining whether sexual reproduction can potentially be homothallic or is exclusively heterothallic. These findings also have implications for the mode of sexual reproduction in related species that propagate unisexually, and indicate a role for specialized sexual cycles in the survival and adaptation of pathogenic fungi.

The hemiascomycetous fungi are a diverse range of species that include the prototypical model yeast, *Saccharomyces cerevisiae*, as well as the prevalent human pathogen, *Candida albicans*. Sexual reproduction in both fungi is driven by the secretion of sex-specific pheromones that promote mating between partners of the opposite sex<sup>11–13</sup>. Pheromone gradients are sensed by G-protein-coupled cell-surface receptors that initiate the mating response<sup>14,15</sup>. *C. albicans* mating is thought to be exclusively heterothallic, whereas isolates of *S. cerevisiae* that express HO endonuclease are homothallic because of mating-type switching<sup>16</sup>. The discovery that unisexual populations of *C. albicans* can express both *a* and  $\alpha$  mating pheromones<sup>17</sup> led us to test whether autocrine pheromone signalling and homothallism can occur in this species.

*C. albicans* *a* cells derived from the laboratory strain SC5314 were treated with synthetic  $\alpha$ -pheromone and the quantitative polymerase chain reaction used to compare the induction of both *a*- and  $\alpha$ -pheromone genes (*MFa* and *MF $\alpha$* , respectively). Opaque-phase cells were used for these experiments, as these are the mating-competent form of *C. albicans*<sup>6</sup>. Both *MFa* (300-fold) and *MF $\alpha$*  (373-fold) were highly induced in response to  $\alpha$ -pheromone, in contrast to *S. cerevisiae* where only *a*-pheromone is upregulated<sup>18</sup>. In both *C. albicans* and *S. cerevisiae*, an extracellular barrier activity acts to antagonize the

function of  $\alpha$ -pheromone. The activity, encoded by *BAR1*, is an aspartyl protease that cleaves  $\alpha$ -pheromone, inactivating it<sup>7–10</sup>. We therefore analysed a *C. albicans*  $\Delta$ bar1 mutant to determine whether  $\alpha$ -pheromone production has a functional role in these cells. *C. albicans*  $\Delta$ bar1 cells exhibited distinctive colony morphologies when cultured on solid media. Mutant colonies appeared increasingly wrinkled during growth on yeast peptone dextrose (YPD) medium (Fig. 1a). Cells retrieved from these colonies were highly elongated and showed similarities to cells that had undergone extended exposure to pheromone<sup>12</sup>. To confirm that elongated cells were undergoing a mating-type response and were not hyphal (filamentous) cells, green fluorescent protein (GFP) reporters were introduced under the control of pheromone-specific promoters. Both *FIG1* and *FUS1* genes are highly expressed in response to pheromone<sup>17</sup>, and pFIG1-GFP and pFUS1-GFP constructs were therefore used to monitor activation of the mating program. Significantly, both *FIG1* and *FUS1* expression was induced, confirming that cells were undergoing a mating-like response, even in the absence of exogenous pheromone or a mating partner of the opposite sex (Fig. 1b). To confirm that this phenomenon was not limited to strains derived from SC5314,  $\Delta$ bar1 mutants were also generated in P37005, a natural *a/a* isolate of *C. albicans*, and found to exhibit similar cell and colony phenotypes (Supplementary Fig. 1).

Two models were considered for how autocrine pheromone signalling could lead to activation of a mating response. First, *a*-pheromone secretion could signal to Ste3, the receptor for *a*-pheromone (Fig. 2a, model I). Alternatively,  $\alpha$ -pheromone could induce mating via binding to Ste2, the receptor for  $\alpha$ -pheromone (model II). Although not mutually exclusive, these two models were tested by construction of strains lacking different combinations of pheromone or pheromone receptor genes. Significantly, loss of either  $\alpha$ -pheromone (*MF $\alpha$* ) or its receptor (*Ste2*) completely abolished the wrinkled colony appearance of  $\Delta$ bar1 *a* strains (Fig. 2b). In contrast, loss of *STE3* (encoding the receptor for *a* pheromone) had no effect on colony phenotype (Fig. 2b). Thus, autocrine signalling in *a* cells is driven by  $\alpha$ -pheromone production and requires the presence of Ste2, the cognate receptor for  $\alpha$ -pheromone (model II).

Autocrine pheromone signalling was also observed between neighbouring colonies of cells, as  $\Delta$ bar1 *a* cells induced a response in adjacent colonies of *a* cells. Cells from wrinkled colonies again exhibited polarized growth indicative of a mating response (data not shown). Neighbouring cells failed to respond in the absence of *STE2*, indicating that signalling required the receptor for  $\alpha$ -pheromone (Fig. 2c, row 2). Furthermore,  $\Delta$ bar1 cells were unable to induce a response in adjacent cells if either *MF $\alpha$*  or *STE2* was also deleted (Fig. 2c, rows 3 and 4). The dependence of signalling on *STE2* is demonstrative of a positive feedback loop in these cells;  $\alpha$ -pheromone secreted by  $\Delta$ bar1 cells binds to Ste2 receptors on these cells and results in further augmentation of pheromone production. Only when this

<sup>1</sup>Department of Molecular Microbiology and Immunology, Brown University, Providence, Rhode Island 02912, USA.



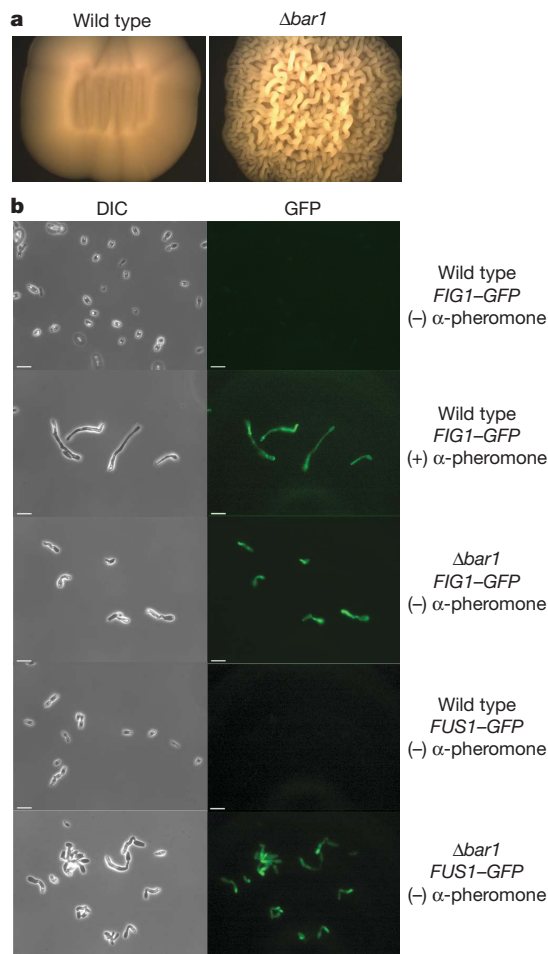


**Figure 1 | Deletion of *BAR1* results in an autocrine mating response.**

**a**, Patches of wild-type and  $\Delta bar1$  *a* cells after 4 days growth on YPD medium. **b**, Mating response of wild-type and  $\Delta bar1$  *a* cells with and without  $\alpha$ -pheromone in Spider medium for 36 h. Differential interference contrast (DIC, left) and GFP fluorescence (GFP, right) images are shown. Induction of the mating response was monitored using GFP reporters under the control of the mating-response genes *FIG1* or *FUS1*. All *C. albicans* cells used in this study were in the opaque phase as this is the mating-competent form of the organism<sup>6,30</sup>. Scale bars, 16  $\mu$ m.

feedback loop is in effect does pheromone secretion reach the levels necessary for autocrine signalling. *STE3*, encoding the receptor for *a*-pheromone, was not involved in this signalling (Fig. 2c, column 4 and row 5). Production of  $\alpha$ -pheromone by  $\Delta bar1$  *a* cells was also evident in halo assays and was shown to increase biofilm formation by these cell types (see Supplementary Information).

The existence of a robust autocrine mating pathway led us to test whether *C. albicans* is capable of homothallic mating. Two different auxotrophic  $\Delta bar1$  strains were mixed and co-incubated on Spider medium for 3 days. Cells were recovered from the mating mixture and plated onto selective medium to detect potential *a*-*a* mating products. A number of prototrophic mating products were obtained and analysis by PCR and flow cytometry revealed that these were stable tetraploid cells of mating type *a* (Fig. 3a, b). To compare the frequency of homothallic and heterothallic mating in *C. albicans*, several quantitative mating crosses were performed (Fig. 3c). Mating between wild-type *a* and  $\alpha$  cells occurred efficiently (94%), whereas no mating was observed between two wild-type *a* strains (<0.00002%). Significant levels of unisexual mating were obtained, however, using two  $\Delta bar1$  *a* strains (0.037%), an increase of more than 1,850-fold over wild-type *a*-*a* mating. The efficiency of unisexual mating was further increased in crosses between  $\Delta bar1$  and

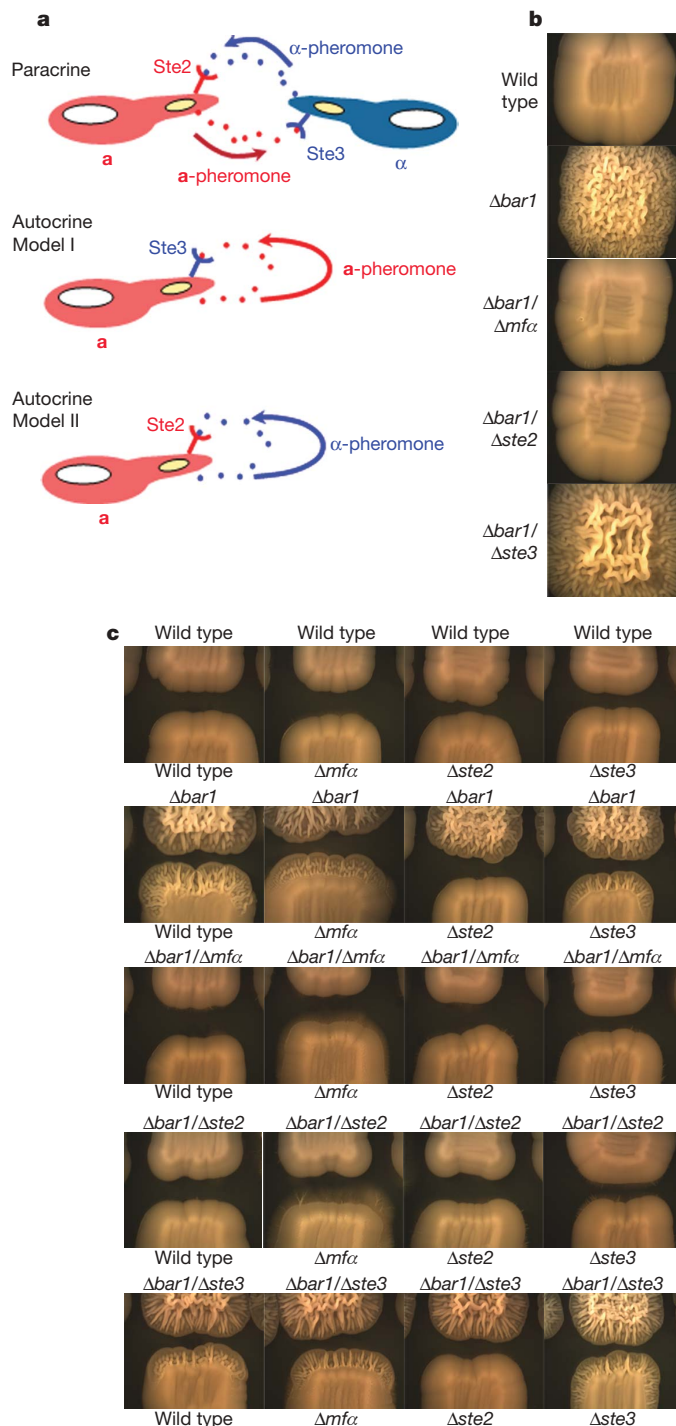


**Figure 2 | Autocrine signalling in *C. albicans* *a* cells. **a**, Model of conventional paracrine signalling between *a* and  $\alpha$  cells and two models for autocrine signalling. Note that 'autocrine' signalling is used here to refer to signalling within populations of *a* cells. **b**, *C. albicans* *a* cells after 4 days growth on YPD medium. Whereas  $\Delta bar1$  strains showed a highly wrinkled morphology, reconstituted strains in which the *BAR1* gene had been reintegrated did not show wrinkling (not shown). **c**, Demonstration of autocrine signalling among different populations of *a* cells after 4 days growth on YPD medium. Wrinkling at the edge of a test colony is indicative of autocrine signalling.**

wild-type *a* strains, with 0.88% of cells undergoing mating, an increase of more than 40,000-fold over that between wild-type *a* strains (Fig. 3c). In fact,  $\Delta bar1$  *a* cells mated as efficiently with other *a* cells as with  $\alpha$  cells (0.80%), indicating a loss in sexual preference for one mating-type partner over the other. These experiments

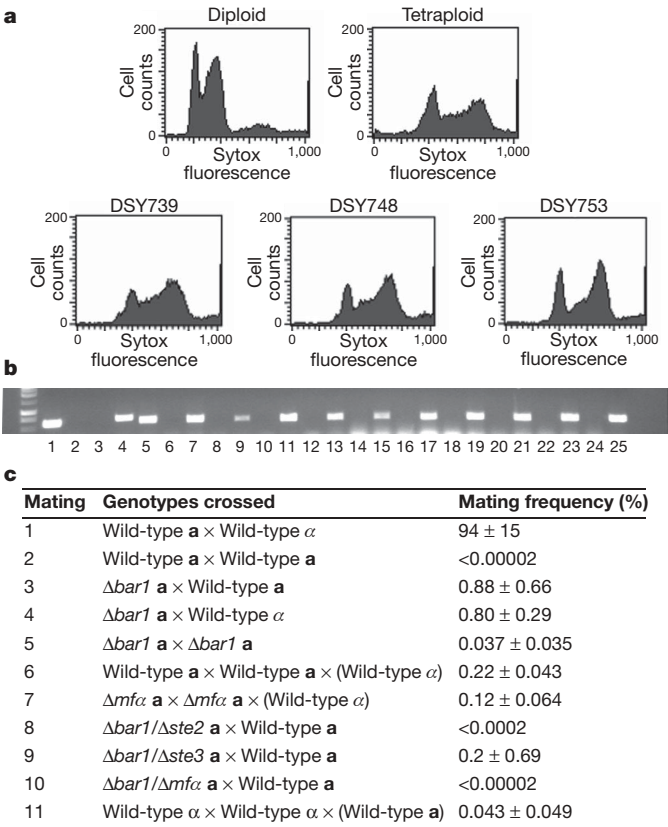


**Figure 3 | Homothallic mating in *C. albicans*.** **a**, Flow cytometric analysis indicating the tetraploid content of progeny isolated from  $\alpha$ - $\alpha$  matings. The x-axis of each graph (Sytox) represents a linear scale of fluorescence and the y-axis (Cell counts) a linear scale of cell number. For analysis of additional same-sex mating products see Supplementary Fig. 6. **b**, PCR confirming the mating type of  $\alpha$ - $\alpha$  mating products using primers directed at *OBP $\alpha$*  and *OBP $\alpha$* . Odd-numbered lanes are *OBP $\alpha$*  reactions, whereas even-numbered lanes are *OBP $\alpha$*  reactions. Lanes 1, 2 and 3, 4 are control reactions for  $\alpha$  and  $\alpha$  cells, respectively. **c**, Table of mating frequencies for different genetic crosses. Values are listed as mean frequency  $\pm$  s.d.

demonstrate that mating can take place even within unisexual populations of *C. albicans* cells, and that Bar1 acts to limit these types of self-fusion events. Notably, mating between wild-type  $\alpha$  cells also occurred at an appreciable frequency (0.22%) if co-cultured with  $\alpha$  cells. In these ménage à trois matings,  $\alpha$  cells presumably provided levels of  $\alpha$ -pheromone that were sufficient to overcome Bar1 activity and drive  $\alpha$ - $\alpha$  mating. Levels of  $\alpha$ -pheromone may be augmented by autocrine pheromone signalling in  $\alpha$  cells, as deletion of *MF $\alpha$*  in  $\alpha$  cells led to a slight reduction in the frequency of ménage à trois mating (0.12%). In addition,  $\alpha$  cells did not need to be in contact with  $\alpha$  cells to drive same-sex mating (Supplementary Fig. 4). Mating between wild-type  $\alpha$  cells (0.043%) was similarly observed when co-cultured with  $\alpha$  cells (see Fig. 3).

If self-mating in unisexual populations is a direct consequence of autocrine pheromone signalling, then mutants deficient in signalling should be unable to self-mate. Both  $\Delta bar1/\Delta ste2$  and  $\Delta bar1/\Delta mfa$  strains did not exhibit autocrine signalling and also showed no detectable mating with wild-type  $\alpha$  strains (<0.0002%; Fig. 3c). In contrast,  $\Delta bar1/\Delta ste3$   $\alpha$  strains were competent for both autocrine signalling and unisexual mating (1.2%). The potential for unisexual mating is therefore dependent on the ability of cells to undergo autocrine pheromone signalling. To examine the efficiency of inbreeding and outbreeding by different *C. albicans* strains, SC5314  $\Delta bar1$   $\alpha$  strains were also mated with different clinical isolates (Fig. 4a). Again,  $\Delta bar1$  strains mated with both  $\alpha$  and  $\alpha$  isolates at a similar frequency (average of 9.8% and 17.6%, respectively). In fact,

mating was generally more efficient between SC5314 and clinical isolates (up to 26%  $\alpha$ - $\alpha$  mating) than that between SC5314 strains alone. Mating zygotes could be detected in unisexual crosses and fluorescent labelling of the nuclei confirmed that karyogamy had taken place (Fig. 4b and Supplementary Fig. 5). The tetraploid products of unisexual mating were generally stable, but could be induced to undergo chromosome loss to produce diploid cells, thereby completing a parasexual mating cycle (Supplementary Fig. 7).

Our findings have implications for sexual reproduction in *C. albicans* and related species, as they reveal a mechanism for same-sex mating in hemiascomycetes. In *C. albicans*, heterothallic mating between  $\alpha$  and  $\alpha$  cells can occur, yet a predominantly clonal population structure suggests that outbreeding is rare<sup>19</sup>. The discovery of self-mating indicates that homothallism could act to create a burst of genetic diversity by increasing recombination within unisexual populations. Completion of the parasexual cycle could promote allele shuffling or increase karyotypic variation within the diploid genome. Furthermore, isolates of some related species are thought to be exclusively homothallic. For example, isolates of *Lodderomyces elongisporus* are able to form asci from identical cells, yet the genome apparently encodes only one pheromone gene (*MF $\alpha$* ) and one receptor gene (*STE2*)<sup>20</sup>. Discovery of autocrine signalling and self-mating reveals a mechanism by which such species could reproduce sexually despite the absence of mating partners of the opposite sex.

Homothallism has been well characterized in *S. cerevisiae* where it is a direct result of mating-type switching. *C. albicans* and related species are unable to undergo mating-type switching, yet we demonstrate two potential pathways by which self-mating can occur. First, inhibition of Bar1 activity promotes autocrine signalling and mating within unisexual populations of *C. albicans*. We hypothesize that certain niches in the mammalian host will favour self-fertilization by downregulating Bar1 activity. Second, we show that same-sex mating can occur because of pheromone signalling in conventional  $\alpha$ - $\alpha$  mixes. In this case, pheromone secretion by even a limiting number of  $\alpha$  cells can promote  $\alpha$ - $\alpha$  mating (Supplementary

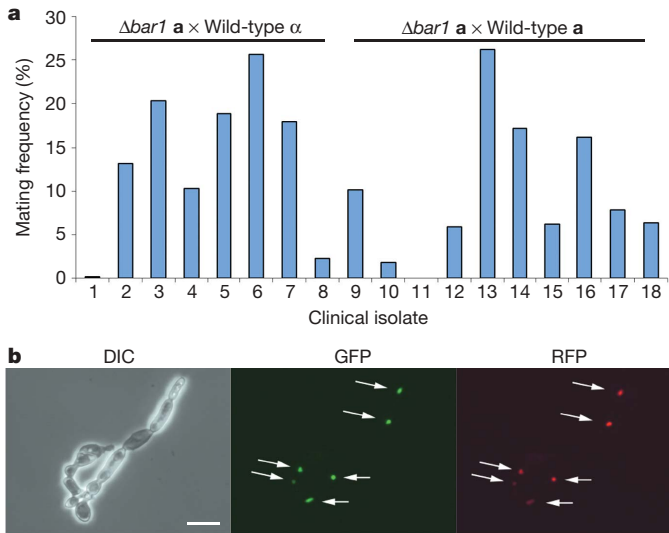


**Figure 4 | Homothallic mating across clades in *C. albicans*.** **a**, Mating frequencies of an SC5314  $\Delta bar1$   $\alpha$  cell crossed with naturally occurring isolates from different clades of *C. albicans*. 1–8 are crosses between  $\Delta bar1$   $\alpha$  cells and clinical  $\alpha$  cells. 9–18 are crosses between  $\Delta bar1$   $\alpha$  cells and clinical  $\alpha$  cells. For a complete list of strains see Methods. **b**, Mating zygote formed between a  $\Delta bar1$   $\alpha$  cell derived from SC5314 (DSY906, expressing *HTB-RFP*; histone H2B gene-red fluorescent protein) and a clinical  $\alpha$  cell derived from IHEM16614 (DSY908, expressing *HTB-YFP*). Arrows indicate fused nuclei expressing both fluorescent proteins. DIC (left), YFP fluorescence (observed using the GFP channel, middle) and RFP fluorescence (right) images are shown. Scale bar, 15  $\mu$ m.

Table 3). In addition, certain combinations of *C. albicans*  $\alpha$  and  $\alpha$  strains are incompatible for heterothallic mating as nuclei fail to undergo karyogamy<sup>21</sup>. Our results show that pheromones produced during contact between two such 'infertile' strains could still result in self-mating within sexes.

The program of same-sex mating in *C. albicans* shows unexpected similarities to that in other human fungal pathogens. In the basidiomycetous fungus *Cryptococcus neoformans* mating between  $\alpha$  and  $\alpha$  isolates can occur, yet clinical and environmental isolates are overwhelmingly of the  $\alpha$  mating type. Same-sex mating between  $\alpha$  isolates of *C. neoformans* has been observed both in the laboratory and in the wild, and is thought to be the predominant mode of sexual reproduction in this organism<sup>22–25</sup>. *Pneumocystis carinii* is another fungal pathogen predicted to undergo a modified sexual cycle involving cells of the same mating type<sup>26</sup>. It thus seems that autocrine pheromone signalling and homothallism may be traits shared by a diverse group of medically relevant fungi. These pathogens have retained the ability to undergo sexual reproduction and yet have evolved modifications to these programs that support their survival and propagation. Elucidating the respective mechanisms of homothallism and heterothallism will therefore be critical to the understanding of these species as human pathogens.

## METHODS SUMMARY

*C. albicans* strains were derived from SC5314 except where otherwise noted. Mutant strains were created using either the PCR fusion or SAT1 flipper methods described previously<sup>27,28</sup>. For a complete list of strains and primers see Supplementary Tables 1 and 2. Media were made as described previously<sup>10</sup>. All *C. albicans* cells used in this study were in the opaque phase as this is the mating-competent form of the organism<sup>6</sup>. Quantitative PCR was performed on  $\alpha$  cells that had been treated with  $10 \mu\text{g ml}^{-1}$   $\alpha$ -pheromone for 4 h in Spider medium, as described previously<sup>10,29</sup>. For analysis of colony morphology, patches of *C. albicans* cells ( $\sim 0.5 \text{ cm}^2$ ) were spaced 0.75 cm apart on YPD medium and imaged after 4 days growth at 30 °C using a Zeiss Stemi 2000-C stereoscope with an Infinity 1 camera. Cells were examined using a Zeiss Axioplan 2 microscope equipped with a Hamamatsu-ORCA camera. Mating frequencies were determined by mixing  $2 \times 10^7$  cells of differently marked auxotrophic strains on Spider medium and incubating at room temperature for 3 days. Cells were then resuspended in water and plated onto selective media to determine frequency of mating products<sup>10</sup>. For analysis of  $\alpha$ - $\alpha$  mating in the presence of  $\alpha$  cells,  $2 \times 10^7$  cells of each of three strains were mixed and incubated on Spider medium (two differently marked  $\alpha$  strains and an  $\alpha$  strain negative for both markers). Cells were recovered and analysed as above. The same strategy (two differently marked  $\alpha$  strains and an  $\alpha$  strain negative for both markers) was applied to detect  $\alpha$ - $\alpha$  mating. Flow cytometry to determine cell ploidy was performed by staining DNA with Sytox Green and analysis on a FACSCalibur<sup>4</sup>. PCR to determine mating type was performed using primers directed at *OBPa*/ $\alpha$  as described previously<sup>30</sup>.

**Full Methods** and any associated references are available in the online version of the paper at [www.nature.com/nature](http://www.nature.com/nature).

Received 6 May; accepted 26 June 2009.

1. Samaranayake, L. P. *et al.* Fungal infections associated with HIV infection. *Oral Dis.* 8 (Suppl. 2), 151–160 (2002).
2. Wisplinghoff, H. *et al.* Nosocomial bloodstream infections in US hospitals: analysis of 24,179 cases from a prospective nationwide surveillance study. *Clin. Infect. Dis.* 39, 309–317 (2004).
3. Hull, C. M. & Johnson, A. D. Identification of a mating type-like locus in the asexual pathogenic yeast *Candida albicans*. *Science* 285, 1271–1275 (1999).
4. Hull, C. M., Raisner, R. M. & Johnson, A. D. Evidence for mating of the "asexual" yeast *Candida albicans* in a mammalian host. *Science* 289, 307–310 (2000).
5. Magee, B. B. & Magee, P. T. Induction of mating in *Candida albicans* by construction of *MTLa* and *MTL $\alpha$*  strains. *Science* 289, 310–313 (2000).
6. Miller, M. G. & Johnson, A. D. White-opaque switching in *Candida albicans* is controlled by mating-type locus homeodomain proteins and allows efficient mating. *Cell* 110, 293–302 (2002).
7. Hicks, J. B. & Herskowitz, I. Evidence for a new diffusible element of mating pheromones in yeast. *Nature* 260, 246–248 (1976).

8. MacKay, V. L. *et al.* The *Saccharomyces cerevisiae* *BAR1* gene encodes an exported protein with homology to pepsin. *Proc. Natl Acad. Sci. USA* 85, 55–59 (1988).
9. Manney, T. R. Expression of the *BAR1* gene in *Saccharomyces cerevisiae*: induction by the  $\alpha$  mating pheromone of an activity associated with a secreted protein. *J. Bacteriol.* 155, 291–301 (1983).
10. Schaefer, D., Cote, P., Whiteway, M. & Bennett, R. J. Barrier activity in *Candida albicans* mediates pheromone degradation and promotes mating. *Eukaryot. Cell* 6, 907–918 (2007).
11. Bennett, R. J., Uhl, M. A., Miller, M. G. & Johnson, A. D. Identification and characterization of a *Candida albicans* mating pheromone. *Mol. Cell. Biol.* 23, 8189–8201 (2003).
12. Lockhart, S. R., Daniels, K. J., Zhao, R., Wessels, D. & Soll, D. R. Cell biology of mating in *Candida albicans*. *Eukaryot. Cell* 2, 49–61 (2003).
13. Panwar, S. L., Legrand, M., Dignard, D., Whiteway, M. & Magee, P. T. *Mfx1*, the gene encoding the  $\alpha$  mating pheromone of *Candida albicans*. *Eukaryot. Cell* 2, 1350–1360 (2003).
14. Jackson, C. L. & Hartwell, L. H. Courtship in *Saccharomyces cerevisiae*: an early cell-cell interaction during mating. *Mol. Cell. Biol.* 10, 2202–2213 (1990).
15. Segall, J. E. Polarization of yeast cells in spatial gradients of  $\alpha$  mating factor. *Proc. Natl Acad. Sci. USA* 90, 8332–8336 (1993).
16. Hall, M. N. & Linder, P. *The Early Days of Yeast Genetics* (Cold Spring Harbor Laboratory Press, 1993).
17. Bennett, R. J. & Johnson, A. D. The role of nutrient regulation and the Gpa2 protein in the mating pheromone response of *C. albicans*. *Mol. Microbiol.* 62, 100–119 (2006).
18. Roberts, C. J. *et al.* Signaling and circuitry of multiple MAPK pathways revealed by a matrix of global gene expression profiles. *Science* 287, 873–880 (2000).
19. Odds, F. C. *et al.* Molecular phylogenetics of *Candida albicans*. *Eukaryot. Cell* 6, 1041–1052 (2007).
20. Butler, G. *et al.* Evolution of pathogenicity and sexual reproduction in eight *Candida* genomes. *Nature* 459, 657–662 (2009).
21. Bennett, R. J., Miller, M. G., Chua, P. R., Maxon, M. E. & Johnson, A. D. Nuclear fusion occurs during mating in *Candida albicans* and is dependent on the *KAR3* gene. *Mol. Microbiol.* 55, 1046–1059 (2005).
22. Lin, X., Hull, C. M. & Heitman, J. Sexual reproduction between partners of the same mating type in *Cryptococcus neoformans*. *Nature* 434, 1017–1021 (2005).
23. Fraser, J. A. *et al.* Same-sex mating and the origin of the Vancouver Island *Cryptococcus gattii* outbreak. *Nature* 437, 1360–1364 (2005).
24. Lin, X. *et al.* Diploids in the *Cryptococcus neoformans* serotype A population homozygous for the  $\alpha$  mating type originate via unisexual mating. *PLoS Pathog.* 5, e1000283 (2009).
25. Bui, T., Lin, X., Malik, R., Heitman, J. & Carter, D. Isolates of *Cryptococcus neoformans* from infected animals reveal genetic exchange in unisexual,  $\alpha$  mating type populations. *Eukaryot. Cell* 7, 1771–1780 (2008).
26. Smulian, A. G., Sesterhenn, T., Tanaka, R. & Cushion, M. T. The *ste3* pheromone receptor gene of *Pneumocystis carinii* is surrounded by a cluster of signal transduction genes. *Genetics* 157, 991–1002 (2001).
27. Noble, S. M. & Johnson, A. D. Strains and strategies for large-scale gene deletion studies of the diploid human fungal pathogen *Candida albicans*. *Eukaryot. Cell* 4, 298–309 (2005).
28. Reuß, O., Vik, A., Kolter, R. & Morschhauser, J. The SAT1 flipper, an optimized tool for gene disruption in *Candida albicans*. *Gene* 341, 119–127 (2004).
29. Guthrie, C. & Fink, G. R. *Guide to Yeast Genetics and Molecular Biology* (Academic Press, 1991).
30. Lockhart, S. R. *et al.* In *Candida albicans*, white-opaque switchers are homozygous for mating type. *Genetics* 162, 737–745 (2002).

**Supplementary Information** is linked to the online version of the paper at [www.nature.com/nature](http://www.nature.com/nature).

**Acknowledgements** The authors would like to thank D. MacCallum and the Aberdeen Fungal Group for strains, and J. Laney, T. Serio, R. Sherwood and M. Tessmer for discussions and critical reading of the manuscript. We also thank D. Koveal and S. Gilman for assistance during the preliminary stages of this work. R.J.B. holds an Investigator in the Pathogenesis of Infectious Disease Award from the Burroughs Wellcome Fund. K.A. was supported by a training grant for Graduate Assistance in Areas of National Need.

**Author Contributions** K.A. constructed mutant strains, analysed mating phenotypes, quantified mating frequencies and performed biofilm assays. D.S. constructed mutant strains, quantified mating frequencies and performed biofilm and halo assays. R.J.B. constructed mutant strains, quantified mating frequencies, performed adherence assays and analysed mating zygotes. K.A. and R.J.B. were involved in study design and writing of the manuscript.

**Author Information** Reprints and permissions information is available at [www.nature.com/reprints](http://www.nature.com/reprints). Correspondence and requests for materials should be addressed to R.J.B. (Richard\_Bennett@brown.edu).



## METHODS

**Strain/plasmid construction.** The parental strains for SC5314-derived mutants were based on auxotrophic strains described previously<sup>10</sup>. Gene deletions were constructed using the fusion PCR or *SAT1* flipper methods described previously<sup>27,28</sup>. All strains are listed in Supplementary Table 1. The *bar1* mutant strains CAY320/321 were generated as described previously<sup>10</sup> except an *ARG4* marker was used in place of the *HIS1* marker. To delete *STE2*, oligonucleotides 1/2 were used to amplify the 5' flank and oligonucleotides 3/4 to amplify the 3' flank of the gene from SC5314. Oligonucleotides 1/4 were then used to generate a disruption cassette containing either the *LEU2* or *HIS1* selectable marker<sup>27</sup>. The cassette was transformed into RBY1118 and integration checked using oligonucleotides 5 or 6 together with primers internal to the marker, and loss of the ORF was confirmed by PCR using oligonucleotides 7/8, resulting in strains RBY1107 and RBY1108. A similar method was used to delete *STE3* and *MF $\alpha$*  genes. For *STE3*, oligonucleotides 9/10 and 11/12 were used to amplify the 5' and 3' flanks, respectively, whereas for *MF $\alpha$* , oligonucleotides 17/18 and 19/20 were used to amplify the flanking regions. Disruption cassettes were then generated using oligonucleotides 9/12 and 17/20 to amplify the selective marker together with flanking gene sequences. Correct integration of the cassette at *STE3* was confirmed using flanking primers 13/14 and loss of the ORF using 15/16, resulting in strains RBY1113 and RBY1114. For *MF $\alpha$* , integration was checked using oligonucleotides 21/22 and deletion of the ORF was confirmed using oligonucleotides 23/24 resulting in strains RBY1081 and RBY1082. To generate the plasmid pDS1 for deletion of *BAR1*, oligonucleotides 25/26 were used to generate a 5' flank that was digested with *ApaI* and *XhoI* and ligated into pSFS2a. Subsequently, oligonucleotides 27/28 were used to generate a 3' flank that was digested with *SacI* and *SacII* and ligated into the vector to generate plasmid pDS1. *ApaI*/*SacI*-digested pDS1 was then used to transform strains RBY1107, RBY1113 and RBY1081, to generate *bar1* mutant strains DSY760/761, DSY792/793 and DSY762/768, respectively. Integration was checked using oligonucleotides 29/30 paired with oligonucleotides internal to pSFS2a, and loss of the ORF was confirmed using oligonucleotides 31/32. To generate plasmids for integration of GFP under the control of a test promoter, GFP was amplified from plasmid pNIM1<sup>31</sup> using oligonucleotides 33/34, cut with *ApaI* and *SalI* and ligated into an *ApaI*/*XhoI*-digested pSFS2a, generating pRS2. The promoters of *FUS1* and *FIG1* were then amplified using oligonucleotides 35/36 and 37/38, respectively. The PCR

products were digested with *KpnI*/*ApaI* and ligated into pRS2 to generate pDS2 and pDS3 respectively. The plasmid pDS2 was linearized with *AflII* and transformed into RBY1117 and RBY1197 and integration checked using oligonucleotides 39/40 to generate DSY702 and DSY690, respectively. The plasmid pDS3 was linearized with *AflII* and transformed into RBY1117 and RBY1220, and integration checked using oligonucleotides 40/41 to generate DSY700 and DSY696, respectively. To generate the mating tester strains DSY170/171, RBY1118 was transformed with a fragment containing *SAT1* from the plasmid pNIM1. This fragment targets an intergenic region of chromosome 5 near *MTL* and was created using oligonucleotides 42/43. To generate the strain CAY371, a *WOR1*-*YFP* fusion construct (white-opaque regulator 1-yellow fluorescent protein) was transformed into CAY320 (ref. 32). To generate fluorescently labelled nuclei, strains RBY1197 and DSY168 were transformed with *HTB*-*RFP* and *HTB*-*YFP* constructs as described previously<sup>21,33</sup> to generate strains DSY906 and DSY908, respectively. Select clinical isolates were also obtained from D. MacCallum of the Aberdeen Fungal group and grown on sorbose media to generate homozygous **a** and  $\alpha$  derivatives, as described previously<sup>34</sup>.

**Clinical mating crosses.** All clinical isolates were crossed with the SC5314  $\Delta$ *bar1* **a** strain, CAY371. Clinical  $\alpha$  isolates correspond as follows: 1, AM2003/0165; 2, L1086 derivative (DSY159); 3, YSU751 derivative (DSY161); 4, Hun92 derivative (DSY165); 5, IHEM16614 derivative (DSY183); 6, 19F; 7, 78048; 8, J981315 derivative (DSY167); CAY371 with WO-1 is not shown. Clinical **a** isolates correspond as follows: 9, L1086 derivative (DSY164); 10, P37005; 11, 12C; 12, L26; 13, AM2003/0191 derivative (DSY162); 14, IHEM16614 derivative (DSY168); 15, T101; 16, J981315 derivative (DSY194); 17, RIH09; 18, AM2005/0377.

31. Park, Y. N. & Morschhauser, J. Tetracycline-inducible gene expression and gene deletion in *Candida albicans*. *Eukaryot. Cell* **4**, 1328–1342 (2005).
32. Alby, K. & Bennett, R. J. Stress-induced phenotypic switching in *Candida albicans*. *Mol. Biol. Cell* **20**, 3178–3191 (2009).
33. Sherwood, R. K. & Bennett, R. J. Microtubule motor protein Kar3 is required for normal mitotic division and morphogenesis in *Candida albicans*. *Eukaryot. Cell* **7**, 1460–1474 (2008).
34. Janbon, G., Sherman, F. & Rustchenko, E. Monosomy of a specific chromosome determines L-sorbose utilization: a novel regulatory mechanism in *Candida albicans*. *Proc. Natl Acad. Sci. USA* **95**, 5150–5155 (1998).

## LETTERS

# Programming cells by multiplex genome engineering and accelerated evolution

Harris H. Wang<sup>1,2,3\*</sup>, Farren J. Isaacs<sup>1\*</sup>, Peter A. Carr<sup>4,5</sup>, Zachary Z. Sun<sup>6</sup>, George Xu<sup>6</sup>, Craig R. Forest<sup>7</sup> & George M. Church<sup>1</sup>

The breadth of genomic diversity found among organisms in nature allows populations to adapt to diverse environments<sup>1,2</sup>. However, genomic diversity is difficult to generate in the laboratory and new phenotypes do not easily arise on practical timescales<sup>3</sup>. Although *in vitro* and directed evolution methods<sup>4–9</sup> have created genetic variants with usefully altered phenotypes, these methods are limited to laborious and serial manipulation of single genes and are not used for parallel and continuous directed evolution of gene networks or genomes. Here, we describe multiplex automated genome engineering (MAGE) for large-scale programming and evolution of cells. MAGE simultaneously targets many locations on the chromosome for modification in a single cell or across a population of cells, thus producing combinatorial genomic diversity. Because the process is cyclical and scalable, we constructed prototype devices that automate the MAGE technology to facilitate rapid and continuous generation of a diverse set of genetic changes (mismatches, insertions, deletions). We applied MAGE to optimize the 1-deoxy-D-xylulose-5-phosphate (DXP) biosynthesis pathway in *Escherichia coli* to overproduce the industrially important isoprenoid lycopene. Twenty-four genetic components in the DXP pathway were modified simultaneously using a complex pool of synthetic DNA, creating over 4.3 billion combinatorial genomic variants per day. We isolated variants with more than fivefold increase in lycopene production within 3 days, a significant improvement over existing metabolic engineering techniques. Our multiplex approach embraces engineering in the context of evolution by expediting the design and evolution of organisms with new and improved properties.

With the advent of next-generation fluorescent DNA sequencing<sup>10</sup>, our ability to sequence genomes has greatly outpaced our ability to modify genomes. Existing cloning-based technologies are confined to serial and inefficient introduction of single DNA constructs into cells, requiring laborious and outdated genetic engineering techniques. Whereas *in vivo* methods such as recombination-based genetic engineering (recombineering) have enabled efficient modification of single genetic targets using single-stranded DNA (ssDNA)<sup>11–14</sup>, no such attempts have been made to modify genomes on a large and parallel scale. MAGE provides a highly efficient, inexpensive and automated solution to simultaneously modify many genomic locations (for example, genes, regulatory regions) across different length scales, from the nucleotide to the genome level (Fig. 1).

Efficiency of the MAGE process was characterized using a modified *E. coli* strain (EcNR2). Mediated by the bacteriophage  $\lambda$ -Red ssDNA-binding protein  $\beta$ , allelic replacement is achieved in EcNR2 by directing ssDNA or oligonucleotides (oligos) to the lagging strand

of the replication fork during DNA replication<sup>14</sup>. We optimized a number of parameters (see Supplementary Information, Supplementary Fig. 2 and Supplementary Table 1) to maximize efficiency of oligo-mediated allelic replacement. To generate sequence diversity in any region of the chromosome by allelic replacement, a pool of targeting oligos is repeatedly introduced into a cell. Under optimized conditions, we can successfully introduce new genetic modifications in >30% of the cell population (Supplementary Fig. 2d) every 2–2.5 h.

Oligo-mediated allelic replacement is capable of introducing a variety of genetic modifications at high efficiency. The efficiency of generating a mismatch or insertion modification is correlated to the amount of homologous sequence between the oligo and its chromosomal target (Fig. 2a, b); the efficiency of producing a deletion modification is correlated to the size of the deletion (Fig. 2c). Figure 2d shows that the predicted two-state hybridization free energy  $\Delta G$  (ref. 15) between the oligo and target chromosomal sequence is a predictor of the allelic replacement efficiency. Thus, in a pool of oligos with degenerate sequences, oligos with more homology to the target will be incorporated in the chromosome at a higher frequency than those with less homology. This feature of MAGE enables tunable generation of divergent sequences along favourable evolutionary paths.

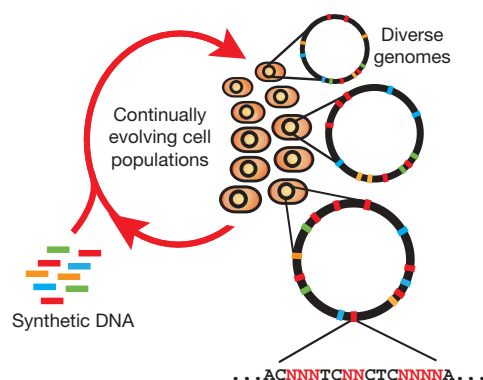


**Figure 1 | Multiplex automated genome engineering enables the rapid and continuous generation of sequence diversity at many targeted chromosomal locations across a large population of cells through the repeated introduction of synthetic DNA.** Each cell contains a different set of mutations, producing a heterogeneous population of rich diversity (denoted by distinct chromosomes in different cells). Degenerate oligo pools that target specific genomic positions enable the generation of a diverse set of sequences at each chromosomal location.

<sup>1</sup>Department of Genetics, Harvard Medical School, Boston, Massachusetts 02115, USA. <sup>2</sup>Program in Biophysics, Harvard University, Cambridge, Massachusetts 02138, USA. <sup>3</sup>Program in Medical Engineering Medical Physics, Harvard-MIT Division of Health Sciences and Technology, <sup>4</sup>The Center for Bits and Atoms, <sup>5</sup>Media Lab, Massachusetts Institute of Technology, Cambridge, Massachusetts 02139, USA. <sup>6</sup>Harvard College, Cambridge, Massachusetts 02138, USA. <sup>7</sup>George W. Woodruff School of Mechanical Engineering, Georgia Institute of Technology, Atlanta, Georgia 30332, USA.

\*These authors contributed equally to this work.

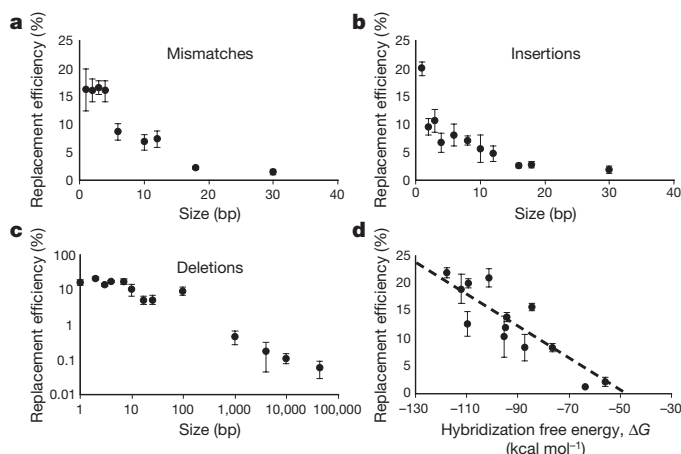


**Figure 2 | Characterization of allelic replacement efficiency as a function of the type and scale of genetic modifications.** **a**, Introducing mismatch mutations of up to 30 bp. **b**, Inserting exogenous sequences of up to 30 bp. **c**, Removing up to 45 kbp of chromosomal sequence using a single oligo. **d**, Correlation of replacement efficiency and two-state hybridization energy  $\Delta G$  between the oligo and the targeted complement region in the genome. See Supplementary Fig. 1 for an illustration of oligo interaction with genomic targets and Supplementary Table 3 for a list of oligos and corresponding  $\Delta G$  values. Dashed line is the linear regression correlation ( $y = -0.288x - 13.7$ ,  $R^2 = 0.799$ ). All oligos used were 90 bp with two phosphorothioate bonds at the 3' and 5' ends. All error bars indicate  $\pm$  s.d.;  $n = 3$ .

To determine the rate at which MAGE generates sequence diversity, we used three different 90-mer oligos to produce mismatch changes in a targeted region of the *lacZ* gene in three distinct cell populations. The *cN6* and *cN30* oligos contained 6 and 30 consecutive degenerate bases, respectively; the *iN6* oligos contained 6 degenerate bases interspersed across a 30-bp region (Fig. 3). For these cell populations, the targeted *lacZ* region was sequenced in 96 random clonal isolates after MAGE cycles 2, 5, 10 and 15 that provided a snapshot of the genotypic variation in each population. Through successive cycles of MAGE, the chromosomal sequence of the *lacZ* region increasingly diverged away from wild type (Fig. 3). For *cN6*, after five MAGE cycles, we detected an average change of 3.1 bp per cell across the population (Fig. 3 inset, blue line), which equates to the generation of more than  $4.3 \times 10^9$  bp

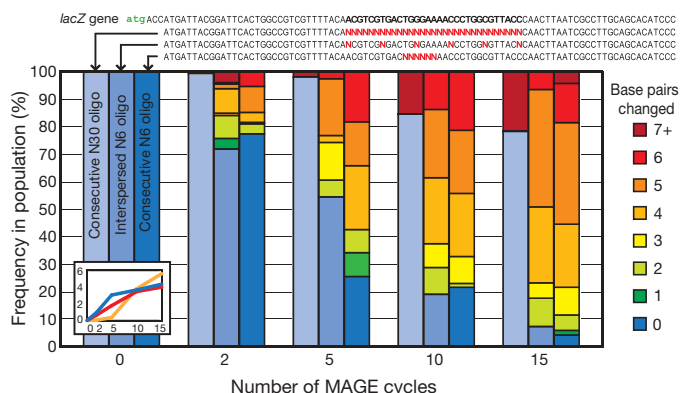


**Figure 3 | Sequence diversity generated across three separate cell populations as a function of the number of MAGE cycles.** Three 90-mer oligo pools were investigated: *cN30*, *iN6* and *cN6*. *cN30* contains oligos with 30 bp of consecutive degeneracy; *iN6* contains oligos with 6 bp of degeneracy spaced every 5 bp; *cN6* contains oligos with 6 bp of consecutive degeneracy. Frequency of strains in each population that contains 0 to 7+ bp of differences from the wild-type *lacZ* sequence are colour-coded. The inset shows average number of base pairs changed from wild type across the whole cell population as a function of the number of MAGE cycles using the three oligo pools *cN30* (orange line), *cN6* (blue line) and *iN6* (red line).

of variation per day (3.1 bp changes per five cycles in  $7 \times 10^8$  cells at 10 cycles per day). Within 15 cycles, cell populations containing all possible *N6* genotype combinations were generated using either *cN6* or *iN6* oligos. Because the replacement efficiency for a 30-bp mismatching oligo is lower (1.5% from Fig. 2a), only 21.8% of the *cN30* cell population had undergone allelic replacement after 15 cycles. We detected an average change of 5.6 bp per cell from the wild-type sequence across the whole *cN30* population (Fig. 3 inset, orange line).

The depth at which MAGE generates diversity is determined by a combination of three factors: (1) the degree of sequence variation desired at each locus; (2) the number of loci targeted; and (3) the number of MAGE cycles performed. When a single locus is targeted using a degenerate oligo pool, genetic diversity is generated across the population at that locus and is a function of the oligo pool complexity only. If more than one locus is targeted simultaneously, diversity is generated through the combinatorial arrangement of the different

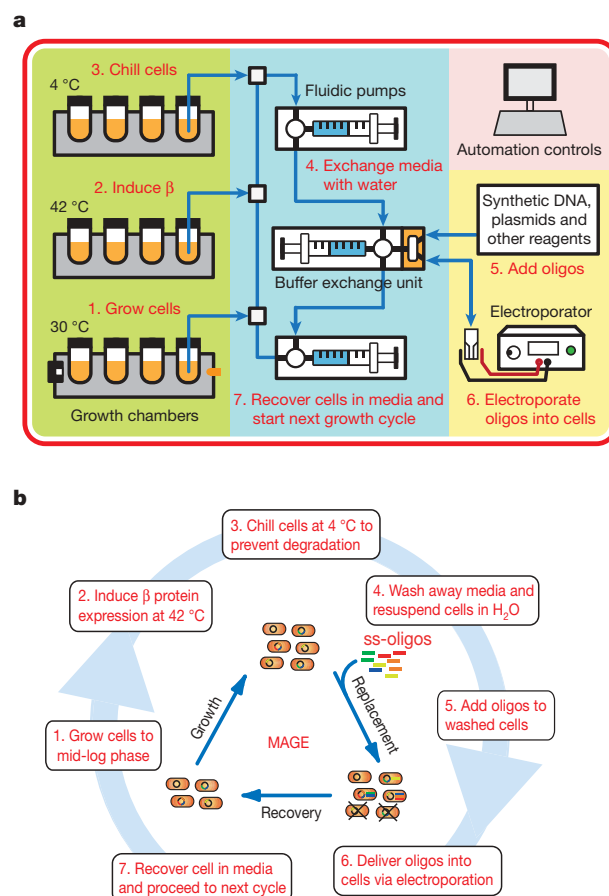


**Figure 4 | MAGE automation.** **a**, Detailed schematic diagram of MAGE prototype including climate-regulated growth chambers with real-time cell density monitors (green), anti-fouling fluidics for transfer of cells between growth chambers and exchange of media and buffers (blue), and real-time generation of competent cells for transformation with synthetic DNA (yellow). Cultures are carried through different MAGE steps (that is, cell growth, heat-shock, cooling). Cells are made electrocompetent by concentration onto a filter membrane and resuspension with wash buffer. Oligos are delivered into cells by electroporation. **b**, Step-by-step diagram of MAGE cycling steps at a total run time of 2–2.5 h per cycle. Owing to high voltage ( $18 \text{ kV cm}^{-1}$ ) electroporation,  $\sim 95\%$  of cells are killed at each cycle. Hence, the electroporation event serves to both introduce oligos into cells and to dilute the cell population, cells are then recovered and grown to mid-log phase ( $7 \times 10^8 \text{ cells ml}^{-1}$ ) in liquid medium for the subsequent cycle.



modified loci. The frequency at which each locus is modified can be computationally predicted through a binomial distribution (Supplementary Fig. 3). Although the cell population at any cycle may reflect only a subset of all variants theoretically possible, we can cumulatively generate more variants than the actual size of the cell population ( $\sim 7 \times 10^8$  cells) through successive MAGE cycles. Thus, we can generate all variants regardless of population size through computational predictions and continuous cycling by MAGE.

Given the cyclical and scalable nature of our approach, we constructed an integrated prototype device that automates the MAGE process to enable fast and reliable cellular programming. The device contains growth chambers to maintain healthy cell cultures and electroporation modules to repeatedly deliver DNA into the cells, thereby facilitating genome engineering and evolution (Fig. 4, Methods and Supplementary Information). Complex culturing conditions can be programmed into the device for growth of a diverse set of organisms and ecosystems.

To demonstrate an application of the MAGE process, we optimized metabolic flux through the DXP biosynthesis pathway to overproduce the isoprenoid, lycopene, in an *E. coli* strain (EcHW2) that contained the pAC-LYC plasmid that is necessary for the final steps of lycopene production. Twenty endogenous genes (*dxs*, *dxr*, *ispD*, *ispE*, *ispG*, *ispH*, *idi*, *ispA*, *appY*, *rpoS*, *crl*, *elbA*, *elbB*, *yjiD*, *purH*, *rnlA*, *yggT*, *ycgZ*, *ymgA*, *ariR*) documented to increase lycopene yield<sup>16,17</sup> were targeted to tune translation (Fig. 5a). Specifically, for each of the 20 genes, 90-mer oligos containing degenerate ribosome binding site

(RBS) sequences (DDRRRRRDDDD; D = A, G, T; R = A, G) flanked by homologous regions on each side were used, with a total pool complexity of  $4.7 \times 10^5$  ( $3^6 \times 2^5 \times 20$ ). The replaced RBS regions were designed to be more similar to the canonical Shine–Dalgarno sequence (TAAGGAGGT)<sup>18</sup>, giving rise to enhanced translation efficiency. Additionally, four genes (*ytjC*, *fdhF*, *aceE*, *gdhA*) from secondary pathways<sup>19</sup> were targeted for inactivation by oligos that introduced two nonsense mutations in the open reading frame, further improving flux through the DXP pathway. In contrast to prior strategies<sup>20–23</sup> that were experimentally limited by the number of genetic components that could be manipulated at once, here we optimized 24 genes simultaneously to maximize lycopene production.

As many as 15 billion genetic variants ( $4.3 \times 10^8$  bp variations per cycle for 35 MAGE cycles) were generated. Screening of variants was done by isolating colonies that produced intense red pigmentation on Luria–Bertani agar plates. Variants were isolated from  $\sim 10^5$  colonies screened after 5–35 cycles of MAGE (see Supplementary Information), some exhibiting as much as a fivefold increase in lycopene production relative to the EcHW2 ancestral strain (Fig. 5b). Under similar experimental conditions, our highest lycopene yield of  $\sim 9,000$  p.p.m. ( $\mu\text{g}$  per g dry cell weight) is better than documented yields<sup>17,19</sup>. Sequencing of six variants (EcHW2a–EcHW2f) revealed RBS convergence towards consensus-like Shine–Dalgarno sequences in genes localized at the beginning and end of the biosynthesis pathway (*dxs*, *dxr*, *idi*, *ispA*) as well as various gene knockouts from secondary pathways ( $\Delta\text{ytjC}$ ,  $\Delta\text{gdhA}$ ,  $\Delta\text{fdhF}$ ) (Fig. 5c and Supplementary Table 2).

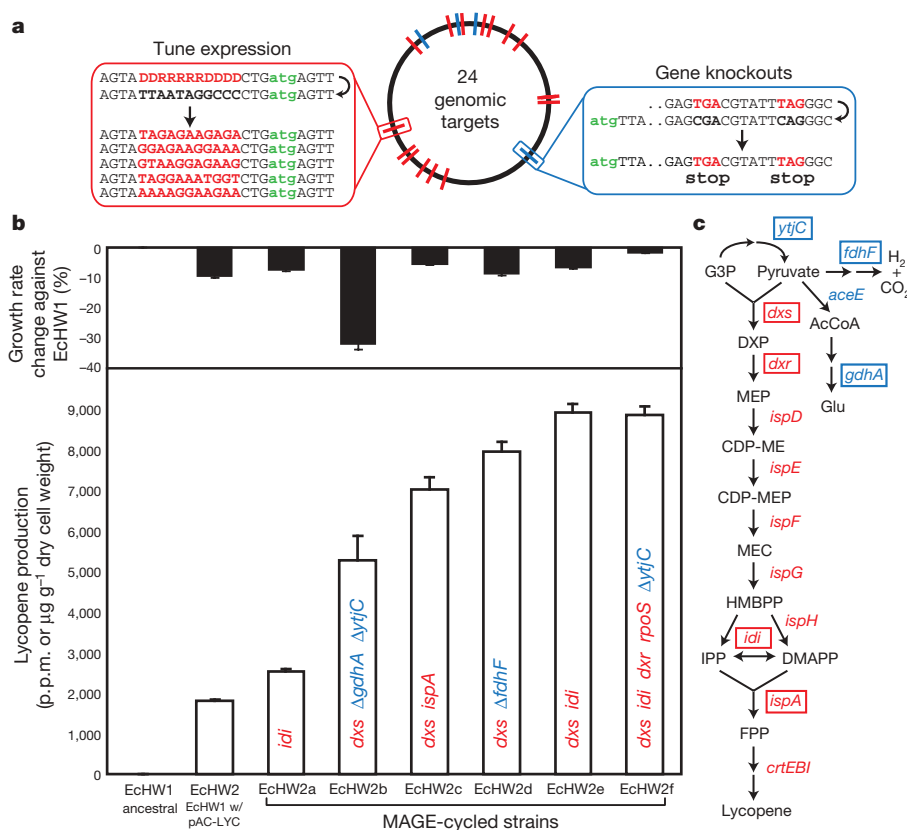


**Figure 5 | Optimization of the DXP biosynthesis pathway for lycopene production.** **a**, Genomic positions of 24 targeted genes with the RBS optimization strategy on the left (red) and gene knockout strategy on the right (blue). The gene knockout strategy involves the introduction of two nonsense mutations. All 90-mer oligos contain two phosphorothioated bases at the 3' and 5' termini. **b**, Black bars represent the growth rate of isolated variants (EcHW2a–f) relative to the ancestral EcHW1 strain. White bars represent lycopene production in p.p.m., which is normalized by dry cell weight in ancestral and mutant strains. Colour-coded labels in each white bar represent genetic modifications found by sequencing. All error

bars indicate  $\pm$  s.d.;  $n = 3$ . **c**, Modifications to the lycopene biosynthesis pathway of isolated variants EcHW2a–f with relevant genes highlighted by rectangular boxes. Blue labels represent knockout targets, red labels represent RBS tuning targets. AcCoA, acetyl-CoA; CDP-ME, 4-diphosphocytidyl-2-C-methyl-D-erythritol; CDP-MEP, 4-diphosphocytidyl-2-C-methyl-D-erythritol-2-phosphate; DMAPP, dimethylallyl diphosphate; FPP, farnesyl diphosphate; G3P, glyceraldehyde 3-phosphate; HMBPP, (E)-4-hydroxy-3-methylbut-2-enyl-diphosphate; IPP, isopentenyl diphosphate; MEP, 2-C-methyl-D-erythritol-4-phosphate; MEC, 2C-methyl-D-erythritol-2,4-cyclodiphosphate.

Different tuning parameters of the lycopene pathway can be individually and combinatorially assessed in the isolated variants. For example, translation optimization of *idi* alone (EcHW2a) increased lycopene production by 40%. Whereas optimizing *dxs* and *idi* increased lycopene production by 390% (EcHW2e), additional optimization at *rpoS* and *dxr*, along with inactivation of *ytjC*, improved the growth rate of EcHW2f to that of the EcHW1 ancestor. Interestingly, *rpoS* is the alternative RNA polymerase subunit sigma factor  $\sigma^S$ , the master stress response regulator, and its upregulation can increase stress resistance to the accumulation of lycopene, a very hydrophobic molecule<sup>17</sup>. *ytjC* is an uncharacterized phosphoglycerate mutase enzyme and is thought to increase metabolic flux through the DXP pathway by increasing the accumulation of glyceraldehyde 3-phosphate intermediates<sup>19</sup>. Inactivation of glutamate dehydrogenase (*gdhA*) increases lycopene production, but causes a 32% decrease in growth rate of EcHW2b relative to wild type. Combinations of genetic modifications can also be assessed against each other. For example, an optimized *dxs* and *idi* strain (EcHW2e) produces 12% more lycopene than a strain with *dxs* and  $\Delta fdhF$  (EcHW2d) and 27% more than a strain with *dxs* and *ispA* modifications (EcHW2c). The optimized DXP biosynthesis pathway presented here can be used to produce many other isoprenoid compounds of industrial and pharmaceutical relevance<sup>24</sup>.

The diversity (that is, the degree of sequence change per target) generated by MAGE is adjustable and the specificity of targeting is always high. Oligos with defined sequences produce well-defined modification, whereas oligos with degenerate sequences produce high-diversity modifications tailored for exploring a vast sequence space. In this study, we used well-defined oligos to inactivate protein-coding sequences and high-diversity degenerate oligos to modify and sample different RBS sequences. We have also used the MAGE platform to perform whole-genome recoding of *E. coli* to enhance the incorporation of non-natural amino acids into proteins<sup>25</sup> and construct safer and multi-virus-resistant strains (F.J.I. *et al.*, manuscript in preparation). MAGE is thus a complementary technology to *de novo* genome synthesis<sup>26</sup>, allowing the tuning of synthetic and natural genomes *in vivo* for various applications.

MAGE is also an accelerated evolution platform that permits the repeated introduction and maintenance of many neutral (or deleterious) mutations in the cell population. Although these mutations would normally disappear in the population via genetic drift or natural selection, MAGE accelerates the rate of their accumulation in any individual cell, thus increasing the likelihood of finding sets of mutations that may interact synergistically to produce a surprisingly beneficial phenotype. Using this technology, we could engineer or evolve cells with higher transfection efficiency (for example, harnessing natural competence systems<sup>27</sup>), increased allelic replacement efficiency (for example, expressing higher levels or mutants<sup>28</sup> of the  $\lambda$ -Red  $\beta$  protein) and perform large-scale bacterial artificial chromosome engineering. The simple allelic replacement mechanism could make this method amenable for use in other organisms, given that other ssDNA-binding protein homologues are functional<sup>29</sup>. Currently, 30 US dollars of commercially synthesized oligos can introduce up to 27 bp of modification at full degeneracy for a single genomic target. To target many loci, obtaining oligos from programmable DNA microchips<sup>30</sup> can significantly decrease the cost in comparison to traditional oligo synthesis. We envision that large-scale pipelines to program synthetic organisms and ecosystems<sup>10</sup> will greatly benefit from integration of hardware, software and wetware to engineer and evolve microbial, plant and animal systems.

## METHODS SUMMARY

**Strains.** The EcNR2 strain is MG1655 with  $\lambda$ -prophage::*bioA/bioB* and *cmR::mutS*. The EcHW2 strain is MG1655 with  $\lambda$ -prophage::*bioA/bioB*, *kanR::mutS* and pAC-LYC plasmid. EcHW2a–f strains were MAGE-cycled EcHW2 derivatives containing DXP pathway modifications. Details of strains used are described in Methods.

**Allelic replacement.** Liquid cell cultures were inoculated from colonies obtained from a plate and grown at 30 °C to an absorbance (600 nm) of  $\sim 0.7$  ( $\sim 7 \times 10^8$  cells ml<sup>-1</sup>) in a rotor drum at 200 r.p.m. To induce expression of the  $\lambda$ -Red recombination proteins (Exo, Beta and Gam), cell cultures were shifted to 42 °C for 15 min and then immediately chilled on ice. In a 4 °C environment, 1 ml of cells was centrifuged at 16,000g for 30 s. Supernatant medium was removed and cells were resuspended in dH<sub>2</sub>O (Gibco catalogue number 15230). This process was repeated twice with water. Supernatant water was removed and oligos suspended in water were added to the cell pellet. The oligos/cells mixture was transferred to a pre-chilled 1 mm gap electroporation cuvette (Bio-Rad) and electroporated with a Bio-Rad GenePulser electroporation system under the following parameters: 1.8 kV, 200  $\Omega$  and 25  $\mu$ F. LB-min medium (1–3 ml) was immediately added to the electroporated cells. The cells were recovered from electroporation and grown at 30 °C for 2–2.5 h. Once cells reached mid-logarithmic growth they were used in additional MAGE cycles, isolated or assayed for genotype and/or phenotype analysis.

**Lycopene assay.** EcHW2 and derivatives (EcHW2a–f) were quantitatively assessed for lycopene production after 24 h of growth in LB-min-chloramphenicol liquid medium at 30 °C. Lycopene was extracted and quantified at an absorbance of 470 nm (see Methods). Lycopene yield was calculated by normalizing the amount of lycopene extracted to the dry cell weight.

**Full Methods** and any associated references are available in the online version of the paper at [www.nature.com/nature](http://www.nature.com/nature).

Received 6 March; accepted 29 May 2009.

Published online 26 July 2009.

- Venter, J. C. *et al.* Environmental genome shotgun sequencing of the Sargasso Sea. *Science* **304**, 66–74 (2004).
- Tringe, S. G. *et al.* Comparative metagenomics of microbial communities. *Science* **308**, 554–557 (2005).
- Elena, S. F. & Lenski, R. E. Evolution experiments with microorganisms: the dynamics and genetic bases of adaptation. *Nature Rev. Genet.* **4**, 457–469 (2003).
- Ellington, A. D. & Szostak, J. W. *In vitro* selection of RNA molecules that bind specific ligands. *Nature* **346**, 818–822 (1990).
- Cramer, A., Raillard, S.-A., Bermudez, E., Stemmer, W. P. & C. DNA shuffling of a family of genes from diverse species accelerates directed evolution. *Nature* **391**, 288–291 (1998).
- Joo, H., Lin, Z. & Arnold, F. H. Laboratory evolution of peroxide-mediated cytochrome P450 hydroxylation. *Nature* **399**, 670–673 (1999).
- Zhang, Y. X. *et al.* Genome shuffling leads to rapid phenotypic improvement in bacteria. *Nature* **415**, 644–646 (2002).
- Pfleger, B. F., Pitera, D. J., Smolke, C. D. & Keasling, J. D. Combinatorial engineering of intergenic regions in operons tunes expression of multiple genes. *Nature Biotechnol.* **24**, 1027–1032 (2006).
- Cadwell, R. C. & Joyce, G. F. Randomization of genes by PCR mutagenesis. *PCR Methods Appl.* **2**, 28–33 (1992).
- Shendure, J. *et al.* Accurate multiplex polony sequencing of an evolved bacterial genome. *Science* **309**, 1728–1732 (2005).
- Zhang, Y., Buchholz, F., Muylers, J. P. & Stewart, A. F. A new logic for DNA engineering using recombination in *Escherichia coli*. *Nature Genet.* **20**, 123–128 (1998).
- Costantino, N. & Court, D. L. Enhanced levels of  $\lambda$  Red-mediated recombinants in mismatch repair mutants. *Proc. Natl Acad. Sci. USA* **100**, 15748–15753 (2003).
- Sharan, S. K., Thomason, L. C., Kuznetsov, S. G. & Court, D. L. Recombineering: a homologous recombination-based method of genetic engineering. *Nature Protocols* **4**, 206–223 (2009).
- Ellis, H. M., Yu, D., DiTizio, T. & Court, D. L. High efficiency mutagenesis, repair, and engineering of chromosomal DNA using single-stranded oligonucleotides. *Proc. Natl Acad. Sci. USA* **98**, 6742–6746 (2001).
- Markham, N. R. & Zuker, M. DINAMelt web server for nucleic acid melting prediction. *Nucleic Acids Res.* **33**, W577–W581 (2005).
- Jin, Y. S. & Stephanopoulos, G. Multi-dimensional gene target search for improving lycopene biosynthesis in *Escherichia coli*. *Metab. Eng.* **9**, 337–347 (2007).
- Kang, M. J. *et al.* Identification of genes affecting lycopene accumulation in *Escherichia coli* using a shot-gun method. *Biotechnol. Bioeng.* **91**, 636–642 (2005).
- Chen, H., Bjerknes, M., Kumar, R. & Jay, E. Determination of the optimal aligned spacing between the Shine – Dalgarno sequence and the translation initiation codon of *Escherichia coli* mRNAs. *Nucleic Acids Res.* **22**, 4953–4957 (1994).
- Alper, H., Jin, Y. S., Moxley, J. F. & Stephanopoulos, G. Identifying gene targets for the metabolic engineering of lycopene biosynthesis in *Escherichia coli*. *Metab. Eng.* **7**, 155–164 (2005).
- Alper, H., Miyaoku, K. & Stephanopoulos, G. Construction of lycopene-overproducing *E. coli* strains by combining systematic and combinatorial gene knockout targets. *Nature Biotechnol.* **23**, 612–616 (2005).
- Farmer, W. R. & Liao, J. C. Precursor balancing for metabolic engineering of lycopene production in *Escherichia coli*. *Biotechnol. Prog.* **17**, 57–61 (2001).

22. Kim, S. W. & Keasling, J. D. Metabolic engineering of the nonmevalonate isopentenyl diphosphate synthesis pathway in *Escherichia coli* enhances lycopene production. *Biotechnol. Bioeng.* **72**, 408–415 (2001).
23. Yuan, L. Z., Rouviere, P. E., Larossa, R. A. & Suh, W. Chromosomal promoter replacement of the isoprenoid pathway for enhancing carotenoid production in *E. coli*. *Metab. Eng.* **8**, 79–90 (2006).
24. Khosla, C. & Keasling, J. D. Metabolic engineering for drug discovery and development. *Nature Rev. Drug Discov.* **2**, 1019–1025 (2003).
25. Cropp, T. A. & Schultz, P. G. An expanding genetic code. *Trends Genet.* **20**, 625–630 (2004).
26. Gibson, D. G. *et al.* Complete chemical synthesis, assembly, and cloning of a *Mycoplasma genitalium* genome. *Science* **319**, 1215–1220 (2008).
27. Metzgar, D. *et al.* *Acinetobacter* sp. ADP1: an ideal model organism for genetic analysis and genome engineering. *Nucleic Acids Res.* **32**, 5780–5790 (2004).
28. Nakayama, M. & Ohara, O. Improvement of recombination efficiency by mutation of Red proteins. *Biotechniques* **38**, 917–924 (2005).
29. Datta, S., Costantino, N., Zhou, X. & Court, D. L. Identification and analysis of recombineering functions from Gram-negative and Gram-positive bacteria and their phages. *Proc. Natl Acad. Sci. USA* **105**, 1626–1631 (2008).
30. Tian, J. *et al.* Accurate multiplex gene synthesis from programmable DNA microchips. *Nature* **432**, 1050–1054 (2004).

**Supplementary Information** is linked to the online version of the paper at [www.nature.com/nature](http://www.nature.com/nature).

**Acknowledgements** We are grateful to J. Jacobson for his insights and advice throughout this work. We thank D. Court for his insights and sharing strain DY330, N. Reppas for advice and sharing strain EcNR2, F. X. Cunningham for sharing pAC-LYC, and B. H. Sterling for assistance in constructing the EcF15 strain. We also thank M. Jewett, J. Aach, D. Bang, S. Kosuri and members of the Church laboratory for advice and discussions. We thank the NSF, DOE, DARPA, the Wyss Institute for Biologically Inspired Engineering and training fellowships from the NIH and NDSEG (H.H.W.) for supporting this research.

**Author Contributions** H.H.W., F.J.I. and G.M.C. conceived the study jointly with P.A.C.; H.H.W. and F.J.I. designed and performed experiments with assistance from P.A.C., Z.Z.S., G.X. and C.R.F.; H.H.W. and F.J.I. wrote the manuscript; G.M.C. supervised all aspects of the study.

**Author Information** Reprints and permissions information is available at [www.nature.com/reprints](http://www.nature.com/reprints). The authors declare competing financial interests: details accompany the full-text HTML version of the paper at [www.nature.com/nature](http://www.nature.com/nature). Correspondence and requests for materials should be addressed to H.H.W. ([hhwang@genetics.med.harvard.edu](mailto:hhwang@genetics.med.harvard.edu)) or F.J.I. ([farren@alumni.upenn.edu](mailto:farren@alumni.upenn.edu)).



## METHODS

**Strains and culture conditions.** The  $\lambda$  prophage was obtained from strain DY330<sup>31</sup>, modified to include the *bla* gene and introduced into wild-type MG1655 *E. coli* by P1 transduction at the *bioA/bioB* gene locus and selected on ampicillin to yield the strain EcNR1 ( $\lambda$ -Red<sup>+</sup>). Replacement of *mutS* with the chloramphenicol resistance gene (*cmR* cassette) in EcNR1 produced EcNR2 (*mutS*<sup>-</sup>,  $\lambda$ -Red<sup>+</sup>). EcNR2 was grown in low salt LB-min medium (10 g tryptone, 5 g yeast extract, 5 g NaCl in 1 l dH<sub>2</sub>O) for optimal electroporation efficiency. A premature stop codon was introduced into the *cmR* gene of EcNR2 with oligo cat\_fwd\_stop (Supplementary Table 3) to produce EcFI5, thus inactivating the *cmR* gene. An oligo (cat\_fwd\_restore) containing the wild-type sequence was used to restore the *CmR* phenotype. The pAC-LYC plasmid<sup>32</sup> containing genes *crtE*, *crtB* and *crtI* was electroporated into EcNR1 to generate EcHW1, which produces lycopene at basal levels. Replacement of *mutS* with a kanamycin resistance gene in EcHW1 produced EcHW2.

**Oligonucleotides and DNA sequencing.** All oligonucleotides were obtained from Integrated DNA Technologies with standard purification. Oligonucleotides used in the MAGE process contained the following modifications: (1) 30–110 bp in length for optimization experiments; (2) different numbers of phosphorothioated bases; and (3) degenerate nucleotides as described elsewhere in this paper. Additional primers were purchased to amplify relevant genetic regions of the lycopene pathway to sequence strains that expressed high levels of lycopene. DNA sequencing to confirm allelic replacements was performed by Agencourt Bioscience.

**LacZ and chloramphenicol replacement efficiency assays.** Replacement efficiency was characterized by performing the allelic replacement protocol on EcNR2 cells using 90-mer oligos (Supplementary Table 3) that produced a premature stop codon in the chromosomal *lacZ* gene. In general, 250–500 cells were plated on LB-min containing 5-bromo-4-chloro-3-indoyl- $\beta$ -D-galactoside and isopropyl- $\beta$ -D-thiogalactoside (USB Biochemicals) agar plates. Efficiency of allelic replacement was calculated by taking the ratio of the number of white colonies to the total number of colonies on plates. A similar strategy was used in the *cmR* gene recovery experiments with strain EcFI5 where 30–110mer oligos were used to determine optimal oligo length for allelic replacement (Supplementary Fig. 2a). These oligos contained two phosphorothioate bonds at both the 5' and 3' termini. Cells were plated on LB-min-chloramphenicol and LB-min agar plates and grown overnight. Efficiency of allelic replacement was calculated by taking the ratio of the number of colonies on LB-min-chloramphenicol plates to the number of colonies on LB-min plates.

**MAGE automation device.** Cells were grown in sterilized 10-ml glass vials placed in thermally conductive blocks. The growth chambers were climate-regulated through temperature controllers that actuate Peltier heating/cooling elements. Cultures acclimatized quickly (<15 s) in chambers held at different temperatures due to small volumes (for example, 3 ml). Aeration of the culture was achieved through agitation of the chambers at 300 r.p.m. using an orbital shaker. Real-time monitoring of growth rates was achieved by detecting changes in light transmittance across the chamber from light-emitting diodes emitting at 600 nm. Cultures were transferred between chambers through solenoid isolation

valves using syringe pumps. Cells were made electrocompetent by a filtration system, which uses a syringe pump to concentrate cells onto a filter membrane (0.22  $\mu$ m pore size) and resuspend them off the membrane with appropriate electroporation buffer (for example, dH<sub>2</sub>O). Single-stranded oligos (or PCR products) were electroporated into cells in a conductive cuvette with an electric pulse (18 kV cm<sup>-1</sup>). After each cycle, the entire system (chambers, syringes, filters) was washed with 70% ethanol followed by dH<sub>2</sub>O three times to reduce contamination and biofilm formation. All instruments were digitally controlled through software written in the LabView programming environment (National Instruments).

Cultures were initially inoculated into 3 ml of medium in the growth chamber. The device then executed repeatedly and continuously through the following steps: (1) grow cells at 30 °C to a pre-set density (that is, OD<sub>600 nm</sub> of 0.7); (2) induce cells for allelic replacement via 42 °C heat shock for 15 min; (3) chill cells at 4 °C to halt cellular metabolism; (4) wash cells through 15–20 iterations of filtration and resuspension with dH<sub>2</sub>O; (5) mix cell suspension and synthetic DNA; (6) deliver DNA into cells by electroporation; and (7) resuspend electroporated cells with growth media.

**Colorimetric screen and assay for lycopene production.** Cells from the cycled EcHW2 population were plated on LB-min-chloramphenicol agar plates and grown for 1 day at 30 °C and 2 days at room temperature to produce red colonies. The 24 gene targets were divided into three oligo pools, one containing 10 targets, a second containing 14 targets and a third containing all 24 targets, which were cycled through the MAGE process in three separate cultures. In total, 10<sup>5</sup> colonies with increased colour intensity by visual inspection were screened after cycles 5, 10, 15, 20, 25, 30 and 35. From 127 isolates, six strains (EcHW2a–f, with representation from each pool) were selected for direct DNA sequencing across all gene targets and quantitatively measured for lycopene production. For lycopene quantification, these isolated colonies were grown in LB-min medium for 24 h. Lycopene was extracted from 1 ml of cells as follows: centrifuged at 16,000g for 30 s, removal of supernatant media and resuspended with water, and re-centrifuged at 16,000g for 30 s. Once the supernatant was removed, the cells were resuspended in 200  $\mu$ l acetone and incubated in the dark for 15 min at 55 °C with intermittent vortexing. The mixture was centrifuged at 16,000g for 30 s and the supernatant lycopene solution was transferred to a clean tube for quantification. Absorbance at 470 nm of the extracted lycopene solution was measured using a spectrophotometer and calibrated against a known lycopene standard (Sigma-Aldrich, catalogue number L9879) to determine the lycopene content. Dry cell weight was determined by baking a washed cell pellet at 105 °C for 24 h in the dark. Lycopene yield of different EcHW2 derivatives (EcHW2a–f) was calculated by normalizing the amount of lycopene extracted to the dry cell weight.

31. Yu, D. *et al.* An efficient recombination system for chromosome engineering in *Escherichia coli*. *Proc. Natl Acad. Sci. USA* **97**, 5978–5983 (2000).
32. Cunningham, F. X. Jr, Sun, Z., Chamovitz, D., Hirschberg, J. & Gantt, E. Molecular structure and enzymatic function of lycopene cyclase from the cyanobacterium *Synechococcus* sp strain PCC7942. *Plant Cell* **6**, 1107–1121 (1994).

# Intrinsic light response of retinal horizontal cells of teleosts

Ning Cheng<sup>1,2,†</sup>, Takashi Tsunenari<sup>1,2,†</sup> & King-Wai Yau<sup>1,2,3</sup>

The discovery of intrinsically photosensitive retinal ganglion cells has overthrown the long-held belief that rods and cones are the exclusive retinal photoreceptors<sup>1,2</sup>. Intrinsically photosensitive retinal ganglion cells use melanopsin<sup>3</sup> as the photopigment, and mediate non-image-forming visual functions such as circadian photoentrainment. In fish, *in situ* hybridization studies indicated that melanopsin is present in retinal horizontal cells<sup>4–6</sup>—lateral association neurons critical for creating the centre-surround receptive fields of visual neurons. This raises the question of whether fish horizontal cells are intrinsically photosensitive. This notion was examined previously in flat-mount roach retina, but all horizontal-cell light response disappeared after synaptic transmission was blocked<sup>6</sup>, making any conclusion difficult to reach. To examine this question directly, we have now recorded from single, acutely dissociated horizontal cells from catfish and goldfish. We found that light induced a response in catfish cone horizontal cells, but not rod horizontal cells, consisting of a modulation of the nifedipine-sensitive, voltage-gated calcium current. The light response was extremely slow, lasting for many minutes. Similar light responses were observed in a high percentage of goldfish horizontal cells. We have cloned two melanopsin genes and one vertebrate ancient (VA) opsin gene from catfish. *In situ* hybridization indicated that melanopsin, but less likely VA opsin, was expressed in the horizontal-cell layer of catfish retina. This intrinsic light response may serve to modulate, over a long time-scale, lateral inhibition mediated by these cells. Thus, at least in some vertebrates, there are retinal non-rod/non-cone photoreceptors involved primarily in image-forming vision.

We performed whole-cell recordings from single, acutely dissociated horizontal cells from catfish retina. This retina has rod-driven horizontal cells and a single type of cone-driven horizontal cell<sup>7,8</sup>. Rod horizontal cells are larger, with >50- $\mu$ m-long dendrites and a smooth somatic membrane (Fig. 1a, right)<sup>7,8</sup>. Cone horizontal cells are more compact, with short processes and a slender axon-like process often still attached after dissociation, and spine-like protrusions from the soma<sup>7,8</sup> (Fig. 1a, left). We examined cone horizontal cells first because they have been studied more extensively<sup>8–13</sup>. When held steadily at  $-20$  to  $-30$  mV (approximate *in situ* membrane potential in darkness) or more hyperpolarized/depolarized potentials, there was no obvious light-induced current. Catfish cone horizontal cells have four reported voltage-gated currents<sup>9,12</sup>: nifedipine-sensitive calcium current, tetrodotoxin-sensitive sodium current, delayed-rectifier potassium current, and inward-rectifier potassium current (see Supplementary Fig. 1). Accordingly, to screen for a light response more closely, we isolated each current pharmacologically (see Methods) and tested the effect of light. Indeed, we

observed a modulation of the cone horizontal cell's  $\text{Ca}^{2+}$  current by light. Rod horizontal cells did not show this effect (see below).

In physiological concentrations of extracellular ions, the current–voltage ( $I$ – $V$ ) relationship of the isolated  $\text{Ca}^{2+}$  current of a cone horizontal cell showed modulation by light in the range of  $\pm 30$  mV as assayed by voltage ramps. In darkness, the  $\text{Ca}^{2+}$  current was  $160 \pm 62$  pA (mean  $\pm$  s.d.) at peak ( $\sim 0$  mV) from 13 cells. For seven cells, a bright flash ( $1 \times 10^8$  to  $3 \times 10^8$  photons  $\mu\text{m}^{-2}$  at 480 nm, 40- $\mu$ m-diameter spot centred on soma; see Methods) transiently reduced this current, then enhanced it for minutes ('biphasic' response, Fig. 1b; by a maximum of  $10 \pm 4$  and  $28 \pm 12$  pA, respectively, or  $9 \pm 8\%$  and  $20 \pm 9\%$  of dark value, right panel). For five cells, the same flash produced only a slow decrease in the current ('monophasic' response, Fig. 1c; by  $25 \pm 13$  pA, or  $14 \pm 4\%$  of dark value, right panel). One cell was not light sensitive. For both response types, the amplitude of the  $\text{Ca}^{2+}$  current was light sensitive, but not the voltage dependence (Fig. 1b and c, left). The biphasic response was likely the composite of a slow decrease and a slow increase of the  $\text{Ca}^{2+}$  current, with the decrease occurring sooner. In the monophasic response, the current increase could still be present (see later), but was cancelled by a more delayed and superposing current decrease. The light-mediated modulation of the  $\text{Ca}^{2+}$  current can explain why no light response was detected at steady  $-30$  mV or more negative membrane potentials, in that the current was not activated. At steady, more positive potentials, on the other hand, the  $\text{Ca}^{2+}$  current was probably inactivated<sup>9</sup>. We attempted to measure a light-induced change in intracellular  $\text{Ca}^{2+}$  concentration with Fura-2 under current clamp, but, owing to spontaneous, wide swings in the membrane potential between positive and negative values (also observed by others<sup>9,12–14</sup> in dissociated horizontal cells) in darkness triggering spontaneous  $\text{Ca}^{2+}$  concentration changes, such measurements were not feasible.

The dark  $\text{Ca}^{2+}$  current and its light modulation tended to run down with time, possibly due to washout by the whole-cell-pipette solution. A second, identical flash almost invariably elicited a smaller response (for example, see Supplementary Fig. 5a), and a third flash gave an even smaller, or no, response. This run down and the response slowness precluded quantitative measurements such as the intensity–response relationship. If flashes were delivered in rapid succession, before the cell's recovery from each flash, then multiple responses could be observed (Supplementary Fig. 2). With a step of light, the response was more prolonged as expected (not shown). Light did not affect the voltage-gated  $\text{Na}^+$  current, the delayed-rectifier  $\text{K}^+$  current, the inward-rectifier  $\text{K}^+$  current (Fig. 1d), or the ionotropic glutamate- and GABA ( $\gamma$ -aminobutyric acid)-induced currents<sup>8,10</sup> (Fig. 1e; also Supplementary Fig. 3). Thus, light

<sup>1</sup>Solomon H. Snyder Department of Neuroscience, <sup>2</sup>Center for Sensory Biology and <sup>3</sup>Department of Ophthalmology, Johns Hopkins University School of Medicine, Baltimore, Maryland 21205, USA. <sup>†</sup>Present addresses: Unit of Developmental Neural Plasticity, National Institute of Neurological Disorders and Stroke, National Institutes of Health, Bethesda, Maryland 20892, USA (N.C.); Graduate Program of Human Sensing and Functional Sensor Engineering, Graduate School of Science and Engineering, Yamagata University, Yonezawa City, Yamagata 992-8510, Japan (T.T.).

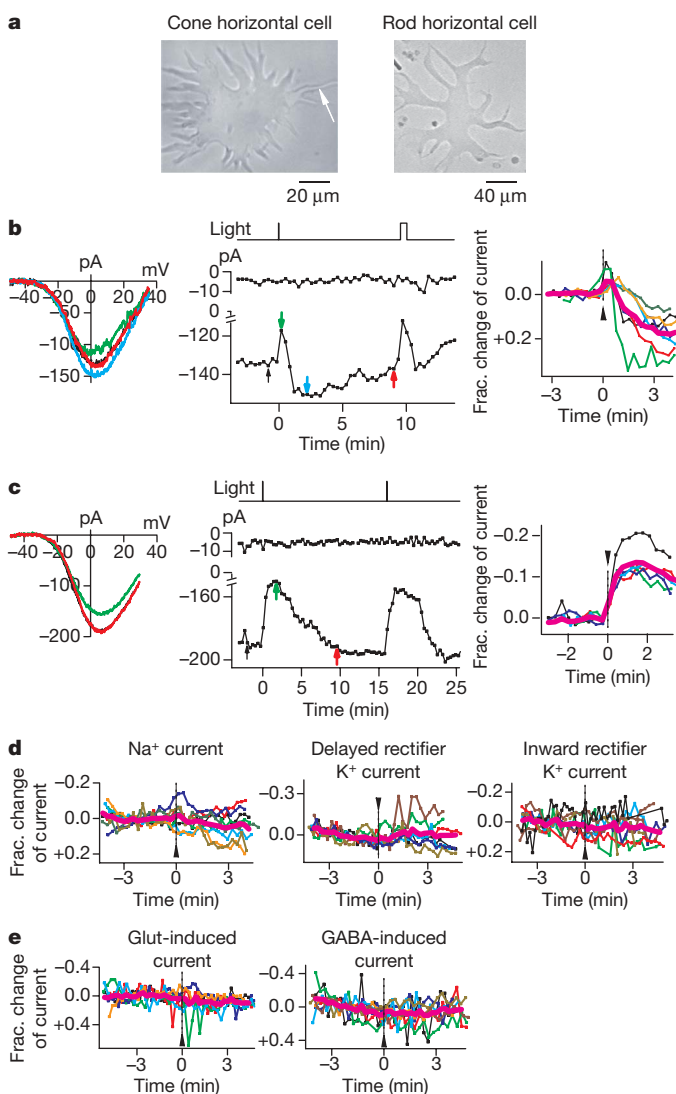


**Figure 1 | Light modulated the voltage-gated  $\text{Ca}^{2+}$  current on catfish cone horizontal cells.** **a**, Dissociated cone horizontal cell (left; arrow indicates axon-like process) and rod horizontal cell (right). **b**, Biphasic light response of some cone horizontal cells in  $\text{Ca}$ -Ringer and  $\text{K}$ -methanesulphonate pipette solution. Left:  $\text{Ca}^{2+}$  current  $I$ - $V$  relationship before (black), shortly after (green), intermediately after (blue) and a long period after bright flash (red). Middle: time course of peak  $\text{Ca}^{2+}$  current modulation by light. Vertical bars at top indicate flashes. Coloured arrows correspond to measurements on left panel. In this and subsequent figures, input resistance of the recorded cell (to monitor recording stability) is indicated at the top by the membrane current elicited by repetitive, 200 ms,  $-3$  mV voltage steps. Time 0 designates onset of first light stimulus, as in other panels. Light stimulus was a spot ( $40 \mu\text{m}$  diameter,  $480 \text{ nm}$ ) centred on soma, delivering  $3 \times 10^8$  photons  $\mu\text{m}^{-2} \text{ s}^{-1}$  for 1 (first) and 30 s (second). Right: collected results ( $n = 7$ ) showing fractional change in  $\text{Ca}^{2+}$  current by light, magenta shows average. Flash (arrowhead) was  $1 \times 10^8$ – $3 \times 10^8$  photons  $\mu\text{m}^{-2} \text{ s}^{-1}$  for 1 s. **c**, Monophasic light response (decrease in  $\text{Ca}^{2+}$  current) of other cone horizontal cells. Same solutions and flash intensity as in **b**. Collected results ( $n = 5$ ) and average (magenta) are shown in the right panel. **d**, Light had no effect on the other voltage-gated currents. Membrane potential stepped from  $-50$  to  $0$  mV for  $\text{Na}^{+}$  current ( $n = 8$ ), to  $+60$  mV for delayed-rectifier  $\text{K}^{+}$  current ( $n = 7$ ), and to  $-100$  mV for inward-rectifier  $\text{K}^{+}$  current ( $n = 8$ ). Same flash intensity as above but for 2–30 s. Other wavelengths were also tried (400, 440, 540, 600 and  $680 \text{ nm}$ ), but gave no responses either (not shown).  $\text{K}$ -methanesulphonate pipette solution. **e**, Light had no effect on glutamate- and GABA-induced currents. Same light as in **d**. Glutamate current recorded in  $\text{Mg}^{2+}$ -free catfish Ringer and  $\text{K}$ -methanesulphonate pipette solution,  $n = 6$ ; GABA current recorded in normal catfish Ringer and  $\text{KCl}$  pipette solution,  $n = 8$ . Both pipette solutions had  $20 \mu\text{M}$   $\text{Cd}^{2+}$  to block  $\text{Ca}^{2+}$  current.  $V_{\text{hold}}$   $-50$  mV. Glut, glutamate.

modulated specifically the  $\text{Ca}^{2+}$  current. We found the same light effect when all methanesulphonate (standard anion in the pipette solution and impermeant through  $\text{Cl}^{-}$  channels) was replaced by  $\text{Cl}^{-}$  to give a  $\text{Cl}^{-}$  equilibrium potential of  $\sim 0$  mV, which is evidence against  $\text{Cl}^{-}$  involvement in the light response. Finally, although larger than cone horizontal cells, dissociated rod horizontal cells had a smaller  $\text{Ca}^{2+}$  current<sup>8</sup> ( $30 \pm 11 \text{ pA}$ ,  $n = 3$ ) in darkness and showed no detectable photosensitivity (data in normal solution not shown, but see Fig. 2c).

Substitution of extracellular  $\text{Ba}^{2+}$  for  $\text{Ca}^{2+}$  (Methods) increased the current through the  $\text{Ca}^{2+}$  channels on cone horizontal cells by  $\sim 80\%$  (from  $217 \pm 41 \text{ pA}$  to  $400 \pm 128 \text{ pA}$ ,  $n = 5$ ) and slowed its run down<sup>13,15</sup>. The associated light response was also larger. Interestingly, light produced only an increase but no initial decrease in  $\text{Ba}^{2+}$  current, which lasted many minutes; again, the amplitude but not the voltage dependence was affected (Fig. 2a). Even a cone horizontal cell that gave only a light-induced decrease in  $\text{Ca}^{2+}$  current in normal solution showed a light-induced increase in  $\text{Ba}^{2+}$  solution (Fig. 2a). Altogether, we observed a light response in  $\text{Ba}^{2+}$  solution in 108 out of 132 recorded cone horizontal cells, with a 'threshold' flash intensity of  $\sim 1 \times 10^6$  photons  $\mu\text{m}^{-2}$  ( $480 \text{ nm}$ ) for eliciting any detectable response. The dark  $\text{Ba}^{2+}$  current and its modulation by light was blocked by  $10 \mu\text{M}$  nifedipine (Fig. 2b,  $n = 6$ ), suggesting L-type  $\text{Ca}^{2+}$  channels were involved and consistent with their presence in catfish cone horizontal cells<sup>9,13</sup>. Again, only cone horizontal cells, but not rod horizontal cells (even with greater light intensity and at different wavelengths), showed light-mediated modulation of the  $\text{Ba}^{2+}$  current (Fig. 2c), although the  $\text{Ba}^{2+}$  current on rod horizontal cells was also nifedipine sensitive (Supplementary Fig. 4).

A light-induced decrease in  $\text{Ca}^{2+}$  current, but not  $\text{Ba}^{2+}$  current, suggested that a  $\text{Ca}^{2+}$  influx through the  $\text{Ca}^{2+}$  channel was necessary. Indeed, a light-induced current decrease reappeared when  $\text{Ca}^{2+}$  was added to the  $\text{Ba}^{2+}$  solution (Fig. 2d, left). Also, the strong  $\text{Ca}^{2+}$  buffering in our typical pipette solution ( $10 \text{ mM}$  BAPTA and no  $\text{Ca}^{2+}$ ; see Methods) did not eliminate the light-induced decrease in  $\text{Ca}^{2+}$  current, whereas removing all  $\text{Ca}^{2+}$  buffering in the pipette did not make much difference either, although the light-induced  $\text{Ca}^{2+}$  current decrease seemed faster and larger (Fig. 2d, right). Thus,  $\text{Ca}^{2+}$  might act very close to the  $\text{Ca}^{2+}$  channel, where it entered the cell, to affect a light-sensitive target. The possibility that the light-induced current decrease originated instead from the opening of a  $\text{Ca}^{2+}$ -activated  $\text{K}^{+}$  current<sup>16</sup> is unlikely, because this is inconsistent with the constant form of the  $I$ - $V$  relationship in light and darkness as we observed.

We probed the spectral sensitivity of the cone horizontal-cell light response. We used only the  $\text{Ba}^{2+}$  solution because of the faster run-down of the  $\text{Ca}^{2+}$  current; thus, we could examine only the light-induced current increase. By reiterated pair-wise comparisons between two wavelengths in a given cell (Supplementary Information and Supplementary Fig. 5), we inferred a spectral-effectiveness ordering of  $400 < 440 < 480 > 520 > 540 > 560 > 600 > 680 \text{ nm}$ . Thus, the  $\lambda_{\text{max}}$  of the underlying pigment is between 440 and  $520 \text{ nm}$ . This ordering is tentative because the method in principle applies only to bleachable pigments, which nonetheless include all known vertebrate pigments except possibly for melanopsin (see below), the bleachability of which remains unclear<sup>17</sup>.

Some teleosts have been reported to express melanopsin or vertebrate ancient (VA) opsin, or both, in their horizontal cells<sup>4–6,18,19</sup>. VA opsin is a pigment of largely unknown function. By degenerate polymerase chain reaction with reverse transcription (RT-PCR) based on known melanopsins and VA opsins (Methods), we isolated from catfish retina the complementary DNA clones for two distinct melanopsin genes (catfish *OPN4m1* and *OPN4m2*, based on sequence comparison with other fish melanopsins<sup>20</sup>) and two alternatively spliced cDNAs of a VA opsin gene (catfish VA and VAL, with VAL having a longer and different C terminus<sup>19</sup>) (see Methods, Supplementary Fig. 6 and Supplementary Tables 1 and 2). *In situ* hybridization



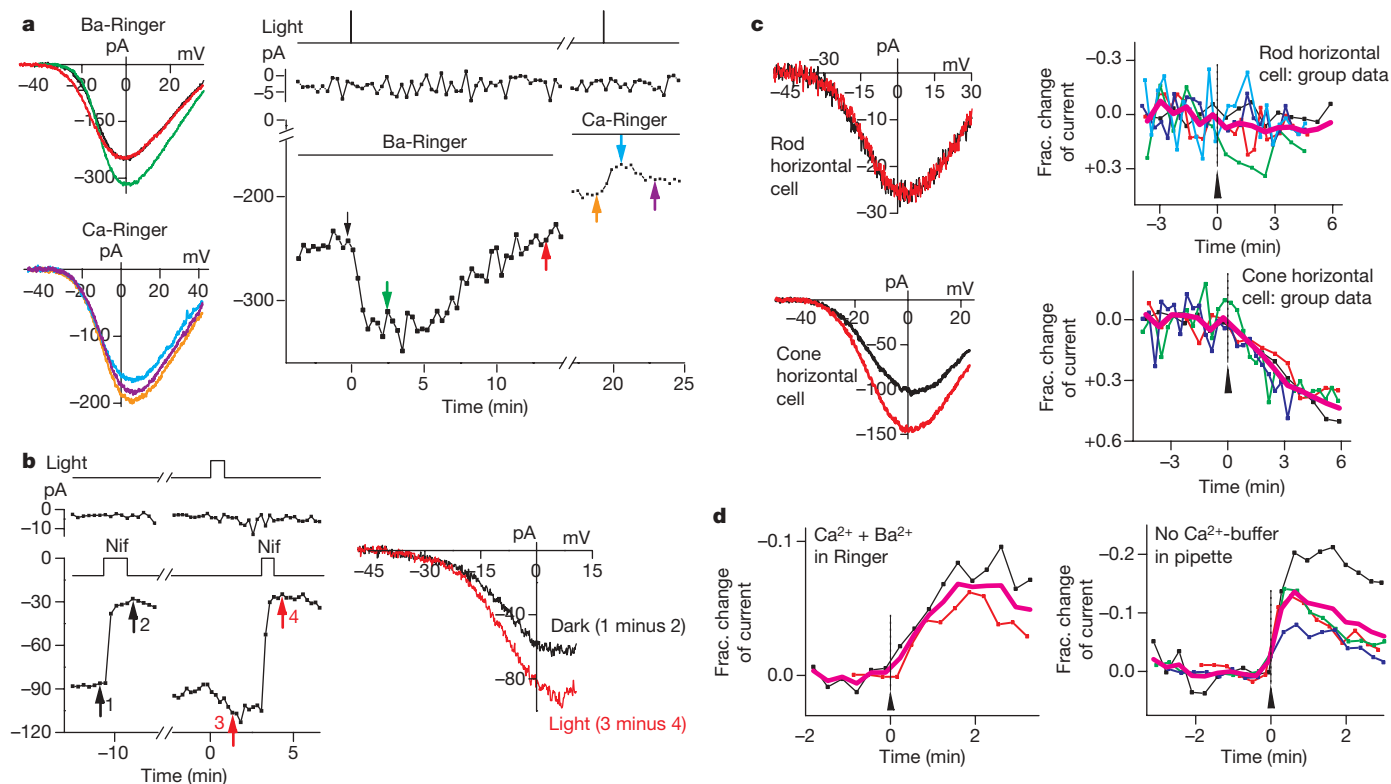


**Figure 2 | Characterization of catfish cone horizontal-cell light response.** **a**, Light only increased current in Ba<sup>2+</sup> solution. Time gap ~2 min, identical flashes, K-methanesulphonate pipette solution. **b**, Ba<sup>2+</sup> current and its light-induced increase were both sensitive to nifedipine (Nif, 10  $\mu$ M). Time gap ~5 min. **c**, Ba<sup>2+</sup> current of cone horizontal cells (bottom), but not rod horizontal cells (top), was light sensitive. Left shows sample cell (black, before light; red, ~3 min after light).  $n = 5$  (top) and  $n = 4$  (bottom) in group data. Simplified Ba-Ringer and Cs-methanesulphonate pipette

solution in **b** and **c**. **d**, Ca<sup>2+</sup> influx was required for light-induced current decrease. Left, Ca<sup>2+</sup> (3 mM) in Ba-Ringer restored light-induced current decrease. Collected results ( $n = 2$ ) and average (magenta) are shown. K-methanesulphonate pipette solution. Right, omitting 10 mM BAPTA in pipette still gave light-induced current decrease ( $n = 4$ ; magenta, average). K-methanesulphonate pipette solution and Ca<sup>2+</sup>-Ringer. In all cases, light was 480 nm,  $0.8 \times 10^8$ – $1 \times 10^9$  photons  $\mu\text{m}^{-2} \text{s}^{-1}$  for 1–50 s.

labelling on flat-mount retina (Fig. 3a, left) indicated that, based on its depth of location in the retinal thickness and other landmarks, the *OPN4m1*- and *OPN4m2*-positive cells were situated near the outer margin of the inner nuclear layer, where horizontal cells are situated. The same labelling in retinal cross-sections supported this conclusion (Fig. 3a, right, and Supplementary Fig. 7). *OPN4m1* was found also in cells near the inner margin of the inner nuclear layer, probably amacrine cells and/or displaced ganglion cells. This distribution pattern of melanopsin mRNA was found in most other fishes examined<sup>4–6</sup>. VA/VAL opsin transcripts were found predominantly in the ganglion cell layer and less in the inner nuclear layer (Fig. 3b and Supplementary Fig. 7), therefore less likely in horizontal cells<sup>6,18,19</sup>. Thus, the intrinsic light response of catfish cone horizontal cells is possibly triggered by melanopsin, although the involvement of VA and VAL cannot be completely excluded. There are other putative pigments in the retina, including teleost multiple tissue (TMT) opsin<sup>21</sup> and neuropsin (OPN5)<sup>22</sup>, but their exact locations remain unknown.

We also examined goldfish retina. Dissociated horizontal cells from goldfish are identifiable by their relatively large size and flat somata with stellar processes<sup>14</sup> (Fig. 4a). However, it is difficult to distinguish these horizontal cells further into subtypes I through IV, which have been identified in the whole goldfish retina<sup>23</sup>. In Ba<sup>2+</sup> solution, the only solution tried, we observed a light-induced, similarly slow current increase in most horizontal cells recorded (Fig. 4b, 18 out of 24 cells; by  $34 \pm 20$  pA at peak, or  $37 \pm 33\%$  over that in darkness, triggered by  $5 \times 10^8$  photons  $\mu\text{m}^{-2} \text{s}^{-1}$  for 0.5–1.0 s at 480 nm). The remaining horizontal cells gave no light responses (Fig. 4c). This percentage of photoresponsive goldfish horizontal cells was remarkably high, but could have resulted from the

dissociation procedure biasing the yield of particular horizontal-cell subtypes.

We have established the presence of intrinsically photosensitive horizontal cells in the fish retina. In catfish, these are specifically cone horizontal cells, with a flash threshold of perhaps  $\sim 10^6$  photons  $\mu\text{m}^{-2}$  (480 nm), or  $10^4$ – $10^5$ -fold less sensitive than fish cones (see Supplementary Information), not greatly different from that of intrinsically photosensitive retinal ganglion cells in mouse<sup>17</sup>. With this low sensitivity, it makes sense at least that the intrinsically photosensitive horizontal cells are associated with cone rather than rod circuitry. In compensation, the prolonged response (lasting for minutes) should make temporal summation extremely effective, especially for sensing steady ambient light. If the intrinsic photosensitivity exists all over the cell, the large surface area of horizontal cells will also capture ambient light quite effectively. The horizontal-cell light response in this study seems distinct from the supposed intrinsic light response previously reported by others<sup>6</sup> for *in situ* horizontal cells in the roach flat-mount retina. This other response<sup>6</sup>, although having an action-spectrum  $\lambda_{\text{max}}$  ( $\sim 477$  nm) distinct from those of roach rods and cones, was observed in only 43 out of more than 1,000 cells, was found in rod horizontal cells and, finally, disappeared in the presence of synaptic blockers, which made a definitive conclusion of intrinsic photosensitivity difficult.

Unlike mammalian intrinsically photosensitive retinal ganglion cells, which mediate predominantly non-image-forming visual functions<sup>2</sup>, albeit not exclusively<sup>24,25</sup>, the intrinsically photosensitive horizontal cells are almost certainly involved primarily in image vision because horizontal cells are principal elements in the retinal circuitry generating the antagonistic surround of the bipolar cell's receptive field. With the operating range of horizontal-cell membrane

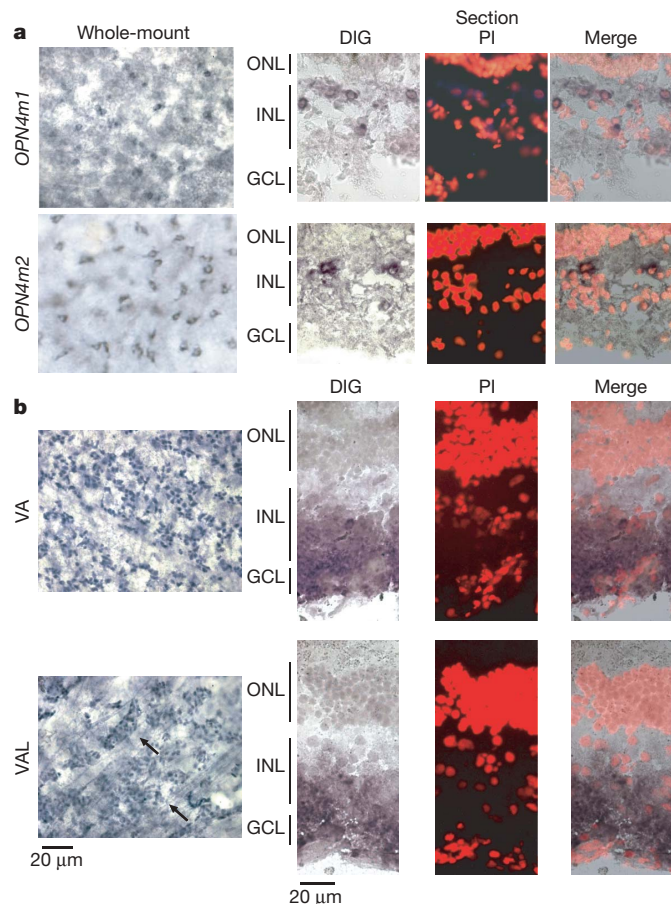


**Figure 3 | Melanopsin, but perhaps not VA/VAL opsin, was expressed in the horizontal cell layer of catfish retina.** **a**, *In situ* hybridization of *OPN4m1* and *OPN4m2* mRNA. Left: digoxigenin (DIG) staining of flat-mount retina. Small, dark-blue areas surrounding hollow cores (presumably the nuclei) indicate stained cell cytoplasm. The right panel shows the same experiments on retinal cross-sections with DIG signal, propidium iodide (PI) nuclear staining to mark retinal layers, and the two merged as indicated. Catfish retinal layers are not very distinctive, with sparse nuclei in the inner nuclear layer<sup>7</sup>. **b**, *In situ* hybridization of *VA/VAL* opsin mRNA. Left: DIG staining of flat-mount retina. Dark-blue dots are the stained cells, situated close to the retina inner surface with blood vessels (arrows) evident in the same focal plane. Right: same experiments on retinal cross-sections. In both **a** and **b**, cells appear smaller in the flat-mount retina than in retinal cross-sections owing to some tissue shrinkage during processing. GCL, Ganglion cell layer; INL, inner nuclear layer; ONL, outer nuclear layer.

potential under *in situ* conditions being typically  $-20$  to  $-65$  mV, the corresponding range for light modulation would be approximately  $-20$  to  $-30$  mV, within which the  $\text{Ca}^{2+}$  current is active. This narrow range means that the effect of light is probably subtle. Because of the extremely slow intrinsic horizontal-cell light response, ambient light may alter, on a slow timescale, the bipolar-cell receptive-field surround, such as by modulating the horizontal cells' electrical coupling or synaptic properties. The relationships of intracellular  $\text{Ca}^{2+}$  concentration to horizontal-cell electrical coupling and to horizontal-cell synaptic-transmitter release in fish have been studied, but the details are nonetheless unsettled, especially on a slow timescale<sup>11,26–28</sup>. Many questions remain, such as by what mechanism light affects the horizontal-cell  $\text{Ca}^{2+}$  current, what specific function this intrinsic photosensitivity serves in the fish retina, and whether light has additional (and possibly electrically silent) effects in these horizontal cells. What is clear from this work on intrinsically photosensitive horizontal cells and previous work on intrinsically photosensitive retinal ganglion cells<sup>1,2</sup>, however, is that the types of intrinsically photosensitive retinal neurons can be much more complex than previously thought.

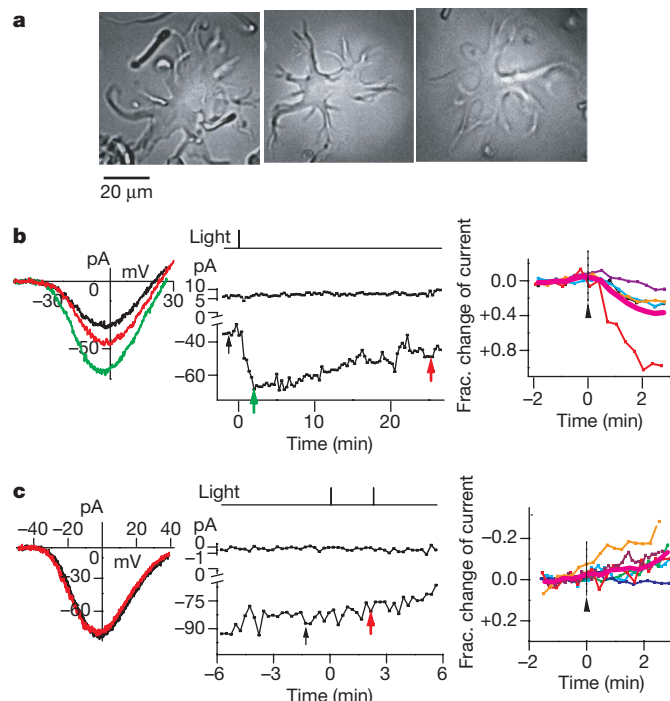


**Figure 4 | Many goldfish horizontal cells also showed light responses.** **a**, Dissociated goldfish horizontal cells. Horizontal cells shown in left and middle panels responded to light, but the horizontal cell shown in the right one did not. **b**, Light increased  $\text{Ba}^{2+}$  current in some horizontal cells. Left and middle panels show a representative cell (left cell in **a**). Right panel shows collected data ( $n = 5$ ) and average (magenta). **c**, Non-photoresponsive horizontal cells under the same conditions as in **b**. Left and middle panels show a representative cell (right cell in **a**). Right panel shows collected data ( $n = 6$ ) and average (magenta). In both **b** and **c**, the flash was  $5 \times 10^8$  photons  $\mu\text{m}^{-2}$  (480 nm), and simplified Ba-Ringer and Cs-methanesulphonate pipette solution were used.

## METHODS SUMMARY

**Retina dissociation and electrophysiology.** The fish was killed and the eyes removed in dim red light. Subsequent procedures were performed under infrared light. The retina-dissociation procedure for obtaining horizontal cells followed published methods<sup>12,29</sup>. After visual identification, a horizontal cell was voltage-clamped with whole-cell, patch-clamp recording at  $23^\circ\text{C}$ . The access resistance (generally  $20$ – $40$  M $\Omega$ ) was not compensated, but should introduce an error of under a few millivolts because the measured  $\text{Ca}^{2+}$  current was small. Liquid-junction potentials were measured and corrected. Voltage ramps ( $45$ – $100$  mV  $\text{s}^{-1}$ ) were used to elicit  $\text{Ca}^{2+}/\text{Ba}^{2+}$  currents in most experiments (Supplementary Fig. 8). Light stimuli were delivered via an optical fibre to the microscope, with strength varied by changing the intensity and/or duration of the flash. Perforated-patch recording (with nystatin, amphotericin B or gramicidin) was also attempted, but the membrane under the pipette invariably ruptured to become whole-cell recording in  $<30$  min, as indicated by Lucifer yellow entering the cell from the pipette solution. With the light response being extremely slow, this time duration would allow at most one or two light responses. Accordingly, this method was not used.

**Cloning of melanopsin and VA/VAL opsin genes from catfish retina.** cDNA was synthesized from catfish retina total RNA, and used as a template for nested degenerate PCR. Primers were designed based on the conserved regions in known melanopsin and VA opsin amino-acid sequences. Conventional 5'- and 3'-rapid amplification of cDNA ends (RACE) was performed to obtain full-length cDNA sequences. Products were cloned into a commercial vector and sequenced. Sequences with more than three identical clones were considered true.

***In situ* hybridization of melanopsins and VA/VAL opsin mRNA in catfish retina.** RNA probes were made against cloned catfish *OPN4m1* and *OPN4m2* sequences, and against the C termini of catfish VA and VAL opsins. Conventional *in situ* hybridization method for whole-mount embryos was adapted for whole-mount staining of catfish retina. *In situ* hybridization of fresh-frozen retinal sections was also performed (see Methods).

**Full Methods** and any associated references are available in the online version of the paper at [www.nature.com/nature](http://www.nature.com/nature).

**Received 25 March; accepted 20 May 2009.**

**Published online 26 July 2009.**

- Berson, D. M., Dunn, F. A. & Takao, M. Phototransduction by retinal ganglion cells that set the circadian clock. *Science* **295**, 1070–1073 (2002).
- Hattar, S., Liao, H. W., Takao, M., Berson, D. M. & Yau, K. W. Melanopsin-containing retinal ganglion cells: architecture, projections, and intrinsic photosensitivity. *Science* **295**, 1065–1070 (2002).
- Provencio, I., Jiang, G., De Grip, W. J., Hayes, W. P. & Rollag, M. D. Melanopsin: an opsin in melanophores, brain, and eye. *Proc. Natl Acad. Sci. USA* **95**, 340–345 (1998).
- Bellingham, J., Whitmore, D., Philp, A. R., Wells, D. J. & Foster, R. G. Zebrafish melanopsin: isolation, tissue localisation and phylogenetic position. *Mol. Brain Res.* **107**, 128–136 (2002).
- Drivenes, O. *et al.* Isolation and characterization of two teleost melanopsin genes and their differential expression within the inner retina and brain. *J. Comp. Neurol.* **456**, 84–93 (2003).
- Jenkins, A. *et al.* VA opsin, melanopsin, and an inherent light response within retinal interneurons. *Curr. Biol.* **13**, 1269–1278 (2003).
- Naka, K. & Carraway, N. R. Morphological and functional identifications of catfish retinal neurons. I. Classical morphology. *J. Neurophysiol.* **38**, 53–71 (1975).
- Dong, C.-J., Picaud, S. A. & Werblin, F. S. GABA transporters and GABA<sub>A</sub>-like receptors on catfish cone- but not rod-driven horizontal cells. *J. Neurosci.* **14**, 2648–2658 (1994).
- Shingai, R. & Christensen, B. N. Excitable properties and voltage-sensitive ion conductances of horizontal cells isolated from catfish (*Ictalurus punctatus*) retina. *J. Neurophysiol.* **56**, 32–49 (1986).
- O'Dell, T. J. & Christensen, B. N. Horizontal cells isolated from catfish retina contain two types of excitatory amino acid receptors. *J. Neurophysiol.* **61**, 1097–1109 (1989).
- DeVries, S. H. & Schwartz, E. A. Modulation of an electrical synapse between solitary pairs of catfish horizontal cells by dopamine and second messengers. *J. Physiol.* **414**, 351–375 (1989).
- Davis, S. F. & Linn, C. L. Activation of NMDA receptors linked to modulation of voltage-gated ion channels and functional implications. *Am. J. Physiol. Cell Physiol.* **284**, C757–C768 (2003).
- Takahashi, K., Dixon, D. B. & Copenhagen, D. R. Modulation of a sustained calcium current by intracellular pH in horizontal cells of fish retina. *J. Gen. Physiol.* **101**, 695–714 (1993).
- Tachibana, M. Membrane properties of solitary horizontal cells isolated from goldfish retina. *J. Physiol.* **321**, 141–161 (1981).
- Bean, B. P. Whole-cell recording of calcium channel currents. *Methods Enzymol.* **207**, 181–193 (1992).
- Heyer, C. B. & Lux, H. D. Control of the delayed outward potassium currents in bursting pace-maker neurones of the snail, *Helix pomatia*. *J. Physiol.* **262**, 349–382 (1976).
- Do, M. T. H. *et al.* Photon capture and signalling by melanopsin retinal ganglion cells. *Nature* **457**, 281–287 (2009).
- Soni, B. G., Philp, A. R., Foster, R. G. & Knox, B. E. Novel retinal photoreceptors. *Nature* **394**, 27–28 (1998).
- Kojima, D., Mano, H. & Fukada, Y. Vertebrate ancient-long opsin: a green-sensitive photoreceptive molecule present in zebrafish deep brain and retinal horizontal cells. *J. Neurosci.* **20**, 2845–2851 (2000).
- Bellingham, J. *et al.* Evolution of melanopsin photoreceptors: discovery and characterization of a new melanopsin in nonmammalian vertebrates. *PLoS Biol.* **4**, e254 (2006).
- Moutsaki, P. *et al.* Teleost multiple tissue (*tmt*) opsin: a candidate photopigment regulating the peripheral clocks of zebrafish? *Mol. Brain Res.* **112**, 135–145 (2003).
- Tarttelin, E. E., Bellingham, J., Hankins, M. W., Foster, R. G. & Lucas, R. J. Neuroopsin (Opn5): a novel opsin identified in mammalian neural tissue. *FEBS Lett.* **554**, 410–416 (2003).
- Stell, W. K. & Lightfoot, D. O. Color-specific interconnections of cones and horizontal cells in the retina of the goldfish. *J. Comp. Neurol.* **159**, 473–502 (1975).
- Barnard, A. R., Hattar, S., Hankins, M. W. & Lucas, R. J. Melanopsin regulates visual processing in the mouse retina. *Curr. Biol.* **16**, 389–395 (2006).
- Dacey, D. M. *et al.* Melanopsin-expressing ganglion cells in primate retina signal colour and irradiance and project to the LGN. *Nature* **433**, 749–754 (2005).
- McMahon, D. G. & Mattson, M. P. Horizontal cell electrical coupling in the giant danio: synaptic modulation by dopamine and synaptic maintenance by calcium. *Brain Res.* **718**, 89–96 (1996).
- Ayoub, G. S. & Lam, D. M. The release of  $\gamma$ -aminobutyric acid from horizontal cells of the goldfish (*Carassius auratus*) retina. *J. Physiol.* **355**, 191–214 (1984).
- Schwartz, E. A. Depolarization without calcium can release gamma-aminobutyric acid from a retinal neuron. *Science* **238**, 350–355 (1987).
- Zenisek, D., Horst, N. K., Merrifield, C., Sterling, P. & Matthews, G. Visualizing synaptic ribbons in the living cell. *J. Neurosci.* **24**, 9752–9759 (2004).

**Supplementary Information** is linked to the online version of the paper at [www.nature.com/nature](http://www.nature.com/nature).

**Acknowledgements** This work was supported by an NIH grant and the António Champalimaud Vision Award (Portugal) to K.-W.Y. We thank R. Johnson, C. Liu and D. Liu for advice on molecular cloning and *in situ* hybridization staining, Y. Shen, C. Linn and G. Matthews for suggestions on retinal dissociation. D. Bergles, P. Fuchs and J. Nathans offered comments throughout the work. L. Belluscio let N.C. take a brief leave of absence from her postdoctoral work to return to Hopkins in order to complete some experiments. Members of the Yau laboratory, especially M. Do and D.-G. Luo, as well as K. Murari, have provided comments on the manuscript.

**Author Contributions** N.C., T.T. and K.-W.Y. discussed and designed the experiments. N.C. performed all of the experiments, with T.T. offering technical advice. N.C. and K.-W.Y. wrote the paper.

**Author Information** Reprints and permissions information is available at [www.nature.com/reprints](http://www.nature.com/reprints). Correspondence and requests for materials should be addressed to N.C. ([chengn2@mail.nih.gov](mailto:chengn2@mail.nih.gov)) or K.-W.Y. ([kwyau@mail.jhmi.edu](mailto:kwyau@mail.jhmi.edu)).



## METHODS

**Retina dissociation and electrophysiology.** Channel catfish (*Ictalurus punctatus*) about 1 ft long were purchased from Osage Catfisheries (Missouri) and maintained in 14/10 h light/dark cycles (light on 7:00–21:00) at the Johns Hopkins School of Medicine animal facility. Experiments were done in daytime hours of 12:00–20:00. The procedure for dissociating the catfish retina was largely as published<sup>12</sup>. Before experiments, a catfish dark-adapted for ~60 min was killed in dim-red light with an institution-approved protocol, the eyes were excised and the cornea, iris and lens removed. The posterior eyecup was incubated in catfish low- $\text{Ca}^{2+}$  dissociation Ringer (123 mM NaCl, 0.3 mM  $\text{CaCl}_2$ , 4 mM KCl, 2 mM  $\text{MgCl}_2$ , 15 mM glucose, 10 mM HEPES, 1 mM sodium pyruvate, pH 7.4) with 0.2–0.3 mg ml<sup>-1</sup> hyaluronidase type I-S (Sigma-Aldrich) for 4 min, then in the same base dissociation solution with 20–28 U ml<sup>-1</sup> papain (Fluka) for 4–6 min. Afterwards, the retina was peeled from the eyecup, cut into six to eight pieces and incubated further in base dissociation solution with 4–20 U ml<sup>-1</sup> papain for 3–12 min. The retina pieces were rinsed four times in base dissociation Ringer with 0.1 mg ml<sup>-1</sup> bovine serum albumin and transferred into normal catfish Ringer (118 mM NaCl, 3 mM  $\text{CaCl}_2$ , 4 mM KCl, 2 mM  $\text{MgCl}_2$ , 15 mM glucose, 10 mM HEPES, pH 7.4) and kept on ice until use. When needed, horizontal cells were dissociated from pieces of tissue by mechanical trituration with a fire-polished Pasteur pipette.

The dissociation procedure for goldfish (*Carassius auratus*) retina also followed a published procedure<sup>29</sup>. Goldfish 4–6-inch long were purchased from local pet stores and maintained in 12/12 h light/dark cycles. Experimental procedures were largely similar to above. Goldfish low- $\text{Ca}^{2+}$  dissociation Ringer contained 117 mM NaCl, 0.5 mM  $\text{CaCl}_2$ , 2.5 mM KCl, 5 mM  $\text{MgCl}_2$ , 16 mM glucose, 10 mM HEPES, 1 mM sodium pyruvate, 1 mM  $\text{NaHCO}_3$ , 1 mM  $\text{NaH}_2\text{PO}_4$ , pH 7.3. Eyecups were prepared, and the retina was peeled off and incubated in hyaluronidase type I-S solution (Sigma-Aldrich, 1 mg ml<sup>-1</sup> in base dissociation Ringer) for 10 min. The retina was rinsed in base dissociation Ringer, cut into four to six pieces, transferred into papain solution (Fluka, 1 mg ml<sup>-1</sup> in base dissociation Ringer) for 30 min, and rinsed four times in base dissociation Ringer containing 0.1 mg ml<sup>-1</sup> bovine serum albumin. The retinal pieces were transferred to normal goldfish Ringer (122 mM NaCl, 2.5 mM KCl, 2.5 mM  $\text{CaCl}_2$ , 1 mM  $\text{MgCl}_2$ , 10 mM HEPES, 16 mM glucose, pH 7.3) and kept on ice until used as above.

To pharmacologically isolate each of the four known voltage-gated ion currents in catfish cone horizontal cells, the following blockers or their combinations were added, or equimolar-substituted, to the normal fish Ringer<sup>9,12</sup>. Tetrodotoxin (10  $\mu\text{M}$ ) was added to block the voltage-gated  $\text{Na}^+$  current.  $\text{Cd}^{2+}$  (20  $\mu\text{M}$ ) was added to block the voltage-gated  $\text{Ca}^{2+}$  current. Tetraethylammonium ion (TEA-Cl, 20 mM) and 4-aminopyridine (10 mM) were equimolar-substituted for NaCl to block the delayed-rectifier  $\text{K}^+$  current, and 1 mM  $\text{Ba}^{2+}$  was added to block the inward-rectifier  $\text{K}^+$  current. For example, the Ringer ('Ca-Ringer') for isolating the  $\text{Ca}^{2+}$  current contained 94 mM NaCl, 3 mM  $\text{CaCl}_2$ , 4 mM KCl, 2 mM  $\text{MgCl}_2$ , 15 mM glucose, 10 mM HEPES, 10  $\mu\text{M}$  tetrodotoxin, 20 mM TEA-Cl, 10 mM 4-aminopyridine, 1 mM  $\text{BaCl}_2$ , pH 7.4. 'Ba-Ringer' had 3 mM  $\text{Ba}^{2+}$  in place of the 3 mM  $\text{Ca}^{2+}$ , in addition to the 1 mM  $\text{Ba}^{2+}$  to block the inward-rectifier  $\text{K}^+$  current. The substitution of  $\text{Ba}^{2+}$  for  $\text{Ca}^{2+}$  shifted the  $I$ - $V$  relationship by a few millivolts in the hyperpolarized direction<sup>30</sup> (see Fig. 2a). Normal internal (that is, pipette-) solution contained 105 mM K-methanesulphonate, 10 mM BAPTA, 10 mM HEPES, 10 mM NaCl, 4 mM ATP-Mg, 0.3 mM GTP-Na, pH 7.3 ('K-methanesulphonate-based pipette solution'). In later experiments, to record

a stable  $\text{Ba}^{2+}$  current for a longer period, we replaced all external  $\text{Na}^+$  and  $\text{K}^+$  with TEA<sup>+</sup>: 4 mM  $\text{BaCl}_2$ , 120 mM TEA-Cl, 3 mM  $\text{MgCl}_2$ , 15 mM glucose, 10 mM HEPES, pH 7.4 (referred to as 'simplified Ba-Ringer'), and substituted  $\text{Cs}^+$  for  $\text{K}^+$  in the pipette solution: 95 mM Cs-methanesulphonate, 10 mM BAPTA, 10 mM HEPES, 20 mM TEA-Cl, 4 mM ATP-Mg, 0.3 mM GTP-Na, pH 7.3 ('Cs-methanesulphonate-based pipette solution')<sup>15</sup>. Pipette solution without  $\text{Ca}^{2+}$  buffer contained: 120 mM K-methanesulphonate, 10 mM HEPES, 10 mM NaCl, 4 mM ATP-Mg, 0.3 mM GTP-Na, pH 7.3. 'KCl-based pipette solution' contained 100 mM KCl, 10 mM BAPTA, 10 mM HEPES, 10 mM NaCl, 4 mM ATP-Mg, 0.3 mM GTP-Na, pH 7.3. All solutions had 260–265 mOsm.

Membrane currents elicited with voltage ramps gave similar results to those with voltage steps (Supplementary Fig. 8). The  $\text{Ca}^{2+}$  current was measured from recordings as shown in Supplementary Fig. 9.

The light stimulus was generally a 40- $\mu\text{m}$ -diameter spot centred on the soma of the cell. The light-spot size was chosen to illuminate enough membrane area yet to avoid other dissociated cells and debris. Larger light spots (with twice the diameter) were occasionally used, but gave qualitatively similar results. Bigger light spots (200  $\mu\text{m}$  diameter) were used for catfish rod horizontal cells because these cells were larger. The microscope did not allow changing the light-spot size or moving it to different parts of the cell during the experiment without disturbing the recording.

**Cloning melanopsins and VA/VAL opsin from catfish retina.** Total RNA was isolated from catfish retina using TRIzol Reagent (Invitrogen), and reverse-transcribed into cDNA with SuperScript II reverse transcriptase (Invitrogen). Degenerate PCR primers were manually designed from a highly conserved region of 8–10 amino acids. Degeneracy was generally kept below 100-fold and idenosine was used when necessary in the 5' region of the primers. A second set of primers were designed using the program CODEHOP (consensus-degenerate hybrid oligonucleotide primers: [http://blocks.fhcr.org/help/CODEHOP/CODEHOP\\_help.html](http://blocks.fhcr.org/help/CODEHOP/CODEHOP_help.html)). Nested degenerate PCR was performed with Taq polymerase. Phusion DNA polymerase (Finnzymes) was used for PCR in 5'- and 3'-RACE.

The DNA sequences of degenerate PCR products were translated into amino-acid sequences and aligned with those of known melanopsins and VA opsins using Vector NTI (Invitrogen). The translated sequences were also used as templates to search for similar sequences in the genome database using NCBI Blast.

The accession numbers for catfish *OPN4m1* and *OPN4m2* are, respectively, FJ839437 and FJ839438. The accession numbers for VA and VAL opsins are FJ839435 and FJ839436, respectively.

**In situ hybridization of melanopsins and VA/VAL opsin mRNAs in catfish retina.** T7 or Sp6 RNA polymerase (New England Biolabs) was used to synthesize both sense and antisense RNA probes tagged with digoxigenin. For whole-mount staining, retinas were fixed in 4% paraformaldehyde, digested by proteinase K, post-fixed, washed with PBS, pre-hybridized and then hybridized overnight at 68 °C, followed by post-hybridization steps. Anti-digoxigenin alkaline phosphatase was used for colour development. Cross-sections (25  $\mu\text{m}$  thick) of fresh-frozen eyecups were made using a cryostat and processed to examine more clearly in which layer(s) the DIG signal was located.

30. Linn, C. L. & Gafka, A. C. Activation of metabotropic glutamate receptors modulates the voltage-gated sustained calcium current in a teleost horizontal cell. *J. Neurophysiol.* 81, 425–434 (1999).

## LETTERS

# Gain-of-function of mutated *C-CBL* tumour suppressor in myeloid neoplasms

Masashi Sanada<sup>1,5\*</sup>, Takahiro Suzuki<sup>7\*</sup>, Lee-Yung Shih<sup>8\*</sup>, Makoto Otsu<sup>9</sup>, Motohiro Kato<sup>1,2</sup>, Satoshi Yamazaki<sup>6</sup>, Azusa Tamura<sup>1</sup>, Hiroaki Honda<sup>11</sup>, Mamiko Sakata-Yanagimoto<sup>12</sup>, Keiki Kumano<sup>3</sup>, Hideaki Oda<sup>13</sup>, Tetsuya Yamagata<sup>14</sup>, Junko Takita<sup>1,2,3</sup>, Noriko Gotoh<sup>10</sup>, Kumi Nakazaki<sup>1,4</sup>, Norihiko Kawamata<sup>15</sup>, Masafumi Onodera<sup>16</sup>, Masaharu Nobuyoshi<sup>7</sup>, Yasuhide Hayashi<sup>17</sup>, Hiroshi Harada<sup>18</sup>, Mineo Kurokawa<sup>3,4</sup>, Shigeru Chiba<sup>12</sup>, Hiraku Mori<sup>18</sup>, Keiya Ozawa<sup>7</sup>, Mitsuhiro Omine<sup>18</sup>, Hisamaru Hirai<sup>3,4</sup>, Hiromitsu Nakauchi<sup>6,9</sup>, H. Phillip Koeffler<sup>15</sup> & Seishi Ogawa<sup>1,5</sup>

Acquired uniparental disomy (aUPD) is a common feature of cancer genomes, leading to loss of heterozygosity. aUPD is associated not only with loss-of-function mutations of tumour suppressor genes<sup>1</sup>, but also with gain-of-function mutations of proto-oncogenes<sup>2</sup>. Here we show unique gain-of-function mutations of the *C-CBL* (also known as *CBL*) tumour suppressor that are tightly associated with aUPD of the 11q arm in myeloid neoplasms showing myeloproliferative features. The *C-CBL* proto-oncogene, a cellular homologue of *v-Cbl*, encodes an E3 ubiquitin ligase and negatively regulates signal transduction of tyrosine kinases<sup>3–6</sup>. Homozygous *C-CBL* mutations were found in most 11q-aUPD-positive myeloid malignancies. Although the *C-CBL* mutations were oncogenic in NIH3T3 cells, *c-Cbl* was shown to functionally and genetically act as a tumour suppressor. *C-CBL* mutants did not have E3 ubiquitin ligase activity, but inhibited that of wild-type *C-CBL* and *CBL-B* (also known as *CBLB*), leading to prolonged activation of tyrosine kinases after cytokine stimulation. *c-Cbl*<sup>+/–</sup> haematopoietic stem/progenitor cells (HSPCs) showed enhanced sensitivity to a variety of cytokines compared to *c-Cbl*<sup>+/+</sup> HSPCs, and transduction of *C-CBL* mutants into *c-Cbl*<sup>+/–</sup> HSPCs further augmented their sensitivities to a broader spectrum of cytokines, including stem-cell factor (SCF, also known as KITLG), thrombopoietin (TPO, also known as THPO), IL3 and FLT3 ligand (FLT3LG), indicating the presence of a gain-of-function that could not be attributed to a simple loss-of-function. The gain-of-function effects of *C-CBL* mutants on cytokine sensitivity of HSPCs largely disappeared in a *c-Cbl*<sup>+/+</sup> background or by co-transduction of wild-type *C-CBL*, which suggests the pathogenic importance of loss of wild-type *C-CBL* alleles found in most cases of *C-CBL*-mutated myeloid neoplasms. Our findings provide a new insight into a role of gain-of-function mutations of a tumour suppressor associated with aUPD in the pathogenesis of some myeloid cancer subsets.

Myelodysplastic syndromes (MDS) are heterogeneous groups of blood cancers originating from haematopoietic precursors. They are

characterized by deregulated haematopoiesis showing a high propensity to acute myeloid leukaemia (AML)<sup>7</sup>. Some MDS cases have overlapping clinico-pathological features with myeloproliferative disorders, and are now classified into myelodysplasia/myeloproliferative neoplasms (MDS/MPN) by the World Health Organization (WHO) classification<sup>8</sup>. To obtain a comprehensive profile of allelic imbalances in these myeloid neoplasms, we performed allele-specific copy number analyses of bone marrow samples obtained from 222 patients with MDS, MDS/MPN, or other related myeloid neoplasms (Supplementary Tables 1 and 2) using high-density single nucleotide polymorphism (SNP) arrays combined with CNAG/AsCNAR software<sup>9,10</sup>.

Genomic profiles of MDS and MDS/MPN showed characteristic unbalanced genetic changes, as reported in previous cytogenetic studies<sup>11</sup> (Supplementary Fig. 1a); however, they were detected more sensitively by SNP array analyses (Supplementary Table 3). aUPD was detected in 70 samples (31.5%) on the basis of the allele-specific copy number analyses, which substantially exceeded the detection rate obtained using a SNP call-based detection algorithm (20.7%) (Supplementary Figs 2 and 4, and Supplementary Tables 4 and 5). Long stretches of homozygous SNP calls caused by shared identical-by-descent alleles in parents were empirically predicted and excluded (Supplementary Fig. 3). aUPDs were more common in MDS/MPN than in MDS. They preferentially affected several chromosomal arms (1p, 1q, 4q, 7q, 11p, 11q, 14q, 17p and 21q) in distinct subsets of patients, and frequently associated with mutated oncogenes and tumour suppressor genes (Supplementary Figs 1b and 5). Among these, the most common aUPDs were those involving 11q ( $n = 17$ ), which defined a unique subset of myeloid neoplasms that were clinically characterized by frequent diagnosis of chronic myelomonocytic leukaemia (CMML) with normal karyotypes (13 cases) (Fig. 1a and Supplementary Table 6). We identified a minimum overlapping aUPD segment of approximately 1.4 megabases (Mb) in 11q, which contained a mutated *C-CBL* proto-oncogene (Fig. 1b).

<sup>1</sup>Cancer Genomics Project, <sup>2</sup>Department of Pediatrics, <sup>3</sup>Cell Therapy and Transplantation Medicine, and <sup>4</sup>Hematology and Oncology, Graduate School of Medicine, The University of Tokyo, 7-3-1 Hongo, Bunkyo-ku, Tokyo 113-8655, Japan. <sup>5</sup>Core Research for Evolutional Science and Technology, <sup>6</sup>Exploratory Research for Advanced Technology, Japan Science and Technology Agency, 4-1-8 Honcho, Kawaguchi-shi, Saitama 332-0012, Japan. <sup>7</sup>Division of Hematology, Department of Medicine, Jichi Medical University, 3311-1 Yakushiji, Shimotsuke-shi, Tochigi 329-0498, Japan. <sup>8</sup>Division of Hematology-Oncology, Department of Internal Medicine, Chang Gung Memorial Hospital, Chang Gung University, 199 Tung Hwa North Road, Taipei 105, Taiwan. <sup>9</sup>Division of Stem Cell Therapy, Center for Stem Cell and Regenerative Medicine, <sup>10</sup>Division of Systems Biomedical Technology, Institute of Medical Science, The University of Tokyo, 4-6-1 Shirokanedai, Minato-ku, Tokyo 108-8639, Japan. <sup>11</sup>Department of Developmental Biology, Research Institute of Radiation Biology and Medicine, Hiroshima University, 1-2-3 Kasumi, Minami-ku, Hiroshima 734-8553, Japan. <sup>12</sup>Department of Clinical and Experimental Hematology, Institute of Clinical Medicine, University of Tsukuba, 1-1-1 Tennodai, Tsukuba-shi, Ibaraki, 305-8571, Japan. <sup>13</sup>Department of Pathology, Tokyo Women's Medical University, 8-1 Kawada-cho, Shinjuku-ku, Tokyo 162-8666, Japan. <sup>14</sup>Department of Hematology, Dokkyo University School of Medicine, 800 Kitabayashi, Mibu, Tochigi 321-0293, Japan. <sup>15</sup>Hematology/Oncology, Cedars-Sinai Medical Center, 8700 Beverly Boulevard, Los Angeles, California 90048, USA. <sup>16</sup>Department of Genetics, National Research Institute for Child Health and Development, 2-10-1 Okura, Setagaya-ku, Tokyo, 157-8535, Japan. <sup>17</sup>Gunma Children's Medical Center, 779 Shimohakoda, Hokenchi-machi, Shibukawa-shi, Gunma 377-8577, Japan. <sup>18</sup>Division of Hematology, Internal Medicine, Showa University Fujigaoka Hospital, 1-30 Fujigaoka, Aoba-ku, Yokohama, Kanagawa 227-8501, Japan.

\*These authors contributed equally to this work.

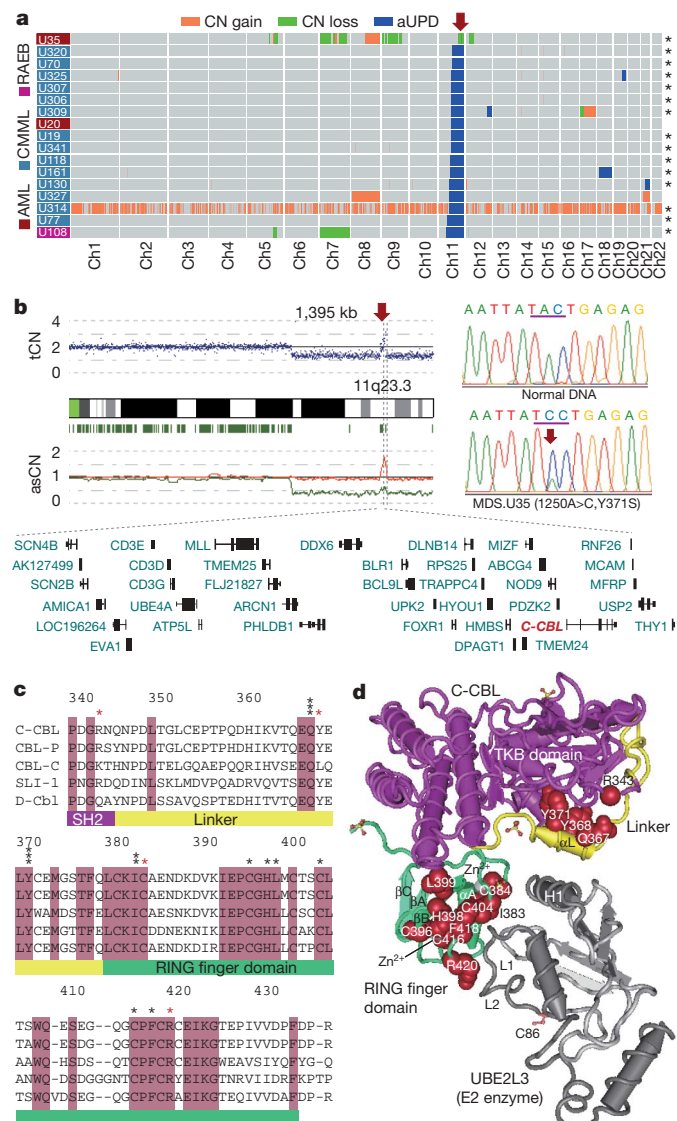


**Figure 1 | Common UPD on the 11q arm and *C-BL* mutations in myeloid neoplasms.** **a**, Copy number profiles of 17 cases with myeloid neoplasms showing 11qUPD. Regions of copy number (CN) gains, losses and aUPD are depicted in different colours. Histologies are shown by coloured boxes. Asterisks denote *C-BL*-mutated cases. Ch, chromosome; RAEB, refractory anaemia with excess blasts. **b**, CNAG output for MDS.U35. Total copy number (tCN) and allele-specific copy number (asCN) plots show a focal copy number gain spanning a 1.4-Mb segment within 3 Mb of an 11q-aUPD region (left), which contained mutated *C-BL* in MDS.U35 (right). **c**, Alignments of amino acid sequences for human *CBL* family proteins and their homologues in *Caenorhabditis elegans* (SLI-1) and *Drosophila* (D-Cbl). Amino acid numbering is on the basis of human *C-BL*. Conserved amino acids are highlighted. Positions of mutated amino acids are indicated by asterisks. Heterozygous mutations are shown in red. **d**, Mutated amino acid positions in the three-dimensional structure of a human *C-BL*-UBE2L3 complex. TKB, tyrosine kinase binding domain.

*C-BL* is the cellular homologue of the *v-Cbl* transforming gene of the Cas NS-1 murine leukaemia virus<sup>5,12</sup>. It was recently found to be mutated in human AML cases<sup>13–15</sup>. Together with its close homologue, *CBL-B*, *C-BL* is thought to be involved in the negative modulation of tyrosine kinase signalling, primarily through their E3 ubiquitin ligase activity that is responsible for the downregulation of activated tyrosine kinases<sup>3–5</sup>. By sequencing all *C-BL* exons in all 222 samples, we found *C-BL* mutations in 15 of the 17 cases with 11q-aUPD, whereas only 3 out of 205 cases without 11q-aUPD had *C-BL* mutations, showing a strong association of *C-BL* mutations with 11q-aUPD ( $P = 1.46 \times 10^{-18}$ ) (Supplementary Fig. 6 and

Supplementary Tables 6 and 7), as also indicated in a recent report<sup>16</sup>. Thus, *C-BL* was thought to be the major, if not the only, target of 11q-aUPD in myeloid neoplasms. Two different *C-BL* mutations co-existed in three cases (Supplementary Fig. 6b). Somatic origins of the mutations were confirmed in three evaluable cases (Supplementary Fig. 6c).

In most cases, *C-BL* mutations were missense, involving the evolutionarily conserved amino acids within the linker-RING finger domain that is central to the E3 ubiquitin ligase activity<sup>17</sup> (Fig. 1c). Another case with a predominant Cys384Tyr mutation also contained a nonsense mutation (Arg343X) in a minor subclone, which resulted in a v-Cbl-like truncated protein (Supplementary Fig. 6b). In the remaining two cases, mutations led to amino acid deletions ( $\Delta 369-371$  and  $\Delta 368-382$ ) involving the highly conserved  $\alpha$ -helix ( $\alpha$ L) of the linker domain and the first loop of the RING finger. According to the published crystal structure of *C-BL*<sup>17</sup>, most of the mutated or deleted amino acids were positioned on the interface for the binding to the E2 enzyme (Fig. 1d), making contact with either the tyrosine kinase binding domain (Tyr 368 and Tyr 371) or E2 ubiquitin-conjugating enzymes (Ile 383, Cys 404 and Phe 418). Especially, all seven linker-domain mutations selectively involved just three amino acids (Gln 367, Tyr 368 and Tyr 371) within the conserved  $\alpha$ L helix (Fig. 1d). Mutations were clearly homozygous in nine cases, and the apparently heterozygous chromatograms in the other six cases could also be compatible with homozygous mutations affecting the aUPD-positive tumour clones, given the presence of substantial normal cell components within these samples. Mutations in the remaining three cases were considered to be heterozygous. About half of the *C-BL*-mutated cases carried coexisting mutations of *RUNX1* (four cases), *TP53* (one case), *FLT3* internal tandem duplication (1 case) or *JAK2* (3 cases). *NRAS* and *KRAS* mutations were prevalent among CMM1 (15.1%) but occurred within discrete clusters from *C-BL*-mutated cases (Supplementary Tables 2 and 6 and Supplementary Fig. 5). The mutation status of *C-BL* did not substantially affect the clinical outcome (Supplementary Fig. 7).

All tested *C-BL* mutants induced clear oncogenic phenotypes in NIH3T3 fibroblasts, as demonstrated by enhanced colony formation in soft agar and tumour generation in nude mice (Supplementary Fig. 8). Transformed NIH3T3 cells showed PI3 kinase-dependent activation of Akt and the transformed phenotype was reverted by treatment with the PI3 kinase inhibitor Ly294002 (Supplementary Fig. 9). When introduced into Lin<sup>−</sup> Sca1<sup>+</sup> c-Kit<sup>+</sup> (LSK) HSPCs, *C-BL* mutants (*C-BL*(Gln367Pro) and *C-BL*(Tyr371Ser)), as well as a mouse lymphoma-derived oncogenic mutant (*C-BL*(70Z)), significantly promoted the replating capacity of these progenitors (Fig. 2a). Because c-Cbl negatively modulates tyrosine kinase signalling, and all *C-BL* mutations, including those previously reported<sup>13–16</sup>, affected the critical domains for its enzymatic activity involved in this modulation, *C-BL* was postulated to have a tumour suppressor function; loss-of-function could be a mechanism for the oncogenicity of these *C-BL* mutants<sup>3,5</sup>. To assess this possibility and to clarify further the role of *C-BL* mutations in the pathogenesis of myeloid neoplasms, we generated *c-Cbl*<sup>−/−</sup> mice and examined their haematological phenotypes (Supplementary Fig. 10).

In agreement with previous reports<sup>18–20</sup>, *c-Cbl*<sup>−/−</sup> mice exhibited splenomegaly and an augmented haematopoietic progenitor pool, as was evident from the increased colony formation of bone marrow cells in methylcellulose culture and higher numbers of LSK and CD34-negative LSK cells in bone marrow and/or spleen compared to their wild-type littermates (Fig. 2b–d and Supplementary Fig. 11). Furthermore, when introduced into a *BCR-ABL* transgenic background<sup>21</sup>, the *c-Cbl*<sup>−/−</sup> allele accelerated blastic crisis depending on the allele dosage (Fig. 2e, f). These observations supported the notion that wild-type *C-BL* has tumour suppressor functions, whereas ‘mutant’ *C-BL* acts as an oncogene; *C-BL* can therefore be both a proto-oncogene and a tumour suppressor gene.



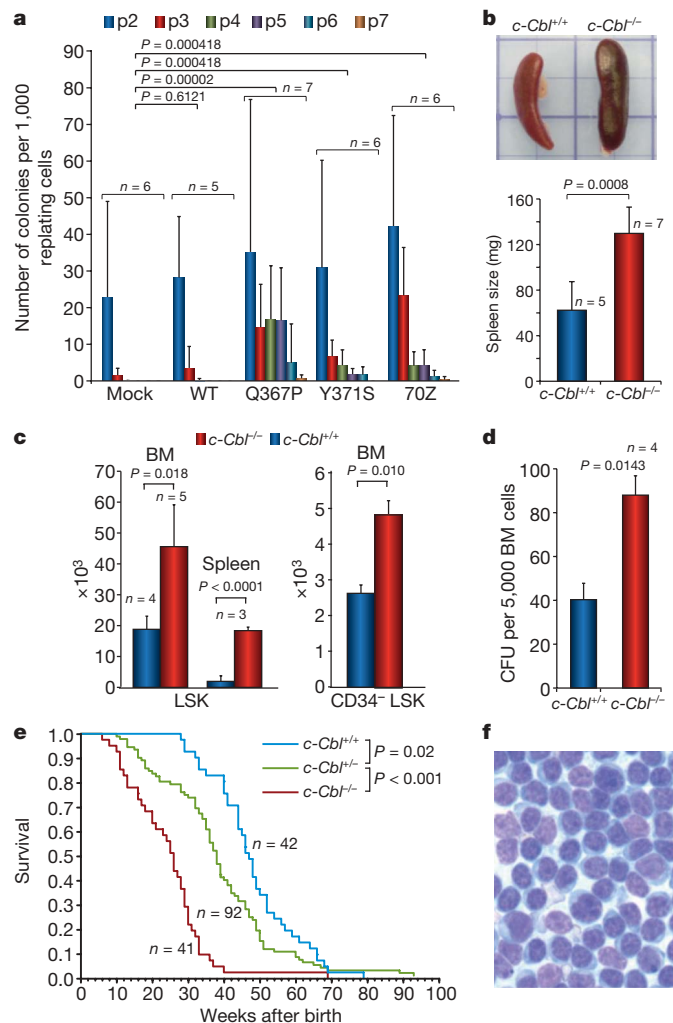


**Figure 2 | Tumour-suppressor functions of wild-type C-CBL.** **a**, Prolonged replating capacity of LSK cells transduced with mutant *C-CBL* (*C-CBL*(Gln367Pro) and *C-CBL*(Tyr371Ser)), compared to mock- or wild-type *C-CBL*-transduced cells. Replating capacity in methylcellulose culture is shown as mean colony number (and s.d.) per 1,000 replating cells at indicated times of replating. **b**, Increased spleen mass in *c-Cbl*<sup>-/-</sup> mice compared to *c-Cbl*<sup>+/+</sup> mice (mean spleen weight and s.d.). **c**, Mean number of total LSK (left) and CD34<sup>+</sup>-negative LSK (right) cells (plus s.d.) in bone marrow (BM) and/or spleen in *c-Cbl*<sup>+/+</sup> (blue columns) and *c-Cbl*<sup>-/-</sup> mice (red columns). Bone marrow cells from bilateral tibias and femurs were counted for each mouse. **d**, Augmented colony-forming potential of bone marrow cells from *c-Cbl*<sup>-/-</sup> mice (mean colony number and s.d. per 5,000 bone marrow cells). CFU, colony-forming units. **e**, Kaplan-Meier survival curves of *c-Cbl*<sup>+/+</sup>, *c-Cbl*<sup>+/+</sup> and *c-Cbl*<sup>-/-</sup> mice carrying a *BCR-ABL* transgene, showing acceleration of blastic crisis in *c-Cbl*<sup>+/+</sup> and *c-Cbl*<sup>-/-</sup> mice. **f**, Wright-Giemsa staining of an enlarged lymph node in a *Bcr-Abl*<sup>+</sup> *c-Cbl*<sup>-/-</sup> mouse during blastic crisis shows massive infiltrates of immature leukaemic blasts. Original magnification, ×600.

Mouse LSK HSPCs expressed two Cbl family member proteins: wild-type *c-Cbl* and *Cbl-b* (Supplementary Fig. 12)<sup>22</sup>. When transduced into NIH3T3 cells stably expressing human epidermal growth factor receptor (EGFR), both Cbl proteins enhanced ubiquitination of EGFR after EGF stimulation, which was suppressed by coexpression of the *C-CBL* mutants (Fig. 3a, b). In haematopoietic cells, overexpression of wild-type *C-CBL* enhanced ligand-induced ubiquitination of a variety of tyrosine kinases, including *c-KIT*, *FLT3* and *JAK2*. In contrast, *C-CBL* mutants not only showed compromised enzymatic activity, but also inhibited the ubiquitinating activities in these haematopoietic cells (Fig. 3c), leading to prolonged tyrosine kinase activation after ligand stimulation (Fig. 3d).

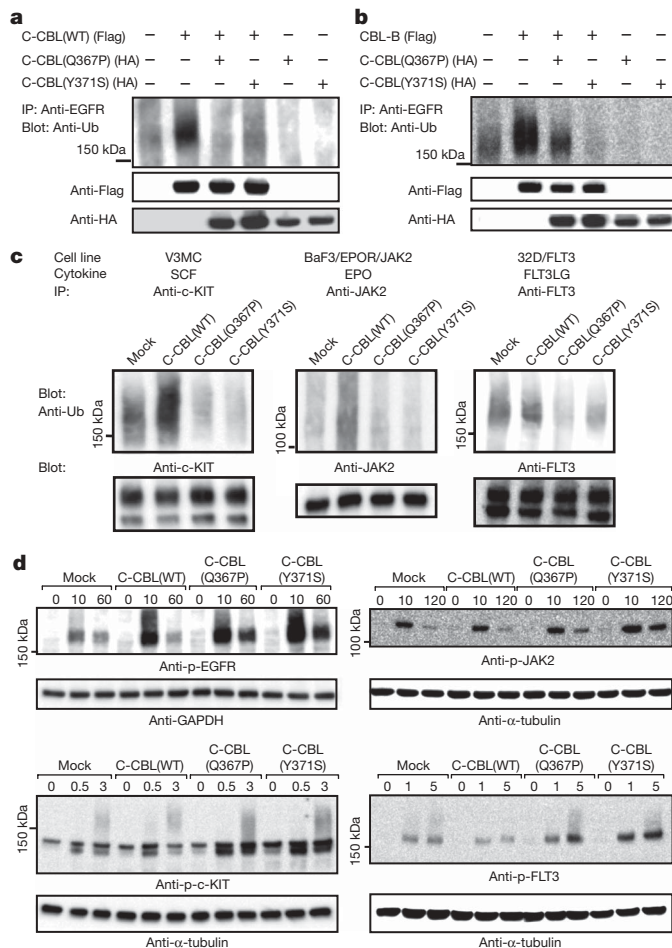


**Figure 3 | Inhibitory actions of C-CBL mutants on wild-type C-CBL.**

**a**, **b**, Flag-tagged wild-type *C-CBL* (a) or *CBL-B* (b) were transfected into NIH3T3 cells stably transduced with human EGFR plus indicated HA-tagged *C-CBL* mutants. Anti-ubiquitin blots of immunoprecipitated EGFR after EGF stimulation show the inhibitory actions of the *C-CBL* mutants on ubiquitinating activity of *C-CBL* (a) and *CBL-B* (b). Bottom panels are anti-HA and anti-Flag blots of total cell lysates. **c**, Effects of wild-type and mutant *C-CBL* on cytokine-induced ubiquitination of *c-KIT*, *JAK2* and *FLT3* in haematopoietic cells V3MC, BaF3 co-transduced with human erythropoietin receptor (EPOR) and *JAK2* (BaF3/EPOR/*JAK2*), and *FLT3*-transduced 32D (32D/*FLT3*), respectively. Each cell line was further transduced with indicated *C-CBL* mutants, and ubiquitination of immunoprecipitated kinases was detected by anti-ubiquitin blots at 1 min after stimulation with SCF, EPO and *FLT3LG*. Anti-kinase blots of the precipitated kinases are shown below each panel. **d**, Kinase phosphorylation was examined at indicated time points (shown in minutes) after ligand stimulation using immunoblot analyses of total cell lysates using antibodies to phosphorylated (p-) EGFR, *c-KIT*, *JAK2* and *FLT3* in which anti- $\alpha$ -tubulin or anti-GAPDH blots are provided as a control.

Because tyrosine kinase signalling is central to cytokine responses in haematopoietic cells and its deregulation is a common feature of myeloproliferative disorders<sup>23</sup>, we next examined the effects of *C-CBL* mutations (*C-CBL*(Gln367Pro) and *C-CBL*(Tyr371Ser)) and the loss of wild-type *C-CBL* alleles on the responses of LSK HSPCs to various cytokines. In serum-free conditions, *c-Cbl*<sup>-/-</sup> LSK cells showed a modestly enhanced proliferative response to a variety of cytokines, including SCF, IL3 and TPO, compared to *c-Cbl*<sup>+/+</sup> cells (mock columns in Fig. 4a). However, the enhanced response in *c-Cbl*<sup>-/-</sup> cells was markedly augmented and extended to a broader spectrum of cytokines, including *FLT3* ligand by the transduction of *C-CBL* mutants. Of note, the effect of *C-CBL* mutant transduction was not remarkable in *c-Cbl*<sup>+/+</sup> LSK cells except for the response to SCF, which was clearly enhanced by *C-CBL* mutants

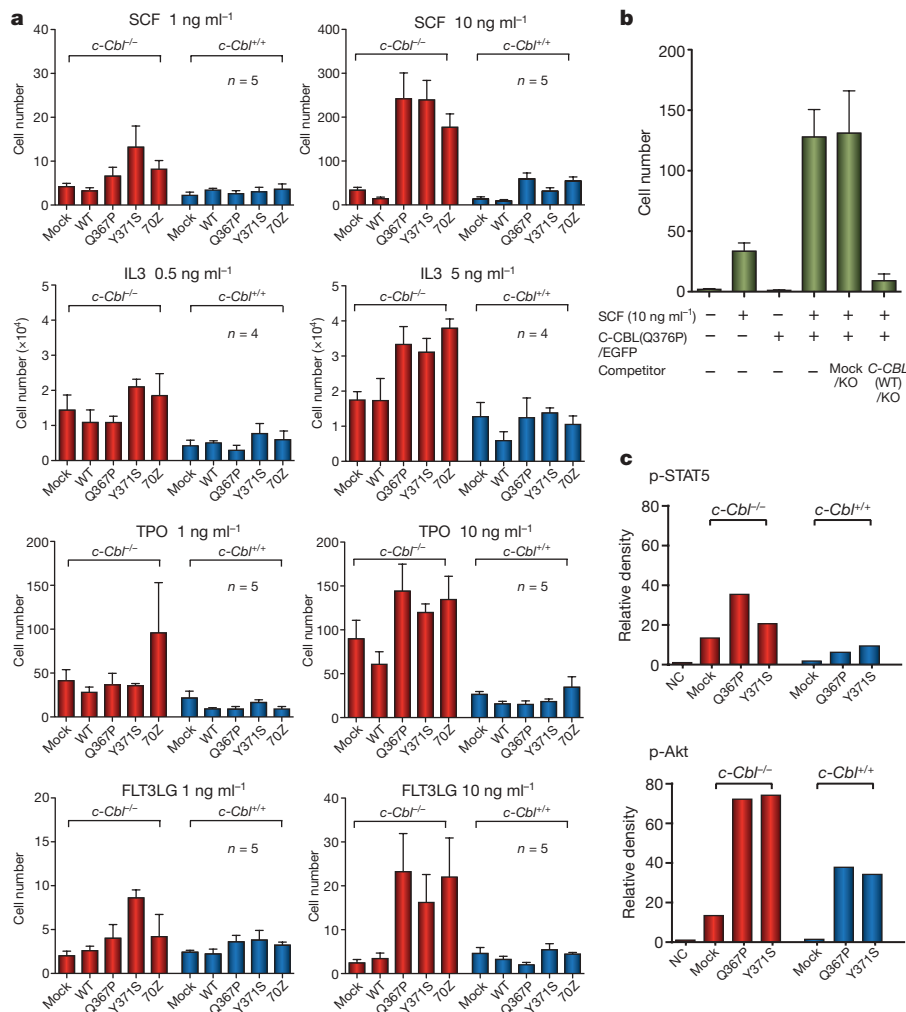


**Figure 4 | Gain-of-function of mutant C-CBL augmented by loss of wild-type C-CBL.** **a**, *c-Cbl*<sup>+/+</sup> and *c-Cbl*<sup>-/-</sup> LSK cells were transfected with various C-CBL internal ribosome entry site (IRES)/green fluorescent protein (GFP) constructs, and 50 GFP-positive cells were sorted for serum-free culture containing indicated concentrations of SCF, IL3, TPO and FLT3LG. Mean cell numbers (plus s.e.m.) on day 5 are plotted. **b**, *c-Cbl*<sup>+/+</sup> LSK cells were co-transduced with C-CBL(Gln367Pro)-IRES-EGFP (C-CBL(Q367P)/EGFP) and mock-IRES-Kusabira-Orange (mock/KO) or wild-type C-CBL-IRES-Kusabira-Orange (C-CBL(WT)/KO), and 50 GFP/KO double-positive

cells were sorted into each well for cell proliferation assays in serum-free culture containing 10 ng ml<sup>-1</sup> SCF. Mean cell numbers on day 5 (plus s.e.m., *n* = 5) are plotted. **c**, Ten thousand *c-Cbl*<sup>+/+</sup> and *c-Cbl*<sup>-/-</sup> LSK cells transduced with various C-CBL constructs were stimulated with 10 ng ml<sup>-1</sup> SCF and 10 ng ml<sup>-1</sup> TPO for 15 min. Total cell lysates were analysed by immunoblotting, using antibodies to STAT5, Akt and their phosphorylated forms. The intensities of phosphorylated proteins relative to total STAT5 (top panel) and Akt (bottom panel) are plotted. NC indicates the mean background signal obtained with nonspecific IgG.

even with a *c-Cbl*<sup>+/+</sup> background (Fig. 4a and Supplementary Fig. 13). To clarify further the effect of wild-type C-CBL on C-CBL mutants, both wild-type C-CBL and C-CBL mutants were co-transduced into *c-Cbl*<sup>-/-</sup> LSK cells, and their effects on the response to SCF were examined. As shown in Fig. 4b, the hyperproliferative response induced by C-CBL mutants was almost completely abolished by the co-transduction of wild-type C-CBL, suggesting the pathogenic importance of loss of wild-type C-CBL alleles found in most C-CBL-mutated cases. LSK cells transduced with C-CBL mutants also showed enhanced activation of the STAT5 and Akt pathways on cytokine stimulation (SCF and TPO), which was more pronounced in *c-Cbl*<sup>-/-</sup> than *c-Cbl*<sup>+/+</sup> LSK cells (Fig. 4c and Supplementary Fig. 14).

The modest enhancement of sensitivity to cytokines found in *c-Cbl*<sup>-/-</sup> LSK cells was a consequence of loss of C-CBL functions. In contrast, the hypersensitive response of mutant-transduced *c-Cbl*<sup>-/-</sup> LSK cells to a broad spectrum of cytokines represents gain-of-function of the mutants that could not be ascribed to a simple loss of C-CBL functions, which was also predicted from the strong association of C-CBL mutations with 11q-aUPD by analogy to the gain-of-function JAK2 mutations associated with 9p-aUPD in polycythemia vera<sup>2</sup>. The gain-of-function of C-CBL mutants became

more evident under a *c-Cbl*<sup>-/-</sup> background. The hypersensitive response to cytokines induced by mutant C-CBL under the *c-Cbl*<sup>-/-</sup> background was largely offset by the presence of the wild-type *c-Cbl* allele or by the transduction of the wild-type C-CBL gene, suggesting that the gain-of-function could be closely related to loss of C-CBL-like functions, probably by inhibition of Cbl-b. Supporting this view is a previous report that *c-Cbl/Cbl-b* double knockout T cells showed more profound impairments in the downregulation of the T-cell receptor (TCR), more sustained TCR signalling, and more vigorous proliferation, than *c-Cbl* or *Cbl-b* single knockout T cells after anti-CD3 (also known as CD3e) stimulation<sup>24</sup>. This is analogous to the gain-of-function found in some TP53 mutants, which has been explained by functional inhibition of two TP53 homologues, TP73 and TP63 (refs 25, 26). Of note, TP53 was also originally isolated as an oncogene through its mutated forms<sup>27</sup>. The Cbl-b inhibition-based gain-of-function model could be tested directly by comparing the behaviour of *c-Cbl/Cbl-b* double knockout LSK cells with that of LSK cells carrying homozygously knocked-in mutant C-CBL alleles. On the other hand, there remains a possibility that the gain-of-function could be mediated by a mechanism other than the simple inhibition of the homologue, because C-CBL mutants retained several motifs

that interacted with numerous signal-transducing molecules. Furthermore, considering the ubiquitous expression of CBL proteins, it would be of interest to explore the possible involvement of mutations in all CBL family members in other human cancers.

## METHODS SUMMARY

Genomic DNA from 222 bone marrow samples with myeloid neoplasms were analysed using GeneChip SNP-genotyping microarrays (Affymetrix GeneChip) as described<sup>28</sup>. Allelic imbalances were detected from the allele-specific copy numbers calculated using CNAG/AsCNAR software (<http://www.genome.umin.jp>)<sup>9,10</sup>. C-CBL mutations were examined by sequencing PCR-amplified genomic DNA. For functional assays, haemagglutinin (HA)- or Flag-tagged complementary DNAs of wild-type and mutant C-CBL were generated by *in vitro* mutagenesis, constructed into a MSCV-based retroviral vector, pGCDNsamIRESGFP or pGCDNsamIRESKO, and used for retrovirus-mediated gene transfer. For the evaluation of oncogenicity of C-CBL mutants, NIH3T3 cells were transfected with various C-CBL constructs and used for colony assays in soft agar and tumour formation assays in nude mice. c-Cbl-deficient mice were generated using a conventional strategy of gene-targeting and crossed with BCR-ABL transgenic mice to evaluate the effect of the c-Cbl allele on the acceleration of blastic crisis. LSK cells sorted from c-Cbl<sup>+/+</sup> and c-Cbl<sup>-/-</sup> mice were transduced with various C-CBL constructs. Their responses to cytokines were evaluated by cell proliferation assays, followed by immunoblot analyses of c-KIT, FLT3 and JAK2, as well as their downstream signalling molecules. The effects of C-CBL mutant expression on the ubiquitination of EGFR, c-KIT, FLT3 and JAK2 were examined by transducing C-CBL mutants into relevant cells, followed by anti-ubiquitin blots of the immunoprecipitated kinases after ligand stimulation. Functional competition of C-CBL mutants with wild-type C-CBL was assessed by cell proliferation assays of LSK cells co-transduced with both wild-type and mutant C-CBL genes. This study was approved by the ethics boards of the University of Tokyo, Chang Gung Memorial Hospital and Showa University. Antibodies and primers used in this study are listed in Supplementary Tables 8 and 9.

**Full Methods** and any associated references are available in the online version of the paper at [www.nature.com/nature](http://www.nature.com/nature).

Received 9 October 2008; accepted 30 June 2009.

Published online 20 July 2009.

- Knudson, A. G. Two genetic hits (more or less) to cancer. *Nature Rev. Cancer* **1**, 157–162 (2001).
- James, C. *et al.* A unique clonal JAK2 mutation leading to constitutive signalling causes polycythaemia vera. *Nature* **434**, 1144–1148 (2005).
- Ryan, P. E. *et al.* Regulating the regulator: negative regulation of Cbl ubiquitin ligases. *Trends Biochem. Sci.* **31**, 79–88 (2006).
- Schmidt, M. H. & Dikic, I. The Cbl interactome and its functions. *Nature Rev. Mol. Cell Biol.* **6**, 907–918 (2005).
- Thien, C. B. & Langdon, W. Y. Cbl: many adaptations to regulate protein tyrosine kinases. *Nature Rev. Mol. Cell Biol.* **2**, 294–307 (2001).
- Thien, C. B. & Langdon, W. Y. c-Cbl and Cbl-b ubiquitin ligases: substrate diversity and the negative regulation of signalling responses. *Biochem. J.* **391**, 153–166 (2005).
- Corey, S. J. *et al.* Myelodysplastic syndromes: the complexity of stem-cell diseases. *Nature Rev. Cancer* **7**, 118–129 (2007).
- Jaffe, E., Harris, N., Stein, H. & Vardiman, J. *World Health Organization Classification of Tumours: Pathology and Genetics of Tumours of Haematopoietic and Lymphoid Tissues* 62–73 (IARC Press, 2002).
- Nannya, Y. *et al.* A robust algorithm for copy number detection using high-density oligonucleotide single nucleotide polymorphism genotyping arrays. *Cancer Res.* **65**, 6071–6079 (2005).
- Yamamoto, G. *et al.* Highly sensitive method for genomewide detection of allelic composition in nonpaired, primary tumor specimens by use of affymetrix single-nucleotide-polymorphism genotyping microarrays. *Am. J. Hum. Genet.* **81**, 114–126 (2007).

- Haase, D. Cytogenetic features in myelodysplastic syndromes. *Ann. Hematol.* **87**, 515–526 (2008).
- Langdon, W. Y. *et al.* v-cbl, an oncogene from a dual-recombinant murine retrovirus that induces early B-lineage lymphomas. *Proc. Natl Acad. Sci. USA* **86**, 1168–1172 (1989).
- Abbas, S. *et al.* Exon 8 splice site mutations in the gene encoding the E3-ligase CBL are associated with core binding factor acute myeloid leukemias. *Haematologica* **93**, 1595–1597 (2008).
- Caligiuri, M. A. *et al.* Novel c-CBL and CBL-b ubiquitin ligase mutations in human acute myeloid leukemia. *Blood* **110**, 1022–1024 (2007).
- Sargin, B. *et al.* FLT3-dependent transformation by inactivating c-Cbl mutations in AML. *Blood* **110**, 1004–1012 (2007).
- Dunbar, A. J. *et al.* 250K single nucleotide polymorphism array karyotyping identifies acquired uniparental disomy and homozygous mutations, including novel missense substitutions of c-Cbl, in myeloid malignancies. *Cancer Res.* **68**, 10349–10357 (2008).
- Zheng, N. *et al.* Structure of a c-Cbl-UbcH7 complex: RING domain function in ubiquitin-protein ligases. *Cell* **102**, 533–539 (2000).
- Murphy, M. A. *et al.* Tissue hyperplasia and enhanced T-cell signalling via ZAP-70 in c-Cbl-deficient mice. *Mol. Cell. Biol.* **18**, 4872–4882 (1998).
- Naramura, M. *et al.* Altered thymic positive selection and intracellular signals in Cbl-deficient mice. *Proc. Natl Acad. Sci. USA* **95**, 15547–15552 (1998).
- Rathinam, C. *et al.* The E3 ubiquitin ligase c-Cbl restricts development and functions of hematopoietic stem cells. *Genes Dev.* **22**, 992–997 (2008).
- Honda, H. *et al.* Acquired loss of p53 induces blastic transformation in p210(bcr/abl)-expressing hematopoietic cells: a transgenic study for blast crisis of human CML. *Blood* **95**, 1144–1150 (2000).
- Zeng, S. *et al.* Regulation of stem cell factor receptor signaling by Cbl family proteins (Cbl-b/c-Cbl). *Blood* **105**, 226–232 (2005).
- Kaushansky, K. Hematopoietic growth factors, signaling and the chronic myeloproliferative disorders. *Cytokine Growth Factor Rev.* **17**, 423–430 (2006).
- Naramura, M. *et al.* c-Cbl and Cbl-b regulate T cell responsiveness by promoting ligand-induced TCR down-modulation. *Nature Immunol.* **3**, 1192–1199 (2002).
- Dittmer, D. *et al.* Gain of function mutations in p53. *Nature Genet.* **4**, 42–46 (1993).
- Lang, G. A. *et al.* Gain of function of a p53 hot spot mutation in a mouse model of Li-Fraumeni syndrome. *Cell* **119**, 861–872 (2004).
- Finlay, C. A., Hinds, P. W. & Levine, A. J. The p53 proto-oncogene can act as a suppressor of transformation. *Cell* **57**, 1083–1093 (1989).
- Chen, Y. *et al.* Oncogenic mutations of ALK kinase in neuroblastoma. *Nature* **455**, 971–974 (2008).

**Supplementary Information** is linked to the online version of the paper at [www.nature.com/nature](http://www.nature.com/nature).

**Acknowledgements** This work was supported by the Core Research for Evolutional Science and Technology, Japan Science and Technology Agency, a Grant-in-Aid from the Ministry of Health, Labor and Welfare of Japan and from the Ministry of Education, Culture, Sports, Science and Technology, and a grant from National Health Research Institute, Taiwan, NHRI-EX96-9434SI, and NIH-2R01CA026038-30. We thank W. Y. Langdon for providing a human C-CBL cDNA. A mast-cell line expressing c-KIT V3MC was a gift from M. F. Gurish. We also thank Y. Ogino and K. Fujita for their technical assistance.

**Author Contributions** M.S. and M.Kato performed microarray experiments and subsequent data analyses. T.S., T.Y., H.Honda and H.Hirai generated and analysed c-Cbl-null mice. M.S., M.Otsu, S.Y., M.N., K.K., N.G., M.Onodera, M.S.-Y. and H.N. conducted functional assays of C-CBL mutants. L.-Y.S., M.S., M.Kato, K.N., J.T. and A.T. performed mutation analysis. H.O. performed pathological analysis of c-Cbl-null mice. L.-Y.S., N.K., H.Harada, M.Kurokawa, S.C., H.M., H.P.K. and M.Omine prepared MDS specimens. M.S., M.Otsu, Y.H., K.O., H.M., H.N., L.-Y.S., H.P.K. and S.O. designed the overall study, and S.O. wrote the manuscript. All authors discussed the results and commented on the manuscript.

**Author Information** Full copy number data for the 222 samples are accessible from the Gene Expression Omnibus public database (<http://ncbi.nlm.nih.gov/geo/>) with the accession number GSE15187. Reprints and permissions information is available at [www.nature.com/reprints](http://www.nature.com/reprints). Correspondence and requests for materials should be addressed to S.O. (sogawa-ky@umin.ac.jp) or L.-Y.S. (sly7012@adm.cgmh.org.tw).



## METHODS

**Genome-wide analysis of allelic imbalances in primary myeloid neoplasms.** Bone marrow specimens were obtained from 222 patients diagnosed with myeloid neoplasms according to the WHO classification (Supplementary Tables 1 and 2). High molecular weight genomic DNA was extracted and used for microarray analysis using Affymetrix GeneChip 50K XbaI, HindIII or 250K NspI, according to the manufacturer's instructions. Genome-wide detection of allelic imbalances was performed using CNAG/AsCNAR software (<http://www.genome.umin.jp>)<sup>9,10</sup>.

**Mutation analysis.** Mutation analysis was performed by direct sequencing of PCR-amplified coding exons of the relevant genes, using an ABI PRISM 3100 genetic analyser (Applied Biosystems). The target genes, exons and PCR primers are listed in Supplementary Table 8. Tandem duplication of the *FLT3* gene was examined by genomic PCR and sequencing.

**Preparation of high-titre vesicular stomatitis virus glycoprotein (VSV-G)-pseudotyped retroviral particles.** HA-tagged human *C-CBL* cDNA was a gift from W. Y. Langdon. Nine mutant cDNAs of *C-CBL*, including eight from patients' specimens and a 70Z mutant corresponding to a mutant isolated from mouse lymphoma<sup>29</sup>, were generated on the basis of this construct, using a QuickChange site-directed mutagenesis kit (Stratagene). These were then constructed into the retrovirus vectors pGCDNsmIRESGFP and pGCDNsmIRESKO<sup>30–32</sup>. Vector plasmids were co-transfected with a VSV-G cDNA into 293GP cells (provided by R. C. Mulligan) to obtain retrovirus-containing supernatant, which was then transduced into 293GPG cells to establish stable cell lines capable of producing VSV-G-pseudotyped retroviral particles on induction<sup>33,34</sup>. The average titre of retrovirus stocks prepared from these cell lines routinely exceeded approximately  $1\text{--}10 \times 10^7$  inclusion-forming units per ml, as estimated using Jurkat cells.

**Assays for anchorage-independent growth and tumorigenicity in nude mice.** NIH3T3 cells (the Japan Cell Resource Bank) were stably transduced with wild-type and mutant *C-CBL* by retrovirus-mediated gene transfer. For colony formation assays,  $1.0 \times 10^3$  stable cells for each construct were inoculated in 0.33% top agar, and the numbers of colonies  $>1$  mm in diameter were counted 3 weeks after inoculation ( $n = 8$ ). Experiments were repeated four times. For tumour formation in nude mice,  $1.0 \times 10^7$  stable cells were inoculated subcutaneously at two sites per mouse. Cells were inoculated at six sites in three mice for each construct.

**Purification of LSK HSPCs.** LSK HSPCs were purified from bone marrow and spleen as described<sup>35,36</sup>. Multicolour flow cytometry analysis and cell sorting were performed using a MoFlo cell Sorter (Beckman Coulter). The purity of sorted cell fractions consistently exceeded 98%.

**Replating assays of bone marrow progenitor cells.** Bone marrow LSK cells were infected with IRES/GFP-containing retrovirus carrying mock, wild-type *C-CBL* and three *C-CBL* mutants (*C-CBL*(Gln367Pro), *C-CBL*(Tyr371Ser) and *C-CBL*(Cys384Gly)) as well as *C-CBL*(70Z) on RetroNectin-coated dishes. After 48 h infection in culture in StemSpan supplemented with SCF ( $50 \text{ ng ml}^{-1}$ ; Peprotech), TPO ( $20 \text{ ng ml}^{-1}$ ) and FLT3LG ( $20 \text{ ng ml}^{-1}$ ),  $1.0 \times 10^2$  GFP-positive cells were inoculated in MethoCult M3231 supplemented with TPO ( $20 \text{ ng ml}^{-1}$ ), IL3 ( $10 \text{ ng ml}^{-1}$ ), IL6 ( $10 \text{ ng ml}^{-1}$ ), FLT3LG ( $10 \text{ ng ml}^{-1}$ ) and SCF ( $50 \text{ ng ml}^{-1}$ ) for colony formation. Colony-forming cells were collected 7 days after each inoculation, from which  $1.0 \times 10^3$  cells were repeatedly subjected to replating until no colonies were produced. Experiments were repeated at the indicated times for each *C-CBL* construct.

**Generation of *c-Cbl*<sup>+/−</sup> mice and evaluation of their tumour-prone phenotype.** *c-Cbl*<sup>+/−</sup> mice were generated using a conventional method of gene targeting (Supplementary Fig. 10). *c-Cbl*<sup>+/+</sup>, *c-Cbl*<sup>+/−</sup> and *c-Cbl*<sup>−/−</sup> mice were crossed with *BCR-ABL* transgenic mice, and their survival and the development of blastic crises were monitored.

**Evaluation of haematopoietic pool size in *c-Cbl*<sup>+/−</sup> mice.** LSK and CD34<sup>+</sup> LSK cells were sorted from bone marrow cells or spleens of *c-Cbl*<sup>+/−</sup> mice, and their numbers were compared to those in *c-Cbl*<sup>+/+</sup> littermates (8 week old). Approximately  $5 \times 10^3$  bone marrow cells collected from *c-Cbl*<sup>+/+</sup> and *c-Cbl*<sup>+/−</sup> mice were inoculated into MethoCult M3231 culture supplemented with TPO ( $20 \text{ ng ml}^{-1}$ ), IL3 ( $10 \text{ ng ml}^{-1}$ ), IL6 ( $10 \text{ ng ml}^{-1}$ ), EPO ( $3 \text{ U ml}^{-1}$ ) and SCF ( $50 \text{ ng ml}^{-1}$ ). The number of colonies was counted 7 days after culturing.

**In vitro cell proliferation assays.** Approximately  $6 \times 10^3$  LSK cells from *c-Cbl*<sup>+/−</sup> mice and their *c-Cbl*<sup>+/+</sup> littermates (8 week old) were sorted into RetroNectin-coated 96-well U-bottom plates containing  $\alpha$ -minimum essential medium supplemented with 1% fetal bovine serum (FBS), mouse SCF ( $50 \text{ ng ml}^{-1}$ ), and human TPO ( $100 \text{ ng ml}^{-1}$ ). After 24 h pre-incubation, retrovirus supernatant was added to each well at a multiplicity of infection of about

10. The plates were incubated for another 24 h in the presence of protamine sulphate ( $10 \mu\text{g ml}^{-1}$ ), followed by repeated infection and extended culture for 2 days in S-Clone SF-O3 medium (Sanko Junyaku) supplemented with 1% BSA,  $50 \text{ ng ml}^{-1}$  SCF and  $50 \text{ ng ml}^{-1}$  TPO. On day 4, fluorescent-marker-positive cells were sorted for subsequent analyses. Cell survival and proliferation of LSK cells transduced with different *C-CBL* constructs were assessed in serum-free liquid culture in 96-well U-bottom plates in the presence of various cytokines. Each well received 50 fluorescent-marker-positive LSK cells, and the cells were cultured in S-Clone supplemented with 1% BSA plus SCF, TPO, IL3 or FLT3LG at the indicated concentrations. Cell numbers were counted either by analysing well images or by flow cytometry using FlowCount beads (Beckman Coulter). After 6 h serum starvation,  $1 \times 10^4$  LSK cells transduced with various *C-CBL* constructs were stimulated with SCF ( $10 \text{ ng ml}^{-1}$ ) and TPO ( $10 \text{ ng ml}^{-1}$ ) for 15 min. Whole-cell lysates were examined for activation of STAT5 and Akt by immunoblots using the respective antibodies.

**Immunoblot analysis of physical interactions between mutant C-CBL and CBL-B.** Flag-tagged CBL-B or C-CBL was co-transfected into NIH3T3 cells with each of three HA-tagged C-CBL mutants (*C-CBL*(Gln367Pro), *C-CBL*(Tyr371Ser) and *C-CBL*(70Z)). Total cell lysates of these NIH3T3 cells were immunoprecipitated with anti-Flag antibody, followed by immunoblot analysis with anti-HA antibody.

**Detection of ubiquitination and phosphorylation of kinases.** After overnight serum starvation, NIH3T3 cells stably transduced with human EGFR, and indicated HA-tagged C-CBL mutants and Flag-tagged wild-type C-CBL were stimulated with human EGF ( $10 \text{ ng ml}^{-1}$ ) for 2 min. Cell lysates were immunoprecipitated with anti-EGF antibody, followed by immunoblotting using anti-ubiquitin antibody. Constructs for wild-type C-CBL and mutant C-CBL were stably transduced into a mast cell line, V3MC, FLT3-transduced 32D cells (32D/FLT3) and BaF3 cells transduced with human EPOR and JAK2 (BaF3/EPOR/JAK2) using retrovirus-mediated gene transfer. After overnight serum starvation, the transduced cells were stimulated with  $10 \text{ ng ml}^{-1}$  SCF (V3MC),  $10 \text{ U ml}^{-1}$  EPO (BaF3/EPOR/JAK2) or  $10 \text{ ng ml}^{-1}$  FLT3LG (32D/FLT3) for 1 min. The specific kinases were immunoprecipitated with relevant antibodies, and their ubiquitination was detected by immunoblotting with anti-ubiquitin antibody. Tyrosine phosphorylation of EGFR, c-KIT, JAK2 and FLT3 was examined by immunoblot analyses of total cell lysates after cytokine stimulation at indicated time points, using antibodies specifically recognizing phosphorylated kinases, anti-p-EGFR, anti-p-c-KIT, anti-p-JAK2 and anti-p-FLT3, respectively. Anti-GAPDH or anti- $\alpha$ -tubulin immunoblot was performed as a control. Antibodies used in this study are listed in Supplementary Table 9.

**Statistical analysis.** Statistical significance of prolonged replating capacity of mutant *C-CBL*-transduced LSK cells was tested by counting the total number of dishes that produced colonies, followed by Fisher's exact test. Survival curves of *c-Cbl*<sup>+/+</sup>, *c-Cbl*<sup>+/−</sup> and *c-Cbl*<sup>−/−</sup> mice containing the *BCR-ABL* transgene were generated using the Kaplan–Meier method. Overall survivals of *C-CBL*-mutated and non-mutated CML cases were analysed according to the proportional hazard model, using STATA software. Statistical differences in survival were evaluated using the log-rank test, and statistical differences in  $2 \times 2$  contingency tables were tested according to Fisher's exact method. Student's *t*-tests were used to evaluate the significance of difference in spleen mass, number of haematopoietic progenitors and colony-forming cells between *c-Cbl*<sup>+/+</sup> and *c-Cbl*<sup>+/−</sup>.

29. Blake, T. J. *et al.* The sequences of the human and mouse *c-cbl* proto-oncogenes show *v-cbl* was generated by a large truncation encompassing a proline-rich domain and a leucine zipper-like motif. *Oncogene* **6**, 653–657 (1991).
30. Hamaoka, S. *et al.* Stable transgene expression in mice generated from retrovirally transduced embryonic stem cells. *Mol. Ther.* **15**, 560–565 (2007).
31. Nabekura, T. *et al.* Potent vaccine therapy with dendritic cells genetically modified by the gene-silencing-resistant retroviral vector GCDNsp. *Mol. Ther.* **13**, 301–309 (2006).
32. Sanuki, S. *et al.* A new red fluorescent protein that allows efficient marking of murine hematopoietic stem cells. *J. Gene Med.* **10**, 965–971 (2008).
33. Ory, D. S., Neugeboren, B. A. & Mulligan, R. C. A stable human-derived packaging cell line for production of high titer retrovirus/vesicular stomatitis virus G pseudotypes. *Proc. Natl Acad. Sci. USA* **93**, 11400–11406 (1996).
34. Suzuki, A. *et al.* Feasibility of *ex vivo* gene therapy for neurological disorders using the new retroviral vector GCDNsp packaged in the vesicular stomatitis virus G protein. *J. Neurochem.* **82**, 953–960 (2002).
35. Ema, H. *et al.* Adult mouse hematopoietic stem cells: purification and single-cell assays *Nature Protoc.* **1**, 2979–2987 (2006).
36. Osawa, M. *et al.* Long-term lymphohematopoietic reconstitution by a single CD34-low/negative hematopoietic stem cell. *Science* **273**, 242–245 (1996).

# A role for *Lin28* in primordial germ-cell development and germ-cell malignancy

Jason A. West<sup>1,2</sup>, Srinivas R. Viswanathan<sup>1,2</sup>, Akiko Yabuuchi<sup>1,2</sup>, Kerianne Cuniff<sup>1,2</sup>, Ayumu Takeuchi<sup>1,2</sup>, In-Hyun Park<sup>1,2</sup>, Julia E. Sero<sup>3</sup>, Hao Zhu<sup>1,2</sup>, Antonio Perez-Atayde<sup>3</sup>, A. Lindsay Frazier<sup>1,4</sup>, M. Azim Surani<sup>5</sup> & George Q. Daley<sup>1,2,6,7</sup>

The rarity and inaccessibility of the earliest primordial germ cells (PGCs) in the mouse embryo thwart efforts to investigate molecular mechanisms of germ-cell specification. *stella* (also called *Dppa3*) marks the rare founder population of the germ lineage<sup>1,2</sup>. Here we differentiate mouse embryonic stem cells carrying a *stella* transgenic reporter into putative PGCs *in vitro*. The *Stella*<sup>+</sup> cells possess a transcriptional profile similar to embryo-derived PGCs, and like their counterparts *in vivo*, lose imprints in a time-dependent manner. Using inhibitory RNAs to screen candidate genes for effects on the development of *Stella*<sup>+</sup> cells *in vitro*, we discovered that *Lin28*, a negative regulator of let-7 microRNA processing<sup>3–6</sup>, is essential for proper PGC development. Furthermore, we show that *Blimp1* (also called *Prdm1*), a let-7 target and a master regulator of PGC specification<sup>7–9</sup>, can rescue the effect of *Lin28* deficiency during PGC development, thereby establishing a mechanism of action for *Lin28* during PGC specification. Overexpression of *Lin28* promotes formation of *Stella*<sup>+</sup> cells *in vitro* and PGCs in chimaeric embryos, and is associated with human germ-cell tumours. The differentiation of putative PGCs from embryonic stem cells *in vitro* recapitulates the early stages of gamete development *in vivo*, and provides an accessible system for discovering novel genes involved in germ-cell development and malignancy.

The transcriptional program responsible for specifying PGCs has been investigated through molecular analysis of cDNA created from single cells<sup>10,11</sup>, but because transgenic or knockout methods required to verify roles in germ-cell formation are cumbersome, only a small number of genes has been demonstrated to be essential in germ-cell formation, most notably *Blimp1* and *Prdm14* (refs 8, 9, 12). Building on our previous demonstration of germ-cell formation from embryonic stem (ES) cells *in vitro*<sup>13</sup>, we have further characterized differentiation into putative PGCs, and now exploit the system to screen candidate genes via RNA interference (RNAi) to discover novel regulators of PGC development. For these studies, we used embryoid body (EB) differentiation of ES cells carrying a transgenic *Stella*–GFP reporter that specifically marks the germ-cell lineage *in vivo*<sup>2</sup> (Fig. 1a and Supplementary Fig. 1). The *Stella*–GFP reporter, which is expressed in approximately 20% of cells within each ES cell colony, was rapidly downregulated during EB differentiation (Fig. 1a and Supplementary Fig. 2a). Reporter gene expression in ES cells reflects known *Stella* expression in the inner cell mass and does not seem to represent pre-existing germ cells<sup>14,15</sup>. Rather, as shown below, a small percentage of *Stella*<sup>+</sup> cells arises in punctate structures within the EB, which represent putative PGCs (Fig. 1a and Supplementary Fig. 2)<sup>2,15</sup>.

During mouse development, loss of genomic imprinting occurs solely in the germ line and is a prerequisite for the sex-specific re-establishment of imprints during gametogenesis, thus establishing loss of imprinting as a unique marker of the germ lineage<sup>16</sup>. Given the fidelity of the *stella* reporter *in vivo*<sup>1</sup>, we predicted that the *Stella*<sup>+</sup> population derived during ES cell differentiation would demonstrate a time-dependent loss of imprints when compared to *Stella*–negative fractions and the parental ES cells. Indeed, *Stella*<sup>+</sup> cells purified directly from EBs or clonally derived under growth conditions for embryonic germ cells (EGCs) showed extensive loss of methylation at imprinted loci from day 7 of differentiation onwards (Fig. 1b and Supplementary Figs 3 and 4). These EB-derived EGCs displayed pluripotency properties similar to their embryo-derived counterparts (Supplementary Fig. 5)<sup>17</sup>.

Quantitative gene expression analysis revealed that germ-cell-specific genes become highly enriched within the EB-derived *Stella*<sup>+</sup> cell fraction in a temporal pattern that recapitulates gene activation during germ-cell specification *in vivo* (Fig. 1c–e). Using microarrays, we observed that *Stella*<sup>+</sup> cells purified from day 7 EBs show a transcriptional profile with significant similarities to embryo-derived PGCs. Unsupervised principal component analysis (PCA) of the microarray data revealed the close clustering of day 7 *Stella*<sup>+</sup> EB-derived cells with embryo-derived E10.5 PGCs (Fig. 1f). Additionally, among a set of 178 genes that displayed at least a twofold change in expression in *Stella*<sup>+</sup> cells from day 7 EBs (when compared to *Stella*<sup>+</sup> ES cells, *Stella*–negative ES cells and *Stella*–negative cells from day 7 EBs), germ-cell-specific transcripts were highly represented in the EB-derived *Stella*<sup>+</sup> cell population ( $P = 0.0009$ ; Supplementary Fig. 6a, b). Scatter plot representations of the microarray data comparing *Stella*<sup>+</sup> cells purified from day 7 EBs versus either *Stella*–GFP ES cells or embryo-derived E10.5 PGCs were created to highlight individual gene expression similarities and differences (Supplementary Fig. 6c, d). These microarray data reveal that the overall transcriptional profile of EB-derived *Stella*<sup>+</sup> cells is highly correlated with PGCs.

We next sought to use this system of *in vitro* germ-cell specification to characterize the loss-of-function phenotypes for a number of candidate genes ( $n = 30$ ) identified through our microarray analysis and reports of transcriptional profiling of PGCs<sup>10</sup>. We assessed the effects of gene knockdown on both tissue-nonspecific alkaline phosphatase-positive (TNAP<sup>+</sup>) EGC colony formation and on the loss of imprints during differentiation to link candidate gene function to germ lineage specification. TNAP staining is a hallmark of PGCs and EGCs. We knocked down endogenous expression of each gene within *Stella*–GFP

<sup>1</sup>Division of Pediatric Hematology/Oncology, Children's Hospital Boston and the Dana-Farber Cancer Institute, <sup>2</sup>Department of Biological Chemistry and Molecular Pharmacology, Harvard Medical School, Harvard Stem Cell Institute, Boston, Massachusetts 02115, USA. <sup>3</sup>Department of Pathology, Children's Hospital Boston and Harvard Medical School, Boston, Massachusetts 02115, USA. <sup>4</sup>Channing Laboratory, Brigham and Women's Hospital, Harvard Medical School, Boston, Massachusetts 02115, USA. <sup>5</sup>Wellcome Trust Cancer Research UK Gurdon Institute of Cancer and Developmental Biology, University of Cambridge, Tennis Court Road, Cambridge CB2 1QN, UK. <sup>6</sup>Manton Center for Orphan Disease Research, Boston, Massachusetts 02115, USA. <sup>7</sup>Howard Hughes Medical Institute, Boston, Massachusetts 02115, USA.

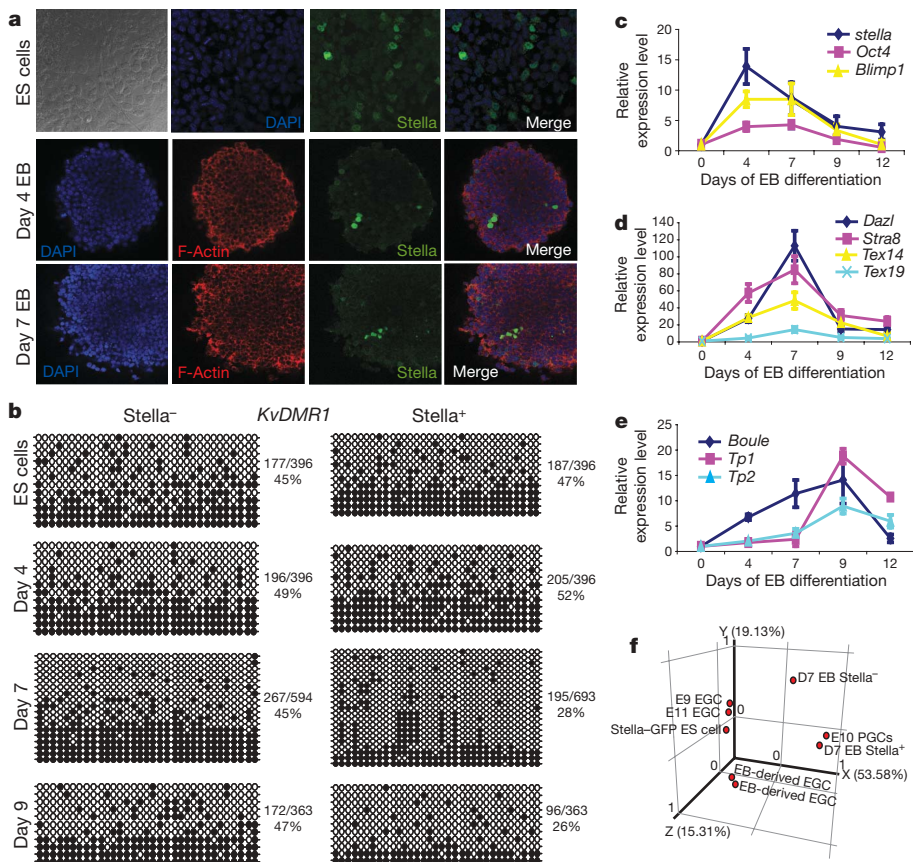


**Figure 1 | ES cell differentiation into putative PGCs *in vitro* is marked by *stella* expression.**

**a**, Immunofluorescent detection of *Stella*-GFP, F-actin and DAPI expression in ES cells and EBs at days 4 and 7 ( $\times 63$  confocal objective). **b**, Bisulphite sequencing at the *KvDMR1* imprinted locus, a differentially methylated region within the *Kcnq1ot1* gene. White circles, unmethylated CpG dinucleotides; black circles, methylated CpGs. The percentage of methylated CpGs is noted next to each panel. **c-e**, Relative gene expression within *Stella*<sup>+</sup> cells during EB differentiation, including the pre-migratory PGC markers *stella*, *Oct4* and *Blimp1* (**c**), migratory and post-migratory markers *Dazl*, *Stra8*, *Tex14* and *Tex19* (**d**), and *Boule* (also called *Boll*), a marker of meiosis, and the transition proteins *Tp1* and *Tp2* (**e**), by real-time PCR. Levels are relative to day 0 *Stella*<sup>+</sup> cells and the data are represented as mean  $\pm$  s.d.  $n = 3$ . **f**, PCA of *Stella* ES cells, EB-derived and embryo-derived EGCs (E9 and E11), day 7 EB cells (both *Stella*<sup>+</sup> and *Stella*<sup>-</sup>) and E10.5 embryo-derived PGCs.

ES cells by delivering short hairpin RNAs (shRNAs) via lentiviral transduction (Supplementary Fig. 7). shRNAs directed against *Blimp1*, an established regulator of PGC development<sup>8,9</sup>, and *lacZ* served as controls. We differentiated ES cells carrying shRNAs for 9 days and assayed *Stella*-GFP<sup>+</sup> cells for their ability to form TNAP<sup>+</sup> EGC colonies after 5 days of retinoic acid treatment. The addition of retinoic acid to our selection media after EB differentiation served to promote the self-renewal of PGCs and to differentiate potential contaminating ES cells. Notably, transgenic *Stella*-GFP expression during EB differentiation was largely unaffected under all conditions, including *Blimp1* knockdown (data not shown), whereas endogenous *Stella* is modulated by gene manipulation (see below). This suggests that the endogenous *stella* locus is more tightly regulated than the transgene *in vitro*. Although *Blimp1* knockdown would be expected to abrogate *Stella* expression completely, *Blimp1* homozygous knockout mice still form *stella*-expressing cells, although these cells are rare and fail to proliferate and develop properly<sup>8,10</sup>. Thus, we focused on functional aspects of germ-cell formation, including TNAP colony formation and loss of genomic imprints. Among the candidate genes that we assessed, knockdown of *Lin28* demonstrated the most quantitative reduction in TNAP-positive colony formation (Fig. 2a and Supplementary Fig. 8a). Further corroborating the loss of germ cells, we verified that knockdown of *Lin28* abrogates the ability to derive imprint-erased clones after retinoic acid selection of EB-derived *Stella*<sup>+</sup> cells (Fig. 2b).

*Lin28* selectively blocks the processing of let-7 precursors into the corresponding mature microRNA (miRNA) species<sup>3-6</sup>. Although not previously suspected as a regulator of PGC formation, we included *Lin28* in our screen because it was more highly expressed in day 7 EB-derived *Stella*<sup>+</sup> cells than in ES cells and EB-derived *Stella*-negative cells (as determined by microarray). Interrogation of a microarray data set of embryo-derived single cells from the mouse PGC lineage indicated high *Lin28* expression in the proximal epiblast, PGC precursors and lineage-restricted PGCs, as well as in the posterior mesoderm surrounding these cells<sup>10</sup>. We evaluated *Lin28* protein

expression during PGC development in mouse embryos and observed high levels of *Lin28* staining within *Stella*<sup>+</sup> PGCs at E7.5, and only diffuse low-level *Lin28* staining in surrounding somatic cells. We observed diminishing yet persistent expression of *Lin28* within PGCs through E12.5, at which time *Lin28*-negative PGCs become apparent (Fig. 2c).

To elucidate further the role of *Lin28* in the development of germ cells, we characterized the effects of modulating *Lin28* expression on germ-cell-marker gene expression during ES cell differentiation *in vitro*. Quantitative gene expression analysis revealed that *Lin28* RNAi decreased the expression of multiple germ-cell markers in *Stella*-GFP<sup>+</sup> cells during EB differentiation, including key genes implicated in PGC commitment, such as *Blimp1*, *Prdm14* and endogenous *stella* (Supplementary Fig. 9a-i). Moreover, we confirmed that *Lin28* RNAi resulted in increased levels of mature let-7 miRNA family members by approximately five- to sixfold in *Stella*<sup>+</sup> cells (Supplementary Fig. 9z-b'). *Lin28* RNAi markedly reduced TNAP colony formation throughout EB differentiation of *Stella*-GFP ES cells, consistent with a reduction in the generation of putative PGCs (Fig. 2d). Three individual shRNAs directed against *Lin28* resulted in a similar phenotype, and ectopic *Lin28* expression resistant to shRNA inhibition was able to stimulate formation of TNAP<sup>+</sup> colonies and re-expression of germ-cell-specific genes, thereby arguing against off-target effects of *Lin28* RNAi (Supplementary Fig. 10).

We next drove ectopic *Lin28* expression during EB differentiation from a tetracycline-inducible ES cell line (i*Lin28* ES cells). Addition of doxycycline to the media resulted in a pronounced upregulation of *Lin28* throughout differentiation, and a corresponding suppression of let-7 maturation (Supplementary Fig. 9j, q, c'-e'). Induction of *Lin28* during EB differentiation was accompanied by increased expression of multiple germ-cell markers, including *stella*, *Prdm14* and *Tex14* within whole EBs as well as within SSEA1<sup>+</sup> cells (Supplementary Fig. 9j-y). Notably, we found no evidence that ectopic *Lin28* expression influenced *Blimp1* messenger RNA levels (Supplementary Fig. 9l, s), which could be a result of the reported



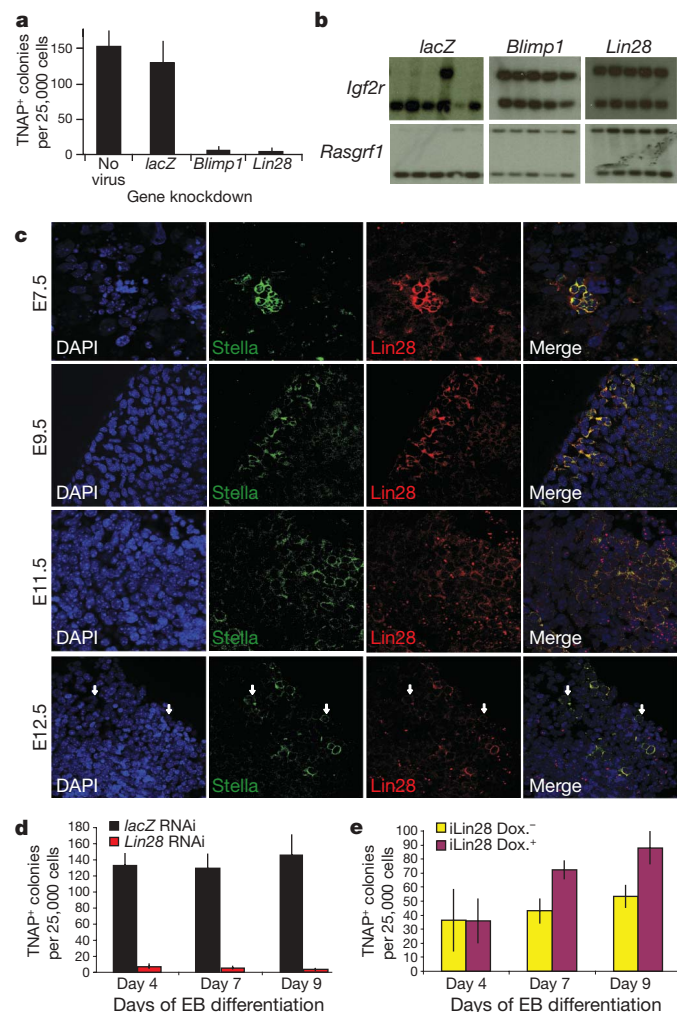


**Figure 2 | *Lin28* regulates PGC development.** **a**, The effects of candidate gene knockdown on TNAP<sup>+</sup> EGC colony formation from day 9 EB-derived Stella<sup>+</sup> cells after *in vitro* differentiation of ES cells carrying shRNA-mediated gene knockdown, as indicated.  $n = 3$ . **b**, Imprint status at the *Igf2r* and *Rasgrf1* loci of individual clones derived from day 9 EB-derived Stella<sup>+</sup> cells carrying gene knockdown of either *lacZ*, *Blimp1* or *Lin28*. **c**, Expression of *Lin28* during embryonic PGC development. By E12.5, multiple Stella<sup>+</sup> PGCs within the genital ridge are negative for *Lin28* (white arrows;  $\times 63$  confocal objective). **d**, *Lin28* RNAi prevents TNAP<sup>+</sup> EGC colony formation during EB differentiation.  $n = 3$ . **e**, Induced *Lin28* expression enhances TNAP<sup>+</sup> EGC colony formation on and after day 7 of EB differentiation compared to the uninduced control.  $n = 3$ . Dox., doxycycline. All error bars represent s.e.m.

post-transcriptional regulation of *Blimp1* by let-7 (ref. 7). Functionally, ectopic *Lin28* expression during EB differentiation resulted in significant increases in TNAP<sup>+</sup> EGC colony formation when compared to uninduced controls, indicating that enforced expression of *Lin28* promotes expansion of PGC pools (Fig. 2e).

To corroborate our *in vitro* results of *Lin28* knockdown within a physiological setting *in vivo*, we injected knockdown ES cells into blastocysts and monitored the germ-cell contribution in the resulting chimaeric embryos via Stella–GFP transgenic reporter expression. Control embryos injected with Stella–GFP ES cells expressing a constitutive *lacZ* RNAi construct showed extensive contribution of GFP<sup>+</sup> germ cells in the genital ridge, whereas *Blimp1* RNAi ablated germ-cell commitment (Fig. 3a, b). *Lin28* knockdown compromised PGC formation to the same extent as *Blimp1* knockdown. Failure of *Lin28* RNAi ES cells to contribute to the germ line was not due to a generalized deficit in the potential to chimaerize tissues, as *Lin28* RNAi ES cells were detected in the tissues of the head and limbs in virtually all embryos tested (Supplementary Fig. 11). Stella–GFP

expression was not observed in somatic areas of chimaeric embryos, indicating the specificity of the Stella reporter<sup>2</sup>. Furthermore, these data suggest a cell-autonomous role for *Lin28* in PGC formation, as chimaeric embryos possess mosaic tissues with presumably normal elements derived from the host that would be expected to complement deficits caused by *Lin28* deficiency in non-germ cells. Thus, our data indicate a physiological role for *Lin28* in PGC development *in vivo*.

As a complementary approach to examine the impact of *Lin28* on PGC numbers *in vivo*, we transduced Stella–GFP ES cells with a retrovirus that drives the ectopic expression of *Lin28*, injected blastocysts, and quantified ES cell contribution to the genital ridge. Ectopic *Lin28* expression resulted in a significant enhancement of PGC number in chimaeric embryos (Fig. 3a, b), thus suggesting that *Lin28* can both positively and negatively regulate the pool of germ cells.

As the 3' untranslated region (UTR) of *Blimp1* has been identified as a direct target for let-7 miRNAs<sup>7</sup>, we hypothesized that *Lin28* influences PGC development through let-7-mediated effects on *Blimp1*. *Blimp1* is a key regulator of germ-cell commitment<sup>8,9</sup>, and we sought to determine if ectopic expression of *Blimp1* lacking its 3' UTR could rescue PGC development in the setting of *Lin28* depletion. We engineered Stella–GFP ES cells possessing both *Lin28* RNAi and ectopic *Blimp1* expression and assayed the ability of these cells to contribute to the germ line in chimaeric E12.5 embryos. In this context, *Blimp1* rescues PGC numbers to control levels (Fig. 3a, b). Additionally, *Blimp1* RNAi ablates PGC development from ES cells ectopically expressing *Lin28* (Fig. 3a, b). These data suggest that *Lin28* is as an upstream regulator of PGC development relative to *Blimp1*, potentially acting via repression of the let-7 miRNA family within PGCs or their precursors. To test this hypothesis further, we engineered a doxycycline-inducible ES cell line to express a form of let-7 (let-7s-21L) that is resistant to *Lin28* by virtue of a terminal loop substitution with that of miR-21 (a miRNA not regulated by *Lin28*)<sup>18</sup>, and determined the effect of induction on *Blimp1* expression in EBs. We found that induction of let-7s-21L abrogates *Blimp1* protein expression during EB differentiation (Fig. 3c); further supporting *Lin28* regulation of *Blimp1* via let-7.

Expression of *Lin28b*, a homologue of *Lin28*, is largely absent in early PGCs<sup>10</sup>, but is expressed in ES cells. Thus, we also assessed the impact of *Lin28b* RNAi on PGC formation. We observed a compromised ability to form EB-derived PGCs owing to *Lin28b* knockdown and an intermediate phenotype *in vivo* (Supplementary Fig. 8). Knockdown of *Lin28b* in ES cells similarly results in upregulation of let-7 and compromises germ-cell formation, further linking let-7 to PGC development but indicating that *Lin28* is the dominant regulator *in vivo*.

Given our data linking *Lin28* and germ-cell numbers, we surmised that aberrant overexpression of *Lin28* might dysregulate the growth or differentiation of pluripotent cells including germ cells. Furthermore, recent reports have linked *Lin28* and its homologue *Lin28b* to oncogenesis<sup>19–21</sup>. In teratomas formed from ES cells engineered to express *Lin28* in response to doxycycline induction (iLin28 ES cells) we observed that primitive neural tissue predominated in regions of transgene induction (Supplementary Fig. 12a). High-grade, aggressive human teratocarcinomas contain abundant immature neural tissue, whereas low-grade, benign teratomas contain no immature neural tissue. This phenomenon is also observed in teratomas formed from inducible Oct4 ES cells<sup>22</sup>. In contrast, *Lin28* RNAi during teratoma formation resulted in reduced tumour size, and these teratomas were comprised of mature tissues from all three germ layers (Supplementary Fig. 12b, c). *Lin28* and *Lin28b* are more prominently over-expressed in the transformed embryonal carcinoma (EC) cell line P19 relative to ES cells than corresponding Oct4 levels in these cells (Supplementary Fig. 13a). Modulation of *Lin28* expression by RNAi in P19 cells reduces both cell proliferation and tumour formation in immunodeficient mice, suggesting that *Lin28* contributes to the

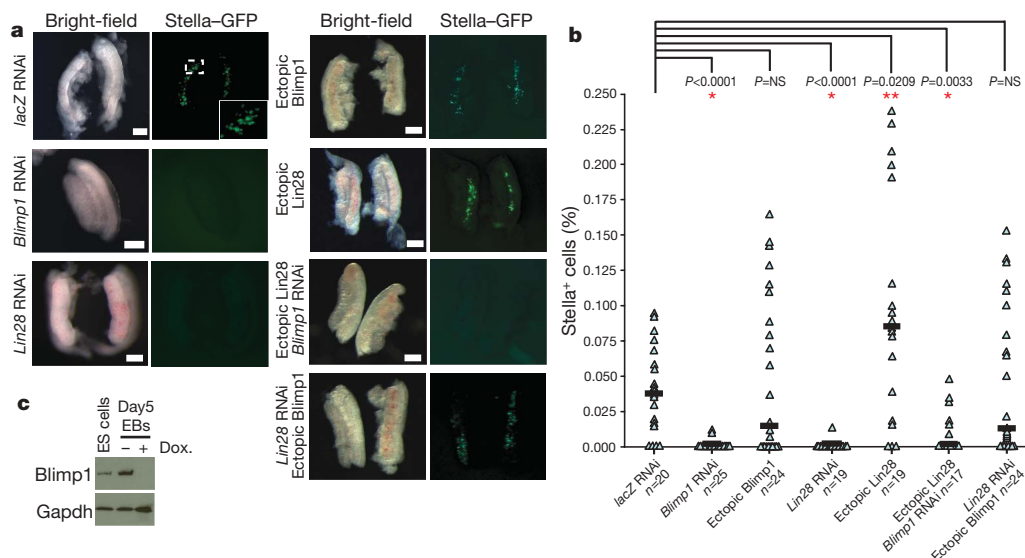


**Figure 3** | *Lin28* and *Blimp1* regulate PGC development in vivo.

**a**, Representative images of genital ridges from E12.5 embryos injected with Stella-GFP ES cells harbouring either *lacZ* RNAi, *Blimp1* RNAi, ectopic *Blimp1* expression, *Lin28* RNAi, ectopic *Lin28* expression, *Lin28* RNAi plus ectopic *Blimp1* expression, or ectopic *Lin28* plus *Blimp1* RNAi. Scale bar, 100  $\mu$ m. **b**, Quantification by flow cytometry of the percentage of Stella<sup>+</sup> PGCs in E12.5 genital ridges dissected from chimaeric embryos created with

Stella-GFP ES cells containing the following: *lacZ* RNAi, *Blimp1* RNAi, ectopic *Blimp1* expression, *Lin28* RNAi, ectopic *Lin28* expression, ectopic *Lin28* plus *Blimp1* RNAi, or *Lin28* RNAi plus ectopic *Blimp1* expression. Black horizontal bars represent the median. NS, nonsignificant *P* values. **c**, Immunoblot for *Blimp1* expression in extracts from ES cells and day 5 EBs with or without doxycycline induction of let-7s-21L. Gapdh served as a loading control.

malignant phenotype of embryonal carcinoma cells (Supplementary Fig. 13b–e). In addition, tumours with ectopic *Lin28* displayed local invasion into the host tissues, whereas teratomas formed from pluripotent cells treated with *Lin28* RNAi were differentiated, non-invasive and well encapsulated (Supplementary Fig. 13d, e), paralleling recent reports linking *Lin28* to metastasis<sup>20,21</sup>.

We sought to determine whether *LIN28* is expressed in human germ-cell tumours. We interrogated a germ-cell tumour microarray data set and profiled multiple primary human tumours for the expression of *LIN28*, *LIN28B* and *OCT4*, a known marker of germ-cell tumours<sup>23</sup>. We observed that malignant tumours of a germ-cell origin, including mixed germ-cell tumours, yolk-sac tumours, choriocarcinomas, embryonal carcinomas and seminomas, demonstrated overexpression of *LIN28* and/or *LIN28B* (Fig. 4a). Importantly, benign teratomas and normal testis do not show high levels of *LIN28* and *LIN28B* expression relative to malignant tumour types, and *OCT4* is not expressed in yolk-sac tumours or choriocarcinomas<sup>24</sup>. The expression of *LIN28* and/or *LIN28B* in all malignant

germ-cell tumour subtypes implicates *LIN28* as a consistent marker of germ-cell tumours. We confirmed *LIN28* protein expression in a primary human embryonal carcinoma by immunohistochemistry (Fig. 4b). Importantly, we noted that *LIN28* expression was specifically observed in malignant components of the tumour, but not in benign elements of the tumour or in the adjacent stroma. Interestingly, regions of intratubular germ-cell neoplasia (a precursor lesion for most germ-cell tumours) stained strongly positive for *LIN28* whereas normal seminiferous tubules displayed little to no staining (Fig. 4b, right panel), suggesting that aberrant expression of *LIN28* might be an early lesion in germ-cell tumorigenesis. In a separate study, we have documented that *LIN28* overexpression facilitates cellular transformation in NIH-3T3 and BaF3 cells, consistent with a functional role for *LIN28* in malignancy<sup>21</sup>.

*Lin28* selectively blocks the processing of the let-7 family of miRNAs<sup>3–6</sup>. let-7 miRNAs are upregulated only during later stages of PGC development<sup>25</sup>, establishing that let-7 expression is dynamically regulated within the germ lineage. Our data suggest that *Lin28*

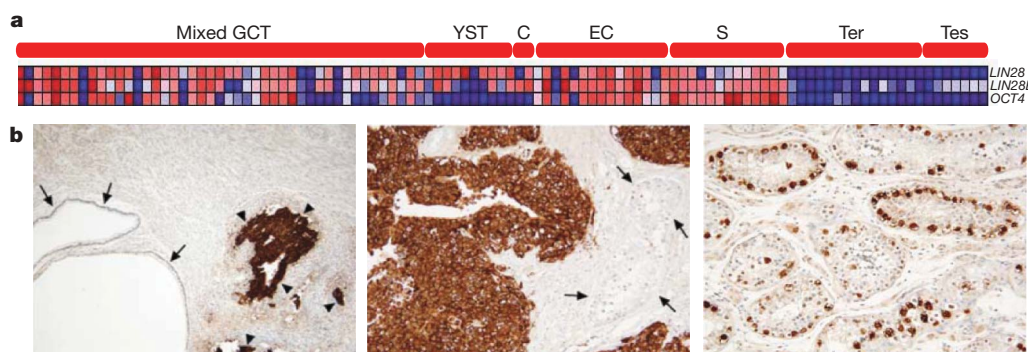


**Figure 4** | *LIN28* expression in human germ-cell tumours. **a**, Primary malignant germ-cell tumours of multiple histologies show consistent high expression of *LIN28* and *LIN28B*. Benign teratomas and normal testis show no significant expression of *LIN28* or *LIN28B*. C, choriocarcinoma; EC, embryonal carcinoma; GCT, germ-cell tumour; S, seminoma; Ter, teratoma; Tes, normal testis; YST, yolk-sac tumour. **b**, Immunohistochemical detection of *LIN28* in primary embryonal carcinoma. Left: cytoplasmic

immunoreactivity of embryonal carcinoma cells for *LIN28* (between arrowheads). Endodermal epithelial elements of the teratoma (arrows) and tumoural stroma are not immunoreactive. Middle: higher magnification of immunoreactive embryonal carcinoma. Adjacent seminiferous tubules are negative (between arrows). Right: intratubular germ-cell neoplasia within the embryonal carcinoma demonstrates *LIN28* immunoreactivity.  $\times 40$  magnification.



suppression of let-7 maturation is required for proper *Blimp1*-mediated development of the germ lineage. Consistent with this hypothesis, we have observed that *Lin28* RNAi is associated with upregulation of let-7 miRNAs and the abrogation of *Blimp1* expression in *Stella*<sup>+</sup> cells during *in vitro* differentiation (Supplementary Fig. 9c, z, a'–e'). Additionally, ectopic *Blimp1* expression rescues PGC formation from ES cells harbouring *Lin28* knockdown. Our *Lin28* expression data in PGCs correlate inversely with the expression of let-7 miRNAs<sup>25</sup> and are coincident with *Blimp1* protein dynamics in PGCs<sup>26</sup>. Although *Blimp1* seems critical, additional let-7 targets may yet prove relevant to PGC specification.

Our functional data indicate that *Lin28* is a key lineage regulator for germ-cell numbers (Supplementary Fig. 14). As multiple lineage-specifying factors such as *MITF* (microphthalmia-associated transcription factor)<sup>27</sup> and *SCL* (stem cell leukaemia gene)<sup>28</sup> have been implicated as oncogenes, *Lin28* could have a dual role in both germ-cell development and malignancy. As let-7 miRNAs function as tumour suppressors by directly and indirectly repressing a number of cell proliferation pathways, *Lin28* de-repression of let-7 oncogenes has been established as a key oncogenic factor<sup>19–21</sup>. Multiple tumour types show reduced levels of let-7 miRNAs, and several let-7 targets, including *c-Myc*, *k-Ras* and *HMGA2*, are oncogenic<sup>21,29</sup>. In addition, somatic cell reprogramming factors (including presumably *Lin28*) also have prominent roles in cellular transformation. *Oct4* has been identified as an oncogenic driver for certain germ-cell tumours, including embryonal carcinomas and seminomas but not yolk-sac tumours and choriocarcinomas<sup>22,24</sup>. Here we show that *Lin28* and its homologue *Lin28b* are more consistently expressed in malignant germ-cell tumours than even *Oct4*, including within yolk-sac tumours and choriocarcinomas. Together, our data implicate *Lin28* as a novel regulator of germ-cell development and a consistent marker of germ-cell malignancy, and provide new insights into germ-cell formation, development and cancer.

## METHODS SUMMARY

shRNA constructs in the pLKO.1-Puro vector system for RNAi-mediated gene knockdown were obtained from Sigma and Open Biosystems (MISSION TRC-Mm 1.0). TRC numbers for individual hairpins as well as primer information for real-time PCR analysis can be found in Supplementary Tables 1 and 2. EB-derived PGC microarray analysis used Affymetrix mouse 430 2.0 whole genome arrays, and data analysis used MAS5.0 standard normalization and differential expression analysis techniques using GeneSpring GX 7.3 software. Embryo-derived PGC and PGC-precursor microarray data sets were published previously<sup>10</sup> and have the Gene Expression Omnibus (GEO) accession number GSE11128. Primary human tissue microarray data sets were published previously<sup>23</sup> and have the GEO accession number GSE3218. R. Yu and C. Estrada provided the pCDH-CMV-mPrdm1 construct. Antibodies used in this study include: mouse anti-SSEA1 (MC480; Developmental Studies Hybridoma Bank at the University of Iowa), rabbit anti-GFP (BioVision), goat anti-*Lin28* for immunofluorescence and western blotting (Santa Cruz), anti-*Lin28* for human germ-cell tumour immunohistochemistry (Proteintech Group), anti-*Blimp1* (R&D Systems), and Alexa-594 phalloidin (Molecular Probes). In Fig. 3b, *P* values were calculated by the Mann–Whitney rank-sum test and are relative to the control, *lacZ* RNAi.

**Full Methods** and any associated references are available in the online version of the paper at [www.nature.com/nature](http://www.nature.com/nature).

Received 19 April; accepted 16 June 2009.

Published online 5 July 2009.

1. Payer, B. *et al.* *Stella* is a maternal effect gene required for normal early development in mice. *Curr. Biol.* **13**, 2110–2117 (2003).
2. Payer, B. *et al.* Generation of *stella*-GFP transgenic mice: a novel tool to study germ cell development. *Genesis* **44**, 75–83 (2006).
3. Heo, I. *et al.* *Lin28* mediates the terminal uridylation of let-7 precursor MicroRNA. *Mol. Cell* **32**, 276–284 (2008).
4. Newman, M. A., Thomson, J. M. & Hammond, S. M. *Lin-28* interaction with the Let-7 precursor loop mediates regulated microRNA processing. *RNA* **14**, 1539–1549 (2008).

5. Rybak, A. *et al.* A feedback loop comprising *lin-28* and let-7 controls pre-let-7 maturation during neural stem-cell commitment. *Nature Cell Biol.* **10**, 987–993 (2008).
6. Viswanathan, S. R., Daley, G. Q. & Gregory, R. I. Selective blockade of microRNA processing by *Lin28*. *Science* **320**, 97–100 (2008).
7. Nie, K. *et al.* MicroRNA-mediated down-regulation of PRDM1/*Blimp-1* in Hodgkin/Reed-Sternberg cells: a potential pathogenetic lesion in Hodgkin lymphomas. *Am. J. Pathol.* **173**, 242–252 (2008).
8. Ohinata, Y. *et al.* *Blimp1* is a critical determinant of the germ cell lineage in mice. *Nature* **436**, 207–213 (2005).
9. Vincent, S. D. *et al.* The zinc finger transcriptional repressor *Blimp1/Prdm1* is dispensable for early axis formation but is required for specification of primordial germ cells in the mouse. *Development* **132**, 1315–1325 (2005).
10. Kurimoto, K. *et al.* Complex genome-wide transcription dynamics orchestrated by *Blimp1* for the specification of the germ cell lineage in mice. *Genes Dev.* **22**, 1617–1635 (2008).
11. Saitou, M. Specification of the germ cell lineage in mice. *Front. Biosci.* **14**, 1068–1087 (2009).
12. Yamaji, M. *et al.* Critical function of *Prdm14* for the establishment of the germ cell lineage in mice. *Nature Genet.* **40**, 1016–1022 (2008).
13. Geijsen, N. *et al.* Derivation of embryonic germ cells and male gametes from embryonic stem cells. *Nature* **427**, 148–154 (2004).
14. Hayashi, K., Lopes, S. M., Tang, F. & Surani, M. A. Dynamic equilibrium and heterogeneity of mouse pluripotent stem cells with distinct functional and epigenetic states. *Cell Stem Cell* **3**, 391–401 (2008).
15. Wei, W. *et al.* Primordial germ cell specification from embryonic stem cells. *PLoS ONE* **3**, e4013 (2008).
16. Reik, W. & Walter, J. Genomic imprinting: parental influence on the genome. *Nature Rev. Genet.* **2**, 21–32 (2001).
17. Donovan, P. J. & de Miguel, M. P. Turning germ cells into stem cells. *Curr. Opin. Genet. Dev.* **13**, 463–471 (2003).
18. Piskounova, E. *et al.* Determinants of microRNA processing inhibition by the developmentally regulated RNA-binding protein *Lin28*. *J. Biol. Chem.* **283**, 21310–21314 (2008).
19. Chang, T. C. *et al.* *Lin-28B* transactivation is necessary for *Myc*-mediated let-7 repression and proliferation. *Proc. Natl Acad. Sci. USA* **106**, 3384–3389 (2009).
20. Dangi-Garimella, S. *et al.* Raf kinase inhibitory protein suppresses a metastasis signalling cascade involving *Lin28* and let-7. *EMBO J.* **28**, 347–358 (2009).
21. Viswanathan, S. R. *et al.* *Lin28* promotes transformation and is associated with advanced human malignancies. *Nature Genet.* advance online publication doi:10.1038/ng.392 (31 May 2009).
22. Gidekel, S., Pizov, G., Bergman, Y. & Pikarsky, E. Oct-3/4 is a dose-dependent oncogenic fate determinant. *Cancer Cell* **4**, 361–370 (2003).
23. Korkola, J. E. *et al.* Down-regulation of stem cell genes, including those in a 200-kb gene cluster at 12p13.31, is associated with *in vivo* differentiation of human male germ cell tumors. *Cancer Res.* **66**, 820–827 (2006).
24. Cheng, L. Establishing a germ cell origin for metastatic tumors using OCT4 immunohistochemistry. *Cancer* **101**, 2006–2010 (2004).
25. Hayashi, K. *et al.* MicroRNA biogenesis is required for mouse primordial germ cell development and spermatogenesis. *PLoS ONE* **3**, e1738 (2008).
26. Ancelin, K. *et al.* *Blimp1* associates with *Prmt5* and directs histone arginine methylation in mouse germ cells. *Nature Cell Biol.* **8**, 623–630 (2006).
27. Garraway, L. A. *et al.* Integrative genomic analyses identify *MITF* as a lineage survival oncogene amplified in malignant melanoma. *Nature* **436**, 117–122 (2005).
28. Shivdasani, R. A., Mayer, E. L. & Orkin, S. H. Absence of blood formation in mice lacking the T-cell leukaemia oncoprotein *tal-1/SCL*. *Nature* **373**, 432–434 (1995).
29. Lu, J. *et al.* MicroRNA expression profiles classify human cancers. *Nature* **435**, 834–838 (2005).

**Supplementary Information** is linked to the online version of the paper at [www.nature.com/nature](http://www.nature.com/nature).

**Acknowledgements** We thank M. W. Lensch for comments on this manuscript; D. K. Gifford, G. Gerber, C. Reeder and J. Baughman for comments and input regarding microarray analysis; G. Losyev for flow cytometry expertise; and S. Winkler of the British Consulate for providing support for collaboration between the Daley and Surani laboratories. This study was supported by grants from the NIH, the NIH Director's Pioneer Award of the NIH Roadmap for Medical Research, and by support from the germ cell program of the Harvard Stem Cell Institute. G.Q.D. is a recipient of the Burroughs Wellcome Fund Clinical Scientist Award in Translational Research.

**Author Contributions** J.A.W., project planning, experimental work, manuscript preparation; S.R.V., A.Y., A.T., K.C., I.-H.P., J.E.S., H.Z., A.P.-A., A.L.F., experimental work; M.A.S., contributed reagents and critical feedback; G.Q.D., project planning, data analysis and manuscript preparation.

**Author Information** The microarray data have been deposited in the Gene Expression Omnibus (GEO) and given the series accession number GSE7948. Reprints and permissions information is available at [www.nature.com/reprints](http://www.nature.com/reprints). Correspondence and requests for materials should be addressed to G.Q.D. ([george.daley@childrens.harvard.edu](mailto:george.daley@childrens.harvard.edu)).



## METHODS

**ES cell culture, EB differentiation, PGC selection and EGC culture.** Transgenic Stella-GFP and Stella BAC ES cells (B6/CBA) were cultured as described<sup>2,13,30–32</sup>. All data presented used the Stella-GFP transgenic ES cell line unless indicated<sup>2</sup>. Inducible Lin28 ES cells (iLin28 ES cells) and inducible let-7s-21L ES cells were created from the KH2 ES cell line as described<sup>18,33</sup>, and 2  $\mu\text{g ml}^{-1}$  doxycycline was added for induced expression during differentiation.

For PGC selection, EBs were dissociated and the single-cell suspension was subjected to FACS using a BD FACS Aria cell sorting system to purify Stella-GFP-positive cells. For the iLin28 ES cell line, SSEA1 purification was used for germ-cell isolation, as described<sup>13,32</sup>. For EGC culture, FACS-processed cells were plated on MEFs, with mouse ES cell media containing 15  $\text{ng ml}^{-1}$  of bFGF (Invitrogen) and 30  $\text{ng ml}^{-1}$  of SCF (Peprotech), plus 2  $\mu\text{M}$  trans-retinoic acid (Sigma). Retinoic acid promotes germ-cell self-renewal while serving as a differentiation agent for ES cells<sup>34</sup>. After 5–7 days, replacing the media daily, cultures were fixed and stained for tissue-nonspecific alkaline phosphatase (TNAP), a germ-cell-specific marker<sup>35</sup>, or clonal EGC colonies were isolated and cultured as previously described and expanded for analysis<sup>32</sup>. For TNAP staining, cultured cells were washed once with PBS, fixed in 4% paraformaldehyde (PFA) for 1 min, and then washed in PBS three times. AB staining solution (10 ml buffer (100 mM Tris HCl pH 9.5, 50 mM  $\text{MgCl}_2$ , 100 mM NaCl and 0.1% Tween-20), 22.5  $\mu\text{l}$  of 50  $\text{mg ml}^{-1}$  nitro-blue tetrazolium in 70% dimethylformamide (NBT; Promega), and 17.5  $\mu\text{l}$  of 50  $\text{mg ml}^{-1}$  5-bromo-4-chloro-3-indolyl-1-phosphate in 100% dimethylformamide (BCIP; Promega)) was added to the cells and incubated at room temperature for 5–10 min, and then the cells were washed in PBS several times and imaged.

**Confocal imaging.** Embryos or EBs were fixed in 4% PFA (in PBS) for 1 h at room temperature, washed 3 $\times$  in PBS (5 min per wash) and permeabilized for 1 h at room temperature in 1 $\times$  IF buffer (PBS plus 0.1% BSA, 0.2% Triton X-100, 0.04% Tween-20). They were then incubated with 1:200 primary rabbit anti-GFP (BioVision) or 1:200 primary goat anti-Lin28 (Santa Cruz) in IF buffer at 37 °C for 1 h, washed 3 $\times$  with IF buffer 5 min each at room temperature with a final wash in IF buffer at 37 °C for 10 min. They were then incubated with 1:500 secondary (Alexa488 and/or Alexa594, Molecular Probes) or 1:200 Alexa-594 phalloidin (Molecular Probes) and DAPI (1:100 from 5  $\text{mg ml}^{-1}$  stock) in IF buffer for 1 h at 37 °C. Samples were placed in coverslip-bottom dishes (MatTek) in Fluoromount G mounting medium (Southern Biotech) and imaged on a Leica confocal microscope ( $\times 63$  objective with oil).

**Quantitative real-time RT-PCR.** Quantitative real-time PCR of gene expression used SYBR green. Multiple, independent biological samples were obtained for RNA isolation. Levels of mature miRNAs were measured using Taqman probes (Applied Biosystems).  $\beta$ -actin expression was used to normalize all samples except for miRNA expression, which were normalized to sno142 RNA. Relative fold changes were calculated using the  $\Delta\Delta C_t$  method. See Supplementary Table 1 for primer sequences.

**Microarray hybridization and data analysis.** Each sample contained two to four biological replicates. RNA was isolated using an RNeasy kit (Qiagen) according to the manufacturer's protocol. Biotin-labelled RNA was hybridized to Affymetrix mouse 430 2.0 whole genome arrays at the Dana-Farber Cancer Institute Microarray Core. GeneSpring GX 7.3 software was used for all data analysis, including scatter plot generation, using MAS5.0 standard normalization and differential expression analysis techniques. Principal component analysis (PCA) was performed via GeneSpring using mean centring and scaling for all genes. Raw data for EB-derived PGCs and associated cell types are deposited in the public gene expression database GEO (<http://www.ncbi.nlm.nih.gov/geo/>) under the accession number GSE7948. Embryo-derived PGC and PGC-precursor microarray data sets were published previously<sup>10</sup> and have the GEO accession number GSE11128.

**Southern blot analysis.** Imprint analysis for the *Igf2r* locus was at the maternally methylated differentially methylated region 1 (DMR1). Genomic (g) DNA was digested with PvuII/MluI and probed via Southern blot hybridization as described<sup>36</sup>. For the paternally methylated *Rasgrf1* locus, Southern blot hybridization of gDNA digested with PstI/NotI was probed as described<sup>37</sup>.

**Bisulphite sequencing.** Bisulphite treatment of gDNA was carried out using a Chemicon CpGenome DNA Modification Kit according to the manufacturer's protocol. Sample treatment and processing were performed simultaneously for

quality control. Nested PCR was then used to amplify *KvDMR1*<sup>38</sup> and the *Snrpn* DMR1 as described<sup>39</sup>. The *KvDMR1* region examined is on distal chromosome 7, contains 33 CpGs within intron 10 of the *Kcnq* gene, and controls the expression of six paternally repressed genes: *Ascl2*, *Tssc4*, *Kcnq*, *Cdkn1c*, *Slc22a18* and *Tssc3*<sup>38</sup>. The maternally repressed *Snrpn* DMR1 examined is located on central chromosome 7 and contains 11 CpGs<sup>39</sup>. PCR products were cloned from two independent PCR reactions. Bisulphite conversion efficiency ranged from 85% to 99%, and 83% to 100% of individual clones for each sample showed unique patterns of conversion.

**RNA interference.** shRNA constructs in the pLKO.1-Puro vector system for RNAi-mediated gene knockdown were obtained from Sigma and Open Biosystems (MISSION TRC-Mm 1.0). Expression of the shRNA was constitutively driven by the human U6 promoter whereas the human phosphoglycerate kinase promoter (PGK) independently drove the expression of a puromycin resistance gene to allow selection for cells harbouring the shRNA-mediated gene knockdown. TRC numbers for hairpins used are listed in Supplementary Table 2. For Lin28, only shRNA TRCN0000102579 was used for all experiments, unless otherwise noted. Viral production in 293T cells and ES cell infection were performed according to product literature and as described<sup>40</sup>. Puromycin selection was applied continuously during all subsequent cell culture including EB differentiation.

**Ectopic gene expression vectors.** Ectopic Lin28 was provided by either pBABE-puro-Lin28 or MSCV-neo-Lin28, whereas ectopic Blimp1 was driven by pCDH-CMV-mPrdm1 (System Biosystems; provided by R. Yu and C. Estrada).

**Tumour formation.** All tumour-forming assays, including teratoma formation, were performed using NOD-SCID mice (Charles River Laboratories).  $1 \times 10^6$  cells in 150  $\mu\text{l}$  PBS were injected subcutaneously for all experiments.

**Production of chimaeric embryos.** C57BL6 females were superovulated by PMSG followed 48 h later by hCG and were mated with C57BL6 males. Blastocysts were collected from the uterus 3.5 days after vaginal plugging. 12–15 ES cells were injected into each blastocyst which was then transferred to the uterus of a 2.5-day postcoitum pseudo-pregnant CD-1 female. Ectopic Lin28 expression was accomplished by retroviral infection of Stella-GFP ES cells with pBABE-Lin28. Statistical significance of germ-cell chimaerism was determined by the Mann-Whitney rank-sum test.

**Human primary tumour and cell line information.** Primary tissue microarray data sets were published previously<sup>23</sup> and have the GEO accession number GSE3218. Log<sub>2</sub> transformed expression data were normalized to the average expression signal for normal tissue. Cutoff for overexpression was as a normalized expression value of 2 or greater. Immunohistochemistry of paraffin-embedded tissues was performed using standard techniques with LIN28 primary antibody staining (1/200; Proteintech Group) followed by streptavidin peroxidase incubation (Lab Vision) and DAB kit colour developing (Vector Laboratories) according to the manufacturers' protocol. Sections were counterstained with haematoxylin.

30. Keller, G. M. *In vitro* differentiation of embryonic stem cells. *Curr. Opin. Cell Biol.* **7**, 862–869 (1995).
31. Kyba, M., Perlingeiro, R. C. & Daley, G. Q. HoxB4 confers definitive lymphoid-myeloid engraftment potential on embryonic stem cell and yolk sac hematopoietic progenitors. *Cell* **109**, 29–37 (2002).
32. West, J. A., Park, I. H., Daley, G. Q. & Geijsen, N. *In vitro* generation of germ cells from murine embryonic stem cells. *Nature Protocols* **1**, 2026–2036 (2006).
33. Beard, C., Hochedlinger, K., Plath, K., Wutz, A. & Jaenisch, R. Efficient method to generate single-copy transgenic mice by site-specific integration in embryonic stem cells. *Genesis* **44**, 23–28 (2006).
34. Koshimizu, U., Watanabe, M. & Nakatsuji, N. Retinoic acid is a potent growth activator of mouse primordial germ cells *in vitro*. *Dev. Biol.* **168**, 683–685 (1995).
35. Ginsburg, M., Snow, M. H. & McLaren, A. Primordial germ cells in the mouse embryo during gastrulation. *Development* **110**, 521–528 (1990).
36. Stoger, R. *et al.* Maternal-specific methylation of the imprinted mouse *Igf2r* locus identifies the expressed locus as carrying the imprinting signal. *Cell* **73**, 61–71 (1993).
37. Yoon, B. J. *et al.* Regulation of DNA methylation of *Rasgrf1*. *Nature Genet.* **30**, 92–96 (2002).
38. Mager, J., Montgomery, N. D., de Villena, F. P. & Magnuson, T. Genome imprinting regulated by the mouse Polycomb group protein Eed. *Nature Genet.* **33**, 502–507 (2003).
39. Lucifero, D., Mertineit, C., Clarke, H. J., Bestor, T. H. & Trasler, J. M. Methylation dynamics of imprinted genes in mouse germ cells. *Genomics* **79**, 530–538 (2002).
40. Zaehres, H. & Daley, G. Q. Transgene expression and RNA interference in embryonic stem cells. *Methods Enzymol.* **420**, 49–64 (2006).

## LETTERS

## Multiple roles for MRE11 at uncapped telomeres

Yibin Deng<sup>1\*†</sup>, Xiaolan Guo<sup>1,3\*†</sup>, David O. Ferguson<sup>4</sup> & Sandy Chang<sup>1,2</sup>

Progressive telomere attrition or uncapping of the shelterin complex elicits a DNA damage response as a result of a cell's inability to distinguish dysfunctional telomeric ends from DNA double-strand breaks<sup>1</sup>. Telomere deprotection activates both ataxia telangiectasia mutated (ATM) and telangiectasia and Rad3-related (ATR) kinase-dependent DNA damage response pathways, and promotes efficient non-homologous end-joining (NHEJ) of dysfunctional telomeres<sup>2–5</sup>. The mammalian MRE11–RAD50–NBS1 (MRN; NBS1 is also known as NBN) complex interacts with ATM to sense chromosomal double-strand breaks and coordinate global DNA damage responses<sup>6,7</sup>. Although the MRN complex accumulates at dysfunctional telomeres, it is not known whether mammalian MRN promotes repair at these sites. Here we address this question by using mouse alleles that either inactivate the entire MRN complex or eliminate only the nuclease activities of MRE11 (ref. 8). We show that cells lacking MRN do not activate ATM when telomeric repeat binding factor 2 (TRF2) is removed from telomeres, and ligase 4 (LIG4)-dependent chromosome end-to-end fusions are markedly reduced. Residual chromatid fusions involve only telomeres generated by leading strand synthesis. Notably, although cells deficient for MRE11 nuclease activity efficiently activate ATM and recruit 53BP1 (also known as TP53BP1) to deprotected telomeres, the 3' telomeric overhang persists to prevent NHEJ-mediated chromosomal fusions. Removal of shelterin proteins that protect the 3' overhang in the setting of MRE11 nuclease deficiency restores LIG4-dependent chromosome fusions. Our data indicate a critical role for the MRN complex in sensing dysfunctional telomeres, and show that in the absence of TRF2, MRE11 nuclease activity removes the 3' telomeric overhang to promote chromosome fusions. MRE11 can also protect newly replicated leading strand telomeres from NHEJ by promoting 5' strand resection to generate POT1a–TPP1-bound 3' overhangs.

The proper maintenance of telomeres is essential for global genome stability. Mammalian telomeres are composed of TTAGGG repeats bound to shelterin—a complex of six core proteins including the double-stranded DNA-binding proteins TRF1 and TRF2, and protection of telomeres 1 (POT1) that interacts with its binding partner TPP1 to protect single-stranded G-rich overhangs<sup>1</sup>. Telomeres rendered dysfunctional by the removal of TRF2 are recognized as double-strand breaks (DSBs), activate ATM and are ligated by the NHEJ pathway to generate fused chromosomes<sup>3</sup>. The MRN complex recruits ATM to sites of DSBs, where it initiates a signalling cascade leading to checkpoint responses<sup>9,10</sup>. Although MRN localizes to deprotected telomeres<sup>11,12</sup>, its role in NHEJ-mediated repair is not well understood. We sought to uncover the roles of the MRN complex in NHEJ by using two mouse alleles of MRE11: the *Mre11*<sup>Δ/Δ</sup> null allele that also abolishes the formation of the MRN complex, and the *Mre11*<sup>H129N/Δ</sup> nuclease-deficient allele—in which His 129 was mutated to Asn—that eliminates both endo- and exonuclease functions of MRE11 (ref. 8).

To engage the NHEJ pathway, we removed TRF2 from telomeres with retrovirus-mediated short hairpin RNA (shRNA) to *Trf2* in SV40LT immortalized mouse embryonic fibroblasts (MEFs) (Supplementary Fig. 1a). Metaphase spreads collected 72 to 120 h after *Trf2* shRNA treatment showed a progressive increase in the number of fused telomeres until nearly all chromosomes are joined end-to-end (Supplementary Fig. 1b). This telomere fusion phenotype was suppressed when MEFs were first complemented with shRNA-resistant murine *Trf2* complementary DNA before *Trf2* shRNA treatment (Supplementary Fig. 1c, d and Supplementary Table 1), indicating that the telomere fusions observed are not due to off-target effects of *Trf2* shRNA treatment.

To determine whether MRE11 is required for the DNA damage response (DDR) initiated by dysfunctional telomeres, MEFs containing the conditional *Mre11*<sup>F/Δ</sup> allele were infected with adenovirus expressing Cre recombinase. The floxed *Mre11* allele was efficiently deleted, with concomitant loss of MRE11 protein as confirmed by western blotting (Supplementary Fig. 2b, c). Because TRF2 represses ATM activation at telomeres<sup>4,5</sup>, removal of TRF2 from *Mre11*<sup>F/Δ</sup> cells resulted in robust ATM activation, phosphorylation of CHK2 and induction of phosphorylated histone 2AX (γ-H2AX, also known as H2AFX) and 53BP1 telomere-induced DNA damage foci (TIF) that colocalized with telomeric DNA in 90% of cells examined (Fig. 1a, c and Supplementary Fig. 3a). However, both ATM phosphorylation and TIF formation were reduced to 12% in *Mre11*<sup>Δ/Δ</sup> MEFs in response to TRF2 depletion (Fig. 1a, c and Supplementary Fig. 3a). To determine whether the MRE11 nuclease activity is required for ATM activation after induction of telomere dysfunction, *Mre11*<sup>H129N/Δ</sup> MEFs were generated (Supplementary Fig. 2a–c). In contrast to *Mre11*<sup>Δ/Δ</sup> MEFs, the phosphorylation of ATM and induction of TIF after TRF2 depletion in *Mre11*<sup>H129N/Δ</sup> MEFs remained robust (Fig. 1b, d and Supplementary Fig. 3b). These results indicate that ATM phosphorylation in response to TRF2 depletion requires MRN, whereas the MRE11 nuclease activity is dispensable for this function. At murine telomeres, ATR activation is repressed by POT1a<sup>4,5</sup>. To test whether ATR activation at telomeres requires MRN or MRE11 nuclease activity, *Pot1a* shRNA was used to deplete POT1a in *Mre11*<sup>Δ/Δ</sup> and *Mre11*<sup>H129N/Δ</sup> MEFs. Removal of POT1a resulted in robust ATR phosphorylation and TIF formation in both cell types (Fig. 1e, f and Supplementary Fig. 3c, d), suggesting that MRE11 is not required to activate an ATR-dependent DDR at telomeres after POT1a loss.

Our data demonstrate that the removal of TRF2 results in telomeres being recognized as DSBs that elicit MRN-dependent DDR. To determine whether the repair of dysfunctional telomeres is impacted in the setting of MRE11 nuclease deficiency or after removal of the MRN complex, TRF2 was depleted in *Mre11*<sup>F/Δ</sup>, *Mre11*<sup>Δ/Δ</sup> and *Mre11*<sup>H129N/Δ</sup> MEFs. Although *Mre11*<sup>F/Δ</sup> cells showed extensive end-to-end chromosome fusions in a LIG4-dependent manner, *Mre11*<sup>Δ/Δ</sup> cells showed a 15-fold reduction in the number of

<sup>1</sup>Department of Genetics, Box 1010, <sup>2</sup>Department of Hematopathology, The M.D. Anderson Cancer Center, 1515 Holcombe Boulevard, Houston, Texas 77030, USA. <sup>3</sup>Institute of Rheumatology and Immunology North Sichuan Medical College, Nanchong, Sichuan 637000, China. <sup>4</sup>Department of Pathology, The University of Michigan Medical School, Ann Arbor, Michigan 48109, USA. <sup>†</sup>Present address: Section of Cancer Genetics, The Hormel Institute, University of Minnesota, Austin, Minnesota 55912, USA.

\*These authors contributed equally to this work.



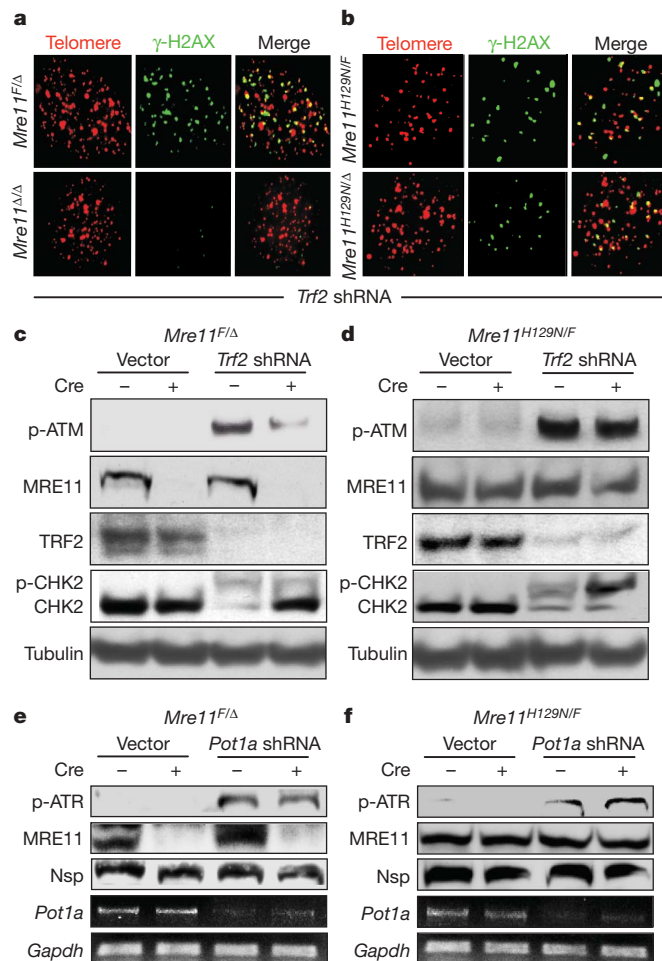


**Figure 1 | Activation of ATM but not ATR after TRF2 depletion requires the MRN complex but not MRE11 nuclease activity.** **a, b**,  $\gamma$ -H2AX-positive TIF in MEFs of the indicated genotypes after TRF2 depletion in MRE11-deficient SV40LT immortalized MEFs (**a**) and MRE11-nuclease-activity-deficient MEFs (**b**). Original magnification,  $\times 630$ . **c, d**, Western blots detecting TRF2, MRE11, p-ATM, total and phosphorylated CHK2 (p-) after *Trf2* shRNA treatment in MRE11-deficient SV40LT immortalized MEFs (**c**) and MRE11 nuclease-deficient MEFs (**d**). Tubulin served as loading control. **e, f**, Immunoblots for MRE11 and ATR phosphorylation, and RT-PCR to detect *Pot1a* and *Gapdh* transcripts, after *Pot1a* shRNA infection of MRE11-deficient SV40LT immortalized MEFs (**e**) and MRE11 nuclease-activity-deficient MEFs (**f**). Nsp, nonspecific protein used as a loading control.

chromosome–chromosome fusions (Fig. 2a, Supplementary Fig. 4a–c and Supplementary Table 2). Unexpectedly, chromosome–chromosome fusions were similarly reduced in nuclease-deficient *Mre11*<sup>H129N/Δ</sup> cells, even though the DDR is activated after TRF2 loss (Figs 1d, 2a and Supplementary Table 2). These results indicate a critical role of the MRE11 nuclease activity in mediating NHEJ of dysfunctional telomeres.

The marked reduction in the number of chromosome–chromosome fusions observed in *Mre11*<sup>H129N/Δ</sup> cells treated with *Trf2* shRNA suggests that nucleolytic processing of telomeric ends might be required for NHEJ of dysfunctional telomeres. To test this hypothesis, we examined the status of the 3' single-strand overhang using an in-gel hybridization assay. In contrast to *Trf2*-shRNA-treated *Mre11*<sup>F/Δ</sup> cells, which showed rapid reduction of the 3' overhang due to NHEJ-mediated processing<sup>13</sup>, the 3' overhang persists in *Mre11*<sup>Δ/Δ</sup> and *Mre11*<sup>H129N/Δ</sup> cells with uncapped telomeres (Fig. 2b). Treatment with the 3' end specific exonuclease ExoI revealed that these overhangs are indeed single-stranded telomeric repeats (Supplementary Fig. 5a, b). The lack of overhang degradation in *Mre11*<sup>H129N/Δ</sup> cells treated with *Trf2* shRNA suggests that nucleolytic processing of the 3' telomeric

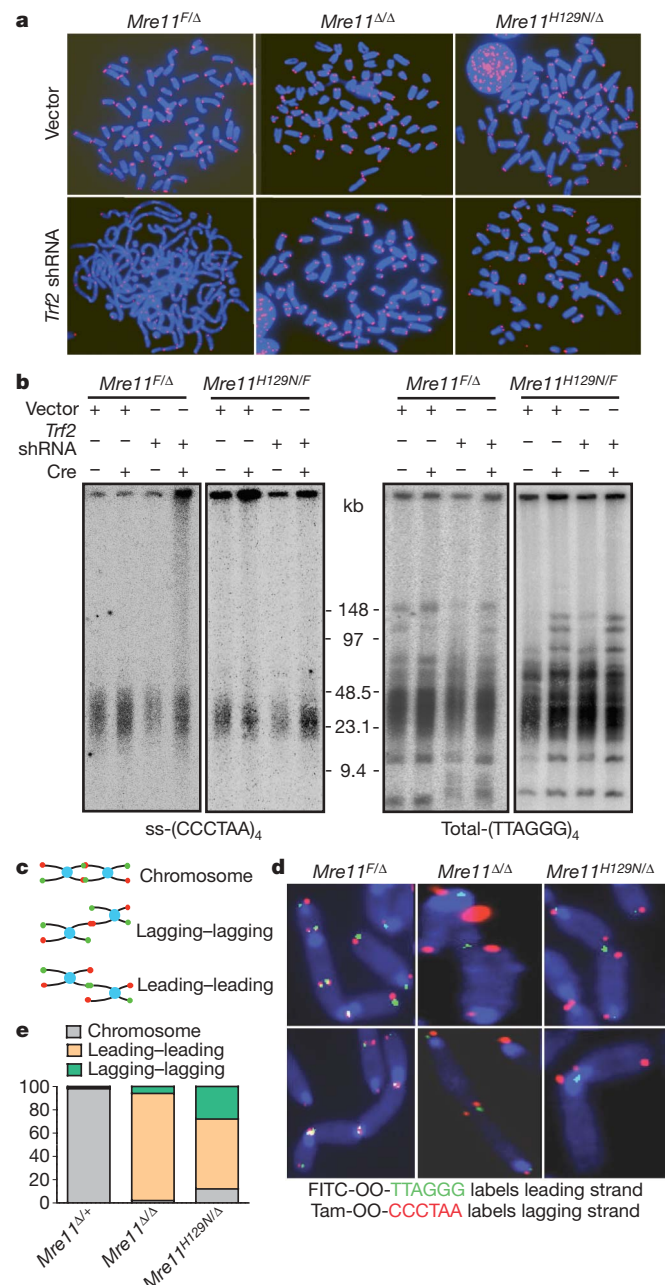


**Figure 2 | Requirement for MRN and MRE11 nuclease activity in NHEJ of telomeres lacking TRF2.** **a**, MEFs of the indicated genotypes were treated with control vector or *Trf2* shRNA for 120 h, metaphases were prepared and telomere fusions were visualized by telomere peptide nucleic acid (PNA)-FISH (red) and 4,6-diamidino-2-phenylindole (DAPI; blue). **b**, In-gel hybridization assay using a clamped homogenous electric field (CHEF) gel to fractionate genomic DNA, then hybridized *in situ* to a (CCCTAA)<sub>4</sub> probe to detect the 3' single strand (SS) overhang under native conditions (left) and under denatured condition (right) to detect total TTAGGG repeats (right). **c**, Schematic of fusion products expected in chromosome–chromosome, leading–leading chromatid and lagging–lagging chromatid fusions. **d**, Fusion products of *Trf2*-shRNA-treated cells of the indicated genotypes analysed by CO-FISH. DNA was detected by DAPI (blue). Telomeric probes used in CO-FISH experiments are FITC-OO-(TTAGGG)<sub>4</sub> to label the leading strand, and Tam-OO-(CCCTAA)<sub>4</sub> to label the lagging strand. Representative images are shown. **e**, Quantification of the types of fusions observed in cells of the indicated genotypes expressed as a percentage of total fusions observed after TRF2 depletion. A minimum of 150 independent fusion events with telomeric signals at the sites of fusions were characterized per genotype. Original magnification for all images,  $\times 630$ .



overhang by MRE11 nuclease activity is required for efficient NHEJ of telomeres rendered dysfunctional by the removal of TRF2.

Interestingly, telomere fusions were not completely abolished in *Trf2*-shRNA-treated *Mre11*<sup>Δ/Δ</sup> cells. Instead, chromosome-orientation fluorescent in situ hybridization (CO-FISH) showed that ~90% of these rare fusions involved the leading strands of sister chromatids (Fig. 2c–e). After telomeric replication, telomeres formed by leading strand synthesis are initially blunt, whereas lagging strand DNA synthesis results in the formation of a 3' overhang after the removal of the last synthesis primer. Leading strand telomeric ends have to be enzymatically processed after replication to produce a 3' overhang that is protective against NHEJ-mediated fusion. We postulate that the MRN complex prevents NHEJ of newly synthesized leading strand telomeres by mediating 5' end resection of the leading strand to generate a 3' overhang. In support of this notion, leading–leading chromatid fusions comprised ~60% of all chromatid fusions in *Trf2*-shRNA-treated *Mre11*<sup>H129N/Δ</sup> cells, suggesting that the nuclease activity of MRE11 is at least in part responsible for the formation of the 3' overhang at the leading strand (Fig. 2d, e).

Although the POT1a–TPP1 shelterin sub-complex<sup>14</sup> binds to the 3' single-stranded telomeric overhang and represses ATR-mediated DDR<sup>4,5</sup>, little is known about how the overhang is protected from engaging DNA repair pathway(s). The presence of an intact single-stranded telomeric overhang in *Trf2*-shRNA-treated *Mre11*<sup>Δ/H129N</sup> cells, and the ability of this mutant to activate ATM and ATR signaling pathways, represent a unique opportunity to address this question. Using immunostaining and telomere FISH to detect the localization of endogenous TPP1 at single-stranded overhangs and the double-stranded telomeric binding protein TRF1 to mark telomeres, we observed a 3.5-fold reduction of TPP1, but not TRF1, at telomeres in *Mre11*<sup>H129N/F</sup> cells after TRF2 depletion (Supplementary Fig. 6a–c), reinforcing the idea that telomeric accumulation of the POT1a–TPP1 complex is reduced when TRF2 is depleted<sup>15</sup>. In contrast, TPP1 immunostaining remained robust in *Trf2*-shRNA-treated *Mre11*<sup>H129N/Δ</sup> cells (Supplementary Fig. 6a–c), suggesting that POT1a–TPP1 remains complexed to the single-stranded telomeric overhangs in these cells.

We next addressed whether the removal of POT1a–TPP1 rendered the overhang amenable to DSB repair. We first depleted TRF2 in *Mre11*<sup>H129N/Δ</sup> MEFs, then removed POT1a, POT1b or TPP1 from the single-stranded overhang using shRNAs (Supplementary Fig. 7a). Depletion of POT1a but not POT1b resulted in a threefold increase in telomere end-to-end fusions (Fig. 3a, b), supporting the hypothesis that in mouse cells, POT1a helps protect telomeres from engaging in inappropriate repair, whereas POT1b is involved in the protection of the C strand<sup>16–19</sup>. Removal of TPP1 (ref. 4) from the 3' overhang of *Trf2*-shRNA-treated *Mre11*<sup>H129N/Δ</sup> cells resulted in a fivefold increase in chromosome end-to-end fusions, with 30% of all chromosomes fused (Fig. 3a, b and Supplementary Figs 7a and 8a, b). Taken together, these results demonstrate that at telomeres lacking TRF2 and MRE11 nuclease activities, the POT1a–TPP1 complex is able to protect telomeres from participating in inappropriate repair pathways.

ATM, ATR and 53BP1 have been implicated in mediating NHEJ of dysfunctional telomeres after the removal of TRF2 (refs 4, 5, 20). We found that the depletion of ATR, but not of ATM, resulted in a fourfold reduction in the number of end-to-end chromosomal fusions induced by retroviral expression of full-length *Tpp1*<sup>ARD</sup> (a TPP1 mutant in which the POT1a recruitment domain is deleted; ref. 4) in *Trf2*-shRNA-treated *Mre11*<sup>H129N/Δ</sup> cells (Fig. 3c, d and Supplementary Figs 7b and 9a–c). Similarly, depletion of 53BP1 led to a fourfold reduction of chromosomes fused in *Mre11*<sup>H129N/Δ</sup> MEFs expressing *Tpp1*<sup>ARD</sup> (Fig. 3c, d and Supplementary Fig. 7c). Collectively, these data argue that in the absence of the POT1a–TPP1 complex, processing of the single-stranded overhang does not require MRE11 nuclease activity to mediate ATR and 53BP1-dependent chromosomal fusions. We postulate that other nucleases

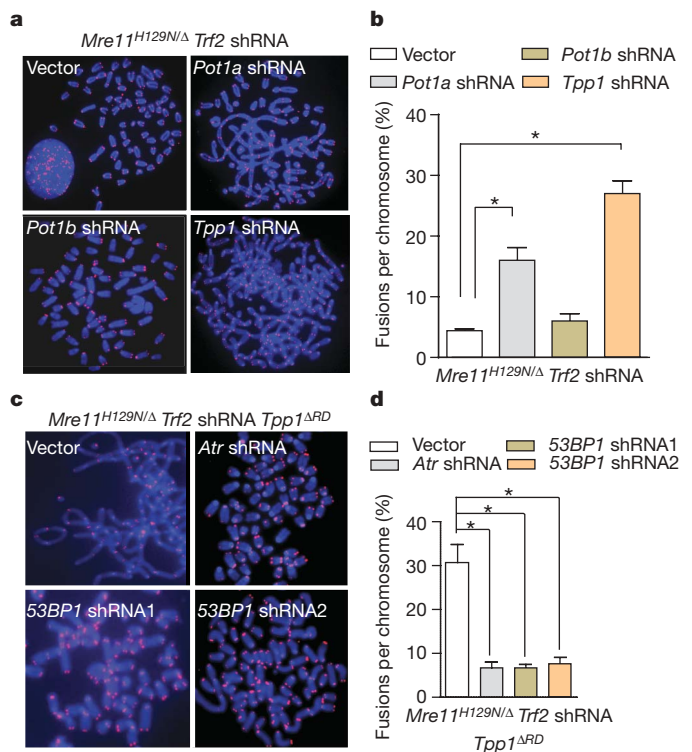


**Figure 3 | POT1a–TPP1 complex protects single-stranded overhangs from DNA repair.** **a**, Depletion of POT1a or TPP1, but not POT1b, results in pronounced telomere fusions in metaphase spreads from *Trf2*-shRNA-treated *Mre11*<sup>H129N/Δ</sup> MEFs, with telomeric PNA-FISH (red) and DAPI (blue). **b**, Quantification of telomere fusions from representative images shown in **a**. Error bars, s.d.;  $n \geq 350$ , asterisk,  $P < 0.001$ . **c**, Depletion of ATR or 53BP1 inhibits chromosomal fusions generated by expression of *Tpp1*<sup>ARD</sup> cDNA and removal of TRF2 in *Mre11*<sup>H129N/Δ</sup> MEFs. **d**, Quantification of telomere fusions from representative images shown in **c**. Error bars, s.d.;  $n \geq 900$ , asterisk,  $P < 0.001$ . Original magnification for all images,  $\times 630$ .

in the cell, for example the nucleotide excision repair nuclease ERCC1 (also known as XPF) that has been shown to remove the 3' overhang when coupled to the NHEJ machinery<sup>13</sup>, might substitute for MRE11 nuclease function at this stage.

Furthermore, we asked which pathway (NHEJ versus homologous recombination) is required for repair of the single-stranded overhang. Removal of POT1a–TPP1 from *Mre11*<sup>H129N/F</sup> MEFs resulted in increased homologous recombination at telomeres, detected as a fivefold increase in telomere sister chromatid exchanges (T-SCEs)<sup>21</sup> (Supplementary Fig. 10a, b). Notably, T-SCEs were not increased significantly in POT1a–TPP1-depleted *Mre11*<sup>H129N/Δ</sup> cells, suggesting that the MRE11 nuclease activity has an important role in telomeric homologous recombination (Supplementary Fig. 10a–c). When TRF2 is removed from POT1a–TPP1-depleted *Mre11*<sup>H129N/Δ</sup> cells, robust LIG4-dependent chromosomal fusions were observed (Fig. 4a–c). However, T-SCE levels in these cells remained similar to those observed in control cells (Fig. 4d and Supplementary Fig. 11). These results support the hypothesis that the main function of POT1a–TPP1 is to repress homologous recombination at telomeres, whereas TRF2 is primarily responsible to repress NHEJ at telomeres.

The data presented here reveal several roles for the MRN complex at telomeres. MRN interacts with TRF2 and localizes to telomeres throughout the cell cycle<sup>11</sup>. Together with TRF2, MRE11 has a protective role in preventing NHEJ-mediated fusion of leading strand telomeric DNA after replication by promoting 5' leading strand resection to generate POT1a–TPP1 bound 3' overhangs that prevent NHEJ (Supplementary Fig. 12). Although the MRE11 nuclease activity has a role in this process, additional factors are likely to be involved<sup>22</sup>. One such candidate is CtIP (also known as RBBP8)<sup>23,24</sup>, because recent data indicate that the yeast homologue SAE2 (also known as UBA2)

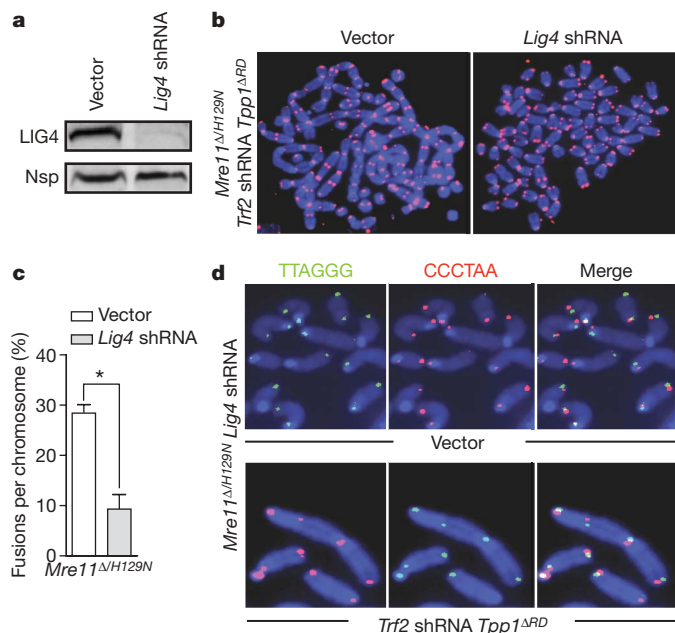


**Figure 4 | LIG4 is required for repair of unprotected single-stranded telomeric overhangs.** **a**, Immunoblot demonstrating that *Lig4* shRNA efficiently depletes LIG4 from *Mre11*<sup>H129N/Δ</sup> nuclease-deficient MEFs expressing *Tpp1*<sup>ΔRD</sup> and *Trf2* shRNA. Nsp, nonspecific protein used as loading control. **b**, LIG4 is required for chromosomal fusions in *Mre11*<sup>H129N/Δ</sup> nuclease-deficient MEFs expressing *Tpp1*<sup>ΔRD</sup> and *Trf2* shRNA. **c**, Quantification of the number of fusions per chromosome from representative images shown in **b**. Error bars, s.d.;  $n \geq 850$ ; asterisk,  $P < 0.001$ . **d**, T-SCEs in *Mre11*<sup>H129N/Δ</sup> nuclease-deficient MEFs depleted in LIG4, TRF2 and expressing TPP1<sup>ΔRD</sup>. CO-FISH was performed using FITC-OO-(TTAGGG)<sub>4</sub> (green) and Tam-OO-(CCCTAA)<sub>4</sub> (red) probes. Original magnification for all images,  $\times 630$ .

cooperates with MRE11 to remove nucleotides at DSBs in a 5'–3' endonucleolytic manner before extensive resection is performed by other nucleases, including ExoI and Dna2 (refs 25, 26). However, the generation of 3' single-stranded overhangs has the undesired consequence of initiating inappropriate homologous recombination at telomeres. Indeed, the MRE11 nuclease activity is required for telomere homologous recombination after POT1a–TPP1 is removed from the 3' overhang. Because initiation of homologous recombination requires RPA binding to single-stranded DNA, we speculate that the POT1a–TPP1 complex represses homologous recombination by preventing RPA access to the 3' overhang.

Removal of TRF2 from telomeres stimulates the MRN complex to activate ATM and 53BP1 to promote NHEJ. Surprisingly, removal of TRF2 also liberates the MRE11 3'–5' nuclease activity to process 3' telomeric overhangs before NHEJ of chromosome ends. Because single-stranded telomeric overhangs are incompatible with DNA ligation<sup>3</sup>, we speculate that degradation of the 3' overhang by MRE11 (ref. 27), probably in conjunction with other components of the NHEJ pathway<sup>13,20</sup>, is required to generate telomeric substrates amenable for joining by LIG4. This model is supported by the observation that MRE11 nuclease activities are required for efficient NHEJ during class-switch recombination in developing lymphocytes<sup>28</sup>.

Our studies also uncover an unexpected role for the POT1a–TPP1 complex in protecting the 3' overhang from NHEJ in the absence of TRF2 and MRE11 nuclease activity. Because TRF2 is thought to be essential for the formation of the telomeric-loop structure proposed to protect chromosome ends from engaging the NHEJ pathway, our result support the notion that under certain conditions the telomeric loop is dispensable for telomere end protection<sup>29</sup>. We speculate that the POT1a–TPP1 complex cooperates with TRF2–RAP1 during telomere replication, when the telomeric loop is transiently lost, to protect the integrity of linear chromosomal ends<sup>30</sup>.

## METHODS SUMMARY

**Generation of MEFs and conditional deletion of MRE11.** MEFs were isolated from embryonic day (E)13.5 embryos obtained from crosses between *Mre11*<sup>F1Δ</sup> and *Mre11*<sup>H129N</sup> mice, and grown in standard culture conditions. PCR-based genotyping was performed as described<sup>8</sup>. Primary MEFs were immortalized at passage 2 by transfection with pBabeSV40LT. To delete MRE11, MEFs with different genotypes were treated with Cre-expressing adenoviruses at multiplicities of infection of 500. Depletion of MRE11 was confirmed by PCR and western blot.

**shRNA interference.** Two *Trf2* shRNAs were generated in pSuper. To generate Retro-pSuper constructs, EcoRI- and XhoI-digested insert from pSuper was subcloned into the same site into Retro-pSuper vector. The shRNA target sequences for mouse *Trf2* are: shRNA1, 5'-CTGTCATTATTTGTATCAA-3'; and shRNA2, 5'-GAACAGCTGTGATGATTAA-3'. The target sequence of *Trf2* shRNA2 was changed to 5'-CGTACTGCAGTCATGATC-3' by standard site-directed mutagenesis to create *Trf2*-shRNA-resistant construct Retro-pSuper shTRF2-2M (Stratagene). Lentivirus-based shRNAs for *Lig4*, *Mre11* and *53BP1* were purchased from Sigma (sequences available on request). Published target sequences<sup>5</sup> were constructed into Retro-pSuper and used for knockdown of ATR. shRNAs for *Pot1a*, *Pot1b*, *Tpp1* and the TPP1<sup>ΔRD</sup> construct *Tpp1*<sup>ΔRD</sup> were as described<sup>4</sup>. Retrovirus or lentivirus-mediated efficient knockdown of target genes was verified by either RT-PCR or immunoblotting.

**Full Methods** and any associated references are available in the online version of the paper at [www.nature.com/nature](http://www.nature.com/nature).

Received 19 February; accepted 11 June 2009.

Published online 26 July; corrected 13 August 2009 (see full-text HTML version for details).

- Palm, W. & de Lange, T. How shelterin protects mammalian telomeres. *Annu. Rev. Genet.* **42**, 301–334 (2008).
- van Steensel, B., Smogorzewska, A. & de Lange, T. TRF2 protects human telomeres from end-to-end fusions. *Cell* **92**, 401–413 (1998).
- Celli, G. B. & de Lange, T. DNA processing is not required for ATM-mediated telomere damage response after TRF2 deletion. *Nature Cell Biol.* **7**, 712–718 (2005).
- Guo, X. *et al.* Dysfunctional telomeres activate an ATM-ATR-dependent DNA damage response to suppress tumorigenesis. *EMBO J.* **26**, 4709–4719 (2007).
- Denchi, E. L. & de Lange, T. Protection of telomeres through independent control of ATM and ATR by TRF2 and POT1. *Nature* **448**, 1068–1071 (2007).
- D'Amours, D. & Jackson, S. P. The Mre11 complex: at the crossroads of DNA repair and checkpoint signalling. *Nature Rev. Mol. Cell Biol.* **3**, 317–327 (2002).
- Lee, J. H. & Paull, T. T. ATM activation by DNA double-strand breaks through the Mre11-Rad50-Nbs1 complex. *Science* **308**, 551–554 (2005).
- Buis, J. *et al.* Mre11 nuclease activity has essential roles in DNA repair and genomic stability distinct from ATM activation. *Cell* **135**, 85–96 (2008).
- Falck, J., Coates, J. & Jackson, S. P. Conserved modes of recruitment of ATM, ATR and DNA-PKcs to sites of DNA damage. *Nature* **434**, 605–611 (2005).
- Deng, Y., Chan, S. S. & Chang, S. Telomere dysfunction and tumour suppression: the senescence connection. *Nature Rev. Cancer* **8**, 450–458 (2008).
- Zhu, X. D., Kuster, B., Mann, M., Petrini, J. H. & de Lange, T. Cell-cycle-regulated association of RAD50/MRE11/NBS1 with TRF2 and human telomeres. *Nature Genet.* **25**, 347–352 (2000).
- Takai, H., Smogorzewska, A. & de Lange, T. DNA damage foci at dysfunctional telomeres. *Curr. Biol.* **13**, 1549–1556 (2003).
- Zhu, X. D. *et al.* ERCC1/XPF removes the 3' overhang from uncapped telomeres and represses formation of telomeric DNA-containing double minute chromosomes. *Mol. Cell* **12**, 1489–1498 (2003).
- O'Connor, M. S., Safari, A., Xin, H., Liu, D. & Songyang, Z. A critical role for TPP1 and TIN2 interaction in high-order telomeric complex assembly. *Proc. Natl Acad. Sci. USA* **103**, 11874–11879 (2006).
- Hockemeyer, D. *et al.* Telomere protection by mammalian Pot1 requires interaction with Tpp1. *Nature Struct. Mol. Biol.* **14**, 754–761 (2007).
- Hockemeyer, D., Daniels, J. P., Takai, H. & de Lange, T. Recent expansion of the telomeric complex in rodents: Two distinct POT1 proteins protect mouse telomeres. *Cell* **126**, 63–77 (2006).
- Wu, L. *et al.* Pot1 deficiency initiates DNA damage checkpoint activation and aberrant homologous recombination at telomeres. *Cell* **126**, 49–62 (2006).
- Hockemeyer, D., Palm, W., Wang, R. C., Couto, S. S. & de Lange, T. Engineered telomere degradation models dyskeratosis congenita. *Genes Dev.* **22**, 1773–1785 (2008).
- He, H. *et al.* Pot1b deletion and telomerase haploinsufficiency in mice initiate an ATR-dependent DNA damage response and elicit phenotypes resembling dyskeratosis congenita. *Mol. Cell Biol.* **29**, 229–240 (2009).
- Dimitrova, N., Chen, Y. C., Spector, D. L. & de Lange, T. 53BP1 promotes non-homologous end joining of telomeres by increasing chromatin mobility. *Nature* **456**, 524–528 (2008).
- Bailey, S. M., Cornforth, M. N., Kurimasa, A., Chen, D. J. & Goodwin, E. H. Strand-specific postreplicative processing of mammalian telomeres. *Science* **293**, 2462–2465 (2001).

22. Hopkins, B. B. & Paull, T. T. The *P. furiosus* MRE11/RAD50 complex promotes 5' strand resection at a DNA double-strand break. *Cell* **135**, 250–260 (2008).
23. Limbo, O. *et al.* Ctp1 is a cell-cycle-regulated protein that functions with Mre11 complex to control double-strand break repair by homologous recombination. *Mol. Cell* **28**, 134–146 (2007).
24. Sartori, A. A. *et al.* Human CtIP promotes DNA end resection. *Nature* **450**, 509–514 (2007).
25. Mimitou, E. P. & Symington, L. S. Sae2, Exo1 and Sgs1 collaborate in DNA double-strand break processing. *Nature* **455**, 770–774 (2008).
26. Zhu, Z., Chung, W. H., Shim, E. Y., Lee, S. E. & Ira, G. Sgs1 helicase and two nucleases Dna2 and Exo1 resect DNA double-strand break ends. *Cell* **134**, 981–994 (2008).
27. Paull, T. T. & Gellert, M. The 3' to 5' exonuclease activity of Mre11 facilitates repair of DNA double-strand breaks. *Mol. Cell* **1**, 969–979 (1998).
28. Dinkelmann, M. *et al.* Multiple functions of MRN in end-joining pathways during isotype class switching. *Nature Struct. Mol. Biol.* (in the press).
29. Wang, X. & Baumann, P. Chromosome fusions following telomere loss are mediated by single-strand annealing. *Mol. Cell* **31**, 463–473 (2008).
30. Verdun, R. E. & Karlseder, J. The DNA damage machinery and homologous recombination pathway act consecutively to protect human telomeres. *Cell* **127**, 709–720 (2006).

**Supplementary Information** is linked to the online version of the paper at [www.nature.com/nature](http://www.nature.com/nature).

**Acknowledgements** We are grateful to M. Zhao, Z. Lu, P. Iyengar and J. Buis for technical help. Both J. Karlseder and P. Carpenter are thanked for providing antibodies. S.C. acknowledges financial support from the National Institute on Aging (NIA) (RO1 AG028888), the National Cancer Institute (NCI) (RO1 CA129037), the Welch Foundation, the Susan G. Koman Race for the Cure Foundation, the Abraham and Phyllis Katz Foundation and the Michael Kadoorie Cancer Genetic Research Program. Y.D. was supported by an NCI Howard Temin Award (K01CA124461).

**Author Contributions** Y.D. designed and guided all experiments, helped write the paper and generated figures. X.G. performed all the experiments presented. D.O.F. provided MRE11 mouse cell lines for this study and assisted in the interpretation of results. S.C. conceived this study, analysed and interpreted the data, wrote the paper and finalized the figures.

**Author Information** Reprints and permissions information is available at [www.nature.com/reprints](http://www.nature.com/reprints). Correspondence and requests for materials should be addressed to S.C. ([schang@mdanderson.org](mailto:schang@mdanderson.org)).



## METHODS

**Mouse genotyping.** *Mre11* genotyping was performed as described<sup>8</sup>. The following primers were used: forward, 5'-TACAAAAGGTTGAAAATTGAGAAGC-3', reverse, 5'-TGTAATTGCAGGT-CCTTAAAGGC-3'. The thermocycling conditions were 36 cycles of 95 °C for 30 s, 52 °C for 1 min, and 72 °C for 1 min.

**RNA isolation, RT-PCR.** RNA was isolated from approximately 10<sup>6</sup> cells with the Qiagen RNeasy kit. RT-PCR was performed with the oligo-dT RT-PCR system according to the protocol provided by the manufacturer (Invitrogen). The following primers were used: mouse *Pot1a* forward, 5'-GATGACGTCA CAGGCGCCTAGG-3'; reverse, 5'-TCCCATACACACTGCACTCAATGG-3'; mouse *Pot1b* forward, 5'-CTTTAAGCCTCCGGCCTTAAGCAAAGG-3'; reverse, 5'-CTTGGACATGATTATCAGCAACGACAATGTCTAC-3'; mouse *Tpp1* forward, 5'-ATGTCCGATTCAGGGTTGCTGG-3'; reverse, 5'-TCATAC CTGGGTAACTCAGACTCTGACTC-3'; mouse *Gapdh* forward, 5'-TCACCA CCATGGAGAAGGC-3'; reverse, 5'-GCTAAGCAGTTGGTGGTGCA-3'.

**Immunoblotting.** Cell extracts were isolated and western blot was performed as described<sup>4</sup>. Antibodies were: phospho-ATM Ser 1981 from Rockland; phospho-ATR, ATR and MRE11 from Cell Signaling; CHK2 from BD Biosciences;  $\gamma$ -tubulin and haemagglutinin from Sigma;  $\gamma$ -H2AX from Upstate; anti-53BP1 antibody was obtained from P. Carpenter at UT Medical School; anti-TRF1 and -TRF2 antibodies were obtained from J. Karlseder at Salk Institute.

**Immunofluorescence and TIF analysis.** Immunofluorescence and TIF analysis assays for cells with different genotypes grown on coverslips were performed as described previously<sup>4</sup> using the primary antibody TRF1, TPP1, 53BP1 or  $\gamma$ -H2AX. Secondary antibodies against mouse or rabbit were labelled with Alexa 488 (Molecular Probes). For the TIF assay, the same primary and secondary antibodies were used with a Tam-OO-(CCCTAA)<sub>4</sub> PNA telomere probe (Applied Biosystems). DNA was counterstained with DAPI and slides were mounted in 90% glycerol, 10% PBS containing 1  $\mu$ g ml<sup>-1</sup> p-phenylene diamine (Sigma). Digital images were acquired and analysed as described<sup>4</sup>, using a Nikon Eclipse 800 microscope,  $\times 63$  apo-plan objective and a CCD camera with a 5

megapixel, 9  $\times$  9 micron chip. Bias, dark and flat-field frames were taken for image processing. Only cells with  $\geq$  five 53BP1 or  $\gamma$ -H2AX signals co-localized with telomere signals were scored.

**Telomere FISH and CO-FISH.** Cells were collected at indicated time points and fixed; FISH and CO-FISH were performed as described previously<sup>4,17</sup>. Hybridization of metaphase spreads was performed with Tam-OO-(CCCTAA)<sub>4</sub> peptide nucleic-acid probes (Applied Biosystems). For CO-FISH, metaphase spreads were incubated sequentially with 5'- Tam-OO-(CCCTAA)<sub>4</sub>-3' and 5'-FITC-OO-(TTAGGG)<sub>4</sub>-3' probes. Control experiments were performed to ensure that the CO-FISH signals were dependent on the incorporation of BrdU, and that the procedure did not generate signals owing to unintended denaturation of the telomeric DNA. A minimum of 500 chromosome ends were scored blindly for each genotype, and pairwise comparisons for statistical significance were made by Student's *t*-test. Differences between genetic backgrounds were considered significant only when *P* values were less than 0.01. Digital Images were captured as described earlier and processed with MetaMorph Premier (Molecular Devices).

**In-gel telomeric G-overhang assay.** In-gel G-overhang assays were performed essentially as described<sup>17</sup>. After pulse-field gel electrophoresis, gels were dried down at 40 °C and prehybridized at 50 °C for 1 h in Church mix (0.5 M Na<sub>2</sub>HPO<sub>4</sub>, pH 7.2, 1 mM EDTA, 7% SDS and 1% BSA), followed by hybridization at 50 °C overnight with an end-labelled (CCCTAA)<sub>4</sub> oligonucleotide. After hybridization, gels were washed three times with 4 $\times$  SSC for 30 min and once with 4 $\times$  SSC, 0.1% SDS. Gels were exposed to PhosphorImager screens. After G-overhang assays, gels were alkali denatured (0.5 M NaOH and 1.5 M NaCl), neutralized (3 M NaCl and 0.5 M Tris-HCl, pH 7.0), rinsed with H<sub>2</sub>O, and reprobed with labelled (TTAGGG)<sub>4</sub> oligonucleotide at 55 °C and then processed as previously. To determine the relative overhang signal, the signal intensity for each lane was determined before and after denaturation using Imagequant software. The G-overhang signal was normalized to the total telomeric DNA and this normalized value was compared between samples.

# Canadian changes in the air

British Columbia aims to become a leader in clean-energy technology. **Virginia Gewin** tracks progress.

**T**he Canadian province of British Columbia has a simple strategy for becoming a hub of clean technology — be bold. Under its premier Gordon Campbell, the province has established aggressive clean-energy initiatives, including North America's first carbon tax (see <http://tiny.cc/HkvYn>) to meet its goal of reducing greenhouse-gas emissions to 33% below 2007 levels by 2020. Carbon-based fuels will be taxed at a rate of Can\$10/tonne (US\$9.28) of carbon emissions now and at Can\$30 per tonne by 2012. Campbell's government has also made reducing carbon emissions part of a wider plan to stimulate job growth in the region, where the traditional natural-resources industries of forestry and fisheries are struggling. From biofuels to wave energy, the province's government and the Canadian federal government have made sizeable investments in the research, development and commercialization of clean-energy alternatives to fossil fuels.

The plan seems to be paying off. Early-stage companies are getting the funding they need to hire additional staff, and energy-related training opportunities abound. The big challenge, however, will be bringing these technologies to fruition. In the face of an uncertain market and the significant up-front costs of commercializing a new energy technology, British Columbia's leaders have encouraged investment in clean energy. "The real prize is becoming a 'go-to' place to sell technologies to the rest of the world," says Andrew Walls, director of the British Columbia Innovation Council's ocean sciences and energy programme.

To complement the federally funded Can\$1-billion Sustainable Development Technology Canada (SDTC) fund, devoted to developing clean energy, most notably biofuels, British Columbia has created its own clean-tech funds. The Can\$25-million annual Innovative Clean Energy Fund (ICE) and the Can\$25-million British Columbia Bioenergy Network (BCBN) emphasize help to companies that are developing biofuels. In 2008, the provincial government released a bioenergy strategy to help guide its energy plan. "This is one of the few sectors that has legs, and people actively developing technologies," says Michael Weedon, executive director of the BCBN.

Lignol, an emerging biofuel company based in Burnaby, has received funding from the ICE, the SDTC and the BCBN to support its efforts to produce ethanol from



J. F. RAGA/CORBIS

Sited in the southwestern corner of British Columbia, Vancouver is one of the region's skills centres.

woody materials. It wants to recruit scientists, primarily those with biology and chemistry backgrounds, to explore and develop new technologies. Lignol's chief operating officer Michael Rushton says the company looks for people with skills in chemical processing or enzyme chemistry as it continues to

improve the efficiency of the conversion of lignocellulose into ethanol.

Despite the emphasis on biofuels, there are also job opportunities in the areas of wave energy and carbon sequestration. In

March, SyncWave, a company in Pemberton, received Can\$2.7 million from the SDTC to field test its technology, which taps the energy of ocean swells. Chief executive Nigel Protter says he needs scientists and engineers who understand hydrodynamics and fluid dynamics. British Columbia will also be the site of one of eight Canada-wide projects that will share Can\$140 million in government funds to conduct carbon-capture and storage demonstrations. Spectra Energy, based in Houston, Texas, which specializes in natural-gas infrastructure, will oversee the carbon-capture project in British Columbia from its offices in Vancouver and Calgary, Alberta. Tony Irwin, the company's director of climate change and energy efficiency, says he is looking for people who can combine multiple skills, including chemistry, hydrogeology, policy and engineering.

Both the public and the private sectors are taking steps to ensure that British Columbia's human scientific resources match the clean-tech initiative. The provincial government has established the Leading Edge Endowment Fund, a Can\$56.25-million joint government-private sector initiative to create 29 permanent endowed chairs at British Columbia universities and colleges in areas including health, technology and the environment. The hope is that 20 permanent leadership research chairs will attract top talent and that nine 'regional innovation chairs' will spur technology transfer at smaller colleges and technical institutes.

## Training grounds

The Natural Sciences and Engineering Research Council of Canada's Collaborative Research and Training Experience (CREATE) programme aims to fill interdisciplinary gaps. For example, the CREATE program in interdisciplinary climate science will partner with the Canadian Centre for Climate Modelling and Analysis at the University of Victoria with the Institute of Ocean Sciences on Vancouver Island, run by Fisheries and Oceans Canada. The programme will carry out research in areas crucial to industry and government, such as developing new ways of predicting the evolution of terrestrial and oceanic ecosystems, and climate diagnostics research to uncover signatures of climatic variation. Other CREATE programmes

**"Bioenergy is one of the few sectors that has legs."**

— Michael Weedon

will target British Columbia's health and life-sciences industries, and those devoted to the environment and energy include bioenergy, biorefining and biodiversity. Each programme receives Can\$1.65 million to split among stipends for undergraduate, graduate and postdoctoral students.

Meanwhile, a new climate-science initiative should mean several million dollars in funding for graduate students, postdocs and visiting scientists. In March 2008, the Pacific Institute for Climate Solutions (PICS) was established with a Can\$90-million endowment. PICS, a partnership between the University of British Columbia in Vancouver, the University of Victoria, Simon Fraser University in Burnaby and the University of Northern British Columbia in Prince George, will spend around Can\$1 million of its operating budget on training. Projects are still being planned but scientists will be needed to address how ecosystems and humans can adapt to climate change, says Nancy Olewiler,



**British Columbia premier Gordon Campbell (top), and innovation council head Andrew Walls see clean energy as the future.**



director of the public-policy programme at Simon Fraser University and a member of the PICS programme committee. She expects teams from each university to participate in interdisciplinary projects such as developing solutions to water shortage, tracking climate-induced emerging health issues and exploring how timber can meet bioenergy needs (see 'Bioenergy investment benefits cash-strapped life-sciences sector').

Formal partnerships with two recently established oceanography initiatives should extend PICS's interdisciplinary reach. The newly established Can\$100-million North-East Pacific Time-Integrated Undersea Networked Experiments (Neptune Canada) and the Can\$25-million Victoria Experimental Network Under the Sea (Venus) project, a deep-sea and coastal ocean observatory, will provide climate-science opportunities for oceanography graduate students and postdocs.

They will have the task of sifting through an unprecedented variety and amount of data, which can be used, for example, to visualize the sea floor and monitor conditions such as oxygen depletion and ocean acidification, says Verena Tunnicliffe, professor of deep-sea research at the University of Victoria and Venus's project director. Tunnicliffe's team is exploring ways to help oceanographers handle the huge amount of data generated by the Neptune and Venus programmes. She says the training possibilities for young scientists in British Columbia are endless.

Connecting graduate research to burgeoning industries in British Columbia is the goal of the Accelerate programme, run by the mathematical and science research network MITACS, in Vancouver, which fosters graduate internships with potential employers in high-tech industry, government and non-profit organizations. The aim is to give companies, and in particular those in the clean-tech sector, access to cutting-edge university research, while students get a first-hand experience of what industry needs. "British Columbia is moving away from its history as a resource extractor," says Tunnicliffe, "to a region using technology to find exciting ways to use and develop these resources sustainably."

**Virginia Gewin is a freelance writer based in Portland, Oregon.**

## BIOENERGY INVESTMENT BENEFITS CASH-STRAPPED LIFE-SCIENCES SECTOR

The economic downturn is hitting Canadian life-science companies hard. On 15 July, BIOTEC Canada, Canada's biotechnology industry organization, released survey data suggesting that, including jobs already lost, 7,000 highly skilled researchers and scientists could be laid off throughout the country in the next year if short-term financing from private or government sources cannot be obtained to keep struggling companies afloat.

Although British Columbia has a relatively mature biopharmaceutical sector that is better placed to weather the storm, the recession has had an impact, says Bob Ingratta, bioproducts and bioenergy sector specialist at the non-profit industry-support organization LifeSciences British Columbia, based in Vancouver.

The Canadian government's investment in bioenergy and clean technology could offer a welcome respite, and create opportunities for those with genomics or bioinformatics skills. For example, Jörg Bohlmann, a forest biologist at the University of British Columbia in Vancouver, has a grant of

Can\$7.5 million (US\$7 million) from Genome British Columbia, one of six centres that vie for funds from the central organization Genome Canada.

Bohlmann is hunting for genomic clues to the outbreaks of mountain pine beetle that threaten Canada's forests (pictured), and is exploring how the biofuels sector might use infested wood as biomass. He wants to train people in genomics, bioinformatics and ecological risk modelling. "If we can't truly stop forest impact of the pine mountain beetle, we may be able to better utilize forest resources that are infected," he says.

Pierre Meulien, Genome British Columbia's chief scientific officer, says that although Genome Canada did not receive any new funding in this year's budget, it is funded up to the end of 2013. Genome British Columbia also receives money from the provincial government specifically for research on local priorities such as bioenergy. For example, researchers funded by Genome British Columbia at the University of British Columbia in Vancouver and the University of Victoria are investigating how



to maximize the fermentation of lignocellulose to bioethanol, using poplars.

The Canada Foundation for Innovation has provided Can\$71 million in funding for 16 major infrastructure projects in British Columbia, with particular emphasis on ocean research and the life sciences. The focus is on maintaining cutting-edge research platforms in life sciences, including a Can\$10 million ultra-high-throughput DNA sequencing platform for large-scale genome analysis at the University of British

Columbia. Such investments are considered key to maintaining British Columbia's success.

Christoph Borchers, director of the University of Victoria-Genome British Columbia Proteomics Centre, sees ample promise in the province's diverse portfolio of genomics research despite funding woes. "Genome British Columbia has a lot of funding from the provincial government, which wants to see the community broadly apply 'omics to all areas that affect human health from trees to fisheries," he says.

**V.G.**



# Bombs away!

Happy landings.

**Paul Di Filippo**

Having left the McConnell Air Force Base in Kansas just a few hours earlier, the squadron of long-range B-5 'Shelly O' Stealth bombers arrived over Igboland in south-eastern Nigeria at 3:13 a.m., local time. The air defences of the reclusive and hostile dictatorship (a failed state since the collapse of the global petroleum industry after the advent of microbe-generated electricity from trash) could not detect the invaders.

The payloads unleashed by the bombers, however, were a different matter.

Each package measured some 4 cubic metres, big as a freestanding urban street toilet, swaddled in protective foam and with a chute on top.

Soon, mushroom-like synthetic blooms dotted the night sky all over Igboland.

Nigerian troops scrambled to meet their descent.

Each package, as it touched down in countryside, town or city, automatically jettisoned its self-destructing foam coating and parachute, removing evidence of the landing.

Revealed was what, indeed, appeared to be an urban street-toilet: a shed-sized, streamlined plastic structure, windowless, with a curving door panel.

In 90% of the landings, soldiers arrived on the scene first, surrounding the structures menacingly, weapons raised, until military trucks arrived to haul the invaders away.

Occasionally, average citizens reached the bombs first. The finders generally cooperated. They sought to shift the structures out of sight of the authorities. But sometimes fights erupted, or pirate bands intervened. For the most part, unless the citizens moved very fast, the soldiers soon showed up and took the prizes away, brutally and with bloodshed.

But in a very small number of instances, the bombs passed safely and secretly into the hands of non-state individuals.

A young, orphaned bachelor, Okoronkwo Mmadufo grew pearl millet and raised goats on the edge of an abandoned and decaying Chinese coltan-processing plant; land no one else coveted as it was seeded with toxic waste. His farm struggled to provide even one person with a subsistence living. The soil made his crops sick and the vegetation did the same to his animals. Okoronkwo despaired of ever being rich enough to afford a wife and family.

The night of the bombing run the farmer was awake, tending a sick goat. He looked up when he heard a muffled but sizable thump, and saw the bomb settle atop a patch of scrawny millet plants. He left the goat and rushed to the structure.

He began to push futilely at the big bomb, which was nearly as large as his house. But then he saw a large red unlabelled button near the door panel, and he slapped it.

The bomb lifted itself up on a set of wheels and an air-cushion effect.

Okoronkwo ran with the bomb towards the deserted, ruined factory. A small outbuilding looked impenetrably collapsed upon itself. But Okoronkwo knew the secret of its access.

He moved some timbers and hauled aside a wall of galvanized tin and got the bomb hidden. After grabbing a branch, he erased any slight tracks leading back to the landing site.

The soldiers found him cradling his sick goat.

After interrogation and discussion, the soldiers decided not to investigate the abandoned plant, as they had heard that the effect of the toxic waste would be to cause their penises to disappear. They had much sport speculating on Okoronkwo's genital shrinkage, then left.

Okoronkwo waited until the next night to investigate the bomb in the outbuilding.

When the curving plastic portal opened, light flooded the interior of the bomb. Okoronkwo quickly stepped inside and shut the door.

The interior of the structure was much smaller than he expected, indicating concealed machinery or reservoirs. The only visible features were an intake hopper, a dispensing chute and a docked cellphone.

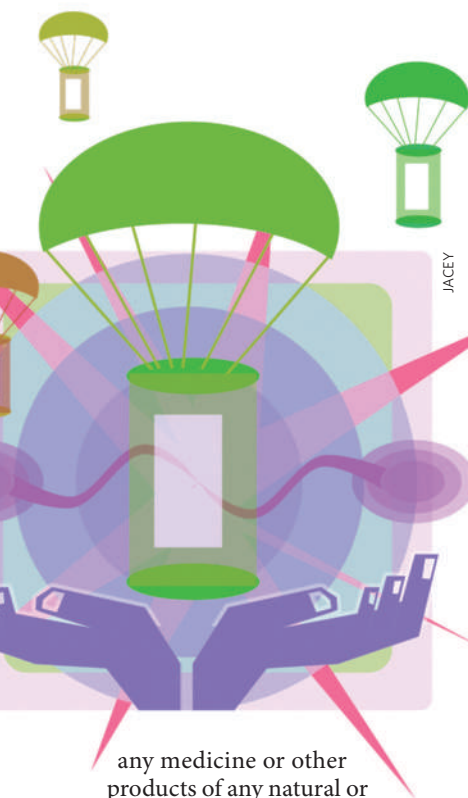
Okoronkwo picked up the phone and it came alive.

Speckled with animated glyphs, the face of a young white guy appeared.

"Sticky here. What's your name?"

"Okoronkwo Mmadufo."

"Gonna call you OM. Here's the tranche. You're now the proud owner of a Biofab Field Unit. A BFU. It comes supplied with feedstocks — just common stuff you'll be able to replace — and smart microbes that will handle their own reproduction, as well as diagnostic, engineering and interface instrumentation. PCR, nucleotide decouplers and linkers, sequencers — the works. You can use the BFU to make nearly



any medicine or other products of any natural or synthetic organic processes. The unit will tailor doses of active agents, as well, for dispersal into the environment. You run everything via the cellphone. You'll see the control panel now on the touchscreen, with a link to an interactive tutorial. Click on the terms of agreement, please, OM — Swell! Goodbye."

"Wait! I have many questions!"

"Sorry, the feds aren't paying me to answer questions. Strictly freelance. So, I'm gone. Unless — can you get me any rare highlife recordings?"

"You like live shows of Dr Sir Warrior?"

"Hell yeah!"

"I can get those."

"Bring me tracks I don't have, and I'm yours to command."

Over the next week, Okoronkwo and his new friend used the BFU to tailor a remediation treatment for the soil, a cure for pearl millet top rot, and nutraceuticals for the goats.

Okoronkwo came to feel confident in his prowess with the BFU, and eventually bade Sticky goodbye. He knew now that he could continue to help himself and his neighbours, and that his personal future would include a woman and children.

But first he had to tailor a certain lethal smart bug, keyed only to the genomes of Nigeria's rulers. These men were lax with their condom use, and obtaining their seed would be no chore at all.

**Having celebrated his thirtieth year as a professional writer, Paul Di Filippo believes he still detects potential for self-improvement.**

**Join the discussion of Futures in Nature at <http://tinyurl.com/kkh3kt>**